Forschungszentrum Karlsruhe
in der Helmholtz-Gemeinschaft

Wissenschaftliche Berichte

FZKA 7516

Contributions to the 31st International Cosmic Ray Conference, Łódź, Poland, 2009

J. Blümer, R. Engel, A. Haungs

Institut für Kernphysik
Institut für Prozessdatenverarbeitung und Elektronik

Universität Karlsruhe
Institut für Experimentelle Kernphysik

Oktober 2009

Forschungszentrum Karlsruhe

in der Helmholtz-Gemeinschaft

Wissenschaftliche Berichte

FZKA 7516

Contributions to the 31st International Cosmic Ray Conference, Łódź, Poland, 2009

by

Forschungszentrum Karlsruhe

Institut für Kernphysik,

Institut für Prozessdatenverarbeitung und Elektronik

and

Universität Karlsruhe

Institut für Experimentelle Kernphysik

Johannes Blümer, Ralph Engel, Andreas Haungs (Editors)

Institut für Kernphysik

Forschungszentrum Karlsruhe GmbH, Karlsruhe

2009

Forschungszentrum Karlsruhe GmbH
Postfach 3640, 76021 Karlsruhe

Mitglied der Hermann von Helmholtz-Gemeinschaft
Deutscher Forschungszentren (HGF)

ISSN 0947-8620

urn:nbn:de:0005-075161

ABSTRACT

The bi-annual International Cosmic Ray Conferences have become the most central meetings for discussing new results and recent progress in the field of cosmic ray research. The contributions to these conferences cover a wide range of subjects extending from the physics of the sun and heliosphere, over gamma-ray observations to direct and indirect cosmic ray measurements and their interpretation. Many new results are announced at these meetings for the first time.

The present volume is a compilation of the contributions of Institutes of the KIT to the 31st International Cosmic Ray Conference (ICRC), held in Łódź, Poland from July 7 to 15, 2009. KIT, the Karlsruhe Institute of Technology, is the merger of Forschungszentrum Karlsruhe and University Karlsruhe. The collection of contributions provides an up-to-date review of the current activities and research projects related to cosmic rays that are pursued in Karlsruhe. The articles also demonstrate the enormous progress that has been made during the last years, in particular in the field of ultra-high energy cosmic rays. Most of these contributions are the result of close and fruitful collaboration of many different groups worldwide, first of all within international collaborations such as the Pierre Auger, KASCADE-Grande and LOPES Collaborations, but also within smaller groups.

The articles compiled in this report are sorted according to the main research foci of the Karlsruhe groups. These include the physics of the knee in the cosmic ray spectrum, the transition between galactic and extra-galactic cosmic rays, and extragalactic cosmic rays of the highest energies.

Cosmic rays in the energy range from just below the knee in the cosmic ray spectrum ($10^{14.5}$ eV) to the energy of the conjectured transition between galactic and extra-galactic cosmic rays are studied with the **KASCADE-Grande** detector at the site of Forschungszentrum Karlsruhe. KASCADE-Grande is a multi-detector air shower array, which combines the electron and muon detectors of the KASCADE (KArlsruhe Shower Core and Array Detector) array with a 0.5 km^2 array of scintillators. At this conference the collaboration presented the all-particle cosmic ray energy spectrum in the range of 10^{16}-10^{18} eV. The quality of the experimental set-up is expressed in the fact that the spectrum could be reconstructed consistently by four different methods, allowing a high confidence on the presented results. The results were of such importance that they could be presented in an invited highlight talk at the conference.

An alternative method of air shower detection is the measurement of radio signals produced by the particles showers in the atmosphere. The physics potential of this detection technique is investigated with the **LOPES** (LOFAR PrototypE Station) array of dipole antennas at the site of the KASCADE-Grande installation. The full amplitude and time calibration of the antennas allow measuring the field strength per single antenna and therefore the lateral distribution for individual events, as well as the polarization of the emitted signal could be studied. The investigation of the influence of thunderstorms on the measured field strength, progress in developing self-triggering and optimized antenna systems for future large-scale applications were also presented as well as simulation studies on the intrinsic capability of this new detection technique.

The event-by-event study of cosmic rays at the highest energies is the aim of the **Pierre Auger Project**. The Pierre Auger Observatory is the largest cosmic ray detector with one installation in the northern and southern hemisphere to ensure full sky coverage. The southern detector in the Province of Mendoza, Argentina is now completed. It consists as baseline set-up of 24 fluorescence telescopes and a surface detector array of 1600 water Cherenkov tanks, covering an area of 3000 km^2. Several enhancements (**HEAT**, AMIGA, AERA) to measure in more detail showers of lower energy, i.e. the transition between galactic and ex-

tra-galactic cosmic rays, are under construction. In particular HEAT, the 'high elevation Auger telescopes', will be able to measure the energy spectrum and composition down to $10^{17.25}$ eV, and will have a good overlap with KASCADE-Grande. A site near Lamar in Colorado, USA has been selected for the northern observatory and preparatory R&D work has begun.

The analysis of data taken with the southern observatory has since the last conference led to first results on the elemental composition, where an unexpected high contribution of heavy nuclei has been found. A significant discrepancy between the characteristics of simulated and measured air showers at ultra-high energy has been found. Together with the updates presented on the energy spectrum and on anisotropy studies, still the physics of the highest energy cosmic rays remains an unsolved puzzle. Due to the indirect character of cosmic ray measurements with air showers, all analyses discussed above depend on the detailed simulation of cosmic ray interactions and extensive air showers. Recent progress in this field is summarized in the contributions related to the **CORSIKA** (Cosmic Ray Simulations for KASCADE and Auger) and CONEX simulation packages, the measurement of the characteristics of hadronic interactions, and air shower simulation studies.

In addition, contributions to the conference in Poland include measurements with the CERN fix target experiment **NA61/SHINE** in order to improve the reliability of air-shower simulations and solar event observations with smaller muon detection devices.

Beiträge zur *31st International Cosmic Ray Conference (ICRC), Łódź, Polen, 2009* des Karlsruher Instituts für Technogie – KIT, Institut für Kernphysik und Institut für Prozessdatenverarbeitung und Elektronik des Forschungszentrums Karlsruhe, und dem Institut für experimentelle Kernphysik der Universität Karlsruhe

Zusammenfassung

Die zweijährlich stattfindende internationale Konferenz zur kosmischen Strahlung (ICRC) ist die in diesem Forschungsbereich weltweit wichtigste Tagung um Resultate und neueste Entwicklungen vorzustellen und zu diskutieren. Beiträge zu diesen Konferenzen umfassen einen weiten wissenschaftlichen Bereich mit experimentellen Ergebnissen aus der Sonnen- und Heliosphären-Physik, über die Quellenbeobachtung mit hochenergetischen Gamma-Strahlen bis zu direkter und indirekter Messung kosmischer Teilchen, sowie die Interpretation all dieser Beobachtungen. Viele neue Resultate werden bei dieser Konferenzreihe erstmalig der Öffentlichkeit vorgestellt.

Die in diesem Band zusammengestellten Beiträge sind von den herausgebenden Instituten des KIT, dem Karlsruher Institut für Technologie, dem Zusammenschluss von Forschungszentrum und Universität Karlsruhe, in enger und fruchtbarer Zusammenarbeit mit weiteren nationalen und internationalen Universitäten und Instituten entstanden und auf der diesjährigen ICRC in Łódź, Polen vom 7. bis 15. Juli 2009 vorgestellt worden. Die Zusammenarbeit betrifft insbesondere Studien und Datenanalysen innerhalb der großen internationalen Kollaborationen wie der Pierre-Auger-, der KASCADE-Grande-, und der LOPES-Kollaboration, aber auch Arbeiten innerhalb kleinerer Gruppen.

Die Beiträge in diesem Band sind geordnet gemäß den Forschungsschwerpunkten der Karlsruher Gruppen. Dies betrifft die kosmische Strahlung im Energiebereich des so genannten Knies, dem Bereich des Übergangs von galaktischer zu extragalaktischer kosmischer Strahlung und der Messung extragalaktischer Teilchen höchster Energien. Die Sammlung stellt damit einen Überblick über alle die kosmische Strahlung betreffenden, aktuellen Karlsruher Aktivitäten und Projekte dar. Die Beiträge belegen auch den enormen Fortschritt in diesem Forschungsgebiet der letzten Jahre, insbesondere bei der Messung und Analyse der hochenergetischen kosmischen Strahlung.

Luftschauer von kosmischen Teilchen mit einer Energie gerade unterhalb des Knies im Spektrum ($10^{14.5}$ eV) bis in etwa zu einem Energiebereich, bei dem der Übergang von galaktischem zu extragalaktischem Teilchenursprung vermutet wird, werden mit dem **KASCADE-Grande** Experiment gemessen, das sich auf dem Gelände des Forschungszentrums Karlsruhe befindet. KASCADE-Grande ist ein Multi-Detektor Aufbau, der die Detektoren des ursprünglichen KASCADE Experimentes mit einem neuen Detektorfeld verbindet, das aus 37 Stationen besteht, verteilt auf einer Fläche von 0.5 km^2. Bei der diesjährigen ICRC konnte die Kollaboration das Spektrum im Energiebereich von 10^{16}-10^{18} eV präsentieren. Die Qualität der experimentellen Messungen drückt sich dadurch aus, dass das Spektrum mit konsistentem Ergebnis mittels vier verschiedener Methoden rekonstruiert werden konnte, was ein hohes Vertrauen in die Resultate erlaubt. Die erzielten Ergebnisse waren von solcher Bedeutung, dass sie in einer eingeladenen Highlight-Rede bei der Konferenz diskutiert wurden.

Als alternative Messmethode hochenergetischer Teilchen wird die Messung der Radioemission während der Luftschauerentwicklung in der Atmosphäre betrachtet. Das physikalische Potential dieser neuen Messtechnik wird mit Hilfe der **LOPES** (LOFAR PrototypE Station) Dipolantennen untersucht. LOPES ist aufgebaut innerhalb des KASCADE-Grande Experimentes und misst in Koinzidenz mit den Teilchendetektoren. Die vollständige Amplituden-

und Zeitkalibrierung der Antennen erlaubt die Bestimmung der Feldstärke pro Antenne und damit die Rekonstruktion der Lateralverteilung des Radiosignals, sowie die Bestimmung der Polarisation des emittierten Signals Basis einzelner Luftschauer-Ereignisse. Die Untersuchung des Einflusses von Gewittern auf die gemessene Feldstärke, Fortschritte in der Entwicklung eines Radio-Selbsttriggers sowie neuartige, für zukünftige groß-skalige Anwendungen optimierte Antennensysteme wurden auf der Tagung ebenso vorgestellt, wie auch Simulationsstudien zum intrinsischen Potential dieser neuen Detektionstechnik.

Das Studium der höchstenergetischsten kosmischen Teilchen ist das Ziel des Pierre Auger Projektes. Das **Pierre Auger Observatorium** ist der weltweit größte Detektor für kosmische Strahlung mit je einer Installation auf der Nord- und der Südhalbkugel der Erde. Der südliche Observatorium in der Provinz Mendoza in Argentinien ist inzwischen fertig gestellt. Es besteht aus 24 Fluoreszenz-Teleskopen und einem Feld von 1600 Wasser-Tscherenkow Detektoren mit einer Flächenabdeckung von 3000 km^2. Im Aufbau befinden sich einige Erweiterungen des Süd-Experimentes (**HEAT**, AMIGA, AERA), die es ermöglichen werden, niederige Energien zu messen, d.h. den Übergang von galaktischer zu extragalaktischer kosmischer Strahlung genauer zu untersuchen. Insbesondere wird HEAT (High Elevation Auger Telescopes) in der Lage sein, das Spektrum und die Elementzusammensetzung bis hinunter zu einer Energie von 10^{17}eV zu messen und hat damit auch einen guten Überlapp mit KASCADE-Grande. Ein Gebiet bei der Kleinstadt Lamar in Colorado, USA wurde als Areal für das Nord-Observatorium ausgesucht, und vorbereitende Entwicklungsarbeiten vor Ort begonnen, welche auf der Konferenz präsentiert wurden.

Die Analyse der mit dem südlichen Observatorium aufgenommenen Daten konzentrierte sich seit der letzten Konferenz auf die Rekonstruktion der Elementzusammensetzung, wobei ein unerwartet hoher Beitrag von schweren Kernen gefunden wurde. Zusammen mit den aktualisierten Ergebnissen des Energiespektrums und der Analyse von Anisotropien ergeben sich unerwartete neue Fragestellungen, insbesondere auch weil eine signifikante Diskrepanz in der Charakteristik von simulierten zu gemessenen Luftschauern bei den allerhöchsten Energien herrscht. Auf der Konferenz wurde dieses Rätsel ausführlich diskutiert. Da die Interpretation aller Messungen hochenergetischer kosmischer Teilchen nur indirekt über den Nachweis von Luftschauer durchgeführt werden können, basiert sie auf detaillierten Simulationen der Luftschauerentwicklung und hier insbesondere der hadronischen Wechselwirkungen. Fortschritte auf diesem Gebiet wurden präsentiert in Beiträgen im Zusammenhang mit der Weiterentwicklung und Verbesserung der **CORSIKA** (Cosmic Ray Simulations for KASCADE and Auger) und CONEX Simulations-Programme, einer besseren Beschreibung hadronischer Wechselwirkungen auch durch Beteiligung an Beschleunigerexperimenten, und allgemeinen Studien zur Luftschauerentwicklung.

Weiter Beiträge zur Konferenz in Polen umfassten Messungen mit dem CERN-Fix-Target-Experiment **NA61/SHINE** zur Verbesserung der Luftschauersimulationen, sowie die Beobachtung von solaren Ereignissen mit kleineren experimentellen Aufbauten zur Myonbeobachtung.

CONTENTS

KASCADE-Grande

Results on the cosmic ray energy spectrum measured with KASCADE-Grande 1
A. Haungs et al., KASCADE-Grande Collaboration

Cosmic ray energy spectrum based on shower size measurements of KASCADE-Grande 5
D. Kang et al., KASCADE-Grande Collaboration

The Energy Spectrum of Primary Cosmic Rays Reconstructed with the KASCADE-Grande Muon Data 9
J.C. Arteaga-Velázquez et al., KASCADE-Grande Collaboration

The all particle energy spectrum of KASCADE-Grande in the energy region 10^{16} - 10^{18} eV by means of the N_{ch} - N_{μ} technique 13
M. Bertaina et al., KASCADE-Grande Collaboration

Primary energy reconstruction from the S(500) observable recorded with the KASCADE-Grande detector array 17
G. Toma et al., KASCADE-Grande Collaboration

Performance of the KASCADE-Grande array 21
F. Di Pierro et al., KASCADE-Grande Collaboration

Muonic Component of Air Showers Measured by the KASCADE-Grande Experiment 25
D. Fuhrmann et al., KASCADE-Grande Collaboration

The sensitivity of KASCADE-Grande to the cosmic ray primary composition between 10^{16} and 10^{18} eV 29
E. Cantoni et al., KASCADE-Grande Collaboration

A direct measurement of the muon component of air showers by the KASCADE-Grande Experiment 33
V. de Souza et al., KASCADE-Grande Collaboration

Study of EAS development with the Muon Tracking Detector in KASCADE-Grande 37
J. Zabierowski et al., KASCADE-Grande Collaboration

Lateral distribution of EAS muons measured with the KASCADE-Grande Muon Tracking Detector 41
P. Łuczak et al., KASCADE-Grande Collaboration

Muon Production Height and Longitudinal Shower Development 45
P. Doll et al., KASCADE-Grande Collaboration

Restoring Azimuthal Symmetry of Lateral Density Distributions of EAS Particles 49
O. Sima et al., KASCADE-Grande Collaboration

Quantitative tests of hadronic interaction models with KASCADE-Grande air shower data 53
J.R. Hörandel et al., KASCADE-Grande Collaboration

LOPES and radio signal simulation studies

Lateral Distribution of the Radio Signal in Extensive Air Showers Measured with LOPES 57
S. Nehls, F. Schröder et al., LOPES Collaboration

Polarization studies of the EAS radio emission with the LOPES experiment 61
P.G. Isar et al., LOPES Collaboration

Time Calibration of the Radio Air Shower Array LOPES 65
F. Schröder et al., LOPES Collaboration

Radio Emission of Extensive Air Showers during Thunderstorms 69
M. Ender et al., LOPES Collaboration

Self-Trigger for Radio Detection of UHCR 73
A. Schmidt et al., LOPES Collaboration

New Antenna for Radio Detection of UHECR 77
O. Krömer et al., LOPES Collaboration

Universal behavior of electrons & positrons in extensive air showers 81
S. Lafebre, R. Engel, H. Falcke, J. Hörandel, T. Huege, J. Kuijpers and R. Ulrich

Effects of atmospheric electric fields on the evolution and radio emission of extensive air showers 85
S. Buitink, T. Huege, H. Falcke, D. Heck and J. Kuijpers

Prospects for using geosynchrotron emission arrival times to determine air shower characteristics 89
S. Lafebre, H. Falcke, J. Hörandel, T. Huege and J. Kuijpers

Pierre-Auger-Project

Measurement of the cosmic ray energy spectrum above 10^{18} eV using the Pierre Auger Observatory 93
F. Schüssler for the Pierre Auger Collaboration

Extension of the Pierre Auger Observatory using high-elevation fluorescence telescopes (HEAT) 97
M. Kleifges for the Pierre Auger Collaboration

Energy scale derived from Fluorescence Telescopes using Cherenkov Light and Shower Universality 101
S. Müller for the Pierre Auger Collaboration

The electromagnetic component of inclined air showers at the Pierre Auger Observatory 105
I. Valino for the Pierre Auger Collaboration

Rapid atmospheric monitoring after the detection of high-energy showers at the Pierre Auger Observatory 109
B. Keilhauer for the Pierre Auger Collaboration

UHE neutrino signatures in the surface detector of the Pierre Auger Observatory 113
D. Gora for the Pierre Auger Collaboration

Sensitivity of Extensive Air Showers to Features of Hadronic Interactions at Ultra-High Energies 117
R. Ulrich, R. Engel, S. Müller, T. Pierog, F. Schüssler and M. Unger

Fluorescence emission induced by extensive air showers in dependence on atmospheric conditions 121
B. Keilhauer and M. Unger

A MC simulation of showers induced by microscopic black holes 125
D. Gora, M. Haag and M. Roth

3D Air Shower Simulations Using CONEX in CORSIKA 129
T. Pierog, R. Engel and D. Heck

How to Relate Particle Physics and Air Shower Development: the EPOS Model 133
T. Pierog and K. Werner

Pierre-Auger-Project: Abstracts of all contributions 137

Further articles

Hadron Production Measurements with the NA61/SHINE Experiment and their Relevance for Air Shower Simulations 149
I.C. Maris for the NA61/SHINE Collaboration

Correlations between solar events and the cosmic muon flux measured with WILLI detector 153
I.M. Brancus, A. Saftoiu, B. Mitrica, M. Petcu, O. Sima, A. Haungs, G. Toma, M. Duma and A. Bercuci

Studies of hadronic interaction models by measuring the flux and the charge ratio of atmospheric muons with the WILLI detector 157
B. Mitrica, I.M. Brancus, A. Saftoiu, H. Rebel, O. Sima, A. Haungs, G. Toma, M. Petcu and M. Duma

Observation of Forbush Degreases and Solar Events in the 10-20 GeV Energy Range with the Karlsruhe Muon Telescope 161
I. Braun, J. Engler, J.R. Hörandel and J. Milke

Collaboration lists 165

Results on the cosmic ray energy spectrum measured with KASCADE-Grande

A. Haungs[*], W.D. Apel[*], J.C. Arteaga[†,xi], F. Badea[*], K. Bekk[*], M. Bertaina[‡], J. Blümer[*,†], H. Bozdog[*] I.M. Brancus[§], M. Brüggemann[¶], P. Buchholz[¶], E. Cantoni[‡,‖], A. Chiavassa[‡], F. Cossavella[†], K. Daumiller[*], V. de Souza[†,xii], F. Di Pierro[‡], P. Doll[*], R. Engel[*], J. Engler[*], M. Finger[*], D. Fuhrmann[**], P.L. Ghia[‖], H.J. Gils[*], R. Glasstetter[**], C. Grupen[¶], D. Heck[*], J.R. Hörandel[†,xiii], T. Huege[*], P.G. Isar[*], K.-H. Kampert[**], D. Kang[†], D. Kickelbick[¶], H.O. Klages[*], P. Łuczak[††], H.J. Mathes[*], H.J. Mayer[*], J. Milke[*], B. Mitrica[§], C. Morello[‖], G. Navarra[‡], S. Nehls[*], J. Oehlschläger[*], S. Ostapchenko[*,xiv], S. Over[¶], M. Petcu[§], T. Pierog[*], H. Rebel[*], M. Roth[*], H. Schieler[*], F. Schröder[*], O. Sima[‡‡], M. Stümpert[†], G. Toma[§], G.C. Trinchero[‖], H. Ulrich[*], A. Weindl[*], J. Wochele[*], M. Wommer[*], J. Zabierowski[††]

[*]*Institut für Kernphysik, Forschungszentrum Karlsruhe, 76021 Karlsruhe, Germany*
[†]*Institut für Experimentelle Kernphysik, Universität Karlsruhe, 76021 Karlsruhe, Germany*
[‡]*Dipartimento di Fisica Generale dell'Università, 10125 Torino, Italy*
[§]*National Institute of Physics and Nuclear Engineering, 7690 Bucharest, Romania*
[¶]*Fachbereich Physik, Universität Siegen, 57068 Siegen, Germany*
[‖]*Istituto di Fisica dello Spazio Interplanetario, INAF, 10133 Torino, Italy*
[**]*Fachbereich Physik, Universität Wuppertal, 42097 Wuppertal, Germany*
[††]*Soltan Institute for Nuclear Studies, 90950 Lodz, Poland*
[‡‡]*Department of Physics, University of Bucharest, 76900 Bucharest, Romania*
[xi]*now at: Universidad Michoacana, Morelia, Mexico*
[xii]*now at: Universidade de São Paulo, Instituto de Física de São Carlos, Brasil*
[xiii]*now at: Dept. of Astrophysics, Radboud University Nijmegen, The Netherlands*
[xiv]*now at: University of Trondheim, Norway*

***Abstract*. KASCADE-Grande is an extensive air shower experiment at Forschungszentrum Karlsruhe, Germany. The present contribution attempts to provide a synopsis of the actual results of the reconstruction of the all-particle energy spectrum in the range of 10^{16} eV to 10^{18} eV based on four different methods with partly different sources of systematic uncertainties. Since the calibration of the observables in terms of the primary energy depends on Monte-Carlo simulations, we compare the results of the various methods applied to the same sample of measured data.**

***Keywords*: High-energy cosmic rays, energy spectrum, KASCADE-Grande**

I. KASCADE-GRANDE

Main parts of the experiment are the Grande array spread over an area of $700 \times 700\,\mathrm{m}^2$, the original KASCADE array covering $200 \times 200\,\mathrm{m}^2$ with unshielded and shielded detectors, and additional muon tracking devices. This multi-detector system allows us to investigate the energy spectrum, composition, and anisotropies of cosmic rays in the energy range up to 1 EeV. The estimation of energy and mass of the primary particles is based on the combined investigation of the charged particle, the electron, and the muon components measured by the detector arrays of Grande and KASCADE.

The multi-detector experiment KASCADE [1] (located at 49.1°n, 8.4°e, 110 m a.s.l.) was extended to KASCADE-Grande in 2003 by installing a large array of 37 stations consisting of $10\,\mathrm{m}^2$ scintillation detectors each (fig. 1). KASCADE-Grande [2] provides an area of $0.5\,\mathrm{km}^2$ and operates jointly with the existing KASCADE detectors. The joint measurements with the KASCADE muon tracking devices are ensured by an additional cluster (Piccolo) close to the center of KASCADE-Grande for fast trigger purposes. While the Grande detectors are sensitive to charged particles, the KASCADE array detectors measure the electromagnetic component and the muonic component separately. The muon detectors enable to reconstruct the total number of muons on an event-by-event basis also for Grande triggered events.

II. RECONSTRUCTION

Basic shower observables like the core position, angle-of-incidence, and total number of charged particles are provided by the measurements of the Grande stations. A core position resolution of $\approx 5\,\mathrm{m}$, a direction resolution of $\approx 0.7°$, and a resolution of the total particle number in the showers of $\approx 15\%$ is reached [3]. The total number of muons (N_μ resolution $\approx 25\%$) is calculated using the core position determined by the Grande array and the muon densities measured by the KASCADE muon array detectors [4]. Full efficiency for triggering and reconstruction of air-showers is reached at primary energy of $\approx 2 \cdot 10^{16}$ eV, slightly varying on the cuts needed for the reconstruction of the different observables.

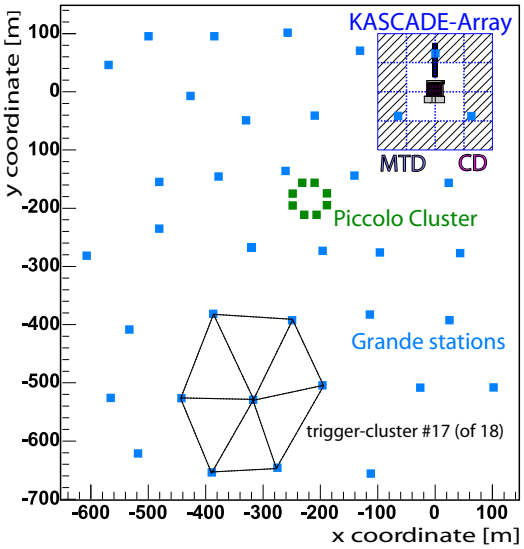

Fig. 1: Layout of the KASCADE-Grande experiment: The original KASCADE, the distribution of the 37 stations of the Grande array, and the small Piccolo cluster for fast trigger purposes are shown. The outer 12 clusters of the KASCADE array consist of μ- and e/γ-detectors, the inner 4 clusters of e/γ-detectors, only.

Applying different methods to the same data sample has advantages in various aspects: One would expect the same result for the energy spectrum by all methods when the measurements are accurate enough, when the reconstructions work without failures, and when the Monte-Carlo simulations describe correctly the shower development. But, the fact that the various observables have substantial differences in their composition sensitivity hampers a straightforward analysis. However, investigating results of different methods can be used to

- cross-check the measurements by different subdetectors;
- cross-check the reconstruction procedures;
- cross-check the influence of systematic uncertainties;
- test the sensitivity of the observables to the elemental composition;
- test the validity of hadronic interaction models underlying the simulations.

III. Analysis

The estimation of the all-particle energy spectrum is presently based on four different methods using different observables of KASCADE-Grande:

- N_{ch}-method: The reconstructed charge particle shower size per individual event is corrected for attenuation by the constant intensity cut method and calibrated by Monte-Carlo simulations under the assumption of a dependence $E_0 \propto N_{ch}^{\alpha_{ch}}$ and a particular primary composition [5].
- N_μ-method: The reconstructed muon shower size per individual event is corrected for attenuation and calibrated by Monte-Carlo simulations under the assumption of a dependence $E_0 \propto N_\mu^{\alpha_\mu}$ and a particular primary composition [6].
- $N_{ch}-N_\mu$-method: This method combines the information provided by the two observables. By help of Monte-Carlo simulations a formula is obtained to calculate the primary energy per individual shower on basis of N_{ch} and N_μ. The formula takes into account the mass sensitivity in order to minimize the composition dependence. The attenuation is corrected for by deriving the formula for different zenith angle intervals independently and combining the energy spectrum afterwards [7].
- $S(500)$-method: The reconstructed particle density at the specific distance to the shower axis of 500 m per individual event is corrected for attenuation and calibrated by Monte-Carlo simulations under the assumption of a dependence $E_0 \propto S(500)^{\alpha_{S(500)}}$.

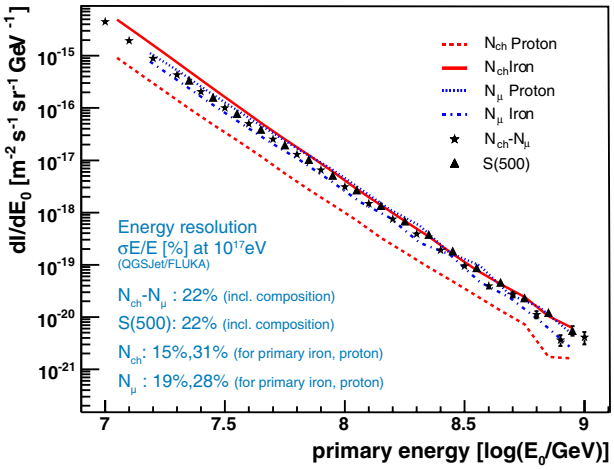

Fig. 2: Reconstructed all-particle energy spectrum by four different methods applied to KASCADE-Grande data. Given are also the energy resolution for the methods.

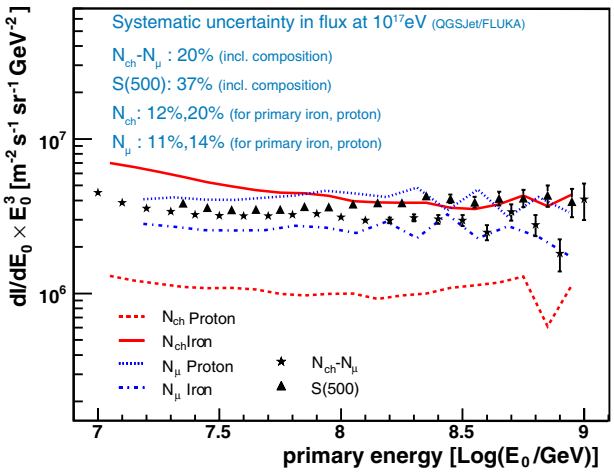

Fig. 3: Same as figure 2, but the flux multiplied by E_0^3. Values for the uncertainty in the flux determination are given for the different methods.

The distance of 500 m is chosen to have a minimum influence of the primary particle type, therefore a smaller dependence on primary composition is expected [8].

In figures 2 and 3 the resulting spectra are compiled. Due to the different procedures, the results for the first two methods are shown under proton and iron assumption, respectively, only, whereas for the other two methods the resulting all-particle energy spectrum is displayed. Figure 3 shows the same results but with the flux multiplied by a factor of $E^{3.0}$.

A. Systematic uncertainties and attenuation

The application of the different methods allows us to compare and cross-check the influence of various sources of systematic uncertainties. The N_{ch}-method uses the basic measurements of the Grande array only, resulting in a high accuracy of N_{ch} with better than 15% over the whole range of shower size, without any energy dependent bias. But, using only one observable, there is a large dependence on the primary elemental composition, reflected by the distance between the spectra obtained for proton and iron assumption at the calibration. The N_μ-method on the other hand is based on the muon shower size, which can be estimated less accurate (25% with a little bias dependent on the distance of the shower core to the muon detectors which is corrected for), but with a much less composition dependence. The N_{ch}-N_μ-method, due to the combination of the reconstruction uncertainty of two variables shows basically a larger uncertainty in the reconstruction, but this is compensated by taking into account the correlation of these observables at individual events. Furthermore, by this procedure the composition dependence is strikingly decreased. The $S(500)$ value by construction yields a larger uncertainty of the variable reconstruction, but has also a minor composition dependence.

For all methods, the energy resolution is estimated using full Monte-Carlo simulations and comparing the reconstructed with the simulated primary energy (for instance figure 2 gives the numbers for an energy of $E_0 = 10^{17}$ eV). Values of systematic uncertainties in the flux determination for the different methods are shown in fig. 3 (again for $E_0 = 10^{17}$ eV). These uncertainties are to a large amount due to the reconstruction of the observables, but there are additional sources of systematics which belong to all methods: e.g., concerning the Monte-Carlo statistics, the assumed Monte-Carlo spectral slope, or the fits of the calibration procedures. The different attenuation (and its handling to correct for) of the various observables ($\Lambda(N_{ch}) \approx 495 \pm 20\,\mathrm{g/cm^2}$; $\Lambda(N_\mu) \approx 1100 \pm 100\,\mathrm{g/cm^2}$; $\Lambda(S(500)) \approx 347 \pm 22\,\mathrm{g/cm^2}$ at $E_0 = 10^{17}$ eV) however, lead again to slightly different contribution to the total systematic uncertainty. The total uncertainties (energy resolution and systematics) for the various methods are discussed in refs. [5], [6], [7], [8] and can be displayed as a band surrounding the reconstructed energy spectrum (e.g., see fig. 4).

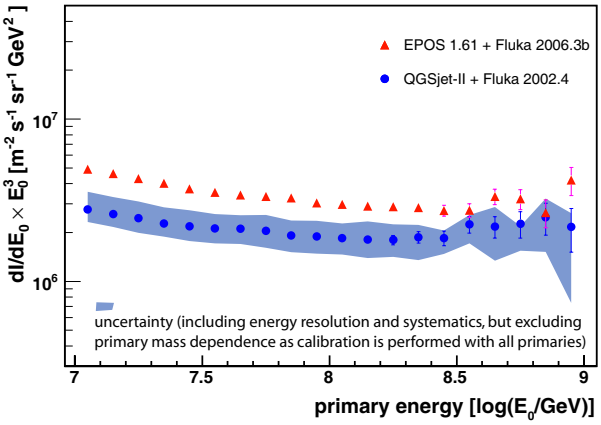

Fig. 4: Reconstructed all-particle energy spectrum with the N_{ch}-method and the calibration function obtained by assuming mixed composition, but based on two different hadronic interaction models.

B. Discussion

Taking into account the systematic uncertainties, there is a fair agreement between the all-particle energy spectra of the different applications (fig. 3).

Of particular interest is the fact that by using N_{ch}, the iron assumption predicts a higher flux than the proton assumption, whereas using N_μ the opposite is the case. That means that the 'true' spectrum has to be a solution in between the range spanned by both methods. If one has only the possibility of applying one method, than there is a large variance in possible solutions (everything in the range spanned by proton and iron line, not even parallel to these lines). However, more detailed investigations have shown, that a structure in the spectrum or a sudden change in composition would be retained in the resulting spectrum, even if the calibration is performed with an individual primary, only. Interestingly, over the whole energy range there is only little room for a solution satisfying both ranges, spanned by N_{ch} and N_μ, and this solution has to be of relative heavy composition - in the framework of the QGSJet-II hadronic interaction model. The narrower range for a solution provided by the N_μ-method compared to N_{ch} confirms the finding of KASCADE that at sea-level the number of mostly low-energy muons N_μ is a very good and composition insensitive energy estimator.

The results of the composition independent N_{ch}-N_μ-, and $S(500)$-methods lie inside the area spanned by the composition dependent methods, which is a very promising result. The $S(500)$-method results in a slightly higher flux than the N_{ch}-N_μ-method, but the two spectra are consistent taking into account the systematic uncertainties.

All the discussed results show a smooth all-particle energy spectrum without any hint to a distinct structure over the whole energy range from 10 PeV to 1 EeV. Another conclusion is that, taking into account the systematic uncertainties for all methods, the underlying

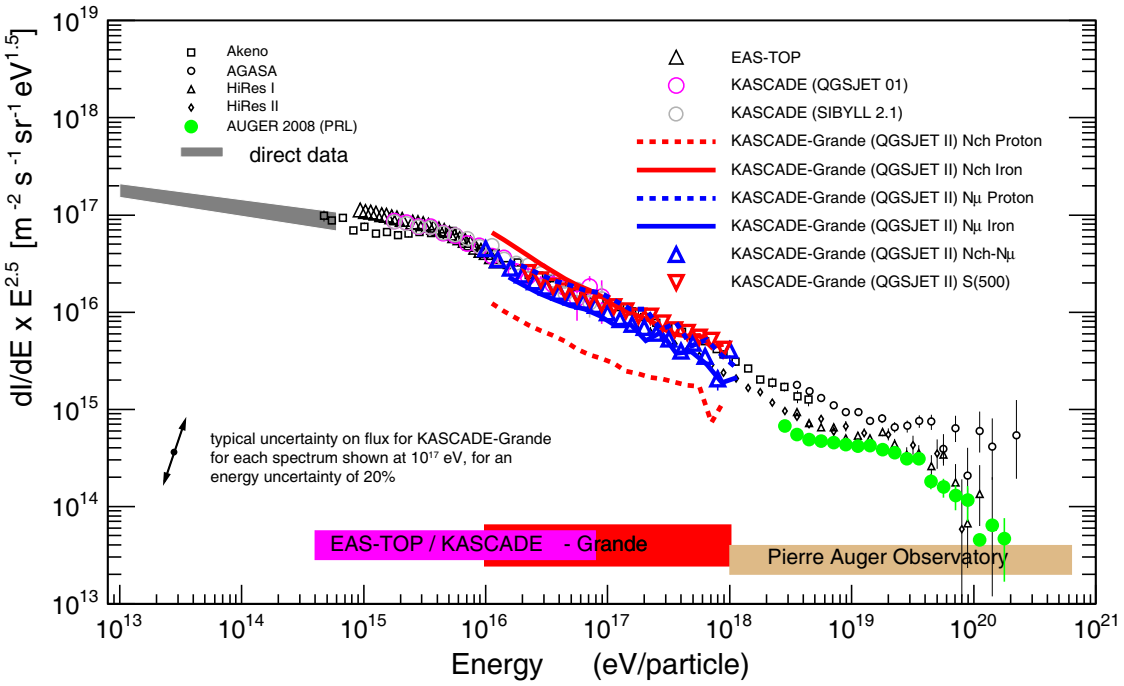

Fig. 5: Compilation of the all-particle energy spectrum obtained by four different methods applied to KASCADE-Grande data and in comparison to results of other experiments.

hadronic interaction model (QGSJet-II/FLUKA) is intrinsically consistent, i.e. the correlation between the different observables, respectively the particle components can describe the global features of our measurements.

C. Hadronic interaction models

By now, for all the considerations the models QGSJet-II and FLUKA [9], [10], [11] are used, only. Other interaction models would probably change the interpretation of the data. We investigated the influence of the hadronic interaction model exemplarily by performing the N_{ch}-method based on simulations with the hadronic interaction model EPOS vers.1.61 [12]. As the Monte-Carlo statistics is limited in case of EPOS, both spectra were obtained by generating the calibration curve with an equally mixed composition of five primaries (H,He,C,Si,Fe). Figure 4 compares the all-particle energy spectrum obtained with the KASCADE-Grande data set for both cases. The interpretation of the KASCADE-Grande data with EPOS leads to a significantly higher flux compared to the QGSJet-II result. Though we know, that version 1.61 of the EPOS model is not consistent with air shower data (in particular, it cannot describe the correlation of hadronic observables with the muon and electron content of the EAS [13]) this example shows that by applying and comparing various reconstruction methods on the same data set will be useful for a better understanding of the interaction processes in the air shower development.

IV. Conclusion

Applying various different reconstruction methods to the KASCADE-Grande data the obtained all-particle energy spectra are compared for cross-checks of reconstruction, for studies of systematic uncertainties and for testing the validity of the underlying hadronic interaction model. The resulting energy spectra are consistent to each other and in the overlapping energy range in a very good agreement to the spectrum obtained by the KASCADE and EAS-TOP experiments (fig. 5).

References

[1] T. Antoni et al - KASCADE Coll., Nucl. Instr. and Meth. A 513 (2003) 490.
[2] A. Chiavassa et al. - KASCADE-Grande Coll., Proc. 21^{st} Europ. Cosmic Ray Symp., Kosice (Slovakia), (2008).
[3] F. Di Pierro et al. - KASCADE-Grande Coll., 31^{th} ICRC, Lodz (Poland) 2009, these proceedings.
[4] D. Fuhrmann et al. - KASCADE-Grande Coll., 31^{th} ICRC, Lodz (Poland) 2009, these proceedings.
[5] D. Kang et al. - KASCADE-Grande Coll., 31^{th} ICRC, Lodz (Poland) 2009, these proceedings.
[6] J.C. Arteaga et al. - KASCADE-Grande Coll., 31^{th} ICRC, Lodz (Poland) 2009, these proceedings.
[7] M. Bertaina et al. - KASCADE-Grande Coll., 31^{th} ICRC, Lodz (Poland) 2009, these proceedings.
[8] G. Toma et al. - KASCADE-Grande Coll., 31^{th} ICRC, Lodz (Poland) 2009, these proceedings.
[9] D. Heck et al., Report FZKA 6019, Forschungszentrum Karlsruhe (1998).
[10] S.S. Ostapchenko, Nucl. Phys. B (Proc. Suppl.) 151 (2006) 143&147; S.S. Ostapchenko, Phys. Rev. D 74 (2006) 014026.
[11] A. Fassò et al., Proc. Monte Carlo 2000 Conf., Lisbon, 23-26 October 2000, Springer, Berlin (2001) 955.
[12] K. Werner, F.M. Liu, T. Pierog, Phys. Rev. C 74 (2006) 044902.
[13] W.D. Apel et al. - KASCADE-Grande Coll., J. Phys. G: Nucl. Part. Phys. 36 (2009) 035201.

Cosmic ray energy spectrum based on shower size measurements of KASCADE-Grande

D. Kang[†], W.D. Apel[*], J.C. Arteaga[†,xi], F. Badea[*], K. Bekk[*], M. Bertaina[‡], J. Blümer[*,†], H. Bozdog[*], I.M. Brancus[§], M. Brüggemann[¶], P. Buchholz[¶], E. Cantoni[‡,‖], A. Chiavassa[‡], F. Cossavella[†], K. Daumiller[*], V. de Souza[†,xii], F. Di Pierro[‡], P. Doll[*], R. Engel[*], J. Engler[*], M. Finger[*], D. Fuhrmann[**], P.L. Ghia[‖], H.J. Gils[*], R. Glasstetter[**], C. Grupen[¶], A. Haungs[*], D. Heck[*], J.R. Hörandel[†,xiii], T. Huege[*], P.G. Isar[*], K.-H. Kampert[**], D. Kickelbick[¶], H.O. Klages[*], P. Łuczak[††], H.J. Mathes[*], H.J. Mayer[*], J. Milke[*], B. Mitrica[§], C. Morello[‖], G. Navarra[‡], S. Nehls[*], J. Oehlschläger[*], S. Ostapchenko[*,xiv], S. Over[¶], M. Petcu[§], T. Pierog[*], H. Rebel[*], M. Roth[*], H. Schieler[*], F. Schröder[*], O. Sima[‡‡], M. Stümpert[†], G. Toma[§], G.C. Trinchero[‖], H. Ulrich[*], A. Weindl[*], J. Wochele[*], M. Wommer[*], J. Zabierowski[††]

[†]*Institut für Experimentelle Kernphysik, Universität Karlsruhe, 76021 Karlsruhe, Germany*
[*]*Institut für Kernphysik, Forschungszentrum Karlsruhe, 76021 Karlsruhe, Germany*
[‡]*Dipartimento di Fisica Generale dell'Università, 10125 Torino, Italy*
[§]*National Institute of Physics and Nuclear Engineering, 7690 Bucharest, Romania*
[¶]*Fachbereich Physik, Universität Siegen, 57068 Siegen, Germany*
[‖]*Istituto di Fisica dello Spazio Interplanetario, INAF, 10133 Torino, Italy*
[**]*Fachbereich Physik, Universität Wuppertal, 42097 Wuppertal, Germany*
[††]*Soltan Institute for Nuclear Studies, 90950 Lodz, Poland*
[‡‡]*Department of Physics, University of Bucharest, 76900 Bucharest, Romania*
[xi]*now at: Universidad Michoacana, Morelia, Mexico*
[xii]*now at: Universidade São Paulo, Instituto de Fisica de São Carlos, Brasil*
[xiii]*now at: Dept. of Astrophysics, Radboud University Nijmegen, The Netherlands*
[xiv]*now at: University of Trondheim, Norway*

***Abstract*. The KASCADE-Grande (KArlsruhe Shower Core and Array DEtector and Grande array), located on site of the Forschungszentrum Karlsruhe in Germany, is designed for observations of cosmic ray air showers in the energy range of 10^{16} to 10^{18} eV. The measurement of the all-particle energy spectrum of cosmic rays is based on the size spectra of the charged particle component, measured for different zenith angle ranges and on the "Constant Intensity Cut" method to correct for attenuation effects. The all-particle energy spectrum, calibrated by Monte-Carlo simulations, is presented and systematic uncertainties discussed.**

***Keywords*: cosmic rays; KASCADE-Grande; constant intensity cut method.**

I. Introduction

The energy spectrum and composition of primary cosmic rays around 10^{17} eV are very important since they might be related to the existence of extragalactic cosmic ray sources, which might have a significantly different elemental composition from the one observed at lower energies [1]. The aim of KASCADE-Grande is the examination of the iron-knee in the cosmic ray energy spectrum, i.e. the end of the bulk of cosmic rays of galactic origin. It is expected at around 10^{17} eV following previous KASCADE observations [2]. KASCADE-Grande will allow investigations in detail about the elemental composition giving the possibility to distinguish between astrophysical models for the transition region from galactic to extragalactic origin of cosmic rays. The KASCADE-Grande array covering an area of 700×700 m^2 is optimized to measure extensive air showers up to primary energies of 1 EeV [3]. It comprises 37 scintillation detector stations located on a hexagonal grid with an average spacing of 137 m for the measurements of the charged shower component. Each of the detector stations is equipped with plastic scintillator sheets covering a total area of 10 m^2. The stations contain 16 scintillator sheets read-out by photo-multipliers providing a dynamic range up to about 10000 charged particles per station for the reconstruction of particle densities and timing measurements. The timing accuracy of Grande stations allows an excellent angular resolution [4]. Grande is electronically subdivided in 18 hexagonal trigger clusters formed by six external and one central stations. A trigger signal is build when all stations in a hexagon are fired, and its total rate is about 0.5 Hz. Full efficiency for the shower size is reached at the number of charged particles of around 10^6, which approximately corresponds to a primary energy of 10^{16} eV, so that a large overlap for cross-checks with measurements of the original KASCADE experiment is attained. The limit at high energies is due to the restricted area of the Grande array.

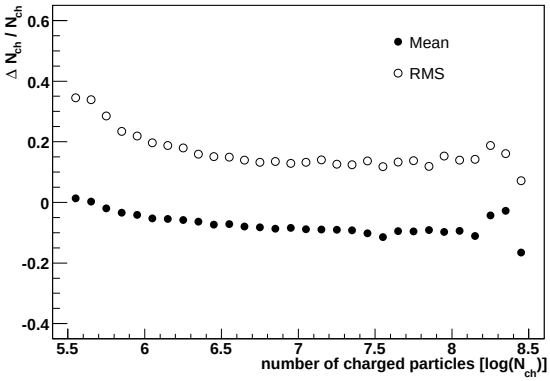

Fig. 1: Reconstruction accuracy of the number of charged particles obtained by Monte-Carlo simulations. The closed and open circles represent the values of mean and Root Mean Square, respectively.

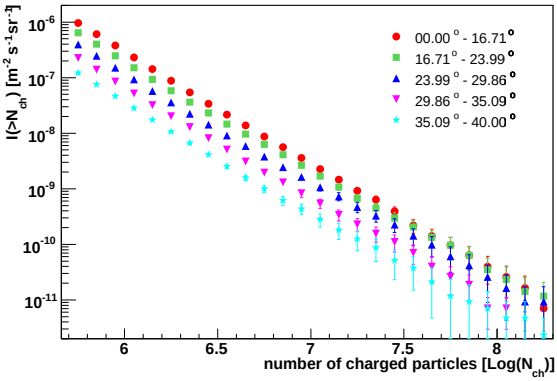

Fig. 2: Integral shower size spectra of the number of charged particles for different zenith angle ranges.

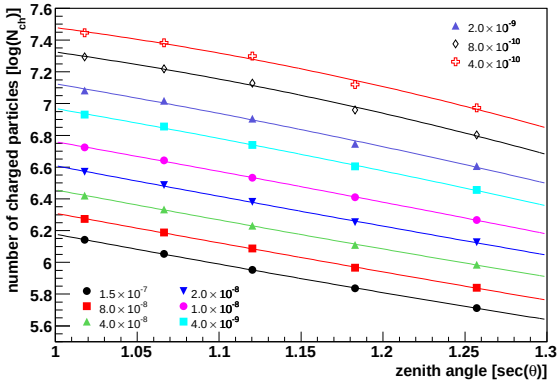

Fig. 3: The number of charged particles resulting from the constant intensity cuts as a function of the zenith angle. The unit of each flux (symbol) is $m^{-2}s^{-1}sr^{-1}$.

II. Reconstruction accuracy

The primary energy of cosmic rays is reconstructed by the observed electron and muon numbers at ground. While the Grande detectors are sensitive to all charged particles, the KASCADE detectors measure separately the electromagnetic and muonic components due to the shielding above the muon counters. Therefore, the shower core position, the arrival direction, and the total number of charged particles in the shower are reconstructed from Grande array data, whereas the total number of muons is extracted from the data of the KASCADE muon detectors. Performing CORSIKA air shower simulations [5] including the detector response of the Grande array, the parameters were optimized for the lateral density distribution of KASCADE-Grande [4], and well reconstructed with sufficient accuracies for the further physics analysis. Figure 1 shows the accuracy of the reconstructed number of charged particles obtained by Monte-Carlo simulations. The accuracy could be confirmed by combining information of KASCADE with Grande reconstruction on a subsample of commonly measured events (Ref. [4]). In order to avoid misreconstruction effects of shower core positions on the border of the Grande array, a fiducial area of about 0.2 km^2 centered in the middle of the Grande array is chosen. The statistical uncertainty of the shower size is of the order of 20% for the total number of charged particles. Above a threshold of 10^6 charged particles, the reconstruction accuracies of the core position and the arrival direction are better than 8 m and 0.5°, respectively, for zenith angles below 40°.

III. Data analysis

KASCADE-Grande has started combined data acquisition with all detector components since the end of 2003. The data presented here were taken from December 2003 to March 2009. It corresponds to the effective measuring time of 987 days, where all components of KASCADE and KASCADE-Grande were operating without failures in data acquisition. In this analysis, all showers with zenith angles smaller than 40° have been analyzed. After some quality cuts approximately 10 million events are available for the physics analysis. As the first step to determine the all-particle energy spectrum, the constant intensity cut method was introduced. This method assumes that cosmic rays arrive isotropically from all directions, i.e. the primary energy of a cosmic ray particle corresponds to a certain intensity regardless of its arrival direction. In KASCADE-Grande, an isotropic distribution is assumed in the considered energy range up to 10^{18} eV, so that it allows us to apply the constant intensity method to the integral shower size spectra for different zenith angular bins (Fig. 2).

Above a certain shower size, the intensity should be constant due to the assumption of the uniform intensity distribution when binned in $\cos^2\theta$. For a given intensity, the number of charged particles is calculated for each zenith angle range. The intensity cut is mostly located in between two neighboring points of the distributions, and thus the exact values of the corresponding shower size are estimated by interpolation between these two

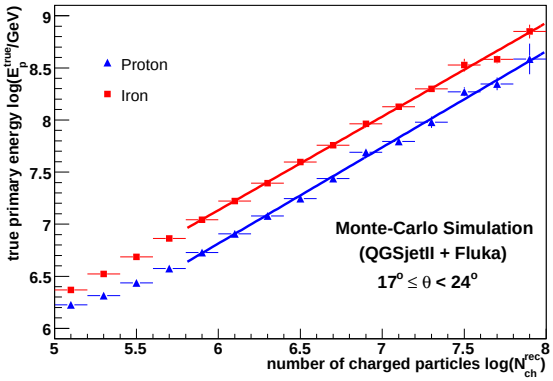

Fig. 4: The true primary energy as a function of the number of charged particles for proton and iron components. The lines show the applied fits to the points.

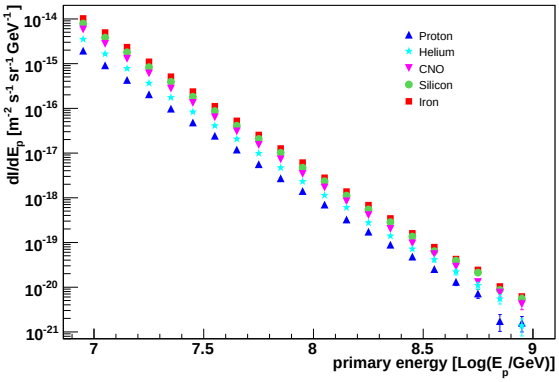

Fig. 5: All-particle energy spectrum reconstructed from KASCADE-Grande shower size for five different primary particle type assumptions together with its statistical uncertainties.

points. From the values of N_{ch} we obtain the attenuation curves (Fig. 3). It represents how the number of charged particles for a given intensity attenuates through the atmosphere with increasing zenith angle, i.e. with increasing atmospheric depth. Each curve is individually fitted by a second-degree polynomial function, where the reference angle θ_{ref} of 20° is chosen by the mean value from a Gaussian fit to the measured zenith angle distribution. Due to a negligible variation of the fit parameters only one value is used to correct the number of charged particles event by event for the attenuation in the atmosphere. The zenith angle dependence of the number of charged particles was therefore eliminated by using informations from the measurements only.

In order to determine the energy conversion relation between the number of charged particles N_{ch} and the primary energy E_p, Monte-Carlo simulations were used. Extensive air showers were simulated using the program CORSIKA with QGSjetII [6] and FLUKA as hadronic interaction models, including full simulations of the detector response. The simulated data sets contain air shower events for five different primary mass groups: proton, helium, carbon, silicon and iron. For the simulation, events for the zenith angle ranges of $17° \leq \theta < 24°$, i.e. around the reference angle, are selected to reduce systematic effects. The relation of the primary energy as a function of the number of charged particles is shown in Fig. 4. Assuming a linear dependence $\log E_p = a + b \cdot \log N_{ch}$, the correlation between the primary energy and the number of charged particles is obtained, where the fit is applied in the range of full trigger and reconstruction efficiencies. The fit yields $a = 1.28 \pm 0.08$ and $b = 0.92 \pm 0.01$ with a reduced χ^2 of 1.42 for proton, and $a = 1.74 \pm 0.07$ and $b = 0.90 \pm 0.01$ with a reduced χ^2 of 0.98 for iron. The same procedure is also performed for helium, carbon and silicon to examine the dependence of the calibration on the assumed primary particle type, where the fit parameters are also in between above values. Using these

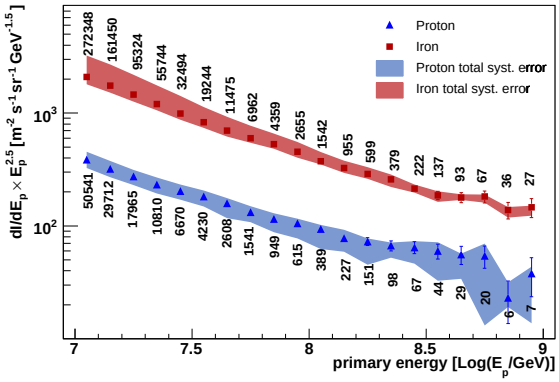

Fig. 6: The reconstructed energy spectrum for proton and iron, together with statistical error bars (vertical lines) and uncertainties (energy resolution and systematics) (bands). The numbers indicate the events per bin for the points.

correlations the all-particle energy spectrum is obtained. The reconstructed energy spectra for the assumption of five different primary particle types are shown in Fig. 5.

IV. Systematic Uncertainty

The energy resolution is estimated from the difference between simulated energy and derived energy, where the derived energy is obtained by applying the measured attenuation correction to the Monte-Carlo simulation. The energy resolutions for proton and iron are about 31% and 15% over the whole energy ranges, where the uncertainties of the reconstructed number of charged particles give the largest contribution. In addition, the systematic uncertainties on the reconstructed energy spectrum are investigated considering various possible contributions. Firstly, the fit of the attenuation curve was performed in order to correct the zenith angle dependence of the number of charged particles. Each fit parameter has an associated error and it effects on the

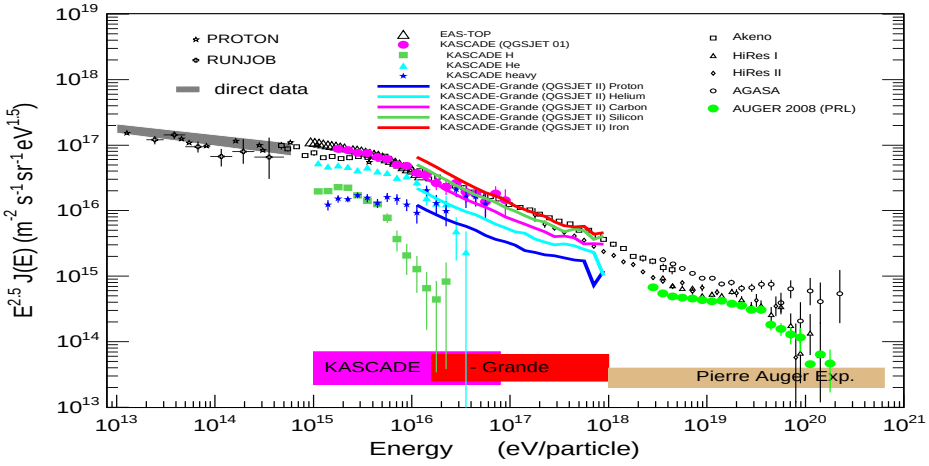

Fig. 7: All-particle energy spectrum in comparison with results of other experiments. The lines represent the KASCADE-Grande spectrum for the calibration assuming five different primary mass groups.

determination of the energy spectrum. The fit parameters are correlated with each other, so that the propagation of errors is used to calculate the systematic uncertainty induced by the attenuation fit. This uncertainty is estimated to be less than 2% for both proton and iron in the full energy range. Secondly, for the correlation of N_{ch} with E_p a power law fit was applied. As the same procedure above, the estimated systematic uncertainties due to the fit of the energy calibration contribute with 1% for proton and 3% for iron to the total uncertainty. The shower fluctuations are another source of systematic uncertainties, which is basically caused by the nature of the development of extensive air showers. The influence of these fluctuations on the reconstructed primary energy spectrum is estimated by using simulation data. For the calibration a spectral index of γ = -3 is used in the simulations. By varying this spectral index, i.e. varying the effect of fluctuations on the reconstructed spectrum, the systematic uncertainty is estimated. The systematic deviation due to the shower fluctuation is evaluated by this procedure to be about 15% and 4% for proton and iron, respectively. Uncertainties due to a possible misdescription of the attenuation in the Monte-Carlo simulation are estimated by using two different reference zenith angles, together with the corresponding correlation of N_{ch} and E_p. The systematic uncertainties of 14% for proton and 11% for iron on the energy estimation are obtained for varying the reference angle from 10° to 30° for the calibration. All these individual systematic contributions were considered to be uncorrelated, and combined thus in quadrature to obtain the total systematic uncertainty (Fig. 6), where the composition dependence was not taken into account. The systematic uncertainty (i.e. sum in quadrature of all terms discussed above except the energy resolution) in the energy scale is of the order of about 20% for proton and 12% for iron at the primary energy of 10^{17} eV. The uncertainties on the flux for proton and iron are 32% and 21%, respectively, at energies of 10^{17} eV. Further checks are currently being performed to reduce the systematic uncertainties on the energy estimation.

V. Conclusion

The air shower experiment KASCADE-Grande measures cosmic rays in the energy range of 10^{16}-10^{18} eV. The multi detector setup of KASCADE-Grande allows us to reconstruct charged particles, electron and muon numbers of the showers separately with high accuracies. In the present contribution the reconstructed all-particle energy spectrum by means of the shower size measurements of the charged particle component by Grande array is presented by using the hadronic interaction model QGSjetII. The resulting spectrum is shown in Fig. 7 in comparison with results of other experiments. The obtained intensity values have been shown to depend on the nature of the primary particle as expected for an observable dominated by the electromagnetic components. Such values, inside the systematic uncertainties, are consistent with other KASCADE-Grande analysis based on different observables and methodologies. Their combination is a basic tool to provide an unbiased measurement of the primary energy spectrum and first indications on average primary composition [7].

References

[1] T. K. Gaisser *et al.*, Phys. Rev. **D 47** 1919 (1993).
[2] T. Antoni *et al.*, KASCADE Collaboration, Astrop. Phys. **24** 1 (2005).
[3] G. Navarra *et al.*, KASCADE-Grande Collaboration, Nucl. Instr. Meth. **A 518** 207 (2004).
[4] F. Di Pierro *et al.*, KASCADE-Grande Collaboration, These Conference Proceedings.
[5] D. Heck *et al.*, Rep. FZKA 6019, Forschungszentrum Karlsruhe (1998).
[6] S.S. Ostapchenko, *Phys. Rev. D* **74** 014026 (2006).
[7] A. Haungs *et al.*, KASCADE-Grande Collaboration, These Conference Proceedings.

The Energy Spectrum of Primary Cosmic Rays Reconstructed with the KASCADE-Grande Muon Data

J.C. Arteaga-Velázquez[†,xi], W.D. Apel[*], F. Badea[*], K. Bekk[*], M. Bertaina[‡], J. Blümer[*,†], H. Bozdog[*], I.M. Brancus[§], M. Brüggemann[¶], P. Buchholz[¶], E. Cantoni[‡,‖], A. Chiavassa[‡], F. Cossavella[†], K. Daumiller[*], V. de Souza[†,xii], F. Di Pierro[‡], P. Doll[*], R. Engel[*], J. Engler[*], M. Finger[*], D. Fuhrmann[**], P.L. Ghia[‖], H.J. Gils[*], R. Glasstetter[**], C. Grupen[¶], A. Haungs[*], D. Heck[*], J.R. Hörandel[†,xiii], T. Huege[*], P.G. Isar[*], K.-H. Kampert[**], D. Kang[†], D. Kickelbick[¶], H.O. Klages[*], P. Łuczak[††], H.J. Mathes[*], H.J. Mayer[*], J. Milke[*], B. Mitrica[§], C. Morello[‖], G. Navarra[‡], S. Nehls[*], J. Oehlschläger[*], S. Ostapchenko[*,xiv], S. Over[¶], M. Petcu[§], T. Pierog[*], H. Rebel[*], M. Roth[*], H. Schieler[*], F. Schröder[*], O. Sima[‡‡], M. Stümpert[†], G. Toma[§], G.C. Trinchero[‖], H. Ulrich[*], A. Weindl[*], J. Wochele[*], M. Wommer[*], J. Zabierowski[††]

[*]*Institut für Kernphysik, Forschungszentrum Karlsruhe, 76021 Karlsruhe, Germany*
[†]*Institut für Experimentelle Kernphysik, Universität Karlsruhe, 76021 Karlsruhe, Germany*
[‡]*Dipartimento di Fisica Generale dell'Università, 10125 Torino, Italy*
[§]*National Institute of Physics and Nuclear Engineering, 7690 Bucharest, Romania*
[¶]*Fachbereich Physik, Universität Siegen, 57068 Siegen, Germany*
[‖]*Istituto di Fisica dello Spazio Interplanetario, INAF, 10133 Torino, Italy*
[**]*Fachbereich Physik, Universität Wuppertal, 42097 Wuppertal, Germany*
[††]*Soltan Institute for Nuclear Studies, 90950 Lodz, Poland*
[‡‡]*Department of Physics, University of Bucharest, 76900 Bucharest, Romania*
[xi]*now at: Instituto de Física y Matemáticas, Universidad Michoacana, Morelia, Mexico*
[xii]*now at: Universidade de São Paulo, Instituto de Fîsica de São Carlos, Brasil*
[xiii]*now at: Dept. of Astrophysics, Radboud University Nijmegen, The Netherlands*
[xiv]*now at: University of Trondheim, Norway*

***Abstract*. A detailed analysis based on the Constant Intensity Cut method was applied to the KASCADE-Grande muon data in order to reconstruct an all-particle energy spectrum of primary cosmic rays in the interval $2.5 \times 10^{16} - 10^{18}$ eV. To interpret the experimental data, Monte Carlo simulations carried out for five different primary nuclei (H, He, C, Si and Fe) using the high-energy hadronic interaction model QGSJET II were employed. For each case, the derived all-particle energy spectrum is presented. First estimations of the main systematic uncertainties are also shown.**

***Keywords*: Ground arrays, cosmic ray energy spectrum, muons**

I. Introduction

One of the main goals of the cosmic ray research is the measurement of the primary energy spectrum, which encloses important keys about the origin, acceleration and propagation of cosmic rays. This task can be done directly or indirectly, depending on the energy of the primary particle. At high energies, above 10^{15} eV, where direct detection is not feasible, the energy spectrum must be determined indirectly from the measured properties of the extensive air showers (EAS) that cosmic rays induce in the Earth's atmosphere. Depending on the experimental apparatus and the detection technique, different sets of EAS observables are available to estimate the energy of the primary cosmic ray [1]. In ground arrays the total number of charged particles in the shower and the corresponding density at observation level are more commonly employed [1], [2]. However, the muon content is also at disposal for this enterprise [3]. One reason in favor of this observable is that, in an air shower, muons undergo less atmospheric interactions than the charged component (dominated by electromagnetic particles for vertical EAS) and present in consequence less fluctuations. Another reason is that, according to MC simulations, the muon shower size (N_μ) grows with the energy of the primary particle following a simple power law. Although these advantages, the muon number as an energy estimator is expected to be limited by the hadronic-interaction model, the experimental error and the uncertainty in the primary composition, among other things. In this work, the KASCADE-Grande muon data is used as a tool to derive the energy spectrum for cosmic rays in the range from 2.5×10^{16} to 10^{18} under different composition scenarios. The method is explained and the main systematic uncertainties behind the calculations are presented.

II. Description of the detector and the data

The KASCADE-Grande experiment was conceived as a ground-based air shower detector devoted to the search of the *iron knee* in the cosmic ray spectrum [4]. KASCADE-Grande, with an effective area of $0.5\,\mathrm{km}^2$,

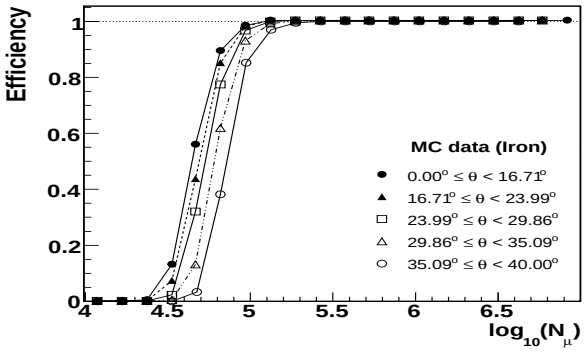

Fig. 1: KASCADE-Grande triggering and reconstruction efficiency shown as a function of the muon number for different zenith angle intervals. The efficiency was estimated from MC simulations assuming a pure iron composition.

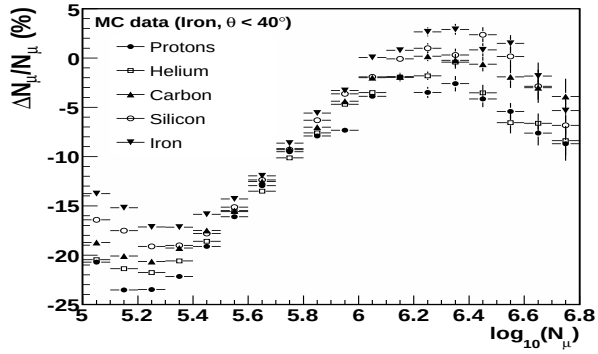

Fig. 2: Average values of the muon correction functions plotted versus the total muon number. Results for different primaries are displayed.

is composed by several types of particle detectors dedicated to study different components of the EAS. Important for this analysis is the $200 \times 200\,\mathrm{m}^2$ muon detector array integrated by $192 \times 3.2\,\mathrm{m}^2$ shielded scintillator detectors, which are sensitive to muons with energy threshold above $230\,\mathrm{MeV}$ for vertical incidence [4], [5], [6]. The muon array was implemented to measure the lateral distribution of muons in the shower front and to extract the muon shower size. The latter is performed, event by event, from a fit to the observed lateral muon densities [6].

The present analysis was based on a muon data set collected with the KASCADE-Grande array during the period December 2003 - February 2009 for zenith angles, θ, below 40°. In order to reduce the influence of systematic uncertainties in this data, a fiducial area of $370 \times 520\,\mathrm{m}^2$ located at the center of KASCADE-Grande was employed. Moreover various experimental cuts were imposed. As a result the effective time of observation of the selected data was approximately 754.2 days. For the conditions above described, full efficiency is achieved for $\log_{10}(N_\mu) > 5.1 - 5.4$, according to MC simulations. Here the lower threshold corresponds to the case of light primaries and/or vertical air showers (see, for example, Fig. 1).

The systematic uncertainties of the instrument and the reconstruction procedures were also investigated with MC simulations. The EAS events were generated with an isotropic distribution with spectral index $\gamma = -2$ and were simulated with CORSIKA [7] and the hadronic MC generators FLUKA [8] and QGSJETII [9]. MC data sets were produced for five different representative mass groups: H, He, C, Si and Fe. In each case the simulated data was weighted with a proper function to describe a steeper energy spectrum with $\gamma = -3$, which was chosen as reference for the purpose of this study.

III. The path to the spectrum

For the current analysis the experimental muon data was divided in five zenith angle intervals ($\Delta\theta$), each of them with the same value of acceptance. In addition, N_μ was corrected for systematic effects through a correction

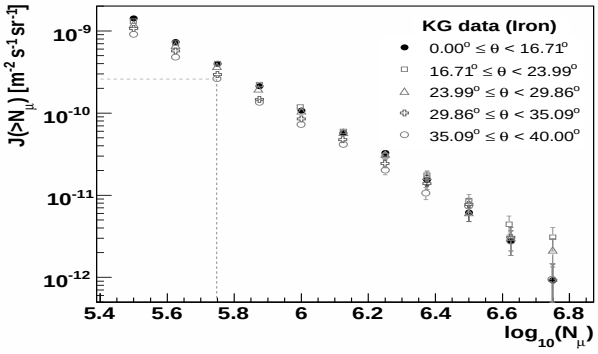

Fig. 3: Integral muon spectra obtained from the KASCADE-Grande data using the muon correction function for iron nuclei. The vertical error bars represent statistical uncertainties. In this figure, a CIC cut is represented by the horizontal line. The intersection of the CIC cut with a given integral flux defines a corresponding N_μ value, here indicated by the vertical line.

function, which was parameterized in terms of the zenith and azimuth angles, the core position and the muon size according to MC results. The precise magnitude of the corrections change with the primary mass, but on average they are under 25 % and tend to decrease with N_μ in the region of full efficiency (see Fig. 2). Along the paper muon correction functions were already applied to the data according to the primary composition assumed.

In order to reconstruct the all-particle energy spectrum, in a first step the CIC method was applied to the corrected muon data [2], [3], [10]. The objective was to extract a muon attenuation curve to correct the muon shower size at different atmospheric depths and convert it into an equivalent N_μ for a given zenith angle of reference to combine in this way muon data measured at different atmospheric depths. To start with, the integral muon spectra, $J(> N_\mu)$, were calculated for all $\Delta\theta$ bins. As an example, in Fig. 3 the integral fluxes derived with a N_μ correction function for iron nuclei were plotted. Unless otherwise indicated an iron primary composition will be assumed from now on to illustrate the procedure. Once the integral spectra were calculated, cuts at a fixed frequency rate or integral intensity were

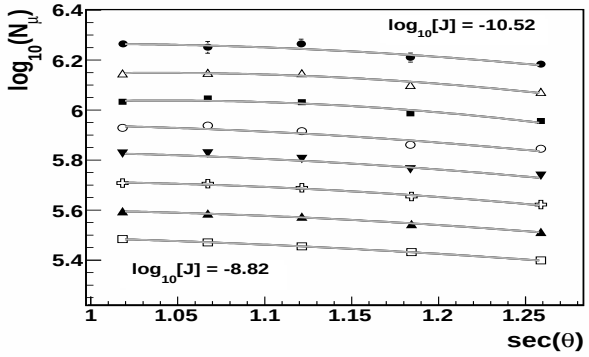

Fig. 4: Muon attenuation curves as extracted from several constant intensity cuts applied to the integral N_μ spectra of figure 3. From the bottom to the top, the CIC cuts decrease in steps of $\Delta \log_{10}[J/(m^{-2}s^{-1}sr^{-1})] \approx 0.24$.

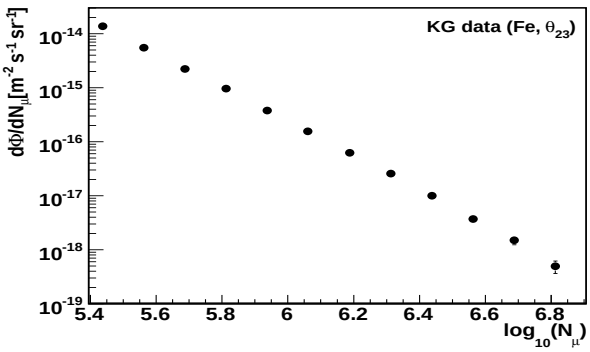

Fig. 5: The KASCADE-Grande muon spectrum obtained with the CIC method for $\theta_{ref} = 23.1^\circ$. The muon correction function for iron nuclei was employed.

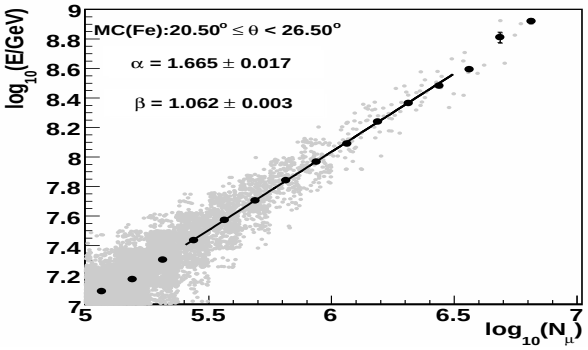

Fig. 6: Mean distribution of true energy vs muon number for iron nuclei and $\theta = 20.5^\circ - 26.5^\circ$ calculated with MC simulations. The fit with formula $\mathrm{E[GeV]} = \alpha \cdot N_\mu^\beta$ is shown.

applied covering only the region of maximum efficiency and statistics. Then from the intersection of each cut and the integral fluxes (see Fig. 3) a muon attenuation curve was built plotting the intersected muon numbers as a function of $\sec\theta$, as displayed in Fig. 4. This can be in principle done since, according to the CIC method (where isotropy of cosmic rays is assumed) all EAS muon sizes connected through a specific cut belong to showers of identical energy. A technical point should be mentioned before continuing, that linear interpolation between two adjacent points was used in order to find the crossing between a given cut and a certain spectrum. The uncertainty introduced by the interpolation procedure in the extracted value of N_μ was properly taken into account along with the statistical errors of the integral spectra.

With the attenuation curves finally at disposal, one can calculate the equivalent muon number of an EAS for a zenith angle of reference, θ_{ref}. This angle was chosen to be the mean of the measured zenith angle distribution, which was found around 23.1°. Event by event, the equivalent EAS muon size for the selected atmospheric depth was estimated through the formula:

$$N_\mu(\theta_{ref}) = N_\mu(\theta) \exp\left[P(\theta_{ref}) - P(\theta)\right], \qquad (1)$$

where $P(\theta)$ is a fit, with a second degree polynomial in $\sec\theta$, to the attenuation curves (see Fig. 4). In the above equation $P(\theta)$ is the closest curve to a given $N_\mu(\theta)$ data point. In Fig. 5 the equivalent muon spectrum for θ_{ref} as calculated with the CIC method is presented.

In a final step, to derive the energy spectrum from the above data a conversion relation from muon content into primary energy was invoked. The calibration formula was obtained from MC simulations by fitting the mean distribution of true energy versus N_μ for data with zenith angles around θ_{ref}. The fit was done with a power law relation, $\mathrm{E[GeV]} = \alpha \cdot N_\mu^\beta$, for the N_μ interval of full efficiency and high statistics (see Fig. 6). To test the reconstruction method the same analysis was applied to the MC data. Differences between the magnitude of the true and the estimated MC energy spectra were found. At $E \approx 10^{17}$ eV, they are smaller than 30%. Deviations are due to fluctuations in the reconstructed energy, which are bigger for light primary masses. They vary in the range of $18 - 29$ % at 10^{17} eV. That defines our energy resolution at this energy scale.

IV. Results and Conclusions

The all-particle energy spectrum reconstructed from the KASCADE-Grande muon data is displayed in Fig. 7 for different primary composition assumptions. Measurements of the original KASCADE experiment [5] are also shown for comparison. It can be seen that the KASCADE data points are found inside the region that covers the KASCADE-Grande results, showing agreement between both experiments. Total uncertainties are also presented in the same figure. They take into account the following sources: 1) the influence of the energy resolution distribution, 2) uncertainties in the N_μ correction functions and 3) the energy conversion relation, both arising from the fits to MC data, 4) uncertainties in the estimation of the equivalent muon number, 5) a small shift observed in the estimated energy, which is introduced by the analysis, 6) uncertainties in the primary spectral index ($\gamma = -3 \pm 0.5$) and 7) the effect of selecting another reference angle θ_{ref}, using for example 10 and 30°. Each of these contributions introduces a

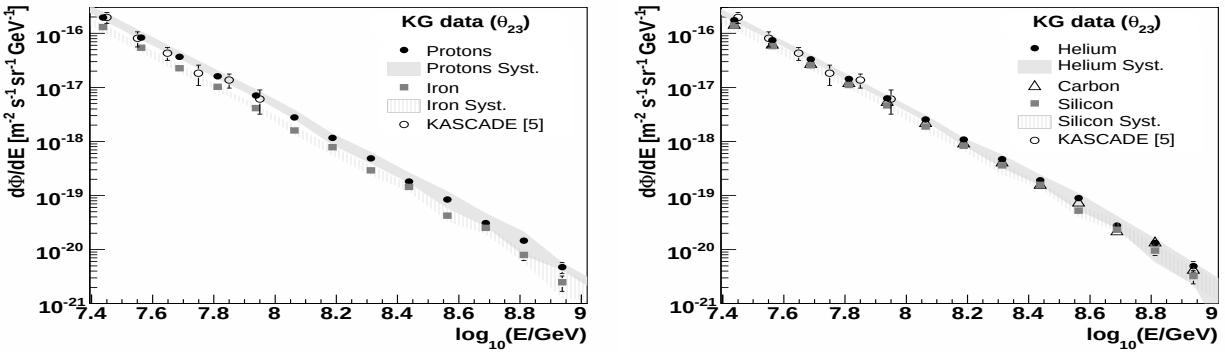

Fig. 7: The all-particle energy spectrum derived from the KASCADE-Grande muon data assuming different primary compositions. The bands for the total uncertainties (energy resolution plus systematic errors) are displayed (except for Carbon). Vertical error bars represent statistical uncertainties.

TABLE I: Percentual contributions to the total uncertainty (energy resolution and systematics) of the energy spectrum around 10^{17} eV. Sources are enumerated as described in the text. At the same energy scale, the average energy systematic uncertainty and energy resolution are also shown. The muon attenuation length is presented in the last column.

Composition	$\Phi \pm$ tot. $\pm$ stat. $10^{-18}[\mathrm{m^{-2}\,s^{-1}\,sr^{-1}\,GeV^{-1}}]$	(1) [%]	(2) [%]	(3) [%]	(4) [%]	(5) [%]	(6) [%]	(7) [%]	ΔE/E [%] $\pm$syst. $\pm$ res.	Λ_μ [g/cm^2]
H	$2.75^{+1.09}_{-0.21} \pm 0.07$	$+35$	$^{+2}_{-1}$	±1	$^{+3}_{-1}$	$+11$	$^{+13}_{-7}$	$^{+8}_{-0}$	$^{+9}_{-8} \pm 29$	1136 ± 115
He	$2.52^{+0.53}_{-0.20} \pm 0.07$	$+19$	$^{+1}_{-0.4}$	$^{+1}_{-0.4}$	$^{+2}_{-1}$	-3	$^{+6}_{-5}$	±5	$^{+6}_{-12} \pm 26$	1111 ± 112
C	$2.29^{+0.23}_{-0.229} \pm 0.06$	$+9$	$^{+0.2}_{-2}$	$^{+0.2}_{-1}$	$^{+1}_{-2}$	-2	$^{+2}_{-6}$	$^{+3}_{-10}$	$^{+6}_{-13} \pm 19$	1137 ± 121
Si	$1.88^{+0.20}_{-0.35} \pm 0.06$	$+6$	$^{+2}_{-3}$	$^{+0.4}_{-0.1}$	±2	-3	$^{+4}_{-1}$	$^{+7}_{-18}$	$^{+5}_{-15} \pm 20$	1056 ± 146
Fe	$1.58^{+0.36}_{-0.26} \pm 0.05$	$+22$	$^{+0.5}_{-0.1}$	$^{+0}_{-0.1}$	$^{+1}_{-4}$	$+2$	$^{+2}_{-0.1}$	$^{+1}_{-16}$	$^{+4}_{-13} \pm 18$	1123 ± 182

modification in the estimated energy of the events, which is propagated to the flux. The differences between the reference spectrum and the modified ones were interpreted as the corresponding uncertainties. They were added in quadrature to get the total error. In cases (2), (3) and (4) usual error propagation formulas were employed to find the energy uncertainty of the events. (1) and (5) were estimated from MC simulations. In the case of (1), the energy of an event was assigned in a probabilistic way using the energy resolution distributions per energy bin obtained with MC simulations. In (6) MC relations employed in the whole analysis were recalculated with simulations characterized by the new spectral indexes. Finally, for (7) both the equivalent N_μ and the energy calibration formula were estimated for the new values of θ_{ref}. The resulting uncertainties (energy resolution (1) and systematics (2)-(7)) for the energy and the spectrum around 10^{17} eV are presented in table I. In general, for the interval $\log_{10}[\mathrm{E/GeV}] = 7.4 - 8.3$ from all the estimated contributions to the total uncertainty of the flux the biggest one is related to composition ($\lesssim$ 50%). The second most important contribution ($\lesssim$ 35%) comes from (1). The uncertainties associated to (6) and (7) together occupy the third place ($\lesssim$ 31%), but sometimes they can be as important as (1). For light primaries (5) can become the next influent source ($\lesssim$ 12%). The rest contributions, (2)-(4), are always the smaller ones (added they are $\lesssim$ 12%). Both the energy and flux total uncertainties change with the value of E. They tend to increase near the energy threshold and in the high-energy region, where statistics decreases. These first estimations are very encouraging. They show that muons can be used in KASCADE-Grande as a tool to reconstruct the primary all-particle energy spectrum. More work is to come in order to improve the reconstruction method. Plans are also underway to investigate the muon attenuation length, Λ_μ. Some values extracted from the N_μ attenuation curves are shown in Table I for $E \approx 10^{17}$ eV. A good agreement is seen among the experimental attenuation lengths under the assumption of different primary masses at this energy.

V. Acknowledgments

J.C. Arteaga acknowledges the partial support of CONACyT and the Coordinación de la Investigación Científica de la Universidad Michoacana.

References

[1] M. Nagano and A.A. Watson., Rev. Mod. Phys. **72**, 689 (2000).
[2] D. M. Edge *et al.*, J. Phys. **A6**, 1612-34 (1973).
[3] M. M. Winn *et al.*, J. Phys. **G12**, 653-674 (1986). M. Nagano *et al.*, J. Phys. **G10** 1295-1310 (1984).
[4] A. Haungs *et al.*, KASCADE-Grande Coll., these proceedings.
[5] T. Antoni *et al.*, Astrop. Phys. **24**, 1-25 (2005).
[6] D. Fuhrmann *et al.*, KASCADE-Grande Coll., these proceedings.
[7] D. Heck *et al.*, Forschungszentrum Karlsruhe, Report FZKA 6019 (1998).
[8] A. Fassò *et al.*, Proc. Monte Carlo 2000 Conf., Lisbon, 955 (2001).
[9] S. S. Ostapchenko, Phys. Rev **D74**, 014026 (2006).
[10] J. Alvarez-Muñiz *et al.*, Phys. Rev **D66**, 123004 (2002).

The all particle energy spectrum of KASCADE-Grande in the energy region 10^{16} - 10^{18} eV by means of the N_{ch} - N_{μ} technique

M. Bertaina[‡], W.D. Apel[*], J.C. Arteaga[†,xi], F. Badea[*], K. Bekk[*], J. Blümer[*,†], H. Bozdog[*] I.M. Brancus[§], M. Brüggemann[¶], P. Buchholz[¶], E. Cantoni[‡,‖], A. Chiavassa[‡], F. Cossavella[†], K. Daumiller[*], V. de Souza[†,xii], F. Di Pierro[‡], P. Doll[*], R. Engel[*], J. Engler[*], M. Finger[*], D. Fuhrmann[**], P.L. Ghia[‖], H.J. Gils[*], R. Glasstetter[**], C. Grupen[¶], A. Haungs[*], D. Heck[*], J.R. Hörandel[†,xiii], T. Huege[*], P.G. Isar[*], K.-H. Kampert[**], D. Kang[†], D. Kickelbick[¶], H.O. Klages[*], P. Łuczak[††], H.J. Mathes[*], H.J. Mayer[*], J. Milke[*], B. Mitrica[§], C. Morello[‖], G. Navarra[‡], S. Nehls[*], J. Oehlschläger[*], S. Ostapchenko[*,xiv], S. Over[¶], M. Petcu[§], T. Pierog[*], H. Rebel[*], M. Roth[*], H. Schieler[*], F. Schröder[*], O. Sima[‡‡], M. Stümpert[†], G. Toma[§], G.C. Trinchero[‖], H. Ulrich[*], A. Weindl[*], J. Wochele[*], M. Wommer[*], J. Zabierowski[††]

[*]*Institut für Kernphysik, Forschungszentrum Karlsruhe, 76021 Karlsruhe, Germany*
[†]*Institut für Experimentelle Kernphysik, Universität Karlsruhe, 76021 Karlsruhe, Germany*
[‡]*Dipartimento di Fisica Generale dell'Università, 10125 Torino, Italy*
[§]*National Institute of Physics and Nuclear Engineering, 7690 Bucharest, Romania*
[¶]*Fachbereich Physik, Universität Siegen, 57068 Siegen, Germany*
[‖]*Istituto di Fisica dello Spazio Interplanetario, INAF, 10133 Torino, Italy*
[**]*Fachbereich Physik, Universität Wuppertal, 42097 Wuppertal, Germany*
[††]*Soltan Institute for Nuclear Studies, 90950 Lodz, Poland*
[‡‡]*Department of Physics, University of Bucharest, 76900 Bucharest, Romania*
[xi]*now at: Universidad Michoacana, Morelia, Mexico*
[xii]*now at: Universidade de São Paulo, Instituto de Fîsica de São Carlos, Brasil*
[xiii]*now at: Dept. of Astrophysics, Radboud University Nijmegen, The Netherlands*
[xiv]*now at: University of Trondheim, Norway*

Abstract. **The KASCADE-Grande experiment, located at Forschungszentrum Karlsruhe (Germany) is a multi-component extensive air-shower experiment devoted to the study of cosmic rays and their interactions at primary energies 10^{14} - 10^{18} eV. One of the main goals of the experiment is the measurement of the all particle energy spectrum in the 10^{16} - 10^{18} eV region. For this analysis the Grande detector samples the charged component of the air shower while the KASCADE array provides a measurement of the muon component. An independent fit of the lateral distributions of charged particle and muon densities allows to extract the charged particle and muon sizes of the shower. The size of the charged particles, combined with the ratio between charged particle and muon sizes, which is used to take into account shower-to-shower fluctuations, is used to assign the energy on an event-by-event basis, in the framework of the CORSIKA-QGSjetII model. The method itself, and the energy spectrum derived with this technique are presented.**

Keywords**: Energy spectrum, KASCADE-Grande, 10^{16} - 10^{18} eV**

I. INTRODUCTION

The KASCADE-Grande experiment [1] is a multi-component air-shower experiment with the aim of measuring the all particle energy spectrum in the 10^{16} - 10^{18} eV region by sampling the charged particle and muon densities. A fit to the lateral distribution of the charged particle densities allows to reconstruct the shower parameters (core position, angular direction) and the size of the charged component (see [2] for details). An independent fit of the lateral distribution of the muon densities (see [3],[4]), gives the size of the muon component of the shower. The performance of the KASCADE-Grande array, and, therefore, its high accuracy up to energies 10^{17} -10^{18} eV, essential to derive an accurate energy spectrum, is summarized in [2].

The conversion between the observed quantities (charged particle and muon sizes) of the Extensive Air Shower (EAS) to the energy of the primary particle requires the assumption of a specific hadronic interaction model, whose suitability has to be verified beforehand. In this work, the energy estimations are based on the CORSIKA-QGSjetII model [5], [6], motivated by the fact that such model reproduces fairly well the distributions of the ratio of the muon and electron sizes measured by KASCADE-Grande as a function of both the electron size and the atmospheric depth [7].

The method described in this paper uses the combined information of the charged particle and muon sizes on an event-by-event basis, with the aim of reducing the systematics on the primary composition in the energy assignment, systematics which are the main sources of uncertainty on methods based on a single component

information ([4], [8]).
The analysis presented here is based on ∼981 days of data collected on the central area of KASCADE-Grande array (∼0.2 km^2) at zenith angles $\theta < 40^\circ$ corresponding to a total acceptance $A = 2.50 \cdot 10^9$ cm$^2\cdot$ sr (exposure $E = 2.12 \cdot 10^{17}$ cm$^2\cdot$ s·sr).

II. TECHNIQUE

The technique has been defined on simulated data assuming a power law with index γ=-3 for the energy spectrum and then applied to the experimental ones. Proton and iron nuclei have been selected as primaries, to represent the two extreme cases. The simulation includes the full air shower development in atmosphere, the response of the detector and its electronics, as well as their uncertainties. Therefore, the reconstructed parameters from simulated showers are obtained exactly in the same way as for real data. Data have been subdivided in 5 angular bins of same acceptance ($\theta <$ 16.7, 16.7 $\leq \theta <$ 24.0, 24.0 $\leq \theta <$ 29.9, 29.9 $\leq \theta <$ 35.1, 35.1 $\leq \theta <$ 40.0) and the analysis is conducted independently in each angular bin. The difference in the results obtained among the angular bins will be considered as one of the sources in the final systematic uncertainty on the energy spectrum. In this way, possible differences in the air shower attenuation in atmosphere (i.e. the zenith angle) between real and simulated data, will be included directly into the systematic uncertainties of the measurement, without applying any correction. The energy assignment is defined as $E = f(N_{ch}, k)$ (see eq. 1), where N_{ch} is the size of the charged particle component and the parameter k is defined through the ratio of the sizes of the N_{ch} and muon (N_μ) components: $k = g(N_{ch}, N_\mu)$ (see eq. 2). The main aim of the k variable is to take into account the average differences in the N_{ch}/N_μ ratio among different primaries with same N_{ch}, and the shower to shower fluctuations for events of the same primary mass:

$$log_{10}(E[GeV]) = [a_p + (a_{Fe} - a_p) \cdot k] \cdot log_{10}(N_{ch}) + \\ + b_p + (b_{Fe} - b_p) \cdot k \quad (1)$$

$$k = \frac{log_{10}(N_{ch}/N_\mu) - log_{10}(N_{ch}/N_\mu)_p}{log_{10}(N_{ch}/N_\mu)_{Fe} - log_{10}(N_{ch}/N_\mu)_p} \quad (2)$$

where,

$$log_{10}(N_{ch}/N_\mu)_{p,Fe} = c_{p,Fe} \cdot log_{10}(N_{ch}) + d_{p,Fe}. \quad (3)$$

The coefficients a, b, c, d are obtained through the fits to the scatter plots $(N_{ch}, N_{ch}/N_\mu)$ and (N_{ch}, E) in the region $6 < log_{10}(N_{ch}) < 8$, which means above the ∼100% trigger efficiency, and up to the energy for which the simulated statistics is sufficiently high. The k parameter is, by definition of eq. 2, a number centered around 0 for a typical proton shower and 1 for a typical iron shower. As an example, figs. 1 and 2 show such scatter plots for the iron component in the 1^{st} angular bin. Similar plots are obtained in the other 4 angular bins as well as for proton primaries.

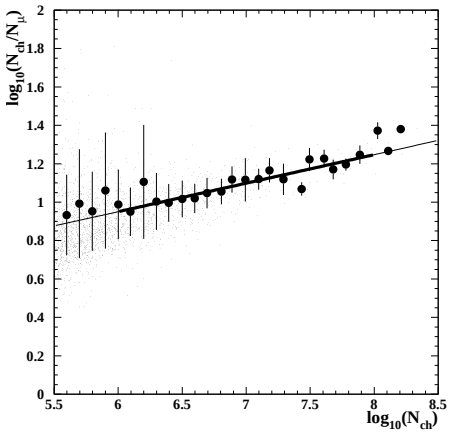

Fig. 1: Scatter plot of N_{ch}/N_μ vs N_{ch} for primary iron nuclei. The small dots indicate single events, while full ones refer to the average values in each N_{ch} interval (ΔN_{ch} = 0.1). The error bar of the full dots indicates the RMS of the distribution of the small dots in each N_{ch} interval. The linear fit is performed on the full dots and their uncertainties in the region $6 < log_{10}(N_{ch}) < 8$ (thick line). Such fit is used to obtain the parameters c and d of expression 3.

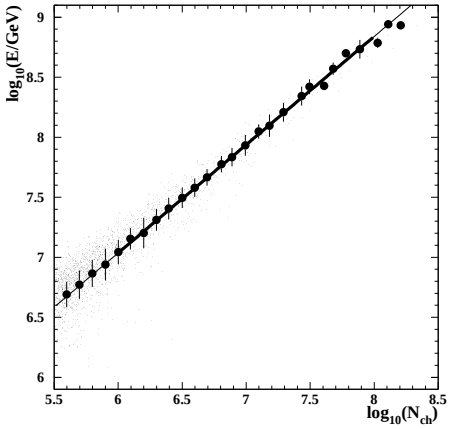

Fig. 2: Scatter plot of E vs N_{ch} for iron primary nuclei. See fig. 1 for detailed explanation of the meaning of dots and error bars. The fit is used to obtain the parameters a and b of expression 1.

In order to check the capability of this technique of correctly reproducing the original energy spectrum, the expressions 1 and 2 have been applied to: a) the simulated energy spectra they have been derived from (H and Fe); b) to other three mass groups (He, C, Si) simulated using the same criteria; c) to the mixture of the five mass groups with 20% abundance each. Fig. 3 shows a comparison between the reconstructed and true energy spectra obtained for the 1^{st} angular bin in case of iron primary nuclei. Similar plots are obtained for the other mass groups and for all angular bins. Fig. 4 summarizes

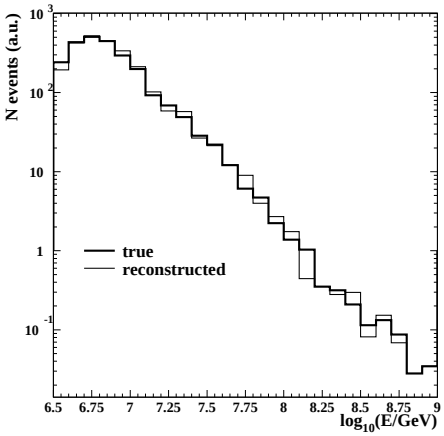

Fig. 3: True (thick line), and reconstructed (thin line) energy spectrum in the 1^{st} angular bin for iron primary nuclei according to expressions 1 and 2.

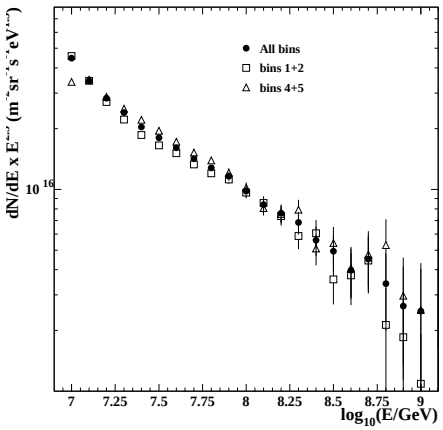

Fig. 5: The experimental energy spectrum (differential intensity multiplied by $E^{2.5}$) as a function of $\log_{10}$(E/GeV) for vertical (bins 1+2), more inclined (bins 4+5) and all events (only statistical uncertainties).

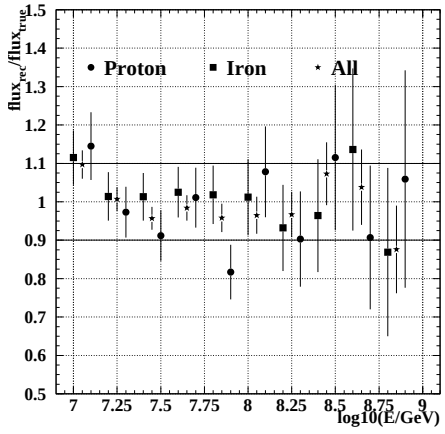

Fig. 4: Ratio between the reconstructed and true spectra (as shown in fig. 3) for protons, iron and all mixed primaries (all angular bins together).

the results on the ratio between reconstructed and true spectra for protons, iron and all mixed primaries. The original energy spectra are fairly well reproduced. The systematic uncertainties are discussed in section III.

III. The reconstructed energy spectrum and its uncertainties

Expressions 1 and 2 have been applied to the experimental data obtaining the intensities shown in fig. 5. A detailed analysis of the systematic uncertainties on the intensities has been conducted taking into account the following effects:

a) Systematic uncertainty from the comparison of the intensity in different angular bins.
b) Systematic uncertainty on the $E(N_{ch})$ relation.
c) Systematic uncertainty related to the capability of reproducing an, *a priori* assumed, single primary spectrum with slope γ = -3 (i.e. difference between true and reconstructed spectra of fig. 3).
d) Systematic uncertainty on the muon lateral distribution function (l.d.f.).

Possible systematic uncertainties on the reconstructed N_{ch} and N_{μ} values compared to the true ones, are already taken into account by the technique itself as the same reconstruction procedure is applied to simulated and real data.

Concerning a), in fig. 5 data points of the 1^{st} and 2^{nd} angular bins have been summed together, and the same for data of the 4^{th} and 5^{th} bins. The semi-difference of the intensity in each energy interval (subtracted from the statistical uncertainty) between vertical and more inclined angular bins provides an estimation of the uncertainty on the relative energy calibration among the angular bins, together with the systematic uncertainty related to possible differences in the air shower attenuation in the atmosphere between real and simulated data. At E $\sim 10^{17}$ ($\sim 3 \cdot 10^{16}$) eV (at higher energies the results are dominated by the statistical uncertainty) the systematic uncertainty is $\sim$5% ($\sim$15%). This result confirms the fact that the technique is self-consistent in the entire angular range used in this analysis and that the QGSjetII model reproduces quite consistently the shower development at least up to zenith angles $\theta < 40$ degrees. The uncertainty on the intensity provides only an indication on the relative uncertainty among expressions 1 and 2 for different angular bins, but doesn't take into account a common systematic effect of all $E = f(N_{ch}, k)$. For this reason, $E = f(N_{ch}, k)$ in simulated data have been artificially modified, at a level in which the systematic effect is clearly visible between the true and reconstructed simulated energy spectra as in fig. 3 and an upper limit has been set and used as systematic effect on the $E(N_{ch})$ conversion relation: at E $\sim 10^{17}$ eV such uncertainty is $< 10\%$.

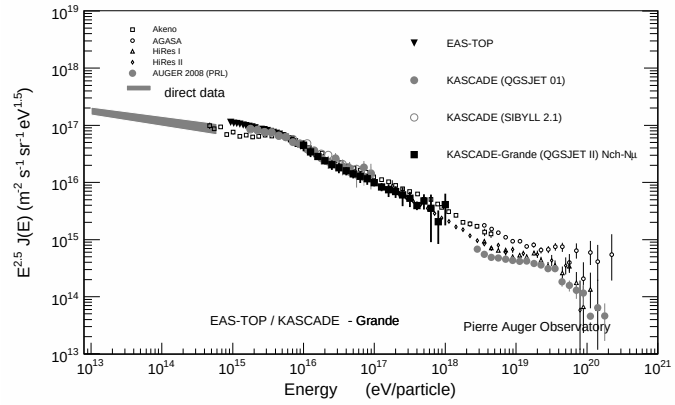

Fig. 6: All primaries energy spectrum (intensity multiplied by $E^{2.5}$) obtained with KASCADE-Grande data applying the N_{ch} - N_{μ} technique. A comparison with other experimental results is also presented.

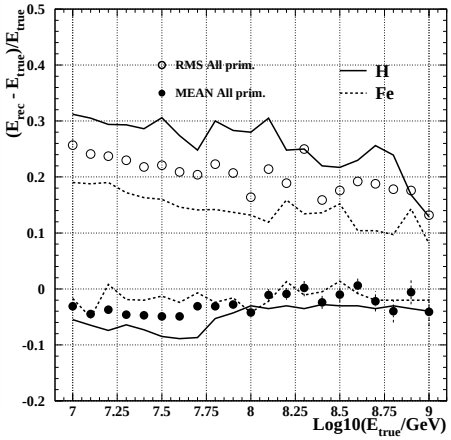

Fig. 7: Resolution in the energy assignment for a mixture of primaries of the 5 simulated mass groups (relative abundance of each group 20%), for H and Fe. The full dots show the offset of the reconstructed energy E_{rec} in bins of true energy E_{true}. The open dots show the RMS of such distributions (see text for details).

A further systematic uncertainty comes from the capability of reproducing the original energy spectrum assuming a single mass composition as shown in fig. 4. In general the ratio between the reconstructed and true fluxes obtained in each energy bin are compatible, inside the statistical uncertainty, with unity. Only at the threshold a systematic effect of $\sim$12% is visible. The typical relative differences in flux at energies E$<10^{17}$ eV are $<$5%.

Regarding d), the energy spectrum has been obtained for different ranges of distance of the shower core from the muon detector. The relative difference in intensity as a function of energy is used to compute a systematic uncertainty due to the assumed l.d.f., and it amounts to $\sim$3% at E $\sim 10^{17}$, slightly increasing with energy.

Finally, it is interesting to look at the relative uncertainty in the energy assignment on an event-by-event basis. Simulated data using the mixture of all primaries have been divided in bins of true energy (E_{true}) and the distributions of the relative differences between reconstructed (E_{rec}) and true energies have been created. As shown in fig. 7 the RMS of such distributions (energy resolution) is $\sim$26% at the energy threshold and decreases with energy, due to the lower fluctuations of the shower development, becoming $<$ 20% at the highest energies. The small offset in the mean values of the distributions at low energies is necessary to take into account the effect of shower fluctuations on a steep spectrum. Such offset does not appear in fig. 4, which indicates that the correct energy spectrum is well reproduced. Results for pure H and Fe primaries are also indicated by lines.

The statistical uncertainty on the intensity is $<$10% up to E$\sim 3 \cdot 10^{17}$ eV. The total uncertainty (statistical and systematic squared together) on the intensity is $<$20% at energies E $< 10^{17}$ eV in the frame of the CORSIKA-QGSjet model.

IV. Results

The all particle energy spectrum of KASCADE-Grande in the 10^{16} - 10^{18} eV energy region using the N_{ch} - N_{μ} technique is shown in fig. 6. The uncertainty in each intensity point is obtained as squared sum of all systematic and statistical uncertainties. At the threshold, the spectrum overlaps well with KASCADE and EAS-TOP spectra. Moreover, it is in agreement with the energy spectra of KASCADE-Grande obtained using other techniques ([4], [8], [9]) which have partially different systematic uncertainties (see [10]).

The mean of the average $\overline{k}$ obtained in different bins of N_{ch} in the range $6 < log_{10}(N_{ch}) < 8$ is $< \overline{k} >$ = 0.64, with bin to bin fluctuations of $\sigma_{\overline{k}} \sim$ 0.06, therefore, perfectly compatible with the limits set by eq. 2 using QGSjetII simulations.

References

[1] G. Navarra et al. - KASCADE-Grande Collaboration, Nucl. Instr. and Meth. A 518 (2004).
[2] F. Di Pierro et al. - KASCADE-Grande Collaboration, These Conference Proceedings.
[3] D. Fuhrmann et al. - KASCADE-Grande Collaboration, These Conference Proceedings.
[4] J.C. Arteaga et al. - KASCADE-Grande Collaboration, These Conference Proceedings.
[5] D. Heck et al. Forschungszentrum Karlsruhe, Report FZKA 6019 (1998).
[6] S. Ostapchenko, *QGSjetII:results for extensive air showers*, astro-ph/0412591.
[7] E. Cantoni et al. - KASCADE-Grande Collaboration, These Conference Proceedings.
[8] D. Kang et al. - KASCADE-Grande Collaboration, These Conference Proceedings.
[9] G. Toma et al. - KASCADE-Grande Collaboration, These Conference Proceedings.
[10] A. Haungs et al. - KASCADE-Grande Collaboration, These Conference Proceedings.

Primary energy reconstruction from the S(500) observable recorded with the KASCADE-Grande detector array

G. Toma[§], W.D. Apel[*], J.C. Arteaga[†,xi], F. Badea[*], K. Bekk[*], M. Bertaina[‡], J. Blümer[*,†], H. Bozdog[*], I.M. Brancus[§], M. Brüggemann[¶], P. Buchholz[¶], E. Cantoni[‡,‖], A. Chiavassa[‡], F. Cossavella[†], K. Daumiller[*], V. de Souza[†,xii], F. Di Pierro[‡], P. Doll[*], R. Engel[*], J. Engler[*], M. Finger[*], D. Fuhrmann[**], P.L. Ghia[‖], H.J. Gils[*], R. Glasstetter[**], C. Grupen[¶], A. Haungs[*], D. Heck[*], J.R. Hörandel[†,xiii], T. Huege[*], P.G. Isar[*], K.-H. Kampert[**], D. Kang[†], D. Kickelbick[¶], H.O. Klages[*], P. Łuczak[††], H.J. Mathes[*], H.J. Mayer[*], J. Milke[*], B. Mitrica[§], C. Morello[‖], G. Navarra[‡], S. Nehls[*], J. Oehlschläger[*], S. Ostapchenko[*,xiv], S. Over[¶], M. Petcu[§], T. Pierog[*], H. Rebel[*], M. Roth[*], H. Schieler[*], F. Schröder[*], O. Sima[‡‡], M. Stümpert[†], G.C. Trinchero[‖], H. Ulrich[*], A. Weindl[*], J. Wochele[*], M. Wommer[*], J. Zabierowski[††]

[*]*Institut für Kernphysik, Forschungszentrum Karlsruhe, 76021 Karlsruhe, Germany*
[†]*Institut für Experimentelle Kernphysik, Universität Karlsruhe, 76021 Karlsruhe, Germany*
[‡]*Dipartimento di Fisica Generale dell'Università, 10125 Torino, Italy*
[§]*National Institute of Physics and Nuclear Engineering, 7690 Bucharest, Romania*
[¶]*Fachbereich Physik, Universität Siegen, 57068 Siegen, Germany*
[‖]*Istituto di Fisica dello Spazio Interplanetario, INAF, 10133 Torino, Italy*
[**]*Fachbereich Physik, Universität Wuppertal, 42097 Wuppertal, Germany*
[††]*Soltan Institute for Nuclear Studies, 90950 Lodz, Poland*
[‡‡]*Department of Physics, University of Bucharest, 76900 Bucharest, Romania*
[xi]*now at: Universidad Michoacana, Morelia, Mexico*
[xii]*now at: Universidade de São Paulo, Instituto de Fîsica de São Carlos, Brasil*
[xiii]*now at: Dept. of Astrophysics, Radboud University Nijmegen, The Netherlands*
[xiv]*now at: University of Trondheim, Norway*

***Abstract*. Previous EAS investigations have shown that the charged particle density becomes independent of the primary mass at large but fixed distances from the shower core and that it can be used as an estimator for the primary energy. The particular radial distance from the shower axis where this effect takes place is dependent on the detector layout. For the KASCADE-Grande experiment it was shown to be around 500 m. A notation S(500) is used for the charged particle density at this specific distance. Extensive simulation studies have shown that S(500) is mapping the primary energy. We present results on the reconstruction of the primary energy spectrum of cosmic rays from the experimentally recorded S(500) observable using the KASCADE-Grande array. The constant intensity cut (CIC) method is applied to evaluate the attenuation of the S(500) observable with the zenith angle. A correction is subsequently applied to correct all recorded S(500) values for attenuation. The all event S(500) spectrum is obtained. A calibration of S(500) values with the primary energy has been worked out by simulations and has been used for conversion thus providing the possibility to obtain the primary energy spectrum (in the energy range accessible to the KASCADE-Grande array, 10^{16}-10^{18} eV). An evaluation of systematic uncertainties induced by different factors is also given.**

***Keywords*: KASCADE-Grande, EAS, primary energy spectrum**

I. INTRODUCTION

Hillas has shown that the EAS particle density distributions at a certain distance from the shower core (dependent on the EAS detection array) becomes independent of the primary mass and can be used as a primary energy estimator [1]. Following this feature, a method can be derived to reconstruct the primary energy spectrum from the particular value of the charged particle density, observed at such specific radial ranges. The technique has been used by different detector arrays in order to reconstruct the primary energy spectrum of the cosmic radiation [2]. In the case of the KASCADE-Grande array (at Forschungszentrum Karlsruhe, Germany, 110 m a.s.l.) [3], detailed simulations [4] have shown that the particular distance for which this effect takes place is about 500 m (see fig. 1). Therefore an observable of interest in the case of KASCADE-Grande is the charged particle density at 500 m distance from the shower core, noted as S(500) in the following. The study has been performed for both simulated (fig. 1) and experimental (fig. 2) events, using identical reconstruction procedures [5]. The reconstruction begins with recording the energy deposits of particles in the KASCADE-Grande detector stations and the associated temporal information (arrival times of particles). The

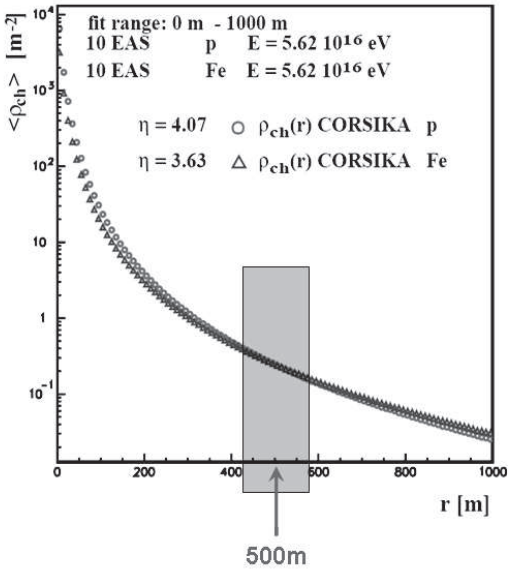

Fig. 1: Simulations show that, for the case of the KASCADE-Grande experimental layout, the particle density becomes independent of the primary mass around 500 m distance from shower core; this plot shows averaged simulated lateral distributions for different primary types with equal energy.

arrival direction of the shower is reconstructed from the particle arrival times. Using appropriate **L**ateral **E**nergy **C**orrection **F**unctions (**LECF**), the energy deposits are converted into particle densities. The LECF functions are dependent on the shower zenith angle [6] and take into account the fact that an inclined particle will deposit more energy in detectors due to its longer cross path. For every event, the obtained lateral density distribution is approximated by a Linsley [7] **L**ateral **D**ensity **F**unction (**LDF**) in order to evaluate the particle density at the radial range of interest, 500 m. To ensure good reconstruction quality, the approximation is performed over a limited range of the lateral extension, namely only in the 40 m $-$ 1000 m radial range.

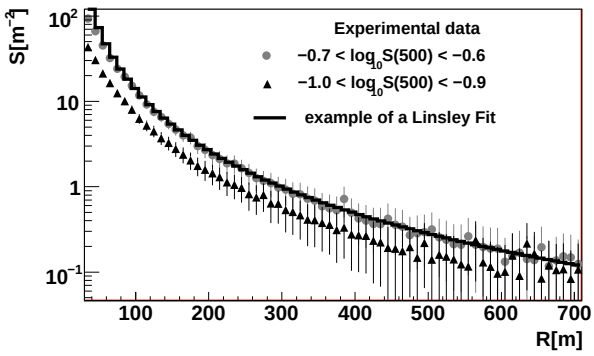

Fig. 2: Averaged lateral density distributions of experimentally recorded EAS samples for two $S(500)$ ranges.

II. Efficiency and quality cuts

For the experimental EAS sample, the total time of acquisition was ≈902 days. Showers were detected on a 500 x 600 m^2 area up to 30° zenith angle. The 30° zenith angle limit was imposed due to certain systematic effects affecting the reconstruction of small showers above this threshold. In order to ensure good reconstruction quality, several quality cuts were imposed on the data. The same cuts were used for both simulated and experimental events. Only those events are accepted for which the reconstructed shower core is positioned inside the detector array and not too close to the border. A good quality of the fit to the Linsley distribution is a further important criterion. Fig. 3 shows the total reconstruction efficiency for different zenith angle intervals (the full efficiency is reached at around $\log_{10}(E_0/\mathrm{GeV})$=7.5).

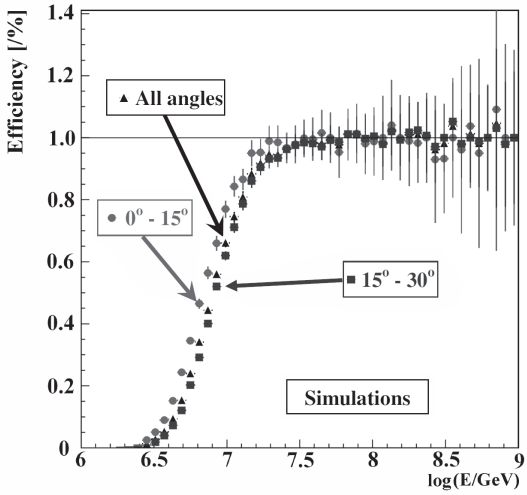

Fig. 3: Reconstruction efficiency for different zenith angle ranges and for the entire shower sample (events triggering more than 24 stations).

III. The Constant Intensity Cut method

Before converting the recorded $S(500)$ values into the corresponding primary energy values (via a relation derived from simulation studies), one has to take into account the atmospheric attenuation affecting the charged particle densities observed on ground. For more inclined showers, the particles have to cross a longer path through the atmosphere before reaching the detector level. In such a case, events generated by identical primaries reach the detector level at different stages of EAS development, dependent on their angles of incidence. In order to bring all recorded EAS events to the same level of consistency, one has to eliminate the influence of the zenith angle on the recorded $S(500)$ observables. This is achieved by applying the **C**onstant **I**ntensity **C**ut (**CIC**) method. The $S(500)$ attenuation is visible if $S(500)$ spectra are plotted for different EAS incident angles. For this, the recorded events are separated into several

sub-samples characterized by their angle of incidence. The angular intervals are chosen in a way that they open equal solid angles: 0° - 13.2°, 13.2° - 18.8°, 18.8° - 23.1°, 23.1° - 26.7° and 26.7° - 30.0°. In fig. 4 the attenuation is visible, as $S(500)$ spectra are shifted towards lower values for increasing zenith angles. The CIC method assumes that a given intensity value in the energy spectrum corresponds to a given primary energy of particles and, since the $S(500)$ is mapping the primary energy spectrum, it is expected that this property of the intensity is true also in the case of $S(500)$ spectra. Therefore a constant intensity cut on integral $S(500)$ spectra is performed, effectively cutting them at a given primary energy. The intersection of the cut line with each spectrum will give the attenuated $S(500)$ value at the corresponding angle of incidence for a given primary energy. A linear interpolation is used between the two neighboring points in the integral spectrum in order to convert the value of the intensity into particle density for each angular bin. The observed attenuation can be corrected by parameterizing the attenuation curve and correcting all events by bringing their $S(500)$ value to their corresponding value at a given reference angle of incidence (see fig. 5; the parameterization with the lowest χ^2 was chosen, namely the one corresponding to intensity 3000). For the present study this angle is considered to be 21°, since the zenith angular distribution for the recorded EAS sample peaks at this value. The CIC method implies several mathematical transformations of data before obtaining the values corrected for attenuation of the $S(500)$ observable: interpolations and analytical parameterizations (as mentioned in the above description of the CIC method). These operations introduce some systematic uncertainties on the final result of the CIC method. The CIC-induced systematic uncertainty of the corrected $S(500)$ value is evaluated by propagating the errors of fit parameters. The resulting CIC-induced error of the $S(500)$ observable will be taken into account later when evaluating the total systematic uncertainty of the reconstructed primary energy.

IV. Conversion to energy

After correcting the recorded $S(500)$ values for attenuation, we can proceed to convert each of them to the corresponding primary energy value. A calibration of the primary energy E_0 with $S(500)$ was derived from simulations (see fig. 6). The Monte-Carlo CORSIKA EAS simulation tool was used to simulate air showers (with QGSJET II model embedded for high energy interactions). In fig. 6, two slightly different dependencies are shown for two primaries, a light primary (proton) and a heavy primary (Fe). The two dependencies are almost identical, a feature that is expected due to the mass insensitivity of the $S(500)$ observable. This calibration is used to convert all $S(500)$ values into the corresponding primary energies. The spectrum of primary energy is thus reconstructed. Fig. 7 shows the reconstructed energy spectrum compared with spectra reconstructed by

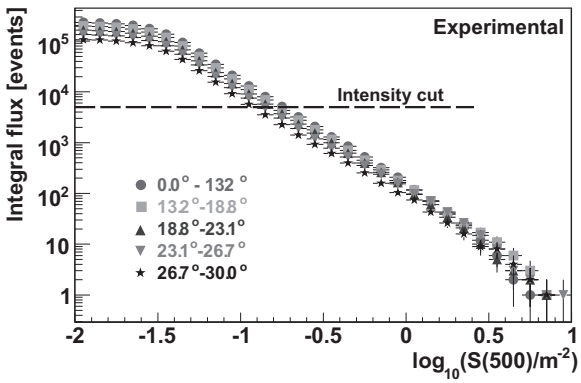

Fig. 4: Integral $S(500)$ spectra; the horizontal line is a constant intensity cut at an arbitrarily chosen intensity; attenuation length of $S(500)$ was evaluated at 347.38 ± 21.65 g·cm^{-2}

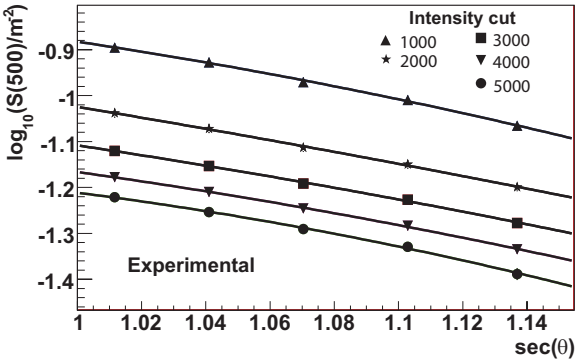

Fig. 5: Attenuation of the $S(500)$ observable with the angle of incidence; the different curves show different arbitrarily chosen intensity cuts.

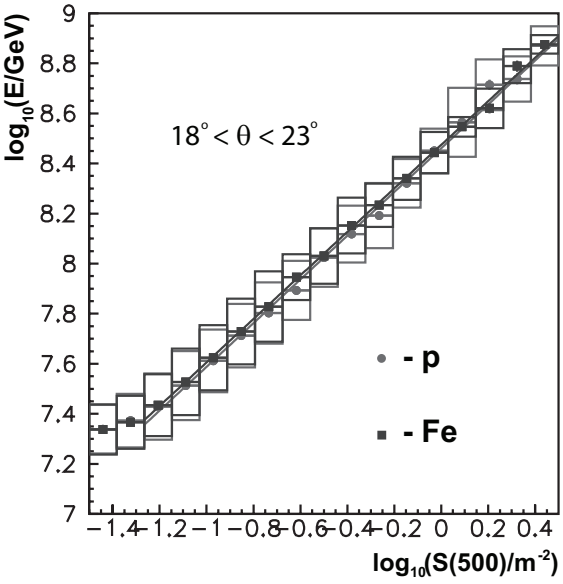

Fig. 6: E_0 - $S(500)$ calibration curve for two different primaries; the box-errors are the errors on the spread; the errors on the mean are represented with bars.

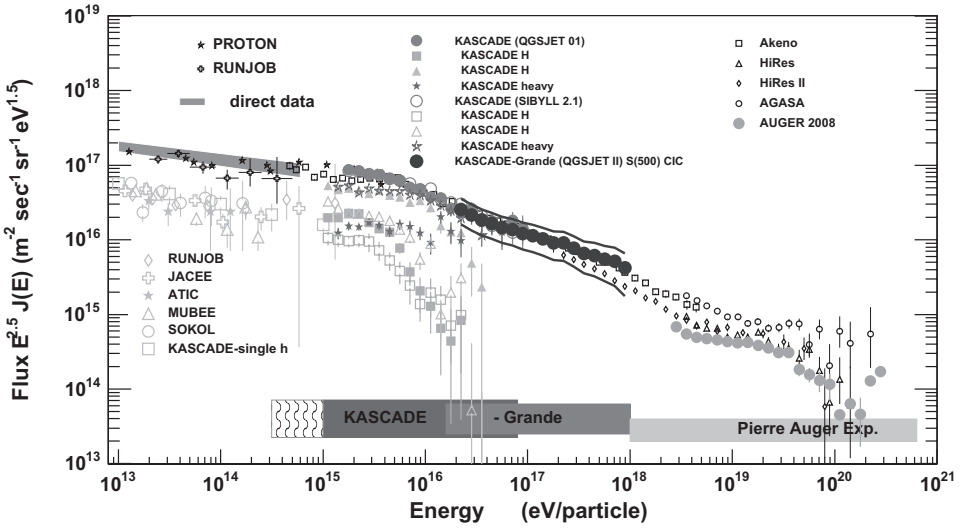

Fig. 7: Reconstructed experimental energy spectrum by KASCADE-Grande from $S(500)$/CIC, multiplied by $E^{2.5}$ compared with results of other experiments; the continuous lines above and below the spectrum are the error envelopes and show combined statistical and systematic uncertainties.

other experiments. The spectrum is plotted starting from the maximum efficiency threshold (see fig. 3). For the systematic contribution to the total error, several sources of systematic uncertainties have been identified and their contributions were evaluated. Thus, the spectral index of the simulated shower sample was equal to -2 and was acting as a source of systematic uncertainty. In a similar fashion, the $S(500)$-E_0 calibration and the CIC method itself were also introducing systematic uncertainties. In all, these three sources were contributing with an uncertainty of $\approx$1% from the total flux value. Other sources that were considered were the Monte-Carlo statistical uncertainty of the simulated shower sample and the choosing of a certain reference angle at which to perform the $S(500)$ attenuation correction (contributing with $\approx$7% and $\approx$30% relative uncertainty). The relative contribution of all identified sources over the full efficiency range was fairly constant for any given source and in total amounts for about 37% of the recorded flux value. The energy resolution has also been evaluated from simulations by calculating the difference between the true and the reconstructed primary energy (applying CIC to the simulated data). The energy resolution was found to be 22% for E_0=10^{17} eV (for all primaries) and is fairly constant over the entire full efficiency range.

V. Conclusions

The primary energy spectrum has been reconstructed from the particle densities recorded in the stations of the KASCADE-Grande array. In the particular case of KASCADE-Grande, the charged particle density at 500 m distance from the shower core was shown to be primary mass insensitive. The CIC method was applied on the recorded $S(500)$ spectrum in order to correct each shower for attenuation effects. Using a simulation-derived calibration between $S(500)$ and E_0 (based on the QGSJET II model for high energy interactions), the attenuation corrected $S(500)$ spectrum has been converted into primary energy spectrum. The $S(500)$ derived KASCADE-Grande spectrum is composition independent and comes in good agreement with the spectrum of lower energies previously reconstructed by the KASCADE array. Future investigations will concentrate also on improving the quality of the reconstruction along with gaining a better understanding of the uncertainties induced by the reconstruction technique.

Acknowledgment

The KASCADE-Grande experiment is supported by the BMBF of Germany, the MIUR and INAF of Italy, the the Polish Ministry of Science and Higher Education (grant 2009-2011), and the Romanian Ministry of Education and Research.

References

[1] A.M. Hillas et al., Proc.12th ICRC, Hobart 3 (1971) 1001
[2] D.M. Edge et al., J. Phys. A: Math. Nucl. Gen.6 (1973) 1612; M. Nagano et al., J. Phys. G:Nucl. Part. Phys.10(1984) 1295; Y. Dai et al., J.Phys.G: Nucl. Part. Phys. 14(1998) 793; M. Roth et al.- Auger collaboration Proc. 28th ICRC, Tsukuba, Japan, vol. 2 (2003) 333
[3] A. Haungs et al., KASCADE-Grande collaboration, Proc. 28th ICRC, Tsukuba, Japan, vol.2 (2003)985
[4] H. Rebel and O. Sima et al. KASCADE-Grande collaboration, Proc. 29th ICRC, Pune, India, vol.6 (2005)297 I.M. Brancus et al. KASCADE-Grande collaboration, Proc. 29th ICRC, Pune, India, vol.6 (2005)361
[5] O. Sima et al., Report FZKA 6985, Forschungszentrum Karlsruhe 2004
[6] G. Toma et al., Proc. 26th ECRS 2006, Lisbon, Portugal, so-134; CERN program library, GEANT users guide, (1997)
[7] J. Linsley et al., Journ. Phys. Soc. Japan 17 (1962) A-III

Performance of the KASCADE-Grande array

F. Di Pierro[‡], W.D. Apel[*], J.C. Arteaga[†,xi], F. Badea[*], K. Bekk[*], M. Bertaina[‡], J. Blümer[*,†], H. Bozdog[*], I.M. Brancus[§], M. Brüggemann[¶], P. Buchholz[¶], E. Cantoni[‡,‖], A. Chiavassa[‡], F. Cossavella[†], K. Daumiller[*], V. de Souza[†,xii], P. Doll[*], R. Engel[*], J. Engler[*], M. Finger[*], D. Fuhrmann[**], P.L. Ghia[‖], H.J. Gils[*], R. Glasstetter[**], C. Grupen[¶], A. Haungs[*], D. Heck[*], J.R. Hörandel[†,xiii], T. Huege[*], P.G. Isar[*], K.-H. Kampert[**], D. Kang[†], D. Kickelbick[¶], H.O. Klages[*], P. Łuczak[††], H.J. Mathes[*], H.J. Mayer[*], J. Milke[*], B. Mitrica[§], C. Morello[‖], G. Navarra[‡], S. Nehls[*], J. Oehlschläger[*], S. Ostapchenko[*,xiv], S. Over[¶], M. Petcu[§], T. Pierog[*], H. Rebel[*], M. Roth[*], H. Schieler[*], F. Schröder[*], O. Sima[‡‡], M. Stümpert[†], G. Toma[§], G.C. Trinchero[‖], H. Ulrich[*], A. Weindl[*], J. Wochele[*], M. Wommer[*], J. Zabierowski[††]

[*]*Institut für Kernphysik, Forschungszentrum Karlsruhe, 76021 Karlsruhe, Germany*
[†]*Institut für Experimentelle Kernphysik, Universität Karlsruhe, 76021 Karlsruhe, Germany*
[‡]*Dipartimento di Fisica Generale dell'Università, 10125 Torino, Italy*
[§]*National Institute of Physics and Nuclear Engineering, 7690 Bucharest, Romania*
[¶]*Fachbereich Physik, Universität Siegen, 57068 Siegen, Germany*
[‖]*Istituto di Fisica dello Spazio Interplanetario, INAF, 10133 Torino, Italy*
[**]*Fachbereich Physik, Universität Wuppertal, 42097 Wuppertal, Germany*
[††]*Soltan Institute for Nuclear Studies, 90950 Lodz, Poland*
[‡‡]*Department of Physics, University of Bucharest, 76900 Bucharest, Romania*
[xi]*now at: Universidad Michoacana, Morelia, Mexico*
[xii]*now at: Universidade de São Paulo, Instituto de Fîsica de São Carlos, Brasil*
[xiii]*now at: Dept. of Astrophysics, Radboud University Nijmegen, The Netherlands*
[xiv]*now at: University of Trondheim, Norway*

***Abstract*. The KASCADE-Grande experiment consists of the basic KASCADE complex and of an extended array, Grande, made of 37x10 m^2 scintillation detectors spread over an area of 700 x 700 m^2. Grande enables triggers and reconstruction of primary cosmic rays in the energy range of 10^{16} to 10^{18} eV through the detection of the all-charged particle component of the related Extensive Air Showers. The experimental set-up allows, for a subsample of the registered showers, detailed comparisons of the data with measurements of the original KASCADE array (252 unshielded detectors, with 490 m^2 sensitive area and 192 shielded muon detectors with 622 m^2 sensitive area spread over 200 x 200 m^2) on an event by event basis. We discuss the Grande reconstruction procedures and accuracies. The lateral charged particle distributions are measured over a wide range of core distances, the results of the measurement are presented.**

***Keywords*: KASCADE-Grande, Reconstruction, LDF**

I. Introduction

The extensive air shower experiments KASCADE and EAS-TOP have shown that the change of the slope in the energy spectrum ("the knee") for different elemental groups occurs at different energies [1], [2]. For the lightest nuclei the knee has been measured at $3 \cdot 10^{15}$ eV. These results support the general view which attributes the change of the spectral index to processes of magnetic confinement, occurring either at acceleration regions, or as diffusive leakage from the Galaxy (or both). Such processes predict that the maximum energy for a specific primary nucleus depends on its atomic number Z.
The Grande array increases the collecting area of KASCADE in order to extend the measured energy range. The aim of KASCADE-Grande [3] is to perform energy, composition and anisotropy studies up to 10^{18} eV, i.e. in the region where the transition from galactic to extragalactic cosmic rays is supposed to happen.

II. Experimental setup

The KASCADE-Grande experiment is located at Forschungszentrum Karlsruhe, Germany (49.1^o N, 8.4^o E) at 110 m a.s.l., corresponding to an average atmospheric depth of 1023 g/cm^2. It consists of an extension of the KASCADE [4] experiment with Grande, an array of plastic scintillators obtained reassembling the EAS-TOP [5] electromagnetic detector, which expands the collecting area, and Piccolo a smaller array providing a fast trigger common to all components.
The KASCADE-Grande detectors and their main characteristics are listed in table I and their layout is shown in fig. 1.

The KASCADE array is composed of 252 detector stations on a square grid with 13 m spacing.
It is composed of:

- e/γ-detectors which mainly consists of 2/4 liquid scintillator units (1 m diameter, 5 cm thick);

Detector	Particle	Area m^2	Threshold
Grande array (plastic scintillators)	charged	370	3 MeV
Piccolo array (plastic scintillators)	charged	80	3 MeV
KASCADE array (liquid scint.)	e/γ	490	5 MeV
KASCADE array (shielded pl. scint.)	μ	622	230 MeV
Muon tracking det. (streamer tubes)	μ	3×128	800 MeV
Multi wire proportional chambers	μ	2×129	2.4 GeV
Limited streamer tubes	μ	250	2.4 GeV
Calorimeter	h	9×304	50 GeV

TABLE I: The KASCADE-Grande detectors, their total sensitive area and threshold for vertical particle.

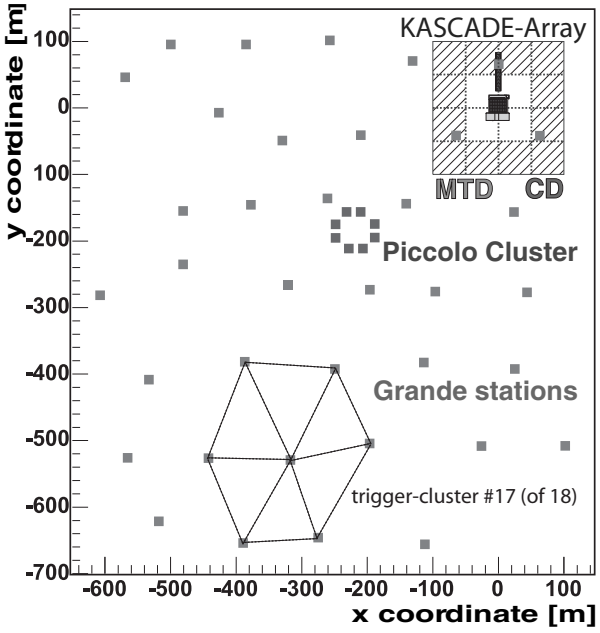

Fig. 1: Layout of the KASCADE-Grande experiment.

- μ-detectors which mainly consists of 4 plastic scintillators (90 x 90 x 3 cm^3), placed below the e/γ-detectors and a shielding (10 cm of lead and 4 cm of iron, which entails a threshold of 230 MeV for vertical muons).

The Grande array consists of 37 stations with an average spacing of 137 m over a 700 x 700 m^2 area. Every detector station consists of 10 m^2 of plastic scintillator organized in 16 units (80 x 80 x 4 cm^3). Each unit is equipped with a high gain (HG) photomultiplier (pmt) and the 4 central units are additionally equipped with a low gain (LG) photomultiplier to increase the dynamic range. The signals from the pmts are added up through passive mixers, one for the HG and one for the LG pmts. The output signals are preamplified and shaped by Shaping Amplifiers into 3 analog signals, digitized by 3 Peak-ADCs, covering the dynamic ranges $0.3 \div 8$, $2 \div 80$, $20 \div 800$ particles/m^2 respectively. The overlapping ranges between the scales are used for cross-calibration. Each detector is continuously monitored and calibrated by means of single muon spectra. The systematic uncertainty on the measured particle density by each detector is less than 15% and the statistical uncertainties are dominated by poissonian fluctuations.

The array is divided in 18 trigger clusters of 7 modules each (6 modules in an hexagon and a central one). The trigger rate is 0.5 Hz and becomes fully efficient for all primaries at $E_0 = 10^{16}$ eV.

III. Reconstruction of extensive air showers

Core position, arrival direction and total number of charged particles are reconstructed in an iterative fit procedure of the energy deposit and timing measurements by the Grande array detectors. The energy deposit is converted to charged particle density through a function of the core distance, derived from shower and detector simulations, taking into account energy deposit of charged particles and gamma conversion [6]. The fitting functions have been derived from full shower and detector simulations. The shower front is fitted with:

$$\overline{t} = 2.43 \cdot (1 + \frac{r}{30})^{1.55}\mathrm{ns}$$

with a time spread:

$$\sigma_{\overline{t}} = 1.43 \cdot (1 + \frac{r}{30})^{1.39}\mathrm{ns}$$

where r is the distance from shower axis in meter. The lateral distribution is fitted with a modified NKG function:

$$\rho_{ch} = C(s) N_{ch} \left(\frac{r}{30}\right)^{s-1.6} \left(1 + \frac{r}{30}\right)^{s-3.4}$$

and the normalization factor is:

$$C(s) = \frac{\Gamma(3.4-s)}{2\pi \cdot 30^2 \cdot \Gamma(s-1.6+2) \cdot \Gamma(1.6+3.4-2s-2)}$$

The total number of muons is obtained by means of a fit of the muon densities measured by the KASCADE array with a Lagutin function (core position is fixed):

$$\rho_\mu(r) = N_\mu \cdot f(r)$$

$$f(r) = \frac{0.28}{320^2}\left(\frac{r}{320}\right)^{-0.69}\left(1+\frac{r}{320}\right)^{-2.39}\left(1+\left(\frac{r}{10 \cdot 320}\right)^2\right)^{-1.0}$$

Reconstruction procedure and accuracy of the muonic component are described in [7].

A single event reconstruction, with the particle densities measured by Grande and by the KASCADE array muon detectors and the corresponding lateral distribution fits, is shown in figure 2.

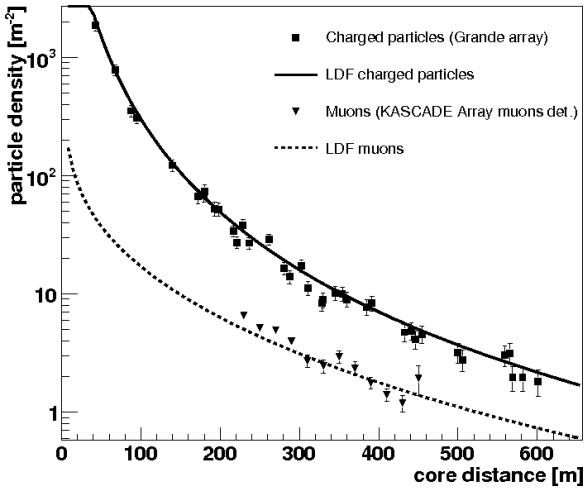

Fig. 2: Lateral distributions of a single event: muon densities measured by KASCADE array muon detector and muon ldf (black triangles represent the average densities in rings of 20 m, while the fit is performed on individual detector measurements); all-charged particles measured by Grande detectors and all-charged ldf. The parameters of the shown event are:
x_{core} = -307 m, y_{core} = -86 m, lg N_{ch} = 7.9, lg N_{μ} = 6.7, Θ = 16.5^o, Φ = 245.5^o.

IV. Reconstruction accuracies

For a subsample of the events collected by the Grande array it is possible to compare on an event by event basis the two independent reconstructions of KASCADE and Grande. This provides the unique opportunity of evaluating the reconstruction accuracies of the Grande array by a direct comparison with an independent experiment instead of the usual procedure involving simulations. Since the KASCADE array is much more dense (sensitive area over fiducial area = 0.06) than Grande (sensitive area over fiducial area = 0.002), the contribution to the differences in the reconstructed observables from KASCADE is negligible and its reconstruction can be taken as reference. The subsample is obtained accordingly to the following selection criteria: maximum energy deposit in the central station of the hexagon overlapping with KASCADE, core position within a circle of 90 m radius from KASCADE center, zenith angle less than 40^o. The scatter plot with the shower sizes reconstructed by both arrays is shown in fig. 3. By means of such a comparison the Grande reconstruction accuracies are found to be:

- shower size (fig. 4): systematic $\leq$ 5%, statistical $\leq$ 15%;
- arrival direction (figs. 5, 6): $\sigma_{\Psi} \approx 0.7^o$;
- core position (fig. 7): $\sigma_{core} \approx$ 5 m.

V. Mean lateral distribution of charged particles

In fig. 8 the experimental mean lateral distributions for vertical showers ($0^o \div 18^o$) and for different shower sizes in the range 6.2 $<$ lg N_{ch} $<$ 7.8 are shown.

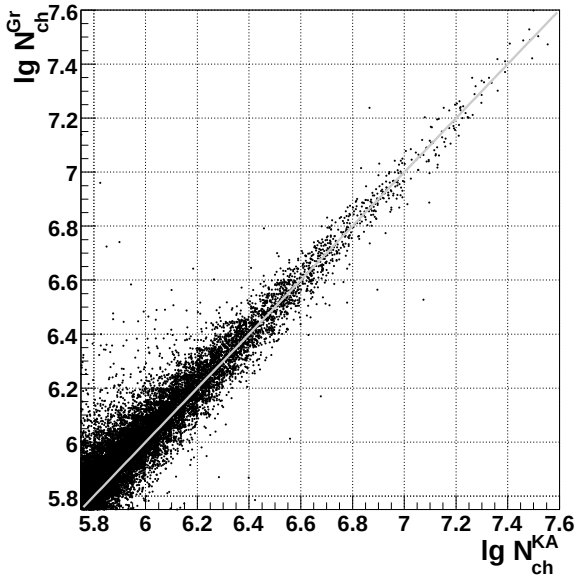

Fig. 3: Scatter plot of the shower sizes (charged particles) reconstructed by KASCADE (x-axis) and Grande (y-axis).

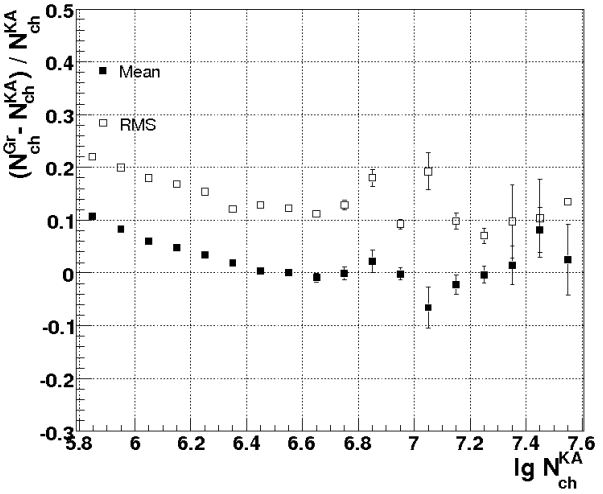

Fig. 4: Mean value and Root Mean Square of the distribution of the shower size differences over shower size reconstructed by KASCADE (N_{ch}^{KA}) as function of N_{ch}^{KA}.

The lines represent the lateral distribution functions with mean N_{ch} and s-parameter values of the corresponding N_{ch} bin. The lateral distributions measured by the Grande array extend up to more than 700 m and the used lateral distribution function represents the data well over the whole range.
In fig. 9 the lateral distributions are shown in a region closer to the core and with the core position reconstructed independently by KASCADE, showing that the good description of measured particle densities by the functions is not just a consequence of the fit procedure.

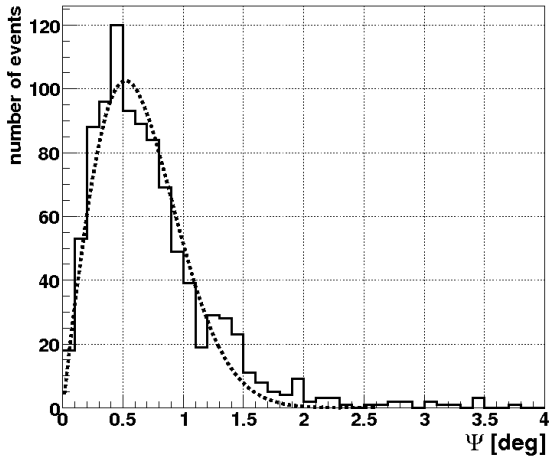

Fig. 5: Angle (Ψ) between the arrival directions reconstructed by KASCADE and Grande, in a bin of N_{ch}^{KA} ($6.2 < \lg N_{ch}^{KA} < 6.3$).

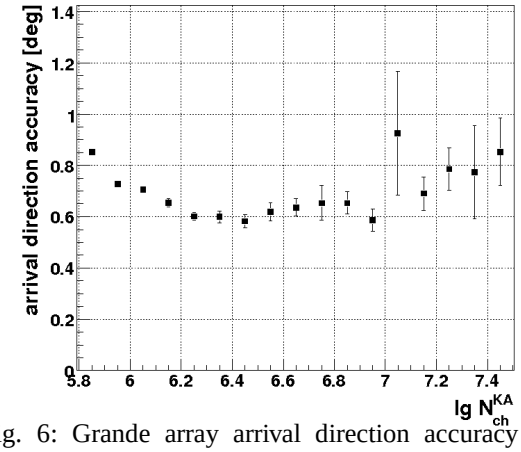

Fig. 6: Grande array arrival direction accuracy from Rayleigh distribution of angular differences (Ψ).

VI. Conclusions

The reconstruction procedures and the achieved accuracies of the Grande array have been studied experimentally and shown. The result is that Grande provides a large acceptance ($2.5{\cdot}10^9$ cm$^2{\cdot}$sr for $E_0 > 10^{16}$eV, zenith angle $< 40^o$) and it is accurate enough (N_{ch} uncertainty: systematic $< 5\%$, statistical $< 15\%$) for the aims of present analysis [8]. The used lateral distribution function describes experimental lateral distributions over the whole 700 m range. Finally the mean lateral distributions of charged particle have been shown.

References

[1] T. Antoni et al. - KASCADE Coll., Astrop. Phys. 24, 1 (2005),
[2] M. Aglietta et al. EAS-TOP Coll., Astrop. Phys. 21, 583 (2004),
[3] G. Navarra et al. - KASCADE-Grande Coll., Nucl.Instr. and Meth. A 518 (2004),
[4] T. Antoni et al KASCADE Coll., Nucl. Instr. and Meth. A 513, 490 (2003),
[5] M. Aglietta et al. - EAS-TOP Coll., Nucl.Instr. and Meth. A 336 (1993),
[6] R. Glasstetter et al. - KASCADE-Grande Coll. - Proc. 28^{th} ICRC, Tsukuba, Japan, vol. 2 (2003) 781,
[7] D. Fuhrmann for the KASCADE-Grande Coll., these proceedings,
[8] E. Cantoni for the KASCADE-Grande Coll., these proceedings.

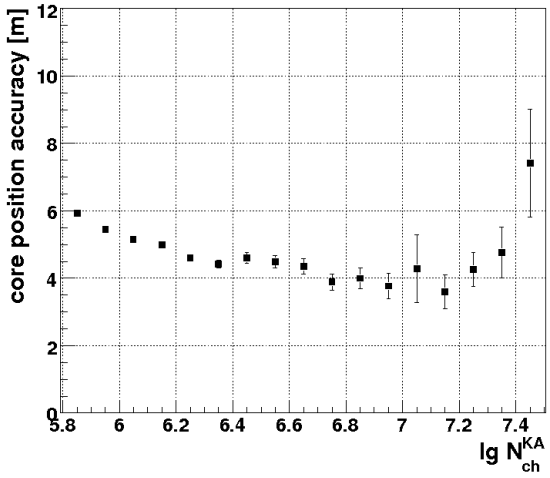

Fig. 7: Grande array core position accuracy from Rayleigh distribution of core position differences.

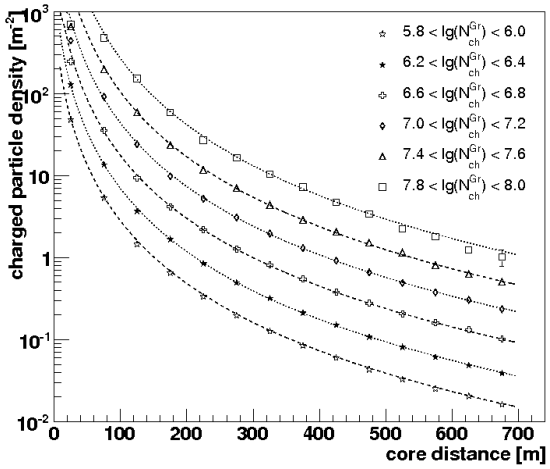

Fig. 8: Mean lateral distributions of charged particles, grouped in $\lg N_{ch}^{Gr}$ bins.

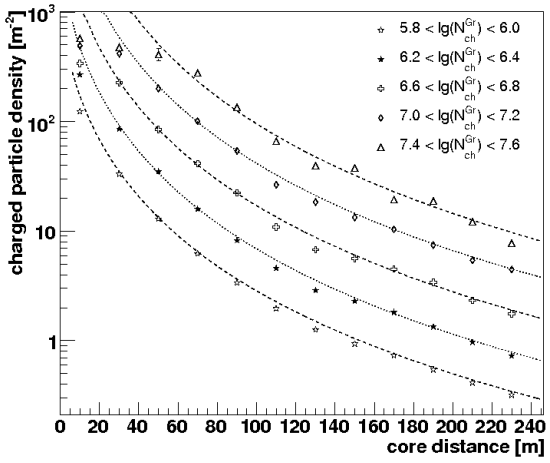

Fig. 9: Mean lateral distributions of charged particles closer to the core and with core position reconstructed independently by KASCADE.

Muonic Component of Air Showers Measured by the KASCADE-Grande Experiment

D. Fuhrmann[**], W.D. Apel[*], J.C. Arteaga[†,xi], F. Badea[*], K. Bekk[*], M. Bertaina[‡], J. Blümer[*,†], H. Bozdog[*] I.M. Brancus[§], M. Brüggemann[¶], P. Buchholz[¶], E. Cantoni[‡,‖], A. Chiavassa[‡], F. Cossavella[†], K. Daumiller[*], V. de Souza[†,xii], F. Di Pierro[‡], P. Doll[*], R. Engel[*], J. Engler[*], M. Finger[*], P.L. Ghia[‖], H.J. Gils[*], R. Glasstetter[**], C. Grupen[¶], A. Haungs[*], D. Heck[*], J.R. Hörandel[†,xiii], T. Huege[*], P.G. Isar[*], K.-H. Kampert[**], D. Kang[†], D. Kickelbick[¶], H.O. Klages[*], Y. Kolotaev[¶], P. Łuczak[††], H.J. Mathes[*], H.J. Mayer[*], J. Milke[*], B. Mitrica[§], C. Morello[‖], G. Navarra[‡], S. Nehls[*], J. Oehlschläger[*], S. Ostapchenko[*,xiv], S. Over[¶], M. Petcu[§], T. Pierog[*], H. Rebel[*], M. Roth[*], H. Schieler[*], F. Schröder[*], O. Sima[‡‡], M. Stümpert[†], G. Toma[§], G.C. Trinchero[‖], H. Ulrich[*], W. Walkowiak[¶], A. Weindl[*], J. Wochele[*], M. Wommer[*], J. Zabierowski[††]

[*]*Institut für Kernphysik, Forschungszentrum Karlsruhe, 76021 Karlsruhe, Germany*
[†]*Institut für Experimentelle Kernphysik, Universität Karlsruhe, 76021 Karlsruhe, Germany*
[‡]*Dipartimento di Fisica Generale dell'Università, 10125 Torino, Italy*
[§]*National Institute of Physics and Nuclear Engineering, 7690 Bucharest, Romania*
[¶]*Fachbereich Physik, Universität Siegen, 57068 Siegen, Germany*
[‖]*Istituto di Fisica dello Spazio Interplanetario, INAF, 10133 Torino, Italy*
[**]*Fachbereich Physik, Universität Wuppertal, 42097 Wuppertal, Germany*
[††]*Soltan Institute for Nuclear Studies, 90950 Lodz, Poland*
[‡‡]*Department of Physics, University of Bucharest, 76900 Bucharest, Romania*
[xi]*now at: Universidad Michoacana, Morelia, Mexico*
[xii]*now at: Universidade de São Paulo, Instituto de Fîsica de São Carlos, Brasil*
[xiii]*now at: Dept. of Astrophysics, Radboud University Nijmegen, The Netherlands*
[xiv]*now at: University of Trondheim, Norway*

***Abstract*. The KASCADE-Grande experiment consists of a large array of scintillators for the detection of charged particles from extensive air showers in the primary energy range 10^{16} eV – 10^{18} eV. In combination with the detectors of the KASCADE array it provides the means to investigate the composition in the expected transition region of galactic to extragalactic cosmic rays and the possible existence of a second knee in the total energy spectrum at E $\sim 10^{17}$ eV caused by heavy primaries.**
For the goals described it is indispensable to reconstruct the shower sizes with highest accuracy. The reconstruction of the muonic component as well as the muon lateral distribution will be discussed and the precision and systematic uncertainties in the reconstruction of the muon number will be studied based on Monte Carlo simulations.

***Keywords*: muonic component, lateral distribution, KASCADE-Grande**

I. Introduction and Experimental Setup

The combined KASCADE and KASCADE-Grande Experiment [1], located on the site of the Forschungszentrum Karlsruhe (110 m a.s.l.), consists of various detector components [2] for measuring the particles of extensive air showers in the primary energy range from 10^{16} eV – 10^{18} eV. The measurement at the upper part of that energy range is possible due to a large scintillator array, the Grande array, covering a collecting area of approximately 0.5 km^2. The 37 Grande stations located on a hexagonal grid with an average mutual distance of 137 m measure the total number of *charged particles* in an air shower.
With the colocated KASCADE array the *muon component* of the extensive air shower can be measured separately from the electronic one. Using an appropriate lateral distribution function, one can derive the total muon number of air showers from the muon signals measured locally with the KASCADE array. This method can be applied even in cases where the core is located in the KASCADE-Grande array, but not in the KASCADE array itself (Fig. 1, left). Subtracting the estimated number of muons from the total number of charged particles measured with KASCADE-Grande yields the total number of shower electrons [3]. The scintillators of the KASCADE detector array cover an area of 200 $\times$ 200 m^2 and are housed in 252 stations on a grid with 13 m spacing. While the inner stations of the KASCADE array are only equipped with liquid scintillators measuring primarily electrons and gammas, the outer stations are also containing plastic scintillators underneath a shielding[1] of 10 cm

[1]corresponding to 20 radiation lengths, muon threshold: 230 MeV.

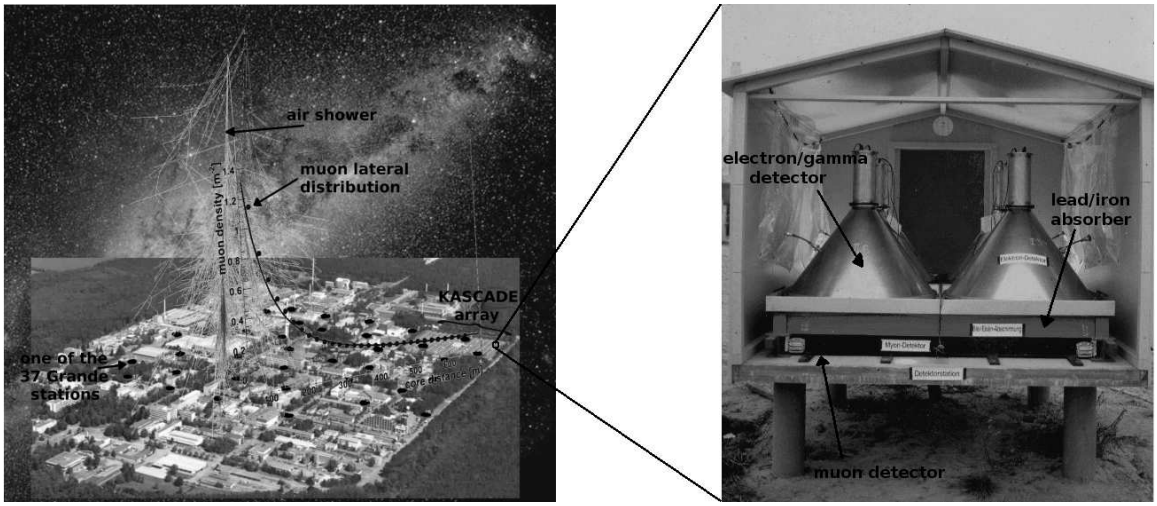

Fig. 1: *Left:* An air shower with the core located in the Grande array. Although the KASCADE detector field is far away from the core, non-zero muon densities can be measured there. *Right:* Detector station of the KASCADE-array equipped with electron/gamma and separate muon detectors.

lead and 4 cm iron, which allows the measurement of muons separately from electrons and gammas (Fig. 1, right). These muon detectors consist of four plastic scintillators per station. The scintillators are of 3 cm thickness and their surface area is 90×90 cm^2. The light is coupled out by wavelength shifters and read out by 1.5 inch photomultipliers. The energy resolution has been determined to about 10% at 8 MeV, the mean energy deposit of a MIP[2].

II. Reconstruction of the Muon Number

As described in the previous chapter the local muon densities can be measured even in cases where the shower core is located in the KASCADE-Grande array, but not in the KASCADE array itself. For these purposes the energy deposits in the muon detectors must be converted to particle numbers by means of a conversion function, the so-called LECF[3]. The LECF is derived from simulated air showers based on CORSIKA [4] and a detailed GEANT [5] detector simulation. It has been determined based on two primaries (H and Fe) and three different simulated energies, 3×10^{16} eV, 1×10^{17} eV and 3×10^{17} eV. The average energy deposit in the KASCADE muon detectors per shower muon at a distance r (in meter) from the shower core is given by the following LECF:

$$\frac{E_{\mathrm{dep}}}{muon}(r) = \left(7.461 + \mathrm{e}^{(1.762-0.017\cdot r)} + 0.0003 \cdot r\right) \text{ MeV} \quad (1)$$

For small radii up to approximately 160 m the energy deposit per muon decreases in order to correct the high energetic electromagnetic punch through close to the shower core. At larger radii the deposited energy per muon reaches a constant value of approximately 7.6 MeV (Fig. 2).

For most analyses it is convenient not only to know the local muon densities given by the LECF but also the total number of muons in the shower disk. Assuming the locally detected muons fluctuate according to a poisson distribution, one can derive the total muon number N_μ^{rec} from a maximum likelihood estimation, which yields:

$$N_\mu^{\mathrm{rec}} = \sum_{i=1}^{k} n_i \,/\, \sum_{i=1}^{k} \Big(f(r_i) \cdot A_i \cdot \cos(\theta) \Big) \,, \quad (2)$$

where n_i is the number of particles measured at a core distance r_i (in meter) in one of the k muon detectors within an area A_i (in square meters), θ is the zenith angle (in degree) of the air shower, and f is an appropriate

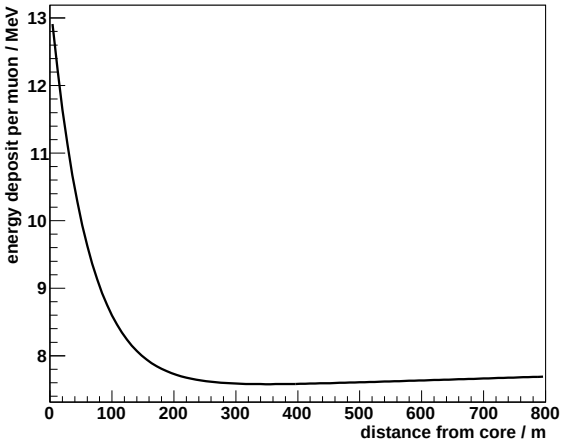

Fig. 2: Average energy deposit per muon in a KASCADE muon detector as a function of the distance of this detector from the shower core (muon LECF according to Eq. 1).

[2]Minimum Ionizing Particle.
[3]Lateral Energy Correction Function.

lateral distribution function.
In case of the KASCADE-Grande Experiment the lateral distribution of muon densities ρ_μ is fitted with a function based on the one proposed by Lagutin and Raikin [6] for the electron component:

$$\rho_\mu(r) = N_\mu \cdot f(r), \text{ with}$$
$$f(r) = \frac{0.28}{r_0^2}\left(\frac{r}{r_0}\right)^{p_1} \cdot \left(1+\frac{r}{r_0}\right)^{p_2} \cdot \left(1+\left(\frac{r}{10\cdot r_0}\right)^2\right)^{p_3}. \quad (3)$$

The parameters $p_1 = -0.69$, $p_2 = -2.39$, $p_3 = -1.0$ and $r_0 = 320$ m are based on CORSIKA simulations using the interaction model QGSJet 01. Both proton and iron primaries were simulated at energies of 10^{16} eV and 10^{17} eV and then the average of the fit results is taken. Since the muon densities are very low, except for the highest energy showers, stable fits on the shower-by-shower basis are only obtained if the lateral distribution function is kept constant and only the muon number N_μ is taken as a fit parameter.
Substituting the lateral distribution function f from Eq. 3 into Eq. 2 yields a formula for calculating the total muon number of the KASCADE-Grande event.

III. Reconstruction Accuracy

The muon number is reconstructed based on the local muon densities measured only on the small area of the KASCADE detector field. The measured densities are typically very small and subject to large fluctuations. The reconstruction of the total number of muons is strongly affected by these uncertainties.

The to some extent *directly measured* muon density distribution and the lateral distribution function f (Eq. 3) with the muon number N_μ set to the *reconstructed* mean muon number $\overline{N_\mu^{\rm rec}}$ (Eq. 2) in each muon size bin are shown in Fig. 3. The measured densities are in general well described by the lateral distribution function. This means a good conformity between *directly measured* sizes and *reconstructed* ones. Only in case of relatively small and large core distances one can see deviations due to the fixed shape of the lateral distribution function which does not account for the primary energy or the zenith angle of the air shower.

The reconstruction quality has been tested based on CORSIKA simulations using the interaction model QGSJet II. Different primaries (H, He, C, Si and Fe) in equal abundances, with an E^{-3} power law spectrum, zenith angles up to 40° and cores scattered over the Grande array were considered in the simulations. The full detector response was also simulated (GEANT [5] detector simulation) and the usual reconstruction techniques were applied to the resulting data. The mean deviation of the reconstructed muon number $N_\mu^{\rm rec}$ from the true muon number $N_\mu^{\rm tru}$ as a function of the true muon number itself or the distance of the shower core to the centre of the KASCADE array are shown in Fig. 4. In the latter case, only events with muon numbers above $\log_{10} N_\mu^{\rm tru} \geq 5.0$ are taken into account, that

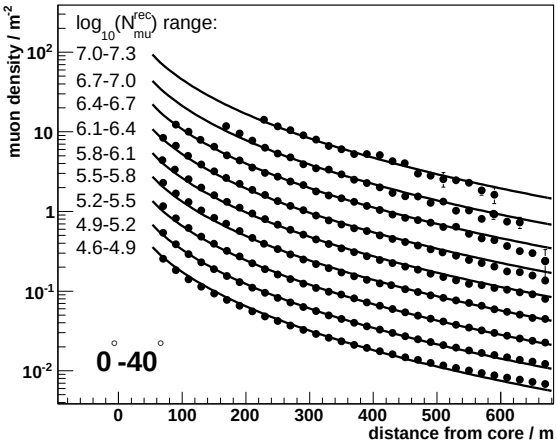

Fig. 3: Measured muon density distribution (dots) for zenith angles 0°–40° and different intervals of the reconstructed muon number. The lateral distribution function of Eq. 3 (curves) with the muon number N_μ set to the measured mean muon number $\overline{N_\mu^{\rm rec}}$ in each interval describes the data quite well.

means only muon numbers above full reconstruction efficiency[4]. In case of muon numbers above a threshold of $\log_{10} N_\mu^{\rm tru} \approx 5.6$, which corresponds to an energy of approximately 5×10^{16} eV, the systematic deviation of the reconstructed total muon number is smaller than 5% and to some extent constant in this range (Fig. 4a). Above the mentioned threshold, the statistical error (represented by the error bars, RMS) decreases from around 20% to 7% with increasing muon number. Showers below 100% efficiency are characterized by a rather large statistical uncertainty up to 40%. In Fig. 4b the dependence of the reconstructed accuracies on the distance of the core to the centre of the KASCADE array is shown. An increase of the statistical uncertainty with increasing distances from approximately 15% at 100 m to 30% at 700 m distance is observed. The under- or overestimation of the local muon densities by the lateral distribution function (discussed above, Fig. 3) in cases of small and large core distances results in an under- or overestimation of the total muon number in these distance ranges. The deviation of the reconstructed muon number from the true one starts from $\sim -7\%$ for small distances, gets zero for ~ 240 m distance and increases to $\sim +12\%$ for larger core distances. Taking into account the fact that quite small particle densities are measured across a small detection area far away from the shower core, one can draw the conclusion, that the reconstruction of the total muon number works surprisingly well. Furthermore the features of the accuracies are well understood and open the possibility to correct the reconstructed muon number to the true one using appropriate correction functions and to perform analyses based on these corrected muon numbers (see [7]).

[4] 100% reconstruction efficiency of muon number is obtained above $\log_{10} N_\mu^{\rm tru} \approx 5.0$.

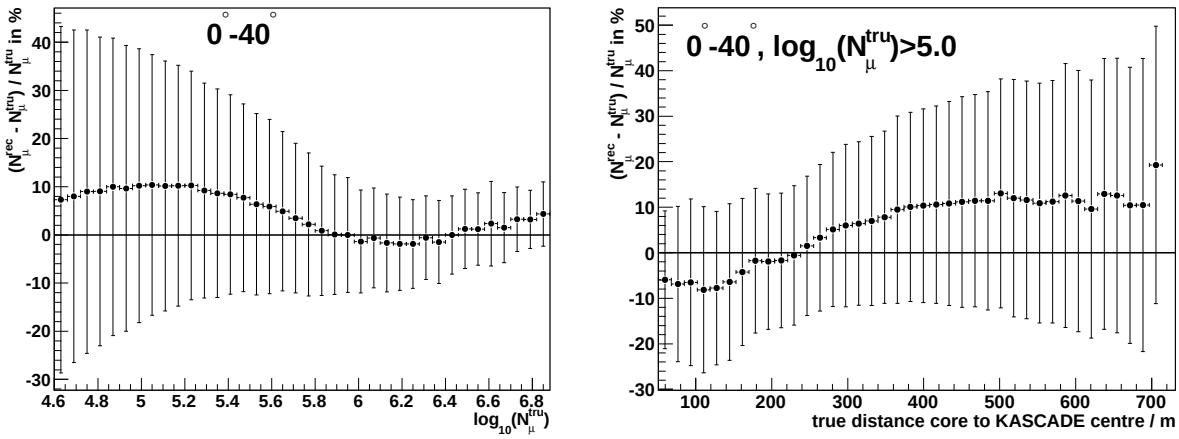

(a) (b)

Fig. 4: Reconstruction quality tested based on Monte Carlo simulations. In case *a)* the deviation of the reconstructed to the true muon number is shown as a function of the true muon number, in case *b)* as a function of the distance of the shower core to the centre of the KASCADE array. In both cases the error bars represent the statistical uncertainty (RMS) in a single measurement.

IV. Conclusion

The reconstruction of the total muon number in the shower disk has been presented using the KASCADE scintillator array as a part of the KASCADE-Grande experiment. The procedure of converting the energy deposits to particle numbers was explained as well as the calculation of the total muon number using a maximum likelihood method. The reconstruction accuracies have been discussed and reveal a good reconstruction quality, despite the fact that the total muon number is reconstructed based on just a small fraction of radial detector coverage. Deviations between reconstructed and true shower sizes are well understood such that it is possible to derive correction functions allowing to correct the reconstructed muon number to the true one. Hence, KASCADE-Grande analyses taking into account the total muon number can be performed.

References

[1] K.-H. Kampert et al. (KASCADE-Grande collaboration), *Nucl. Phys. B (Proc. Suppl.)* **122** (2003) 422.
[2] T. Antoni et al. (KASCADE collaboration), *Nucl. Instr. and Meth.* **A 513**, 490 (2003).
[3] J. van Buren et al. (KASCADE-Grande collaboration), Proc. 29th ICRC Pune (2005) **00**, 101–106.
[4] D. Heck et al., *CORSIKA: A Monte Carlo code to simulate extensive air showers*, Wiss. Ber. FZKA, **6010** (1998).
[5] R. Brun and F. Carminati, *GEANT-Detector Description and Simulation Tool*, CERN Program Library Long Writeup (1993).
[6] A. A. Lagutin and R. I. Raikin, *Lateral distribution of electrons in EAS at superhigh energies: predictions and experimental data*, *Nucl. Phys. Proc. Suppl.* **97**: 274–277 (2001).
[7] J. C. Arteaga-Velazquez et al. (KASCADE-Grande collaboration), *The Energy Spectrum of Primary Cosmic Rays Reconstructed with the KASCADE-Grande muon data*, Proc. 31st ICRC Lodz (2009), these proceedings.

The sensitivity of KASCADE-Grande to the cosmic ray primary composition between 10^{16} and 10^{18} eV

E. Cantoni[‡,‖], W.D. Apel[*], J.C. Arteaga[†,xi], F. Badea[*], K. Bekk[*], M. Bertaina[‡], J. Blümer[*,†], H. Bozdog[*] I.M. Brancus[§], M. Brüggemann[¶], P. Buchholz[¶], A. Chiavassa[‡], F. Cossavella[†], K. Daumiller[*], V. de Souza[†,xii], F. Di Pierro[‡], P. Doll[*], R. Engel[*], J. Engler[*], M. Finger[*], D. Fuhrmann[**], P.L. Ghia[‖], H.J. Gils[*], R. Glasstetter[**], C. Grupen[¶], A. Haungs[*], D. Heck[*], J.R. Hörandel[†,xiii], T. Huege[*], P.G. Isar[*], K.-H. Kampert[**], D. Kang[†], D. Kickelbick[¶], H.O. Klages[*], Y. Kolotaev[¶], P. Łuczak[††], H.J. Mathes[*], H.J. Mayer[*], J. Milke[*], B. Mitrica[§], C. Morello[‖], G. Navarra[‡], S. Nehls[*], J. Oehlschläger[*], S. Ostapchenko[*,xiv], S. Over[¶], M. Petcu[§], T. Pierog[*], H. Rebel[*], M. Roth[*], H. Schieler[*], F. Schröder[*], O. Sima[‡‡], M. Stümpert[†], G. Toma[§], G.C. Trinchero[‖], H. Ulrich[*], W. Walkowiak[¶], A. Weindl[*], J. Wochele[*], M. Wommer[*], J. Zabierowski[††]

[*]*Institut für Kernphysik, Forschungszentrum Karlsruhe, 76021 Karlsruhe, Germany*
[†]*Institut für Experimentelle Kernphysik, Universität Karlsruhe, 76021 Karlsruhe, Germany*
[‡]*Dipartimento di Fisica Generale dell'Università, 10125 Torino, Italy*
[§]*National Institute of Physics and Nuclear Engineering, 7690 Bucharest, Romania*
[¶]*Fachbereich Physik, Universität Siegen, 57068 Siegen, Germany*
[‖]*Istituto di Fisica dello Spazio Interplanetario, INAF, 10133 Torino, Italy*
[**]*Fachbereich Physik, Universität Wuppertal, 42097 Wuppertal, Germany*
[††]*Soltan Institute for Nuclear Studies, 90950 Lodz, Poland*
[‡‡]*Department of Physics, University of Bucharest, 76900 Bucharest, Romania*
[xi]*now at: Universidad Michoacana, Morelia, Mexico*
[xii]*now at: Universidade de São Paulo, Instituto de Fîsica de São Carlos, Brasil*
[xiii]*now at: Dept. of Astrophysics, Radboud University Nijmegen, The Netherlands*
[xiv]*now at: University of Trondheim, Norway*

***Abstract*. The goal of the KASCADE-Grande experiment is the study of the cosmic ray energy spectrum and chemical composition in the range 10^{16} - 10^{18} eV detecting the charged particles of the respective Extensive Air Showers. The observables here taken into account for discussion are the measured electron size (N_e) and muon size (N_μ). It is crucial to verify: the sensitivity to different chemical components, the data reproducibility with the hadronic interaction model in use as a function of the electron size and the athmospheric depth, the consistency with the results obtained by other experiments sensitive to composition in overlapping energy regions. The analysis is presented using KASCADE as reference experiment and using QGSjetII as hadronic interaction model.**

***Keywords*: KASCADE-Grande, sensitivity, interaction model.**

I. Introduction

The KASCADE-Grande experiment is located at Forschungszentrum Karlsruhe (Germany). It consists of an array of 37 scintillator modules 10 m^2 each (the Grande array) spread over an area of 700 x 700 m^2, working jointly with the co-located and formerly present KASCADE experiment [1], made of 252 scintillation detectors, 490 m^2 sensitive area spread over 200 x 200 m^2. The extension from KASCADE to KASCADE-Grande is meant to increase the experimental acceptance of a factor $\sim$10, the achieved accuracies showing there is no significant loss in resolution for the present analysis (see [2]). For each recorded EAS the charged particle size N_{ch} is measured through Grande, the reconstruction procedure being fine tuned over the whole experimental area (see [2]), and the muon size N_μ is obtained from KASCADE, the reconstruction and accuracy of the muonic component being described in [3]. The electron size is obtained subtracting the muon from the charged particle density. As to validate the experimental results and verify the applicability of the interaction model in use for data interpretation[1] it is first of all important to achieve an accurate event reconstruction, the next step is to test the sensitivity of the extended apparatus to observables, to verify the data reproducibility with the hadronic interaction model in use and to test the consistency of this reproducibility with the former KASCADE data. For this aims, in the following analysis, the total number of electrons N_e and the total number of muons N_μ of each recorded event are considered and the distribution of N_μ/N_e is studied in different intervals of N_e[2] and zenith angle (athmospheric depth).

[1]Both for energy measurements and composition studies.
[2]Corresponding to different energy intervals (see IV).

TABLE I: The results for the chi square minimization on the selected experimental data using just one chemical component.

chemical element	protons (p)	Helium (He)	Carbon (CNO)	Silicium (Si)	Iron (Fe)
χ^2/ν	6798.09	404.59	26.44	17.20	10.44

II. The features of the analysis

KASCADE-Grande data are chosen, at first, in an electron size range providing full reconstruction efficiency (see [5]) and high statistics: $6.49 \leq \mathrm{Log}(N_e) < 6.74$ in $0° \leq \theta < 23.99°$ (see figure 1). The same event selection is made on the simulated QGSjetII [4] data sets at disposal for each cosmic ray primary[3]. The experimental distribution of the observable N_μ/N_e is taken into account and fitted with a linear combination of elemental contributions from simulations, expressed as follows:

$$F_{sim}(i) = \sum_j \alpha_j f_{sim,j}(i) \quad (1)$$

where $F_{sim}(i)$ is the total theoretical fraction of simulated events falling in the channel i of the distribution considered as a histogram, $f_{sim,j}(i)$ is the fraction for the single chemical component j, Σ_j is the sum over the different components and α_j is the fit parameter representing the *relative abundance* of the component j. The fit parameters fulfill the conditions

$$0. < \alpha_j < 1., \forall j \quad (2)$$

and

$$\sum_j \alpha_j = 1. \quad (3)$$

The fit is performed through the minimization of the following Chi Square function:

$$\chi^2 = \sum_i \frac{(F_{exp}(i) - F_{sim}(i))^2}{\sigma(i)^2} \quad (4)$$

where $F_{exp}(i)$ is the fraction of experimental events falling in the histogram channel i and $\sigma(i)$ is the error on the theoretical expression (1).

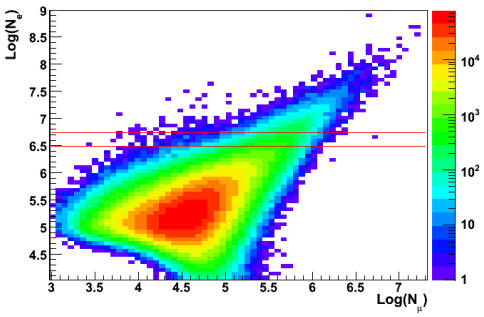

Fig. 1: The KASCADE-Grande data as they appear in the observables N_e and N_μ. The considered selection lies between the lines.

[3]p,He, C, Si, Fe. (simulated with an energy spectrum γ = 3)

A. The fit with a single chemical component

A chi square minimization is performed at first with the use of a single chemical component. This shows to give not a good description of the data, as it can be seen in table I, summarizing the results for the chi square minimization with single elements (see also figure 2 as example).

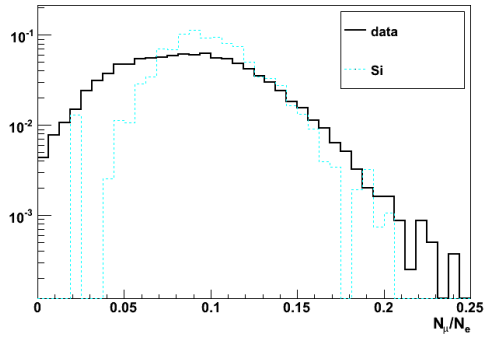

Fig. 2: The distributions (normalized to 1) of the KASCADE-Grande data in $6.49 \leq \mathrm{Log}(N_e) < 6.74$ ($0° \leq \theta < 23.99°$) and of QGSjetII Silicium in the same selection range.

B. The fit with two chemical components

The experimental selection is then fitted with a combination of a light and a heavy chemical component that, at a qualitative glance, seem necessary to describe well the tails of the experimental histogram. Indeed, performing a minimization with two components steps up the fit, as it can be seen in table II and figures 3 and 4. It can be observed that Iron seems necessary to describe well the right tail of the experimental distribution, while Helium seems not to fit well on the left tail. Moreover, the shapes of the fits suggest the requirement of a third element in the middle.

TABLE II: The results for the chi square minimization on the selected experimental data using two chemical components.

chemical elements	p + Fe	He + Fe
α_p	0.41 ± 0.02	–
α_{He}	–	0.49 ± 0.02
α_{Fe}	0.59 ± 0.02	0.51 ± 0.02
χ^2/ν	3.51	1.48

C. The fit with three chemical components

The fit is then performed with a combination of three elements: Protons, Helium and Iron are chosen, matching the light elements with the heaviest element.

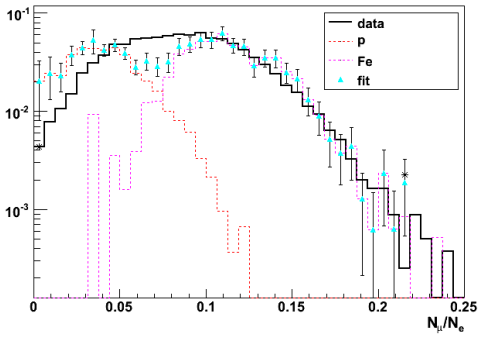

Fig. 3: The KASCADE-Grande data in $6.49 \leq \mathrm{Log}(N_e) < 6.74$ ($0° \leq \theta < 23.99°$) described by Protons and Iron primaries. Here and in the next pictures, the experimental plot is normalized to 1 and every simulated component is normalized to its relative abundance. Each tail of the experimental distribution (>2·RMS and <2·RMS) is treated counting the events in a single bin: the star indicates the total experimental value the fit must be compared with in that bin.

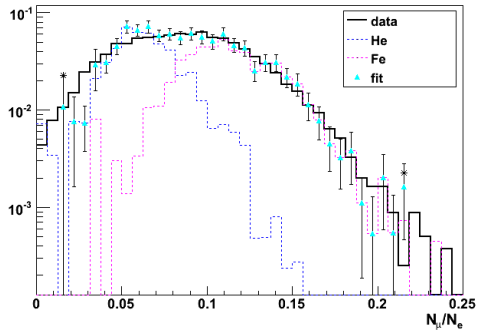

Fig. 4: The KASCADE-Grande data in $6.49 \leq \mathrm{Log}(N_e) < 6.74$ ($0° \leq \theta < 23.99°$) described by a Helium and Iron primaries.

It can be seen that a three elements combination is well fitting the data (see table III and figure 5). It is possible to use also another combination: Protons, Carbon and Iron (see table III and figure 6). These results show that the theoretical model describes well the shape and the tails of the experimental distribution.

TABLE III: The results for the chi square minimization on the selected experimental data using three chemical components.

chemical elements	p + He + Fe	p + CNO + Fe
α_p	0.15 ± 0.02	0.23 ± 0.02
α_{He}	0.31 ± 0.03	–
α_C	–	0.34 ± 0.03
α_{Fe}	0.54 ± 0.02	0.43 ± 0.02
χ^2/ν	0.68	1.14

III. Analysis on inclined showers

To check the consistency of the result at higher zenith angles, the same fits with three chemical components are performed on a higher angular interval of equal

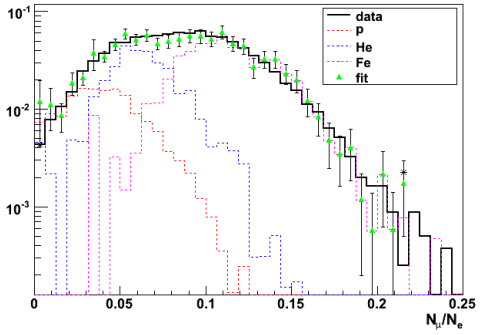

Fig. 5: The KASCADE-Grande data in $6.49 \leq \mathrm{Log}(N_e) < 6.74$ ($0° \leq \theta < 23.99°$) described by Protons, Helium and Iron primaries.

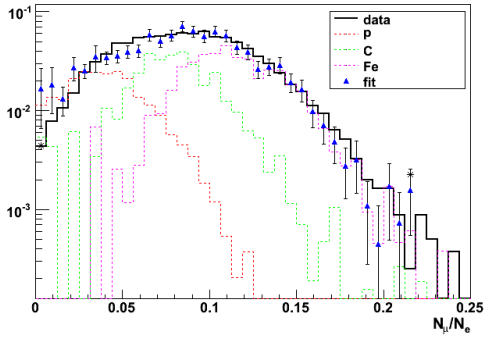

Fig. 6: The KASCADE-Grande data in $6.49 \leq \mathrm{Log}(N_e) < 6.74$ ($0° \leq \theta < 23.99°$) described by Protons, Carbon and Iron primaries.

acceptance, $29.86° \leq \theta < 40°$, in an electron size interval providing a similar number of events, $6.11 \leq \mathrm{Log}(N_e) < 6.36$. Also at higher angles, using three elements, it is found that the model reproduces the data, as it can be seen in table IV and figure 7.

TABLE IV: The results for the chi square minimization on the selected experimental data using p + He + Fe. Comparison between vertical and inclined showers.

angular bin	$0° \leq \theta < 23.99°$	$29.86° \leq \theta < 40°$
α_p	0.15 ± 0.02	0.17 ± 0.04
α_{He}	0.31 ± 0.03	0.31 ± 0.05
α_{Fe}	0.54 ± 0.02	0.52 ± 0.03
χ^2/ν	0.68	0.77

IV. Analysis at higher energies

Selecting the KASCADE-Grande experimental data for higher values of the electron size N_e means to chose showers that were generated by higher energy events (see [5]). Also in this case, it is found that the model reproduces the data, the minimization of the N_μ/N_e distribution with three chemical components still providing a good result, as it can be seen in table V and figure 8.

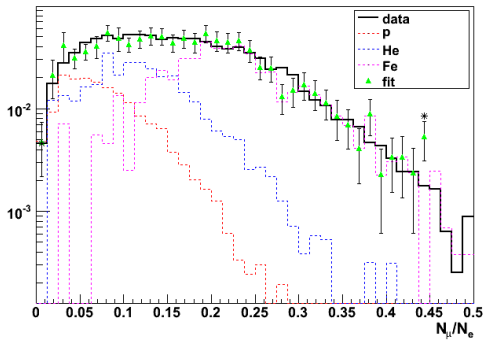

Fig. 7: The KASCADE-Grande data in $6.11 \leq \mathrm{Log}(N_e) < 6.36$ ($29.86° \leq \theta < 40°$) described by Protons, Helium and Iron primaries.

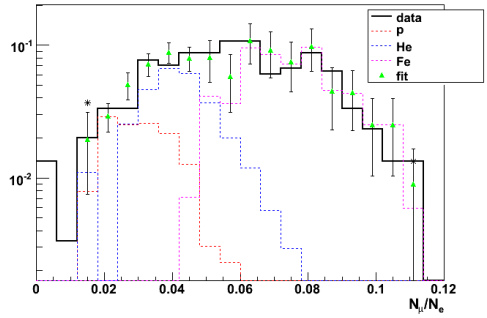

Fig. 8: The KASCADE-Grande data in $7.24 \leq \mathrm{Log}(N_e) < 7.49$ ($0° \leq \theta < 23.99°$) described by Protons, Helium and Iron primaries.

TABLE V: The results for the chi square minimization in a low and a high electron size interval, using p + He + Fe.

Δ Log(N_e)	$6.49 \leq \mathrm{Log}(N_e) < 6.74$	$7.24 \leq \mathrm{Log}(N_e) < 7.49$
α_p	0.15 ± 0.02	0.13 ± 0.02
α_{He}	0.31 ± 0.03	0.29 ± 0.04
α_{Fe}	0.54 ± 0.02	0.58 ± 0.04
χ^2/ν	0.68	0.83

V. Comparison with KASCADE data

Being the electron size range $6.11 \leq \mathrm{Log}(N_e) < 6.36$ ($29.86° \leq \theta < 40°$) common to KASCADE and KASCADE-Grande data, the correspondent N_μ^{tr}/N_e distribution from KASCADE is taken into account. Applying the same analysis, it is found that three chemical components fit the data, as for KASCADE-Grande (see table VI and figure 9). Even with KASCADE data, the combination p + C + Fe is also fitting (see figure 10).

TABLE VI: The results for the chi square minimization on the selected data from KASCADE.

chemical elements	p + He + Fe	p + C + Fe
α_p	0.20 ± 0.03	0.33 ± 0.06
α_{He}	0.30 ± 0.04	–
α_C	–	0.26 ± 0.07
α_{Fe}	0.50 ± 0.03	0.41 ± 0.04
χ^2/ν	1.12	1.25

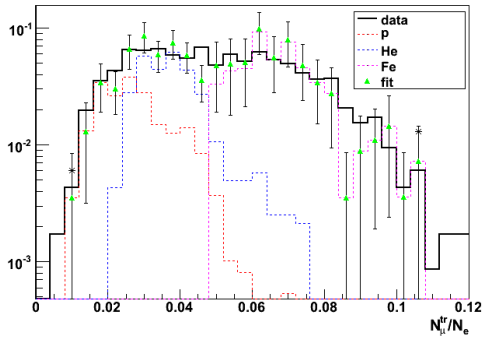

Fig. 9: The KASCADE data in $6.11 \leq \mathrm{Log}(N_e) < 6.36$ ($29.86° \leq \theta < 40°$) described by Protons, Helium and Iron primaries. Here the number of muons with distances to the shower core between 40 m and 200 m ("truncated") is considered.

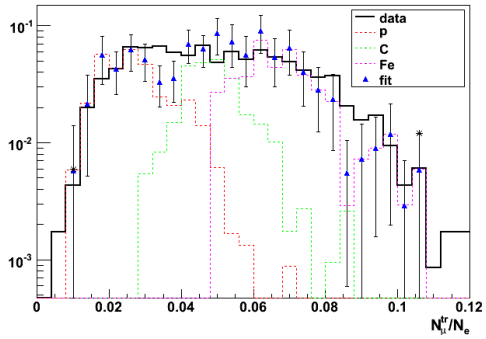

Fig. 10: The KASCADE data in $6.11 \leq \mathrm{Log}(N_e) < 6.36$ ($29.86° \leq \theta < 40°$) described by Protons, Carbon and Iron primaries.

VI. Conclusions

In this work it has been shown that, with the use of a method exploiting a chi square minimization of a linear combination of different simulated primaries, the KASCADE-Grande N_μ/N_e distributions are fitted using at least three elements. QGSjetII, the hadronic interaction model in use, can fairly reproduce the data and, in particular, the tails of the distributions, that represent a main constraint being related to the lightest and heaviest cosmic ray primaries. Finally, this kind of analysis, performed on the correspondent N_μ^{tr}/N_e distribution from KASCADE experiment, gives a consistent result, thus showing that, in the superposition energy region, KASCADE-Grande is fairly well reproducing KASCADE data.

References

[1] T. Antoni et al., Nucl. Instr. and Meth., A513(2003)490-510.
[2] F. Di Pierro for the KASCADE-Grande Coll., this conference.
[3] D. Fuhrmann for the KASCADE-Grande Coll., this conference..
[4] S. Ostapchenko, astro-ph/0412591.
[5] F. Cossavella for the KASCADE-Grande Coll., in *Proceedings of the 30th International Cosmic Ray Conference*, Merida (Mexico), 2007.

A direct measurement of the muon component of air showers by the KASCADE-Grande Experiment

V. de Souza[†,xii], W.D. Apel[*], J.C. Arteaga[†,xi], F. Badea[*], K. Bekk[*], M. Bertaina[‡], J. Blümer[*,†], H. Bozdog[*] I.M. Brancus[§], M. Brüggemann[¶], P. Buchholz[¶], E. Cantoni[‡,‖], A. Chiavassa[‡], F. Cossavella[†], K. Daumiller[*], F. Di Pierro[‡], P. Doll[*], R. Engel[*], J. Engler[*], M. Finger[*], D. Fuhrmann[**], P.L. Ghia[‖], H.J. Gils[*], R. Glasstetter[**], C. Grupen[¶], A. Haungs[*], D. Heck[*], J.R. Hörandel[†,xiii], T. Huege[*], P.G. Isar[*], K.-H. Kampert[**], D. Kang[†], D. Kickelbick[¶], H.O. Klages[*], P. Łuczak[††], H.J. Mathes[*], H.J. Mayer[*], J. Milke[*], B. Mitrica[§], C. Morello[‖], G. Navarra[‡], S. Nehls[*], J. Oehlschläger[*], S. Ostapchenko[*,xiv], S. Over[¶], M. Petcu[§], T. Pierog[*], H. Rebel[*], M. Roth[*], H. Schieler[*], F. Schröder[*], O. Sima[‡‡], M. Stümpert[†], G. Toma[§], G.C. Trinchero[‖], H. Ulrich[*], A. Weindl[*], J. Wochele[*], M. Wommer[*], J. Zabierowski[††]

[†]*Institut für Experimentelle Kernphysik, Universität Karlsruhe, 76021 Karlsruhe, Germany*
[*]*Institut für Kernphysik, Forschungszentrum Karlsruhe, 76021 Karlsruhe, Germany*
[‡]*Dipartimento di Fisica Generale dell'Università, 10125 Torino, Italy*
[§]*National Institute of Physics and Nuclear Engineering, 7690 Bucharest, Romania*
[¶]*Fachbereich Physik, Universität Siegen, 57068 Siegen, Germany*
[‖]*Istituto di Fisica dello Spazio Interplanetario, INAF, 10133 Torino, Italy*
[**]*Fachbereich Physik, Universität Wuppertal, 42097 Wuppertal, Germany*
[††]*Soltan Institute for Nuclear Studies, 90950 Lodz, Poland*
[‡‡]*Department of Physics, University of Bucharest, 76900 Bucharest, Romania*
[xi]*now at: Universidad Michoacana, Morelia, Mexico*
[xii]*now at: Universidade de São Paulo, Instituto de Física de São Carlos, Brasil*
[xiii]*now at: Dept. of Astrophysics, Radboud University Nijmegen, The Netherlands*
[xiv]*now at: University of Trondheim, Norway*

***Abstract*. The muon component of atmospheric air showers is a very relevant information in astroparticle physics due to its direct relation to the primary particle type and dependence on the hadronic interactions. In this paper, we study the muon densities measured by the KASCADE-Grande experiment and illustrate its importance in composition studies and testing of hadronic interaction models. The data analysed here was measured by the KASCADE-Grande detector and lies in the $10^{16}-10^{18}$ eV energy range. The measured muon density is compared to predictions of EPOS 1.61 and QGSJet II hadronic interaction models.**

***Keywords*: Muon Density, Composition and Simulation test.**

I. Introduction

Cosmic rays with energy range between 10^{16} and 10^{18} eV have the potential to reveal interesting astrophysical phenomena occurring in the Universe. This might be the energy range in which a transition in the predominance of the particle flux from galactic to extragalactic sources is happening what could be followed by changes in the primary cosmic abundance. If such a transition is not occurring in this energy range, galactic sources would have an acceleration power beyond the predictions of conservative theories.

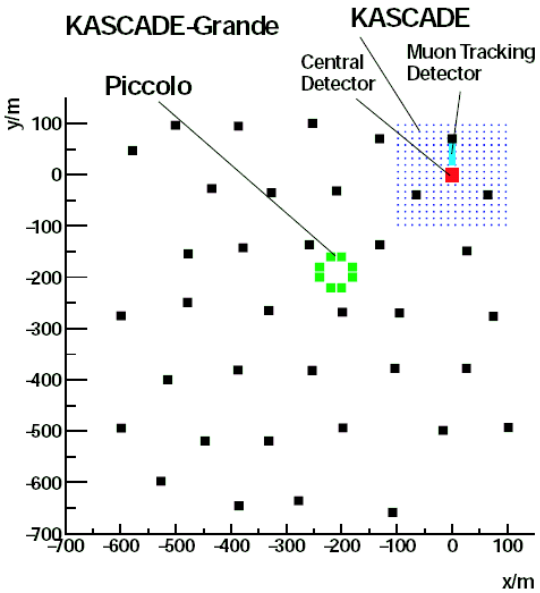

Fig. 1: Representation of the KASCADE-Grande detectors.

The KASCADE-Grande experiment (see figure 1) has been set up to measure primary cosmic rays in this energy range in order to help in the understanding

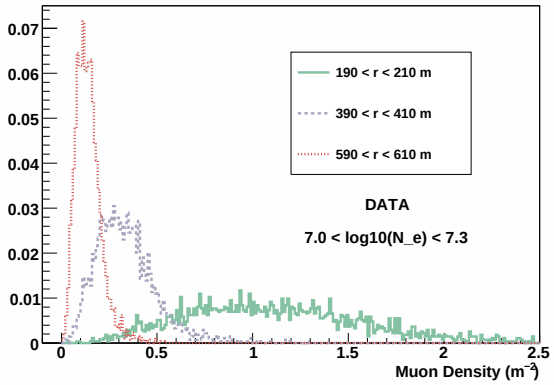

Fig. 2: Distribution of the density of muons for three distances from the shower axis.

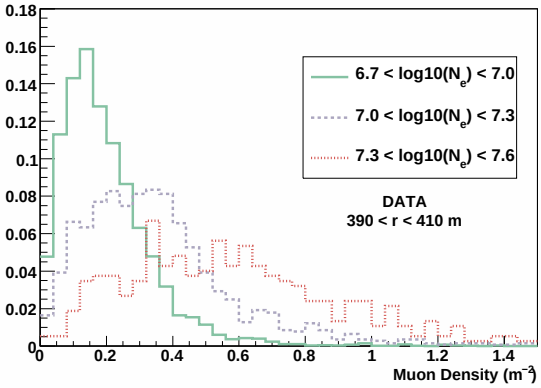

Fig. 3: Distribution of the density of muons for three cuts in the total number of electrons.

of these questions. The experiment is located at the Forschungszentrum Karlsruhe, Germany, where, beside the existing KASCADE [1] array, two new detector set ups (Grande and Piccolo) have been installed. The experiment is able to sample different components of extensive air showers (electromagnetic, muonic and hadronic) with high accuracy and covering a surface of 0.5 km^2. For an overview of the actual setup of the KASCADE-Grande Experiment see ref. [2].

In this article we present studies of the muon component of the shower. Muons are the messengers of the hadronic interactions of the particles in the shower and therefore are a powerful tool to determine the primary particle mass and to study the hadronic interaction models.

II. Reconstruction

The main parameters used in this study are the density of muons and the total number of electrons in the shower for which the reconstruction accuracy is going to be discussed below. For the reconstruction accuracy of the shower geometry see ref. [3].

The density of muons is directly measured by the KASCADE 622 m^2 scintillators. These detectors are shielded by 10 cm of lead and 4 cm of iron, corresponding to 20 radiation lengths and a threshold of 230 MeV for vertical muons. The error in the measurement of the energy deposit was experimentally determined to be smaller than 10% [1].

For each shower, the density of muons is calculated as follows. The muon stations are grouped in rings of 20 m distance from the shower axis. The sum of the signals measured by all muon stations inside each ring is divided by the effective detection area of the stations. Therefore the muon density as a function of the distance from the shower axis is measured in a very direct way. No fitting of lateral distributions is needed in these calculations.

The total number of electrons in the shower is reconstructed in a combined way using KASCADE and KASCADE-Grande stations. A lateral distribution function (LDF) of the Lagutin type can be fitted to the density of muons measured by the KASCADE detector [4]. After that, using the fitted function, the number of muons at any distance from the shower axis can be estimated. The KASCADE-Grande stations measure the number of charged particles. The number of electrons at each KASCADE-Grande stations is determined by subtracting from the measured number of charged particles the number of muons estimated with the LDF fitted to the KASCADE stations.

At this stage, the number of electrons at each KASCADE-Grande station is known. Finally, a modified NKG [5] function is fitted to this data and the total number of electrons is determined in the fit.

Quality cuts have been applied to the events in this analysis procedure. We have required more than 19 KASCADE-Grande stations with signal. The showers used in all analysis along this paper were reconstructed with zenith angle between 0 and 42 degrees. The same quality cuts were applied to the simulated events used for reconstruction studies and to the data presented in the following section. After the quality cuts, the total number of electrons can be estimated with a systematic shift smaller than 10% and a statistical uncertainty smaller than 20% along the entire range considered in this paper [3].

Figure 2 shows the measured density of muons at three distances from the shower axis for events with a total number of electrons (N_e) in the range $7.0 < Log10(N_e) < 7.3$ ($\approx 10^{17}$ eV). Similar plots were obtained for other N_e ranges.

Figure 3 shows the density of muons at 400 m from the shower axis for events with total number of electrons (N_e) in the range $6.7 < Log10(N_e) < 7.0$, $7.0 < Log10(N_e) < 7.3$ and $7.3 < Log10(N_e) < 7.6$. Similar plots were obtained for other distances from the shower axis.

Figure 2 and Figure 3 show the general expected

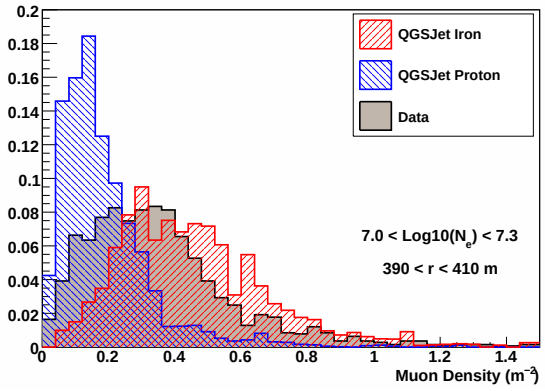

Fig. 4: Measured distribution of the density of muons at 400 m compared to the predictions of QGSJet II.

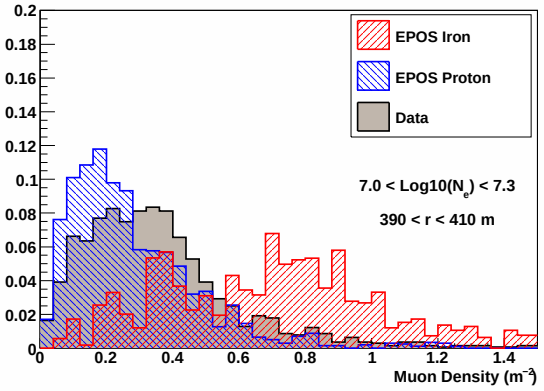

Fig. 5: Measured distribution of the density of muons at 400 m compared to the predictions of EPOS 1.61.

trend: a) decrease of the muon density with increasing distance from the shower axis and b) increase of the muon density with increasing total number of electrons. In the next sections we explore these relations in order to show the capabilities of the KASCADE-Grande experiment for a composition study and for tests of the hadronic interaction models.

We present data for $7.0 < Log10(N_e) < 7.3$ and $390 < r < 410\ m$, these cuts have been chosen in order to minimize the fluctuation of the signal and the reconstruction inaccuracy and to maximize the number of showers for which we have data, however the same conclusions would be drawn for all parameter cuts.

III. Simulation

For all studies in this paper we have used the CORSIKA [6] simulation program with the FLUKA [7] option for low energy hadronic interactions. Two high energy hadronic interaction models were used EPOS 1.61 [8] and QGSJet II [9]. No thinning is used [6].

CORSIKA showers are simulated through the detectors and reconstructed in the same way as the measured data, such that a direct comparison between data and simulation is possible.

Figures 4 and 5 show the comparison of the measured density of muons to values predicted by QGSJet II and EPOS 1.61. For both hadronic interactions models we show the limiting cases of proton and iron nuclei as primary particles. It can be seen in figures 4 and 5 that the data lie well within the proton and iron limits for QGSJet II and EPOS 1.61. These graphics are going to be further discussed in the next sections.

IV. Analysis

Figure 6 shows the mean muon density as a function of the distance from the shower axis compared to the predictions of QGSJet II and EPOS 1.61. Both hadronic interaction models include the data within the proton and iron limits for the entire range of distances from 100 to 750 meters. For distances further than 750 meters the statistics is not enough for a conclusion.

Interesting to note is also the slope of the LDF. Considering an equal probability trigger for protons and iron primaries as a function of distance from the shower axis, one should expect the LDF to be parallel to pure composition primaries. Note that the LDF of simulated proton and iron shower are parallel. However the measured LDF is not parallel to the QGSJet II nor to the EPOS 1.6 curves. That shows that the slope of the LDF can not be well described by neither models.

Figure 7 shows the evolution of the mean muon density as a function of N_e. The calculations done with QGSJet II and EPOS 1.61 using proton and iron nuclei as primary particles bracket the data in the entire range of $5 < Log10(N_e) < 8$.

Nevertheless, both figures 6 and 7 show that EPOS 1.61 would require a very light primary composition in order to fit the data. On the other hand, QGSJet II could fit the data with an intermediate primary abundance between proton and iron nuclei.

Besides that, in figure 7 it is possible to analyse a possible transition of the primary component with increasing total number of electrons. The analysis done with both models show no abrupt change in the compositon in the entire energy range.

The change in slope seen in figure 7 for $Log10(N_e) < 6.0$ corresponds to the threshold of the experiment and the fact that both data and simulation show the same behavior illustrates the good level of understanding of our detectors.

V. Conclusions

The Grande array is in continuous and stable data taking since December 2003. The quality of the detector can be illustrated by the smooth data curve and small fluctuations in figures 6 and 7.

In this article, we have briefly described the procedure used to measure the density of muons with the KASCADE array and we have studied its correlation with

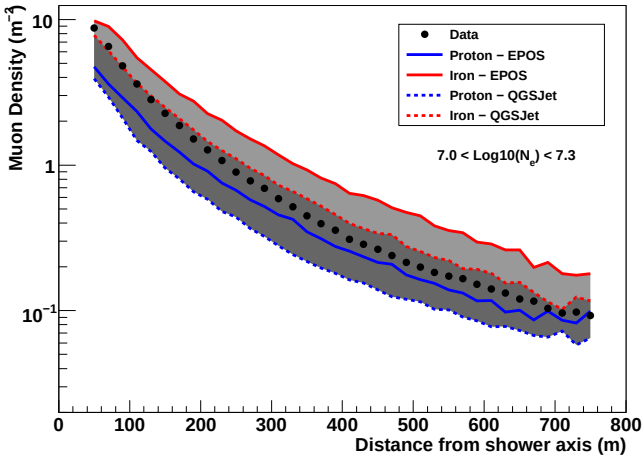

Fig. 6: Lateral distribution of muons compared to the predictions of QGSJet II and EPOS 1.61.

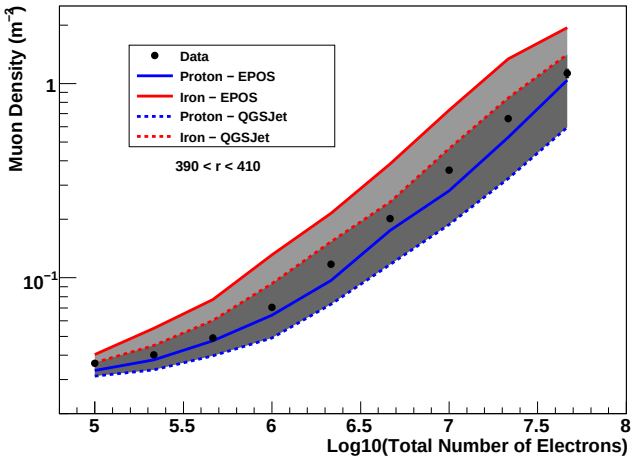

Fig. 7: Muon density as a function of the total number of electrons compared to the predictions of QGSJet II and EPOS 1.61.

the distance from the shower axis and the total number of electrons in the shower.

The density of muons in the shower is measured directly by the KASCADE detectors. We have used this data to study the hadronic interaction models QGSJet II and EPOS 1.61. The data taken with KASCADE-Grande confirms at higher energies the recent results published by the KASCADE [10] experiment. EPOS 1.61 would require a very light abundance of primary particles in order to fit the data. QGSJet II could fit the data with an intermediate primary abundance.

Figure 7 shows no abrupt change with increasing total number of electrons up to $Log10(N_e) = 7.5 \approx 5 \times 10^{17}$ eV. The mean primary mass estimation would depend on the hadronic interaction model used.

REFERENCES

[1] T. Antoni et al. KASCADE Coll., Nucl. Instr. and Meth. A 513, (2003) 490.
[2] A. Haungs et al. KASCADE-Grande Coll., Proc. 31th ICRC, Lodz (2009).
[3] F. di Piero et al. KASCADE-Grande Coll., Proc. 31th ICRC, Lodz (2009).
[4] D. Fuhrmann et al. KASCADE-Grande Coll., Proc. 31th ICRC, Lodz (2009)
[5] K. Greisen, Progress in Cosmic Ray Physics 3 (1956) 1. K. Kamata and J. Nishimura, Suppl. Prog. Theor. Phys. 6 (1958) 93.
[6] D. Heck et al., Report FZKA 6019 (1998).
[7] G. Battistonia et al., ISVHECRI (2006) hep-ph/0612075v1.
[8] K. Werner, M.F. Liu, and T. Pierog Phys. Rev. C 74 (2006) 044902.
[9] S.S. Ostapchenko, Phys. Rev. D 74 (2006) 014026.
[10] W. D. Apel et al. KASCADE-Grande Collab., ,J. Phys. G 36 (2009) 035201

Study of EAS development with the Muon Tracking Detector in KASCADE-Grande

J. Zabierowski[*], W.D. Apel[†], J.C. Arteaga[‡,xi], F. Badea[†], K. Bekk[†], M. Bertaina[§], J. Blümer[†,‡], H. Bozdog[†] I.M. Brancus[¶], M. Brüggemann[‖], P. Buchholz[‖], E. Cantoni[§,], A. Chiavassa[§], F. Cossavella[‡], K. Daumiller[†], V. de Souza[‡,xii], F. Di Pierro[§], P. Doll[†], R. Engel[†], J. Engler[†], M. Finger[†], D. Fuhrmann[††], P.L. Ghia[**], H.J. Gils[†], R. Glasstetter[††], C. Grupen[‖], A. Haungs[†], D. Heck[†], J.R. Hörandel[‡,xiii], T. Huege[†], P.G. Isar[†], K.-H. Kampert[††], D. Kang[‡], D. Kickelbick[‖], H.O. Klages[†], Y. Kolotaev[‖], P. Łuczak[*], H.J. Mathes[†], H.J. Mayer[†], J. Milke[†], B. Mitrica[¶], C. Morello[**], G. Navarra[§], S. Nehls[†], J. Oehlschläger[†], S. Ostapchenko[†,xiv], S. Over[‖], M. Petcu[¶], T. Pierog[†], H. Rebel[†], M. Roth[†], H. Schieler[†], F. Schröder[†], O. Sima[‡‡], M. Stümpert[‡], G. Toma[¶], G.C. Trinchero[**], H. Ulrich[†], W. Walkowiak[‖], A. Weindl[†], J. Wochele[†], M. Wommer[†],**

[*]*Soltan Institute for Nuclear Studies, 90950 Lodz, Poland*
[†]*Institut für Kernphysik, Forschungszentrum Karlsruhe, 76021 Karlsruhe, Germany*
[‡]*Institut für Experimentelle Kernphysik, Universität Karlsruhe, 76021 Karlsruhe, Germany*
[§]*Dipartimento di Fisica Generale dell'Università, 10125 Torino, Italy*
[¶]*National Institute of Physics and Nuclear Engineering, 7690 Bucharest, Romania*
[‖]*Fachbereich Physik, Universität Siegen, 57068 Siegen, Germany*
[**]*Istituto di Fisica dello Spazio Interplanetario, INAF, 10133 Torino, Italy*
[††]*Fachbereich Physik, Universität Wuppertal, 42097 Wuppertal, Germany*
[‡‡]*Department of Physics, University of Bucharest, 76900 Bucharest, Romania*
[xi]*now at: Universidad Michoacana, Morelia, Mexico*
[xii]*now at: Universidade São Paulo, Instituto de Fisica de São Carlos, Brasil*
[xiii]*now at: Dept. of Astrophysics, Radboud University Nijmegen, The Netherlands*
[xiv]*now at: University of Trondheim, Norway*

Abstract. **The Muon Tracking Detector (MTD) in KASCADE-Grande allows to measure with high accuracy muon directions in EAS up to 700 m distance from the shower center. According to the simulations this directional information allows to study longitudinal development of showers by means of such quantities like muon radial angles and, derived out of radial and tangential angle values, muon pseudorapidities. Shower development depends on the hadronic interactions taking place in the atmosphere, therefore, such study is a good tool for testing interaction models embedded in the Monte-Carlo shower simulations.**

Sensitivity of the muon radial angles and their pseudorapidities to the shower development will be discussed and examples of measured distributions will be shown. Experimental results will be compared with simulation predictions showing the possibility to validate hadronic interaction models with the MTD data.

Keywords**: KASCADE-Grande, muon tracking,**

I. INTRODUCTION

The Muon Tracking Detector (MTD) [1], registering muons above an energy threshold 800 MeV, is one of the detector components in the KASCADE-Grande EAS experiment [2] operated on site of the Research Center Karlsruhe in Germany by an international collaboration (see Fig.1). The directions of muon tracks in EAS are measured by the MTD with excellent angular resolution of $\approx 0.35^{\circ}$. These directional data allow to investigate the longitudinal development of the muonic component in showers which is a signature of the development of the hadronic EAS core. Among the various EAS components there are only four, that are the penetrating ones: optical photons, muons, neutrinos and radio emission. As a result of their penetrating ability they provide practically undisturbed information about their origin. Out of these four, optical photons (of eV energy or smaller) as the most numerous particles, have been used most successfully so far (e.g. ref. [3]) in the study of the longitudinal shower development of individual showers. Muon information has usually been integrated over a large sample of showers and over the whole longitudinal profile.

However, muons have some advantage compared with optical photons and the radio emission: they reflect the development of the nuclear cascade with no mediation from the electromagnetic part of the shower. They are also "seen" the whole day long, not only on clear moonless nights. This feature they share with the EAS radio emission. Evident disadvantage of muons is that they are less numerous than photons and are therefore subject to large fluctuations. Moreover, being charged particles they are subjected to deflection in the geomagnetic field. Therefore, attempts to use them as an independent

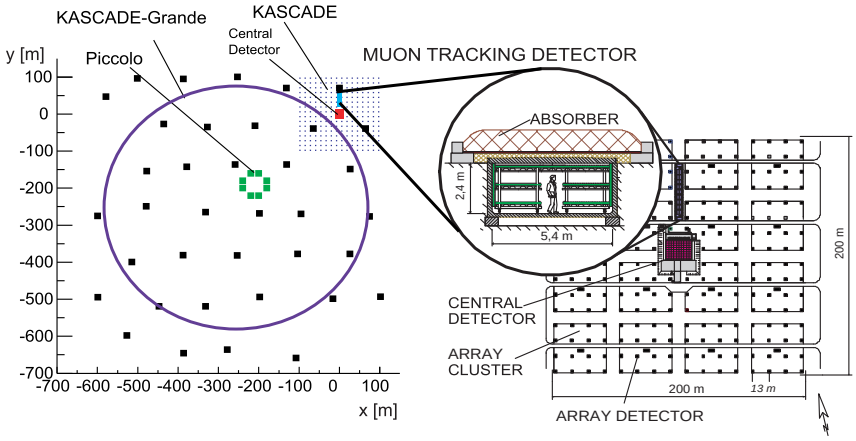

Fig. 1: Layout of the KASCADE-Grande experiment distributed over the Research Center Karlsruhe. KASCADE is situated in the North-East corner of the Center: note the position of the Muon Tracking Detector.

source of information on EAS development were rather rare in the past, but now, with the development of such sophisticated detectors as the MTD, they become more feasible and gain importance. On the other hand, muons have never been used up to now to reconstruct the hadron longitudinal development of EAS with sufficient accuracy, due to the difficulty of building large area ground-based muon telescopes.

Muons are produced mainly in decay processes of charged pions and kaons - most numerous products of the hadronic interations driving the development of EAS. The longitudinal profile of the hadronic cascade depends on the primary mass, and thus, can be used for testing the hadronic interaction models.

The most straightforward method of investigation of the longitudinal shower development is to reconstruct the muon production heights by means of triangulation [4], [5]. Results of such a research are presented on this conference by P. Doll et al. [6]. The longitudinal development of a shower has its imprint also in the lateral distribution of muon densities, presented on this conference by P. Łuczak et al. [7]. Here we will show, that the directional data of muons in EAS obtained with the MTD can be used to reconstruct such quantities like radial (ρ) and tangential (τ) angles and, as a next step, muon pseudorapidies [8], which are also sensitive to the longitudinal shower development. Therefore they can also serve to validate hadronic interaction models used in Monte-Carlo EAS simulations [9].

II. Radial, tangential angles, and muon pseudorapidity

Investigation of muons registered in the MTD is based on the two ortogonal projections of the muon angle in space with respect to the shower axis direction, namely the radial (ρ) and tangential (τ) angles. Their definition is given in Fig. 2 and their properties are discussed in [8]. Here we remind only, that the value of muon radial angle

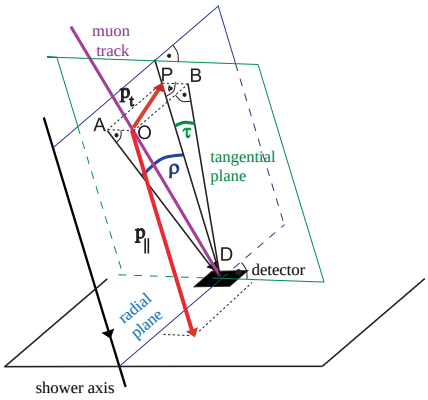

Fig. 2: Definition of radial (ρ) and tangential (τ) angles.

is dominated by the value of the transverse momentum of its parent meson.

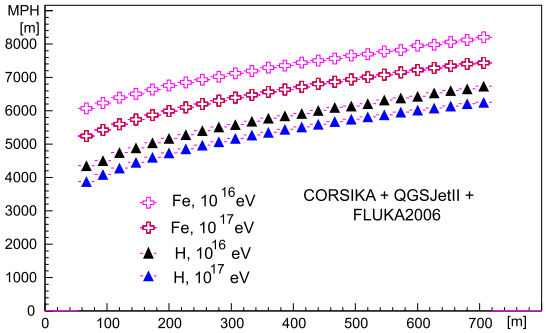

Fig. 3: Lateral distribution of the mean muon production height (MPH) in vertical showers for the two primary particle types and two energies.

In [8] it was also shown that using τ and ρ one can reconstruct the pseudorapidity of muons in the shower reference system (z-axis parallel to the shower direction): η = - $\ln \frac{\zeta}{2}$, where ζ=$\sqrt{\tau^2 + \rho^2}$. This pseudorapidity is

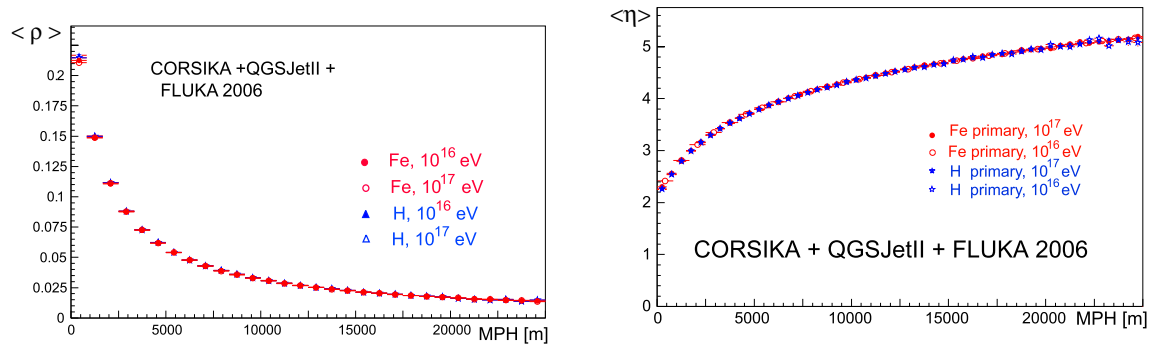

(a) (b)

Fig. 4: Mean radial angle (a) and mean pseudorapidity (b) of muons registered in the MTD and produced at a given height above the detector is independent of the primary mass and energy.

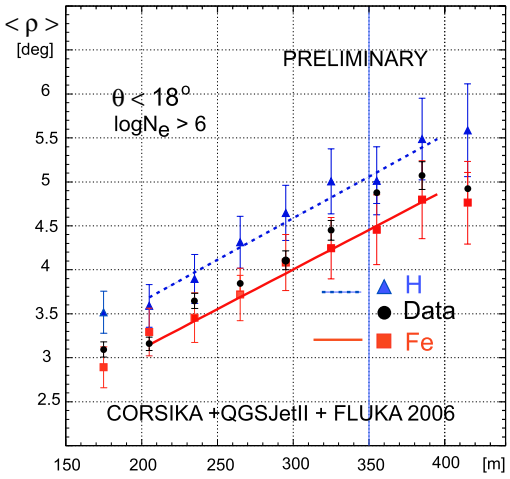

Fig. 5: Reconstructed lateral distribution of the mean radial angle compared with CORSIKA simulation results for proton and iron primaries. Lines are fits to the simulations.

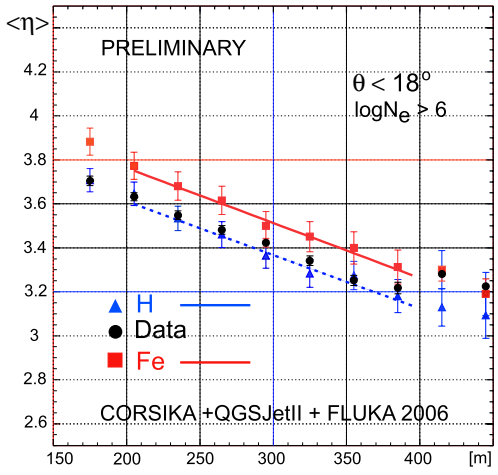

Fig. 6: Reconstructed lateral distribution of the mean muon pseudorapidity compared with CORSIKA simulation results for proton and iron primaries. Lines are fits to the simulations.

closely related with the rapidity of parent mesons [10], thus being a good tool for testing interaction models.

In Fig. 3 the sensitivity of the MTD to the longitudinal shower development is demonstrated. At each distance to the shower core registered muons have certain average production height (MPH), being dependent on the type of primary and its energy. Muons in proton induced showers are per average produced deeper than in iron showers; with increase of the primary energy mean MPH moves deeper into the atmosphere.

As it is seen from the CORSIKA [11] simulation results shown in Fig. 4 muons from a given production height carry to the observation level a certain mean value of ρ and η, irrespective to the primary type and energy. Having in mind Fig. 3 we conclude, that radial angles and pseudorapidity of muons in the showers are parameters sensitive to the longitudinal shower development. Therefore, they can be used to test the hadronic interaction models.

III. Experimental data and simulation results

The MTD data collected in the period from March 2004 to November 2008 have been used to reconstruct muon mean radial angles and mean muon pseudorapidities. Vertical showers ($\theta \leq 18°$) with the size $\lg N_e > 6$ have been selected. The fiducial area for core positions was: -550 m $\leq$ x_{core} $\leq$ 50 m and -580 m $\leq$ y_{core} $\leq$ 20 m.

Then the lateral distributions of those two quantities have been obtained and compared with the results reconstructed out of the simulated data for two primary species: proton and iron. The simulations were done with CORSIKA code using the QGSJETII model [12] for high energy interactions above 200 GeV and FLUKA2006 [13] below that energy.

In Fig. 5 experimental and simulated radial angle lateral distributions are compared. The comparison is done in limited ranges of muon distances to the core, where the saturation effects (seen below 150 m) and trigger inefficiencies (seen above 400 m) are not present. The lines are linear fits to the simulation results. The error bars in the simulations are still too large and the number of simulated data will be increased, thus the results are marked "Preliminary".

We can conclude here that the experimental data is compatible with the CORSIKA simulations done using QGSJETII - FLUKA model combination - data points are in-between the simulated ones. Similar concusions about intrinsic consistency of these models is found in [14]. We can also notice that experimental data tend to be positioned closer to the radial angles in iron initiated showers rather than proton ones.

In Fig. 6 lateral distributions of mean muon pseudorapidity for the same data sets, experimental and simulated, are compared. Here, one can also conclude that the experimental data points are bracketed by the simulated distributions showing compatibility of the simulations with the experiment, same as it is in the case of radial angles, discussed above.

However, there is one striking difference in this figure compared to Fig. 5. The data points here are closer to the proton simulation results rather than to the iron ones, as it is in the case of radial angle distribution. And for the shower sizes in our investigation one would really expect the result being shown by the radial angle distributions (at primary energies in the region of $10^{16}eV$ and above rather heavier than lighter composition is seen in the analyses of many other shower parameters).

This difference may be an indication of the features of the models. Mean radial angle distribution (Fig. 5) suggests that the transverse momentum of pions produced in hadronic interactions is reproduced by the models in a way close to the reality.

On the other hand, Fig. 6 shows that the rapidity of those pions is in simulations too large, by 0.05 - 0.1 in the mean values.

Mean radial angles and mean pseudorapidities of muons registered by the MTD in a given distance range from the shower core are quantities sensitive to the primary mass (what was shown also in section II).

However, for the investigation of the mass composition (e.g. in terms of the determination of the $<\ln A>$ parameter) with the model combination used in this research, one should rather wait for the increased statistics of Monte-Carlo simulations.

IV. Acknowledgements

The KASCADE-Grande experiment is supported by the BMBF of Germany, the MIUR and INAF of Italy, the Polish Ministry of Science and Higher Education (grant for 2009-2011), and the Romanian Ministry of Education, Research and Innovation. This work was supported in part by the German-Polish bilateral collaboration grant (PPP - DAAD) for the years 2009-2010.

References

[1] P. Doll et al.,"Muon tracking detector for the air shower experiment KASCADE", Nucl. Instr. and Meth. A 488, 2002, 517.

[2] M. Bertaina et al. (KASCADE-Grande Coll.),"KASCADE-Grande: An overview and first results", Nucl. Instr. and Meth. A 588, 2008, 162;
G. Navarra et al. (KASCADE-Grande Coll.),"KASCADE-Grande: A large acceptance, high-resolution cosmic-ray detector up to 10^{18} eV",Nucl. Instr. and Meth. A 518, 2004, 207.

[3] S.P. Swordy and D.B. Kieda,"Elemental composition of cosmic rays near the knee by multiparameter measurements of air showers", Astropart. Phys. vol. 13, 2000, 137.

[4] J. Linsley, J.Phys.G:Part.Phys.,"Thickness of the particle swarm in cosmic-ray air showers", vol. 1, 1986, 51;
J. Linsley, Nuovo Cim., "Interpretation of EAS observations by time-track complementarity (TCC)" vol. C 15, 1992, 743.

[5] M.Ambrosio et al.,"Performances of RPC detectors with tracking and timing electronics", Nucl.Instr. and Meth. A 344, 1994, 350.

[6] P. Doll et al., (KASCADE-Grande Coll.),"Muon Production Height and Longitudinal Shower Development", Proc. 31^{st} ICRC, 2009, Lodz, Poland, vol. HE 1.5, these proceedings.

[7] P. Łuczak et al.,"Lateral distribution of EAS muons measured with the KASCADE-Grande Muon Tracking Detektor", Proc. 31^{st} ICRC, 2009, Lodz, Poland, vol. HE 1.5, these proceedings.

[8] J. Zabierowski, K. Daumiller and P. Doll,"Properties of tangential and radial angles of muons in EAS", Nucl. Phys. B (Proc. Suppl.) vol.122, 2003, 275.

[9] J. Zabierowski et al. (KASCADE-Grande Coll.),"Muon Tracking in KASCADE-Grande:CORSIKA Simulation Study", Proc.29^{th} ICRC, Pune, India, 2005, vo.6, 357.

[10] J. Zabierowski et al. (KASCADE Coll.),"Investigation of the pseudorapidity and momentum of muons in EAS with the KASCADE muon tracking detector" Nucl. Phys. B (Proc. Suppl.) vol. 151, 2006, 291.

[11] D. Heck et al.,"CORSIKA" A Monte-Carlo Code to Simulate Extensive Air Showers", FZKA Report 6019, Forschungszentrum Karlsruhe, 1998.

[12] S.S. Ostapchenko, Nucl. Phys. B (Proc. Suppl.) vol.151, 2006, 143;
S.S. Ostapchenko, "Nonlinear screening effects in high energy hadronic interactions" Phys.Rev D vol.74, 2006, 014026.

[13] A. Fasso et al., Proc CHEP2003, Paper MOMT005, eConf C0303241 (2003), arXiv:hep-ph/0306267.

[14] A.Haungs et al. (KASCADE-Grande Coll.), Proc. 31^{st} ICRC, 2009, Lodz, Poland, vol. HE 1.3, these proceedings.

Lateral distribution of EAS muons measured with the KASCADE-Grande Muon Tracking Detector

P. Łuczak*, W.D. Apel†, J.C. Arteaga‡,[xi], F. Badea†, K. Bekk†, M. Bertaina§, J. Blümer†,‡, H. Bozdog† I.M. Brancus¶, M. Brüggemann‖, P. Buchholz‖, E. Cantoni§,, A. Chiavassa§, F. Cossavella‡, K. Daumiller†, V. de Souza‡,[xii], F. Di Pierro§, P. Doll†, R. Engel†, J. Engler†, M. Finger†, D. Fuhrmann††, P.L. Ghia**, H.J. Gils†, A. Haungs†, R. Glasstetter††, C. Grupen‖, A. Haungs†, D. Heck†, J.R. Hörandel‡,[xiii], T. Huege†, P.G. Isar†, K.-H. Kampert††, D. Kang‡, D. Kickelbick‖, H.O. Klages†, Y. Kolotaev‖, H.J. Mathes†, H.J. Mayer†, J. Milke†, B. Mitrica¶, C. Morello**, G. Navarra§, S. Nehls†, J. Oehlschläger†, S. Ostapchenko†,[xiv], S. Over‖, M. Petcu¶, T. Pierog†, H. Rebel†, M. Roth†, H. Schieler†, F. Schröder†, O. Sima‡‡, M. Stümpert‡, G. Toma¶, G.C. Trinchero**, H. Ulrich†, W. Walkowiak‖, A. Weindl†, J. Wochele†, M. Wommer†, J. Zabierowski***

*Soltan Institute for Nuclear Studies, 90950 Lodz, Poland

†Institut für Kernphysik, Forschungszentrum Karlsruhe, 76021 Karlsruhe, Germany

‡Institut für Experimentelle Kernphysik, Universität Karlsruhe, 76021 Karlsruhe, Germany

§Dipartimento di Fisica Generale dell'Università, 10125 Torino, Italy

¶National Institute of Physics and Nuclear Engineering, 7690 Bucharest, Romania

‖Fachbereich Physik, Universität Siegen, 57068 Siegen, Germany

**Istituto di Fisica dello Spazio Interplanetario, INAF, 10133 Torino, Italy

††Fachbereich Physik, Universität Wuppertal, 42097 Wuppertal, Germany

‡‡Department of Physics, University of Bucharest, 76900 Bucharest, Romania

[xi] now at: Universidad Michoacana, Morelia, Mexico

[xii] now at: Universidade de São Paulo, Instituto de Fîsica de São Carlos, Brasil

[xiii] now at: Dept. of Astrophysics, Radboud University Nijmegen, The Netherlands

[xiv] now at: University of Trondheim, Norway

***Abstract*. The KASCADE-Grande Muon Tracking Detector (MTD) allows to measure with high accuracy directions of EAS muons with energy above 0.8 GeV up to 700 m distance from the shower center. Lateral distribution of muon densities reflects the longitudinal development of the muonic shower component, thus comparison of experimental distributions from different detectors, as well as with the simulated results, allows to check the contemporary understanding of shower physics. Experimental results for EAS muons above 0.8 GeV obtained for the first time with the tracking detector in a wide range of distances from the core will be shown. They will be compared with the lateral distributions of muons above 0.23 GeV, measured with KASCADE Array muon scintillation counters. Comparison with the simulation results will also be shown.**

***Keywords*: KASCADE-Grande, Muon Tracking Detector, lateral muon density distributions**

I. INTRODUCTION

Ivestigations of muonic component in Extensive Air Shower (EAS) is of a primary importance for understanding air shower physics. Muons carry to the observation level nearly undistorted information about their parent particles: pions and kaons, which are the most numerous products of hadronic interactions responsible for the development of the shower in the atmosphere.

A perfect tool for such investigations is the KASCADE-Grande EAS experiment [1], being an extension of the KASCADE experimental setup [2]. It is a multi-detector system located on site of the Research Centre (Forschungszentrum) Karlsruhe in Germany at 110 m a.s.l., measuring all three EAS components: hadrons, electrons and muons (at 4 energy thresholds) in a wide range of distances (up to 700 m) from the shower core, and primary particle energies (5×10^{14}–10^{18} eV). High precision measurements of particle densities and tracks, the latter by means of a dedicated Muon Tracking Detector (MTD) [3] - at different energy thresholds allow to investigate many features of EAS and are the basis for multiparameter analyses (e.g.: [4], [5]). These features of KASCADE-Grande make it also to a very good test field for the development of other shower detection techniques, like radio detection (LOPES [6]).

II. KASCADE-GRANDE

A. The KASCADE experiment

The KASCADE experiment (Fig.1) consists of several detector systems. A description of the performance of the experiment can be found elsewhere ([2]). An array of 252 detector stations 200 m $\times$ 200 m (called the Array), is organized in a square grid of 16 clusters, and equipped with scintillation counters, which measure the electromagnetic (threshold 5 MeV) and in the outer 12 clusters, below a lead iron shielding imposing the energy

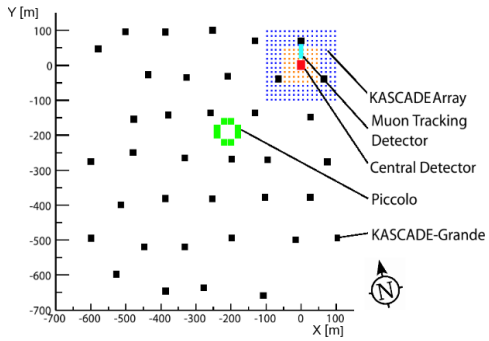

Fig. 1: The layout of the KASCADE-Grande experiment.

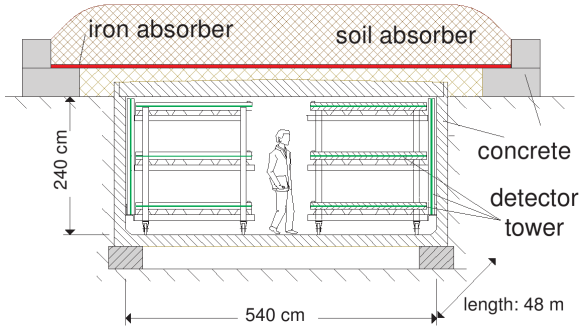

Fig. 2: Cross-section of the Muon Tracking Detector tunnel.

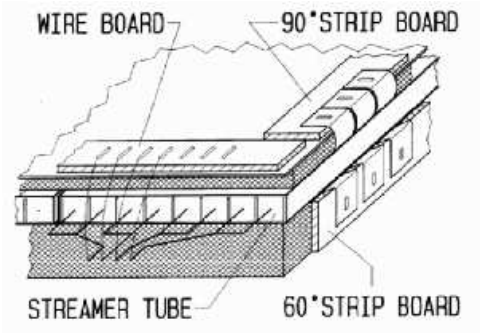

Fig. 3: The MTD module design.

threshold of 230 MeV, also the muonic parts of EAS. In its centre, a 16 m $\times$ 20 m iron sampling calorimeter (a main part of the Central Detector) detects the hadrons in the shower core [7].

Muon detectors located in the third gap of the calorimeter provide a trigger for the calorimeter and additional information about the lateral and time distribution of muons (above 490 MeV energy) near the shower core [2], [8]. Underneath the calorimeter two layers of multi-wire proportional chambers (MWPC) are used to measure tracks of muons with energy above 2.4 GeV. In the northern part of the KASCADE Array the 128 m^2 large Muon Tracking Detector is situated.

B. Grande part of the experiment

Grande is an extension of the KASCADE Array. It is an array of 37 detector stations organized in a hexagon grid of 18 clusters covering an area of 0.5 km^2. Each station contains 10 m^2 of plastic scintillators for registration of charged particles. In the centre there is a small trigger array of plastic scintillation stations, called Piccolo, build to provide additional trigger for the MTD and other KASCADE components.

III. THE MUON TRACKING DETECTOR

The Muon Tracking Detector is installed below ground level in a concrete tunnel. Under the shielding of 18 r.l., made out of concrete, sand and iron (Fig.2), 16 muon telescopes (called detector towers) register tracks of muons which energy exceeds 800 MeV. Each tower contains limited streamer tube (ST) detector modules: three horizontal and one vertical. All towers are connected with a gas supply system, high voltage and electronic chain readout system.

Each ST chamber houses 16 anode copper-beryllium wires in two cathode comb profiles, extruded for eight parallel ST cells of 9$\times$9 mm^2 cross-section and 4000 mm length.

In the MTD an efficient chain-type readout system is used. Front-end electronics boards, mounted to the detector modules are acquiring signals from wires and strips. Each of three wire and nine strip boards in a module creates digital signals being used to reconstruct the tracks. Information from all modules, under certain trigger condition, is send to the acquisition system. Detailed information about the design of the MTD may be found in [3] and [9].

When a particle is passing through the modules of the tower it ionizes the gas in the streamer tubes and a streamer is created. As a result we have a large increase of charge in a small volume of the tube. This charge is inducing a certain charge in the aluminum strips above and below the tubes (perpendicular and diagonal, 60° with respect to the wires), respectively (Fig.3). Coincidence of the signal from the wires and strips in each layer is called a hit. The tracks are reconstructed out of three or two hits, in three or two modules, respectively. The algorithm is first searching for three hit tracks and the remaining hits are used next to create two hit tracks out of them.

IV. TRACKING MUONS IN EAS

Combined information of the muon tracks, direction of the shower axis and the shower core position allows to investigate the muonic component of the EAS more precisely than it is done with the scintillator array alone. With the MTD we count muons and, in addition, have very precise (better than 0.3°) information about their directions. This allows to investigate the longitudinal development of the muon component, and due to its close relation to EAS hadrons, the development of showers themselves. This investigation is done by studying quantities derived from the experimental data, like mean muon production height [10] and shower

muon pseudorapidities [11]. The way shower develops in the atmosphere (and its muon component in particular) leaves its imprint in the lateral distributions of muons – also a subject of our investigations with the MTD data.

V. LATERAL MUON DENSITY DISTRIBUTIONS

Lateral distribution of EAS particles is an important characteristic of the shower cascade in the atmosphere. In particular, such distributions of EAS muons, being closely related to the hadronic shower component, are a good tool to test the quality of experimental detector setup and our understanding of shower physics. Therefore, every EAS experiment, equipped with sufficiently large muon detectors, provides such distributions. Also KASCADE experiment has done so [4] and first preliminary distributions from KASCADE-Grande were reported [12] , [13].

Usually results were obtained with arrays of shielded scintillator detectors, the most popular device in EAS experiments. With the MTD in KASCADE-Grande, for the first time with high angular resolution, it is possible to obtain lateral distributions of muons registered with the tracking devices, like limited streamer tube telescopes. Muon numbers (muon densities) are obtained by counting particle tracks instead of measuring energy deposits, as it is the case with shielded scintillator arrays.

A. Selection of events

This analysis is based on the showers measured in a period from March 2004 till November 2008 fulfilling the following conditions:

1) All clusters in the KASCADE-Grande array and the MTD work properly,
2) Reconstruction of shower parameters from Grande array was succesful,
3) Zenith angle of the shower $\Theta \leq 18^{\circ}$,
4) Shower core was reconstructed in fiducial area where $\mathrm{x_{core}} \in \langle -550\mathrm{m}; 50\mathrm{m} \rangle$ and $\mathrm{y_{core}} \in \langle -580\mathrm{m}; 20\mathrm{m} \rangle$.

B. Calculation of the number of tracks and the area of the MTD

The detector area is divided into 30 meter radial bins around the reconstructed shower core position (see Fig.4). Muon tracks are reconstructed from hits in two or three MTD modules and the position of each hit is known. Distance from the hit in the middle module to the shower axis is the muon distance.
The area of the detector in each distance bin is calculated in the following way:

From very precise measurements the position of every wire pair and perpendicular strip is known. Point where the wire pair is crossing the perpendicular strip is a centre of a basic detection unit (cell) in the MTD. Each cell has constant area of ~ 4 cm^2. Distance of each cell to the shower axis is being calculated and the number of cells is accumulated in each distance bin. This number

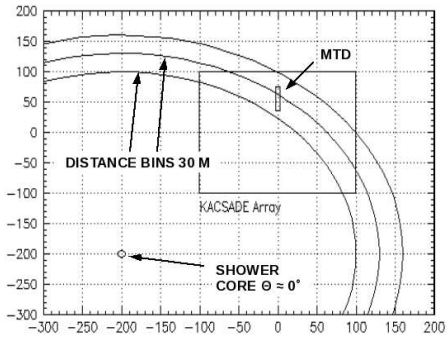

Fig. 4: 30 meter radial bins divide the MTD into parts (from one to three). In each bin the number of muons and the detector area is calculated.

of cells gives information about the detector area in that bin. The number of muon tracks in each distance bin is corrected for the reconstruction efficiency. The track reconstruction efficiency is calculated from the following formula (1):

$$\epsilon = \frac{1}{1 + \frac{N_{tr2}}{3 \cdot N_{tr3}}} \tag{1}$$

where N_{tr2} and N_{tr3} are two and three hit tracks respectively. Becasue of reconstruction procedure two and three hit tracks are not independent and it is necessary to introduce a proper correction factor k, given by the formula (2):

$$k = \frac{1}{3 \cdot \epsilon^3 + 2 \cdot \epsilon^2} \tag{2}$$

Typicaly $\epsilon = 0.74$ and $k = 0.4$
The density ρ_i in each distance bin is calculated as a sum of all muons from all showers corrected for reconstruction efficiency being divided by detector area corrected for zenith angle (A_{MTD}).

$$\rho_i = \frac{\sum_{j=1}^{N_s} (N_{tr2}^j + N_{tr3}^j) \cdot k}{\sum_{j=1}^{N_s} A_{MTD}^{j,i}} \tag{3}$$

where i is distance bin number, N_s is number of showers, $A_{MTD}^{j,i}$ is detector area in i^{th} distance bin for j^{th} shower.

In Fig.5 the preliminary results for the lateral muon density distributions are presented in four muon size bins: from $\lg(\mathrm{N}_\mu)>4.9$ to $\lg(\mathrm{N}_\mu)<6.1$. N_μ is derived from muon densities measured with KASCADE muon detectors and the above mentioned range roughly corresponds to primary energies from 10^{16} eV to 10^{17} eV. Together with the MTD results, represented by symbols, the lateral distributions based on the number of muons reconstructed out of energy deposits in shielded plastic scintillators of the KASCADE Array (represented by lines) are given. One can notice that the presented distributions can be compared in limited distance range (marked by full symbols and solid lines for the MTD and KASCADE distributions respectively). It is due to

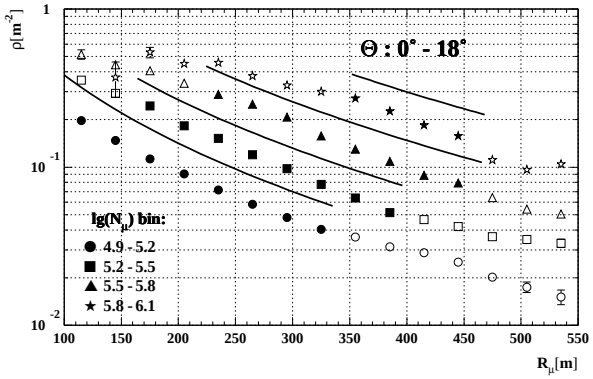

Fig. 5: Lateral muon density distributions obtained with the MTD (symbols) and with the KASCADE Array muon detectors (lines) in four muon size bins (see text).

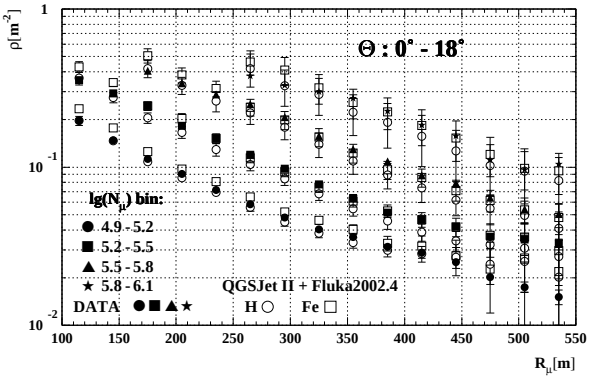

Fig. 6: Lateral muon density distributions obtained with the MTD (solid symbols) and simulations (see text).

saturation effects in the MTD when the core of the shower, initiated by high energy particle, is close to the detector. At large distances the experimental setup is not able to provide an efficient trigger. The absolute values of muon densities for both muon energy thresholds (230 MeV for the KASCADE Array and 800 MeV for the MTD) are still preliminary. Systematic uncertainties (e.g shower and track reconstruction accuracies) and efficiency corrections are under investigation. However, general shape of the distributions has been already established. It can be fitted with a Lagutin-like function (4) [15],[16]. In case of the lower energy muons the function is of the form :

$$f(r) = 0.28 \cdot r_0^{-2} \left(r/r_0\right)^{-0.69} \left(1 + r/r_0\right)^{-2.39} \times \left(1 + \left(r/(10 \cdot r_0)\right)^{-2}\right)^{-1} \quad (4)$$

where r_0=320 m. For the higher energy muons registered by the MTD the distribution is steeper and can be described by similar Lagutin-like function where r_0 is smaller.

In Fig.6 comparison of the MTD distribution with CORSIKA [14] simulations of proton and iron primaries is shown. In muon size bin $\lg(N_\mu)$ from 4.9 to 5.2 the data are between simulations. In higher bins ($\lg(N_\mu)$ from 5.2 to 6.1) the data, in the distance ranges where the MTD results can be compared with KASCADE, seem to lie on top of iron distributions. Close and far away from the shower core the data points have tendency to lie on top of proton distributions. This is due to differences in track reconstruction in data and simulations. However, within our accuracies, the experimental distributions are in a good agreement with simulations.

ACKNOWLEDGEMENTS

The KASCADE-Grande experiment is supported by the BMBF of Germany, the MIUR and INAF of Italy, the Polish Ministry of Science and Higher Education (grant for 2009-2011), and the Romanian Ministry of Education, Research and Innovation. This work was supported in part by the German-Polish bilateral collaboration grant (PPP - DAAD) for the years 2009-2010.

REFERENCES

[1] G. Navarra et al. (KASCADE-Grande Coll.), "KASCADE-Grande: A large acceptance, high-resolution cosmic-ray detector up to 10**18-eV", *Nucl. Instr. Meth.* A518, 2004, pp. 207-209.
[2] T. Antoni et al., "The Cosmic ray experiment KASCADE", *Nucl. Instr. Meth.* A 513 , 2003, pp. 490-510.
[3] P. Doll et al., "Muon tracking detector for the air shower experiment KASCADE", *Nucl. Instr. Meth.* A 488, 2002, pp. 517-535
[4] T. Antoni et al. (KASCADE-Grande Coll.), "Electron, Muon, and Hadron Lateral Distributions Measured in Air-Showers by the KASCADE Experiment", *Astropart. Phys.*, 14, 2001, pp. 245-260
[5] M. Bertaina et al. (KASCADE-Grande Coll.), "KASCADE-Grande: An overview and first results", *Nucl. Instr. Meth.* A 588, 2008, pp. 162-165.
[6] H. Falcke et al. (LOPES Coll.), "Detection and imaging of atmospheric radio flashes from cosmic ray air showers", *Nature*, vol. 435, 2005, pp. 313-316.
[7] J. Engler et al., "A Warm-liquid Calorimeter for Cosmic-ray Hadrons", *Nucl. Instr. Meth.* A427, 1999, pp.528-542.
[8] T. Antoni et al. (KASCADE-Grande Coll.), "Muon Density Measurements with the KASCADE Central Detector", *Astropart. Phys.*, 16, 2002, pp. 373-386.
[9] J. Zabierowski and P. Doll., "Front-end readout boards for streamer tube muon tracking detector in the KASCADE EAS Experiment" , *Nucl.Instr. and Meth.* A 484, 2002, pp. 528-532.
[10] P. Doll et al., "Muon Production Height and Longitudinal Shower Development.", $31^{th} ICRC$, these proceedings.
[11] J. Zabierowski et al., "Study of EAS development with the Muon Tracking Detector in KASCADE-Grande", $31^{th} ICRC$, these proceedings.
[12] A. Haungs et al. (The KASCADE-Grande Coll.), "Investigations of Muons in EAS with KASCADE-Grande", *Nucl. Phys. B (Proc.Suppl.)* 2002, vol. 175-176, pp. 354-357.
[13] D. Furhman et al. , "Muonic Component of Air Showers Measured by the KASCADE-Grande Experiment", $31^{th} ICRC$, these proceedings.
[14] D. Heck, J. Knapp, J.N. Capdevielle, G. Schatz, T. Thouwheck, "CORSIKA: A Monte Carlo Code to Simulate Extensive Air Showers", *Forschungszentrum Karlsruhe Report* FZKA 6019, 1998
[15] A. A. Lagutin, R. I.Raikin, "Latreal distribution of electrons in EAS at superhigh energies: predictions and experimental results", *Nucl. Phys. B (Proc. Suppl.)*, vol. 97, 2001, pp. 274-277.
[16] A. A. Lagutin, R. I. Raikin, N. Inoue and A. Misaki, "Electron lateral distribution in air showers: scaling formalism and its implications", *J. Phys. G* 2002, vol 28, pp. 1259-1274.

Muon Production Height and Longitudinal Shower Development

P. Doll[*], W.D. Apel[*], J.C. Arteaga[†,xi], F. Badea[*], K. Bekk[*], M. Bertaina[‡], J. Blümer[*,†], H. Bozdog[*], I.M. Brancus[§], M. Brüggemann[¶], P. Buchholz[¶], E. Cantoni[‡,‖], A. Chiavassa[‡], F. Cossavella[†], K. Daumiller[*], V. de Souza[†,xii], F. Di Pierro[‡], R. Engel[*], J. Engler[*], M. Finger[*], D. Fuhrmann[**], P.L. Ghia[‖], H.J. Gils[*], R. Glasstetter[**], C. Grupen[¶], A. Haungs[*], D. Heck[*], J.R. Hörandel[†,xiii], T. Huege[*], P.G. Isar[*], K.-H. Kampert[**], D. Kang[†], D. Kickelbick[¶], H.O. Klages[*], Y. Kolotaev[¶], P. Łuczak[††], H.J. Mathes[*], H.J. Mayer[*], J. Milke[*], B. Mitrica[§], C. Morello[¶], G. Navarra[‡], S. Nehls[*], J. Oehlschläger[*], S. Ostapchenko[*,xiv], S. Over[¶], M. Petcu[§], T. Pierog[*], H. Rebel[*], M. Roth[*], H. Schieler[*], F. Schröder[*], O. Sima[‡‡], M. Stümpert[†], G. Toma[§], G.C. Trinchero[§], H. Ulrich[*], W. Walkowiak[¶], A. Weindl[*], J. Wochele[*], M. Wommer[*], J. Zabierowski[††]

[*]*Institut für Kernphysik, Forschungszentrum Karlsruhe, 76021 Karlsruhe, Germany*
[†]*Institut für Experimentelle Kernphysik, Universität Karlsruhe, 76021 Karlsruhe, Germany*
[‡]*Dipartimento di Fisica Generale dell'Università, 10125 Torino, Italy*
[§]*National Institute of Physics and Nuclear Engineering, 7690 Bucharest, Romania*
[¶]*Fachbereich Physik, Universität Siegen, 57068 Siegen, Germany*
[‖]*Istituto di Fisica dello Spazio Interplanetario, INAF, 10133 Torino, Italy*
[**]*Fachbereich Physik, Universität Wuppertal, 42097 Wuppertal, Germany*
[††]*Soltan Institute for Nuclear Studies, 90950 Lodz, Poland*
[‡‡]*Department of Physics, University of Bucharest, 76900 Bucharest, Romania*
[xi]*now at: Universidad Michoacana, Morelia, Mexico*
[xii]*now at: Universidade São Paulo, Instituto de Fisica de São Carlos, Brasil*
[xiii]*now at: Dept. of Astrophysics, Radboud University Nijmegen, The Netherlands*
[xiv]*now at: University of Trondheim, Norway*

***Abstract*. A large area ($128\ m^2$) Muon Tracking Detector (MTD), located within the KASCADE experiment, has been built with the aim to identify muons ($E_\mu > 0.8$ GeV) and their directions in extensive air showers by track measurements under more than 18 r.l. shielding. The orientation of the muon track with respect to the shower axis is expressed in terms of the radial- and tangential angles. By means of triangulation the muon production height H_μ is determined. By means of H_μ, a transition from light to heavy cosmic ray primary particles with increasing shower energy E_o from 1-10 PeV is observed.**

***Keywords*: KASCADE-Grande: Muon Production Height**

I. Introduction

Muons have never been used up to now to reconstruct the longitudinal development of EAS with sufficient accuracy, due to the difficulty of building large area ground-based muon telescopes [1]. Muons are produced mainly by charged pions and kaons in a wide energy range. Usually they are not produced directly on the shower axis. Multiple Coulomb scattering in the atmosphere and in the detector shielding may change the muon direction. It is evident that the reconstruction of the longitudinal development of the muon component by means of triangulation [2], [3] provides a powerful tool for primary mass measurement, giving an information similar to that obtained with the fluorescence technique, but in the energy range not accessible by the detection of fluorescence light. Muon tracking allows to study the angular correlation of the muons with respect to shower axis and,therefore, hadronic interactions in shower development by means of the muon pseudorapidity [6]. Already in the past, analytical tools have been developed which describe the transformation between shower observables recorded on the observation level and observables which represent directly the longitudinal shower development [4]. Fig. 1 shows the experimental environment. Measured core position distributions for showers inside KASCADE range from 40 m-140 m and inside Grande from 140 m-360 m. These core positions stay away from the MTD more than 40 m for KASCADE for shower energies $\sim 10^{15}eV - 10^{16.5}eV$ and more than 140 m for Grande for shower energies $\sim 10^{16}eV - 10^{17.5}eV$. Such shower core distribution for Grande covers almost full trigger efficiency in the Grande specific energy range as confirmed by investigations of muon lateral density distributions as shown in Fig. 5 in the contribution by P. Luczak to this ICRC2009 [7].

II. Muon Production Height

Usually, X_{max} is the atmospheric depth at which the electrons and photons of the air shower reach their maximum numbers and is considered to be mass A sensitive [8]. Concerning muons which stem dominantly from $\pi^{\pm}$ decays, the corresponding height where most muons are created may also provide a mass A and energy sensitive observable. For X_{max}, Matthews [9]

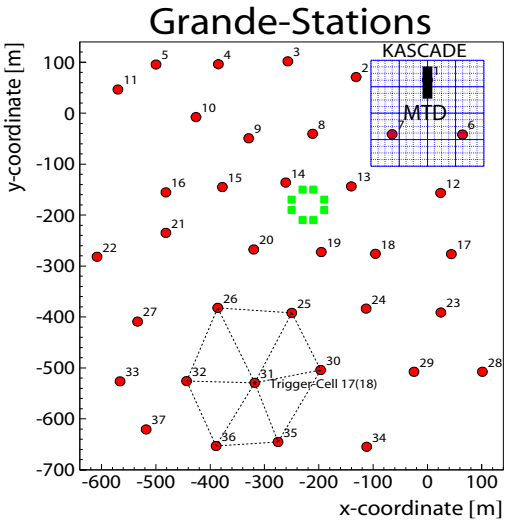

Fig. 1. Layout of the KASCADE-Grande experiment distributed over Research Center Karlsruhe. KASCADE is situated in the North-East corner of the Center: note the position of the Muon Tracking Detector (MTD)

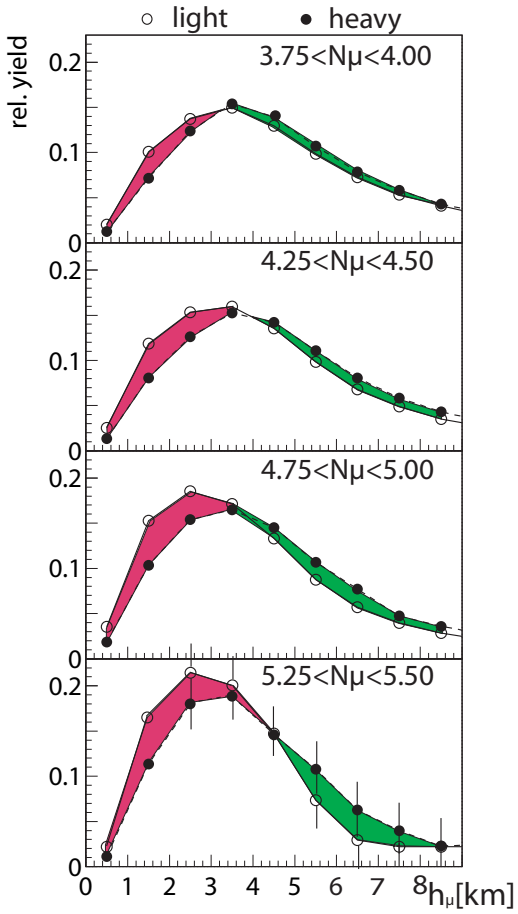

Fig. 2. Muon production height distributions for different muon size bins and different $lg(N_\mu)/lg(N_e)$ ratio above (light) and below (heavy) the solid line in Fig. 5. Colors emphasize the strong mass dependence.

in a phenomenological ansatz gives for the e.m. part the elongation rate of $\sim 60\ gcm^{-2}$ per decade which is in a good agreement with simulations. For the X_{max} value for nuclei ref. [9] reports: $X^A_{max} = X^p_{max} - X_o ln(A)$ (X_o, radiation length in air), therefore, X_{max} from iron induced showers is $\sim 150\ gcm^{-2}$ higher than X_{max} from induced proton showers at all energies. With the integral number of muons for a proton or nucleus A induced shower:

$$N_\mu \sim E_0^\beta \qquad or \qquad N_\mu^A \sim A(E_A/A)^\beta \qquad (1)$$

we assume that $\langle H_\mu \rangle$ exhibits a similar lg(N_e) and lg(N_μ^{tr}) dependence as X_{max}. Note however, $\langle H_\mu \rangle$, because of the long tails in the H_μ distribution towards large heights can be systematically higher than the muon production height, where most of the muons are created in a shower. Some energetic muons may stem from the first interaction and survive down to the MTD detector plane. The almost mass A independent energy estimator in equation (2) was employed.

$$lgE_0[GeV] = 0.19lg(N_e) + 0.79lg(N_\mu^{tr}) + 2.33 \qquad (2)$$

The shower development leads also to various fluctuations in those shower parameters.

For the following analysis the elongation rate was given the value $70\ gcm^{-2}$ per decade in lg(N_μ^{tr}). After subtracting from each track the 'energy' dependent penetration depth

$$H_\mu^A = H_\mu - 70gcm^{-2}lg(N_\mu^{tr}) + 20gcm^{-2}lg(N_e) \qquad (3)$$

the remaining depth H_μ^A may exhibit the mass A dependence. Note the relation lg(N_μ^{tr}) = lg(N_μ) - 0.55 which connects the 'truncated' muon number in KASCADE recorded showers to their total muon number. Under this relation lg(N_μ^{tr}) from KASCADE matches the lg(N_μ) from Grande in the overlap region.

The correction with the electron size $lg(N_e)$ in equation (3) should be of opposite sign because of fluctuations to larger size for this variable (X_{max} also fluctuates to larger values).

Investigating in a closer look the distribution of the parameters, Fig. 2 shows $h_\mu[km]$ distributions for fixed muon number bins which vary with shower energy.

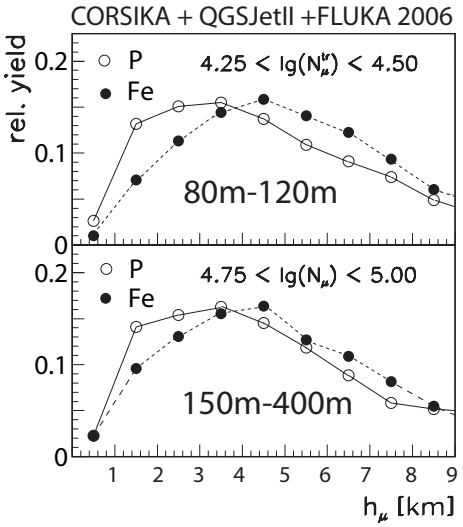

Fig. 3. Simulated muon production height distributions for different muon size bins and the KASCADE (80 m-120 m) and Grande (150 m-400 m) experiment components. Note the relation lg(N_μ^{tr}) = lg(N_μ) - 0.55 which connects the 'truncated' muon number in KASCADE registered showers to their total muon number.

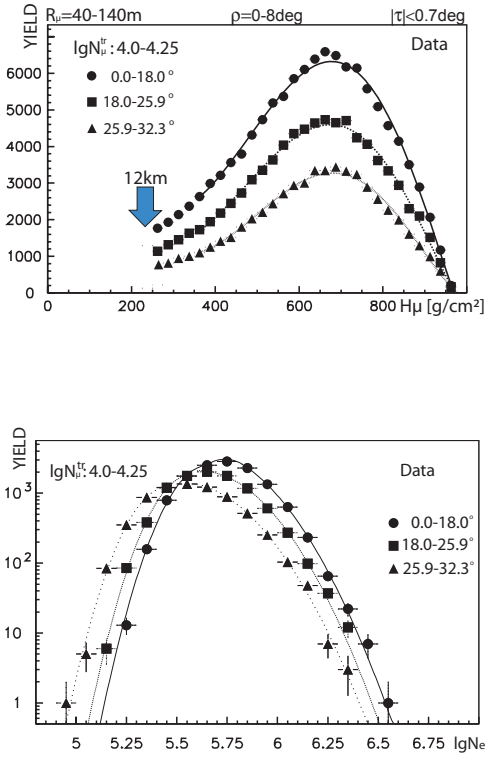

Fig. 4. (Top) Yield of shower size $lg(N_e)$ distributions for 3 different angle (degree) bins. (Bottom) Yield of muon production depth distributions for 3 different angle (degree) bins.

In Fig. 3 simulated muon production height distributions are shown for different experimental configurations within the geometry of KASCADE (80 m-120 m) and within the geometry of Grande (150 m-400 m). Simulation were done with the CORSIKA code [10] using the QGSJETII model [11] for high energy interactions above 200 GeV and FLUKA2006 [12] below that energy. Because of the shift between lg(N_μ^{tr}) and lg(N_μ) both distributions should be very similar. When comparing the simulated distributions to the corresponding distributions in Fig. 2, a longer tail towards larger muon production height is observed in the simulations. These tails may stem from more abundant muon production at high altitudes and appear also in terms of pseudorapidity (see Fig. 4 in contribution to this conference by J. Zabierowski [5]) at large pseudorapidity values.

In Fig. 2 the muon production heights h_μ are plotted for light and heavy primary mass enriched showers, employing the $lg(N_\mu)/lg(N_e)$ ratio to be larger or smaller than 0.84 as indicated by the solid line in Fig. 5. The distributions exhibit a striking dependence on the primary mass range. Further, it is known from earlier studies, that the $lg(N_e)$ parameter exhibits fluctuations to large values in agreement with simulations while the $lg(N_\mu^{tr})$ parameter exhibits little fluctuations. In contrary, the H_μ parameter in Fig. 4 is fluctuating to large heights i.e. smaller values (gcm^{-2}). Therefore, we may argue that the fluctuations in the corrections for H_μ for the elongation rate (equation (3)) will cancel to some extent and, therefore, the resulting mass A dependent muon production height H_μ^A represents a stable mass A observable.

Fig. 5 shows the regions of different mass A dependent mean muon production height $\langle H_\mu^A \rangle$ in the 2-parameter $lg(N_e) - lg(N_\mu)$ space. H_μ^A in Fig. 5 is the mean $\langle H_\mu^A \rangle$ per shower and calculated from all muon tracks in the MTD. The picture shows regions of distinct $\langle H_\mu^A \rangle$ in a colour code with a $40\ gcm^{-2}$ step size. The borders between different regions are for some cases marked with lines which exhibit a slope in the $lg(N_e) - lg(N_\mu^{tr})$ plane. While in the middle of the distribution the slope confirms the previously employed slope $lg(N_\mu) = 0.84(\pm 0.01) lg(N_e)$ for selecting light or heavy primary particles, modified slopes may be recognized for regions away from the middle of the ridge. The slope for the $600\ gcm^{-2}$ line comes close to the slope of the air-shower simulations employed in [13]. Note also that the number of tracks increases with energy and exhibits a specific mass A dependent rise, which is under study.

The lines obtain their slope from the muon number-energy relation in equation (1) combined with equation (2). There, the exponent is according to ref. [9] connected to the amount of inelasticity κ (fraction of energy used up for π production) involved in the processes of the A-air collisions. A comparatively steeper slope $\beta = (1 - 0.14\kappa)$ [9], corresponds to an increased inelasticity. The correction in equation (3) depending on $lg(N_e)$

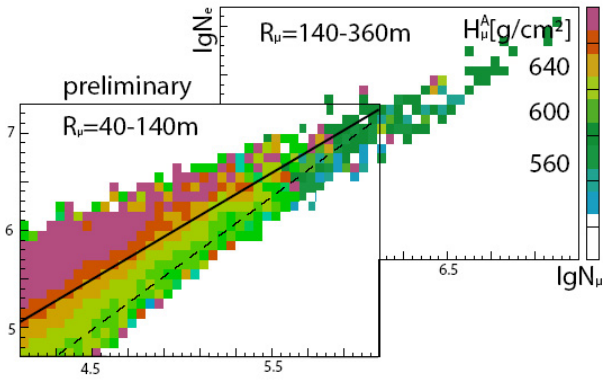

Fig. 5. Effective muon production depth H_μ^A represented by varying contour scale in the 2-parameter presentation $lg(N_e) - lg(N_\mu)$ for $0^o - 18^o$. Pictures are overlayed for separate KASCADE and Grande analyses, respectively.

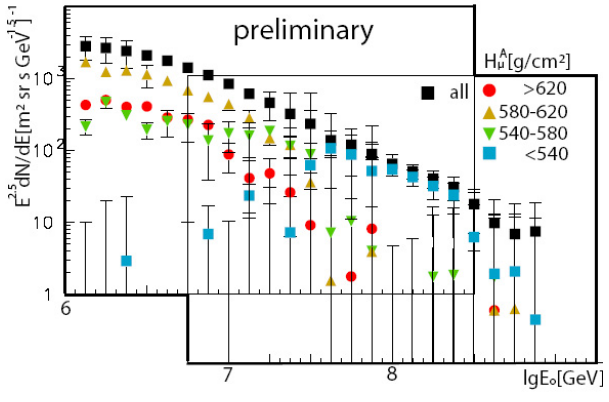

Fig. 6. Energy spectra for different effective muon production depth H_μ^A represented by different symbols for $0^o - 18^o$. Pictures are overlayed for separate KASCADE and Grande analyses, respectively.

and $lg(N_\mu^{tr})$ was found appropriate to get the slope of the H_μ^A profile in the 2-parameter $lg(N_e) - lg(N_\mu)$ presentation (Fig. 5). Differences between two different models in ref. [13] amount to about 20 gcm^{-2} on the H_μ^A scale.

Sorting the $lg(N_e) - lg(N_\mu^{tr})$ events by their range in H_μ^A and employing for the same event the almost mass A independent equation (2) for KASCADE and a corresponding equation for Grande [15] for $lgE_o[GeV]$, energy spectra are obtained and shown in Fig. 6. Sofar, no explicit mass range assignment is given as would be motivated by the equation $X_{max}^A = X_{max}^p - X_o ln(A)$. The spectra in Fig. 6 together with their preliminary error estimations are almost model independent. The error estimations are obtained by varying the effective muon production depth H_μ^A intervals by 20 gcm^{-2}. The preliminary spectra reveal distinct features. While the low 'mass' spectra show a rapid drop with increasing shower energy, the medium 'mass' and heavy 'mass' spectra seem to overtake at large primary energy. The all-particle spectrum exhibits a somewhat steeper slope than the all-particle spectra compiled by A.Haungs [16] which will be further investigated using improved energy estimators. Systematic errors dominate the low and high energy bins for KASCADE and Grande, respectively, and are subject of further investigations. In the KASCADE analysis the detection threshold of the MTD may be effective and a fraction of tracks may be missing leading to a light particle mass interpretation. For the large Grande geometry some flux loss for low energy muons may lead to a bias towards large primary mass.

III. Conclusions

Triangulation allows to investigate H_μ. Future analysis of other shower angle bins and a larger and improved quality data sample will provide a more detailed information on the nature of high energy shower muons. Also muon multiplicities provide valuable parameters to derive the relative contributions of different primary cosmic ray particles. A natural extension towards even larger shower energies is provided by KASCADE-Grande [14]. There is a common understanding that the high energy shower muons serve as sensitive probes to investigate [5], [6] the high energy hadronic interactions in the EAS development. Very inclined muons which can be studied with tracks recorded by the wall modules of the MTD are currently of vital interest.

IV. Acknowledgements

The KASCADE-Grande experiment is supported by the BMBF of Germany, the MIUR and INAF of Italy, the Polish Ministry of Science and Higher Education(grant for 2009-2011), and the Romanian Ministry of Education, Research and Innovation. The support by the PPP-DAAD grant for 2009-2010 is kindly acknowledged.

References

[1] P. Doll *et al.*, Nucl.Instr.and Meth. A488 (2002) 517; J. Zabierowski and P. Doll., Nucl.Instr.and Meth. A484 (2002) 528.
[2] M. Ambrosio *et al.*, Nucl. Phys. (Proc.Suppl.) 75A (1999) 312.
[3] R. Obenland *et al.*, *(KASCADE Coll.)*, Proc. 29^{th} ICRC, Pune, India, Vol.6 (2005) 225.
[4] L. Pentchev and P. Doll, J.Phys.G: Nucl.Part.Phys. 27 (2001) 1459.
[5] J. Zabierowski *et al.*, *(KASCADE-Grande Coll.)* Proc. 31^{th} ICRC, 2009, Lodz, Poland.
[6] J. Zabierowski *et al.*, *(KASCADE Coll.)*, Proc. 29^{th} ICRC, Pune, India, Vol.6 (2005) 357; J. Zabierowski *et al.*, *(KASCADE Coll.)*, Proc. 30^{th} ICRC, Merida, Mexico, Vol.4 (2007) 111.
[7] P. Luczak *et al.*, *(KASCADE-Grande Coll.)*, Proc. 31^{th} ICRC, 2009, Lodz, Poland.
[8] J. Linsley, Proc. 15^{th} ICRC, Vol. 12 (1977) 89; T. K. Gaisser et al., Proc. 16^{th} ICRC, Vol.9 (1979) 275.
[9] J. Matthews, Astropart.Phys.22 (2005) 387
[10] D. Heck *et al.*, CORSIKA, FZKA Report 6019, Forschungszentrum Karlsruhe, 1998.
[11] S. S. Ostapchenko, Nucl. Phys. B. (Proc.Suppl.) 151 (2006) 143; S. S. Ostapchenko, Phys.Rev. D74 (2006) 014026.
[12] A. Fasso *et al.*, Proc. CHEP2003, Paper MOMT005, arXiv:hep-ph/0306267.
[13] T. Antoni *et al.*, *(KASCADE Coll.)*, Astropart. Phys. 24 (2005) 1.
[14] M.Bertaina *et al.*, Nucl.Instr.and Meth. A588 (2008) 162.
[15] J.van Buren *et al.*, *(KASCADE-Grande Coll.)*, Proc. 29^{th} ICRC, Pune, India, Vol.6 (2005) 301.
[16] A. Haungs *et al.* *(KASCADE-Grande Coll.)*, Proc. 31^{th} ICRC, 2009, Lodz, Poland.

Restoring Azimuthal Symmetry of Lateral Density Distributions of EAS Particles

O. Sima[‡‡], W.D. Apel[*], J.C. Arteaga[†,xi], F. Badea[*], K. Bekk[*], M. Bertaina[‡], J. Blümer[*,†], H. Bozdog[*], I.M. Brancus[§], M. Brüggemann[¶], P. Buchholz[¶], E. Cantoni[‡,‖], A. Chiavassa[‡], F. Cossavella[†], K. Daumiller[*], V. de Souza[†,xii], F. Di Pierro[‡], P. Doll[*], R. Engel[*], J. Engler[*], M. Finger[*], D. Fuhrmann[**], P.L. Ghia[‖], H.J. Gils[*], R. Glasstetter[**], C. Grupen[¶], A. Haungs[*], D. Heck[*], J.R. Hörandel[†,xiii], T. Huege[*], P.G. Isar[*], K.-H. Kampert[**], D. Kang[†], D. Kickelbick[¶], H.O. Klages[*], P. Łuczak[††], C. Manailescu[‡‡], H.J. Mathes[*], H.J. Mayer[*], J. Milke[*], B. Mitrica[§], C. Morariu[‡‡], C. Morello[‖], G. Navarra[‡], S. Nehls[*], J. Oehlschläger[*], S. Ostapchenko[*,xiv], S. Over[¶], M. Petcu[§], T. Pierog[*], H. Rebel[*], M. Roth[*], H. Schieler[*], F. Schröder[*], M. Stümpert[†], G. Toma[§], G.C. Trinchero[‖], H. Ulrich[*], A. Weindl[*], J. Wochele[*], M. Wommer[*], J. Zabierowski[††]

[*]*Institut für Kernphysik, Forschungszentrum Karlsruhe, 76021 Karlsruhe, Germany*
[†]*Institut für Experimentelle Kernphysik, Universität Karlsruhe, 76021 Karlsruhe, Germany*
[‡]*Dipartimento di Fisica Generale dell'Università, 10125 Torino, Italy*
[§]*National Institute of Physics and Nuclear Engineering, 7690 Bucharest, Romania*
[¶]*Fachbereich Physik, Universität Siegen, 57068 Siegen, Germany*
[‖]*Istituto di Fisica dello Spazio Interplanetario, INAF, 10133 Torino, Italy*
[**]*Fachbereich Physik, Universität Wuppertal, 42097 Wuppertal, Germany*
[††]*Soltan Institute for Nuclear Studies, 90950 Lodz, Poland*
[‡‡]*Department of Physics, University of Bucharest, 76900 Bucharest, Romania*
[xi]*now at: Universidad Michoacana, Morelia, Mexico*
[xii]*now at: Universidade de São Paulo, Instituto de Fîsica de São Carlos, Brasil*
[xiii]*now at: Dept. of Astrophysics, Radboud University Nijmegen, The Netherlands*
[xiv]*now at: University of Trondheim, Norway*

Abstract. **The lateral distributions of EAS particles are affected by various kinds of azimuthal asymmetries, which arise from different effects: Geometric effects of mapping the horizontal plane observations onto the shower plane, different attenuation of particles on different sides of inclined EAS and the influence of the geomagnetic field on the particle movement. A procedure is described of minimizing the effects of azimuthal asymmetries of lateral density distributions. It is demonstrated and discussed in context of practical cases of data reconstruction by KASCADE-Grande.**

Keywords**: Extensive air showers; lateral density distribution; azimuthal asymmetry**

I. Introduction

A crucial observable for the reconstruction and analysis of Extensive Air Showers (EAS) [1] is represented by the lateral distribution of the EAS particles evaluated in the intrinsic shower plane, hereafter called normal plane. In the case of ground arrays like KASCADE-Grande [2] this observable is obtained first by converting (by the use of appropriate Lateral Energy Correction Functions, LECF) the detector signals in particle densities evaluated in the horizontal plane. In a second step the density in the horizontal plane is mapped into the normal plane by applying specific projection techniques. Typically the detectors sample only a small fraction of the EAS particles; information concerning the complete distribution is obtained by using lateral distribution functions (LDFs) fitted to the measured data. The commonly used LDFs assume that the particle density possesses axial symmetry in the normal plane. This assumption greatly simplifies the problem of fitting the LDFs, but its validity should be investigated, especially in the case of arrays which only sample a limited part of the azimuthal dependence of the particle density. The bias is more important for inclined showers and in the case of observables evaluated far from the core, e.g. the density at 500 m, which can be used as an energy estimator [3]. In this context the purpose of this work is to study the asymmetry of the reconstructed particle density in the range of the KASCADE-Grande experiment and to propose practical methods to restore the symmetry in the intrinsic shower plane.

II. Basic origin of asymmetry

In the absence of the Earth's magnetic field the LDF of shower particles would possess symmetry around the shower axis. Consider an inclined shower and assume for the moment that shower evolution in the vicinity of the ground is negligible. Then in the simplified description of shower particles coming on the surface of a cylinder centered on the shower axis elementary geometrical effects would distort the LDF in the horizontal plane; a simple orthogonal projection of the observed densities

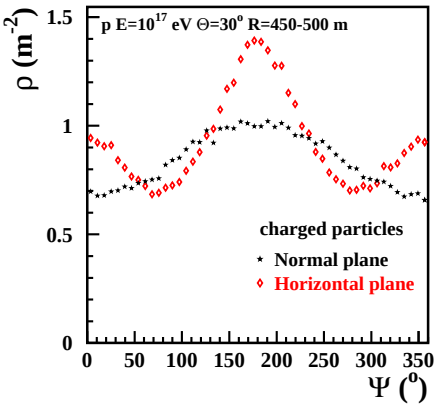

Fig. 1: Charged particle density in the horizontal plane (CORSIKA) and in the normal plane (by orthogonal projection). Coordinate system: $\Psi = 0^\circ$ in the late region, $\Psi = 90^\circ$ along the intersection of the horizontal plane with the normal plane.

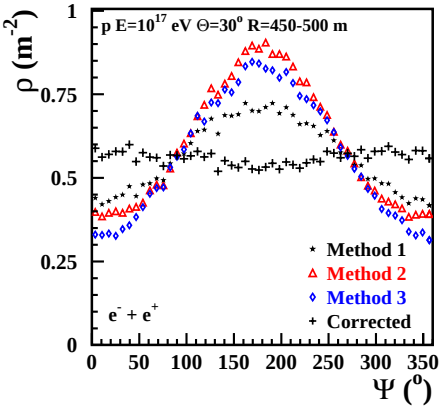

Fig. 2: Electron density reconstructed in the normal plane using the three projection methods, together with the density corrected as detailed in Section IV.

from the horizontal plane to the normal plane would restore the symmetry. If the shower particles would come on a surface of a cone, then the simple orthogonal projection would not completely restore the symmetry, because the particles would be projected outwards from the core with respect to their real trajectory in the region above the shower axis and towards the core in the opposite region. In the normal plane in a given radial bin the error of the reconstructed number of particles depends on the balance between the number of particles that are artificially projected into that bin and the number of particles that are artificially removed from the bin due to this imperfection of the orthogonal projection. As a result, close to the core, the reconstructed density in the region above the shower core is artificially decreased and it is artificially increased in the opposite region. Far from the core the effect is reversed.

In fact shower evolution should also be taken into account. Due to shower development, the particles hitting the ground below the shower axis (the early region) represent an earlier stage of shower development with respect to the shower particles coming above the shower axis (the late region). This evolution additionally distorts the symmetry around the shower core, for e.g. the particles from the late region have traveled longer paths than the particles from the early region and are more attenuated [4], [5], [6]. The magnetic field of the Earth, producing asymmetry also for vertical showers, is especially important when the densities of particles of opposite charge are compared [7], [8].

III. Projection in the intrinsic shower plane

In this work we analyzed proton and Fe induced showers with energy E=10^{17}, $1.78 \cdot 10^{17}$, $3.16 \cdot 10^{17}$ and $5.62 \cdot 10^{17}$ eV and incidence angle Θ=22, 30 and 45°; proton showers with an extended range of angles (Θ=22, 30, 45, 55 and 65°) were also studied for E=10^{15} eV. The showers were produced by CORSIKA version 6.01 [9] in the absence of the magnetic field of the Earth.

Clearly the simple model of shower particles coming on cylindrical surfaces with negligible shower development in the vicinity of ground is contradicted by shower simulations. Indeed, the orthogonal projection of the densities from the horizontal plane into the normal plane does not restore axial symmetry (Figure 1).

To investigate further the role played by the imperfection of the method of orthogonal projection (Method 1) and of the shower evolution we applied two other methods of mapping the particle impact point from the horizontal plane to the normal plane: projection along the particle momentum when it reaches the ground (Method 2) and a method based on triangulation using particle arrival time and assuming that the particles have been produced close to the shower axis (Method 3) [10]. Method 2 would be rigorous if the interactions in the space between the horizontal plane and the normal plane would be negligible, while Method 3 requires negligible interactions along the complete trajectory of the particle. The results demonstrate that shower evolution has an important contribution to the asymmetry of LDF, especially in the case of the electron component (Fig. 2). In the case of the muon component the three methods give almost similar results between each other and the amplitude of the early-late variation is smaller, e.g. it is 14% while for electrons it is 72% in the same conditions (Fig. 2).

IV. Correction function

Along the intersection of the horizontal plane with the normal plane ($\Psi = 90^\circ$ and $\Psi = 270^\circ$) the imperfections of the projection method have minimal effects; also shower development between the two planes is negligible. The density $\rho(r, \Psi)$ in the normal plane at other azimuth angles differs from the density $\rho_{ref}(r)$ at the same radial distance and $\Psi = 90^\circ$ or $\Psi = 270^\circ$ due to the imperfections of the projection method and to shower evolution. The magnitude of the effects should

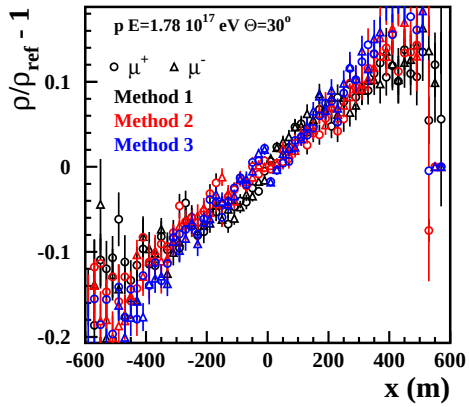

Fig. 3: The dependence of $\rho(r,\Psi)/\rho_{ref}(r) - 1$ on the distance x between the corresponding points in the normal and horizontal planes ($x > 0$ in the early region).

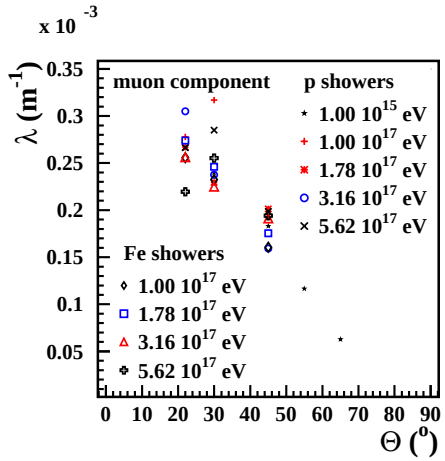

Fig. 5: Attenuation coefficient for the muon component. Note the scale difference between Fig. 4 and Fig. 5.

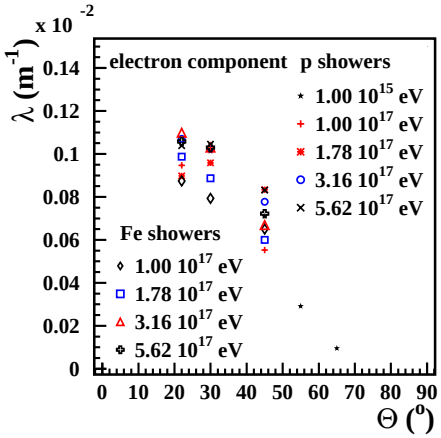

Fig. 4: Attenuation coefficient for the electron component

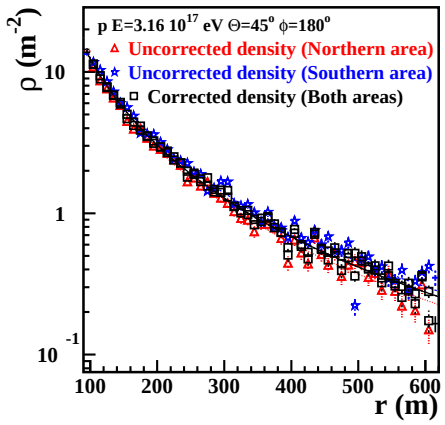

Fig. 6: Comparison of the reconstructed density in the case of showers with the core in the Northern area of Grande with the reconstructed density in the case of showers with the core in the Southern area of Grande

depend on the distance x between the corresponding points in the normal and horizontal planes. The dependence of the average density on x is approximated by an exponential function, $\exp(-\lambda x)$. In Fig. 3 this dependence is represented for the case of muons.

The values of λ incorporate both the attenuation by shower development and the distortions due to the projection method. The results show that λ depends mainly on the angle of the shower axis. The systematic dependence on the primary energy or composition is less obvious; certainly the sensitivity to these parameters is small. A more refined study [11], [12] shows that the imperfections of Method 1 induce a slight dependence of λ on the radial distance from the core: it decreases when the radial coordinate increases from 0 to about 200 m and then remains practically constant. In Figs. 4 and 5 this asymptotic value of λ in each set of simulated showers is represented for the case when Method 1 was applied for projection.

V. Results

The application of the correction procedure greatly removes the asymmetry of lateral distribution (Fig. 2). In order to test the applicability to the KASCADE-Grande experiment, a proton induced shower with E=3.16 $\cdot 10^{17}$ eV, $\Theta = 45°$ incident from North, was repeatedly positioned with the core in various points in the Northern part of KASCADE-Grande, so that most of the Grande detectors were located in the late region of the shower development. The energy deposition in the detectors was realistically simulated, then the density in the observation plane was obtained by applying an appropriate LECF. The density in the normal plane was reconstructed using the Method 1 of projection. The same procedure was applied for a second set of results, obtained in the case when the same shower was repeatedly positioned with the core in various points in the Southern part of the KASCADE-Grande, so that now

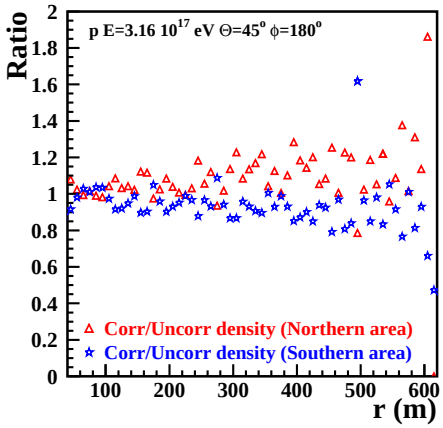

Fig. 7: The ratios of the corrected to the uncorrected densities (proton induced EAS)

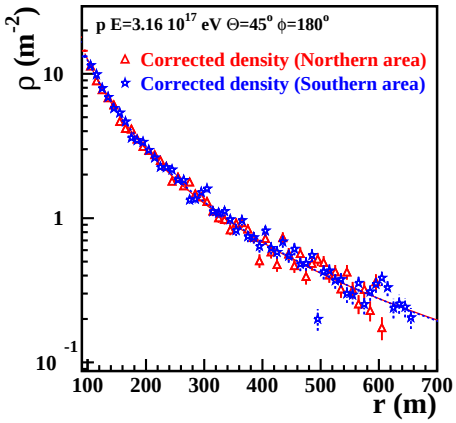

Fig. 8: Corrected lateral density distributions for p induced showers. Linsley fits of the density for showers with the core in the northern area (full line) and southern area (dashed line), respectively

most of the detectors were located in the early region. The reconstructed density in the case of the first set of showers is lower than the reconstructed density in the case of the second set of showers if no correction procedure is applied (Fig. 6).

As can be seen in Fig. 7 the corrections are important, especially at large radial distances. The difference between the mean density at 500 m in the two cases was 23% when the corrections were not applied and negligible when the corrections were applied [11]. After applying the correction method proposed the reconstructed density in the case of the set of showers with the core located in the Northern part of the Grande array does not differ significantly from the reconstructed density in the case of the set of showers with the core located in the Southern part of the array (Fig. 8).

Similar results were obtained in the case of a Fe shower with E=5.62 $\cdot 10^{17}$ eV, $\Theta = 45°$.

ACKNOWLEDGMENT

O. Sima acknowledges the support of the studies by Deutsche Forschungsgemeinschaft. C. Manailescu and C. Morariu thank for the support of the studies from the ERASMUS programme and from KIT (Karlsruhe Institute of Technology).

REFERENCES

[1] A. Haungs, H. Rebel, M. Roth, Rep. Progr. Phys. 66 (2003) 1145
[2] G. Navarra et al. - KASCADE-Grande Coll., Nucl. Instr. Meth. A 518 (2004) 207
[3] G. Toma et al. - KASCADE-Grande Coll., these proceedings (2009)
[4] C. Pryke, Auger Technical Note GAP-98-034 (1997) http://www.auger.org
[5] X. Bertou, P. Billoir, Auger Technical Note GAP-2000-017 (2000) http://www.auger.org
[6] M.T. Dova, L.N. Epele, A.G. Marazzi, Astropart. Phys. 18 (2003) 351
[7] H. Rebel et al., J. Phys. G: Nucl. Part. Phys. 35 (2008) 085203
[8] H. Rebel, O. Sima, Romanian Rep. Phys. 59 (2007) 609; H. Rebel et al., Proc. 30-th ICRC, Merida, Mexico, 2007, vol. 5, p. 1515
[9] D. Heck et al., Report FZKA 6019 Forschungszentrum Karlsruhe (1998)
[10] O. Sima et al., Report FZKA 6985 Forschungszentrum Karlsruhe (2004)
[11] O. Sima et al., Report FZKA 7464 Forschungszentrum Karlsruhe (2009)
[12] C. Morariu et al., Internal Report KASCADE-Grande 2008-01; A. Patrascioiu, O. Sima, H. Rebel, Internal Report KASCADE-Grande 2006-01.

Quantitative tests of hadronic interaction models with KASCADE-Grande air shower data

J.R. Hörandel[†,xi], W.D. Apel[*], J.C. Arteaga[†,xii], F. Badea[*], K. Bekk[*], M. Bertaina[‡], J. Blümer[*,†], H. Bozdog[*] I.M. Brancus[§], M. Brüggemann[¶], P. Buchholz[¶], E. Cantoni[‡,‖], A. Chiavassa[‡], F. Cossavella[†], K. Daumiller[*], V. de Souza[†,xiii], F. Di Pierro[‡], P. Doll[*], R. Engel[*], J. Engler[*], M. Finger[*], D. Fuhrmann[**], P.L. Ghia[‖], H.J. Gils[*], R. Glasstetter[**], C. Grupen[¶], A. Haungs[*], D. Heck[*], D. Hildebrand[†,xiv], T. Huege[*], P.G. Isar[*], K.-H. Kampert[**], D. Kang[†], D. Kickelbick[¶], H.O. Klages[*], P. Łuczak[††], H.J. Mathes[*], H.J. Mayer[*], J. Milke[*], B. Mitrica[§], C. Morello[‖], G. Navarra[‡], S. Nehls[*], J. Oehlschläger[*], S. Ostapchenko[*,xv], S. Over[¶], M. Petcu[§], T. Pierog[*], H. Rebel[*], M. Roth[*], H. Schieler[*], F. Schröder[*], O. Sima[‡‡], M. Stümpert[†], G. Toma[§], G.C. Trinchero[‖], H. Ulrich[*], A. Weindl[*], J. Wochele[*], M. Wommer[*], J. Zabierowski[††]

[*]*Institut für Kernphysik, Forschungszentrum Karlsruhe, 76021 Karlsruhe, Germany*
[†]*Institut für Experimentelle Kernphysik, Universität Karlsruhe, 76021 Karlsruhe, Germany*
[‡]*Dipartimento di Fisica Generale dell'Università, 10125 Torino, Italy*
[§]*National Institute of Physics and Nuclear Engineering, 7690 Bucharest, Romania*
[¶]*Fachbereich Physik, Universität Siegen, 57068 Siegen, Germany*
[‖]*Istituto di Fisica dello Spazio Interplanetario, INAF, 10133 Torino, Italy*
[**]*Fachbereich Physik, Universität Wuppertal, 42097 Wuppertal, Germany*
[††]*Soltan Institute for Nuclear Studies, 90950 Lodz, Poland*
[‡‡]*Department of Physics, University of Bucharest, 76900 Bucharest, Romania*
[xi] *now at: Dept. of Astrophysics, Radboud University Nijmegen, The Netherlands*
[xii] *now at: Universidad Michoacana, Morelia, Mexico*
[xiii] *now at: Universidade de São Paulo, Instituto de Fîsica de São Carlos, Brasil*
[xiv] *now at: ETH Zürich, Switzerland*
[xv] *now at: University of Trondheim, Norway*

***Abstract*. Quantitative tests of hadronic interaction models are described. Emphasize is given on the models EPOS 1.61 and QGSJET II-2. In addition, a new method to measure the attenuation length of hadrons in air showers is introduced. It turns out that this method is in particular sensitive to the inelastic cross sections of hadrons.**

***Keywords*: air showers, hadronic interactions, KASCADE-Grande**

I. Introduction

Measurements of air shower detectors are usually interpreted with an air shower model to obtain physical properties of the shower inducing primary particles. Modern detector installations, such as the KASCADE-Grande experiment comprise well calibrated particle detectors installed with high spatial density. The systematic uncertainties are dominated by uncertainties of the models used to interpret the data. For air shower interpretation the understanding of multi-particle production in hadronic interactions with a small momentum transfer is essential [1]. Due to the energy dependence of the strong coupling constant α_s, soft interactions cannot be calculated within QCD using perturbation theory. Instead, phenomenological approaches have been introduced in different models. These models are the main source of uncertainties in simulation codes to calculate the development of extensive air showers, such as the program CORSIKA [2].

The test of interaction models necessitates detailed measurements of several shower components. The KASCADE experiment [3] with its multi-detector set-up, registering simultaneously the electromagnetic, muonic, and hadronic shower components is particularly suited for such investigations. The information derived on properties of high-energy interactions from air shower observations is complementary to measurements at accelerator experiments since different kinematical and energetic regions are probed.

In the energy range of interest, namely 10^{14} to 10^{17} eV, the composition of cosmic rays is unknown. Therefore, primary protons and iron nuclei are taken as extreme assumptions and corresponding predictions are calculated for different interaction models. The measured data should be in between the results for the extreme assumptions. If the data are outside the proton-iron range for an observable, this is an indication for an incompatibility of the particular hadronic interaction model with the observed values.

II. Experimental set-up

KASCADE consists of several detector systems [3]. A 200×200 m^2 array of 252 detector stations, equipped with scintillation counters, measures the electromagnetic

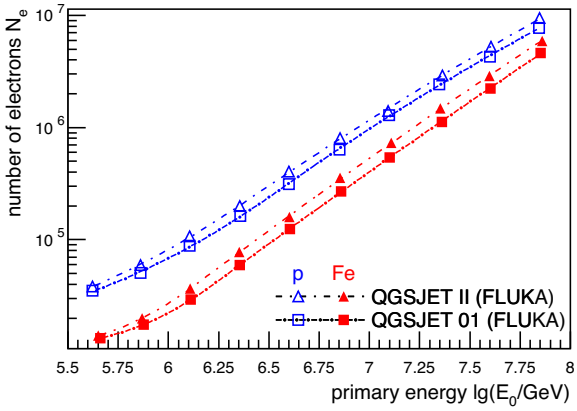

Fig. 1: Number of electrons as predicted by the hadronic interaction models QGSJET II-2 and QGSJET 01 as function of shower energy.

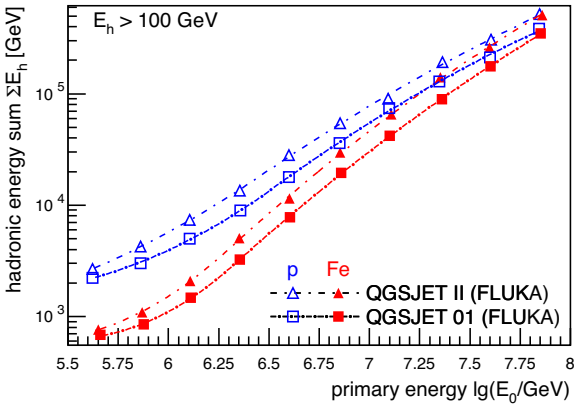

Fig. 2: Hadronic energy sum as predicted by the hadronic interaction models QGSJET II-2 and QGSJET 01 as function of shower energy.

and, below a lead/iron shielding, the muonic parts of air showers. An iron sampling calorimeter of 16×20 m^2 area detects hadronic particles [4]. It has been calibrated with a test beam at the SPS at CERN up to 350 GeV particle energy [5]. For a detailed description of the reconstruction algorithms see [6].

The shower simulations were performed using CORSIKA. Hadronic interactions at low energies ($E_h < 80$ and 200 GeV, respectively) were modeled using the GHEISHA [7] and FLUKA [8], [9] codes. Both models are found to describe the data equally well [10]. High-energy interactions were treated with different models as discussed below. In order to determine the signals in the individual detectors, all secondary particles at ground level are passed through a detector simulation program using the GEANT package [11]. For details on the event selection and reconstruction, see Ref. [10], [12], [13].

III. Earlier tests

Several hadronic interaction models as implemented in the CORSIKA program have been systematically tested over the last decade. First quantitative tests [14], [15], [16] established QGSJET 98 [17] as the most compatible code. Similar conclusions have been drawn for the successor code QGSJET 01 [10].

Predictions of SIBYLL 1.6 [18] were not compatible with air shower data, in particular there were strong inconsistencies for hadron-muon correlations. These findings stimulated the development of SIBYLL 2.1 [19]. This model proved to be very successful, the predictions of this code are fully compatible with KASCADE air shower data [20], [21], [10].

Investigations of the VENUS [22] model revealed some inconsistencies in hadron-electron correlations [16]. The predictions of NEXUS 2 [23] were found to be incompatible with the KASCADE data, in particular, when hadron-electron correlations have been investigated [10].

Analyses of the predictions of the DPMJET model yield significant problems in particular for hadron-muon correlations for the version DPMJET 2.5 [24], while the newer version DPMJET 2.55 is found to be compatible with air shower data [10].

Presently, the most compatible predictions are obtained from the models QGSJET 01 and SIBYLL 2.1.

IV. Hadronic model EPOS

Recently, predictions of the interaction model EPOS 1.61 [25], [26], [27] have been compared to KASCADE air shower data [12]. This model is a recent development, historically emerging from the VENUS and NEXUS codes. The analysis indicates that EPOS 1.61 delivers not enough hadronic energy to the observation level and the energy per hadron seems to be too small. Most likely, the incompatibility of the EPOS predictions with the KASCADE measurements is caused by too high inelastic cross sections for hadronic interactions implemented in the EPOS code.

These findings stimulated the development of a new version EPOS 1.9 introduced at this conference [28]. Corresponding investigations with this new version are under way and results are expected to be published soon.

V. Hadronic model QGSJET II

Also predictions of QGSJET II-2 [29], [30], [31] have been investigated. As discussed above, QGSJET 01 is found to be the most reliable interaction code. Thus, in the following, it serves as reference model and the results can easily be compared to previous publications [16], [10]. The simulations for primary protons and iron nuclei predict about equal numbers of muons as function of energy for QGSJET II and for QGSJET 01. QGSJET II predicts about 20% to 25% more electrons on observation level at a given energy for both primary species relative to QGSJET 01, see Fig. 1. Also the number of hadrons at ground level at a given energy is larger by about 30% to 35% for proton and iron induced showers. The hadronic energy sum and the maximum hadron energy registered at observation level are shown in Figs. 2 and 3, respectively. The values predicted using

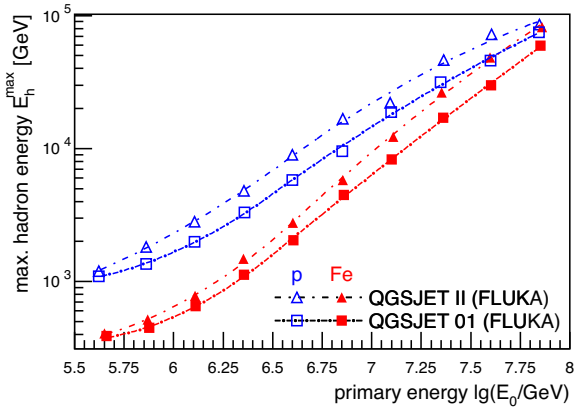

Fig. 3: Maximum hadron energy sum as predicted by the hadronic interaction models QGSJET II-2 and QGSJET 01 as function of shower energy.

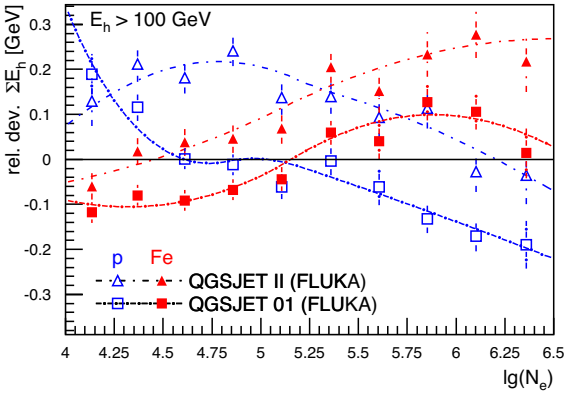

Fig. 4: Relative difference to measured values of the hadronic energy sum as predicted by the models QGSJET II-2 and QGSJET 01.

QGSJET II exceed the ones from QGSJET 01 by a significant amount (up to $\approx 40\%$), as can be inferred from the figures.

The predicted values have been compared to measured data. Investigating the hadronic energy sum and the maximum hadron energy as function of the registered muon number indicates that the predictions for QGSJET II are compatible with the measurements. The measured values are in between the predictions for the extreme assumptions for proton and iron induced showers. Also the correlation between the hadronic energy sum and the number as hadrons as well as the maximum hadron energy and the number of hadrons are compatible with the measurements.

The situation is different for the correlation between the hadronic energy sum and the number of electrons, see Fig. 4. The figure displays the relative deviation of the predicted values from the measured values, i.e. the quantity $(\sum E_h^{sim} - \sum E_h^{meas})/\sum E_h^{meas}$ is shown. That means the data are at the "zero line". The predictions of QGSJET 01 are compatible with the data, since the values bracket the zero line. On the other hand, the predictions of QGSJET II are above the zero line for

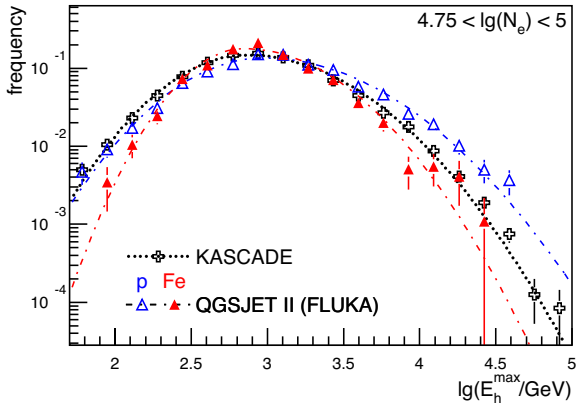

Fig. 5: Energy of the most energetic hadron reconstructed at observation level. Predictions of QGSJET II are compared to measured values.

both primary species – an unrealistic scenario.

The energy of the most energetic hadron reconstructed at observation level is depicted in Fig. 5 for an electron number interval corresponding to a primary energy of about 1 to 2 PeV. Predictions of simulations according to QGSJET II for primary protons and iron nuclei are compared to measured values. It can be recognized that for high maximum hadron energies the measured values are in between the predictions for proton and iron-induced showers. On the other hand, QGSJET II predicts too few hadrons with low energies. A similar behavior is observed for other electron number intervals.

In summary, the investigations reveal incompatibilities in the hadron-electron correlation for the model QGSJET II-2.

VI. Attenuation Length

Recently, a new method to determine the attenuation length of hadrons in air has been introduced, see Ref. [13]. The energy absorbed in a material within a certain atmospheric depth X is used to define an attenuation length. In this new approach we use the number of electrons N_e and muons N_μ to estimate the energy of the shower inducing primary particle E_0. The energy reaching the observation level in form of hadrons $\sum E_H$ is measured with the hadron calorimeter. The fraction of surviving energy in form of hadrons is defined as $R = \sum E_H/E_0$. The attenuation length λ_E is then defined as

$$\Sigma E_H = E_0 \exp\left(-\frac{X}{\lambda_E}\right) \text{ or } R = \exp\left(-\frac{X}{\lambda_E}\right). \quad (1)$$

In contrast to methods using the electromagnetic shower component, the present work focuses directly on measurements of hadrons to derive an attenuation length for this shower component. The values obtained are not a priori comparable to other attenuation lengths, given in the literature since they are based on different definitions. It should be noted that the experimentally obtained attenuation length is affected by statistical fluctuations

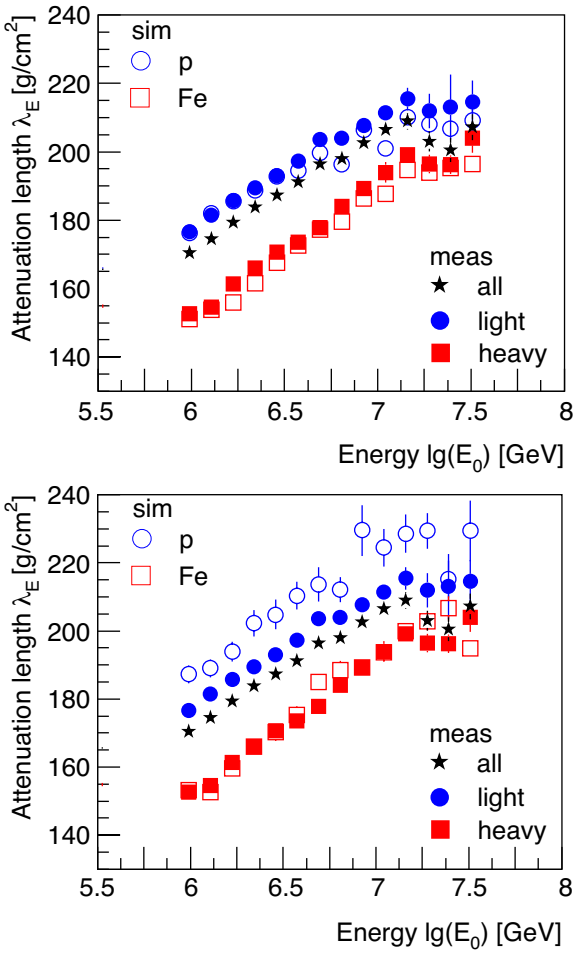

Fig. 6: Attenuation length λ_E as function of estimated primary energy. The light and heavy groups in the measurements are compared to simulations for primary protons and iron-induced showers using CORSIKA with the hadronic interaction model QGSJET 01 (*top*) and a modified version with lower cross sections and higher elasticity (*bottom*, model 3a in Ref. [32]).

during the development of the showers. However, in the present work we do not attempt to correct for this effect.

Measured values of λ_E are shown in Fig. 6. Using a cut in the $N_e - N_\mu$ plane the data have been divided into a "light" and "heavy" sample, the corresponding values for λ_E are depicted as well in the figure. Also predictions of air shower simulations for primary protons and iron nuclei, using the interaction code QGSJET 01 and a modified version with lower cross sections (model 3a in Ref. [32]) are shown. A closer inspection reveals that at high energies the λ_E values of the "light" data selection are greater than the values for proton induced showers according to QGSJET 01. This is an unrealistic behavior. Lowering the inelastic hadronic cross sections by about 5% to 8% changes the situation, see lower panel. The predicted values for protons are now above the values for the "light" selection. This demonstrates the sensitivity of the observable λ_E to hadronic cross sections applied in the simulations.

VII. Conclusions

Quantitative tests of hadronic interaction models implemented in the CORSIKA program have been performed with KASCADE-Grande air shower data in the energy range $10^{14} - 10^{17}$ eV. They indicate that the model EPOS 1.61 is not compatible with air shower data — the new version EPOS 1.9 is presently under investigation. Predictions of the model QGSJET II-2, in particular the hadron-electron correlations are not compatible with measured values. Presently, the most consistent description of all air shower observables as obtained by the KASCADE-Grande experiment is achieved by the interaction models QGSJET 01 and SIBYLL 2.1.

The newly introduced method to measure an attenuation length of hadrons is in particular sensitive to inelastic hadronic cross sections applied in air shower simulations. A comparison of values predicted by QGSJET 01 to measured values suggests that the inelastic cross sections in QGSJET 01 are slightly too large. A version with 5% to 8% smaller cross sections is more compatible with the measurements.

References

[1] R. Engel. Nucl. Phys. B (Proc. Suppl.), **151** (2006) 437.
[2] D. Heck et al. Report FZKA 6019, Forschungszentrum Karlsruhe, 1998.
[3] T. Antoni et al. Nucl. Instr. & Meth. A, **513** (2003) 490.
[4] J. Engler et al. Nucl. Instr. & Meth. A, **427** (1999) 528.
[5] S. Plewnia et al. Nucl. Instr. & Meth. A, **566** (2006) 422.
[6] T. Antoni et al. Astropart. Phys., **14** (2001) 245.
[7] H. Fesefeldt. Report PITHA-85/02, RWTH Aachen, 1985.
[8] A. Fasso et al. CERN-2005-10, INFN/TC-05/11, SLAC-R-773, 2005.
[9] A. Fasso et al. arXiv:hep-ph/0306267, 2003.
[10] W. Apel et al. J. Phys. G: Nucl. Part. Phys., **34** (2007) 2581.
[11] Geant 3.21 detector description and simulation tool. CERN Program Library Long Writeup W5013, CERN, 1993.
[12] W. Apel et al. J. Phys. G: Nucl. Part. Phys., **36** (2008) 035201.
[13] W. Apel et al. submitted to PRD, (2009).
[14] J. R. Hörandel et al. Nucl. Phys. Proc. Suppl., **75A** (1999) 228.
[15] J. Hörandel. Proc. 26th Int. Cosmic Ray Conf., Salt Lake City, **1** (1999) 131.
[16] T. Antoni et al. J. Phys. G: Nucl. Part. Phys., **25** (1999) 2161.
[17] N. Kalmykov et al. Nucl. Phys. B (Proc. Suppl.), **52B** (1997) 17.
[18] J. Engel et al. Phys. Rev. D, **46** (1992) 5013.
[19] R. Engel et al. Proc. 26th Int. Cosmic Ray Conf., Salt Lake City, **1** (1999) 415.
[20] J. Milke et al. Acta Physica Polonica B, **35** (2004) 341.
[21] J. Milke et al. Proc. 29th Int. Cosmic Ray Conf., Pune, **6** (2005) 125.
[22] K. Werner. Phys. Rep., **232** (1993) 87.
[23] H. Drescher et al. Phys. Rep., **350** (2001) 93.
[24] J. Ranft. Phys. Rev. D, **51** (1995) 64.
[25] K. Werner, et al. Phys. Rev. C, **74** (2006) 044902.
[26] T. Pierog et al. Proc. 30th Int. Cosmic Ray Conf., Merida, **4** (2008) 629.
[27] T. Pierog et al. arXiv:astro-ph 0611311, 2006.
[28] T. Pierog et al. Proc. 31th Int. Cosmic Ray Conf., Lodz, (2009) in press.
[29] S. Ostapchenko. astro-ph/0412591, 2005.
[30] S. Ostapchenko. Phys. Rev. D, **74** (2006) 014026.
[31] S. Ostapchenko. Nucl. Phys. B (Proc. Suppl.), **151** (2006) 143 and 147.
[32] J. Hörandel. J. Phys. G: Nucl. Part. Phys., **29** (2003) 2439.

Lateral Distribution of the Radio Signal in Extensive Air Showers Measured with LOPES

S. Nehls[*], F. Schröder[*], W.D. Apel[*], J.C. Arteaga[†,xiv], T. Asch[‡], F. Badea[*], L. Bähren[§], K. Bekk[*], M. Bertaina[¶], P.L. Biermann[‖], J. Blümer[*,†], H. Bozdog[*] I.M. Brancus[**], M. Brüggemann[††], P. Buchholz[††], S. Buitink[§], E. Cantoni[¶,‡‡], A. Chiavassa[¶], F. Cossavella[†], K. Daumiller[*], V. de Souza[†,xv], F. Di Pierro[¶], P. Doll[*], R. Engel[*], H. Falcke[§,x], M. Finger[*], D. Fuhrmann[xi], H. Gemmeke[‡], P.L. Ghia[‡‡], R. Glasstetter[xi], C. Grupen[††], A. Haungs[*], D. Heck[*], J.R. Hörandel[§], A. Horneffer[§], T. Huege[*], P.G. Isar[*], K.-H. Kampert[xi], D. Kang[†], D. Kickelbick[††], O. Krömer[‡], J. Kuijpers[§], S. Lafebre[§], P. Łuczak[xii], M. Ludwig[†], H.J. Mathes[*], H.J. Mayer[*], M. Melissas[†], B. Mitrica[**], C. Morello[‡‡], G. Navarra[¶], A. Nigl[§], J. Oehlschläger[*], S. Over[††], N. Palmieri[†], M. Petcu[**], T. Pierog[*], J. Rautenberg[xi], H. Rebel[*], M. Roth[*], A. Saftoiu[**], H. Schieler[*], A. Schmidt[‡], O. Sima[xiii], K. Singh[§,xvi], G. Toma[**], G.C. Trinchero[‡‡], H. Ulrich[*], A. Weindl[*], J. Wochele[*], M. Wommer[*], J. Zabierowski[xii], J.A. Zensus[‖]

[*]*Institut für Kernphysik, Forschungszentrum Karlsruhe, Germany*
[†]*Institut für Experimentelle Kernphysik, Universität Karlsruhe, Germany*
[‡]*IPE, Forschungszentrum Karlsruhe, Germany*
[§]*Department of Astrophysics, Radboud University Nijmegen, The Netherlands*
[¶]*Dipartimento di Fisica Generale dell' Universita Torino, Italy*
[‖]*Max-Planck-Institut für Radioastronomie Bonn, Germany*
[**]*National Institute of Physics and Nuclear Engineering, Bucharest, Romania*
[††]*Fachbereich Physik, Universität Siegen, Germany*
[‡‡]*Istituto di Fisica dello Spazio Interplanetario, INAF Torino, Italy*
[x]*ASTRON, Dwingeloo, The Netherlands*
[xi]*Fachbereich Physik, Universität Wuppertal, Germany*
[xii]*Soltan Institute for Nuclear Studies, Lodz, Poland*
[xiii]*Department of Physics, University of Bucharest, Bucharest, Romania*
[xiv]*now at: Universidad Michoacana, Morelia, Mexico*
[xv]*now at: Universidade de São Paulo, Instituto de Fîsica de São Carlos, Brasil*
[xvi]*now at: KVI, University of Groningen, The Netherlands*

***Abstract*. The lateral distribution of the radio signal in air showers measured with LOPES is studied in detail. The antenna array LOPES is set up at the location of the KASCADE-Grande extensive air shower experiment in Karlsruhe, Germany and aims to measure and investigate radio pulses from Extensive Air Showers. The antennas have an absolute amplitude calibration. This allows us to reconstruct the electric field strength at observation level in dependence of general EAS parameters. The lateral distribution of the measured electric field strengths in individual EAS can be described by an exponential function. The estimated scale parameters describing the slope of the lateral profiles are in the range of $100\,\mathrm{m}$ to $200\,\mathrm{m}$, and no evidence for a correlation with shower parameters like azimuth or geomagnetic angle, or primary energy could be found. This indicates that the lateral profile is an intrinsic property of the radio emission during the shower development. For about 20% of the events a flattening towards the shower axis is observed, preferentially for showers with large inclination angle and when measured close to the shower center. The measured lateral distributions are compared on an event-to-event basis with expectations of detailed Monte-Carlo simulations using the REAS2 code.**

***Keywords*: extensive air showers, radio emission, lateral distribution**

I. Introduction

In the present study we investigate in detail the lateral profile of the radio signal as measured by LOPES [1]. Due to a precise amplitude calibration [2] of each individual antenna and the event information from KASCADE-Grande [3], [4], this is possible on an event-by-event basis with high accuracy. Such investigations are of great interest as the lateral shape defines the optimum grid size for a radio antenna array in a stand-alone mode. Of particular interest is the scale parameter which describes the amount of the signal decrease with distance from the shower axis and the dependence of that parameter on characteristics of the primary particle. In addition, simulations have shown [5], that the lateral shape is related to important physical quantities such as the primary energy or the mass of the primary.

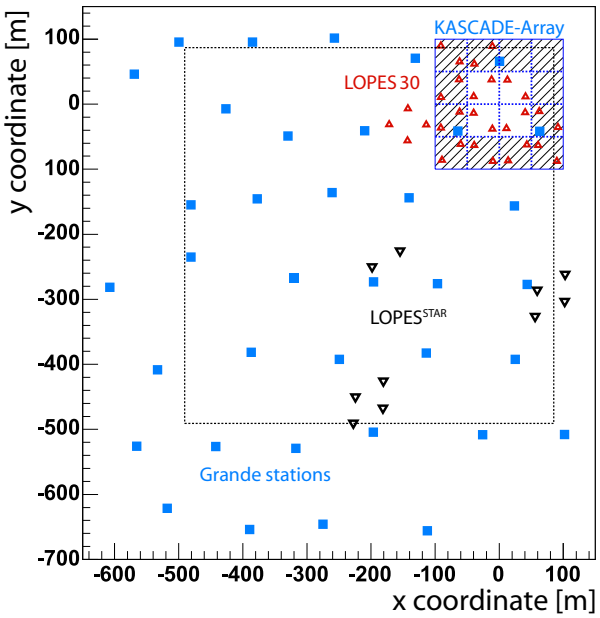

Fig. 1: Sketch of the KASCADE-Grande – LOPES experiments. The dotted line shows the area used for the present analysis.

The LOPES short dipole antennas (LOPES30), positioned within or close to the original KASCADE array (fig. 1), operate in the frequency range of $40 - 80$ MHz and were all (for the period used in this analysis) aligned in east-west direction, i.e. they are mainly sensitive to the linear east-west polarized component of the radiation. This layout was in particular chosen to provide the possibility for a detailed investigation of the lateral extension of the radio signal as it has a maximum baseline of approximately 260 m.

II. Data processing

The data triggered by KASCADE-Grande and recorded by LOPES30 are first generally processed in order to get a calibrated, average field strength value of the received, coherent radio signal, the CC-beam value [6], [7].

The analysis of the data using this CC-beam is based on the RFI cleaned raw data. However, the sampling of the data is done in the second Nyquist domain and a reconstruction of the original 40–80 MHz signal shape is needed to investigate the radio emission properties in more detail, i.e. on basis of single antennas. Therefore, an up-sampling of the data on a single antenna basis is performed (by the zero-padding method applied in the frequency domain) resulting in a band limited interpolation in the time domain [8] to reconstruct the original signal form between the sampled data points with 12.5 ns spacing.

After applying the up-sampling the radio signals can be used to reconstruct the electric field strength in each individual antenna. The systematic uncertainty of these field strengths includes a contribution of the noise level, which is estimated by a calculation using a time window

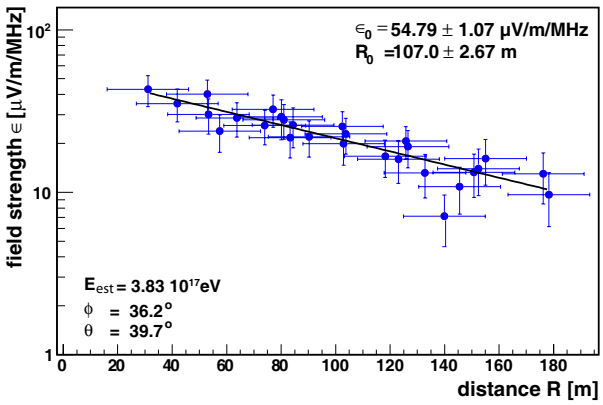

Fig. 2: Lateral distribution reconstructed from single antenna signals, shown for an individual shower.

(520 nanosecond width) before the actual radio pulse from the shower.

III. Lateral Distribution of the Radio Signal

For the analysis of lateral distributions of the radio emission in individual events 110 showers with a high signal-to-noise ratio were selected. The selection requires clear radio signal in all participating antennas and a successful reconstruction of the shower by KASCADE-Grande. To reconstruct the lateral distribution of the radio field strength, the distance of the antennas to the shower axis is obtained with help of the reconstructed shower parameters from KASCADE-Grande. To investigate the lateral behavior of the radio signal an exponential function $\epsilon = \epsilon_0 \cdot \exp(-R/R_0)$ was used to describe the measured field strengths ϵ. The fit contains two free parameters, where the scale parameter R_0 describes the lateral profile and ϵ_0 the extrapolated field strength at the shower axis at observation level. An example of an individually measured event including the resulting lateral field strength function is shown in figure 2.

For roughly 20% of the events lateral distributions have been found which do not show a clear exponential fall-off. Figure 3 displays an example of such behavior. The shower shows apparently an exponential behavior as others do for larger distances, but there appears a flattening for small distances. There are about 15 events that exhibit such a slope change to a flatter lateral distribution close to the shower axis. In addition, there are a few showers being flat over the whole distance range that could be measured. It should be remarked that at field strengths above $5\,\mu$V/m/MHz the ambient noise background cannot affect the measurement. Moreover, no known instrumental effects can explain such shapes, and no strange environmental conditions like a thunderstorm appeared during such events. However, for a statistically reliable analysis, e.g. if two exponential functions with different slopes fit the distribution more reliable, too few of such flat or flattening lateral profiles have been measured so far.

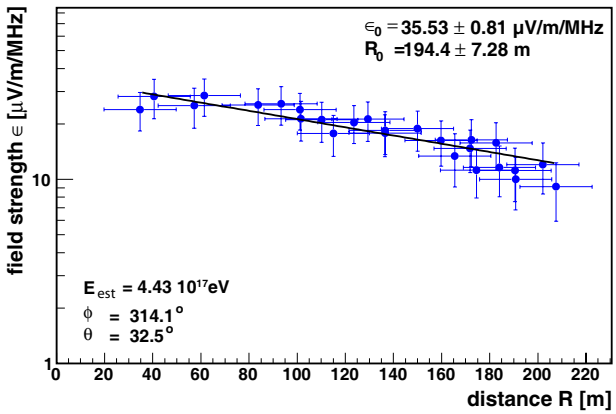

Fig. 3: Lateral distribution reconstructed from single antenna signals, shown for a shower with a clear flattening of the LDF towards the shower center.

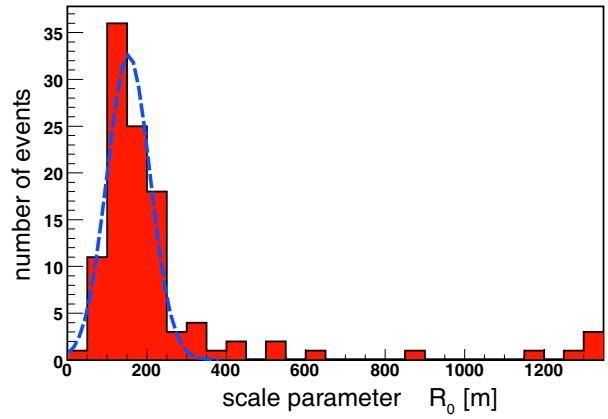

Fig. 4: Distribution of the scale parameter R_0. There are four events set to $R_0 = 1300\,\mathrm{m}$ whose actual R_0 values are higher, i.e. these are very flat events. The dashed line displays a Gaussian fit to the distribution in the range $R_0 = 0 - 300\,\mathrm{m}$ resulting in $\bar{R_0} = 157\,\mathrm{m}$ with a width of $54\,\mathrm{m}$.

IV. The Scale Parameter R_0

Most of the showers have a scale parameter smaller than 300 m (figure 4), including the events with a visible flattening to the shower center. As already mentioned, there are some showers with extremely large scale parameter, $R_0 > 1300\,\mathrm{m}$, those are set to $R_0 = 1300\,\mathrm{m}$ in fig. 4. Fitting a Gaussian function to the distribution of the scale parameter in the range of $0 - 300\,\mathrm{m}$, i.e. neglecting the flat events, a mean value of $\bar{R_0} = 157\,\mathrm{m}$ with a width of $54\,\mathrm{m}$ is obtained.

For a more detailed study [8] of the lateral distributions the properties of the scale parameter and possible correlations with EAS parameters have been investigated. In case of the LOPES experiment this can be done easily, as the general shower parameters are available from the KASCADE-Grande measurements. The scale parameter has been correlated with the geomagnetic angle, the azimuth angle of the incoming shower, the primary energy, and the shower size, where with none of these parameters a distinct correlation is found. The

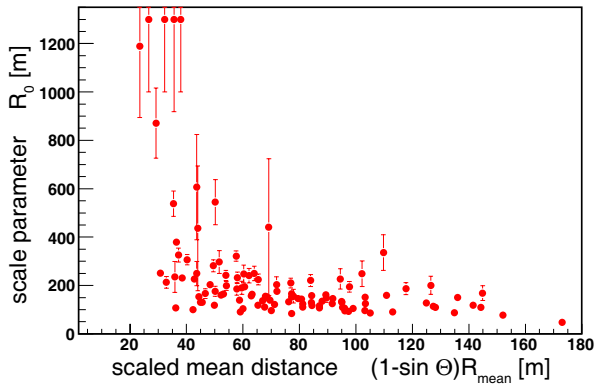

Fig. 5: Relation of the scale parameter R_0 with the mean distance of the antennas to the shower axis scaled with the zenith angle of the axis.

situation is different when the scale parameter has been correlated with the zenith angle of the incoming primary cosmic ray. Here a tendency towards larger values of the scale parameter is seen for inclined events. A clearer feature is even seen, when the scale parameter is analyzed with respect to the corresponding mean distance to the shower axis of all antennas participating in an individual event. It was found that the lateral profile gets flatter when we measure closer to the shower center. In particular, all the very flat events have a mean distance below $R_0 \approx 80\,\mathrm{m}$.

A strongly pronounced dependence of the scale parameter of flat events is seen when the mean distance is combined with the zenith angle information in the form $R'_{\mathrm{mean}} = (1 - \sin\Theta) \cdot R_{\mathrm{mean}}$. Figure 5 shows clearly that the probability of a flattening increases when the shower is inclined and when measured closer to the shower axis. But as not all events with small R'_{mean} show a flattening the reason is still unclear and further investigations with larger statistics are required.

V. Comparisons with REAS2-Simulations

Because of the performed amplitude calibration of LOPES and the estimate of the field strength at individual antennas a detailed comparison of the measured events with Monte Carlo simulations on an event-to-event basis is possible. Due to the simulation strategy, using realistic air shower models with precise, multi-dimensional histograms derived from per-shower CORSIKA [9] simulations, detailed comparisons are performed [10]. The REAS2 Monte Carlo simulation code (see [5] and references therein) is used to simulate the geo-synchrotron radio emission for all the showers detected in the investigated data set. For each single event a shower that represents best the measured one in KASCADE-Grande estimated parameters is selected. The resulting information and the known shower core position is used in the REAS2 code to calculate the radio emission. The output are unlimited bandwidth pulses, that are digitally filtered with a rectangle filter from 43 to 76 MHz for the known antenna positions

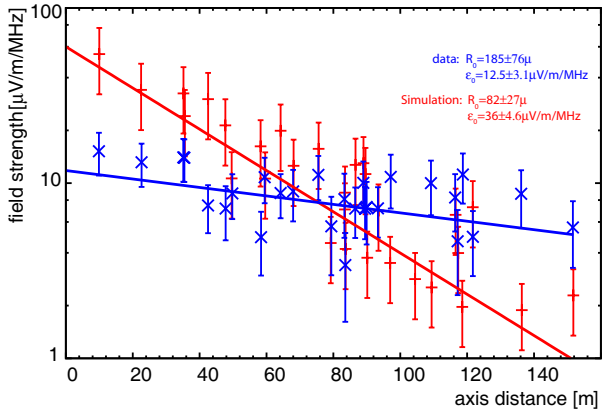

Fig. 6: Lateral distribution obtained for data and simulation for an individual event.

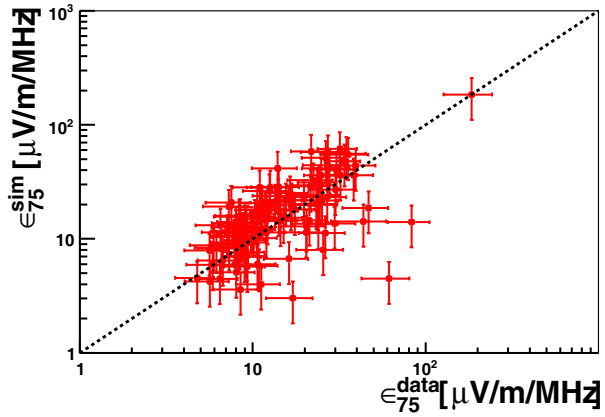

Fig. 7: Comparison of field strength at distance R. Correlations $\epsilon_R^{\rm data}$ obtained from measurements and $\epsilon_R^{\rm sim}$ obtained from simulation. The dashed line represents equal values from simulation and measurement.

at ground, which can be directly compared with the measured lateral distribution.

Like in the example displayed in fig. 6, in general the simulations give steeper lateral distributions than measured. The mean for the distribution of the scale parameter from the simulation is $R_0 = 50$ m. Such small values represent a steep lateral decrease of the field strength. In addition, it was derived that the differences between measurements and simulations can be very large and that the unexpected very flat lateral profiles could not be reproduced by the simulations.

The deviation in the scale parameters enters in systematically higher field strengths at the shower axis $\epsilon_0^{\rm sim}$, compared to the field strengths ϵ_0 obtained from the measured lateral distributions (by approximately factor three). On the other hand we obtain at $R = 75$ m a fairly good agreement between simulations and measurements (fig. 7) for all events. This is a promising result in itself, as such comparisons are performed for the first time for LOPES data.

VI. Conclusions

The lateral distribution of the radio signal in 110 measured LOPES events could be analysed on a single antenna basis. The applied exponential function to these lateral distributions has two free parameters, the field strength ϵ_0 at the shower axis, and the scale parameter R_0. The scale parameter distribution shows a peak value of $R_0 \approx 125$ m and has a tail with very flat lateral distributions. Excluding the flat events a mean value of $\bar{R_0} \approx 150\,\mathrm{m}$ with a width of $\sigma = 50\,\mathrm{m}$ was obtained. No direct evidence for a dependence on the shower parameters azimuth angle, geomagnetic angle, and primary energy could be found. This indicates that the lateral profile is an intrinsic property of the radio emission and the shower development. Comparing the obtained scale parameter with published values of earlier experiments, a good agreement has been found [8].

Studying the lateral distributions in individual events, approximately 20% of the studied showers show a very flat lateral distribution or exhibit a flattening towards the shower center. Preferably, such showers arrive under larger zenith angle and axes are close to the antennas.

The radio emission observed in EAS was compared with detailed Monte Carlo simulations on an event-to-event basis. The REAS2 simulations exhibit in general a steeper lateral slope, i.e. a smaller scale parameter than the measurements. The absolute field strength, however, agrees quite well at a distance of 75 m to the shower axis. The measured flattening towards the shower center could not be reproduced by the present REAS simulations.

References

[1] H. Falcke et al. - LOPES Collaboration, Nature **435**, 313 (2005).
[2] S. Nehls et al., NIM A **589**, 350 (2008).
[3] T. Antoni et al. - KASCADE Collaboration, NIM A **513**, 429 (2003).
[4] G. Navarra et al. - KASCADE-Grande Collaboration, NIM A **518**, 207 (2004).
[5] T. Huege, R. Ulrich, and R. Engel, Astrop. Phys. **30**, 96 (2008).
[6] A. Horneffer et al. - LOPES Collaboration, Int. Journ. Mod. Phys. A **21** Suppl., 168 (2006).
[7] A. Haungs et al. - LOPES Collaboration, NIM A, in press (2009), arXiv:0811.1919.
[8] W.D. Apel et al. - LOPES Collaboration, Astrop. Phys. (2009), submitted
[9] D. Heck et al., Report FZKA 6019, Forschungszentrum Karlsruhe (1998).
[10] S. Nehls, FZKA report **7440**, Forschungszentrum Karlsruhe (2008).

Polarization studies of the EAS radio emission with the LOPES experiment

P.G. Isar[*,xvii], W.D. Apel[*], J.C. Arteaga[†,xiv], T. Asch[‡], F. Badea[*], L. Bähren[§], K. Bekk[*], M. Bertaina[¶], P.L. Biermann[‖], J. Blümer[*,†], H. Bozdog[*] I.M. Brancus[**], M. Brüggemann[††], P. Buchholz[††], S. Buitink[§], E. Cantoni[¶,‡‡], A. Chiavassa[¶], F. Cossavella[†], K. Daumiller[*], V. de Souza[†,xv], F. Di Pierro[¶], P. Doll[*], R. Engel[*], H. Falcke[§,x], M. Finger[*], D. Fuhrmann[xi], H. Gemmeke[‡], P.L. Ghia[‡‡], R. Glasstetter[xi], C. Grupen[††], A. Haungs[*], D. Heck[*], J.R. Hörandel[§], A. Horneffer[§], T. Huege[*], K.-H. Kampert[xi], D. Kang[†], D. Kickelbick[††], O. Krömer[‡], J. Kuijpers[§], S. Lafebre[§], P. Łuczak[xii], M. Ludwig[†], H.J. Mathes[*], H.J. Mayer[*], M. Melissas[†], B. Mitrica[**], C. Morello[‡‡], G. Navarra[¶], S. Nehls[*], A. Nigl[§], J. Oehlschläger[*], S. Over[††], N. Palmieri[†], M. Petcu[**], T. Pierog[*], J. Rautenberg[xi], H. Rebel[*], M. Roth[*], A. Saftoiu[**], H. Schieler[*], A. Schmidt[‡], F. Schröder[*], O. Sima[xiii], K. Singh[§,xvi], G. Toma[**], G.C. Trinchero[‡‡], H. Ulrich[*], A. Weindl[*], J. Wochele[*], M. Wommer[*], J. Zabierowski[xii], J.A. Zensus[‖]

[*] *Institut für Kernphysik, Forschungszentrum Karlsruhe, Germany*
[†] *Institut für Experimentelle Kernphysik, Universität Karlsruhe, Germany*
[‡] *IPE, Forschungszentrum Karlsruhe, Germany*
[§] *Department of Astrophysics, Radboud University Nijmegen, The Netherlands*
[¶] *Dipartimento di Fisica Generale dell' Universita Torino, Italy*
[‖] *Max-Planck-Institut für Radioastronomie Bonn, Germany*
[**] *National Institute of Physics and Nuclear Engineering, Bucharest, Romania*
[††] *Fachbereich Physik, Universität Siegen, Germany*
[‡‡] *Istituto di Fisica dello Spazio Interplanetario, INAF Torino, Italy*
[x] *ASTRON, Dwingeloo, The Netherlands*
[xi] *Fachbereich Physik, Universität Wuppertal, Germany*
[xii] *Soltan Institute for Nuclear Studies, Lodz, Poland*
[xiii] *Department of Physics, University of Bucharest, Bucharest, Romania*
[xiv] *now at: Universidad Michoacana, Morelia, Mexico*
[xv] *now at: Universidade de São Paulo, Instituto de Física de São Carlos, Brasil*
[xvi] *now at: KVI, University of Groningen, The Netherlands*
[xvii] *Leave on absence: ISS, Institute of Space Sciences, Bucharest, Romania*

***Abstract*. During the development of high-energy cosmic ray air showers in the atmosphere the charged particles are deflected by the geomagnetic field. This causes the geo-synchrotron emission leading to a short radio signal observable on ground. This model predicts characteristic dependences of the polarization of the radio signal on general shower parameters, and thus such dependences are investigated with the LOPES experiment. LOPES is an array of dipole radio antennas designed to detect such radio signals in the frequency range between 40-80 MHz. LOPES is located at the area of the ground particle detector array KASCADE-Grande providing the trigger and well-calibrated shower information for primary energies in the range of 10^{16}-10^{18} eV. For investigating the polarization, half of the LOPES antennas are orientated in east-west and respectively half in north-south direction. In this work, the variation of the polarization of the signal with the direction of the incoming air-shower with respect to the geomagnetic field is studied.**

***Keywords*: air showers, radio emission, polarization**

I. Introduction

Due to the interaction with the Earth's atmosphere, an Ultra High Energy Cosmic Ray (UHECR) generates a shower of elementary particles propagating towards the ground with almost the speed of light. Electrons and positrons, as major part of the charged particles in the Extensive Air Shower (EAS), emit synchrotron radiation due to their deflection in the Earth's magnetic field which initiate a short radio flash measurable on ground. The LOPES experiment, a radio array of Λ-shape digital antennas is designed to record such signals and takes data since 2004. In its initial phase, LOPES-10, 10 antennas were equipped with channels sensitive to the east-west polarization direction of the electric field only. After one year of operation [1], the antenna set-up has been changed to a larger array by an addition of further 20 antennas, forming LOPES-30 [2]. Within LOPES-30, the antennas have an absolute amplitude calibration in order to estimate the electric field strength of the radio signal generated in the atmosphere [3]. Moreover,

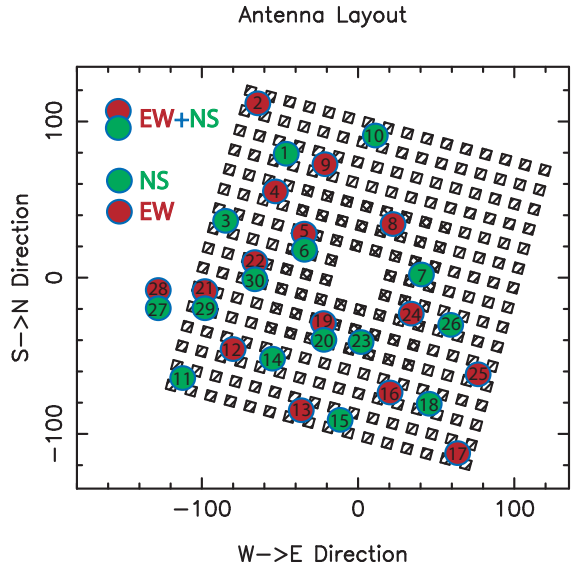

Fig. 1: LOPES antenna layout at the KASCADE array at Forschungszentrum Karlsruhe, Germany.

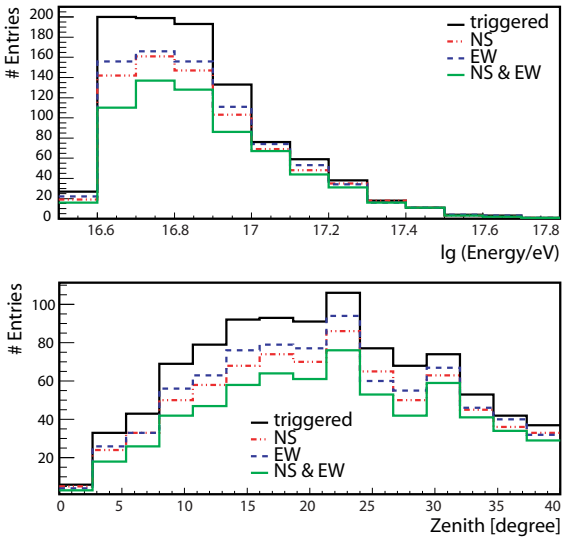

Fig. 2: Primary energy and zenith angular distributions of the triggered (by KASCADE) and of the radio (by LOPES) detected events.

to investigate the radio emission from these EAS in detail and clarify if the technique is useful for large scale application, the LOPES set-up has been changed to perform polarization measurements in 2006.

II. Detector Configuration

East-west polarization measurements alone do not provide the full radio emission information. The recording of both together, the east-west and the north-south polarization components, is a key measure in understanding the radio emission and will allow us to verify the geo-synchrotron effect as the dominant emission mechanism in cosmic ray air showers. Therefore, LOPES-30 was reconfigured to perform polarization measurements by the end of December 2006. Within the new configuration, 15 channels are installed to measure the east-west direction and 15 the north-south direction, where 5 antennas have sensitivity to both polarization components at the same place recording the full radio signal at the same time (Fig. 1). The LOPES antennas are triggered by the original KASCADE and in addition by the KASCADE-Grande particle detector array which benefits from the extended detection area, and allows the analysis of higher-energy events at larger distances with better accuracy [4].

III. Data Selection and Polarization Analysis

For the current studies we have used data recorded during roughly two years of polarization measurements, by using the well-reconstructed shower parameters provided by KASCADE in the energy range of about $10^{16.5}$-$10^{17.8}$ eV. Large statistics in radio detected events are obtained by requiring high particle numbers measured by KASCADE and the shower center close to the antennas. Therefore, only showers falling inside the KASCADE array were used for the moment. The analysis of the radio signal is performed by applying the LOPES standard reconstruction pipeline [2] to each polarization direction separately and independently (15 channels, each). The considered observables are the CC-Beams (cross-correlation beams) calculated per individual polarization component from the measured field strengths per antenna. The total number of triggered events which are used for this analysis is given by 959 selected showers. Fig. 2 shows the energy and zenith angular distributions of the triggered, and the radio detected events. For the following studies an energy cut of

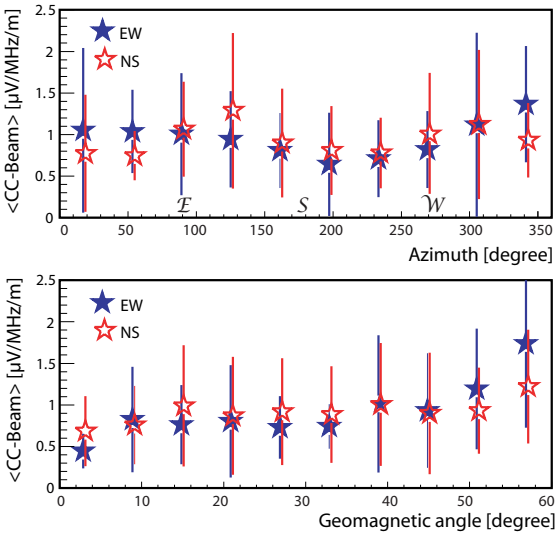

Fig. 3: The normalized CC-Beam values for both polarization components vs. the primary azimuth angle (top panel) and geomagnetic angle (bottom panel). Only events with an estimated primary energy $> 10^{16.9}$ eV are used. Mean values and spread of the distributions are shown.

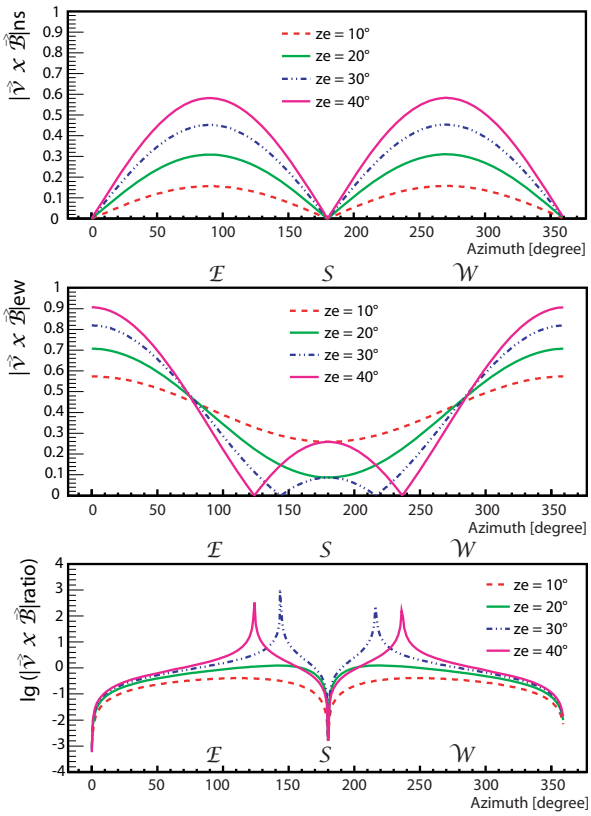

Fig. 4: Relative contributions of the $\vec{v} \times \vec{B}$-vector for the polarization components north-south (top panel), east-west (middle panel), and their ratio (bottom panel) vs. the azimuth angle calculated for different zenith angles.

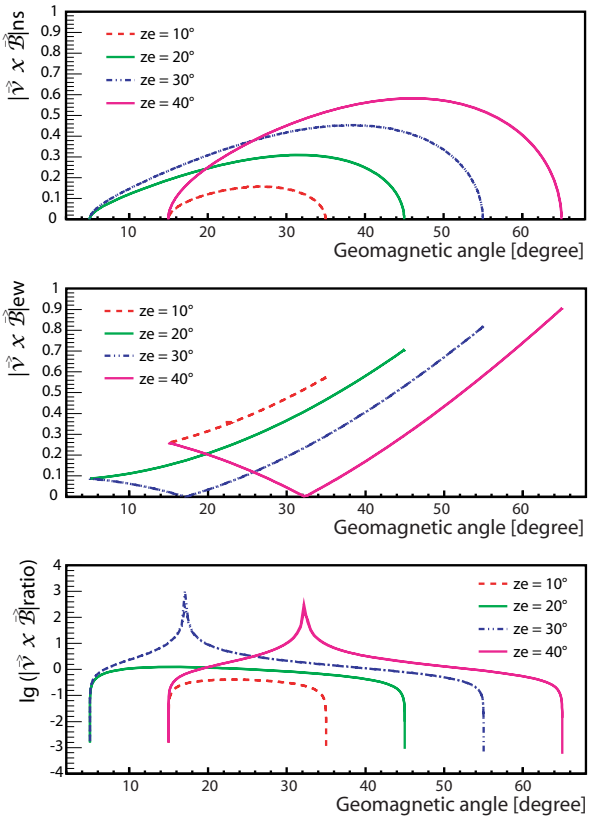

Fig. 5: Same as Fig.4, but vs. the geomagnetic angle.

$E > 10^{16.9}$ eV is chosen in order to avoid any efficiency biased effect on the investigated polarization characteristics. Fig. 3 shows the mean values (and width of the distributions) of the CC-Beam in dependence on shower azimuth and geomagnetic angle (angle between shower axis and the geomagnetic field). The reconstructed CC-Beam value is normalized to the estimated muon number of the EAS and to the mean distance of the antennas to the shower axis in order to minimize the influence of others than directional dependences on the distributions. Slight variations of the radio signal with the azimuth and geomagnetic angles are observed, as well as slight differences between the two polarization directions. A possible origin of these differences is discussed in the following sections.

IV. Polarization characteristics

The radio emission of cosmic ray air showers generated by the geo-synchrotron mechanism is expected to be highly linearly polarized. As predicted by sophisticated Monte Carlo simulations of the radio emission, the signal is usually present in both polarization components whose strengths depend directly on the shower azimuth for a given zenith angle (and therefore also on the geomagnetic angle) [5]. Already in early models of geomagnetic emission mechanisms, the expectation was that, to first order, the emission is polarized in the direction perpendicular to the air shower axis and geomagnetic field, outlined also in [5]. In other words, the polarization characteristics follow a behavior described by a unit polarization vector: $\vec{v} \times \vec{B}$, $\vec{v}$ being the direction of the incoming shower axis and $\vec{B}$ of the Earths magnetic field at the location of the experiment (for Karlsruhe, zenith $= 25°$ and azimuth $= 180°$). Recently, there have been suggestions [6] that, in addition to the polarization characteristics, also the absolute amplitude of the electric field in a first approximation can be considered to be proportional to this Lorentz force. The unit polarization vector is calculated for fixed zenith angles for each individual projection of the polarization, where the north-south part, east-west part, and their ratio (north-south/east-west) are displayed in Figs. 4 and 5. These figures show the dependence of the polarization components of the radio signal on the direction of the shower axis. They emphasize that, in Karlsruhe, considering pure shower geometry the north-south polarized channels are more sensitive to showers coming from east and west directions, and the east-west polarized channels have a higher sensitivity to showers coming from north and south.

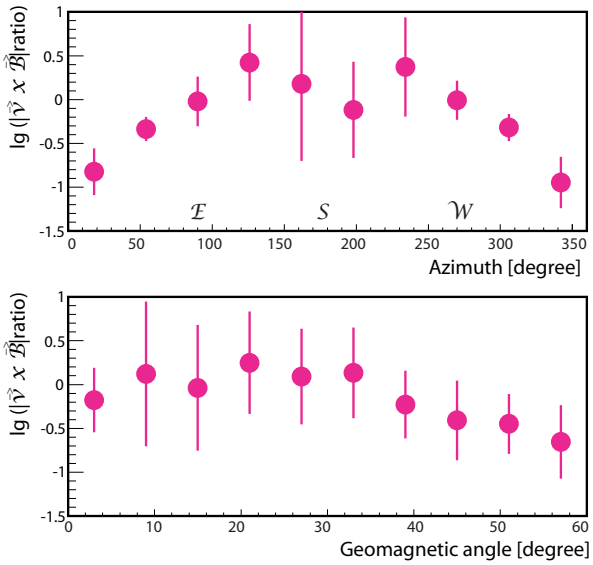

Fig. 6: Ratio of the north-south divided by the east-west component of the $\vec{v} \times \vec{B}$-vector for the measured events taking into account the geometry of the shower axis only vs. the azimuth angle (upper panel) and the geomagnetic angle (lower panel) of the shower. Mean values and spread of the distributions are shown.

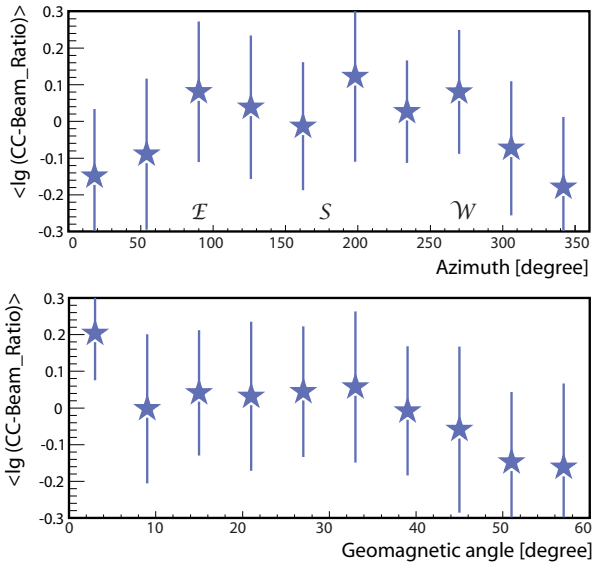

Fig. 7: Ratio of the reconstructed CC-beam values for the north-south and east-west polarization component of the measured events vs. the azimuth angle (upper panel) and the geomagnetic angle (lower panel). Mean values and spread of the distributions are shown.

V. Comparison with data

To investigate if these expected relations are also seen in the measured data, we calculate the ratio of the north-south and east-west polarization contribution in terms of the $\vec{v} \times \vec{B}$-amplitudes for each individual measured event (Fig. 6) using the geometry of the EAS only. Thus, the displayed distributions reflect the dependencies shown in Figs. 4 and 5 for the sample of the selected radio detected events above a primary energy of $10^{16.9}$ eV. The ratio of the two polarization components is chosen in order to be independent of the energy and distance dependence of the measured amplitudes. It is obvious from figure 6, that there is a characteristic correlation of the ratio on the azimuth and geomagnetic angle expected, if the Lorentz force approximation is applicable. Finally, Fig. 7 shows the distributions of the measured events in their CC-Beam value of the pulse height ratio (north-south/east-west), where the same qualitative behavior is observed in their main characteristics.

VI. Summary and Outlook

Within the current configuration, LOPES is continuously performing polarization measurements since December 2006. The digital antenna array is absolutely amplitude calibrated, and thus we can pave the way for a better understanding of the radio signal as a complementary technique to large cosmic ray experiments. By LOPES-30, the signal is recorded in both polarization directions, east-west and north-south, independently. Meanwhile, a large number of events detected in both polarization directions is at disposal for detailed analysis. In this presentation, the ratio of the radio signal recorded in the north-south polarization direction vs. the signal recorded in the east-west direction was studied. Investigating this ratio in individual showers allows us to study the polarization characteristics of the signal independent of primary energy and distance of the antennas to the shower axis, i.e. in particular the dependence of the polarization on the direction of the incoming primary particle. Correlations of the pulse height ratio of both polarization components with the azimuth, as well as with the geomagnetic angle were compared with predictions of a first order approximation of models based on a geomagnetic origin of the emission. By this, the geomagnetic effect could be verified as a main mechanism in the radio emission process of cosmic ray air showers. Nevertheless, in future, detailed simulations are required for more reliable comparisons with the measurements; full detector simulations included.

VII. Acknowledgments

P.G. Isar would like to thank for the PhD support from DAAD-Helmholtz in the frame of the LOPES project.

References

[1] H. Falcke et al. - LOPES coll., *Nature 435, 313-316 (2005)*
[2] A. Horneffer et al. - LOPES coll., *Proceedings of the 30th ICRC, Merida, Mexico 4 (2008) 83*
[3] S. Nehls et al., *Nucl.Instr.and.Meth.A 589 (2008) 350*
[4] P.G. Isar et al. - LOPES coll., *Nucl.Instr.and.Meth.A (2009), doi:10.1016/j.nima.2009.03.118*
[5] T. Huege and H. Falcke, *Astropart.Phys. 24 116-136 (2005)*
[6] D. Ardouin et al. - CODALEMA coll., *Astropart.Phys. (2009), doi:10.1016/j.astropartphys.2009.01.001*

Time Calibration of the Radio Air Shower Array LOPES

F. Schröder[*], W.D. Apel[*], J.C. Arteaga[†,xiv], T. Asch[‡], F. Badea[*], L. Bähren[§], K. Bekk[*], M. Bertaina[¶], P.L. Biermann[‖], J. Blümer[*,†], H. Bozdog[*] I.M. Brancus[**], M. Brüggemann[††], P. Buchholz[††], S. Buitink[§], E. Cantoni[¶,‡‡], A. Chiavassa[¶], F. Cossavella[†], K. Daumiller[*], V. de Souza[†,xv], F. Di Pierro[¶], P. Doll[*], R. Engel[*], H. Falcke[§,x], M. Finger[*], D. Fuhrmann[xi], H. Gemmeke[‡], P.L. Ghia[‡‡], R. Glasstetter[xi], C. Grupen[††], A. Haungs[*], D. Heck[*], J.R. Hörandel[§], A. Horneffer[§], T. Huege[*], P.G. Isar[*], K.-H. Kampert[xi], D. Kang[†], D. Kickelbick[††], O. Krömer[‡], J. Kuijpers[§], S. Lafebre[§], P. Łuczak[xii], M. Ludwig[†], H.J. Mathes[*], H.J. Mayer[*], M. Melissas[†], B. Mitrica[**], C. Morello[‡‡], G. Navarra[¶], S. Nehls[*], A. Nigl[§], J. Oehlschläger[*], S. Over[††], N. Palmieri[†], M. Petcu[**], T. Pierog[*], J. Rautenberg[xi], H. Rebel[*], M. Roth[*], A. Saftoiu[**], H. Schieler[*], A. Schmidt[‡], O. Sima[xiii], K. Singh[§,xvi], G. Toma[**], G.C. Trinchero[‡‡], H. Ulrich[*], A. Weindl[*], J. Wochele[*], M. Wommer[*], J. Zabierowski[xii], J.A. Zensus[‖]

[*] *Institut für Kernphysik, Forschungszentrum Karlsruhe, Germany*
[†] *Institut für Experimentelle Kernphysik, Universität Karlsruhe, Germany*
[‡] *IPE, Forschungszentrum Karlsruhe, Germany*
[§] *Department of Astrophysics, Radboud University Nijmegen, The Netherlands*
[¶] *Dipartimento di Fisica Generale dell' Universita Torino, Italy*
[‖] *Max-Planck-Institut für Radioastronomie Bonn, Germany*
[**] *National Institute of Physics and Nuclear Engineering, Bucharest, Romania*
[††] *Fachbereich Physik, Universität Siegen, Germany*
[‡‡] *Istituto di Fisica dello Spazio Interplanetario, INAF Torino, Italy*
[x] *ASTRON, Dwingeloo, The Netherlands*
[xi] *Fachbereich Physik, Universität Wuppertal, Germany*
[xii] *Soltan Institute for Nuclear Studies, Lodz, Poland*
[xiii] *Department of Physics, University of Bucharest, Bucharest, Romania*
[xiv] *now at: Universidad Michoacana, Morelia, Mexico*
[xv] *now at: Universidade de São Paulo, Instituto de Fîsica de São Carlos, Brasil*
[xvi] *now at: KVI, University of Groningen, The Netherlands*

***Abstract*. LOPES is a digitally read out antenna array consisting of 30 calibrated dipole antennas. It is located at the site of the KASCADE-Grande experiment at Forschungszentrum Karlsruhe and measures the radio emission of cosmic ray air showers in the frequency band from 40 to 80 MHz. LOPES is triggered by KASCADE and uses the KASCADE reconstruction of the shower axis as an input for the analysis of the radio pulses. Thereby LOPES works as an interferometer when the signal of all antennas is digitally merged to form a beam into the shower direction. To be sensitive to the coherence of the radio signal, a precise time calibration with an accuracy in the order of 1 ns is required.**

Thus, it is necessary to know the delay of each antenna which is time and frequency dependent. Several calibration measurements are performed to correct for this delay in the analysis: The group delay of every antenna is measured regularly (roughly once per year) by recording a test pulse which is emitted at a known time. Furthermore, the delay is monitored continuously by the so called phase calibration method: A beacon (a dipole antenna) emits continuously two sine waves at 63.5 MHz and 68.1 MHz. By that a variation of the delay can be detected in a subsequent analysis of the radio events as a change of the phase at these frequencies. Finally, the dispersion of the analog electronics has been measured to account for the frequency dependence of the delay.

***Keywords*: LOPES timing calibration**

I. Introduction

The main part of LOPES (LOfar ProtoypE Station) consists of 30 digitally read out, absolutely calibrated, inverted V-shape dipole antennas [1], [2], [3]. The antennas are co-located with the KASCADE array with a baseline of about 200 m and are triggered about twice per minute by the KASCADE-Grande experiment [4], [5]. Only a few events per day contain a cosmic ray air shower radio pulse which is clearly distinguishable from the noise, as the noise floor is quite high inside the KASCADE array. Due to a precise time calibration of LOPES the digitally measured radio data can be used to form a beam into the shower arrival direction. Furthermore the cross-correlation of the antennas can be calculated to be sensitive to the coherence of the radio signal [6]. This way LOPES is a phased array which can be used as a digital interferometer.

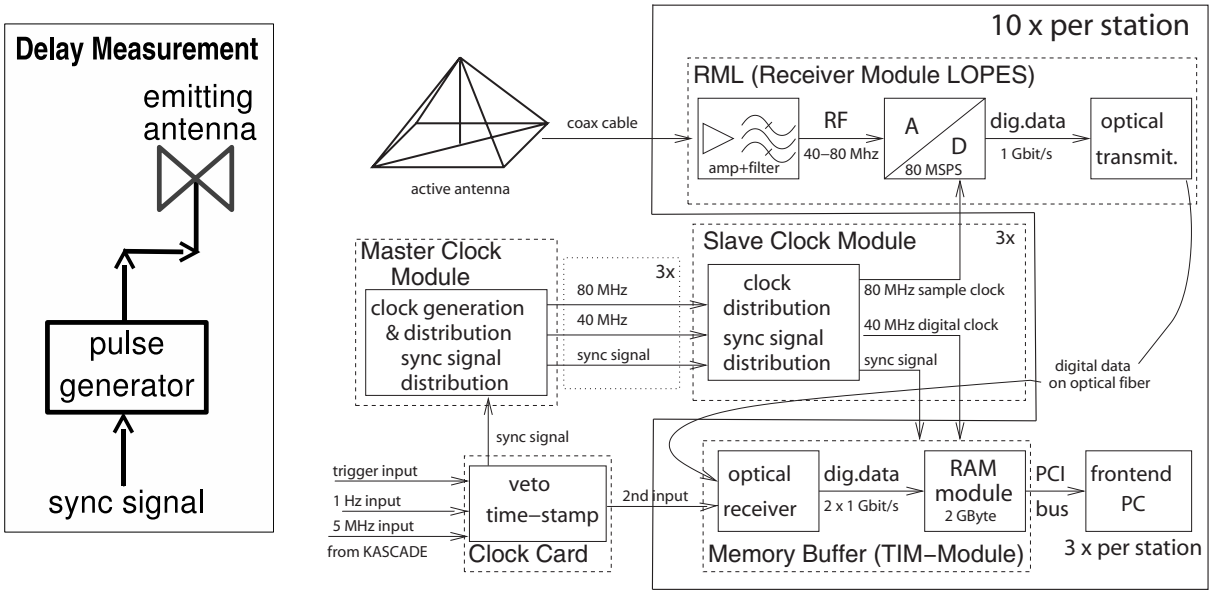

Fig. 1: Right: LOPES hardware and timing setup. Left: extension used for delay measurements; a pulse generator which is connected to a emitting calibration antenna is triggered by the same sync signal as the LOPES DAQ and emits a short calibration pulse. Thus this calibration pulse is recorded with a certain delay within a normal event. Due to the setup, the delay of the pulse contains a certain offset, which is the same for every measurement and therefore can be ignored when determining relative delays between antennas.

Whenever LOPES is triggered a trace of 2^{16} samples with a sampling rate of $80\,\mathrm{MHz}$ is read out at each antenna with the trigger time roughly in the middle of the trace. LOPES is operating in the second Nyquist domain. Thus the full information of the radio signal between $40\,\mathrm{MHz}$ and $80\,\mathrm{MHz}$ is contained in the data and can be retrieved by up-sampling (i.e. the correct interpolation between the samples) with the zero-padding method [7]. With reasonable computing time, data can be up-sampled to a sample spacing below $0.1\,\mathrm{ns}$, so that the sample spacing does not contribute significantly to uncertainties in the timing.

To obtain a stable timing of the antenna array the ADC clock is centrally generated and distributed via cables to all DAQ computers (fig. 1). With the exception of jumps by full clock cycles (see section IV), the jitter of the clock is negligible. Thus the time calibration of LOPES is basically reduced to measure the delay of each antenna and the subsequent electronics, i.e. the time between the arrival of a radio pulse at the antenna and its measurement with the DAQ. This delay is different for each antenna (mainly due to different cable lengths). As for interferometry only the differences of the arrival time of the radio signal between the antennas matters, the absolute delay is of minor importance. In this paper the term delay is therefore meant in a relative sense.

The following section explains how the delay is measured at LOPES. To achieve the necessary precision we also take into account second order effects, like the frequency dependence of the delay (dispersion) and variations of the delay with time.

II. Delay measurements

LOPES as a digital interferometer requires the timing precision of the radio pulse in each antenna to be much smaller than the period of the filter ringing ($\approx 17\,\mathrm{ns}$), when forming a cross-correlation beam into the arrival direction of the cosmic ray air shower. Thus the delay has to be known and measured with a precision of about $1\,\mathrm{ns}$, to be sensitive to the coherence of the radio signal.

At the beginning of LOPES the delay has been measured with solar flare events, but now we have developed a new method which does not depend on any astronomical sources: Simultaneously with the LOPES data acquisition we trigger a pulse generator which is connected to a calibration antenna at a defined angle and distance to each LOPES antenna. The calibration antenna emits a pulse with a known delay after the trigger. Therefore after repeating the calibration for every antenna the pulse should appear in the data of each antenna at exactly the same time, if the delay of each LOPES antenna (and the connected analog electronics) would be the same.

However, e.g. due to different cable lengths, this is not the case, and indeed the calibration pulses are detected at different times for each antenna. The relative delay between different LOPES antennas can then be obtained by measuring the time differences of the detection times of the calibration pulses.

The pulse detection time can be determined by different methods: On the one hand a Hilbert envelope is

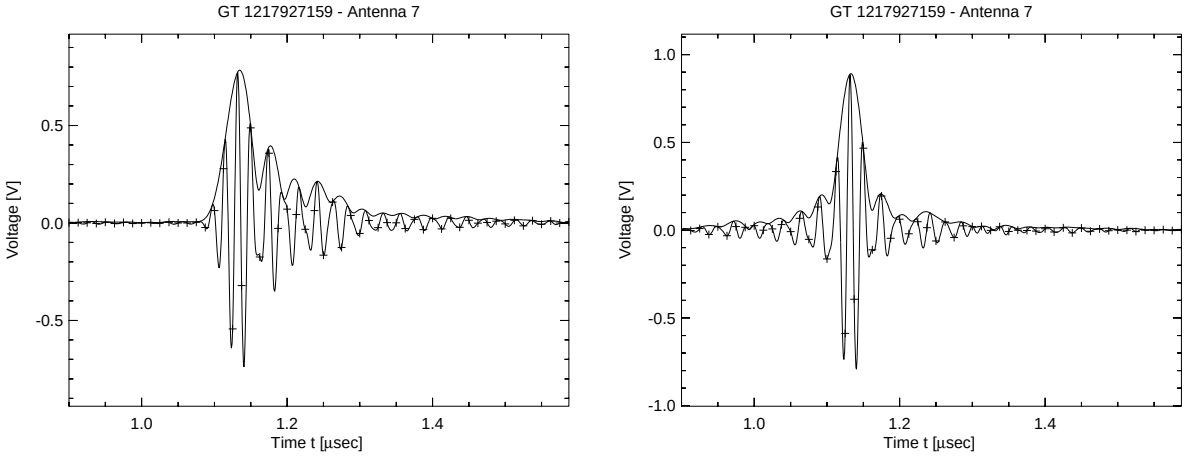

(a) without dispersion correction

(b) after dispersion correction

Fig. 2: A short test pulse (FWHM ≈ 10 ns) emitted by a function generator and recorded by the LOPES DAQ. The crosses indicate the measurement points sampled by the ADC. The lines show the up-sampled signal and the Hilbert envelope of the pulse. In the raw data (a) it can be seen that a part of the pulse is delayed by more than 100 ns due to the dispersion of the filter. After the correction of the dispersion (b), the pulse is more symmetrical, the position of the pulse envelope has moved by about 2 ns, its height (field strength) has increased by about $10\,\%$ and its FWHM (field strength) decreased by about $10\,\%$. The effects on height and width are reduced to a few percent, when using the sub-band from 43 MHz to 74 MHz.

calculated and the pulse position is taken as either the position of the maximum or the crossing of half height. Thereby the position of the maximum shows slightly less jitter (RMS about 0.4 ns) when looking at several events recorded within a few minutes and the delays obtained from the half height crossing and the maximum are consistent within errors. On the other hand the position can be defined as the minimum or the maximum of the up-sampled trace and the jitter for both of them for subsequent events is less than the used sampling spacing of 0.1 ns (after up-sampling). The delays calculated by the maximum and the minimum agree well with each other. Thus in principle the delay can be determined with a precision of better than 0.5 ns.

Although the delays determined by the two methods (pulse position by the trace itself or its envelope) are inconsistent by a few nanosecond, this inconsistency can be explained at least partially with the dispersion of the analog electronics. This difference is reduced to an average of about 2 ns when correcting for this dispersion. The remaining inconsistency could not be explained so far, and is under investigation. Nevertheless, since the calculation of the cross-correlation beam is done with the (up-sampled) trace and not with the envelope, we currently use the delays deferred directly from the trace for the analysis of cosmic ray events.

III. Correction for the dispersion

The frequency dependence of the group delay of a system is called dispersion. For LOPES^{STAR} the dispersion has been measured for the antenna, the analog electronics (filter) and the connecting cable [8]. The dispersion of the cable can be considered negligible and the largest contribution to the overall dispersion comes from the filter.

Unfortunately, the dispersion of the LOPES V-shape antenna is unknown, because it is not easily measurable. But the dispersion of the filter has been measured with a network analyzer and can be corrected in the analysis. This is especially important as the first 10 LOPES antennas are connected to a slightly different filter than the later 20 antennas. The successfull correction of the dispersion in the analysis software has been proven by recording test pulses which are emitted by a function generator connected to the RML (fig. 1).

As expected, the filter creates a response only to the leading and falling edge of pulses. Thus a delta pulse with FWHM $<<$ filter width $^{-1}$ (≈ 25 ns) should be seen as a pulse with a width of ≈ 25 ns (FWHM of the power). This pulse is linearly distorted by the dispersion such that it is partially delayed by more than 100 ns (fig. 2). When correcting for the dispersion this distortion can be significantly reduced and the FWHM of the pulse power is in the order of 30 ns. In addition the pulse is shifted by a few ns and the pulse width and height (field strength) change by roughly 10%. Thus the correction of the dispersion is necessary for precise time and amplitude measurements of radio pulses, and future radio experiments should aim to correct the dispersion of every system in the signal chain.

IV. Phase calibration

The delay of each antenna and the read out electronics can be assumed to be roughly constant. However, there

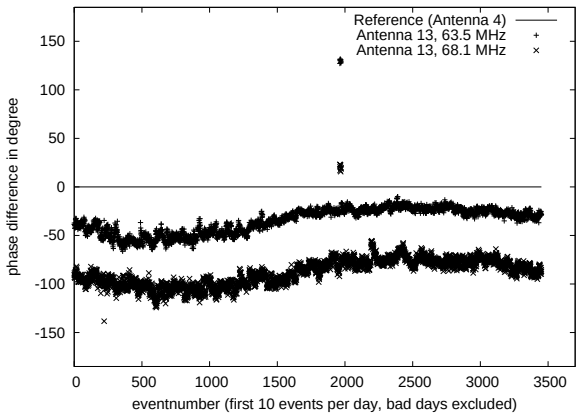

Fig. 3: Example of the phase calibration: The phase differences at the beacon frequencies between one antenna and a chosen reference antenna are shown for the first 10 events of every day for one year of data taking (08 May 2008 - 07 May 2009, excluding a few days of down time and operational problems).

are variations on the scale of a few ns over time. In addition the LOPES clock distribution is not absolutely temperature stable, causing the effective delay of single antennas to increase or decrease from time to time by integer steps of $12.5\,\mathrm{ns}$ (one clock cycle). To correct for these steps, originally the phase of a TV transmitter inside of the LOPES band was monitored. After the shut down of this TV transmitter this method has been further developed by setting up a dedicated transmitter (beacon) inside of the Forschungszentrum Karlsruhe.

The beacon continously emits two sine waves of $63.5\,\mathrm{MHz}$ and $68.1\,\mathrm{MHz}$ at $-21\,\mathrm{dBm}$ each, which have a very narrow band width (FWHM $<$ $100\,\mathrm{Hz}$). This signal is clearly seen above the noise level by all LOPES antennas and the phase can be measured at each of the two beacon frequencies at each antenna. For each of the two frequencies now the following is valid: As a LOPES event contains data from every antenna coincidently, a stable delay should lead to a constant difference between the phases at the same frequency measured by different antennas. Thus a variation in the relative delay between two antennas can be detected as a variation in the phase difference at the same two antennas at one of the beacon frequencies. Subsequently this variations can be taken into account in the analysis of radio events.

In a few events the measurement of the phase is disturbed by RFI noise. To avoid corrections for 'unreal' variations of the delay and to take into account ambiguities of the phase if the difference is larger than 180° ,a consistency check is performed between the phase differences at both frequencies. For most of the events the results agree well, and this way the timing of the antennas can be monitored and significantly improved on a event-by-event basis.

For the given example (fig. 3), the correlated drift which can be seen in both frequencies corresponds to a variation in the effective delay of about $1.5\,\mathrm{ns}$ over the year and can be clearly distinguished from the jitter of the phase differences. The jump in the middle is caused by a change of the effective delay by $25\,\mathrm{ns}$ during one day. The outlier at the beginning is one of the few noisy events, for which the phase calibration method would fail.

The accuracy of the phase calibration on short time scales is thereby determined by the short-term jitter (noise) of the phase measurement. This jitter is a function of the trace length and the amplitude of the beacon signal. Therefore, for a fixed trace length (2^{16} samples at LOPES) an emission power of the beacon can be chosen such that the phase calibration allows a sufficiently accurate correction of the timing. In the case of LOPES the short term jitter of the phase differences is in the order of $0.3\,\mathrm{ns}$. Furthermore, in figure 3 can be seen that there is some additional error on longer time scales, as changes in the phase differences are not completely correlated between both frequencies. But still, the overall accuracy is better than the required timing precision of about $1\,\mathrm{ns}$.

V. Conclusions

It could be shown that the delay of each LOPES antenna and the corresponding electronic chain can be calibrated with a precision of better than $0.5\,\mathrm{ns}$. Nevertheless, there is a not fully understood difference between the measurement of the time of a radio pulse by either looking to the trace or its envelope. In addition, it is possible to continously monitor the relative delay of each antenna with a precision of below $1\,\mathrm{ns}$. Thus long and short term variations of the delay in the order of a few nanoseconds can be corrected in the subsequent data analysis on an event-by-event basis.

Furthermore, the dispersion of the analog electronics has been shown to slightly affect the time, the width and the height of measured radio pulses. Therefore this is taken into account in the LOPES standard analysis pipeline to produce more accurate results. Also future radio experiments should consider the dispersion of the whole detection system.

Finally, the different timing calibration methods of LOPES show that radio air shower experiments can achieve a relative timing accuracy of better than one nanosecond and that this accuracy can be monitored and maintained continuously over long periods.

References

[1] H. Falcke et al., *Nature 435 (2005) 313*
[2] S. Nehls et al., *Nucl.Instr.and.Meth.A 589 (2008) 350*
[3] T. Asch et al., *Proceedings of the 30th International Cosmic Ray Conference, Merida, Mexico 5 (2008) 1081*
[4] T. Antoni et al., *Nucl.Instr.and.Meth.A 513 (2003) 429*
[5] G. Navarra et al., *Nucl.Instr.and.Meth.A 518 (2004) 207*
[6] A. Horneffer et al., *Proceedings of the 30th International Cosmic Ray Conference, Merida, Mexico 4 (2008) 83*
[7] T. Asch, *FZKA report 7459, Forschungszentrum Karlsruhe (2009)*
[8] O. Krömer, *FZKA report 7396, Forschungszentrum Karlsruhe (2008)*

Radio Emission of Extensive Air Showers during Thunderstorms

M. Ender[†], W.D. Apel[*], J.C. Arteaga[†,xiv], T. Asch[‡], F. Badea[*], L. Bähren[§], K. Bekk[*], M. Bertaina[¶], P.L. Biermann[‖], J. Blümer[*,†], H. Bozdog[*] I.M. Brancus[**], M. Brüggemann[††], P. Buchholz[††], S. Buitink[§], E. Cantoni[¶,‡‡], A. Chiavassa[¶], F. Cossavella[†], K. Daumiller[*], V. de Souza[†,xv], F. Di Pierro[¶], P. Doll[*], R. Engel[*], H. Falcke[§,x], M. Finger[*], D. Fuhrmann[xi], H. Gemmeke[‡], P.L. Ghia[‡‡], R. Glasstetter[xi], C. Grupen[††], A. Haungs[*], D. Heck[*], J.R. Hörandel[§], A. Horneffer[§], T. Huege[*], P.G. Isar[*], K.-H. Kampert[xi], D. Kang[†], D. Kickelbick[††], O. Krömer[‡], J. Kuijpers[§], S. Lafebre[§], P. Łuczak[xii], M. Ludwig[†], H.J. Mathes[*], H.J. Mayer[*], M. Melissas[†], B. Mitrica[**], C. Morello[‡‡], G. Navarra[¶], S. Nehls[*], A. Nigl[§], J. Oehlschläger[*], S. Over[††], N. Palmieri[†], M. Petcu[**], T. Pierog[*], J. Rautenberg[xi], H. Rebel[*], M. Roth[*], A. Saftoiu[**], H. Schieler[*], A. Schmidt[‡], F. Schröder[*], O. Sima[xiii], K. Singh[§,xvi], G. Toma[**], G.C. Trinchero[‡‡], H. Ulrich[*], A. Weindl[*], J. Wochele[*], M. Wommer[*], J. Zabierowski[xii], J.A. Zensus[‖]

[*]*Institut für Kernphysik, Forschungszentrum Karlsruhe, Germany*
[†]*Institut für Experimentelle Kernphysik, Universität Karlsruhe, Germany*
[‡]*IPE, Forschungszentrum Karlsruhe, Germany*
[§]*Department of Astrophysics, Radboud University Nijmegen, The Netherlands*
[¶]*Dipartimento di Fisica Generale dell' Universita Torino, Italy*
[‖]*Max-Planck-Institut für Radioastronomie Bonn, Germany*
[**]*National Institute of Physics and Nuclear Engineering, Bucharest, Romania*
[††]*Fachbereich Physik, Universität Siegen, Germany*
[‡‡]*Istituto di Fisica dello Spazio Interplanetario, INAF Torino, Italy*
[x]*ASTRON, Dwingeloo, The Netherlands*
[xi]*Fachbereich Physik, Universität Wuppertal, Germany*
[xii]*Soltan Institute for Nuclear Studies, Lodz, Poland*
[xiii]*Department of Physics, University of Bucharest, Bucharest, Romania*
[xiv]*now at: Universidad Michoacana, Morelia, Mexico*
[xv]*now at: Universidade de São Paulo, Instituto de Fîsica de São Carlos, Brasil*
[xvi]*now at: KVI, University of Groningen, The Netherlands*

***Abstract*. The deflection of relativistic, charged particles in high energy air showers due to the geomagnetic field leads to a coherent emission of radio pulses. This process can be described by the geosynchrotron model. In particular during thunderstorms, there are additional strong electric fields in the atmosphere which can lead to further accelerations of the charged particles and thus can have influence on shape and strength of the radio pulse. To get a reliable energy reconstruction based on the measured radio signal it is mandatory to understand such effects. Furthermore, lightning strikes are a source of broadband radio emissions that are visible over very long distances. This could also cause difficulties in detecting the much lower signal of air showers. The influences of strong electric fields are currently explored with the LOPES experiment in Karlsruhe, Germany. LOPES measures in the frequency range between 40 and 80 MHz and is operated in coincidence with KASCADE-Grande. Additionally, meteorological data as well as the vertical electrical field near the ground are monitored.**

***Keywords*: LOPES, thunderstorm, lightning**

I. INTRODUCTION

Radio detection of air showers is an upcoming new technique to measure the properties of very high energy cosmic rays. Compared to fluorescence or air Čerenkov measurements a much higher duty cycle is achieved. Only during strong and nearby thunderstorms, the measurements are distinctively different compared to fair weather conditions. To determine whether a measurement is reliable or not, it is very important to understand the processes happening in the atmosphere during a thunderstorm and how they affect the radio emission in air showers.

The radio emission of extensive air showers in the energy range from $5 \cdot 10^{16}$ to 10^{18} eV is studied with the LOPES experiment [4][6]. It has been built as a LOFAR prototype station and is located at the site of the KASCADE-Grande experiment in Karlsruhe, Germany [1][7]. LOPES consists of thirty inverted v-shaped dipole antennas, half of them oriented to measure the east-west and half of them the north-south polarization. The frequency is limited to a range between 40 and 80 MHz.

For the purpose of studying the effects of thunderstorms on the radio emission of air showers, an electric

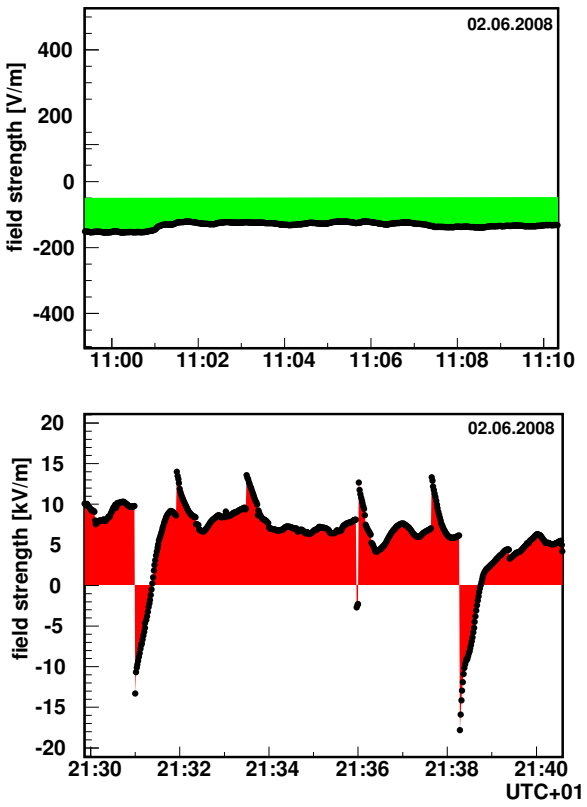

Fig. 1: Vertical component of the static electric field near the surface during fair weather conditions (upper figure) and during a thunderstorm (lower figure). Please note the different scales of the field strength. The lightning discharges are clearly visible as discontinuities. Each plot shows ten minutes of the atmospheric electric field.

field mill has been set up at the LOPES array. It measures the vertical component of the static electric field near the ground once a second. With this information a reliable automatic detection of thunderstorms is possible [8].

II. Monitoring the atmospheric electric field

During fair weather conditions, the static electric field near the surface varies only slowly between -100 and -200 Vm^{-1}. When rain clouds move overhead, the amplitudes become bigger but the changes are still smooth. During thunderstorms this is completely different. The field strength can reach values up to ± 20 kVm^{-1} on ground level. Additionally, discharges are visible as discontinuities that can even invert the polarity of the field. Together, these are reliable indicators to automatically detect thunderstorms [9].

Whenever a thunderstorm is detected (figure 1), LOPES is switched to a special data acquisition mode that records an eight times larger data block. Instead of the usual 0.82 ms, about 6.55 ms of data are taken, while the pre-trigger time of 0.41 ms remains the same. This strongly increases the probability to find in addition

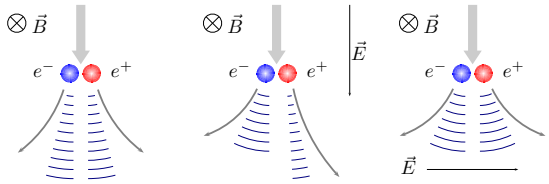

Fig. 2: Additional electric fields lead to different trajectories and therefore different radio emission of the charged particles.

to the shower signal a signal from lightnings inside the recorded trace.

III. Influence of strong electric fields on the radio emission of EAS

The main component of the radio emission from an extensive air shower can be described by the geosynchrotron model. The geomagnetic field causes a Lorentz force which leads to a coherent emission of synchrotron radiation.

The electric fields inside thunderstorm clouds, especially within the convective region, can reach peak values up to 100 kVm^{-1}. This leads to additional forces on the electrons and positrons that are added to the forces caused by the geomagnetic field. Depending on the direction of the electric field, this can lead to an amplification or a weakening of the radio emission [3] as illustrated in figure 2.

Figure 3 shows two air shower events initiated by primary cosmic rays of very similar energy and direction but with different radio signals. This is an example where such an amplification during a thunderstorm has occurred. The upper event was recorded during normal weather conditions and shows no signal from the air shower which would be expected at -1.8 μs, as would be expected for the relative low estimated primary energy of $5.4 \cdot 10^{16}$ eV. The incoherent signal of some antennas after -1.75 μs is noise caused by the particle detectors of KASCADE. The direction of this event has been reconstructed from KASCADE data to $\phi = 110.4\,^\circ$ and $\theta = 31.5\,^\circ$, where ϕ is the azimuth of the shower direction and θ the zenith angle.

The lower figure shows an event with a very similar geometry of $\phi = 110.4\,^\circ$ and $\theta = 32.1\,^\circ$ and even a slightly lower estimated energy of $4.3 \cdot 10^{16}$ eV. Also the average distance of the antennas to the shower core is similar. Nevertheless, the event shows a strong and coherent radio pulse at -1.8 μs, which is not expected at that energy. This can be explained by amplification of the radiosignal in a thundercloud.

Unfortunately, due to low event statistics during thunderstorm conditions only for a few events such a twin can be found. During 2007 and 2008, about 3400 events have been recorded during thunderstorms, which also passed the quality checks for a reliable reconstruction. That corresponds to approximately two days of data taking in thunderstorm mode.

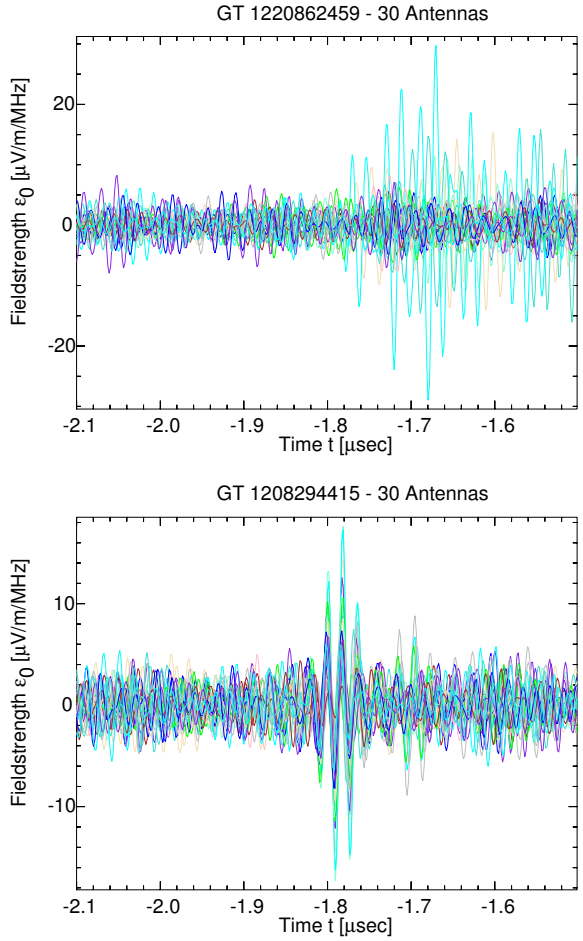

Fig. 3: The upper figure shows an event with no coherent signal from the air shower. In the lower figure which shows an event with similar geometry and even slightly lower estimated energy, there is a clearly visible coherent pulse at -1.8 μs.

Due to the fact that the trigger threshold for LOPES is lower than the detection threshold of about $5 \cdot 10^{16}$ eV and the steep spectrum, only a small fraction of all triggered events shows a radio pulse. The fraction of events with a ratio of peak value of the formed cross-correlation beam to the rms value of the beamformed data larger than a certain value is here defined as detection efficiency.

Only a fraction of $(0.96 \pm 0.12) \cdot 10^{-2}$ of the events recorded during fair weather conditions has a detected coherent signal. During thunderstorms the situation changes. Then a fraction of $(2.39 \pm 0.27) \cdot 10^{-2}$ has a detected coherent signal. That corresponds to 81 air shower events with a cross-correlation beam above threshold, recorded during thunderstorm conditions.

This shows that a significant fraction of the events during thunderstorms is affected by the atmospheric conditions. The influence of atmospheric electric fields with smaller peak amplitudes as they can occur in rain clouds has still to be studied more carefully. At the moment it does not seem as if there is a big effect [3]. The only case might be rain clouds with extraordinary strong field. But they are even less frequent than thunderstorms. Thus, the number of events within such periods is quite low.

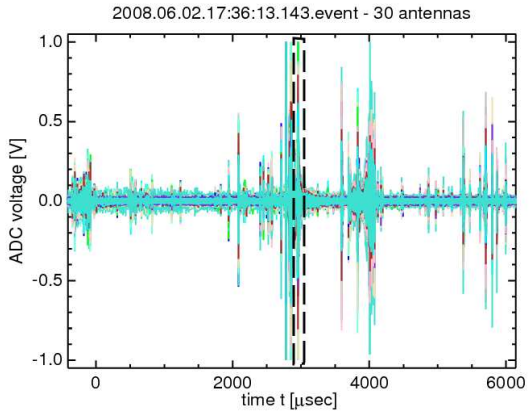

Fig. 4: Example of a thunderstorm event with strong additional signals caused by lightning. An EAS signal would be visible at time zero with an amplitude less than 0.1 V. The dashed frame marks the region which is used for the skymap shown in figure 5.

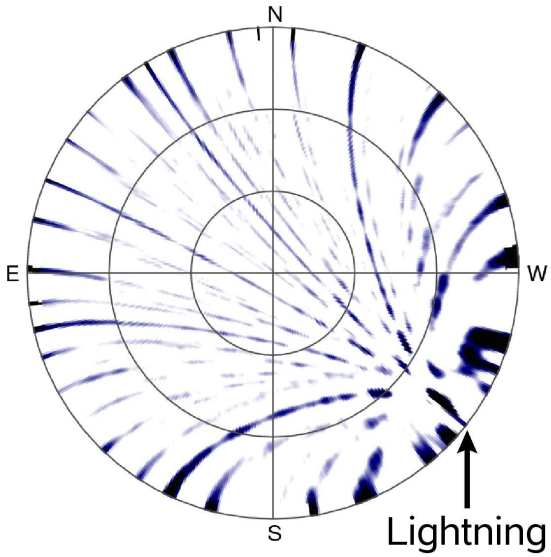

Fig. 5: The figure shows a skymap of the cross-correlation beam of the event shown in figure 4. It shows the whole sky with zenith in the center and horizon at the edge. The strong lightning signal in south-west is the discharge region and the grating lobes of the antenna array cause the signals covering the whole sky.

IV. Background signals caused by lightnings

The strong currents during lightning strikes cause strong broadband radio signals that are detectable over very large distances. Depending on the distance and the kind of the discharge, the time structure of the

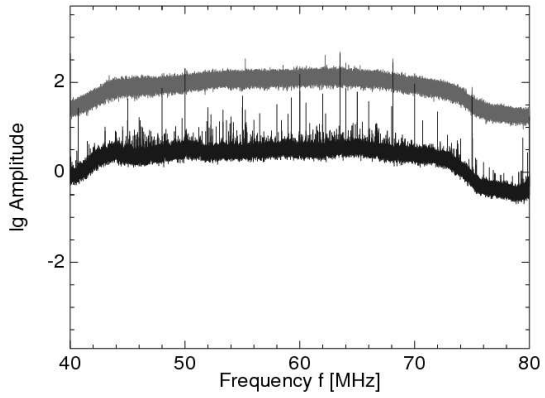

Fig. 6: The figure shows a comparison between the usual background spectrum (black) and the spectrum with a lightning signal inside (grey). The power inside the LOPES frequency range is approximately a hundred times higher than in the usual case. The sine waves emitted by a beacon, that are needed for phase calibration, at 63.5 and 68.1 MHz are almost covered by the lightning signal.

signal varies. Very short and strong pulses from located discharges inside the clouds in altitudes between 5 and 20 km, as described as narrow bipolar pulses by A. V. Gurevich [5]. For large scale applications of the radio detection technique it is aspired to trigger on the radio pulse directly. This self-trigger technique has been developed with LOPES-STAR [2]. The trigger decision is based on various conditions including the shape of the observed pulse. It might be important to know the properties of the short pulses originating from thunderstorms to avoid wrong trigger decisions.

Discharges between clouds or from cloud to ground are the origin of longer lasting signals (figure 4). The lightning signal in all antennas can be used for a beamforming to localize the origin of the lightning (figure 5). Due to the grating lobes of the antenna array, the lightning signal which originates near the horizon causes additional signals all over the sky. With a higher number of time-frames the evolution of the discharge can be watched.

Furthermore there is a beacon, mounted at the roof of a nearby building that is emitting two sine waves at 63.5 and 68.1 MHz as a reference for the timing. The lightning signal can be stronger these sine waves, as shown in figure 6, that are used for the phase calibration. The phase calibration gives a precise relative timing between the recorded traces, which is necessary for beamforming. Therefore a good signal to noise ratio is necessary at these frequencies. Thus the background produced by lightnings can make it impossible to analyse a specific air shower event.

The very sensitive electronics that are necessary in order to measure the low radio signal from air showers is often saturated by lightning signals. In these cases the events cannot be used for the standard analysis.

V. Conclusion

The reconstructed energy of an air shower based on radio measurements is influenced by electric fields during thunderstorms only, and not at normal weather conditions. This leads to a larger fraction of events with a detected coherent signal. To obtain reliable air shower information from the measured radio signal it is mandatory to monitor the electric field of the atmosphere and thus record the signatures of thunderstorms.

Another possibility to prove whether an event has been influenced by additional electric fields or not, is the polarization of the recorded signal. An aberration of the measured polarization from the theoretically expected polarization is a considerable hint to a changed emission process. For this analysis the yet obtained statistics are still too low. There are hardly any events taken in thunderstorm mode that show a visible pulse in both polarization channels.

The exact origin of the radio signal observed during thunderstorms is not yet known for all of the different shapes. Nevertheless it is evident that they form a strong noise background that sometimes causes a failure of the analysis software.

References

[1] T. Antoni et al. - KASCADE Collaboration, NIM A **513**, 429 (2003).
[2] T. Asch, FZKA report **7459**, Forschungszentrum Karlsruhe (2009)
[3] S. Buitink et al. - LOPES Collaboration, A&A, 467, 385, 2007
[4] H. Falcke et al. - LOPES Collaboration, Nature **435**, 313 (2005).
[5] A. V. Gurevich, K. P. Zybin, Physics Letters A 329 (2004) 341-347, 2004
[6] A. Haungs et al. - LOPES Collaboration, NIM A, in press (2009), arXiv:0811.1919.
[7] G. Navarra et al. - KASCADE-Grande Collaboration, NIM A **518**, 207 (2004).
[8] S. Nehls, FZKA report **7440**, Forschungszentrum Karlsruhe (2008).
[9] V. Rakov, M. Uman, ISBN 0-521-03541-4, CAMBRIDGE Univ. Press, 2005

Self-Trigger for Radio Detection of UHCR

A. Schmidt[‡], H. Gemmeke[‡], W.D. Apel[*], J.C. Arteaga[†,xiv], T. Asch[‡], F. Badea[*], L. Bähren[§], K. Bekk[*], M. Bertaina[¶], P.L. Biermann[‖], J. Blümer[*,†], H. Bozdog[*] I.M. Brancus[**], M. Brüggemann[††], P. Buchholz[††], S. Buitink[§], E. Cantoni[¶,‡‡], A. Chiavassa[¶], F. Cossavella[†], K. Daumiller[*], V. de Souza[†,xv], F. Di Pierro[¶], P. Doll[*], R. Engel[*], H. Falcke[§,x], M. Finger[*], D. Fuhrmann[xi], P.L. Ghia[‡‡], R. Glasstetter[xi], C. Grupen[††], A. Haungs[*], D. Heck[*], J.R. Hörandel[§], A. Horneffer[§], T. Huege[*], P.G. Isar[*], K.-H. Kampert[xi], D. Kang[†], D. Kickelbick[††], O. Krömer[‡], J. Kuijpers[§], S. Lafebre[§], P. Łuczak[xii], M. Ludwig[†], H.J. Mathes[*], H.J. Mayer[*], M. Melissas[†], B. Mitrica[**], C. Morello[‡‡], G. Navarra[¶], S. Nehls[*], A. Nigl[§], J. Oehlschläger[*], S. Over[††], N. Palmieri[†], M. Petcu[**], T. Pierog[*], J. Rautenberg[xi], H. Rebel[*], M. Roth[*], A. Saftoiu[**], H. Schieler[*], F. Schröder[*], O. Sima[xiii], K. Singh[‡‡,xvi], G. Toma[**], G.C. Trinchero[‡‡], H. Ulrich[*], A. Weindl[*], J. Wochele[*], M. Wommer[*], J. Zabierowski[xii], J.A. Zensus[‖]

[*] *Institut für Kernphysik, Forschungszentrum Karlsruhe, Germany*
[†] *Institut für Experimentelle Kernphysik, Universität Karlsruhe, Germany*
[‡] *IPE, Forschungszentrum Karlsruhe, Germany*
[§] *Department of Astrophysics, Radboud University Nijmegen, The Netherlands*
[¶] *Dipartimento di Fisica Generale dell' Universita Torino, Italy*
[‖] *Max-Planck-Institut für Radioastronomie Bonn, Germany*
[**] *National Institute of Physics and Nuclear Engineering, Bucharest, Romania*
[††] *Fachbereich Physik, Universität Siegen, Germany*
[‡‡] *Istituto di Fisica dello Spazio Interplanetario, INAF Torino, Italy*
[x] *ASTRON, Dwingeloo, The Netherlands*
[xi] *Fachbereich Physik, Universität Wuppertal, Germany*
[xii] *Soltan Institute for Nuclear Studies, Lodz, Poland*
[xiii] *Department of Physics, University of Bucharest, Bucharest, Romania*
[xiv] *now at: Universidad Michoacana, Morelia, Mexico*
[xv] *now at: Universidade de São Paulo, Instituto de Fîsica de São Carlos, Brasil*
[xvi] *now at: KVI, University of Groningen, The Netherlands*

Abstract. **In a large scale antenna array for the radio detection of cosmic rays the trigger mechanism is one of the key features. While calling for a low trigger threshold for best event acceptance, the trigger rate of each station must be low enough to allow for the limited capacity of wireless communications. Additionally a low power consumption is required, as the stations will be solar powered.**
We have developed a trigger algorithm realized in FPGA-hardware which provides an RFI-suppression by Fourier transforming the radio signal live to frequency domain, eliminating mono-frequent carriers and transforming back to time domain. This improves the signal to noise ratio by a factor of 2. Then a threshold is applied and cuts on particular pulse shape parameters are performed to further reduce the trigger rate. Finally the coincidence between neighboring antennas is built, and the event is read out. The current status of the hardware development and first results of test measurements with 3 prototype antennas is presented.

Keywords**: extensive air shower, radio emission, self trigger**

I. INTRODUCTION

After the first radio measurements of extensive air showers (EAS) with the ground-breaking LOPES experiment [1], the next generation radio detector should show its advantages compared to established detection methods. Similar to a fluorescence detector it measures the integrated energy deposit of the shower along its axis, instead of a single snapshot at ground level, which also improves the acceptance of very inclined showers. At the same time a radio detector has the advantage of a high duty cycle close to 100 % like a particle detector array. To establish radio emission as a new self contained standard detecting method, a self trigger mechanism is essential. Some of the advantages of radio detection, like the expected better acceptance of very inclined air showers are only valid for a self triggered radio array.

The radio signal of an extensive air shower of a given energy shows a steeply falling lateral distribution [2]. This requires the field strength threshold of the trigger to be as low as possible to allow for a reasonable antenna grid spacing. Because of these large distances between antenna stations, the communication and data transfer must be done wireless, which strongly limits the possible data load and asks for a low false trigger rate. As the

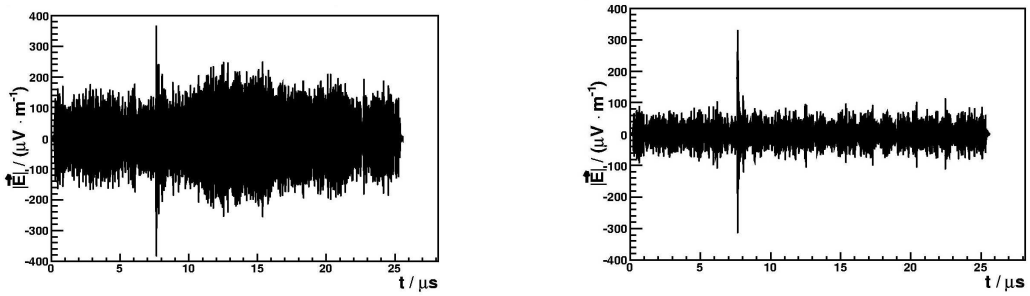

(a) Before RFI-suppression (b) After RFI-suppression

Fig. 1: Enhancement of an example shower event by applying the RFI-suppression.

radio band is traditionally contaminated with plenty of man made noise, only a sophisticated trigger mechanism can meet these requirements. The trigger algorithm must mainly focus on the antenna station level to reduce the amount of readout data as far as possible. Due to the solar power supply of the antenna stations a low power consumption of the trigger implementation is also required.

II. Trigger Approach

To learn about the environmental trigger conditions, $\mathrm{LOPES}^{\mathrm{STAR}}$ (LOPES **S**elf-**T**riggered **A**rray of **R**adio detectors) was developed. This detector consists of antennas arranged in equilateral triangles on the site of the Forschungszentrum Karlsruhe (FZK), triggered by the KASCADE-Grande [3] experiment. The taken data was used to develop a suitable trigger strategy [4].

According to monte carlo simulations [5] radio emission takes place in the frequency range from few MHz up to 100 MHz. Due to radio frequency interference (RFI), the detection of this emission is only applicable above the strongly used short wave band going up to 30 MHz and below the FM radio band starting beyond 80 MHz.

However we also find lesser radio sources in the used frequency band in between. As a first step to improve the trigger situation we filter these mono-frequent carriers. Therefore we Fast Fourier transform (FFT) into frequency domain, where the carriers can easily be removed by replacing the spectrum by its median. A short pulse created by an air shower is not affected by this median filter, as it is distributed widely over all frequencies. After transforming the median filtered spectrum back to time domain, the signal to noise ratio of the pulse is improved by a factor of 2 under fair conditions, the gain under the heavily industrialized radio-loud environment on the site of FZK is much higher (s. fig. 1). In particular this RFI-suppression provides a comparable situation for the subsequent trigger, as independent as possible from the initial recording situation.

As the RFI-suppression performs two FFTs continuously at full sampling rate before the first trigger level, it requires high calculation power and the implementation in a low power system is tricky: The incoming

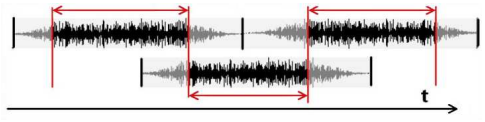

Fig. 2: Illustration of the used block windowing.

continuous data stream must be divided into blocks first to perform the FFT. To avoid leakage effect and signal jumps at the block edges, a trapezoid window function is applied, fading in and out the signal over the first and last eighth of each block. After transforming into frequency domain and back, the affected first and last eighth of each block are dumped before glueing the blocks together again. To conserve a continuous data stream without gaps, the block division is done with one quarter overlap, and the FFTs are calculated for a factor of $^4/_3$ more data (s. fig. 2).

The next task is to identify pulses on the such enhanced data. Therefore a dynamic threshold is applied. The threshold is kept to a fixed factor above the RMS which is calculated over a time period of some seconds. The threshold variation is important to avoid unreasonable trigger rates due to strong background noise variations over the day, caused by the change of the ionospheric reflectivity and the rise and descent of the galaxies as a dominant radio noise source.

To further reduce the trigger rate, the pulse shape is characterized by particular parameters to discriminate shower pulses from background noise pulses. For example measurements in combination with the KASCADE-Grande detector show that EAS-induced pulses seem to be shorter than 125 ns (FWHM) and have a faster signal fall-off after the maximum than background transients [6]. Anyhow final reliable pulse shape cuts require careful further work, as the radio emission mechanism of EAS is not completely understood yet. Of course the measured pulse height and shape are strongly affected by dispersion along the analogue signal path including antenna and filters, which must be taken into account for the trigger decision. Fortunately our trigger approach in principle makes it easily feasible to deconvolve such a frequency response before triggering, as the needed

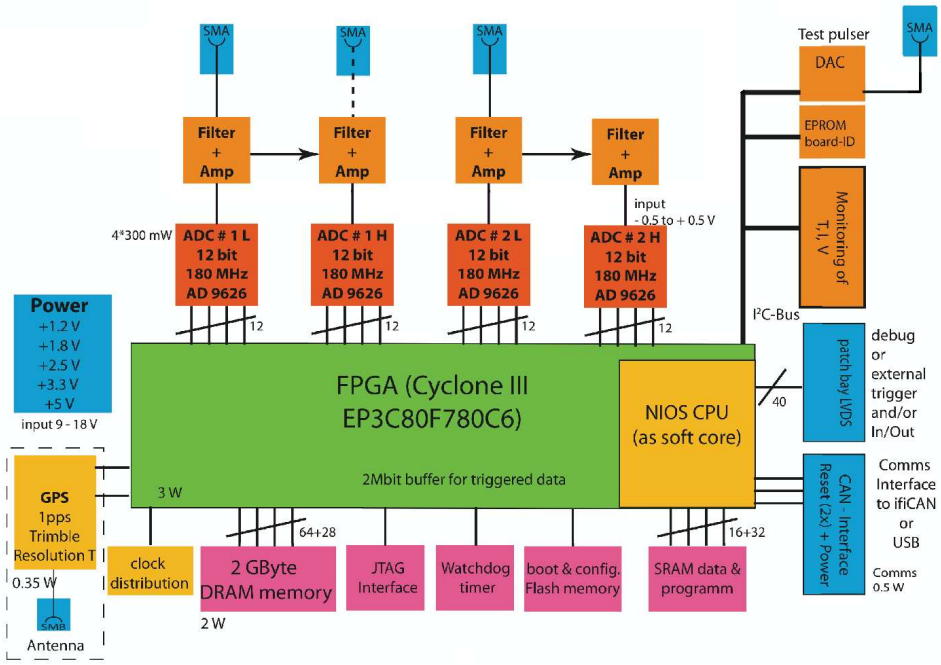

Fig. 3: Block diagram of new electronics design

FFTs are already implemented.

If three adjacent antennas trigger within the coincidence time, the event is finally accepted, read out and stored. By varying the required maximum coincidence time the accepted zenith-angle is set: A vertical shower will trigger the antennas simultaneously, the maximum trigger time difference is the antenna spacing over the speed of light and caused by horizontal events.

III. Prototype electronics

To verify the real-time feasibility of our trigger algorithm, we used existent hardware offering 10 bit ADCs at a sampling rate of 80 MHz connected to a Stratix I FPGA with 40'000 logic elements. As a first step we only use these prototype electronics to create a trigger signal replacing the external trigger from KASCADE-Grande. The data taking is done by our field-tested DAQ-System.

Because of the low sampling rate, we take subsampled data of the limited radio band between 40 and 80 MHz in the second Nyquist domain. Subsampling still conserves full signal information, the RFI-suppression algorithm is not even affected, the frequency spectrum appears just mirrored. Before pulse finding, the signal must be up-sampled to get back the original pulse shape. With this prototype hardware we could well prove the functionality and stability of our sophisticated algorithm in laboratory.

However we did not find any 3-fold coincidences corresponding to an air shower neither during three weeks of measurement at the KASCADE-Grande detector nor during four months of data taking at the Pierre Auger Observatory in Argentina. This is due to different problems:

- The ADC-resolution is too low: When the analogue amplification is high enough to guarantee numerical stability for the background analysis, many pulses get saturated, which renders the pulse shape analysis useless.
- Our elaborate algorithm leads to about 10 W power consumption in the FPGA. Especially during Argentinian summer inside an enclosed container the heat dissipation was underestimated, which lead to longer dead time of the remote stations.
- Because of the high power consumption of our prototype setup, we depend on a power line. This increases the radio background, in particular it introduces plenty of radio spikes.

Nevertheless we continue measurements with the prototype hardware, try different trigger variations and improve our understanding of the radio background. For the development of a trigger which reduced the data rate by more than a factor of 10^5 from permanent recording down to less than one event per second, rare background events can play an important role. Offline analysis of randomly recorded background data hardly helps with such rare background, a live test is essential.

IV. New electronics development

Learning about the problems of our prototype, we currently develop new electronics (s. fig. 3).

To improve dynamic range, we use two 12 bit Flash-ADCs for each antenna polarization. One ADC operating with high analogue gain, the other at low gain, they deliver an effective 18 bit resolution in a cost- and power efficient way. A dedicated test pulser is used to calibrate the analogue signal path. The time resolution is

improved by a high sampling rate of 180 MHz. Sampling in first Nyquist domain not only eases the requirements on the band filter, which can now be optimized for a smooth phase response, but also enables data taking in the whole available radio band from 30 MHz to 80 MHz. This should improve the signal to noise ratio, as air shower simulations predict a more dominant radio emission at lower frequencies [5].

The ADCs are connected to a large Cyclone III FPGA with 80'000 logic elements. The new chip with 65 nm structure together with a reduced core voltage delivers a lower power consumption compared to the 130 nm prototype. In spite of the higher clock frequency, simulations predict a consumption of only 3 W. However we pay highest attention to a decent heat management under the rough ambient conditions in the Argentinian pampa.

These low power needs are very important for the projected $20\,\mathrm{km}^2$ array with 100 antennas, as all stations will be solar powered. The expected advantage of this remoteness is a strongly reduced interference by transients from power lines or passing cars.

Besides the actual trigger-task, the second major topic is the wireless communication between the antenna and the central readout station. For each pulse detected by the antenna's trigger, its timestamp evaluated by a GPS-clock is sent to the central station. This task is fulfilled by a processor implemented as soft core on the FPGA. If the central station finds a coincidence between adjacent antennas, it requests a readout of the event trace from all involved antenna stations. For an improved usage of the communication bandwidth and to avoid collisions, we will use a time division multiple access method (TDMA), where each station only transmits during its particular time slice each second. This approach is for example used for the surface detector of the Pierre Auger Observatory. It optimizes the throughput, but also increases the latency up to a few seconds.

As we are still learning about the radio emission mechanism and its triggering, we want event data as complete as possible. This includes data of antennas that did not trigger, thus the outer ring of an event, where the radio pulse was to faint to trigger on. Anyhow this low pulse contains valuable information, and even if there is no visible pulse at all, it is possible to extract additional information by means of interferometry with several antennas.

The possibility of reading out untriggered data is therefore an important key-feature. Because of the high latency of the communication, this requires a huge buffer memory. With a ring buffer of 2 GByte we get a buffer time of 2 s for raw data or 3 – 4 s including a half-decent online compression. The large buffer in principle also enables external triggering of the radio detector by a regular surface detector to form a new type of hybrid detection.

V. Conclusion

A sophisticated algorithm to trigger the radio emission of extensive air showers was developed on shower data recorded with an external trigger from KASCADE-Grande. At first interfering carrier frequencies are removed from the radio signal by Fourier transforming into frequency domain, replacing the spectrum by its median and transforming back into time domain. This improves the signal to noise ratio by a factor of 2, and compensates for different environments. For each signal pulse exceeding a dynamic threshold the pulse shape parameters are calculated resulting in a trigger decision. If at least three neighboring antennas show an accepted pulse within a certain coincidence time, the radio event is finally accepted and read out.

The real-time feasibility of this trigger mechanism was proven on prototype hardware, single design problems were identified, and the improvements are incorporated into the design of the next generation electronics.

The approach of fully reconfigurable hardware with decent power reserves in buffer memory and FPGA resources permits to continue the advancement of the trigger logic not only during development, but also after some time of data taking, when the radio detection properties are better understood.

References

[1] H. Falcke et al., Nature **435**, 313 (2005).
[2] T. Huege et al., Astop. Phys. **30**, 96, (2008).
[3] G. Navarra et al., NIM A **518**, 207 (2004).
[4] T. Asch et al., Proc. 30th ICRC Merida **5**, 1081 (2007).
[5] T. Huege et al., Astrop. Phys. **27**, 392 (2007).
[6] T. Asch, FKZA report **7459**, Forschungszentrum Karlsruhe (2009).

New Antenna for Radio Detection of UHECR

O. Krömer[‡], H. Gemmeke[‡], W.D. Apel[*], J.C. Arteaga[†,xiv], T. Asch[‡], F. Badea[*], L. Bähren[§], K. Bekk[*], M. Bertaina[¶], P.L. Biermann[‖], J. Blümer[*,†], H. Bozdog[*], I.M. Brancus[**], M. Brüggemann[††], P. Buchholz[††], S. Buitink[§], E. Cantoni[¶,‡‡], A. Chiavassa[¶], F. Cossavella[†], K. Daumiller[*], V. de Souza[†,xv], F. Di Pierro[¶], P. Doll[*], R. Engel[*], H. Falcke[§,x], M. Finger[*], D. Fuhrmann[xi], P.L. Ghia[‡‡], R. Glasstetter[xi], C. Grupen[††], A. Haungs[*], D. Heck[*], J.R. Hörandel[§], A. Horneffer[§], T. Huege[*], P.G. Isar[*], K.-H. Kampert[xi], D. Kang[†], D. Kickelbick[††], J. Kuijpers[§], S. Lafebre[§], P. Łuczak[xii], M. Ludwig[†], H.J. Mathes[*], H.J. Mayer[*], M. Melissas[†], B. Mitrica[**], C. Morello[‡‡], G. Navarra[¶], S. Nehls[*], A. Nigl[§], J. Oehlschläger[*], S. Over[††], N. Palmieri[†], M. Petcu[**], T. Pierog[*], J. Rautenberg[xi], M. Roth[*], H. Rebel[*], A. Saftoiu[**], H. Schieler[*], A. Schmidt[‡], F. Schröder[*], O. Sima[xiii], K. Singh[‡‡,§], G. Toma[**], G.C. Trinchero[‡‡], H. Ulrich[*], A. Weindl[*], J. Wochele[*], M. Wommer[*], J. Zabierowski[xii], J.A. Zensus[‖]

[*] *Institut für Kernphysik, Forschungszentrum Karlsruhe, Germany*
[†] *Institut für Experimentelle Kernphysik, Universität Karlsruhe, Germany*
[‡] *Institut für Prozessdatenverarbeitung und Elektronik, Forschungszentrum Karlsruhe, Germany*
[§] *Department of Astrophysics, Radboud University Nijmegen, The Netherlands*
[¶] *Dipartimento di Fisica Generale dell' Universita Torino, Italy*
[‖] *Max-Planck-Institut für Radioastronomie Bonn, Germany*
[**] *National Institute of Physics and Nuclear Engineering, Bucharest, Romania*
[††] *Fachbereich Physik, Universität Siegen, Germany*
[‡‡] *Istituto di Fisica dello Spazio Interplanetario, INAF Torino, Italy*
[x] *ASTRON, Dwingeloo, The Netherlands*
[xi] *Fachbereich Physik, Universität Wuppertal, Germany*
[xii] *Soltan Institute for Nuclear Studies, Lodz, Poland*
[xiii] *Department of Physics, University of Bucharest, Bucharest, Romania*
[xiv] *now at: Universidad Michoacana, Morelia, Mexico*
[xv] *now at: Universidade de São Paulo, Instituto de Fîsica de São Carlos, Brasil*
[xvi] *now at: KVI, University of Groningen, The Netherlands*

Abstract. **The antenna is the key component for radio detection of cosmic air showers. For large-scale radio detector arrays we designed a crossed polarized short aperiodic loaded loop antenna (SALLA) with only 100 cm diameter, less than 2 kg weight and material cost of about 60 Euro. It is a special type of the well-known Beverage antennas. The E-plane and H-plane directional diagram features a wide main lobe towards zenith with a 3 dB beam width of 150°. SALLA systematically uses internal losses by resistor loading and their sensitivity reaches the theoretical limit given by the omnipresent galactic noise. In return SALLA has in comparison to dipoles and other standard antennas the widest main lobe, the lowest calibration uncertainty, dispersion, weight, material costs, and production time, the smallest dimension, and the highest robustness. SALLA has practically the same directional sensitivity in the E- and H-plane. Thus the sensitivity is rotational invariant. The properties of this new antenna including its delay and transfer function are given.**

Keywords**: extensive air showers, radio emission, antennas**

I. INTRODUCTION

Cosmic ray air showers produce pulsed wideband geosynchrotron radio signals in the frequency range 10 to 100 MHz [1]. Due to man made radio frequency interferences (RFI), see Fig. 1, the useable bandwidth range from 30 to 80 MHz.

The necessary antenna influences the achievable bandwidth, the RFI suppression, and the calibration uncertainty decisively. The different types of antennas have especially different directional diagrams (sky coverage), frequency dependencies, noise immunity and sensitivity to environmental conditions (e.g. conductivity, dielectricity and distance to the ground). On the other hand the antenna design has to be robust, low-cost, and easy to assemble.

The limitation of our antenna-sensitivity to radio signals is given in this frequency range by the galactic noise, first time identified by Jansky 1933 [2], and solar flairs and lightning. But the latter two are limited to short time periods - giving no serious problem for long term radio observation of cosmic rays. The noise level of Galactic noise is frequency dependent [3] and limits by its field strength value in the order of $10\,\mu V/m$ the sensitivity of obersavtion to cosmic radio emission. Furthermore the

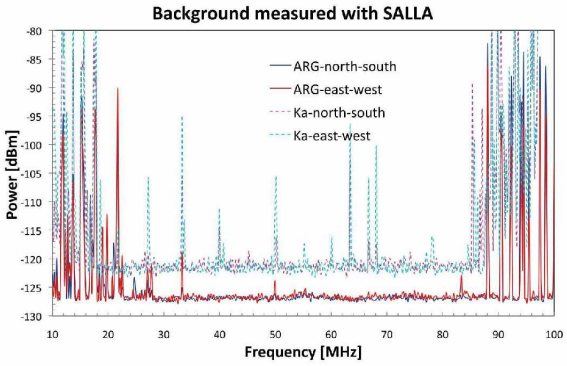

Fig. 1: Measured radio background at Karlsruhe (dashed line, Ka) and at Pierre Auger Observatory, Argentina (solid line, Arg). The differences in the background are due to overload protection outside the shown measuring range.

noise intensity varies over the day as the galactic center is moving through the field of view. In the framework of LOPES (LOFAR PrototypE Station) and $LOPES^{STAR}$ a Self-Triggered Array of Radio antennas is developed. To obtain an optimized design we explored different types of antennas. We started with dipole like antennas, logarithmic periodic dipole antenna (LPDA) and arrive now at a short loop antenna derived from the Beverage antenna [4].

II. Dipole Antennas

Most of cosmic ray radio detectors use dipoles due to their easy assembly and cost effectiveness. For instance the CODALEMA [6] receiver uses short planar dipoles or the LOPES30 [5] experiment uses inverted V-dipoles (Fig. 2a). With a receiver bandwidth a little bit more than one octave most of classical antenna types like dipoles are difficult to handle, because their antenna impedances and directional diagrams are frequency dependent (Fig. 2b). Furthermore due to their double-sided directional diagram (zenith and ground) up to 50% of the antenna output signal may originate from reflections at ground. Thus their characteristics change with ground properties like humidity, conductivity, dielectricity or distance as can be seen in Fig. 2b. The on the first view simple and low cost dipole antennas produce a high calibration uncertainty and possibly require at weather changes an individual antenna calibration.

III. Logarithmic Periodic Dipole Antennas (LPDA)

To avoid the uncertainties of dipoles $LOPES^{STAR}$ uses custom-built wideband directional antennas with a single-sided directional diagram. The first approach was the logarithmic-periodic dipole antenna (LPDA) with crossed polarisation (east/west and north/south), see Fig. 3a. The excellent wideband properties of the LPDA assures an almost frequency independent directional diagram, antenna gain, and impedance. Within the receiver bandwidth the return loss in a $50\,\Omega$ system is less than $15\,dB$. The E-plane directional diagram features a wide main lobe towards zenith with a $3\,dB$ beam width of 100^o at an average antenna gain of $4\,dBi$ (Fig. 3b). The high side lobe attenuation in the horizontal and backward direction suppresses man-made RFI with flat elevations, minimizes the interactions with ground and thus enables a very low calibration uncertainty without individual antenna calibration. In particular this is an important advantage for large scale radio detector arrays. LPDAs widely fulfil all required electrical properties. Only their overhanging dimensions of $4\times4\times4\,m^3$ cause mechanical problems under harsh weather conditions and the construction is not very cost-effective.

IV. Short Beverage antenna

Another way to design wideband directional antennas with dimensions much smaller than the LPDA is given by resistively loaded aperiodic antennas with internal losses. They also have excellent wideband properties as the resistor load dominates in comparison with the capacitive or inductive reactance. The question is whether internal antenna losses are tolerable or not: In this application at frequencies below $100\,\mathrm{MHz}$ the noise is dominated by external noise sources. The omnipresent and unavoidable galactic noise N_e ($T_e = 5000\,K\,@\,60\,\mathrm{MHz}$ [3]) is about 10 dB larger than the internal receiver noise $N_i(T_{Rec} \approx 500\,K)$. Thus the effective signal-to-noise ratio SNR remains unaffected even if antennas with internal losses are used. The maximum permitted antenna loss α_{Ant} without significant lowering of the signal-to-noise ratio is given when the internal receiver noise remains below the attenuated external noise, e.g. $\alpha_{Ant} = 10\,dB$ at 60 MHz.
For large scale radio detector arrays we designed a crossed polarized short aperiodic loaded loop antenna (SALLA) with only $100\,cm$ diameter, less than $2\,kg$ weight and material cost of about 60 Euro (Fig. 4a). It is a special type of the well-known Beverage antennas. The principle of the antenna with its damping resistor responsible for the wide bandwidth is shown in Fig. 4b. The E-plane directional diagram (Fig. 4c) features a wide main lobe towards zenith with a $3\,dB$ beam width of 150^o which is 50^o wider than the LPDA directional pattern an thus enables enough sensitivity also for showers with low elevation angles. The insensitivity to ground properties is better than with the LPDA and enables the lowest calibration uncertainty compared to a dipole as the inverted V-dipole (Fig. 4c).

SALLA is designed to achieve the minimum required gain even at the sole presence of galactic noise (Fig. 5). At the additional presence of man-made noise in a rural environment like the Pierre-Auger-Observatory the antenna gain is about $5\,dB$ above the required minimum.

V. Antenna delay and dispersion

Due to the passive antenna design the LPDA but also SALLA may be used for both transmitting and

(a)

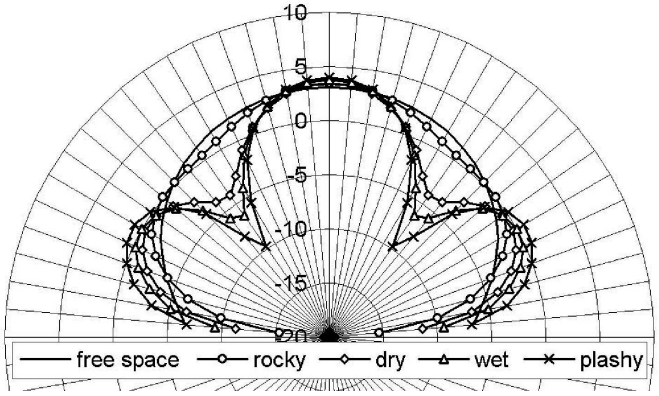

(b)

Fig. 2: (a) Inverted V-dipole, and (b) its calculated E-plane directional diagram in dBi at 2.5 m height above ground for free space, and rocky, dry, wet, and plashy ground (with a dielectricity constant $\epsilon = 1, 3, 15, 30, 80$).

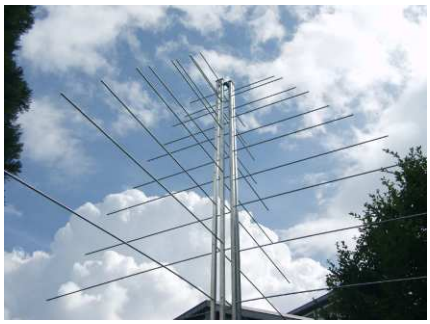

(a)

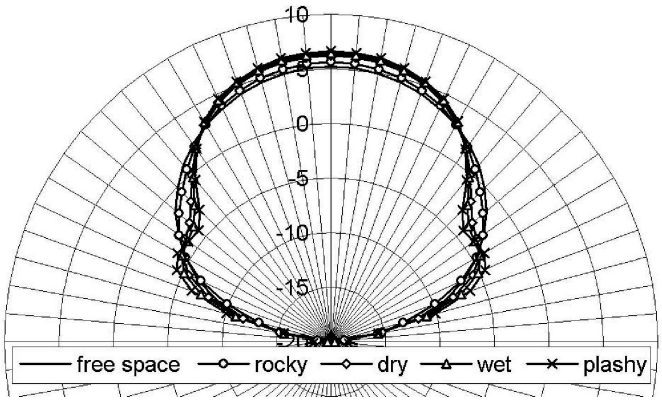

(b)

Fig. 3: (a) Logarithmic Periodic Dipole Antennas (LPDA), (b) its E-plane directional diagram as in Fig. 2b.

(a)

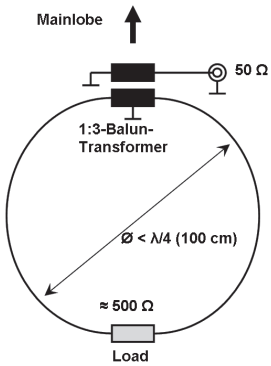

(b)

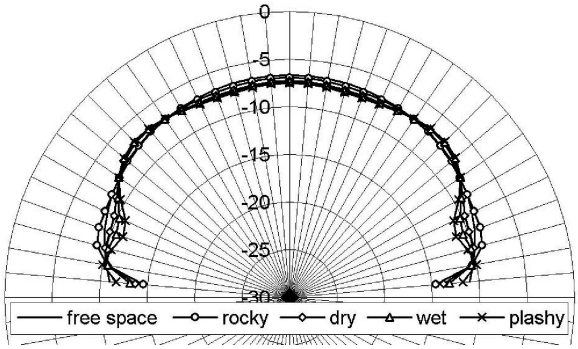

(c)

Fig. 4: (a) Short Aperiodic Loaded Loop Antenna (SALLA), (b) its principle, (c) and its E-plane directional diagram.

receiving. Thus the antennas may be calibrated with the two-antennas-method with high accuracy without the need of a reference antenna. Using a vector-network-analyzer the antenna gain but as well the antenna phase-response and group-delay were analysed and used for the receiver calibration spanning the whole signal path. With the LPDA lower frequencies have a higher delay than frequencies at the upper band limit resulting in a dispersion of $30\,ns$. That is due to the different path lengths at different frequencies: Lower frequencies

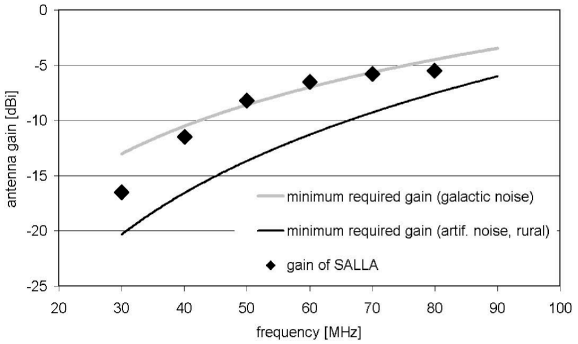

Fig. 5: Minimum required antenna gain without significant lowering the signal-to-noise ratio for external galactic noise (grey) and for man-made noise (black: rural environment) including a characteristic noise of the preamplifier of $2\,dB$. Frequency dependent galactic noise temperatures are derived from [3].

(longer wavelength) have to pass through the dipole structure to reach the corresponding longest dipole sticks and then have to run back to the feed point via the centre wave guide. The SALLA delay response remains widely constant with a delay of $5\,ns$ and a dispersion of $5\,ns$ only. Thus the minimal linear distortion of the pulse shape is achieved with SALLA. These delays have to be included for a precise analysis of the data.

VI. Flatness of antenna transfer function Matched-filter design

The antenna transfer function $T_A(f)$ is the ratio of the antenna output voltage U_A to the electric field strength $|\vec{E}|$. Its dimension is a length, the so-called effective antenna length. The received power P may be calculated by the Poynting vector $|\vec{S}| = |\vec{E} \times \vec{H}| = E^2/\eta_0$ and the effective antenna plane $A_W = G_A(f)^2\lambda^2/4\pi$ and is fed via the output voltage U_A to the receiver input impedance Z_0.

$$P = S \cdot A_W = \frac{E^2 \cdot G_A(f) \cdot c^2}{\eta_0 \cdot 4\pi \cdot f^2} = \frac{U_A^2}{Z_0}, \qquad (1)$$

with the wavelength λ, the vacuum impedance η_0, the magnetic field H, the speed of light c, and the antenna gain related to the isotropic radiator $G_A(f)$. From eq. 1 we get the transfer function (effective length):

$$T_A(f) = \frac{U_A}{E} = \sqrt{\frac{Z_0 \cdot G_A(f) \cdot c^2}{\eta_0 \cdot 4\pi \cdot f^2}} \qquad (2)$$

As both the cosmic radio pulse frequency spectrum and the external noise frequency spectrum decrease at increasing frequencies with similar shape a matched-filter design requires an approximately flat amplitude frequency response [7]. A flat antenna transfer function $T_A(f)$ is not achieved by a frequency independent constant antenna gain but with an antenna gain increasing with frequency $G_A(f) \sim f^2$ (eq. 2).

This is well fulfilled with the SALLA design (Fig. 5). Thus a constant signal-to-noise ratio is enabled over the full frequency range. The LPDA with its widely constant antenna gain $G_A(f) \approx const. \approx 4\,dBi$ (Fig. 3b) produces a transfer function $T_A(f)$ with a $1/f$ characteristic (eq. 2), corresponding to an integration in the time domain. This emphasis of lower frequencies does not fulfil the matched-filter condition and thus has a suboptimal signal-to-noise ratio, if no amplitude frequency response correction is done.

VII. Discussion

The comparison clearly shows that the dipole antennas (as planar or inverted V dipoles) are not very well suited for the radio detection of cosmic ray air showers in large scale radio arrays, if they are mounted on poles with a distance of about $2.5\,m$ from the ground and because their dependence from environmental conditions, such as wetness of the ground, changes their calibration by more than $10\,dB$. These environment conditions cannot be neglected. As conclusion of these calculations and measurements it results, that antennas with no reasonable backward suppression, as dipoles, are not very simple to handle in a calibrated radio experiment with changing conductivity and dielectricity constant of the ground. The required low calibration uncertainties and frequency independent directional diagrams could be achieved more easily with wideband directional antennas, like the LPDA or SALLA. While the LPDA is a conservative approach with a high gain reserve of $10\,dB$ related to the minimum required antenna gain, SALLA systematically uses internal losses by resistor loading and their sensitivity reaches the necessary theoretical limit given by the omnipresent galactic noise. In return SALLA has the widest main lobe, the lowest calibration uncertainty, dispersion, weight, material costs, and production time, the smallest dimension, and the highest robustness. SALLA has practically the same sensitivity in the E- and H-plane and a flat transfer function from the field strength in $\mu V/m$ to the detected voltage in the receiver. In the range of a few dB it is still possible to enhance the sensitivity of the SALLA by its size and a more elaborated preamplifier.

References

[1] T. Huege et al., Astropart. Physics **27**, 392-405 (2007).
[2] K.G. Jansky, Nature **132**, 66 (1933).
[3] ITU 1982, Recommendations and Reports of the CCIR, Genf: Vol. I, Rep. 670 (1982), Vol. VI Rep. 258-4, (1990).
[4] H.H. Beverage, US Patent 2,247,743 (1938).
[5] H. Falcke et al. - LOPES Collaboration, Nature **435**, 313 (2005).
[6] D. Ardouin et al. (CODALEMA Collaboration), Astroparticle Physics **26** (2006) 341-350.
[7] O. Krömer FZKA report **7396**, Forschungszentrum Karlsruhe (2008), page 16-29 and page 89-91.

Universal behavior of electrons & positrons in extensive air showers

S. Lafebre*, R. Engel†, H. Falcke*‡, J. Hörandel*, T. Huege†, J. Kuijpers* and R. Ulrich†

*Department of Astrophysics, IMAPP, Radboud University, P.O. Box 9010, 6500GL Nijmegen, The Netherlands
† Institut für Kernphysik, Forschungszentrum Karlsruhe, P.O. Box 3640, 76021 Karlsruhe, Germany
‡ Radio Observatory, Astron, Dwingeloo, P.O. Box 2, 7990AA Dwingeloo, The Netherlands
§Tyrell Inc., 123 Replicant Street, Los Angeles, California 90210–4321

***Abstract*. Using a large set of CORSIKA simulated extensive air showers at energies 10^{17}–10^{20} eV, we discuss universality features of electron and positron distributions in very-high-energy cosmic-ray air showers. A study of these distributions as a function of particle energy, vertical and horizontal momentum angle, lateral distance, and time distribution of the shower front reveals that most of them depend only on the depth relative to the shower maximum and the number of particles in the cascade at this depth. We empirically derived parameterizations for these distributions, allowing direct access to a realistic description of electron–positron quantities of extensive air showers at very high energy. Data analysis and simulations of electromagnetic effects such as Cherenkov radiation, fluorescence signal, and radio emission can benefit from these parameterizations.**

***Keywords*: Extensive air showers; electron distributions; Shower front structure**

I. Introduction

Secondary radiation effects in extensive air showers, including atmospheric fluorescence, Cherenkov light and radio signal, primarily depend on the distributions of electrons and positrons in extensive air showers. Here, we investigate dependence of these distributions on energy, species, and zenith angle of the primary particle and on the evolution stage of the shower, extending the concept of universality from previous studies [1, 2, 3, 4, 5].

II. Method

Electron and positron distributions in the atmosphere were studied through CORSIKA simulations [6] for protons, photons, and iron nuclei at primary energies of 10^{17}, 10^{18}, 10^{19}, and 10^{20} eV. For each combination of primary particle and energy, showers with zenith angles of 0, 30, 45, and 60° were calculated. Non-vertical showers were injected from different directions to accommodate deviations due to the geomagnetic field. Each parameter set was repeated 20 times, amounting to a total of 3840 simulated showers.

We describe electron and positron distributions in terms of relative evolution stage t, defined in terms of the depth relative to the slant depth $X_{\max}$ where the number of particles in the air shower reaches its maximum:

$$t \equiv \frac{X - X_{\max}}{X_0}, \tag{1}$$

where $X_0 \simeq 36.7$ g/cm^2 is the radiation length of electrons in air. Describing a set of showers in terms of this quantity rather than X or shower age s leads to a higher degree of universality [7, 8].

The total number of particles in the air shower crossing a plane at level t perpendicular to the primary's trajectory is $N(t)$. We define

$$n(t;\mu) \equiv \frac{1}{N(t)}\frac{\partial N(t)}{\partial \mu} \quad \text{and} \tag{2}$$

$$n(t;\mu,\nu) \equiv \frac{1}{N(t)n(t;\mu)}\frac{\partial^2 N(t)}{\partial \mu\, \partial \nu}, \tag{3}$$

as the normalised differential number of particles with respect to some variables μ and ν, with dimension $[\mu]^{-1}$ and $[\nu]^{-1}$, respectively.

III. Energy spectrum

From cascade theory, the energy spectrum of electrons and positrons as a function of shower age takes an analytical form as derived by Rossi & Greisen [9]; a thorough previous study of this parameterization was done by Nerling et al. [4]. Loosely translating this description in terms of t, we replace the equation by

$$n(t;\ln\epsilon) = \frac{A_0 \epsilon^{\gamma_1}}{(\epsilon+\epsilon_1)^{\gamma_1}(\epsilon+\epsilon_2)^{\gamma_2}}, \tag{4}$$

where ϵ is the energy of a given secondary particle in the shower, and $\epsilon_{1,2}$ depend on t. We have performed a fit to this function for electrons, positrons and their sum, indirectly providing a description of the negative charge excess of extensive air showers as a function of evolution stage and secondary energy. In these fits the exponent γ_1 was fixed at $\gamma_1 = 2$ for positrons and $\gamma_1 = 1$ for both electrons and the total number of particles. The parameters for all three cases are explained in [8].

When applied to showers initiated by different species at different energies, the energy distribution (4) is reconstructed accurately. This is shown in Fig. 1, where the simulated energy distributions are compared to their parameterizations for evolution stages $t = 0$ and $t = 6$.

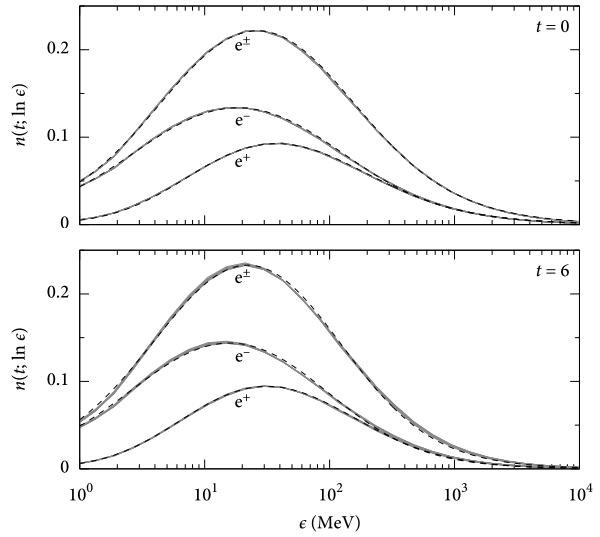

Fig. 1. Average energy distribution for different evolution stages $t = 0$ and $t = 6$ for electrons (marked e^-), positrons (e^+), and their sum ($e^\pm$). Background curves represent simulated distributions for different primaries (p, Fe, and γ) and energies (10^{17}, 10^{18} and 10^{19} eV). The corresponding parameterized distributions from (4) are plotted on top (dashed).

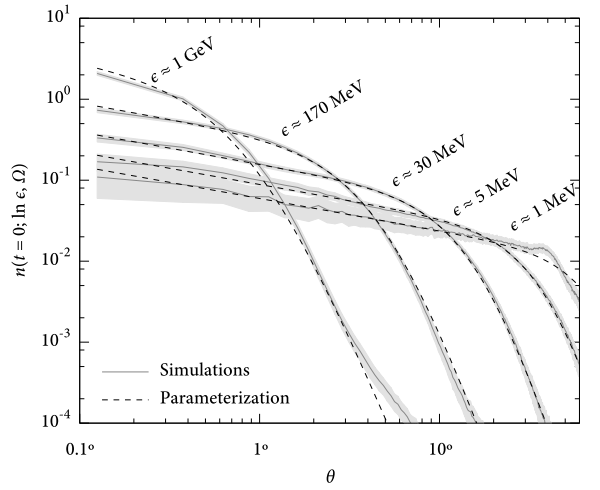

Fig. 2. Normalised average electron distributions $n(t = 0; \ln \epsilon, \Omega)$ (solid) for 20 proton showers at 10^{18} eV with 3σ statistical error margins (filled area). For each energy, corresponding parameterizations according to [8] are also drawn (dashed).

IV. Angular spectrum

The angular distribution of particles is an important factor for observations with Cherenkov and radio telescopes. Fig. 2 shows the average angular distribution of particles at 10^{18} eV as a function of the angle between the shower axis and the particles' direction θ. To compensate for the increase in solid angle with rising θ, the distribution plotted here was divided by $\sin\theta$.

Since the majority of all electrons and positrons stays close to the shower axis, we focus on this part of the distribution. From Fig. 2, it is clear that there is a plateau close to the shower axis at all energies and a sharp drop at a certain angle that depends on secondary energy.

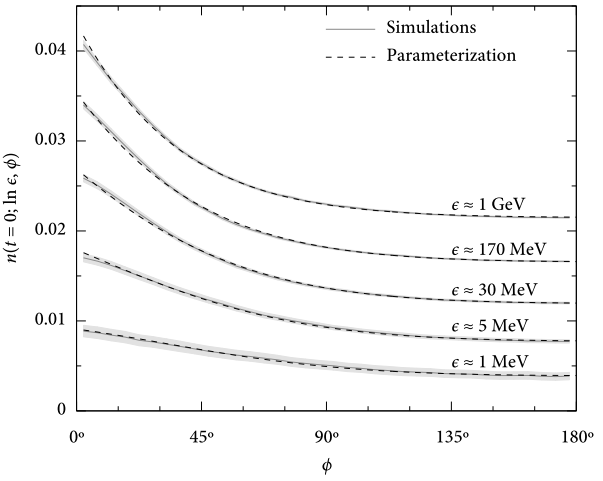

Fig. 3. Normalised average electron distributions $n(t = 0; \ln \epsilon, \phi)$ (solid) for 20 proton showers at 10^{18} eV with 3σ statistical error margins (filled area). Consecutive curves are shifted up by 0.005 to distinguish them better; curves for 1 MeV are at the actual level. For each energy, corresponding parameterizations according to [8] are also drawn (dashed).

Angular distributions were found to be independent of shower stage, as noted earlier [2, 4, 10]. In addition, no dependence on incidence zenith angle or primary energy was found. Looking at different primary species, universality seems somewhat less convincing: spectra for heavier primary species tend to be wider at higher electron energies. The effect is too small to detect, however. The universality with respect to t allows one to parameterize this distribution as a function of two physical quantities only: momentum angle and energy [8].

Because our simulations have no sensitivity in the azimuthal direction by design, no dependence on the geomagnetic field could be determined. Previous work has shown that the effect on the angular distribution is probably small, but not negligible [1, 11]. As accuracy of simulations has rather improved since these studies were carried out, it would be worthwhile to investigate the effect of the geomagnetic field in greater detail.

V. Outward momentum distribution

Let us define ϕ as the angle of a particle momentum vector projected in the plane perpendicular to the shower axis with respect to the outward direction, such that $\phi = 0^\circ$ for a particle moving away from the shower axis, and $\phi = 180^\circ$ for a particle moving towards it. We will refer to this angle as the horizontal momentum angle. For radio measurements, which involve geosynchrotron radiation, this horizontal momentum angle spectrum has to be taken into account [8].

Average simulated distributions $n(t; \ln \epsilon, \phi)$ at $t = 0$ are plotted in Fig. 3 for 20 showers. We observe that high-energy particles tend to move outward more than lower-energy particles. This can be explained by consid-

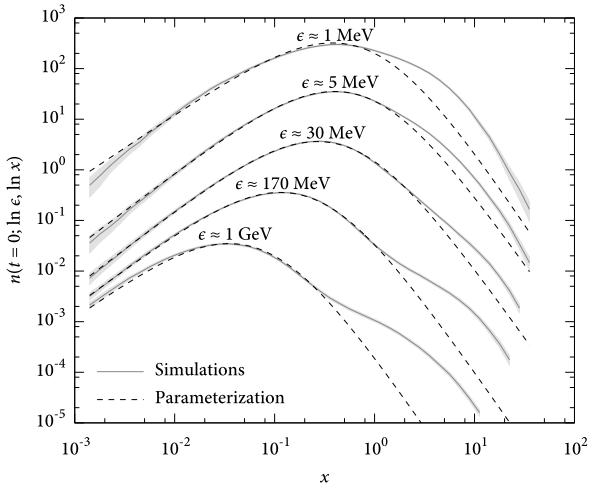

Fig. 4. Normalised average electron distributions $n(t = 0; \ln \epsilon, \ln x)$ (solid) for 20 proton showers at 10^{18} eV with 3σ statistical error margins (filled area). For each energy, corresponding parameterizations according to [8] are also drawn (dashed). Consecutive sets are shifted up by a factor of 10.

ering the collisions in which high-energy electrons and positrons are created, as they primarily occur close to the shower axis. Hence reaction products are transported away from the shower core due to their transverse momenta. Electrons and positrons with lower energies, on the other hand, are also created further away from the shower core.

No significant dependencies on incident zenith angle, primary energy, and primary species were found, so the horizontal momentum angular spectra are universal. Additionally, the shape of the distribution does not change significantly for $\epsilon > 2$ MeV when only electrons or only positrons are considered. There is some dependence in terms of t, however: the distribution appears to soften with evolution stage. This effect can be explained from the expanding spatial structure of the shower with age.

VI. Lateral distribution

When looking at the lateral distribution of electrons and positrons in terms of the lateral distance r from the shower axis, one has to compensate for differences in atmospheric density at the individual values of $X_{\max}$ by expressing the lateral distance in terms of the Molière unit r_{M}, defining $x \equiv r/r_{\mathrm{M}}$ [12].

For different values of ϵ, the normalised average lateral particle distribution at $t = 0$ is shown in Fig. 4 as a function of this quantity. As expected, particles with higher energies tend to remain closer to the shower axis. This agrees with the observation that the angle of their momentum to the shower axis is smaller.

We found no statistically relevant dependence of the lateral distribution on zenith angle of incidence, nor does it change when electrons or positrons are considered separately, except at energies $\epsilon < 10$ MeV. There is, however, a significant effect with shower stage: older showers tend to be wider at the same secondary energy. Therefore, unlike in the case of angular distributions, in any parameterization of the lateral distribution a dependence on t must be incorporated. There is also a minor effect of the energy of the primary on the distribution, but this is only appreciable for secondary energies of $\epsilon > 1$ GeV.

From Fig. 4 it is observed that each curve is a combination of two separate contributions. The left peak, the shape of which does not depend significantly on primary energy or species, is produced through cascading steps of bremsstrahlung and pair creation. The second bulge shows a high level of dependence on primary species, and tends to be less prominent for photon primaries, as for these species there is no significant contribution from the pion production channel. For hadronic primaries it is more significant, especially at higher secondary energies of $\epsilon > 100$ MeV. The magnitude of the variation between different species does not change with t, but its lateral position does slightly.

Theoretically, one could use this difference in lateral distribution to differentiate between primaries on a shower-to-shower basis. But in practice, appreciable difference in density only occurs at high energies and at some distance, implying that the total electron density in the region of sensitivity would be very small. Additionally, the effect does not appear at the same distance for different electron energies, washing out the feature when an integrated energy spectrum is measured.

VII. Delay time distribution

Let us define the delay time Δt of a particle as the time lag with respect to an imaginary particle continuing on the cosmic-ray primary's trajectory with the speed of light in vacuum from the first interaction point. In the distribution of these time lags we must again compensate for differences in Molière radius to obtain a universal description by introducing the variable $\tau \equiv c\Delta t/r_{\mathrm{M}}$, where c is the speed of light in vacuum. The normalised average particle distribution at the shower maximum for different values of ϵ shows a striking resemblance to the time lag distribution to the lateral particle distribution. This similarity is a direct result of the non–planar shape of the shower front as discussed in the next section. Therefore, every characteristic in the lateral distribution will have an equivalent in the time lag distribution. The dependencies on primary energy, species, and angle of incidence closely follow those observed in the lateral distributions in every aspect. This includes the behaviour of the second bulge with primary species. Pion-decay-initiated electrons and positrons are again responsible for the emergence of this peak.

VIII. Shape of the shower front

The similarity between the lateral and delay time distributions of electrons and positrons as investigated in the previous sections is the result of the spatial extent of an air shower at a given time. It makes sense, therefore, to investigate the physical shape of the shower front by

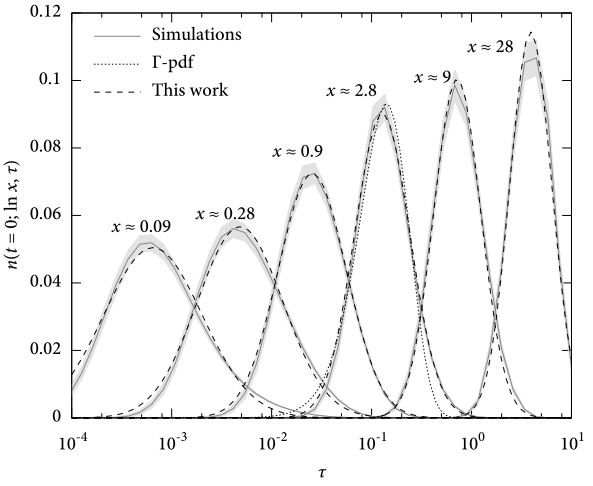

Fig. 5. Average electron distributions $n(t = 0; \ln x, \tau)$ (solid) for 20 proton showers at 10^{18} eV with 3σ statistical error margins (filled area). For each distance, corresponding parameterizations from [8] are drawn as well (dashed). Best-fit Γ-pdfs [13] are also plotted (dotted).

looking at the dependence of the distribution on lateral and delay time simultaneously.

The average shower front shape $n(t; \ln x, \tau)$ for 20 showers at the shower maximum is displayed in Fig. 5 for different distances from the shower core. Though the low number of particles leads to larger fluctuations of the distributions at high distances, the behaviour clearly does not change significantly for $x > 3$.

No significant dependence of the shower front shape on incidence angle or primary energy was found for $x < 15$. There are fluctuations with evolution stage, however: as the shower evolves, the entire distribution shifts to the left. This effect can be explained from the increasing spatial structure of the shower with age, allowing one to estimate $X_{\max}$ from the arrival times of the particles. We also found a non-negligible dependence of the delay time on primary species, which is comparable in nature to the effect of evolution stage. The dependence of the distribution on both species and evolution stage can be removed almost entirely for distances of $0.03 < x < 15$ by applying a simple exponential shift in τ. Additionally, the distributions shown are integrated over energy. Therefore, the shape of the distribution changes when electrons or positrons are considered separately, since their energy distribution is different as well.

The shower front is sometimes approximated as a spherical shell. Close to the shower core, we then expect $\tau \propto x^2$. Going out, the slope should then decrease slowly to a linear relation as x approaches the presumed curvature radius. This spherical shape does not correspond to the situation in our simulations. In the innermost region, we find $\tau \propto x^{1.79}$. Further out, there is an abrupt transition around $x \simeq 0.3$ to $\tau \propto x^{1.45}$.

IX. Conclusion

Analysis of a library of CORSIKA-simulated extensive air showers shows that, to a large extent, their electron–positron distributions show universal behaviour at very high energy, making them dependent on only two parameters: the atmospheric depth $X_{\max}$ and the total number of particles $N_{\max}$ present in the shower at this depth. The entire structure of the shower follows directly from these two values.

Some exceptions to the universality hypothesis were found. Theoretically, these non-universal features can be employed to distinguish primaries on a shower-to-shower basis. In real experiments, however, this would be a difficult task because the effects are very subtle.

X. Acknowledgements

The authors express their gratitude to Markus Risse whose help was indispensable. R.E. acknowledges fruitful discussions with Paolo Lipari on the subject of shower universality. This work is part of the research programme of the 'Stichting voor Fundamenteel Onderzoek der Materie (FOM)', which is financially supported by the 'Nederlandse Organisatie voor Wetenschappelijk Onderzoek (NWO)'. T.H. was supported by grant number VH-NG-413 of the Helmholtz Association.

References

[1] Hillas, A. M. 1982, Journal of Physics G Nuclear Physics, 8, 1461
[2] Giller, M., Kacperczyk, A., Malinowski, J., Tkaczyk, W., & Wieczorek, G. 2005, J. Phys. G, 31, 947
[3] Góra, D., Engel, R., Heck, D., et al. 2006, Astropart. Phys., 24, 484
[4] Nerling, F., Blümer, J., Engel, R., & Risse, M. 2006, Astropart. Phys., 24, 421
[5] Schmidt, F., Ave, M., Cazon, L., & Chou, A. 2008, Astroparticle Physics, 29, 355
[6] Heck, D., Knapp, J., et al. 1998, CORSIKA: A Monte Carlo code to simulate extensive air showers, Tech. Rep. 6019, Forschungszentrum Karlsruhe
[7] Müller. 2008, Diploma Thesis, Univ. Karlsruhe
[8] Lafebre, S., Engel, R., Falcke, H., et al. 2009, Astroparticle Physics, 31, 243
[9] Rossi, B. & Greisen, K. 1941, Reviews of Modern Physics, 13, 240
[10] Giller, M., Stojek, H., & Wieczorek, G. 2005, International Journal of Modern Physics A, 20, 6821
[11] Elbert, J. W., Stanev, T., & Torii, S. 1983, in International Cosmic Ray Conference, Vol. 6, Proc. 18th Int. Cosmic Ray Conf., 227–230
[12] Dova, M. T., Epele, L. N., & Mariazzi, A. G. 2003, Astropart. Phys., 18, 351
[13] Agnetta, G., Ambrosio, M., Aramo, C., et al. 1997, Astroparticle Physics, 6, 301

Effects of atmospheric electric fields on the evolution and radio emission of extensive air showers

S. Buitink[*,‡], **T. Huege**[†], **H. Falcke**[*], **D. Heck**[†] **and J. Kuijpers**[*]

[*]*Radboud Univ. Nijmegen, Dept. of Astrophysics, IMAPP, P.O.Box 9010, 6500 GL Nijmegen*
[†]*Insitut für Kernphysik, Forschungszentrum Karlsruhe, 76021 Karlsruhe, Germany*
[‡]*now at: Lawrence Berkeley National Laboratory, Berkeley, California 94720*

***Abstract*. Atmospheric electric fields can have an influence on the development of extensive air showers and the radio emission they emit. For the radio detection of air showers it is of vital importance to know the magnitude of this effects and the weather conditions under which it becomes significant.**

The physical mechanism that produces the amplified radio pulses is investigated and simulated in two steps. The first step is simulation of the development of air showers in the presence of a background electric field with an upgraded version of CORSIKA. The second step is simulation of the radio emission of air showers in electric fields. The radio simulation code REAS2 is extended with a routine describing the trajectories of charges in an electromagnetic field.

***Keywords*: air showers - radio emission - atmospheric electric fields**

I. Introduction

The electrons and positrons in extensive air showers are separated in the geomagnetic field, giving rise to a detectable radio signal [1]. This radiation can be described in terms of geosynchrotron emission [2] and can be simulated with the Monte Carlo code REAS2 [3][4], which calculates the radio emission of particles from air showers produced with CORSIKA [5]. Alternatively, the radio signals can be analytically derived in terms of a time dependent transverse current [6][7].

Already in the 1970s it was discovered that the radio pulse of an air shower may be larger than anticipated when strong electric fields are present in the atmosphere [8]. Using LOPES data recorded during various weather types it was shown that an amplification of the radio pulse can occur during thunderstorm conditions [9]. In another study it was shown that the arrival direction reconstructed with radio data and particle detector data can differ by a few degrees during thunderstorms [10].

In this work, we simulate the influence of a background electric field on the development of air showers and their radio emission with CORSIKA and REAS2.

In fair weather, i.e. atmospheric conditions in which electrified clouds are absent, there is a downward electric field present with a field strength of $\sim 100\,\mathrm{Vm}^{-1}$ at ground level. The field strength decreases rapidly with altitude and has values below 10 Vm^{-1} at altitudes of a few hunderd meter and higher. Most clouds can typically gain field strengths of a few hundred Vm^{-1}. Nimbostratus clouds, which have a typical thickness of more than 2000 m can have fields of the order of $10\,\mathrm{kVm}^{-1}$. The largest electric fields are found inside thunderstorms, where locally field strengths can reach values up to $100\,\mathrm{kVm}^{-1}$. In most clouds this field is directed vertically, but thunderclouds contain complex charge distributions and can have local fields in any direction. Thunderclouds can have a vertical extent of $\sim$ 10 km [11]. In this work, we use the convention that a positive field points downwards and accelerates the positrons. In the all simulations presented a homogeneous background field is used.

The electric field can influence the radio signal of air showers in several ways. First, the spatial and energy distribution of the electrons and positrons can be altered. Depending on the electric field direction, the electrons are accelerated or slowed down, while the positrons experience the opposite effect. The direction of the particles could also change. Second, the emission mechanism itself is different because the acceleration of particles by the transverse component of the electric field is added to the transverse acceleration due to the magnetic field.

Another issue related to the electric field is the suggestion that air showers of sufficient energy can start an avalanche of runaway electrons in thunderstorm electric fields. Ionization electrons that are produced in collisions of shower particles with air molecules are accelerated in the thunderstorm electric field and can, under the right conditions, gain enough energy to ionize further molecules, an effect described by Gurevich et al. [12]. In thunderstorm research the field strength that can support such avalanches is known as the breakeven field, described in Marshall et al. [13]. In their work, the authors present thunderstorm measurements which show that lightning often occurs when the thunderstorm field exceeds the breakeven field, suggesting that runaway electron breakdown plays a role in lightning initiation. By providing seed electrons for avalanches, air showers from cosmic rays may play an important role in thunderstorm dynamics. The runaway breakdown process can also explain the observation of X-ray and gamma ray emission coming from thunderstorm clouds [14] in terms of bremsstrahlung emitted by the runaway breakdown electrons [15].

II. CORSIKA RESULTS

Electromagnetic interactions are simulated by the standard CORSIKA (version 6.720) routines to treat electromagnetic particles. These routines are taylor-made versions of the EGS4-code [16] adapted to the barometric atmosphere with a density decreasing exponentially with increasing altitude. All possible interactions are considered and a proper treatment of ionization energy loss and multiple scattering is performed.

By including some suitable extra statements into the transport routine ELECTR for $e^{+/-}$ particles the effects of an external electrical field are taken into account which causes an acceleration (energy gain rsp. loss) for particles moving parallel to the field and a deflection for those moving perpendicular to the field. A suitable limitation of the transport step length guarantees small changements of the particle movements to neglect higher order effects on the particle traces. By these means the energy gain/loss in the electrical field and the ionization energy loss can be treated independently for each transport step.

In our simulations we use the high-energy hadronic interaction model QGSJET-II [17] and for low-energy hadronic interactions we use UrQMD 1.3cr [18]. We use the "thinning" option with thinning at 10^{-7} level and optimized weight limitation [19] to keep the computing times below a tolerable level.

When simulating showers with the same primary particle but different random seeds fluctuations will occur from shower to shower. Most importantly the altitude of the first interaction varies, but also the location of the shower maximum, for example, is dependent on number of particles that are produced in the first interaction, and the energy distribution of these particles. Because we are investigating the effect of a background electric field on the shower development we want to suppress the shower-to-shower fluctuations. Therefore, we use CONEX [20] to make 100 proton shower simulations of the same primary energy and direction. From these 100 simulations we select a shower with a large number of secondary particles in the first interaction and a fairly typical longitudinal shower profile. CONEX produces a file that lists all secondary particles after the first interaction and their momenta, which can be used as an input stack for CORSIKA using the STACKIN option. With a CONEX stack of particles created at the first interaction instead of one primary particle as input, different random seeds will produce much smaller variations. For each shower configuration we have selected a CONEX input stack and used this to produce ten showers with different random seeds. In the following plots of shower evolution we plot the mean value of these ten showers and one sigma error bars. Because the fluctuations between simulations are very small with this approach, we are more senstitive to changes that are introduced by the background electric field.

We use the COAST interface code for CORSIKA [4] to get information on electron and positron distributions at 50 layers evenly distributed in atmospheric depth along the shower axis. At each layer histograms are written out, containing information on the position and momentum of the shower particles.

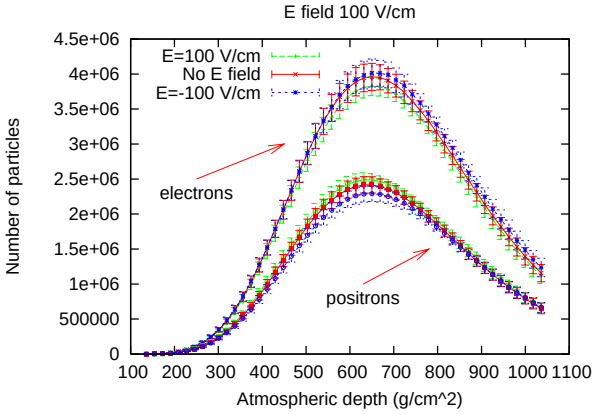

Fig. 1: Number of electrons and positrons as a function of atmospheric depth for a vertical 10^{16} eV proton shower. The different colors correspond to different background electric fields. In a field of $\pm$100 V/cm, the deviations are within 1σ errors.

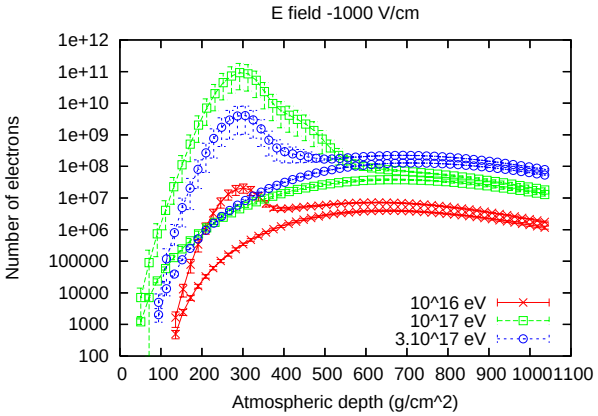

Fig. 2: Number of electrons as a function of atmospheric depth for vertical proton showers of several energies in a background electric field of -1000 V/cm. For each energy the lower line represents the shower development in the absence of a field. The vertical solid line marks the altitude at which the electric field equals the breakeven field.

Fig. 1 shows simulation results for a vertical 10^{16} eV proton air shower. The number of electrons and positrons is plotted as a function of atmospheric depth. The red (solid) lines correspond to the absence of an electric field and the green (dashed) and blue (dotted) lines to fields of 100 V/cm and -100 V/cm respectively. The variations are within the 1 sigma error bars. No significant influence of the electric field on the shower development is observed for this field strength. For fields that are larger by one order of magnitude, however, the influence can be huge.

Fig. 2 shows the shower development in an electric field of -1000 V/cm (accelerating the electrons) for several shower energies. For each energy the lower line represents the same shower in absence of a field. Above the altitude in which the electric field equals the breakeven field [13] an explosive increase in the number of electrons can be seen (note we switched to logarithmic scale). High up in the atmosphere the increase of electrons is nearly exponential. Interestingly, the largest electron content is reached by the shower that had its primary interaction highest up in the atmosphere, not the shower with the highest primary energy. The latter does have the most electrons at lower altitudes, where the breakdown process has stopped and the electrons are injected by pion decay. High up in the atmosphere, the number of electrons increases exponentially reaching a turnover point at $X \approx 300$ g/cm^2, where the electric field is about twice the breakeven field. Note that the point of first interaction for the showers of different energies is random due to the way we selected our showers, and does not follow the dependence of mean first interaction height on primary energy.

An electric field of +1000 V/cm (accelerating the positrons) also strongly influences the energy distribution of positrons and electrons. At some energies the shower can have a positive instead of negative charge excess [21]. In principle, a shower could trigger an upward electron avalanche in such a field, but this does not show up in our simulation as we do not track upgoing particles.

III. REAS2 RESULTS

REAS2 [4] is a Monte Carlo code that calculates the geosynchrotron emission from air showers that are simulated with CORSIKA. For input it uses the histograms produced with COAST. From these distributions REAS2 picks particles, follows a small part of their trajectories and calculates the associated radio emission. In order to do this, an analytic expression for the particle trajectory has to be implemented which gives the particle momentum and acceleration at various points of the trajectory. The electric field effect is included in REAS2 by implementing the equations of motion for a charge inside a homogeneous electric and magnetic field which are under some angle.

The radio emission of air showers is driven by the deflection of electrons and positrons in the magnetic field. When an electric field is present, its contribution to the total radiation can be approximated by comparing the perpendicular component of the electric force to the Lorentz force. Changes in radio pulse height due to an electric field are of the same order of the original pulse height when $E_\perp \sim cB_\perp$. For the geomagnetic field strength in central Europe of $B \sim 0.5$ G, this means an electric field of the order of 100 V/cm can alter the radio pulse height significantly, while fields of the order of 1000 V/cm can dominate the emission mechanism. The geometry of the shower and the fields affects the various contributions. In a shower that propagates parallel to the electric field the charges undergo only linear acceleration, for which the radiation field is suppressed by a factor γ. In a shower that propagates parallel to the magnetic field the charges experience only a small Lorentz force, leading to a small radio pulse. For such showers an electric field can have a relatively large influence.

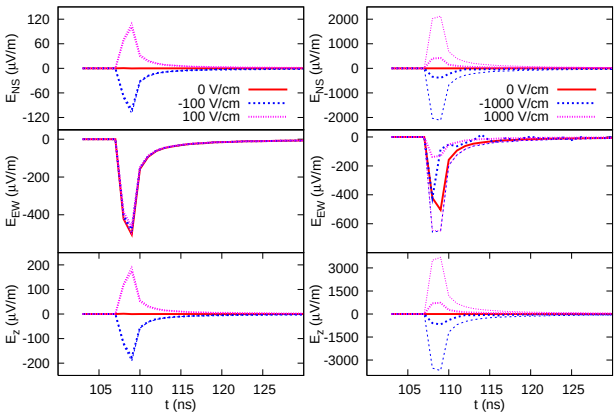

Fig. 3: Radio pulses for an inclined shower (60 degrees zenith angle) of 10^{16} eV propagating towards the north in the presence of electric fields of 100 V/cm (left panel) and 1000 V/cm (right panel). The polarization of pulses in the NS, EW and z directions are shown for an observer located 35 m north of the shower core. Thick lines correspond to simulations in which the electric field effect is switched on in both CORSIKA and REAS2. Thin lines correspond to simulations in which the electric field routine is only switched on in REAS2.

For a single particle, the radio emission is strongly polarized in the direction of the perpendicular component of its acceleration. For the radiation field $\mathbf{A}$ of particle in an electric field $\mathbf{E}$ and magnetic field $\mathbf{B}$ we therefore find:

$$\mathbf{A} \propto (\mathbf{E} - (\mathbf{E} \cdot \hat{n})\hat{n}) + c\,(\hat{n} \times \mathbf{B})\,, \qquad (1)$$

where $\hat{n}$ is the direction of motion of the particle and c is the speed of light. The characteristics of the polarization of the radio emission of full showers, can be roughly explained with this equation.

Fig. 3 shows radio pulses for an observer 35 m north of the shower core for a shower with a zenith angles of 60 degrees propagating towards the north. The three polarization components of the radiation field are plotted separately: north-south (NS), east-west (EW) and vertical (z). For a field of 100 V/cm (left panel) the extra electric field contributions are of the order of the original pulse amplitude, which is to be expected since E and cB are of the same order of magnitude. The polarization properties of the shower radio pulse can be understood in terms of Eqn. 1. Particles propagating towards the north are deflected in the EW direction by the magnetic

field, while the electric field deflects the particles in the NS-z plane. The electric and magnetic acceleration give a contribution to the radio pulse in the corresponding polarization directions.

In this particular case, the polarization directions of the electric and magnetic contributions are orthogonal, but this is only true for a shower propagating towards the north or south. In general, the angle between the polarization directions of the two contributions depends on the direction of the shower propagation and the location of the observer. In most cases, the polarization of an air shower radio pulse that has been significantly influenced by an electric field, will be different from a "regular" geomagnetic pulse. For showers propagating towards the east or west, the polarization of the two components is in the same direction, and it not possible to recognize an electric field contribution by studying the polarization only.

In an electric field of 1000 V/cm, where $E \gg cB$, pulses could be produced that are an order of magnitude larger in amplitude than the pulses in the absence of an electric field. Indeed, in the right panel of Fig. 3, such behaviour is visible, but only for the thin lines, which represent a simulation in which electric field effects are only taken into account in REAS2 and not in CORSIKA. When the CORSIKA electric field routine is switched on, the pulse amplitudes in the NS and z plane drop by an order of magnitude. In the EW plane, the pulse amplitudes are even smaller than the pulse amplitude in absence of an electric field. The reason for this drop in pulse amplitude is the direction of motion of the shower electrons and positrons. In a strong field the charges are deflected strongly into the electric field direction. For inclined showers in a vertical electric field, this means that the particles only move into the direction of an observer close to the shower axis for a much shorter part of their trajectories, and less radiation reaches this observer.

Instead, the particles that are deflected into the (vertical) electric field direction will radiate towards different locations on the ground, but these contributions spread out over a large area and will nowhere give emission of significant intensity.

A large production of runaway electrons, such as shown in Fig. 2, will produce additional radio emission that is not simulated in REAS2. The radio emission that is associated with this pulse of runaway electrons is calculated in Gurevich et al. [22] for a vertical shower. Such pulses have a characteristic frequency of 1-10 MHz, and can be much stronger than the pulses we simulate. Detection of such pulses are reported by the Tien-Shan experiment [23]. The timescale of runaway breakdown radio pulses is of the order of microseconds, while the geomagnetic radio pulse is of the order of tens of nanoseconds. In the latter case the pulse is shortened because the the radio waves and particles travel in the same direction, with almost the same speed.

IV. Conclusions

- For most weather conditions, atmospheric electric fields are not strong enough to significantly influence the radio emission from an air shower. The duty cycle of radio detection of air showers is therefore very high. The technique is reliable in determining the shower energy under all weather conditions except thunderstorms.
- The radio emission of air showers that pass through thunderstorms can be severely influenced by the electric fields present inside the cloud.
- Some other types of clouds, most notably nimbostratus, can contain electric fields with strengths approaching those of thunderstorm electric fields. Although no examples were found in experimental data, we cannot exclude the possibility that such clouds could also have an effect on the radio emission of air showers.
- Pulses that have been influenced by an electric field generally show polarization properties different from pulses that are produced by a pure geomagnetic effect. Polarization measurements therefore contain information of the electric field strength and polarity at a region around the shower maximum.
- An avalanche of runaway electrons can be triggered by an air shower in electric fields exceeding the breakeven field, possibly leading to lightning initiation. The associated fast change in charge distribution can cause strong radio emission.

References

[1] H. Falcke et al., Nature, 435, 313, 2005
[2] H. Falcke and P. Gorham, Astropart. Phys., 19, 477, 2003
[3] T. Huege and H. Falcke, A&A, 430, 779, 2005
[4] T. Huege, R. Ulrich and R. Engel, Astropart. Phys., 27, 392, 2007
[5] D. Heck et al., Forschungszentrum Karlsruhe Report FZKA 6019, 1998
[6] F. Kahn and I. Lerche, Roy. Soc. of London Proc. Series A, 289, 206, 1966
[7] O. Scholten, K. Werner and F. Rusydi, Astropart. Phys., 29, 94, 2008
[8] N. Madolesi, G. Morigi and G. Palumbo, J. Atmos. Terr. Phys., 36, 1431, 1974
[9] S. Buitink et al., A&A, 467, 385, 2007
[10] A. Nigl et al., A&A, 487, 781, 2008
[11] D. MacGorman and W. Rust, "The electrical nature of storms", Oxford Univ. Pres, New York, 1998
[12] A. Gurevich, G. Milikh and R. Roussel-Dupre, Phys. Lett. A., 165, 463, 1992
[13] T. Marshall, M. McCarthy and W. Rust, JGR, 100, 7097, 1995
[14] M. McCarthy and G. Parks, Geophys. Res. Lett., 12, 393, 1985
[15] A. Gurevich and G. Milikh, Phys. Lett. A, 254, 79, 1999
[16] W. Nelson, H. Hirayama and D. Rogers, Report SLAC 265, 1985
[17] S. Ostapchenko, Nucl. Phys. B (Proc. Suppl.), 151, 2006
[18] S. Bass et al., Prog. Part. Nucl. Phys., 41, 225, 1998
[19] M. Kobal et al., Astropart. Phys., 15, 259, 2001
[20] T. Bergman et al., Astropart. Phys., 26, 420, 2007
[21] S. Buitink et al., Astropart. Phys., submitted, 2009
[22] A. Gurevich et al., Phys. Lett. A, 301, 320, 2002
[23] A. Gurevich et al., Phys. Lett. A, 325, 389, 2004

Prospects for using geosynchrotron emission arrival times to determine air shower characteristics

S. Lafebre*, H. Falcke*‡, J. Hörandel*, T. Huege†, J. Kuijpers*

*Department of Astrophysics, IMAPP, Radboud University, P.O. Box 9010, 6500GL Nijmegen, The Netherlands
† Institut für Kernphysik, Forschungszentrum Karlsruhe, P.O. Box 3640, 76021 Karlsruhe, Germany
‡ Radio Observatory, Astron, Dwingeloo, P.O. Box 2, 7990AA Dwingeloo, The Netherlands
§Tyrell Inc., 123 Replicant Street, Los Angeles, California 90210–4321

***Abstract*. From CORSIKA and REAS2 simulations of geosynchrotron radio emission in extensive air showers at 10^{17} to 10^{20} eV, we present an empirical relation between the shape of the radiation front and the distance from the observer to the maximum of the air shower. By analyzing the relative arrival times of radio pulses at several radio antennas in an air shower array, this relation may be employed to estimate the depth of maximum of an extensive air shower if its impact position is known, allowing an estimate for the primary particle's species. Vice versa, the relation provides an estimate for the impact position of the shower's core if an external estimate of the depth of maximum is available.**

***Keywords*: Extensive air showers; Geosynchrotron radiation, Shower front curvature**

I. INTRODUCTION

Lately, there has been a surge of efforts toward the detection of extensive air showers by means of the electromagnetic pulse of geosynchrotron emission emitted by the shower particles [1, 2]. This observational technique allows one to look all the way up to the shower maximum, as there is hardly any attenuation of the signal. It has been shown previously [3] that the position of the maximum of inclined showers can be derived from the lateral slope of the electric field strength at ground level. Here, we use delays in the arrival time of the signal at different positions on the ground to estimate the value of the depth of maximum and the impact position of the shower core.

II. METHOD

Electron and positron distributions at different atmospheric depths were obtained from an air shower library [4] produced with CORSIKA simulations [5] and the COAST library [6]. Photon, proton, and iron-initiated air showers at energies of 10^{16} to $10^{20.5}$ eV, incident from zenith angles up to $60^{\rm o}$ were simulated.

A random sample of $\sim$ 700 simulations from this library was used to calculate the radio signal emitted by these airs showers. The REAS code version 2.58 [7, 8] was used to obtain geosynchrotron pulses associated with each air shower simulation. Antennas were placed on a radial grid at distances of 35 m to 1500 m with intervals of 80–300 m, with one antenna every $45^{\rm o}$.

The magnetic field was taken to match values in northwestern Europe at a field strength of 49 μT and a declination of $68^{\rm o}$ in all simulations. The altitude of the detector array was fixed at 100 m above sea level or a vertical equivalent atmospheric depth of $X \simeq 1024$ g/cm^2.

III. PARAMETERIZATION

One has to compensate for projection effects for showers hitting the detector at an angle. Let θ_0 and ϕ_0 be the zenith and azimuth angle at which the primary particle enters the atmosphere. For a radio antenna a distance d on the ground away from the shower core in the direction δ with respect to the incidence angle ϕ_0, the perpendicular distance r to the shower core is

$$r = d\sqrt{1 - \cos^2\delta \sin^2\theta_0}. \quad (1)$$

The delay τ, converted to length units by multiplying with the speed of light in vacuum, is defined as the lag of the peak strength of the radio signal with respect to the arrival time at the shower impact location. It can be written as

$$\tau = t + d\cos\delta\sin\theta_0, \quad (2)$$

where $t(r, \delta)$ equals the delay caused by the non-planar shape of the shower front expressed in length units. We have included these geometrical compensations in the analysis throughout this paper.

If the particle front is a spherical shell, so will the expected shape of its emitted radio signal be. The delay t can then be written in terms of the distance to the center of the sphere R and the distance from the shower core r as

$$t = \sqrt{R^2 + r^2} - R \approx \frac{r^2}{2R}, \quad (3)$$

where the approximation holds for $r \ll R$. It was shown previously, however, that the assumption of a spherical shower particle front is unrealistic for large air showers [9]. Therefore, the shape of t as a function of r is expected to be different, too.

Analysis of our simulations reveals that, to first order approximation, these delays can be described by the

parameterization

$$t = R_1^{1-\alpha-1/\beta} r^{\alpha} (R + R_0)^{1/\beta}. \quad (4)$$

The distance $R + R_0$ represents the distance from the observer to a virtual source from which the air shower originates. This total distance is subdivided into R_0, representing the distance from the point of origin to the shower maximum, and R, which is the distance from the shower maximum to the observer. R can be converted unambiguously to a value of $X_{\max}$. The value of R_0 is fixed at 6 km. R_1 is a scale parameter, the exponent of which was chosen to match the dimension of t (distance).

The parameters in the above relation do not depend significantly on either primary energy or zenith angle other than through the respective influences on the depth of the shower maximum. This is expected, because the particle distributions responsible for the radiation do not exhibit any dependence on these parameters either [10, 9]. Though the values for R_0, α, and β depend on the orientation of the shower with respect to the magnetic field, the effect of this dependence is much smaller than that of the average statistical variation in showers. Therefore, we will therefore limit geometrical dependence to the angle δ only. A fit to the simulated pulse lags in the region $40 \text{ m} < d < 750 \text{ m}$ yields the following overall best-fit parameters:

$$\begin{aligned} R_1 &= 3.87 + 1.56\cos(2\delta) + 0.56\cos\delta \quad \text{(in km)}, \\ \alpha &= 1.83 + 0.077\cos(2\delta) + 0.018\cos\delta, \\ \beta &= -0.76 + 0.062\cos(2\delta) + 0.028\cos\delta. \end{aligned} \quad (5)$$

The $\cos(2\delta)$ terms in these equations reflect the asymmetries in the east-west versus north-south direction. Note that $\alpha < 2$ for all δ, confirming the non-spherical shape of the wave front.

In a typical array of radio antennas, the delays τ can be determined accurately: using modern equipment, resolutions down to a few ns can be achieved. We can use the delay values to employ our parameterization in two ways: if the position of the shower core is known accurately by scintillator measurements, we can use it to estimate the distance to the shower maximum. If, on the other hand, an estimate for the depth of maximum is available, the position of the shower core can be reconstructed. We will discuss these approaches in detail in the following.

IV. Determining depth of shower maximum

By rearranging (4), we may write

$$R = R_1^{1-\beta+\alpha\beta} \left(\frac{t}{r^{\alpha}} \right)^{\beta} - R_0 \quad (6)$$

to reconstruct the distance to the shower maximum. Using this equation, the reconstructed distance to the shower maximum is plotted versus the simulated value in the left panel of Fig. 1. Each point in this plot represents the reconstructed value of R for one shower

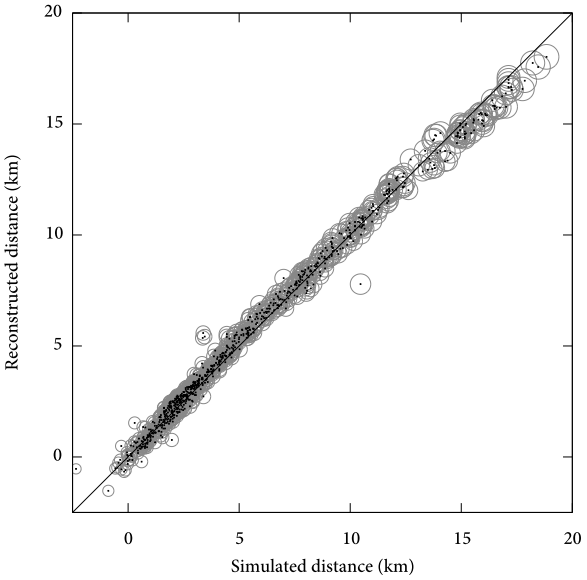

Fig. 1. Scatter plot for $\sim$ 700 showers of various species and energies $E > 10^{17}$ eV of simulated values for R versus the values as reconstructed by the method outlined in the text. Circles around each reconstruction represent error margins of 20 g/cm^2. No error sources were included.

event, obtained by taking a weighted average of the reconstructions from the delays in individual antennas. If the antennas are placed on a regular grid, a weight $\propto r^2$ seems justified to match each time delay to its expected relative error, since $\alpha \simeq 2$. Our simulated array is denser near the shower core, which was compensated for by a total weight for each antenna $\propto r^3$.

The algorithm correctly reconstructs the distance to the shower maximum as simulated, with a standard deviation of 216 m. Note that both simulated and reconstructed events extend to negative distances: showers in this region have a maximum that lies below the observation level of the radio antennas. By design of he algorithm, correct reconstruction of these events is possible only if the downward distance is smaller than R_0.

We have thus far considered ideal circumstances, assuming exact knowledge of the impact angle and position of the shower axis as well as the delay of the radio pulses. A more realistic picture is obtained by introducing error sources in the reconstruction. For a dense array of radio antennas such as LOPES [2] or LOFAR [11], the accuracy in the arrival direction is of the order of 1.0^{o} [12], and a feasible time resolution for determining the maximum pulse height is about 10 ns. We adopt a typical value from the analysis of the KASCADE experiment data of 1 m [13, 14] for the shower core impact location. It is assumed that reconstruction with a dense radio array such as LOFAR will be on a par with this number. All of the above errors are assumed to follow Gaussian distributions. Additionally, we ensure that the signal is sufficiently strong by demanding a certain field strength.

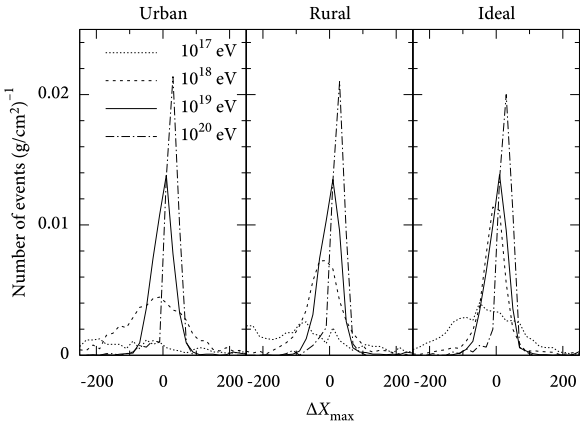

Fig. 2. Distribution of residuals for the reconstruction of the depth of maximum for various primary energies. Plots are shown for urban, rural, and ideal noise level scenarios.

Applying these errors, the correlation is reduced significantly, which is mainly the result of the uncertainty in the arrival direction of the shower. For very inclined showers in particular this can change the expected delay times dramatically. When the accuracy of the shower impact location is reduced, this mostly affects showers for which the maximum lies at a large distance from the observer. When the error is increased to 5 m, for example, hardly any predictions can be made for distances > 10 km.

The distribution of residuals $\Delta X_{\max}$ (i.e. the reconstructed minus the simulated value of the depth of maximum) is shown in Fig. 2 for primary energies between 10^{17} and 10^{20} eV. A homogeneous detector sensitivity up to zenith angles $\theta < 60^{\rm o}$ is assumed. Three background noise scenarios are shown: one for an ideal noise level (requiring a field strength $|\mathbf{E}| > 65$ μV/m for determination of t), one for a rural environment ($|\mathbf{E}| > 180$ μV/m), and one corresponding to an urban area ($|\mathbf{E}| > 450$ μV/m) [3].

From this figure, we observe that the reconstruction accuracy for $X_{\max}$ decreases rapidly at low energies. This is because low-energy showers do not occur very deep in the atmosphere on average, raising the distance to the shower maximum, especially in slanted showers. This results in a radiation front with less curvature, necessitating delay measurements further away from the impact location to obtain the same level of reconstruction accuracy. The produced field strength, however, is proportional to the primary energy, decreasing the patch size that is sufficiently illuminated. The combined effect is that it is hard to make correct estimations for the depth of maximum of low energy showers, unless an array at high altitude is employed.

Additionally, the behaviour of the reconstruction accuracy curve at 10^{18} eV in the three scenarios highlights the importance of low background interference levels: the root mean square deviation σ from the mean decreases from $\sigma = 113$ g/cm^2 (urban) to 102 g/cm^2 (rural) to 62 g/cm^2 (ideal) at this energy. It is also observed that σ does not vary much for energies of 10^{19} and 10^{20} eV at $\sigma \simeq 40$ g/cm^2 and $\sigma \simeq 30$ g/cm^2, respectively. For comparison, the value for Pierre Auger fluorescence detectors is $\sigma \simeq 25$ g/cm^2 for protons, though perfect geometry reconstruction is assumed in that number [15].

If the maximum available distance to the shower core is very small, as would be the case for an array such as LOPES, the fraction of good reconstructions is reduced dramatically. This makes sense, as the shower front shape can no longer be probed accurately. In particular, if the radius of the array shrinks to less than ~ 500 m, the amount of useful reconstructions is negligible.

V. Determining shower core position

If an estimate for $X_{\max}$ (and thus for R) is available, we can employ (4) in an alternative way to estimate values for the distance r of the observer to the shower axis, by writing

$$r = R_1^{1+1/\alpha\beta-1/\alpha} \frac{t^{1/\alpha}}{(R+R_0)^{1/\alpha\beta}}. \qquad (7)$$

In an actual experimental setting, the dependencies of α, β, and R_1 on δ need to be taken into account, for example through an iterative fitting procedure for r and δ. We will only reconstruct the distance to each antenna here, and we will assume the general direction of the core impact position to be known. This decision is motivated by the fact that the effect on the value of r caused by variations in δ is generally small.

In the theoretical limit, the position of the impact location is accurate to within 5 m distance. When similar error sources as in the previous section are introduced, this distance is increased to 15 m or so. In both theoretical and smudged case, there is a substantial difference in reconstruction accuracy between the direction perpendicular to the arrival direction and parallel to it. This results directly from the uncertainty imposed on θ_0: even a small deviation of the zenith angle will make a noticeable difference in the obtained value for t from (2).

Analogous to the situation in the previous section, the average error increases drastically when the radius of the array is smaller than 500 m. The error does not increase significantly, however, when the minimum distance is set to 300 m. This is slightly counterintuitive, but it is again related to the accurate probing of the shower front shape. Of course, the requirement remains that the arrival delay at the impact location is known to 10 ns or so.

VI. Discussion

In this paper, we have worked with the relative delays of geosynchrotron emission from extensive air showers from the raw, unfiltered pulse shape. In real experiments, however, the antennas used are bandwidth-limited, which will be reflected in the shape of the measured pulse. The effect on the arrival time of the pulse is negligible for close antennas ($r < 300$ m), but

for remote antennas it will become important, as the pulse is much broader in these regions. In particular, we expect this to become troublesome for antennas which clip frequencies below ~ 40 MHz.

Another effect that has not been investigated is that of the observer's altitude: in our simulations, this height was fixed at 100 m above sea level. We do not anticipate a significant change of the parameterization or its parameters, however, because the description is valid independent of zenith angle. Changing this angle is comparable to varying the observer's altitude.

Though a deviation from a planar wave is indeed observed in LOPES measurements [2], at only 200 m this array is too small to benefit from the theoretical knowledge of the shape of the radio pulse front. There are currently two other experiments under construction, however, that could make use of the technique outlined in this work. One of these is the initiative in which radio antennas inside the Pierre Auger observatory [16] will be erected [17]. Such an array could use the method in Sect. V to increase the accuracy of the estimated core impact position, since its reconstruction error for the surface detectors is in excess of 100 m. A precise estimate for $X_{\max}$ would have to be provided by fluorescence detectors. The planned spacing of radio antennas is > 500 m, which would allow an accuracy in the reconstruction of around 30 m if the core lies within the radio array.

Another possible experiment is the LOFAR telescope [11], comprising a dense array of approximately 2 km in diameter, with groups of 48 radio antennas every few hundred meters. Its size and spacing make this setup ideally suited to determine $X_{\max}$ using the method outlined in Sect. IV.

VII. Conclusion

We have derived an empirical relation between the relative delay of the radio pulse emitted by the air shower front and the atmospheric depth of the shower maximum through simulations. By analysis of the radio pulse arrival delays in radio antennas in an array of low-frequency radio antennas, this relation can be used to estimate the depth-of-maximum if the impact position is known or vice versa.

We have confirmed that both methods work with no information other than radio signal delays used in the reconstruction. When the algorithm is tested under realistic conditions, however, the accuracy of the method is reduced. In the case of determining the shower maximum, reconstruction down to a useful confidence level is possible only for shower maxima up to ~ 7 km away, and only if the shower core impact position is known down to a few meters. When the parameterization is used to derive this position, the critical quantity is the accuracy in the zenith angle of the shower, which needs to be significantly less than a degree to reconstruct the shower impact location to an accuracy of 10 m at high inclinations up to 60^{o}.

VIII. Acknowledgements

This work is part of the research programme of the 'Stichting voor Fundamenteel Onderzoek der Materie (FOM)', which is financially supported by the 'Nederlandse Organisatie voor Wetenschappelijk Onderzoek (NWO)'. T. Huege was supported by grant number VH-NG-413 of the Helmholtz Association.

References

[1] Huege, T. & Falcke, H. 2003, Astronomy & Astrophysics, 412, 19
[2] Falcke, H. et al. 2005, Nature, 435, 313
[3] Huege, T., Ulrich, R., & Engel, R. 2008, Astropart. Phys., 30, 96
[4] Lafebre, S., Huege, T., Falcke, H., & Kuijpers, J. 2007, in Proc. 30th Int. Cosmic Ray Conf.
[5] Heck, D., Knapp, J., et al. 1998, CORSIKA: A Monte Carlo code to simulate extensive air showers, Tech. Rep. 6019, Forschungszentrum Karlsruhe
[6] Ulrich, R. 2007, http://www-ik.fzk.de/∼rulrich/coast/
[7] Huege, T. & Falcke, H. 2005, Astronomy & Astrophysics, 430, 779
[8] Huege, T., Ulrich, R., & Engel, R. 2007, Astropart. Phys., 27, 392
[9] Lafebre, S., Engel, R., Falcke, H., et al. 2009, Astroparticle Physics, 31, 243
[10] Nerling, F., Blümer, J., Engel, R., & Risse, M. 2006, Astropart. Phys., 24, 421
[11] Falcke, H. D., van Haarlem, M. P., de Bruyn, A. G., et al. 2007, Highlights of Astronomy, 14, 386
[12] Nigl, A., Apel, W. D., Arteaga, J. C., et al. 2008, A&A, 487, 781
[13] Antoni, T., Apel, W. D., Badea, A. F., et al. 2004, ApJ, 608, 865
[14] Glasstetter, R., Antoni, T., Apel, W. D., et al. 2005, in Proc. 29th Int. Cosmic Ray Conf., Vol. 6, 293
[15] Ewers, A., Geenen, H., Kampert, K.-H., et al. 2005, in Proc. 29th Int. Cosmic Ray Conf., Vol. 7, 115
[16] Abraham, J., Aglietta, M., Aguirre, I. C., et al. 2004, Nuclear Instruments and Methods in Physics Research A, 523, 50
[17] Van den Berg, A. M. & et al. 2007, in Proc. 30th Int. Cosmic Ray Conf.

Measurement of the cosmic ray energy spectrum above 10^{18} eV using the Pierre Auger Observatory

F. Schüssler* for the Pierre Auger Collaboration†

* *Karlsruhe Institute of Technology, Karlsruhe, Germany*
† *Observatorio Pierre Auger, Av. San Martin Norte 304, 5613 Malargüe, Argentina*

***Abstract*. The flux of cosmic rays above 10^{18} eV has been measured with unprecedented precision using the Pierre Auger Observatory. Two analysis techniques have been used to extend the spectrum downwards from 3×10^{18} eV, with the lower energies being explored using a novel technique that exploits the hybrid strengths of the instrument. The systematic uncertainties, and in particular the influence of the energy resolution on the spectral shape, are addressed. The spectrum can be described by a broken power-law of index 3.3 below the ankle which is measured at $\lg(E_{\rm ankle}/{\rm eV}) = 18.6$. Above the ankle the spectrum is described by a power-law $\propto E^{-2.6}$ and a flux suppression with $\lg(E_{1/2}/{\rm eV}) = 19.6$.**

***Keywords*: Auger Energy Spectrum**

I. INTRODUCTION

Two independent techniques are used at the Pierre Auger Observatory to study extensive air showers created by ultra-high energy cosmic rays in the atmosphere, a ground array of more than 1600 water-Cherenkov detectors and a set of 24 fluorescence telescopes. Construction of the baseline design was completed in June 2008. With stable data taking starting in January 2004, the world's largest dataset of cosmic ray observations has been collected over the last 4 years during the construction phase of the observatory. Here we report on an update with a substantial increase relative to the accumulated exposure of the energy spectrum measurements reported in [1] and [2].

Due to its high duty cycle, the data of the surface detector are sensitive to spectral features at the highest energies. Its energy scale is derived from coincident measurements with the fluorescence detector. A flux suppression around $10^{19.5}$ eV has been established based on these measurements [1] in agreement with the HiRes measurement [3].

An extension to energies below the threshold of $10^{18.5}$ eV is possible with the use of hybrid observations, i.e. measurements with the fluorescence detectors in coincidence with at least one surface detector. Although statistically limited due to the duty-cycle of the fluorescence detectors of about 13%, these measurements make it possible to extend the energy range down to 10^{18} eV and can therefore be used to determine the position and shape of the ankle at which the power-law index of the flux changes [4], [5], [6], [7]. A precise measurement of this feature is crucial for an understanding of the underlying phenomena. Several phenomenological models with different predictions and explanations of the shape of the energy spectrum and the cosmic ray mass composition have been proposed [8], [9], [10].

II. SURFACE DETECTOR DATA

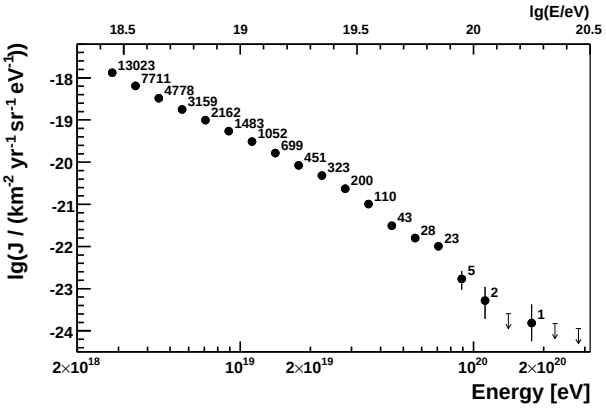

Fig. 1. Energy spectrum derived from surface detector data calibrated with fluorescence measurements. Only statistical uncertainties are shown.

The surface detector array of the Pierre Auger Observatory covers about $3000\,{\rm km}^2$ of the Argentinian Pampa Amarilla. Since its completion in June 2008 the exposure is increased each month by about $350\,{\rm km}^2\ {\rm sr\ yr}$ and amounts to $12,790\,{\rm km}^2\ {\rm sr\ yr}$ for the time period considered for this analysis (01/2004 - 12/2008). The exposure is calculated by integrating the number of active detector stations of the surface array over time. Detailed monitoring information of the status of each surface detector station is stored every second and the exposure is determined with an uncertainty of 3 % [1].

The energy of each shower is calibrated with a subset of high quality events observed by both the surface and the fluorescence detectors after removing attenuation effects by means of a constant-intensity method. The systematic uncertainty of the energy cross-calibration is 7% at 10^{19} eV and increases to 15% above 10^{20} eV [11].

Due to the energy resolution of the surface detector data of about 20%, bin-to-bin migrations influence the

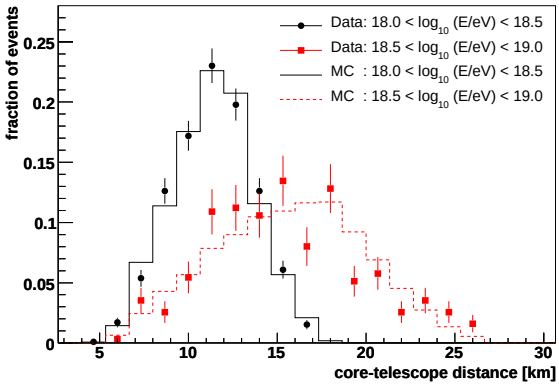

Fig. 2. Comparison between hybrid data and the Monte Carlo simulations used for the determination of the hybrid exposure.

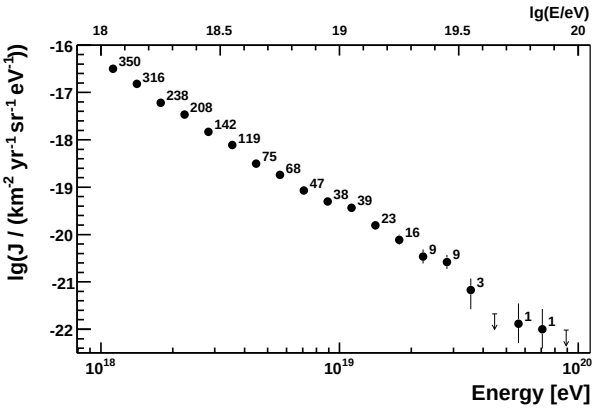

Fig. 3. Energy spectrum derived from hybrid data. Only statistical error bars are shown.

reconstruction of the flux and spectral shape. To correct for these effect, a simple forward- folding approach was applied. It uses MC simulations to determine the energy resolution of the surface detector and derive the bin-to-bin migration matrix. The matrix is then used to derive a flux parameterisation that matches the measured data after forward-folding. The ratio of this parameterisation to the folded flux gives a correction factor that is applied to data. The correction is energy dependent and less than 20% over the full energy range.

The derived energy spectrum of the surface detector is shown in Fig. 1 together with the event numbers of the underlying raw distribution. Combining the systematic uncertainties of the exposure (3%) and of the forward folding assumptions (5%), the systematic uncertainties of the derived flux is 5.8%.

III. Fluorescence Detector Data

The fluorescence detector of the Pierre Auger Observatory comprises 24 telescopes grouped in 4 buildings on the periphery of the surface array. Air shower observations of the fluorescence detector in coincidence with at least one surface detector permit an independent measurement of the cosmic ray energy spectrum. Due to the lower energy threshold of the fluorescence telescopes, these 'hybrid' events allow us to extend the range of measurement down to $10^{18}\,\mathrm{eV}$.

The exposure of the hybrid mode of the Pierre Auger Observatory has been derived using a Monte Carlo method which reproduces the actual data conditions of the observatory including their time variability [12]. Based on the extensive monitoring of all detector components [13] a detailed description of the efficiencies of data-taking has been obtained. The time-dependent detector simulation is based on these efficiencies and makes use of the complete description of the atmospheric conditions obtained within the atmospheric monitoring program [14]. For example, we consider only time intervals for which the light attenuation due to aerosols has been measured and for which no clouds have been detected above the observatory [15].

As input to the detector simulation, air showers are simulated with CONEX [16] based on the Sibyll 2.1 [17] and QGSJetII-0.3 [18] hadronic interaction models, assuming a $50\% - 50\%$ mixture of proton and iron primaries. Whereas the derived exposure is independent of the choice of the hadronic interaction model, a systematic uncertainty is induced by the unknown primary mass composition. After applying restrictions to the fiducial volume [19], the systematic uncertainty related to the primary mass composition is 8% at $10^{18}\,\mathrm{eV}$ and becomes negligible above $10^{19}\,\mathrm{eV}$ (see [12] for details).

Additional requirements limit the maximum distance between air shower and the fluorescence detector. They have been derived from comparisons between data and simulated events and assure a saturated trigger efficiency of the fluorescence detector and the independence of the derived flux from the systematic uncertainty of the energy reconstruction. In addition, events are only selected for the determination of the spectrum if they meet certain quality criteria [12], which assure an energy resolution of better than 6% over the full energy range.

Extensive comparisons between simulations and cosmic ray data are performed at all reconstruction levels. An example is the agreement between data and MC in the determination of the fiducial distance shown in Fig. 2. Additional cross-checks involve laser shots fired into the field of view of the fluorescence telescopes from the Central Laser Facility [20]. They have been used to verify the accuracy of the duty cycle.

The design of the Pierre Auger Observatory with its two complementary air shower detection techniques offers the chance to validate the full MC simulation chain and the derived hybrid exposure using air shower observations themselves. Based on this end-to-end verification, the calculated exposure has been corrected by 4%. The total systematic uncertainty of the derived hybrid spectrum is 10% at $10^{18}\,\mathrm{eV}$ and decreases to about 6% above $10^{19}\,\mathrm{eV}$.

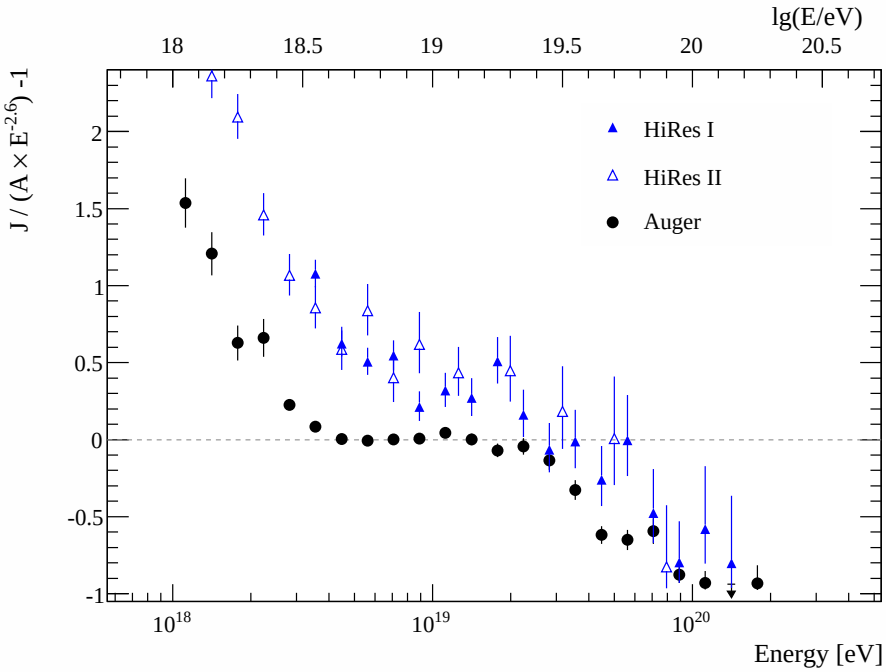

Fig. 4. The fractional difference between the combined energy spectrum of the Pierre Auger Observatory and a spectrum with an index of 2.6. Data from the HiRes instrument [3], [21] are shown for comparison.

The energy spectrum derived from hybrid measurements recorded during the time period 12/2005 - 05/2008 is shown in Fig. 3.

IV. The combined energy spectrum

The Auger energy spectrum covering the full range from $10^{18}\,\mathrm{eV}$ to above $10^{20}\,\mathrm{eV}$ is derived by combining the two measurements discussed above. The combination procedure utilises a maximum likelihood method which takes into account the systematic and statistical uncertainties of the two spectra. The procedure applied is used to derive flux scale parameters to be applied to the individual spectra. These are $k_{\mathrm{SD}} = 1.01$ and $k_{\mathrm{FD}} = 0.99$ for the surface detector data and hybrid data respectively, showing the good agreement between the independent measurements. The systematic uncertainty of the combined flux is less than 4%.

As the surface detector data are calibrated with hybrid events, it should be noted that both spectra share the same systematic uncertainty for the energy assignment. The main contributions to this uncertainty are the absolute fluorescence yield (14%) and the absolute calibration of the fluorescence photodetectors (9.5%). Including a reconstruction uncertainty of about 10% and uncertainties of the atmospheric parameters, an overall systematic uncertainty of the energy scale of 22% has been estimated [11].

The fractional difference of the combined energy spectrum with respect to an assumed flux $\propto E^{-2.6}$ is shown in Fig. 4. Two spectral features are evident: an abrupt change in the spectral index near $4\,\mathrm{EeV}$ (the "ankle") and a more gradual suppression of the flux beyond about $30\,\mathrm{EeV}$.

Some earlier measurements from the HiRes experiment [3], [21] are also shown in Fig. 4 for comparison. A modest systematic energy shift applied to one or both experiments could account for most of the difference between the two. The spectral change at the ankle appears more sharp in our data.

The energy spectrum is fitted with two functions. Both are based on power-laws with the ankle being characterised by a break in the spectral index γ at E_{ankle}. The first function is a pure power-law description of the spectrum, i.e. the flux suppression is fitted with a spectral break at E_{break}. The second function uses a smooth transition given by

$$J(E; E > E_{\mathrm{ankle}}) \quad \propto \quad E^{-\gamma_2} \, \frac{1}{1 + \exp\left(\frac{\lg E - \lg E_{1/2}}{\lg W_c}\right)}$$

in addition to the broken power-law to describe the ankle. This fit is shown as black solid line in Fig. 5. The derived parameters (quoting only statistical uncertainties) are:

In Fig. 5 we show a comparison of the combined energy spectrum with spectral shapes expected from different astrophysical scenarios. Assuming for example a uniform distribution of sources, no cosmological evolution of the source luminosity ($(z+1)^m$, i.e. $m = 0$) and a source flux following $\propto E^{-2.6}$ one obtains a spectrum that is at variance with our data. Better agreement is obtained for a scenario including a strong cosmological evolution of the source luminosity ($m = 5$) in combi-

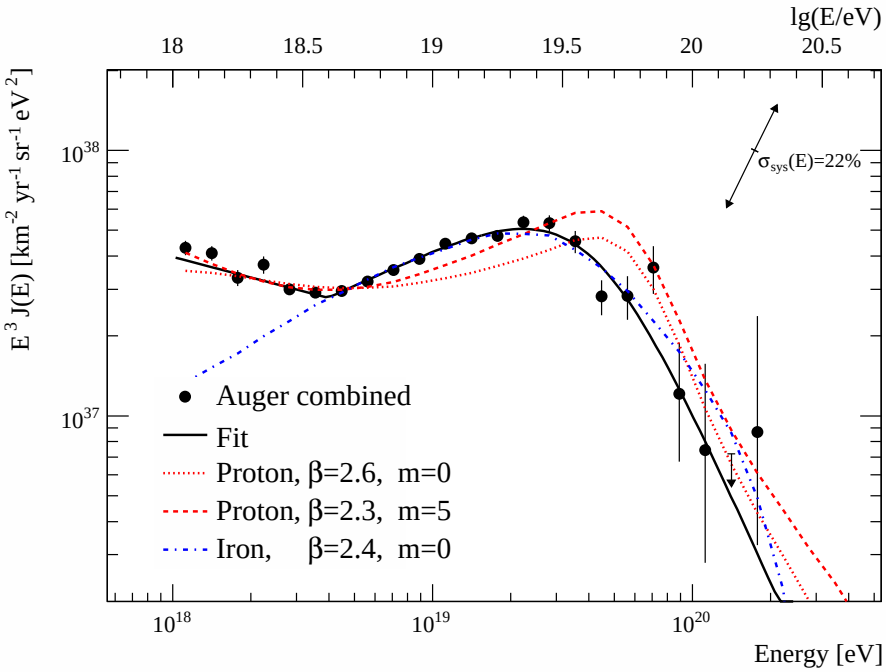

Fig. 5. The combined energy spectrum compared with several astrophysical models assuming a pure composition of protons (red lines) or iron (blue line), a power-law injection spectrum following $E^{-\beta}$ and a maximum energy of $E_{\rm max} = 10^{20.5}\,{\rm eV}$. The cosmological evolution of the source luminosity is given by $(z+1)^m$. The black line shows the fit used to determine the spectral features (see text). A table with the flux values can be found at [22].

parameter	broken power laws	power laws + smooth function
$\gamma_1 (E < E_{\rm ankle})$	3.26 ± 0.04	3.26 ± 0.04
$\lg(E_{\rm ankle}/{\rm eV})$	18.61 ± 0.01	18.60 ± 0.01
$\gamma_2 (E > E_{\rm ankle})$	2.59 ± 0.02	2.55 ± 0.04
$\lg(E_{\rm break}/{\rm eV})$	19.46 ± 0.03	
$\gamma_3 (E > E_{\rm break})$	4.3 ± 0.2	
$\lg(E_{1/2}/{\rm eV})$		19.61 ± 0.03
$\lg(W_{\rm c}/{\rm eV})$		0.16 ± 0.03

nation with a harder injection spectrum ($\propto E^{-2.3}$). A hypothetical model of a pure iron composition injected with a spectrum following $\propto E^{-2.4}$ and uniformly distributed sources with $m = 0$ is able to describe the measured spectrum above the ankle, below which an additional component is required.

V. Summary

We presented two independent measurements of the cosmic ray energy spectrum with the Pierre Auger Observatory. Both spectra share the same systematic uncertainties in the energy scale. The combination of the high statistics obtained with the surface detector and the extension to lower energies using hybrid observations enables the precise measurement of both the ankle and the flux suppression at highest energies with unprecedented statistics. First comparisons with astrophysical models have been performed.

References

[1] J. Abraham et al. (Pierre Auger Collaboration). *Physical Review Letters*, 101:061101, 2008.
[2] L. Perrone for the Pierre Auger Collaboration. *Proc. 30th Int. Cosmic Ray Conf. (Merida, Mexico)*, 4:331, 2007.
[3] R. U. Abbasi et al. *Physical Review Letters*, 100:101101, 2008.
[4] J. Linsley. *Proc of 8th Int. Cosmic Ray Conf., Jaipur*, 4:77–99, 1963.
[5] M. A. Lawrence, R. J. O. Reid, and A. A. Watson. *J. Phys.*, G17:733–757, 1991.
[6] M. Nagano et al. *J. Phys.*, G18:423–442, 1992.
[7] D. J. Bird et al. *Phys. Rev. Lett.*, 71:3401–3404, 1993.
[8] V. Berezinsky, A. Z. Gazizov, and S. I. Grigorieva. *Phys. Lett.*, B612:147–153, 2005.
[9] A. M. Hillas. *J. Phys.*, G31:R95–R131, 2005.
[10] T. Wibig and A. W. Wolfendale. *J. Phys.*, G31:255–264, 2005.
[11] C. Di Giulio for the Pierre Auger Collaboration. *Proc. 31th Int. Cosmic Ray Conf. (Lodz, Poland)*, 2009.
[12] F. Salamida for the Pierre Auger Collaboration. *Proc. 31th Int. Cosmic Ray Conf. (Lodz, Poland)*, 2009.
[13] J. Rautenberg for the Pierre Auger Collaboration. *Proc. 31th Int. Cosmic Ray Conf. (Lodz, Poland)*, 2009.
[14] S. BenZvi for the Pierre Auger Collaboration. *Proc. 31th Int. Cosmic Ray Conf. (Lodz, Poland)*, 2009.
[15] L. Valore for the Pierre Auger Collaboration. *Proc. 31th Int. Cosmic Ray Conf. (Lodz, Poland)*, 2009.
[16] T. Bergmann et al. *Astroparticle Physics*, 26:420–432, 2007.
[17] R. Engel et al. *Proc. 26th Int. Cosmic Ray Conf. (Salt Lake City, USA)*, 415, 1999.
[18] S. Ostapchenko. *Nucl. Phys. B (Proc. Suppl.)*, 151:143, 2006.
[19] M. Unger for the Pierre Auger Collaboration. *Proc 30th Int. Cosmic Ray Conf., Merida*, 4:373, 2007.
[20] B. Fick et al. *JINST*, 1:P11003, 2006.
[21] R. U. Abbasi et al. *Phys. Lett.*, B619:271–280, 2005.
[22] http://www.auger.org/combined_spectrum_icrc09.txt

Extension of the Pierre Auger Observatory using high-elevation fluorescence telescopes (HEAT)

Matthias Kleifges* for the Pierre Auger Collaboration

**Forschungszentrum Karlsruhe, Institut für Prozessdatenverarbeitung und Elektronik, Postfach 3640, 76021 Karlsruhe, Germany*

***Abstract*. The original fluorescence telescopes of the southern Pierre Auger Observatory have a field of view from about 1.5° to 30° in elevation. The construction of three additional telescopes (High Elevation Auger Telescopes HEAT) is nearing completion and measurements with one telescope have started. A second telescope will be operational by the time of the conference. These new instruments have been designed to improve the quality of reconstruction of showers down to energies of 10^{17} eV. The extra telescopes are pivot-mounted for operation with a field of view from 30° to 58°. The design is optimised to record nearby showers in combination with the existing telescopes at one of the telescope sites, as well as to take data in hybrid mode using the measurements of surface detectors from a more compact array and additional muon detectors (AMIGA). The design, expected performance, status of construction, and first measurements are presented.**

***Keywords*: HEAT, high-elevation fluorescence telescope, galactic, extragalactic**

I. Introduction

The Pierre Auger Observatory has been designed to measure the energy, arrival direction and composition of cosmic rays from about 10^{18} eV to the highest energies with high precision and statistical significance. The construction of the southern site near Malargüe, Province of Mendoza, Argentina is completed since mid 2008 and the analysis of the recorded data has provided first results with respect to the energy spectrum [1], the distribution of arrival directions [2], the composition, and upper limits on the gamma ray and neutrino flux [3], [4]. The measured cosmic ray observables at the highest energies are suitable to tackle open questions like flux suppression due to the GZK cut-off, to discriminate between bottom-up and top-down models and to locate possible extragalactic point sources.

However, for best discrimination between astrophysical models, the knowledge of the evolution of the cosmic ray composition in the transition region from galactic to extragalactic cosmic rays in the range 10^{17} eV to 10^{19} eV is required. Tests of models for the acceleration and transport of galactic and extragalactic cosmic rays are sensitive to the composition and its energy dependence in the transition region where the current observatory has low efficiency.

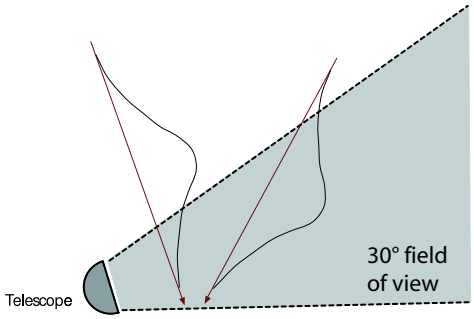

Fig. 1. Effect of limited field of view on reconstruction: Showers approaching the telescope have much higher reconstruction probability than those departing.

The fluorescence technique is best suited to determine the cosmic ray composition by a measurement of the depth of shower maximum. However, it is difficult to lower the energy threshold with the original design of the fluorescence telescopes. As the fluorescence light signal is roughly proportional to the primary particle energy, low energy showers can be detected only at close distance to a telescope. The field of view of the existing Auger fluorescence telescope (FD) is limited to 30° above the horizon (see figure 1). At close distances only the lowest few kilometres of the atmosphere are within the field of view. However, low energy showers reach their maximum of development at higher altitudes. Thus, the crucial region around the shower maximum is generally not observable. The small fraction of the shower development, which falls within the field of view, is mostly very dim and is insufficient to determine the depth of shower maximum $X_{\max}$. In addition, this cut-off effect also depends on primary mass and shower direction. A plain reconstruction of the shower profile using raw data would yield biased results with respect to zenith angle and mass composition. Cuts on the data to remove this bias (anti-bias cuts) are not useful as only very few showers would be left for the $X_{\max}$ determination.

From these arguments it is clear that an effective and unbiased detection of cosmic rays of lower energies requires the extension of the field of view to larger elevations. From the data collected since 2004, we know that the quality of reconstruction is improved considerably if showers are recorded by a hybrid trigger. These hybrid events provide information on the shower profile from the FD telescopes, but in addition at least one surface

detector has detected secondary shower particles simultaneously. The data from the SD system restricts the time and the location of the shower impact point on ground. This improves the reconstruction of the shower geometry significantly [5]. An accurate geometry reconstruction with an uncertainty of about 0.5° is the necessary basis for energy and composition determination. But recording of hybrid data needs also adequate trigger efficiency for the individual surface detectors at lowest energies. Therefore, an enlarged energy range down to 10^{17} eV with high-quality hybrid events requires an extended field of view for FD telescopes in combination with a surface detector array of higher density in a small fraction of the observatory.

Fig. 2. Photo of the 3 HEAT telescopes tilted upward, end of January 2009. In the background the telecommunication tower of Coihueco is visible.

II. Design and properties of HEAT

In 2006 the Auger Collaboration decided to extend the original fluorescence detector, a system consisting of 24 telescopes located at four sites, by three High Elevation Auger Telescopes (HEAT). These telescopes have now been constructed, and they are located 180 m north-east of the Coihueco FD building. At the same time, the collaboration deployed extra surface detector stations as an infill array of 25 km^2 close to and in the field of HEAT. Additional large area muon detectors (AMIGA) [6] will determine the muon content of the shower and further improve the determination of the composition of the primary cosmic ray particles.

The design of HEAT is very similar to the original FD system, except for the possibility to tilt the telescopes upwards by 29°. In both cases a large field of view of about $30^\circ \times 30^\circ$ is obtained using a Schmidt optics. Fluorescence light entering the aperture is focused by a spherical mirror onto a camera containing 440 hexagonal PMTs. An UV transmitting filter mounted at the entrance window reduces background light from stars effectively. An annular corrector ring assures a spot size of about 0.6° despite the large effective aperture of 3 m^2. The high sensitivity of the Auger FD telescopes enables the detection of high energy showers up to 40 km distance. A slow control system for remote operation from Malargüe allows safe handling.

Differences between the conventional FD telescopes and HEAT are caused by the tilting mechanism. While the original 24 FD telescopes are housed in four solid concrete buildings, the 3 HEAT telescopes are installed in individual, pivot-mounted enclosures (see figure 2). Each telescope shelter is made out of lightweight insulated walls coupled to a steel structure. It rests on a strong steel frame filled with concrete. An electric motor can tilt this heavy platform though a commercial hydraulic drive by 29° within two minutes. The whole design is very rigid and can stand large wind and snow loads as required by legal regulations. All optical components are connected to the heavy-weight ground plate to avoid wind induced vibrations and to keep the geometry fixed.

Mirror and camera are adjusted in horizontal position. However, by tilting the telescope the varying gravitational force on camera body and mirror can change their relative position. Supplemental fixing bolts and an improved support structures are foreseen to keep the alignment of the optical system stable, which is essential for telescope pointing and optical resolution. Sensors for inclination are mounted at the mirror top, camera top and bottom, and at the aperture box. Distance sensors monitor the critical distance between camera and several points at the mirror system. These sensors are readout frequently for monitoring purposes.

Another design change for HEAT is the use of an improved DAQ electronics. The concept of the new electronics is the same as before, but as several electronic circuits have become obsolete, every front-end board had to be redesigned. Like the conventional FD electronics, the DAQ of one HEAT telescope contains 20 Analog Boards (AB) for analog signal processing, 20 First Level Trigger (FLT) boards for signal digitizing and storage, and one Second Level Trigger (SLT) board for the recognition of fluorescence light tracks and the initiation of data readout.

Along with faster FPGA logic the sampling rate was increased from 10 MHz to 20 MHz. The cut-off frequency of the anti-aliasing filters on the AB was adapted to about 7 MHz, but the other functions of the board remain the same. The redesigned FLT board implements all functions in FPGA of the Cyclone II FPGA family. A new custom-designed backplane provides dedicated point-to-point links between the FLT and SLT which lead to a factor 40 higher readout speed compared to the previous design. The usage of state-of-the-art FPGA in combination with the higher speed also establishes new fields of application for the DAQ system. The HEAT DAQ system is also the baseline design and the prototype for the Auger North FD electronics.

III. Operation of HEAT

The horizontal (‘down’) position is the only position in which a person can physically enter the enclosure. This configuration is used for installation, commissioning, and maintenance of the hardware. The absolute

calibration of the telescopes will be performed in this position as well. As the field of view of the existing Coihueco telescopes overlaps with HEAT in down position, it is possible to record air showers or laser tracks simultaneously. By comparing the reconstruction results from both installations one can directly determine the telescope resolution in energy and $X_{\max}$. We also want to reserve part of the time at one HEAT telescope for prototype studies for Auger North. Recording the same event in Coihueco and with the Auger North prototype will allow a direct comparison of the trigger and reconstruction efficiencies.

The tilted ('up') position is the default HEAT state. Telescopes are moved into this position at the beginning of a measuring run and stay that way untill the end of the run. From the trigger point of view the telescopes operate like a fifth FD building. Data of of the different installations (HEAT, diffenent FD sites, infill and Amiga, surface detector) are merged offline only, but the exchange of triggers in real time makes the recording of hybrid showers possible. The combined data will improve the accuracy of shower energy and $X_{\max}$ determination at all energies, but especially at the lower end down to 10^{17} eV.

IV. First Measurements

First measurements were performed with HEAT telescope #2 at the end of January 2009. From January, 30^{th} to February, 1^{st} the telescope was operated for two nights in up and down position. At first, the camera was illuminated with a short light pulse from a blue LED located at the center of the mirror. The High Voltage for the PMTs and the individual electronic gains were adjusted to achieve uniform light response in every pixel. Subsequent measurements with the LED pulser were performed at different tilting angles, but with the same settings as found in in down position. No indications were found for a gain change due to changed orientation of the PMTs in the Earth's magnetic field.

In the next step, the mechanical stability of the optical system was verified. The telescope was tilted several times from down to up position and back. The readings of the inclination and distance sensors were recorded during the movement. The analysis of the distance between camera and center of the mirror showed damped oscillations of low amplitude which stopped within seconds after the movement terminated. At rest the distance change between up and down position is less than 0.5 mm which is neglible for the telescope's optical properties.

After these cross-checks several showers were recorded with the telescope tilted in up position and in coincidence with Coihueco telescopes #4 or #5. One of the recorded events is shown in figure 3. The event data of both telescopes match very well in time (colour of the pixels in figure 3). The reconstruction yields a shower distance of 2.83 ± 0.06 km from Coihueco and an energy of the primary particle of $(2.0 \pm 0.2) \cdot 10^{17}$ eV.

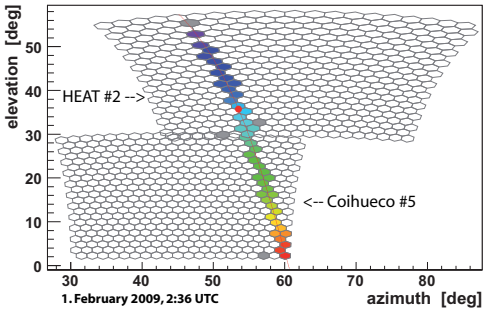

Fig. 3. This shower was recorded by HEAT telescope #2 and Coihueco telescope #5.The relative arrival time of the fluorescence light is coded in the colour of the pixel. The solid line is a fit of the shower detector plane.

In figure 4, the reconstructed longitudinal shower profile is shown together with a fit to a Gaisser-Hillas function. The fit yields a value of (657 ± 12) g cm^{-2} for $X_{\max}$. The plot also accentuates the need for HEAT telescopes for an accurate reconstruction: Using only the data point above a slant depth of 700 g cm^{-2} (Coihueco data) it would not have been possible to fit the profile and find a precise maximum.

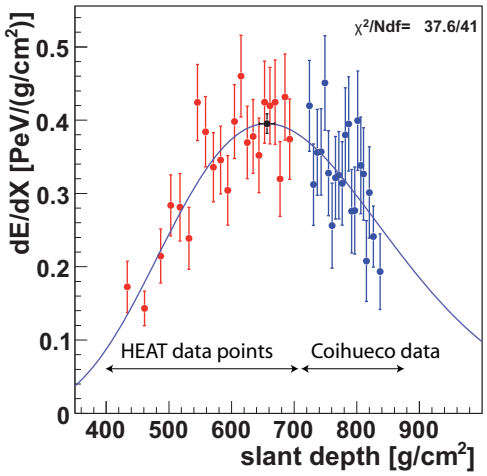

Fig. 4. Longitudinal shower profile of event in figure 3 together with Gaisser-Hillas-fit. Only a fit using both HEAT (left) and Coihueco (right) data points results in a reasonable $X_{\max}$ value.

V. Conclusion and Outlook

First measurements with a single telescope have demonstrated that HEAT will improve the energy threshold of the Pierre Auger Observatory at the Southern site down to about 10^{17} eV. The HEAT design satisfies all requirements with respect to stability and ease of operation. It is expected that all three HEAT telescopes are fully operational in September 2009. They will provide interesting data in the transition region from galactic to extragalactic sources and allow important prototype tests for the design of the Auger North FD system.

REFERENCES

[1] F. Schüssler for the Pierre Auger Colloboration, *Measurement of the cosmic ray energy spectrum above 10^{18} eV with the Pierre Auger Observatory*, these proceedings (2009), ID # 0114

[2] J. D. Hague for the Pierre Auger Collaboration, *Correlation of the highest energy cosmic rays with nearby extragalactic objects in Pierre Auger Observatory data*, these proceedings (2009), ID # 0143

[3] P. Homola for the Pierre Auger Collaboration, *Ultra-high energy photon studies with the Pierre Auger Observatory*, these proceedings (2009), ID # 0030

[4] J. Tiffenberg for the Pierre Auger Collaboration, *Limits on the flux of diffuse ultra high energy neutrinos set using the Pierre Auger Observatory*, these proceedings (2009), ID # 0180

[5] P. Sommers, *Capabilities of a giant hybrid air shower detector*, Astroparticle Physics, Vol. 3 (1995), p349-360

[6] P. Buchholz for the Pierre Auger Collaboration, *Hardware Developments for the AMIGA enhancement at the Pierre Auger Observatory*, these proceedings (2009), ID # 0043

Energy scale derived from Fluorescence Telescopes using Cherenkov Light and Shower Universality

Steffen Mueller[*] **for the Pierre Auger Collaboration**[†]

[*] *Karlsruhe Institute of Technology, Postfach 3640, 76021 Karlsruhe, Germany*
[†] *Observatorio Pierre Auger, Av. San Martin Norte 304, 5613 Malargüe, Argentina*

***Abstract*. We describe a method to determine the energy scale of the fluorescence detection of air-showers based on the universal shape of longitudinal shower profiles. For this purpose, the ratio of scattered Cherenkov and fluorescence light is adopted as a free parameter while fitting the individual profiles of the longitudinal deposit of the energy to the universal shape. We demonstrate the validity of the method using a Monte Carlo study based on the detector simulation of the Pierre Auger Observatory and estimate systematic uncertainties due to the choice of high energy interaction model and atmospheric conditions.**

***Keywords*: Auger Fluorescence Energy**

I. Introduction

Knowing the absolute energy scale of cosmic ray detection is important for the interpretation of physics results such as flux, anisotropy, or composition. At the Pierre Auger Observatory, the energy measured with the fluorescence detector is used to calibrate that of the surface detector [1]. Previous experiments that consisted of a surface array used Monte Carlo simulations for their energy calibration.

In air shower detection with fluorescence telescopes, the atmosphere acts as a calorimeter. The amount of emitted fluorescence light is proportional to the energy deposit in the atmosphere. The light yield is measured in laboratory experiments with a precision that is at present typically 15% [2].

Here, we describe a method to obtain the overall normalization of the fluorescence yield directly from air shower measurements. This method makes use of the universality of the shape of the longitudinal shower profiles of the energy deposit in the atmosphere. It is also dependent on our ability to reliably calculate the Cherenkov light contribution (given the electron number and energy spectra). Only the *relative* fluorescence spectrum is needed, which is known with good precision from laboratory experiments.

As an air shower develops in the atmosphere, a beam of Cherenkov light builds up along the axis of the shower and undergoes Rayleigh and aerosol scattering. In general the scattered Cherenkov light which is observed from a certain point in the shower will have been originally emitted at an earlier stage of shower development. The result is a very different longitudinal light profile from that of the isotropically emitted fluorescence light. Therefore, the shape of the reconstructed longitudinal profile of the energy deposit depends on the assumed composition of the different contributions to the measured light. We modify the fluorescence light yield in the reconstruction of the longitudinal profile to change the light composition in such a way that the energy deposit profile matches the profile expected from universality.

II. Universality of Air Shower Profiles

The energy spectra of shower electrons and the differential energy deposit have been shown to be universal as a function of shower age, $s = 3X/(X + 2X_{\max})$ [3]–[9]. As a result, the shape of energy deposit profiles have been studied for universality when plotted as a function of age. It was found that the profile shape varied much less when plotted in terms of the depth relative to shower maximum, $\Delta X = X - X_{\max}$. Figure 1 shows many normalized energy deposit profiles in ΔX that were simulated with proton primaries using three different high-energy interaction models at 10^{19} eV. In ΔX, the majority of normalized profiles fall within a narrow band.

Consider the average of normalized energy deposit profiles $U_i(\Delta X)$ for a single interaction model and primary particle. Then figure 2 shows the absolute deviations $\delta_i(\Delta X)$ of each average profile from the mean $\langle U(\Delta X)\rangle$ of the average profiles

$$\begin{aligned} U_i(\Delta X) &= \left\langle \left(\frac{dE}{dX}\right) \Big/ \left(\frac{dE}{dX}\right)_{\max} \right\rangle (\Delta X) \\ \delta_i(\Delta X) &= U_i(\Delta X) - \langle U(\Delta X)\rangle \ . \end{aligned}$$

Nowhere does the total systematic difference rise above 3% from the mean and it stays below one percent after the shower maximum. The equivalent plot for shower age shows deviations of up to 5% from the mean both before and after the shower maximum. Due to the weak dependence on primary composition, interaction model and primary particle energy, the average profile $U(\Delta X)$ is henceforth referred to as the Universal Shower Profile (USP). The measurement of the energy scale of fluorescence detection with the method described below is most susceptible to systematic differences in the tail of the USPs for different parameters (cf. figure 3c).

There is a slight dependence of the shape of the energy deposit profile on the primary energy. This effect is relevant for this work only within the uncertainty

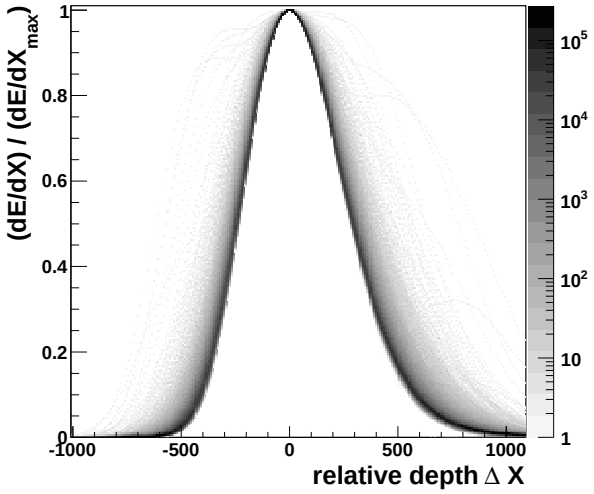

Fig. 1. Superposition of 30000 energy deposit profiles in ΔX. The CONEX [10] simulations are for proton primaries. Equal numbers of showers were generated with the QGSJet, QGSJetII.03, and Sibyll interaction models [11]–[13].

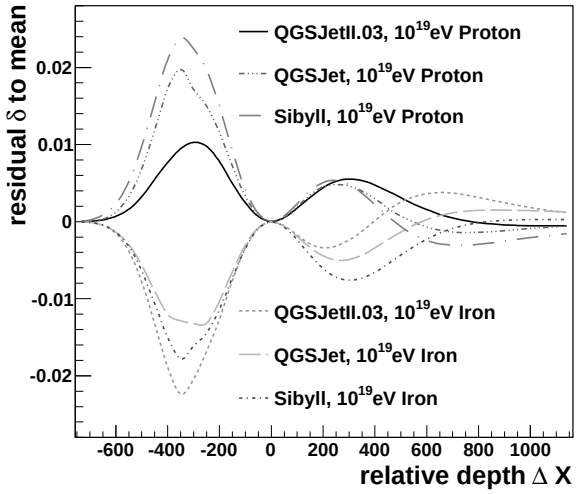

Fig. 2. Residuals $\delta\,(\Delta X)$ of universal shower profiles for various interaction models and primaries to the mean of the profiles.

of the reconstructed primary energy because the USP was recalculated for each event from simulations at the estimated energy. The dependence of the shape on the primary energy introduces a negligible systematic uncertainty (cf. table I).

III. Method

The longitudinal profile reconstruction [14] of the Offline software framework [15] was extended with an additional free parameter f so that the fluorescence yield becomes $Y^f = Y^f_{\rm lab}/f$ where $Y^f_{\rm lab}$ is the fluorescence yield currently used in the standard shower reconstruction by the Auger Collaboration [1]. This fluorescence yield is a parameterization of laboratory measurements, including the corresponding pressure dependence. Since Y^f is inversely related to f, a change in f corresponds to a proportional change in the reconstructed shower energy.

A set of showers is reconstructed many times while varying f. A low f corresponds to assuming a large fluorescence light yield and implies that fewer electrons are required in the shower to produce the observed fluorescence light. Since a smaller number of particles emits less Cherenkov light, the fraction of the measured light that is reconstructed as Cherenkov light is reduced accordingly.

The majority of detected fluorescence photons has not been scattered in the atmosphere before reaching the detector. Therefore, the point on the shower axis from which fluorescence light is observed is also the point at which it was emitted. Showers with significant contributions of direct Cherenkov light are not selected for this analysis (see below). Thus, the bulk of the observed Cherenkov light has propagated along the shower axis before being scattered towards the detector on molecules or aerosols. This means that the detected Cherenkov light carries information from a different stage of shower development than the fluorescence light observed from the same direction. This gives us a handle to change the shape of the reconstructed longitudinal profile of the energy deposit for a given observed light profile by modifying the fluorescence yield scale factor f.

The effect of a modified f parameter on the reconstructed light composition is demonstrated with an example in figure 3a and 3b. The measured light profile is unchanged. But with higher fluorescence yield in 3a, the contribution of Cherenkov light is suppressed. Conversely, it is increased due to the reduced fluorescence yield in 3b.

At the same time, a modified f changes the shape of the reconstructed energy deposit profile as shown in figure 3c. Since the shape is known from universality considerations, a χ^2 minimization can be used to fit each profile to the universal shape in dependence of f.

Each event is assigned an uncertainty that is a combination of the uncertainty from the χ^2 minimization and several propagated uncertainties. These include the uncertainties on the direction of the shower axis, the spread of the showers that make up the Universal Shower Profile, and the uncertainty on the aerosol attenuation lengths. The fit is repeated twice for each of these parameters: once after increasing and once after decreasing each parameter by one standard deviation. The resulting difference to the default result is the propagated uncertainty.

IV. Results

To test the method, a set of showers that roughly corresponds to five years of Auger data was simulated with energies between 10^{18} and 10^{20}eV. The simulation setup follows that used for the Auger fluorescence detector exposure calculation [16]. Basic quality cuts such

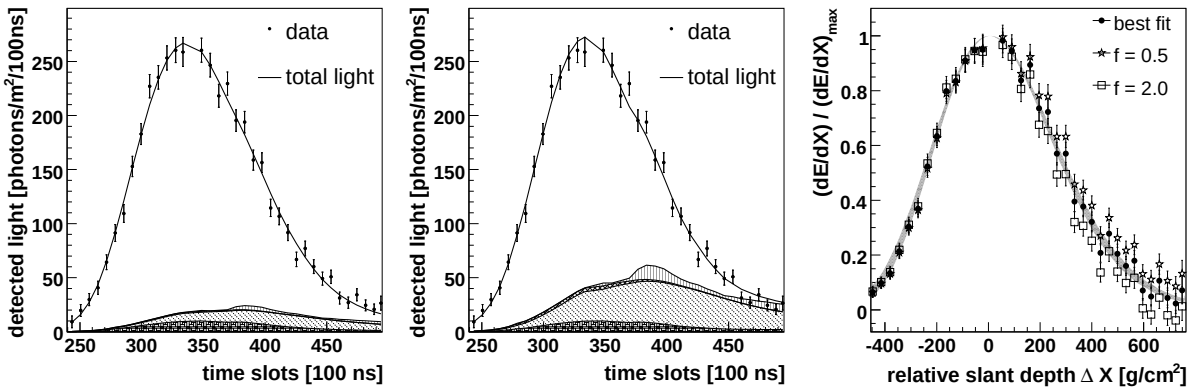

(a) $f = 0.5$ (b) $f = 2.0$ (c)

Fig. 3. Example event (Los Morados detector, run 1392, event 2886). (a)/(b) Measured light profile with reconstructed light components for two modified yield scale factors. Fluorescence light, Cherenkov light (direct, Mie scattered, Rayleigh scattered), multiply scattered light; (c) Normalized, reconstructed energy deposit profiles. Grey band: Universal shower profile with uncertainty band. Graphs: energy deposit profiles for different values of the yield scale factor

as requiring an energy resolution better than 20% and an $X_{\max}$ resolution better than $40\mathrm{g/cm^2}$ were applied. Additionally, since the forward peaked nature of direct Cherenkov light introduces a strong susceptibility to the uncertainties of geometry reconstruction, showers with a significant contribution of direct Cherenkov light were not used for the analysis. This was implemented by selecting showers with a minimum viewing angle in excess of 20°. The minimum viewing angle is the minimum angle between the shower axis and any vector between a point in the observed profile and the fluorescence detector.

Conversely, the showers were required to have significant contributions of Rayleigh scattered Cherenkov light, and a long profile that includes both regions in slant depth where fluorescence light and regions where Cherenkov light dominate the measured light flux.

This requirement was implemented as a two-dimensional cut on the profile length after the shower maximum and a quantity R

$$R \quad = \quad \rho(X_{\mathrm{up}}) \cdot \left(1 + \cos^2 \psi\right) \ .$$

It is the product of atmospheric density ρ in the deepest visible part of the shower track X_{up} and the angular dependence of Rayleigh scattering given the viewing angle ψ. Thus R is a measure for the amount of Cherenkov light scattered from the end of the profile towards the telescope.

The Monte Carlo simulation was carried out for three different fluorescence yields:

- The laboratory measurement $Y^f_{\mathrm{default}} = Y^f_{\mathrm{lab}}$ (corresponding to $f_{\mathrm{true}} = 1.0$),
- an increased fluorescence yield $Y^f_{\mathrm{high}} = Y^f_{\mathrm{lab}}/0.8$ ($f_{\mathrm{true}} = 0.8$),
- and a lowered fluorescence yield $Y^f_{\mathrm{low}} = Y^f_{\mathrm{lab}}/1.2$ ($f_{\mathrm{true}} = 1.2$).

In the shower reconstruction, the fluorescence yield was $Y^f_{\mathrm{lab}}/\tilde{f}$ with the fit parameter $\tilde{f}$.

For the selected set of simulated showers, the resulting, reconstructed fluorescence yield scale factors $\tilde{f}$ are weighted with their respective uncertainties. The distribution of these weighted scale factors is shown in figure 4 for three different input values of f_{true}. As can be seen, we are able to recover the true yield with good accuracy. This shows that the method is sensitive to a true fluorescence yield which differs from the assumed yield Y^f_{lab} because the reconstructed scale factor $\tilde{f}$ has no bias relating to the input parameter f_{true}. The width of the distributions, however, shows that a large number of suitable showers is required for the analysis.

The systematic uncertainties (table I) from various sources were taken into account by repeating the full procedure with various input parameters modified by their respective systematic uncertainties. For the systematics of the method, aerosols play a particularly important role. Both aerosol attenuation and scattering of Cherenkov light on aerosols are non-trivial effects that change the shape of the reconstructed energy deposit profile. The largest contribution is due to the uncertainties of the vertical aerosol optical depth (VAOD) profile. Since the available uncertainty bounds include both statistical and systematic effects, we estimate an upper limit for the systematics on f of about $\pm 7\%$. Another significant systematic uncertainty is introduced by the parameters of the aerosol phase function (APF) which describes the angular dependence of scattering on aerosols [17]. Its parameter g is a measure for the asymmetry of scattering, whereas the APF parameter f determines the relative strength of forward and backwards scattering. The contribution from the exponent γ describing the wavelength dependence of light attenuation due to aerosols is small. Likewise, the slight energy dependence of the shape of the universal shower profile leads to an uncertainty of less than one percent. Using various models or compositions for calculating the universal shower profile yields another contribution to the total of $\pm 1\%$ and $\pm 3\%$ respectively. Two different

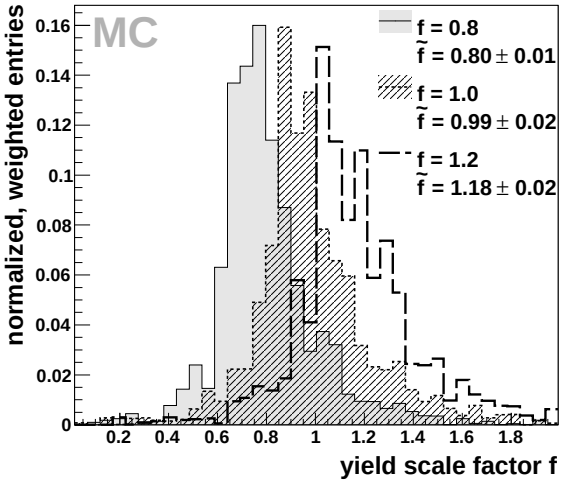

Fig. 4. Reconstructed, weighted yield scale factor distributions for three different input values of the scale factor f

TABLE I
UNCERTAINTIES OF THE SCALE FACTOR
(SEE TEXT)

Source	Uncertainty [%]
APF: g	$+5, -3$
APF: f	± 0.4
wavelength dependence γ	$+0.0, -0.2$
VAODs	$\approx \pm 7$
multiple scattering	± 0.5
energy reconstruction	$+0.4, -0.5$
USP had. int. model	± 1
USP composition	± 3

parameterizations for the multiple scattering of light in the atmosphere [18], [19] produce yield scale factors that differ by 1%. If added in quadrature, these effects add up to a total expected systematic uncertainty of $8 - 9\%$.

V. CONCLUSIONS

We introduced a new method of measuring the energy scale of fluorescence detectors using the universality of shape of the longitudinal shower profile. Its applicability and sensitivity was demonstrated using Monte Carlo simulations of air showers and the detector of the Pierre Auger Observatory. The measurement of the energy scale uses air shower data to determine the absolute fluorescence yield scale directly, and only requires a laboratory measurement of the relative fluorescence spectrum.

The simulated fluorescence yields were reproduced to very good accuracy. The systematic uncertainties of this method could potentially allow for a fluorescence yield determination with a precision better than 10%. The application of this method to Auger data is in progress.

REFERENCES

[1] C. Di Giulio *et al.* (Pierre Auger Collab.), Proc. of 31th Int. Cosmic Ray Conf., Lodz (2009) .
[2] F. Arqueros *et al.*, Nucl. Instrum. Meth. A597 (2008) 1–22 and arXiv:0807.3760 [astro-ph].
[3] A. M. Hillas, J. Phys. G8 (1982) 1461–1473.
[4] M. Giller *et al.*, J. Phys. G31 (2005) 947–958.
[5] F. Nerling *et al.*, Astropart. Phys. 24 (2006) 421–437 and astro-ph/0506729.
[6] D. Gora *et al.*, Astropart. Phys. 24 (2006) 484–494 and astro-ph/0505371.
[7] M. Giller *et al.*, Int. J. Mod. Phys. A20 (2005) 6821–6824.
[8] S. Lafebre *et al.*, Astropart. Phys. 31 (2009) 243–254 and arXiv:0902.0548 [astro-ph.HE].
[9] P. Lipari, Phys. Rev. D 79 (2009) 063001 and arXiv:0809.0190 [astro-ph].
[10] T. Bergmann *et al.*, Astropart. Phys. 26 (2007) 420–432 and astro-ph/0606564.
[11] N. N. Kalmykov and S. S. Ostapchenko, Phys. Atom. Nucl. 56 (1993) 346–353.
[12] S. Ostapchenko, Phys. Rev. D 74 (2006) 014026.
[13] R. Engel *et al.*, Proc. of 26th Int. Cosmic Ray Conf., Salt Lake City 1 (1999) 415.
[14] M. Unger *et al.*, Nucl. Instrum. Meth. A588 (2008) 433–441 and arXiv:0801.4309 [astro-ph].
[15] S. Argiro *et al.*, Nucl. Instrum. Meth. A580 (2007) 1485–1496 and arXiv:0707.1652 [astro-ph].
[16] F. Salamida (Pierre Auger Collab.), Proc. of 31th Int. Cosmic Ray Conf., Lodz (2009) .
[17] S. Y. BenZvi *et al.* (Pierre Auger Collab.), Proc. of 31th Int. Cosmic Ray Conf., Lodz (2009) .
[18] M. D. Roberts, J. Phys. G31 (2005) 1291–1301.
[19] J. Pekala *et al.*, arXiv:0904.3230 [astro-ph] to appear in Nucl. Instrum. Meth. A.

The electromagnetic component of inclined air showers at the Pierre Auger Observatory

Inés Valiño* **for the Pierre Auger Collaboration†**

*Karlsruhe Institute of Technology, POB 3640, D-76021 Karlsruhe, Germany
†Av. San Martin Norte 304, 5613 Malargüe, Argentina

***Abstract*. Muons, accompanied by secondary electrons, dominate the characteristics of inclined air showers above 60°. The characteristics of the signal induced by the electromagnetic component in the water-Cherenkov detectors of the Pierre Auger Observatory are studied using Monte Carlo simulations. The relative contributions of the electromagnetic component to the total signal in a detector are characterised as a function of the primary energy, for different assumptions about mass composition of the primary cosmic rays and for different hadronic models.**

***Keywords*: electromagnetic component, muonic component, Pierre Auger Observatory**

I. Introduction

Inclined air showers are conventionally defined as those arriving at ground with zenith angles θ above 60°. At large zenith angles the electromagnetic (EM) component in air showers, mainly produced by the decay of π^0s, is largely absorbed in the vastly enhanced atmospheric depth crossed by the shower before reaching ground, so in a first approximation only the more penetrating particles such as muons survive to ground. Muons are accompanied by an EM component produced mainly by muon decay in flight and muon interactions such as bremsstrahlung, pair production and nuclear interactions, which amount to $\sim 20\%$ of the muonic component [1]. This is the so-called electromagnetic "halo".

The Surface Detector Array (SD) of the Pierre Auger Observatory [2] is well suited to detect very inclined showers at energies above about 5×10^{18} eV, with high efficiency and unprecedented statistical accuracy. The cosmic ray energy spectrum obtained with inclined events is given in these proceedings [3].

The distribution of the detector signals produced by shower particles is used to estimate shower observables such as the primary energy. The specific characteristics of inclined showers, such as the absorption of the EM component and the deviations suffered by muons in the geomagnetic field, entail that their analysis requires a different approach from the standard one for showers of $\theta < 60^\circ$. The study of the signal distributions of the electromagnetic and muonic components at ground level becomes essential in the reconstruction [3], [4] and analysis of events at large angles.

In this work we have performed a comprehensive characterisation of the electromagnetic component with respect to the well-known behaviour of the muonic component. We have studied the ratio of the EM to muonic contributions to the signal in the water-Cherenkov detector as a function of several parameters. We have examined the effect of the shower evolution, shower geometry and geomagnetic field on the ratio. The dependences of this ratio on the primary energy, mass composition and hadronic model assumed in the simulations are addressed. The resulting parameterisations are used for the reconstruction of inclined events measured with the SD of the Pierre Auger Observatory [3].

The study described here is based on Monte Carlo simulations. A library of proton and iron-induced showers with energies from 10^{18} to 10^{20} eV, zenith angles between 60° and 88° and random azimuthal angle were generated with AIRES 2.6.0 [5] and the hadronic interaction models QGSJET01 [6] and Sibyll 2.1 [7]. The showers were simulated with and without geomagnetic field at the site of the SD of the Pierre Auger Observatory. The detector response is calculated here using a simple method based on parameterisations of the detector response to the passage of shower particles.

II. The ratio of electromagnetic to muonic detector signals

The electromagnetic and muonic particle components have a characteristic behaviour with distance to the shower axis, shower zenith angle and azimuth angle (ζ) of the detector position with respect to the incoming shower direction projected onto the plane transverse to the shower axis (shower plane). Also the different contributions to the electromagnetic component differ from each other as shown below. This is reflected by the ratio of the EM to muonic contributions to the detector signal

$$R_{\mathrm{EM}/\mu} = S_{\mathrm{EM}}/S_\mu \qquad (1)$$

In Fig. 1, we show the average signal distributions of the EM and muonic components (left panel) and their corresponding ratio $R_{\mathrm{EM}/\mu}$ (right panel) as a function of the distance to the core r for different θ. Near the core, the ratio decreases with zenith angle from $\theta = 60^\circ$ to $\sim 70^\circ$ because the remnant of the EM shower due to

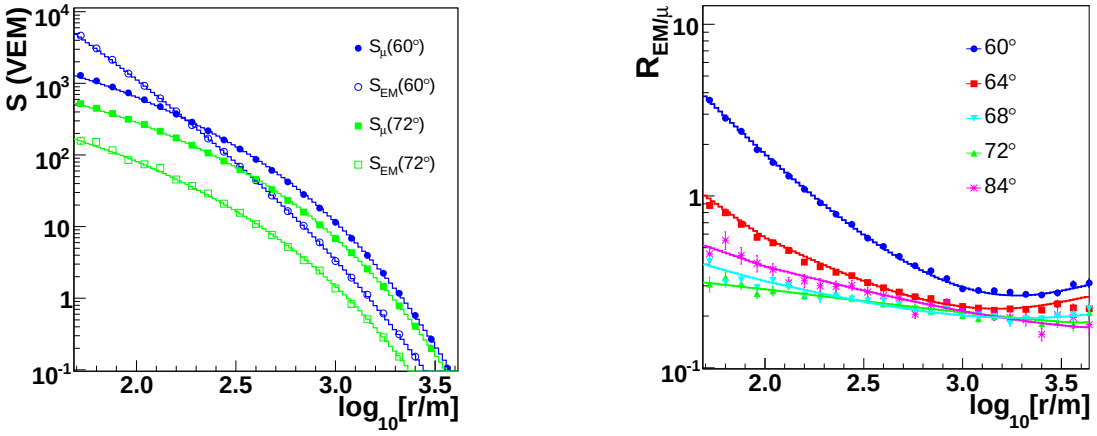

Fig. 1. Left plane: Lateral distribution of the electromagnetic and muonic contributions to the signal in the shower plane. Right panel: The ratio of the electromagnetic to muonic contributions to the detector signal as a function of the distance from the shower axis. Simulations were performed for 10 EeV proton showers at different zenith angles and in absence of geomagnetic field.

cascading processes (π^0 decay) is increasingly absorbed, until it practically disappears at $\theta \sim 70°$. Then the ratio increases again with θ, mainly due to muon hard interaction processes (bremsstrahlung, pair production and nuclear interactions) that are expected to dominate near the core in very inclined showers. Far from the core the lateral distribution of the ratio tends to flatten due to the dominant contribution of the EM halo produced by muon decay in flight. The larger the zenith angle, the ratio levels off closer to shower core. The slight increase of the ratio for $\theta \lesssim 68°$ and far from the core ($r \gtrsim 2$ km) is attributed to the combination of two effects, one is that the number of low energy muons decreases more rapidly at large distances because they decay before reaching the ground, and only energetic muons survive, and on the other hand the presence of the contribution to the EM component due to π^0 decay, particularly in the early region of the shower (the portion of the shower front that hits the ground before the shower axis).

A. Azimuthal asymmetry of the ratio $R_{\mathrm{EM}/\mu}$

There is an azimuthal asymmetry in the ratio of the EM to muonic contributions due to the combination of the geometrical and shower evolution effects [8]. As illustrated in the left panel of Fig. 2 shower particles do not travel parallel to the shower axis in general and therefore they cross different amounts of atmosphere depending on ζ. In particular, particles arrive at ground in the early region of the shower ($\zeta = 0°$) with a smaller local zenith angle than those in the late region ($\zeta = 180°$). This is essentially the basis for the geometrical effect. In inclined showers, the asymmetry induced by the geometrical effect is typically small and the main source of azimuthal asymmetry is the shower evolution effect which can be understood as follows. Particles at the same distance from the shower axis in the shower plane, but arriving with different ζ, travel along different paths and belong to different stages in the evolution of the shower. The importance of this effect depends on the depth-dependent evolution of the lateral particle distribution and on the attenuation of the total number of particles. The asymmetry induced by the shower evolution affects more the remnant of the EM shower than the muonic component or its associated EM halo. As a consequence, the shower evolution is expected to induce a negligible asymmetry in the ratio in showers with $\theta \gtrsim 70°$, because the EM remnant is practically suppressed, and the EM halo approximately has the same asymmetry than the muonic component.

To study further the azimuthal dependence of the asymmetry we divide the shower plane in ζ bins, and we calculate the lateral distributions of the ratio in each bin for a fixed zenith angle: $R_{\mathrm{EM}/\mu}(r, \theta, \zeta)$, and we compare these distributions to the distribution obtained averaging over ζ: $\langle R_{em/\mu}\rangle(r, \theta)$. For this purpose we define the asymmetry parameter Δ_ζ as

$$R_{\mathrm{EM}/\mu}(r, \theta, \zeta) = \langle R_{\mathrm{EM}/\mu}\rangle(r, \theta) \times (1 + \Delta_\zeta) \qquad (2)$$

In Fig. 2, we show the lateral distribution of $R_{\mathrm{EM}/\mu}$ in different ζ bins compared to the mean value (middle panel) and their corresponding asymmetry parameter Δ_ζ (right panel) for showers at $\theta = 60°$. $|\Delta_\zeta|$ increases with distance to the core and it is larger in the early region than in the late region as expected. Moreover, $|\Delta_\zeta|$ decreases as the zenith angle increases for the reasons explained above, becoming negligible for $\theta > 68°$. This plot illustrates the importance of accounting for the asymmetry in the ratio when dealing with inclined showers with $60° < \theta < 70°$.

B. Geomagnetic field effect on $R_{\mathrm{EM}/\mu}$

Muons in inclined showers travel along sufficiently long paths in the atmosphere to be affected by the Earth's magnetic field (GF). Positive and negative muons are deviated in opposite directions and as a consequence the muonic patterns in the shower plane are distorted in elliptical or even 2-lobed patterns [9], [10]. This

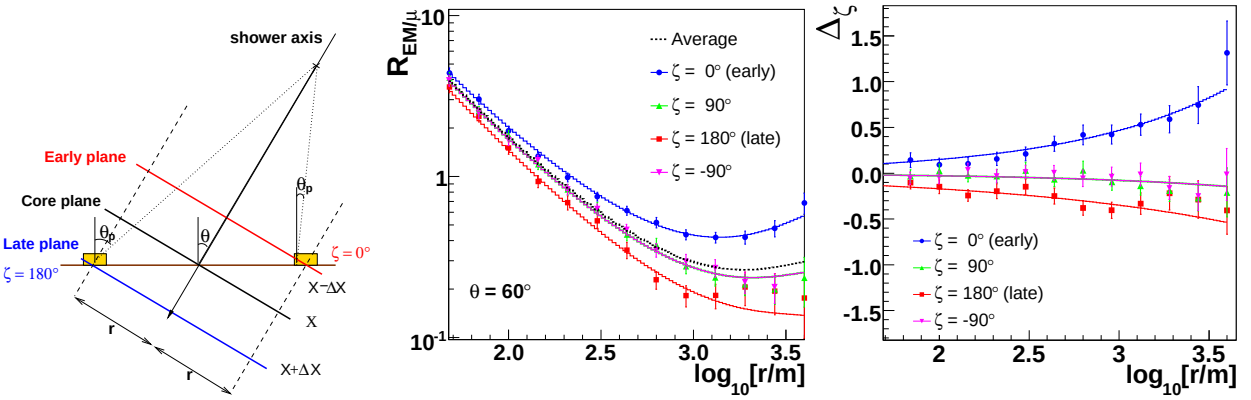

Fig. 2. Azimuthal asymmetry in the ratio $R_{\mathrm{EM}/\mu}$. Left panel: Schematic picture of an inclined shower reaching the ground. Middle panel: The ratio $R_{\mathrm{EM}/\mu}$ as a function of the distance from the shower axis in the shower plane in different bins of ζ for 10 EeV proton showers with $\theta = 60°$. Right panel: Asymmetry of the lateral distribution of the ratio $R_{\mathrm{EM}/\mu}$ in different ζ bins. The size of the bins is $\Delta\zeta = 30°$ centered at ζ.

effect on the muonic distributions is only significant for $\theta \geq 75°$. At these angles, the dominant contribution to the EM signal at ground is due to the EM halo, which inherits the muon spatial distribution and is proportional to the muonic signal distribution. For this reason, the ratio of the EM to muonic signals maintains the symmetry in the azimuthal angle ζ. However, the GF increases the $\langle R_{\mathrm{EM}/\mu}\rangle$ with respect to the value in its absence. The effect depends on the shower zenith (θ) and azimuth (ϕ) angles, and is more important near the core. After studying all these dependences, we have concluded that the effect on the ratio is important for showers at $\theta \gtrsim 86°$. It should be noted that the rate of events at such high zenith angles detected at ground level is small due to the reduced solid angle and the $\cos\theta$ factor needed to project the array area onto the shower plane. Very inclined events are also subject to other uncertainties [3] and we therefore choose to ignore them at this stage without losing much on statistical grounds.

C. Systematic uncertainties

The lateral distributions of the electromagnetic signal due to cascading processes and muonic signal exhibit a different behaviour as a function of the energy and of the depth of the shower maximum, while the contribution to the EM signal due to muon decay in flight mimics the energy dependence of the muonic one. Combining all the results, we expect $R_{\mathrm{EM}/\mu}$ to have a different behaviour depending on whether the EM remnant or the EM halo contributes more to the total signal. We study the energy dependence of $R_{\mathrm{EM}/\mu}$ performing the relative difference Δ_E between the ratio at a given energy with respect to that obtained for 10 EeV proton-induced showers, $\langle R_{\mathrm{EM}/\mu}\rangle$:

$$\Delta_E = \frac{R_{\mathrm{EM}/\mu}(E) - \langle R_{\mathrm{EM}/\mu}\rangle(10\mathrm{EeV})}{\langle R_{\mathrm{EM}/\mu}\rangle(10\mathrm{EeV})} \qquad (3)$$

The dependence of Δ_E on the zenith angle and distance from the shower axis is studied as in the example of Fig. 3 (left panel), where we plot Δ_E in different bins of r, as a function of the zenith angle for 1 EeV proton showers. We find that either for $\theta \gtrsim 68°$ at all the distances to the shower core or for distances beyond 1 km at all the zenith angles the ratio $R_{\mathrm{EM}/\mu}$ remains constant at the same level with energy because only the EM halo contributes to the EM signal. Otherwise, there is a dependence on energy that increases as the distance to the shower axis decreases, and therefore the dependences must be taken into account as systematic uncertainties. We obtain the same general result studying Δ_E for other shower energies.

At present, the chemical composition of the cosmic rays at the highest energies (> 1 EeV) remains unknown. For this reason we have studied the dependence of the ratio on the mass of the primary particle initiating the shower accounting for protons and iron nuclei in our simulations. Following the same procedure as in the case of the energy, we calculate the relative difference Δ_{mass} between the ratio in iron-induced showers at 10 EeV with respect to that obtained for 10 EeV proton shower simulations:

$$\Delta_{\mathrm{mass}} = \frac{R_{\mathrm{EM}/\mu}(\mathrm{Fe}) - \langle R_{\mathrm{EM}/\mu}\rangle(\mathrm{p})}{\langle R_{\mathrm{EM}/\mu}\rangle(\mathrm{p})} \qquad (4)$$

For reasons very similar to those that explain the energy dependence studied before, we conclude that either for $\theta \gtrsim 68°$ at all the distances to the shower core or for distances beyond 1 km at all θ the ratio $R_{\mathrm{EM}/\mu}$ remains constant at the same level with primary mass as shown in Fig. 3 (middle panel).

At the highest energies, there is lack of knowledge about the hadronic interactions which determine the shower development of MC simulations [11]. This fact leads to discrepancies between the different hadronic models on predictions such as the densities of the EM and muonic components at ground.

In this work, we compare two high energy interaction models widely used in cosmic ray physics: QGSJET01

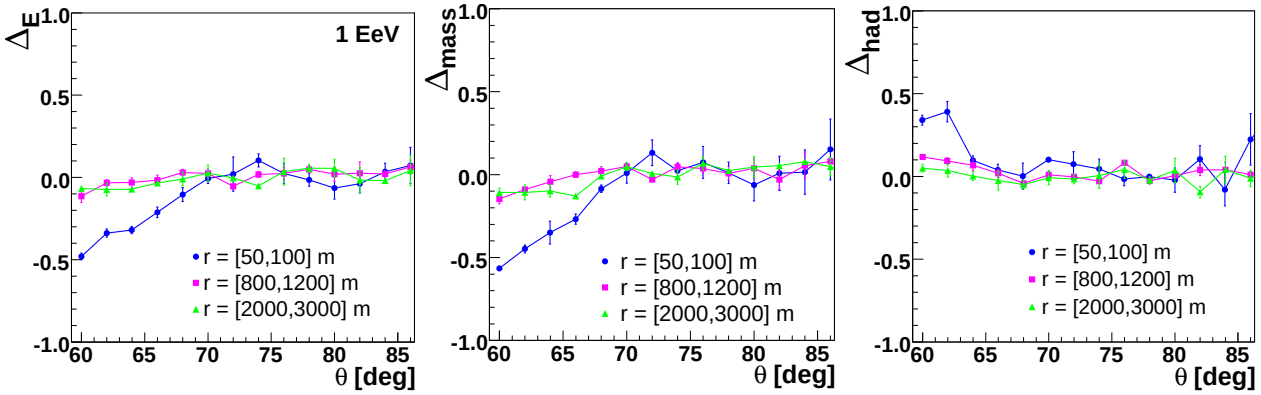

Fig. 3. Left plane: The relative difference $\Delta_{\rm E}$ between the ratio $R_{{\rm EM}/\mu}$ obtained in 1 EeV proton-induced showers with respect to the reference ratio $\langle R_{{\rm EM}/\mu}\rangle$ obtained in 10 EeV proton-induced showers simulated with QGSJET01 (Eq. 3). Middle panel: The relative difference $\Delta_{\rm mass}$ between the ratio $R_{{\rm EM}/\mu}$ obtained in 10 EeV iron-induced showers simulations with respect to $\langle R_{{\rm EM}/\mu}\rangle$ (Eq. 4). Right panel: The relative difference $\Delta_{\rm had}$ between the ratio $R_{{\rm EM}/\mu}$ obtained in 10 EeV proton-induced showers simulated with Sibyll 2.1 with respect to $\langle R_{{\rm EM}/\mu}\rangle$ (Eq. 5). The relative differences are shown as a function of the shower zenith angle in different bins of distance to the shower axis r.

and Sibyll 2.1. For proton primaries at 10 EeV, the QGSJET model predicts showers that on average develop higher in the atmosphere and have 40% more muons than showers simulated with Sibyll.

We calculate the relative difference $\Delta_{\rm had}$ between the ratio for 10 EeV proton showers simulated with Sibyll 2.1 with respect that obtained in showers simulated with QGSJET01:

$$\Delta_{\rm had} = \frac{R_{{\rm EM}/\mu}({\rm Sibyll}) - \langle R_{{\rm EM}/\mu}\rangle({\rm QGSJET})}{\langle R_{{\rm EM}/\mu}\rangle({\rm QGSJET})} \qquad (5)$$

In Fig. 3 (right panel) we show $\Delta_{\rm had}$ as a function of the zenith angle in different bins of r. The differences between both models are more apparent near the shower axis as expected from the dominance of the EM component due to cascading processes near the core. We obtain a similar result to the case of energy and mass dependences, which is that either for $\theta \gtrsim 64^\circ$ at all the distances to the shower axis or for distances beyond 1 km at all zenith angles the ratio $R_{{\rm EM}/\mu}$ remains constant at the same level independently of the model used.

III. Conclusions

We have characterised the signal distributions of the electromagnetic and muonic components of inclined showers at the ground level on the shower plane [12]. We have accounted for the different sources of azimuthal asymmetry and the effect of the geomagnetic field. As a result, we have obtained a parameterisation of the ratio $S_{\rm EM}/S_\mu$ as a function of the shower zenith angle and the detector position that is used in the reconstruction of inclined events measured with the Surface Detector Array of the Pierre Auger Observatory.

We have studied the dependence of this ratio with the primary energy, mass composition and the hadronic interaction model used in the simulations. The general result is that either for zenith angles exceeding $\theta \gtrsim 68^\circ$ or for distances to the shower core beyond 1 km at all the zenith angles $> 60^\circ$, the ratio remains constant because only the electromagnetic halo contributes to the EM signal. Otherwise, the dependences are important and must be taken into account as systematic uncertainties within the event reconstruction.

References

[1] M. Ave et al., *Astropart. Phys.*, 14:109, 2000.
[2] J. Abraham et al. [Pierre Auger Collaboration], *NIMA*, 523:50-95, 2004.
[3] R. Vazquez [Pierre Auger Collaboration], these proceedings.
[4] D. Newton [Pierre Auger Collaboration], Proc. 30$^{\rm th}$ ICRC, Mérida, 4:323, 2007.
[5] http://www.fisica.unlp.edu.ar/auger/aires/
[6] N. Kalmykov et al., *Nucl. Phys. Proc. Suppl.*, 52B:17-28, 1997.
[7] R. Engel et al., Proc. 26$^{\rm th}$ ICRC, Salt Lake City, 1:415, 1999.
[8] M. T. Dova et al., *Astropart. Phys.*, 18:351-365, 2003.
[9] A. M. Hillas et al., Proc. 11$^{\rm th}$ ICRC, Budapest, 3:533, 1969.
[10] M. Ave et al., *Astropart. Phys.*, 14:91, 2000.
[11] T. Pierog et al., *Czech. J. Phys.*, 56:A161-A172, 2006.
[12] I. Valiño et al., in preparation.

Rapid atmospheric monitoring after the detection of high-energy showers at the Pierre Auger Observatory

Bianca Keilhauer*, for the Pierre Auger Collaboration†

*Karlsruhe Institute of Technology (KIT),
Forschungszentrum Karlsruhe, Institut für Kernphysik, P.O.Box 3640, 76021 Karlsruhe, Germany
†Observatorio Pierre Auger, Av. San Martin Norte 304, 5613 Malargüe, Argentina

Abstract. **The atmospheric monitoring program of the Pierre Auger Observatory has been upgraded to make measurements of atmospheric conditions possible after the detection of very high-energy showers. Measurements of the optical transmittance due to aerosols and clouds are time-critical. Therefore, observations of atmospheric regions close to a shower track of interest are performed within ten minutes of a shower detection using LIDAR and telescope monitors. Measurements of the altitude dependence of atmospheric state variables such as air temperature, pressure, and humidity are performed within about two hours following the detection of a very high-energy event using meteorological radio soundings. Both programs are triggered using a full online reconstruction with analysis-level quality cuts. We describe the implementation of the online trigger, and discuss the impact of the monitoring data with high resolution on the analysis of air shower events.**

Keywords**: rapid atmospheric monitoring, Pierre Auger Observatory, high-energy air showers**

I. Introduction

At the Pierre Auger Observatory [1], extensive air showers (EAS) induced by ultra-high energy cosmic rays are studied. The observatory consists of two detector types, a surface detector (SD) for secondary particles of EAS and fluorescence detector (FD) telescopes for UV-emissions by nitrogen molecules in the atmosphere. The fluorescence technique provides an almost calorimetric measurement of the primary energy of cosmic rays.

However, the constantly changing conditions of the atmosphere demand a sophisticated monitoring system [2]. The reconstruction of air showers from their UV-emission requires proper characterisation of atmospheric state variables such as pressure, temperature, and humidity, as well as the optical transmittance due to aerosol contamination and the presence of clouds [3]. The state variables of the atmosphere above the Pierre Auger Observatory are determined using meteorological radio soundings, while aerosol and cloud conditions are measured by two central lasers, four elastic LIDARs, and four cloud cameras [4].

The sounding data have been incorporated into monthly models, and aerosol and cloud data into an hourly database [4]. However, for events of particular physical interest, such as very high-energy showers, it is desirable to measure the properties of the atmosphere as accurately as possible. To improve the resolution of the atmospheric database for such events, dedicated radio soundings and LIDAR measurements can be triggered by an online event reconstruction. We will discuss the motivation for such measurements (Section II), the operation of the online trigger (Section III), and the use of dedicated atmospheric measurements in the offline reconstruction (Section IV).

II. Motivation for Rapid Monitoring

Between 2002 and 2005, radio soundings were performed at the observatory during dedicated measurement campaigns. Since mid-2005, the soundings have been performed approximately every fifth day. The measurements obtained by launching weather balloons provide altitude profiles of the air temperature, pressure, and relative humidity up to about 23 km above sea level. Due to the limited statistics of the measurements, the data have been incorporated into monthly models of conditions near Malargüe, Argentina, the site of the southern part of the Pierre Auger Observatory [4], [5].

Using monthly models instead of actual profiles introduces an uncertainty of the primary energy of $\Delta E/E = 1.5\% - 3\%$ for showers with energies between $\approx 10^{17.7}$ eV and 10^{20} eV, and a corresponding uncertainty $\Delta X_{\max} = 7.2 - 8.4$ g cm^{-2} of the position of the shower maximum. While it is not practical to perform a radio sounding every night, the reconstruction can be improved for a subset of the EAS data by concentrating the soundings in periods when high-quality events are observed. This subset of EAS events is particularly important because they contribute to the energy scale determination of the entire observatory [6].

For aerosol measurements, the LIDAR stations conduct automated hourly sweeps of the atmosphere above the observatory to estimate the vertical aerosol optical depth, cloud height, and cloud coverage [7]. The hourly sweeps are sufficient to characterise changing aerosol conditions, but a more rapid response is necessary to identify moving clouds between shower tracks and the FD telescopes observing the event. To accomplish this, the LIDARs are capable of interrupting their hourly sweeps to scan interesting shower tracks for atmospheric non-uniformities [7], [8].

III. ONLINE TRIGGER

To select events for monitoring with radio soundings and/or LIDAR scans, an online reconstruction is used to trigger balloon launches and the LIDAR hardware. As data are acquired from the FD telescopes and SD, they are merged by an event builder into hybrid event files, and passed to the reconstruction software. The software is the same as that used for Offline event reconstruction [9], including the latest versions of the detector calibration databases. In this way, the LIDAR and balloon triggers can be constructed with the same quality as the offline physics analysis.

The reconstruction loop runs every 60–90 seconds, and reconstructs events between 2 and 10 minutes after their detection[1]. Events with reconstructible dE/dX longitudinal profiles are used to trigger LIDAR and sounding measurements following the application of basic quality cuts. The LIDARs trigger on showers with $E \geq 10^{19}$ eV in combination with given quality cuts on the reconstruction of the shape of the longitudinal profile. These events are typically of high quality and the rapid monitoring is to ensure that no atmospheric impurity has altered the reconstruction result. To allow the investigation of shower observations affected by clouds and other non-uniformities in the atmosphere for possible longitudinal profile corrections in the future, few events of lower quality with $E \gtrsim 10^{18.78}$ eV can also pass the trigger conditions. This yields up to one scan per night. A balloon launch is triggered for events with $E \geq 10^{19.3}$ eV and a profile fit $\chi^2/\mathrm{NDF} < 2.5$. All trigger conditions have in common that the position of shower maximum has to be well in the field of view and that the observed track has an expedient length.

The quality of the online reconstruction has been checked by comparing with results from the Offline reconstruction. Even though some minor differences in the reconstruction chains are present, the reconstruction quality is excellent. Only some events are missed by the online reconstruction below 10^{18} eV, which is well below the required energy threshold for both rapid monitoring programmes. At primary energies of interest, the energy of the primary cosmic ray and the position of the shower maximum are reconstructed very well by comparison with the Offline reconstruction: only below 1% difference for the energy and 2 g cm^{-2} in $X_{\max}$ are expected. The reconstruction cuts for triggering radio soundings yield a trigger rate of 3 to 13 radio soundings per shift[2] depending on season, see Fig 1. In practice, only one launch is performed within 5 hours resulting in about 2 to 6 launches per FD shift.

Triggers for the LIDAR systems are handled automatically by these stations: the hourly scans are halted and the LIDARs sweep into the field of view of the FD telescopes to probe the shower track [7]. To avoid triggering the telescopes with stray light, the FD data acquisition is vetoed for four minutes, the maximum duration of a dedicated scan. In contrast to the LIDAR, the balloon launches require human intervention. Therefore, a sounding trigger initiates a SMS text message to a technician in Malargüe. The technician then drives to the balloon launching facility and performs the sounding typically within two hours of the detection of the event. This measurement has no interference with any other data acquisition of the Pierre Auger Observatory.

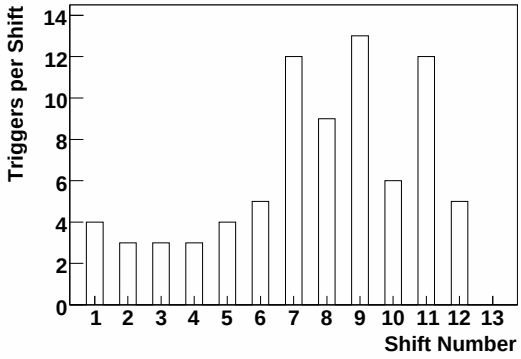

Fig. 1. All triggers for each FD shift in 2008 of events which would have passed the sounding trigger conditions. A seasonal effect due to longer nights in winter can be seen.

IV. ANALYSIS

During the March – April 2009 FD shift, the rapid monitoring with radio soundings was activated for the first time. We had two nights with successful triggers for the radio soundings. In the second night, it was a stereo event. Both radio soundings could be performed within 1.5 hours after the high-energy air shower. The first trigger was sent at the end of March and the second one at the beginning of April. In Fig. 2, the difference between the actual measured atmospheric profiles from the radio soundings and the monthly models for the area of the Auger Observatory valid for that month are displayed for the temperature, atmospheric depth, and vapour pressure. For the event in March, the differences between the measured temperature and atmospheric depth profiles and the monthly average model are small. However the considerable amount of water vapour in the lower atmosphere indicates possible distortions of the longitudinal shower profile compared with a reconstruction using the adequate monthly model. A reconstruction of the first event with the actual atmospheric profiles compared with that using monthly models yields a $\Delta E/E$ of +0.9% and a $\Delta X_{\max}$ of +6 g cm^{-2}. For the event in April, the water vapour content is nearly the same as in the corresponding monthly model. However, the higher temperature close to ground resulting in lower atmospheric depth values will change the reconstructed air shower event. The same two versions of reconstruction as for the first event yield a $\Delta E/E$ of -0.5% and -1.0% for the two different FD

[1]The delay is caused by buffering of station data from the SD.

[2]To infer these numbers, the EAS data sample from 2008 was analysed.

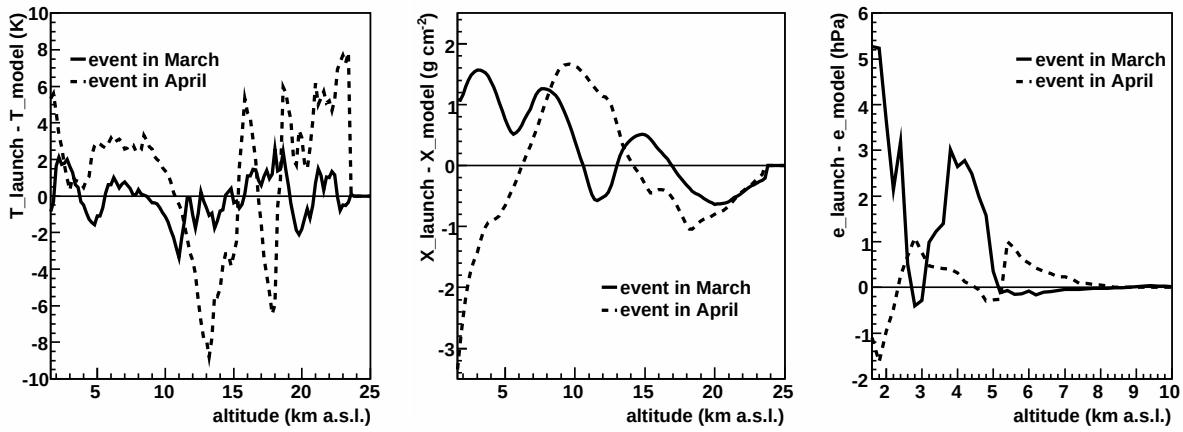

Fig. 2. Difference between two actual measured atmospheric profiles in March and April 2009 from the radio soundings and the corresponding monthly models for the area of the Auger Observatory. Left: Temperature. Middle: Atmospheric Depth. Right: Vapour Pressure.

stations which observed this stereo event and a $\Delta X_{\max}$ of +4 g cm^{-2} and +3 g cm^{-2}.

In the second shift running this programme, we had 10 triggers in 6 nights. The first one was again a stereo event and in the fourth night, there were 3 triggers within 2.5 hours. The fifth night also provided two triggers in 2.5 hours, and in the last night there were 2 triggers within 1 hour. In total, we had 5 radio soundings initiated by high-energy air shower events, because the SMS during the last night were lost.

All events have been reconstructed using two different configurations. The first one represents the status of currently best knowledge, so using the actual atmospheric profiles from the radio soundings in combination with descriptions of fluorescence emission [10] and transmission taking into account all temperature, pressure, density, and humidity effects. The second reconstruction relies on the same descriptions but uses the monthly models for the site of the Pierre Auger Observatory which provide also profiles of water vapour. In Fig. 3, the resulting differences of the reconstruction procedures are shown for all events during March and April 2009. The stereo events have been reconstructed independently for the two FD stations which observed the extensive air shower. The primary energies of these events vary from the threshold energy up to almost $10^{19.7}$ eV and for the position of shower maximum, values between 654 and 924 g cm^{-2} slant depth are observed. The given differences are between reconstruction with actual atmospheric profiles and that with monthly models. For the primary energy, we expect an uncertainty of $\pm$ 2.5% at $E_0 = 10^{19.3}$ eV while using monthly models. The differences between reconstructions using sounding data and the monthly models fit these expectations (Fig. 3 left). For the position of shower maximum, the expected uncertainty at $E_0 = 10^{19.3}$ eV is $\pm$ 8 g cm^{-2}. The reconstruction with monthly models nearly matches these expectation but is biased to one direction for this season (Fig. 3 right).

The rapid monitoring with LIDARs started in February 2009 and through the beginning of May 2009, the four LIDAR stations at the Pierre Auger Observatory were triggered 29 times. The intention is to investigate atmospheric conditions for those high-energy showers that fail strict analysis cuts due to distortions caused by clouds and aerosols.

For high-energy showers of high reconstruction quality, the LIDAR scans can be used to verify the quality of the atmosphere. In this manner, the scans allow for the investigation of atmospheric selection effects on the highest energy showers. Of the 29 showers probed by dedicated LIDAR scans, 17 passed the strict quality cuts used in the analysis of FD data. The energies of these showers ranges from 10^{19} to $10^{19.52}$ eV. The observed shower maxima are between 678 and 808 g cm^{-2}.

In nearly all cases, the profile fit is of high quality, and the LIDAR data do not indicate the presence of large amounts of aerosols or heavy cloud coverage. One exception is shown in Fig. 4, in which the light from the upper segment of a shower track is blocked by a thick cloud layer. The backscattered light from the LIDAR scan shows a strong echo near 8 km above ground level, or 650 g cm^{-2} slant depth along the shower track, confirming the presence of a cloud.

At present, the rapid monitoring with LIDARs is mainly used as a check of the quality of the atmosphere after the observation of high-energy showers. This is quite important for analyses that rely on unusual features in shower tracks, such as exotic particle searches. The LIDAR shots can also be used to remove obscured or distorted sections of a shower track from the analysis. Once sufficient statistics have been collected, it should be possible to use the LIDAR data to correct observed shower tracks for inhomogeneities in the atmosphere.

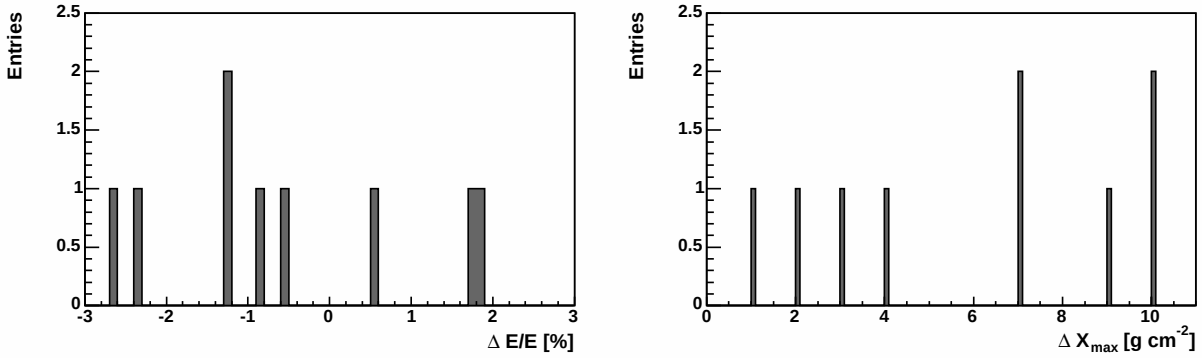

Fig. 3. Comparison of two different versions of reconstruction for air shower events observed in March and April 2009. The first reconstruction uses actual atmospheric profiles from radio soundings performed shortly after the detection of the EAS. The second one uses monthly models developed for the site of the Pierre Auger Observatory.

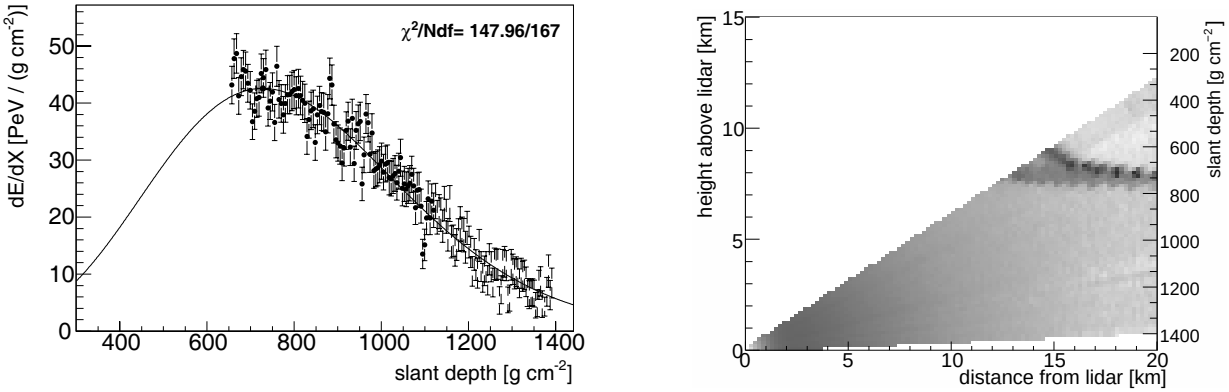

Fig. 4. Left: A $10^{19.48}$ eV shower profile obscured below 650 g cm^{-2} by a cloud. The backscattered light from a LIDAR scan of the shower-detector plane (right) confirms the presence of a cloud layer (the dark horizontal band) in the telescope field of view.

REFERENCES

[1] J. Abraham *et al.* [Pierre Auger Collab.], Nucl. Instr. Meth. **A523** (2004) 50
[2] S. BenZvi for the Pierre Auger Collab., Proc. 31st Int. Cos. Ray Conf. Lodz, Poland, (2009)
[3] L. Valore for the Pierre Auger Collab., Proc. 31st Int. Cos. Ray Conf. Lodz, Poland, (2009)
[4] J. Abraham *et al.* [Pierre Auger Collab.], *A Study of the Effect of Molecular and Aerosol Conditions on Air Fluorescence Measurements at the Pierre Auger Observatory*, submitted to Astropart. Phys. (2009)
[5] J. Blümer *et al.* for the Pierre Auger Collab., Proc. 29th Int. Cos. Ray Conf. Pune, India, **7** (2005) 123
[6] J. Abraham *et al.* [Pierre Auger Collab.], PRL **101** (2008) 061101
[7] S.Y. BenZvi *et al.*, Nucl. Instr. Meth. **A574** (2007) 171
[8] J. Boyer et al. for the HiRes Collab., Proc. 28th Int. Cos. Ray Conf. Tsukuba, Japan, 1 (2003) 481
[9] S. Argiro *et al.*, Nucl. Instr. Meth. **A580** (2007) 1485
[10] B. Keilhauer, M. Unger, Proc. 31st Int. Cos. Ray Conf. Lodz, Poland, (2009)

UHE neutrino signatures in the surface detector of the Pierre Auger Observatory

D. Góra[*†] **for the Pierre Auger Collaboration**[‡]
[*]*Karlsruhe Institute of Technology (KIT), D-76021 Karlsruhe, Germany*
[†]*Institute of Nuclear Physics PAN, ul. Radzikowskiego 152, 31-342 Kraków, Poland*
[‡]*Av. San Martín Norte 304 (5613) Malargüe, Prov. de Mendoza, Argentina*

***Abstract*. The Pierre Auger Observatory has the capability of detecting ultra-high energy neutrinos. The method adopted is to search for very inclined young showers. The properties of such showers that start deep in the atmosphere are very different at ground level from those of showers initiated in the upper atmosphere by protons or nuclei. The neutrino events would have a significant electromagnetic component leading to a broad time structure of detected signals in contrast to nucleonic-induced showers. In this paper we present several observables that are being used to identify neutrino candidates and show that the configuration of the surface detectors of the Auger Observatory has a satisfactory discrimination power against the larger background of nucleonic showers over a broad angular range.**

***Keywords*: UHE neutrino signatures, the Pierre Auger Observatory**

I. INTRODUCTION

The detection of ultra high energy (UHE) cosmic neutrinos, above 10^{18} eV, is important as it may allow us to identify the most powerful sources of cosmic rays (CR) in the Universe. Essentially all models of UHECRs production predict neutrinos as a result of the decay of charged pions produced in interactions of cosmic rays within the sources themselves or while propagating through background radiation fields [1]. For example, UHECR protons interacting with the cosmic microwave background (CMB) give rise to the so called "cosmogenic" or GZK neutrinos [2]. The cosmogenic neutrino flux is somewhat uncertain since it depends on the primary UHECR composition and on the nature and cosmological evolution of the sources as well as on their spatial distribution [3]. In general, about 1% of cosmogenic neutrinos from the ultra-high energy cosmic ray flux is expected.

Due to their low interaction probability, neutrinos need to interact with a large amount of matter to be detected. One of the detection techniques is based on the observation of extensive air showers (EAS) in the atmosphere. In the atmosphere so-called down-going neutrinos of all flavours interacting through charge or neutral currents can produce EAS potentially detectable by a large ground detector such as the Pierre Auger Observatory [4]. When propagating through the Earth only tau neutrinos skimming the Earth and producing an emerging tau lepton which decays in flight may initiate detectable air showers above the ground [5], [6].

One of the experimental challenges is to discriminate neutrino-induced showers from the background of showers initiated by UHECRs. The underlying concept of neutrino identification is rather straightforward. Whereas proton or nuclei and photons interact shortly after having entered the atmosphere, neutrinos may penetrate a large amount of matter undisturbed and generate showers close to the surface array. The differences between showers developing close to the detector – so-called young showers – and showers interacting early in the atmosphere – old showers – becomes more and more pronounced as we consider larger angles of incidence. In case of showers initiated by protons and nuclei, which interact soon after entering the atmosphere, only high-energy muons can survive at high zenith angles. As a result, the detected showers show a thin and flat front which leads to short detected signals (~ 100 ns). In case of young neutrino-induced showers a significant electromagnetic component (EM) is present at the ground as well. The shower front is curved and thick and leads to broad signals, lasting up to a few microseconds.

With the surface detector array (SD) of the Auger Observatory, which consists of 1600 water Cherenkov detectors with 1.5 km spacing, we can identify young showers because the signal in each tank is digitized with 25 ns time resolution, allowing us to distinguish the narrow signals in time expected from old showers, from the broad signals expected from a young shower.

In this contribution, we present the criteria used to identify neutrino-induced showers, the important observables, the neutrino identification efficiencies, and the procedure to simulate neutrino induced showers.

II. "EARTH-SKIMMING" TAU NEUTRINOS

The SD detector of the Auger Observatory is sensitive to Earth-skimming tau neutrinos [7], [8], [9]. These are expected to be observed by detecting showers induced by the decay of emerging τ leptons, after the propagation of of ν_τs through the Earth, see Fig. 1 (upper panel). The first step towards identification of ν_τ induced showers consists of selecting very inclined showers that have most of the stations with signals sufficiently spread in time. Young showers are expected to trigger detector stations with broad signals releasing a so-called 'Time Over Threshold' (ToT) trigger [7]. Counting ToTs stations can help identifying young showers. At this stage

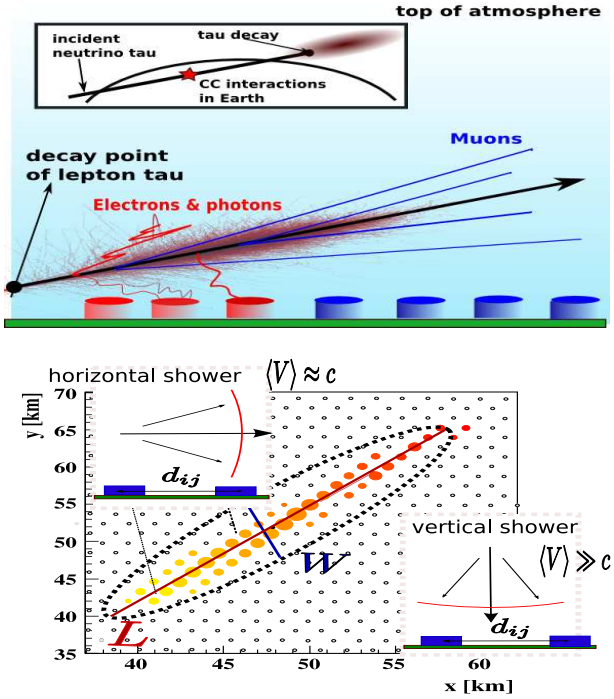

Fig. 1. (Upper panel) The sketch of a shower induced by the decay of a τ lepton emerging from the Earth after originating from an Earth-skimming ν_τ. The earliest stations are mostly triggered by electrons and γs; (bottom panel) sketch of length (L) over width (W) of a footprint and determination of the apparent velocity ($\langle V \rangle$). The $\langle V \rangle$ is given by averaging the apparent velocity, $v_{ij} = d_{ij}/\Delta t_{ij}$ where d_{ij} is the distance between couples of stations, projected onto the direction defined by the length of the footprint, L, and Δt_{ij} the difference in their signal start times.

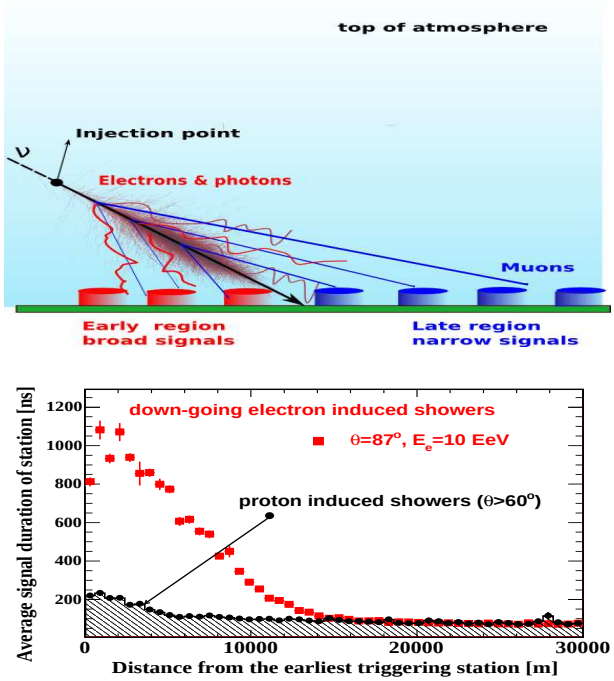

Fig. 2. (Upper panel) Sketch of a down-going shower initiated in the interaction of a ν in the atmosphere close to the ground; In the "early" ("late") region of the shower before (after) the shower axis hits the ground we expect broad (narrow) signals in time due to electromagnetic (muonic) component of the shower; (bottom panel) the average signal duration of the station as a function of the distance from the earliest triggering station.

also a cut of the area of the signal over its peak (AoP)[1] value is applied to reject ToT local triggers produced by consecutive muons hitting a station. Then the elongation of footprint, defined by the ratio of length (L) over width (W) of the shower pattern on ground, and the mean apparent velocity, are basic ingredients to identify very inclined showers [7], see Fig. 1 (bottom panel) for the explanation of these observables.

The mean apparent velocity, $\langle V \rangle$ is expected to be compatible with the speed of light for quasi-horizontal showers within its statistical uncertainty $\sigma_{\langle V \rangle}$ [8]. Finally compact configurations of selected ToTs complete the expected picture of young ν_τ-induced shower footprints. These criteria were used to calculate an upper limit on the diffuse flux UHE ν_τ [8] with the Auger Observatory and an update of this limit [9], [10].

III. "DOWN-GOING" NEUTRINOS

The SD array is also sensitive to neutrinos interacting in the atmosphere and inducing showers close to the ground [11], [12]. Down-going neutrinos of any flavours may interact through both charged (CC) and neutral current (NC) interactions producing hadronic and/or electromagnetic showers. In case of ν_e CC interactions, the resulting electrons are expected to induce EM showers at the same point where hadronic products induce a hadronic shower. In this case the CC reaction are simulated in detail using HERWIG Monte Carlo event generator [13]. HERWIG is an event generator for high-energy processes, including the simulation of hadronic final states and the internal jet structure. The hadronic showers induced by outgoing hadrons are practically indistinguishable in case of ν NC interactions, so they are simulated in the same way for three neutrino flavours. In case of ν_μ CC interactions the produced muon is expected to induce shower which are generally weaker i.e. with a smaller energy transfer to the EAS, and thus with suppressed longitudinal profile and much fewer particles on ground. As a consequence, the detection probability of such shower is low and therefore the produced muon is neglected and only the hadronic component is simulated with the same procedure adopted for ν NC interactions. In case of down-going ν_τ the produced τ lepton can travel some distance in the atmosphere, and then decay into particle which can induce a detectable shower. Thus, the outcoming hadronic showers initiated by ν_τ interactions are usually separated by a certain distance from the shower initiated by the tau decay. In this particular case, τ decays were simulated using TAUOLA [16]. The secondary particles produced by HERWIG or TAUOLA are injected into the extensive air shower generator AIRES [17] to produce lateral profiles of the shower development. Shower simulations were

[1]The peak corresponds to the maximum measured current of recorded trace at a single water-Cherenkov detector.

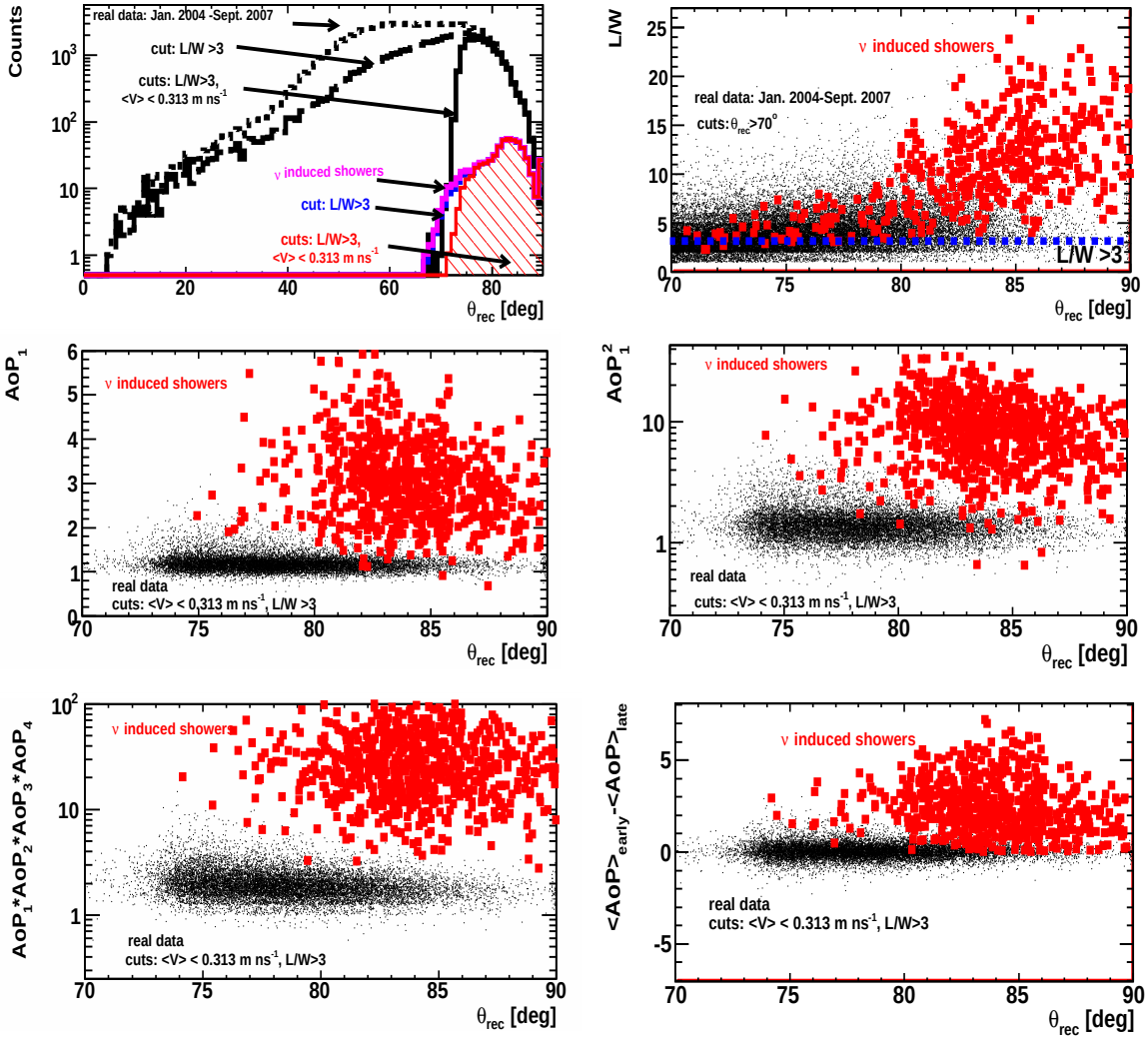

Fig. 3. (Left upper panel) The zenith angle distribution of neutrinos with E^{-2} flux and real events; (right upper panel) the ratio L/W as the function of the reconstructed zenith angle. Neutrino induced showers have larger ratio L/W than real data at high zenith angles. The area over peak for first triggering station (AoP_1) (left middle panel) the square of the area over peak for first triggering station (AoP_1^2) (right middle panel), the product of AoP of four first triggering stations (left bottom panel) and a global early-late asymmetry parameter ($\langle\mathrm{AoP}\rangle_{early} - \langle\mathrm{AoP}\rangle_{late}$) as the function of zenith angle.

performed including the geographic conditions of the site (e.g. geomagnetic field) for different zenith angles $\theta = 75°, 80°, 85°, 87°, 88°$ and $89°$ and random azimuth angles between $0°$ and $360°$ and different hadronic models: QGSJET II [14] and Sibyll [15]. The secondary particles are injected at different slant depths measured from the ground up to a maximum value depending on θ. Finally the response of the SD array is simulated in detail using the Offline simulation package [18]. In total about 20,000 showers induced by down-going decaying τ leptons were simulated and about 36,000 events for electron induced showers. These neutrino simulations were used to estimate the expected neutrino signal and efficiency of detection of the neutrinos.

The criterion to identify young, inclined, down-going showers consists of looking for broad time signals as in the case of up-going neutrinos, at least in the early region, i.e. in those stations triggered before the shower core hits the ground [12]. The physical basis for this criterion is the large asymmetry in the time spread of signals that one expects for very inclined young showers, in which the late front of the shower typically has to cross a much larger grammage of atmosphere than the early front, and as a consequence suffers more attenuation, see Fig. 2 (upper panel). This has been confirmed by simulations of ν-induced showers as is shown in Fig. 2 (bottom panel). The time signal for ν-showers is expected to be broader around the position of the maximum of the shower development. Broader signals are expected to last about 1000 ns, while the duration decreases to a value of about 150 ns downstream in the latest stations which are hit by the muonic tail of the shower development. For hadronic showers with $\theta > 60°$, the expected duration of the signals is almost constant with an average value of about 150 ns. From Fig. 2 (bottom panel) we can see that a good identification criterion is to require broad signals in the first triggered stations of an event.

In the case of down-going neutrinos the general procedure to extract a neutrino induced shower from real

data is similar to the procedure used for Earth-skimming neutrinos, i.e. the inclined events are extracted from real data using the apparent velocity and L/W cut and the criterion for looking for events with broad signal in time are applied. However, there are some differences. The selection criteria cannot be the same as for up-going ν_τ, because in case of down-going neutrinos we are sensitive for a larger zenith angle range (about 15° above the horizon instead about 5° below horizon for up-going ν_τ), which also means a larger background contribution and thus a more demanding selection procedure [10].

In Fig. 3 (left upper panel) the zenith angle distribution of real data and simulated neutrino events is shown. The $\langle V \rangle$ and the ratio L/W cut can extract inclined events from real data, see also Fig. 3 (right upper panel). To extract young showers with broad signals, the area over the peak (AoP) of the first four stations its square (AoP^2), their product (AoP_1*AoP_2*AoP_3*AoP_4) and a global early-late asymmetry parameter of the event $(\langle \mathrm{AoP} \rangle_{early} - \langle \mathrm{AoP} \rangle_{late})^2$ can be used. These observables were used to discriminate neutrino showers by using the Fisher method, see [10] for more details. As an example in Fig. 3 (middle panels) distributions of AoP_1 and AoP_1^2 for the first triggering station are shown. In Fig. 3 (lower panels) we also show the product AoP_1*AoP_2*AoP_3*AoP_4 (left panel) and the global early-late asymmetry parameter $\langle \mathrm{AoP} \rangle_{early} - \langle \mathrm{AoP} \rangle_{late}$ (right panel) for real data and MC simulated neutrinos. The good separation is clearly visible between neutrino simulated showers and measured inclined events. The separation is better at large zenith angles where the background signal (real data events) is less abundant. This example demonstrates that the SD array has a satisfactory discriminating power against the larger background of nucleonic showers at zenith angles larger than about 75°.

In Fig. 4 the neutrino identification efficiency, ϵ (the fraction of ν-induced showers triggering SD array and passing the neutrino identification criteria [10]) is shown. It is clear that ϵ depends on the zenith angle and type of interactions. The efficiency as well as the range of slant depth grows as the zenith angle increases. Only for showers very close to the SD array does it drop dramatically since the shower does not cross sufficient grammage to develop in the direction transverse to the shower axis. The efficiencies for NC are much lower than for CC for the same neutrino energy and zenith angle. This is due to the fact that in NC reactions the fragments of a target nucleus induce a pure hadronic shower with a small fraction (about 20%) of energy transfered to the EAS while in CC ν_e reaction the rest of the energy goes to an additional EM shower. The identification efficiency depends also on the neutrino

[2]The global early-late asymmetry parameter is defined as the difference between average value of AoPs calculated for the first triggered stations and the last triggered stations of the event. If the number of stations is odd the station in middle is ignored. If the event multiplicity is larger than 8 stations only the first/last four stations are used.

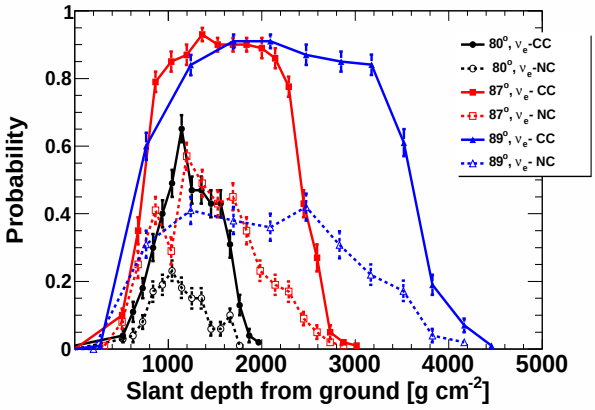

Fig. 4. The ν_e identification efficiency as a function of the neutrino interaction point for different zenith angle and energy 1 EeV.

flavour due to different energy fractions transferred to the induced shower. In CC ν_τ interactions, if the lepton tau decays in flight, only a fraction of its energy is converted into a τ-induced shower. In a ν_μ CC interaction, the produced muon induce a shower which is in general weaker, with a small energy transfer to an EAS with very low probability to trigger the SD array. Thus the ν_e CC induced showers give the main contribution to the expected event rate.

IV. Conclusions

To conclude we have shown that neutrino induced shower can be identified by the SD of the Auger Observatory. The key to for ν identification is the presence of a significant EM component. By means of Monte Carlo simulations we have identified the parameter space where the efficiency of neutrino identification is significant.

References

[1] F. Halzen, D. Hooper, Rep. Prog. Phys. 65 (2002) 1025.
[2] V. S Berezinsky et al.,Phys. Lett. B 28 (1963) 423.
[3] R. Engel et al. Phys. Rev. D 64 (2001) 093010; D. Allard et al., J. Cosmol. Astropart. Phys. 9 (2006) 5, L. Anchordoqui et al., Phys. Rev. D 76, (2007) 123008.
[4] J. Abraham, et al., Nucl. Instrum. Meth. A523 (2004) 50.
[5] A. Letessier-Selvon, AIP Conf. Proc. 566 (2001) 157; D. Fargion, Astrophys. J. 570 (2002) 909.
[6] X. Bertou et al., Astropart. Physc. 17 (2002) 183.
[7] O. Blanch Bigas [The Pierre Auger Collaboration], Procs. of 30th ICRC 2007; P. Billoir, O.Blanch Bigas, Nucl. Phys. Proc. Suppl. 168 (2007) 225.
[8] J. Abraham et al., Phys. Rev. Lett. 100 (2008) 211101.
[9] J. Abraham et al., Phys. Rev. D 79 (2009) 102001.
[10] J. Tiffenberg [The Pierre Auger Collaboration], these proceedings.
[11] K. S. Capelle et al., Astropart. Phys. 8 (1998) 321; P. Billoir et al., Procs. of the Neutrino Oscillation Workshop 2006, Lecce, Italy.
[12] J. Alvarez-Muñiz [The Pierre Auger Collaboration], Proc. 30th ICRC 2007; I. Valiño (PhD thesis) Univ. de Santiago de Compostela, ISBN 9788497509664, 2008.
[13] Herwig 6.5, G. Corcella et al., JHEP 0101 (2001) 010.
[14] S. S. Ostapchenko, Nucl. Phys. Proc. Suppl. 151B (2006) 143.
[15] R. Engel et al., Proc. of the 26th ICRC (1999) 144.
[16] S. Jadach et al., The tau decay library TAUOLA: Version 2.4, Comput. Phys. Commun. 76 (1993) 361.
[17] S. Sciutto, AIRES (AIRshower Extended Simulations) web-site:http://www.fisica.unlp.edu.ar/auger/aires/
[18] S. Argiró et al., Nucl. Instrum. Meth. A580 (2007) 1485.

Sensitivity of Extensive Air Showers to Features of Hadronic Interactions at Ultra-High Energies

Ralf Ulrich, Ralph Engel, Steffen Müller, Tanguy Pierog, Fabian Schüssler and Michael Unger

Karlsruher Institut für Technologie (KIT)[1]
Institut für Kernphysik, P.O. Box 3640, 76021 Karlsruhe, Germany

***Abstract*. We study the dependence of extensive air shower development on the first hadronic interactions at ultra-high energies occurring in the startup phase of the air shower cascade. The interpretation of standard air shower observables depends on the characteristics of these interactions. Thus, it is currently difficult to draw firm conclusions for example on the primary cosmic ray mass composition from the analysis of air shower data. On the other hand, a known primary mass composition would allow us to study hadronic interactions at center of mass energies well above the range that is accessible to accelerators measurements.**

***Keywords*: Hadronic interactions, extensive air showers, ultra-high energies**

I. Introduction

Currently, the interpretation of existing high quality air shower data in terms of important properties as e.g. the primary mass composition, is complicated by the poorly constraint hadronic interaction physics at ultra-high energies (e.g. Ref. [1]). For an unambiguous analysis of air shower data reduced uncertainties of interaction characteristics are needed.

The longitudinal development of extensive air showers is very sensitive to hadronic interaction in the startup of the air shower cascade. These few interactions at ultra-high energies are subject to particularly large uncertainties; Their characteristics must be inferred from extrapolations of accelerator data at much lower energies to cosmic-ray energies and secondary particle production phase space. These extrapolations are not well constraint by theory nor experiment [2]. To explore the importance of these extrapolations to ultra-high energies on the final resulting air shower observables, we modified these extrapolations during air shower simulations.

If, with the help of astrophysical arguments, the composition of cosmic rays of a specific energy can be constraint, then it is possible to learn about the physics of hadronic interactions at energies far above the LHC from the analysis of air shower data. This would allow one to use ultra-high energy cosmic ray observatories as fixed target particle physics experiments at energies up to $\sqrt{s} \sim 450\,\mathrm{TeV}$, which is far above the reach of any Earth-based particle accelerator.

[1]KIT is the cooperation of University Karlsruhe and Forschungszentrum Karlsruhe

II. Modified Air Shower Simulations

For our studies we implemented a modified version of the CONEX [4] air shower simulation program that can modify the characteristics of hadronic interactions during the simulation. We adapt the following factor to re-scale specific properties of hadronic interactions:

$$f(E) = 1 + (f_{19} - 1)\, F(E) \qquad (1)$$

with

$$F(E) = \begin{cases} 0 & E \leq 1\,\mathrm{PeV} \\ \frac{\ln(E/1\,\mathrm{PeV})}{\ln(10\,\mathrm{EeV}/1\,\mathrm{PeV})} & E > 1\,\mathrm{PeV} \end{cases} , \qquad (2)$$

where E is the energy of the projectile of the interaction. The factor $F(E)$ is 0 below 10^{15} eV, and thus $f(E) = 1$, where accelerator data is available to constrain the models (the Tevatron corresponds to $\sim 2 \times 10^{15}$ eV). At higher energies $F(E)$ is increasing logarithmically with energy, reflecting the growing uncertainty of the extrapolation with energy. The resulting impact of $f(E)$ on the extrapolation of the production cross section is shown in Fig. 1. By using Eq. (1) for all interactions during the simulated air shower development with energies above 10^{15} eV, the effect of the modified extrapolation to ultra-high energies affects not only the primary cosmic ray-air interaction, but also the high energy interactions in the startup phase of the air shower, until the energy of the particles drops below 10^{15} eV.

The interactions of hadrons, and thus in particular of primary proton cosmic ray particles, are directly

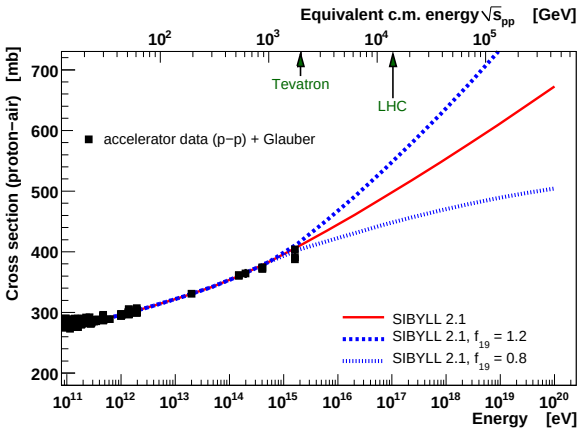

Fig. 1. Example of a modified hadronic production cross section for SIBYLL for a 20 % increase and decrease of f_{19} [8].

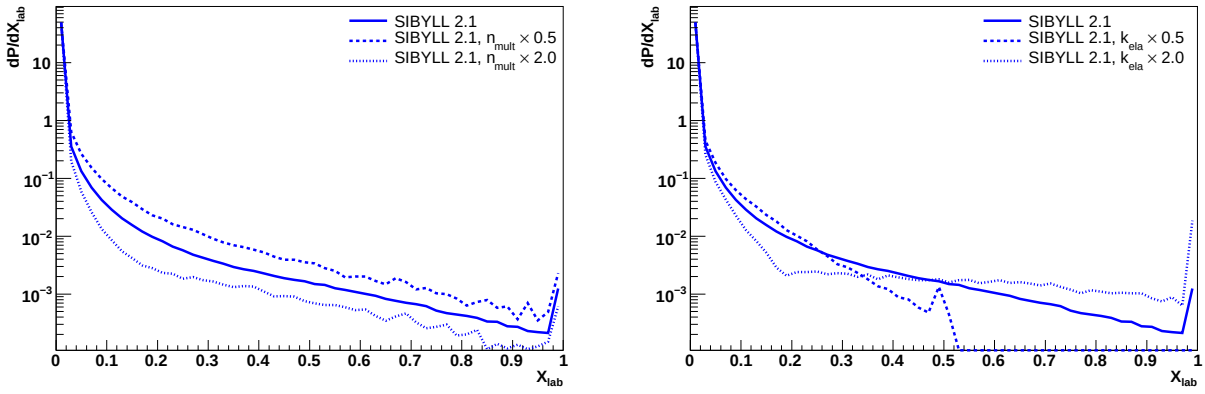

(a) Multiplicity (b) Elasticity

Fig. 2. Impact of secondary particle resampling on $X_{\rm lab}$-distributions [3].

modified by using the factor Eq. (1). For nuclei, however, the semi-superposition model [5, 6] is applied in order to describe the interactions of nuclei based on the fundamental hadronic interactions of the individual nucleons of the nucleus. Since this model is implemented within the SIBYLL event generator [7], the handling of primary nucleons is straightforward and all results presented here are based on the SIBYLL model.

To change characteristics of the secondary particle production, like e.g. the multiplicity or the elasticity, we developed a secondary particle re-sampling algorithm that, by deletion or duplication of existing particles and re-distributing of kinetic energy between secondary particles, can achieve to modify these characteristic properties. At the same time great care is invested to conserve all relevant physical quantities such as the total energy, leading particles, charge, particle types and energy fractions in particle type groups as far as possible. Also the momentum of all particles is consistently re-calculated. A detailed description of the algorithm can be found in Ref. [3]. In Fig. 2 the impact of the resampling algorithm for multiplicity and elasticity on secondary particle $X_{\rm lab}$-distributions is displayed. For the modified multiplicity the number of particles is rescaled, while leaving the shape of the $X_{\rm lab}$-distribution almost untouched, in particular the leading particle is conserved. In the case of a modified elasticity kinetic energy is re-distributed between the leading particle and the rest of the secondaries. For an increased elasticity the leading particle inherits energy from the other particles, so these particles are accumulating at lower energies. For the decreasing elasticity the leading particle looses significance by a reduction of its energy. This leads to a generally more uniform distribution of the total energy on all the secondaries, and in the limiting case to the equal distribution of energy on all secondaries.

For our study we simulated 1000 air showers for each value of f_{19}. All simulations were performed at primary energies of $10^{19.5}$ eV for proton and iron primaries.

III. RESULTS

We are concentrating on three features of hadronic interactions, that can be easily attributed a direct impact on air shower development. These are the hadronic production cross section σ, secondary multiplicity $n_{\rm mult}$ and the elasticity $k_{\rm ela} = E/E_{\rm tot}$. Extended Heitler models (e.g. Ref. [9]) exhibit the relation between these quantities to air shower observable as $X_{\rm max}$

$$X_{\rm max} \approx \lambda_{\rm int} + \lambda_r \cdot \ln \frac{E_0(1-k_{\rm ela})}{n_{\rm mult} \cdot E_{\rm crit}^{\rm e.m.}}\,, \qquad (3)$$

where λ_r is the electromagnetic radiation length and $E_{\rm crit}^{\rm e.m.}$ the critical energy in air.

To demonstrate the impact of these interaction features on the air shower development we simulate the effect on the depth of the shower maximum, $X_{\rm max}$, and on the total number of electrons above $1\,{\rm MeV}$, $N_{\rm e}$, and muons above $1\,{\rm GeV}$, N_μ, after $1000\,{\rm g/cm^2}$ of shower development.

The quantity that is affected most directly is $X_{\rm max}$, see Eq. (3); The effects on $N_{\rm e}$ and N_μ can be mostly understood relative to $X_{\rm max}$ - as the consequence of a changing distance from the shower maximum to the observation level.

The results for proton primaries are summarized in Fig. 3 and for iron primaries in Fig. 4.

A. Cross section

A changing cross section has a strong impact on $X_{\rm max}$. Both the mean as well as the fluctuations are affected. Especially for the fluctuation, the cross section is much more important than any other hadronic interaction feature. The effect on the electron number is related to the changing distance from the shower maximum to the observation level. Muon are only weakly affected.

For iron primaries the effects are very much reduced. Interestingly the impact on the mean $X_{\rm max}$ is still very notable, while it changes the fluctuations only by up to a few g/cm^2.

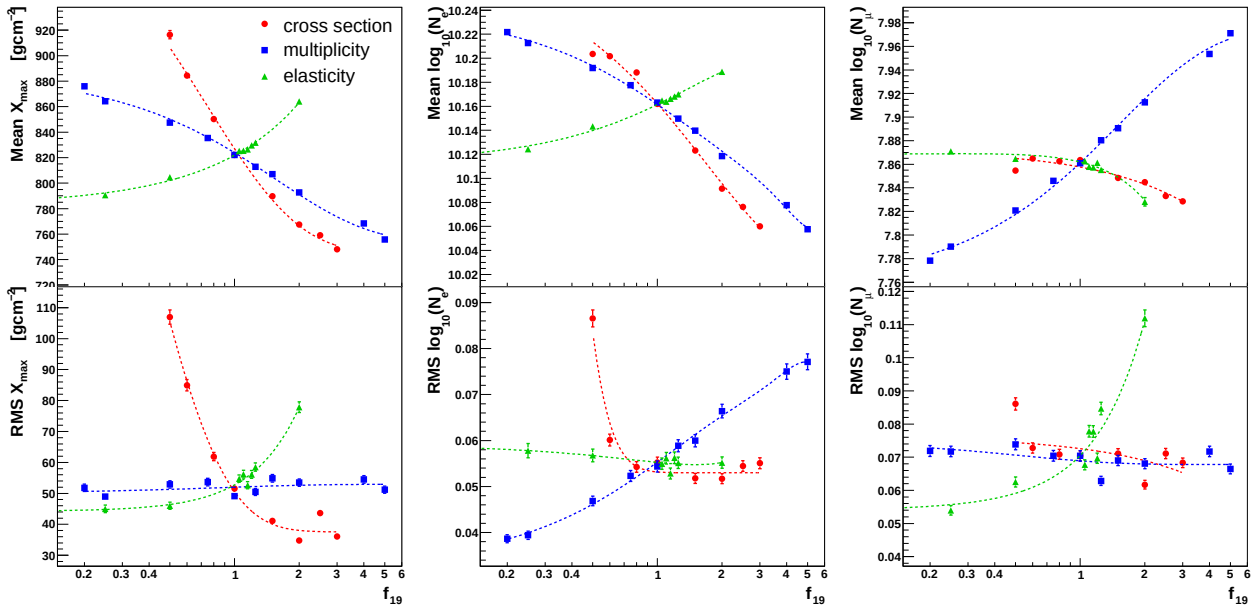

(a) Shower maximum, $X_{\max}$ (b) Electrons, N_{e} (c) Muons, N_{μ}

Fig. 3. Effect of changing interaction characteristics on proton induced air showers. Shown is the impact on the observables $X_{\max}$, N_{e} and N_{μ}. Each data point is the mean value for 1000 simulated air showers at a primary energy of $10^{19.5}$ eV. The lines are just to guide the eye.

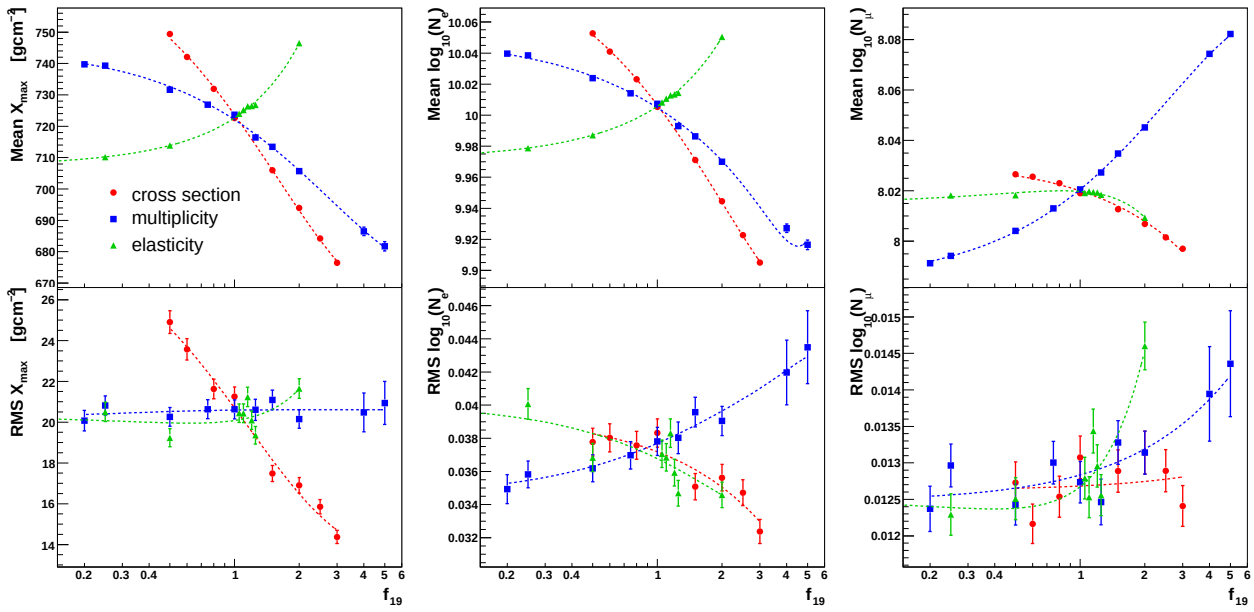

(a) Shower maximum, $X_{\max}$ (b) Electrons, N_{e} (c) Muons, N_{μ}

Fig. 4. Effect of changing interaction characteristics on iron induced air showers. Shown is the impact on the observables $X_{\max}$, N_{e} and N_{μ}. Each data point is the mean value for 1000 simulated air showers at a primary energy of $10^{19.5}$ eV. The lines are just to guide the eye.

B. Multiplicity

The multiplicity shifts the mean value of $X_{\max}$ while leaving its fluctuations almost untouched. The electron number is reduced for a growing multiplicity, since the shower maximum moves further away from the detector level. This is also why the fluctuations are increasing at the same time. The muon number, on the other hand, grows since it does not depend strongly on the distance to the shower maximum. This inverse reaction of electron and muon numbers on a changing multiplicity certainly has interesting implications on N_{e}/N_{μ} unfolding technique, as practiced e.g. by the KASCADE Collaboration [1]; By changing the multiplicity, the model predictions move on diagonal lines in the N_{e}/N_{μ}-plane.

The same effects are observed on a reduced scale for iron primaries.

C. Elasticity

The elasticity has an influence on the mean as well as RMS of the $X_{\max}$ distribution. The case of an increased elasticity by $f_{19} = 2$, as we included it in our results, is the most extreme modification of hadronic interactions that we present; The elasticity is not expected to rise at ultra-high energies. Again, the electron number reacts to the shifting $X_{\max}$. A surprisingly strong effect is observed in the fluctuations of the muon signal.

The latter effect disappears for iron primaries. The impact on $X_{\max}$ and N_{e} is comparable to the one induced by multiplicity and cross section.

IV. SUMMARY

We demonstrate the importance of the extrapolation of hadronic interaction features from accelerator data to ultra-high energies for air shower development. For this purpose hadronic interactions are modified during the air shower simulation process within a customized version of the CONEX program.

It is found that the resulting impact on air shower observables is much larger than by just considering the properties of the single first interaction of the primary cosmic ray particle in the atmosphere. For example the predicted value of $\langle X_{\max} \rangle$ for primary iron nuclei changes by up to $> 30\,\mathrm{g/cm^2}$ while changing the cross section by a factor of 2; Since the mean free path of iron in air itself is only $\sim 8\,\mathrm{g/cm^2}$ a change by a factor of 2 can only explain 4 respectively $16\,\mathrm{g/cm^2}$ of the total impact. The remaining shift of $\langle X_{\max} \rangle$ is in fact originating from a different air shower development after the first interaction.

Currently, the existing uncertainties in interaction physics at cosmic ray energies prevent an unambiguous interpretation of air shower data in terms of e.g. the primary cosmic ray mass composition.

The demonstrated sensitivity of standard air shower observables on hadronic interactions characteristics can be exploited to put constrains on hadronic interaction physics at energies far above the LHC. Furthermore, if the composition of the cosmic ray flux in a specific energy region can be inferred from astrophysical considerations, existing and future high quality air experiments [10 - 13] can be used in order to explore particle physics up to $\sqrt{s} \sim 450\,\mathrm{TeV}$. This is possible for proton cosmic ray primaries but, with somewhat limited sensitivity, also for primary iron nuclei.

REFERENCES

[1] Antoni, T. *et al.* [KASCADE Collaboration], *KASCADE measurements of energy spectra for elemental groups of cosmic rays: Results and open problems*, Astropart. Phys. **24** (2005) 1-25.

[2] R. Engel, *Extensive air showers and accelerator data: The NEEDS workshop*, Nucl. Phys. Proc. Suppl. **122** (2003) 437 [arXiv:hep-ph/0212340].

[3] R. Ulrich, R. Engel, F. Schüssler and M. Unger, *Impact of hadronic interaction characteristics at ultra-high energies on extensive air shower observables*, In preparation

[4] Bergmann, T *et al.*, *One-dimensional hybrid approach to extensive air shower simulation*, Astropart. Phys. **26** (2007) 420-432 [astro-ph/0606564].

[5] Engel, J., Gaisser, T.K., Stanev, T. and Lipari, P., *Nucleus-nucleus collisions and interpretation of cosmic ray cascades*, Phys. Rev. **D46** (1992) 5013-5025.

[6] Bialas, A., Bleszynski, M. and Czyz, W., *Multiplicity Distributions in Nucleus-Nucleus Collisions at High-Energies*, Nucl. Phys. **B111** (1976) 461

[7] Fletcher, R.S., Gaisser, T.K., Lipari, P. and Stanev, T., *SIBYLL: An Event generator for simulation of high-energy cosmic ray cascades*, Phys. Rev. **D50** 5710-5731.

[8] R. Ulrich, R. Engel, S. Müller, F. Schüssler and M. Unger, to appear in Proceedings of the 15^{th} ISVHECRI, Paris 2008.

[9] J. Matthews, *A Heitler model of extensive air showers*, Astropart. Phys. **22** (2005) 387-397

[10] Abbasi, R.U. *et al.* [HiRes Collaboration], *A study of the composition of ultra high energy cosmic rays using the High Resolution Fly's Eye*, Astrophys. J. **622** (2005 910-926 [astro-ph/0407622].

[11] Abraham, J. *et al.* [Pierre Auger Collaboration], *Properties and performance of the prototype instrument for the Pierre Auger Observatory*, Nucl. Instrum. Meth. **A523** (2004) 50

[12] Kawai, H. *et al.* [TA Collaboration], Nucl. Phys. Proc. Suppl. **175-176** (2008) 221-226

[13] Harton, J. [Pierre Auger Collaboration], *The Northern Pierre Auger Observatory*, these proceedings

Fluorescence emission induced by extensive air showers in dependence on atmospheric conditions

Bianca Keilhauer*, Michael Unger*

**Karlsruhe Institute of Technology (KIT),*
Forschungszentrum Karlsruhe, Institut für Kernphysik, P.O.Box 3640, 76021 Karlsruhe, Germany

***Abstract*. Charged particles of extensive air showers (EAS), mainly electrons and positrons, initiate the emission of fluorescence light in the Earth's atmosphere. This light provides a calorimetric measurement of the energy of cosmic rays. For reconstructing the primary energy from an observed light track of an EAS, the fluorescence yield in air has to be known in dependence on atmospheric conditions, like air temperature, pressure, and humidity. Several experiments on fluorescence emission have published various sets of data covering different parts of the dependence of the fluorescence yield on atmospheric conditions.**

Using a compilation of published measurements, a calculation of the fluorescence yield in dependence on altitude is presented. The fluorescence calculation is applied to simulated air showers and different atmospheric profiles to estimate the influence of the atmospheric conditions on the reconstructed shower parameters.

***Keywords*: atmosphere-dependent fluorescence emission, temperature-dependent collisional cross sections, vapour quenching**

I. Introduction

The number of emitted fluorescence photons at the air shower can be written as

$$\frac{d^2N_\gamma^0}{dXd\lambda} = Y(\lambda, P, T, e) \cdot \frac{dE_{\rm dep}^{\rm tot}}{dX}, \tag{1}$$

where $Y(\lambda, P, T, e)$ is the fluorescence yield in dependence on wavelength λ, air pressure P, air temperature T, and vapour pressure e. The deposited energy of the secondary particles is denoted as $dE_{\rm dep}^{\rm tot}/dX$.

In the last couple of years, a lot of effort has been put on the investigation of atmospheric dependences on nitrogen fluorescence in air [1]. The fluorescence yield Y_λ can be written as

$$Y_\lambda = \Phi_\lambda^0 \cdot \lambda/hc \cdot \frac{1}{1 + P/P_v'}, \tag{2}$$

where Φ_λ^0 is the fluorescence efficiency at zero pressure, P is the air pressure, and P' is the characteristic pressure for which the probability of collisional quenching equals that of radiative de-excitation. The index v indicates the vibrational level of the exited state. Several groups have already investigated aspects of the fluorescence emission from nitrogen molecules in air (e.g. Bunner [2], Davidson & O'Neil [3], Kakimoto et al. [4], MACFLY [5] and FLASH [6]). In addition there are various ongoing experimental activities, e.g. AIRFLY [7], [8], [9], [10], Nagano & Sakaki et al. [11], [12], AirLight [13] and Ulrich & Morozov et al. [14]. One major goal of all experiments is to obtain an absolute fluorescence yield $Y_\lambda^0 = \Phi_\lambda^0 \cdot \lambda/hc$ either for the main contributing band at 337.1 nm or for the entire spectrum in the range of interest between about 300 – 420 nm. Y_λ^0 represents the intrinsic radiative de-excitation of the nitrogen molecules. However, in gas like air quenching processes have to be taken into account because the rate of radiative de-excitations is reduced by collisions between excited nitrogen molecules and further molecules in the gas. These quenching processes depend on atmospheric conditions and are described by $(1+P/P_v')^{-1}$ in Eq. (2). Accounting all currently known effects, we can write

$$\begin{aligned}\frac{P}{P_v'} = {} & \frac{\tau_{0,v} \cdot P_{\rm air} \cdot N_A}{R \cdot T_{\rm air}} \cdot \sqrt{\frac{k \cdot T_{\rm air} \cdot N_A}{\pi}} \\ & \cdot \Bigg(4C_{\rm vol}({\rm N}_2) \cdot \sigma_{{\rm NN},v}(T) \sqrt{M_{\rm N}^{-1}} \\ & + 2C_{\rm vol}({\rm O}_2) \cdot \sigma_{{\rm NO},v}(T) \sqrt{2\Big(M_{\rm N}^{-1} + M_{\rm O}^{-1}\Big)} \\ & + 2C_{\rm vol}({\rm H_2O}) \cdot \sigma_{{\rm NH_2O},v}^0 \sqrt{2\Big(M_{\rm N}^{-1} + M_{\rm H_2O}^{-1}\Big)} \Bigg),\end{aligned} \tag{3}$$

with $\tau_{0,v}$ as the mean life time of the radiative transition to any lower state, the index v indicates again the vibrational level of the exited state as for P_v', N_A is Avogadro's number, R is the universal gas constant, $T_{\rm air}$ is the air temperature, k is the Boltzmann constant, $C_{\rm vol}$ is the fractional part per volume of the relevant gas constituents, and M_x is the mass per mole where x stands for the relevant gas constituents. Up to now, the collisional cross sections $\sigma_{{\rm N}x,v}$ have been taken as temperature-independent even though it was known from theory that there has to be a temperature dependence. Recently, first experiments could confirm this dependence for nitrogen-nitrogen and nitrogen-oxygen quenching. The temperature-dependence of the nitrogen-vapour quenching has not been measured yet. First estimates indicate only minor importance with an effect of less than 1% change in the reconstructed energy of an air shower [15]. An independent measurement of the temperature-dependent collisional cross sections in air has been performed quite recently. First analyses of data indicate compatible results with the measurements from AIRFLY and will be published soon [15].

Adopting this description of fluorescence emission for air shower reconstruction, we have to apply atmospheric profiles for temperature, pressure, and vapour pressure. This cannot be provided by simple atmospheric models as these usually do not include vapour profiles. However, profiles obtained with meteorological radio soundings do provide all necessary quantities [16].

II. Fluorescence Models in Reconstruction

For this study, we could use the simulation and reconstruction framework Offline [17] of the Pierre Auger Observatory [18]. Within this framework, we could obtain standard monthly models for the area of that observatory which do not include water vapour profiles [16]. Additionally, we had access to 109 actual nightly atmospheric profiles from local radio soundings that cover all conditions within a year. One of the advantages of the framework is that it features many implementations of different fluorescence models which can easily be interchanged.

The first implementation of a fluorescence model in Offline, referred to as K96, is based on measurements by Kakimoto et al. [4]. The fluorescence yield is parametrised in dependence on deposited energy and on altitude by considering the pressure and $\sqrt{T}$-dependences. The second fluorescence model, N04, has the same functional form of parametrisation and describes data from Nagano et al. [19], [11]. These measurements provide spectrally resolved data for 15 wavelengths between 300 and 430 nm. Also in this description, only the pressure and $\sqrt{T}$-dependences are considered. The third fluorescence description in Offline is given by the AIRFLY Collaboration in 2007, labelled with A07. The fluorescence yield is given as [9]

$$Y_\lambda(P,T) = Y^{337}_{P_0,T_0} \cdot I^\lambda_{P_0,T_0} \cdot \frac{1+\frac{P_0}{P'(\lambda,T_0)}}{1+\frac{P_0}{P'(\lambda,T_0)\sqrt{T/T_0}}}. \quad (4)$$

$Y^{337}_{P_0,T_0}$ is the fluorescence yield at 337.1 nm as measured at their standard experimental conditions which are P_0 = 800 hPa and T_0 = 293 K. The other transitions have been measured relatively to that at 337.1 nm and are given by $I^\lambda_{P_0,T_0}$. Overall, 34 transitions could be resolved between 295 and 430 nm. Since the absolute calibration of this experiment is still under study, Y_{337} is normalised to the corresponding value of N04. It should be pointed out that the description in this model can easily be expanded to account for vapour quenching and temperature-dependent collisional cross sections. The fourth implementation of a fluorescence model follows the calculation from Keilhauer et al. in 2008 [20]. Here, 23 wavelengths between 300 and 430 nm are considered by applying Eq. (2) and (3). The model uses a compilation of different measurements [20], [21]. For the temperature-dependent collisional cross sections, the data from AIRFLY [9] are used. These α-coefficients are obtained in air, so the same α_λ is applied to NN-collisions and NO-collisions. The temperature-dependent collisional cross sections in Eq. (3) are written as $\sigma_{\mathrm{N}x,\nu}(T) = \sigma^0_{\mathrm{N}x,\nu} \cdot T^{\alpha_\nu}$ where $\sigma^0_{\mathrm{N}x,\nu} = \sigma_{\mathrm{N}x,\nu} \cdot 293^{-\alpha_\nu}$ is the measured temperature-independent cross section at standard experimental conditions of T = 293 K. Cross sections for nitrogen - water vapour collisions have been measured by two experiments [22], [23].

III. Atmosphere-dependent Fluorescence Emission

To study the overall effect of different fluorescence models on reconstructed air shower observables, primary energy E and position of shower maximum $X_{\max}$, it is important to account for only that part of the fluorescence spectrum that a detector is sensitive to as well as the wavelength dependent attenuation in the atmosphere (see for instance Fig. 8d in [11]). Moreover, since the atmospheric parameters P, e and T depend on altitude, different fluorescence models will propagate differently to E and $X_{\max}$ if the shower reached its maximum high in the atmosphere or close to the ground.

To include all these effects, we proceeded as follows: Proton and iron showers with energies between $10^{17.5}$ and 10^{20} eV were generated using Conex [24] and QGSJETII [25]. The fluorescence light was generated according to the K08 model including water vapour quenching and temperature-dependent collisional cross sections. The events were generated with time stamps that corresponds to nights with balloon launches, such that realistic profiles for P, e and T could be obtained. In the following, we will compare the difference in the reconstructed E and $X_{\max}$ values of these simulated showers.

A. Fluorescence Models

The $X_{\max}$ and energy differences for reconstructions with different fluorescence models is shown in Fig. 1. For this figure, the water vapour quenching and temperature-dependent collisional cross sections were *not* switched on in the K08-model, thus this comparison is only sensitive to the $Y(P,T)$ implementations. As explained above, the A07 model is normalised to N04, therefore they are not independent and show correspondingly the smallest differences.

B. Temperature-dependent collisional cross sections and vapour quenching

The influence of the water vapour quenching (σ_e) and temperature-dependent collisional cross sections (σ_T) on $X_{\max}$ and E was studied by subsequently switching off the effects in the reconstruction using the K08-model. As can be seen in the left panel of Fig. 2, ignoring σ_e- and σ_T-effects leads to an underestimation of the reconstructed energy by about 5%. Both σ_e- and σ_T-dependences affect the shape of the longitudinal profile. Since the σ_e-dependence is most important close to ground and the σ_T-dependence affects mainly higher altitudes, the two effects partially compensate (see right

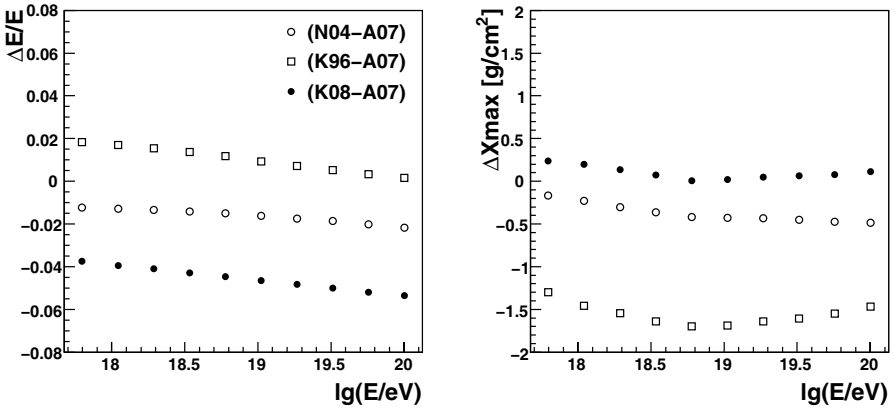

Fig. 1. Comparison of the influence of different fluorescence models on E and $X_{\max}$ (without vapour quenching and temperature-dependent collisional cross sections). The abbreviations of the different fluorescence models are defined in Sec. II.

panel of Fig. 2) leading to only a small $X_{\max}$ shift of $\leq$ 2 g cm^{-2}.

Interchanging the water vapour quenching from [22] with the independent measurement from [23] affects the shower observables very little (see solid black dots in Fig. 2).

The varying strengths of the σ_e- and σ_T-dependences at different altitudes can be seen in Fig. 3. Ignoring the σ_T-effect, the energy is misreconstructed up to -7% for showers with $X_{\max}$ high up in the atmosphere. Ignoring the σ_e-dependence, the energy is underestimated also up to 7% for showers with $X_{\max}$ close to ground. The position of shower maximum is also affected with the largest biases being observed for deep and shallow showers. The overall shift of $X_{\max}$ is strongest for showers with a position of shower maximum at about 3 km a.s.l. with -5 g cm^{-2} or for showers with $X_{\max}$ at 9 km a.s.l. with 5 g cm^{-2}. It can clearly be seen in the right-hand plot of Fig. 3 that the σ_e-dependence cancels out partly the σ_T-dependence concerning $X_{\max}$.

IV. Discussion of Results

In the fluorescence model K08, all currently known effects of the fluorescence light emission are included in dependence on varying atmospheric conditions. Running this model in combination with actual atmospheric profiles, gives a good estimate of the overall misreconstruction and uncertainties of a standard reconstruction. However, it must be stressed that all of the models used in this study have a reported uncertainty of the absolute fluorescence yield well above 10%. In particular, the AIRFLY and AirLight experiments will perform an absolute fluorescence yield calibration with higher accuracy and results can be expected within one year.

In Fig. 4, the difference of the reconstruction of E and $X_{\max}$ using the K08 model with all effects in combination with actual atmospheric profiles and a standard reconstruction with the A07 fluorescence model with monthly models can be seen. More or less independent of energy, the reconstructed primary energy E is higher by about 5% using K08 compared with A07 model. The position of shower maximum $X_{\max}$ is nearly unaffected. These results are very similar to the comparison of the full K08 model and that without σ_e- and σ_T-dependences. Thus, no additional systematics are introduced while changing the fluorescence model apart from those obtained by the σ_e- and σ_T-dependences.

Studying the variation in E and $X_{\max}$ in dependence on the height of the shower maximum, two extreme cases can be found: The average shift in E can be up to -7% for E and -5 g cm^{-2} for $X_{\max}$ for deeply-penetrating showers and up to -7% for E and +5 g cm^{-2} for $X_{\max}$ for showers that develop high in the atmosphere.

Furthermore, we studied the influence of different types of primary particle in terms of proton- and iron-induced showers. Comparing the widths of the distribution, no difference could be found between proton- and iron-induced air showers.

The change in the atmosphere description from monthly models to actual sounding profiles do hardly affect the reconstructed energy nor the position of shower maximum. For E, the difference is well below 1% and for $X_{\max}$ below 2 g cm^{-2}.

Obviously, the fluctuation of the atmosphere around the monthly average atmosphere values adds an additional contribution to the statistical uncertainty of the reconstructed energy and $X_{\max}$ of one shower. The 'end-to-end' comparison of the A07 model with monthly averages to the K08 model with sounding data yields RMS$(\Delta E/E) \in [1.5, 3.0]$% and RMS$(X_{\max}) \in [7.2, 8.4]$ g cm^{-2}(cf. Fig. 4).

Finally, the systematic difference in the collisional cross section data from two independent measurements [22], [23] are negligible. The reconstructed energy varies less than 1% and the position of shower maximum about 1 g cm^{-2} while interchanging the cross sections. Varying the α-coefficients for the temperature-dependent collisional cross sections within their given uncertainties, yields in less than 1% change in reconstructed energy as well.

Acknowledgements

The authors would like to thank the Pierre Auger Collaboration for providing the simulation and reconstruction framework used in this work. Part of this work is supported by the BMBF under contract 05A08VK1.

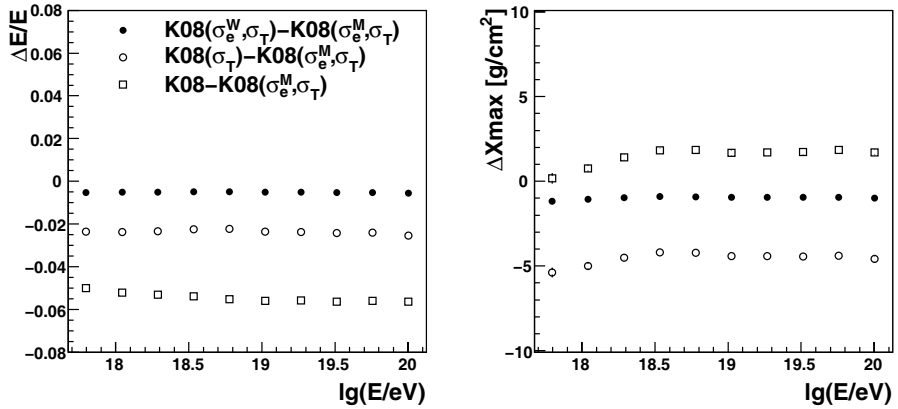

Fig. 2. Comparison of the effect of switching off σ_e and the collisional cross sections σ_T on E and $X_{\max}$ as well as the influence of different vapour quenching, σ_e^W [23] and σ_e^M [22].

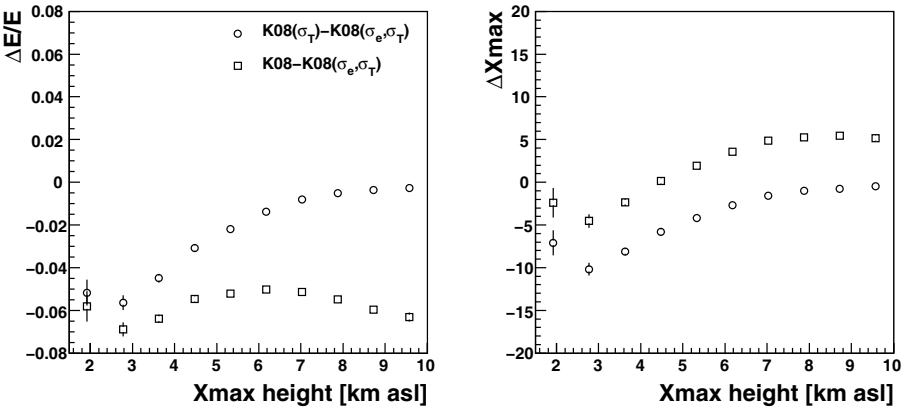

Fig. 3. Difference in reconstructed energy and $X_{\max}$ in dependence the vertical height of the shower maximum ($E = 10^{19}$ eV).

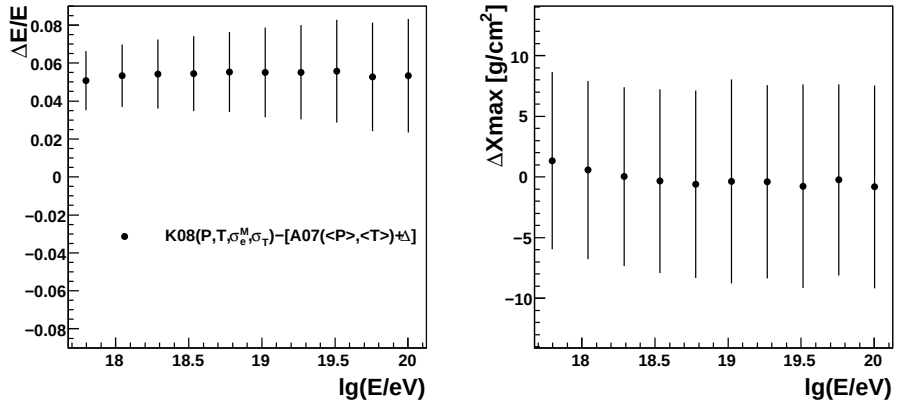

Fig. 4. Difference of the reconstruction using the full K08 model to A07. Error bars denote the RMS spread. Note that we corrected for the 'trivial' yield difference, Δ, from Fig. 1.

REFERENCES

[1] F. Arqueros, J. Hörandel, B. Keilhauer, Nucl. Instr. Meth. **A 597** (2008) 1
[2] A.N. Bunner, Cosmic ray detection by atmospheric fluorescence, Ph.D. Thesis, Cornell University, 1967
[3] G. Davidson, R. O'Neil, J. Chem. Phys. **41** (1964) 3946; R. O'Neil, G. Davidson, American Science and Engineering, Inc., Report AFCRL-67-0277, Cambridge, MA, 1968
[4] F. Kakimoto *et al.*, Nucl. Instr. Meth. **A 372** (1996) 527
[5] P. Colin *et al.* [MACFLY Coll.], Astropart. Phys. **27** (2007) 317
[6] R. Abbasi *et al.* [FLASH Coll.], Nucl. Instr. Meth. **A 597** (2008) 32 and 37
[7] M. Ave *et al.* [AIRFLY Coll.], ibid., 41
[8] M. Ave *et al.* [AIRFLY Coll.], ibid., 46
[9] M. Ave *et al.* [AIRFLY Coll.], ibid., 50
[10] M. Ave *et al.* [AIRFLY Coll.], ibid., 55
[11] M. Nagano *et al.*, Astropart. Phys. **22** (2004), 235
[12] N. Sakaki *et al.*, Nucl. Instr. Meth. **A 597** (2008), 88
[13] T. Waldenmaier *et al.*, ibid., 67
[14] A. Morozov *et al.*, ibid., 105
[15] A. Ulrich, private communication (2009)
[16] B. Keilhauer *et al.*, for the Pierre Auger Collaboration, Proc. 29th Int. Cos. Ray Conf., Pune, India, **7** (2005) 123
[17] S. Argiro *et al.*, Nucl. Instr. Meth. **A580** (2007) 1485; L. Prado *et al.*, Nucl. Instrum. Meth. A **545** (2005) 632
[18] J. Abraham *et al.* [Pierre Auger Coll.], Nucl. Instr. Meth. **A523** (2004) 50
[19] M. Nagano *et al.*, Astropart. Phys. **20** (2003), 293
[20] B. Keilhauer *et al.*, Nucl. Instr. Meth. **A 597** (2008) 99
[21] B. Keilhauer *et al.*, Astropart. Phys. **25** (2006) 259
[22] A. Morozov *et al.*, Eur. Phys. J. **D 33** (2005) 207
[23] T. Waldenmaier, J. Blümer, H. Klages, Astropart. Phys. **29** (2008) 205
[24] T. Bergmann *et al.*, Astropart. Phys. **26** (2007) 420.
[25] S. Ostapchenko, Nucl. Phys. Proc. Suppl. **151**, 143 (2006).

A MC simulation of showers induced by microscopic black holes

D. Góra[*†], **M. Haag**[*] **and M. Roth**[*]
[*]*Karlsruhe Institute of Technology (KIT), D-76021 Karlsruhe, Germany*
[†]*Institute of Nuclear Physics PAN, ul. Radzikowskiego 152, 31-342 Kraków, Poland*

***Abstract*. Large surface detectors might be sensitive not only with respect to extensive air showers induced by ultra high energy neutrinos but also to showers induced by hypothetical objects like microscopic black-holes. Microscopic black-holes might be produced in high energy particle collisions with the center of mass energies above the fundamental scale of gravity. These black-holes would decay rapidly by Hawking radiation into characteristic high multiplicity states of Standard Model particles and induce extensive air showers potentially detectable by a large surface neutrino detector. In this paper we study the possibility to detect microscopic black-holes exemplifying it in case of the surface detector of the Pierre Auger Observatory. The expected event rate is calculated for up-going and down-going showers induced by microscopic black-holes. Our calculations show a significant deviation of the expected rate compared to the rate expected by Standard Model predictions. The rates of up-going neutrinos are almost completely suppressed, whereas the rate of down-going neutrinos increase by a factor of about 50 with respect to standard model calculations. The non observation of up-going neutrinos by the Pierre Auger Observatory in conjunction with a high rate of down-going neutrino-induced showers, would be a strong indication of physics beyond the Standard Model.**

***Keywords*: UHECR, neutrinos microscopic black-hole**

I. Introduction

Searching for ultra high-energy (UHE) neutrinos ($10^{18}\,\mathrm{eV}$ or above) emitted from astrophysical objects is one of the most challenging tasks in Astroparticle Physics. Neutrinos offer a unique opportunity to open a new observation window, since they are only weakly interacting and neutral. After having traveled cosmological distances without being perturbed and/or deflected in the interstellar medium, neutrinos behave as messengers of the most mysterious regions of astrophysical sources. Several theoretical models predict a significant flux of high-energy neutrinos as a result of the decay of charged pions, produced in interactions of UHE cosmic rays within the sources themselves or while propagating through background radiation fields.

The expected neutrino rates possibly detected by large surface detectors do not only depend on the predicted flux of neutrinos but also on the neutrino-nucleon cross section. It has been noted [1] that Earth-skimming ν_τ's will generate upward going air showers when they interact in the earth crust. By contrast neutrinos of all flavours will generate deeply penetrating quasi-horizontal (down-going) air showers which are distinctive in having an electromagnetic component unlike hadron induced showers [2]. The rate for down-going ν induced showers is proportional to neutrino-nucleon cross section, while the rate of Earth-skimming ν_τ is not. Thus, the detection rate for down-going νs, and the rate for up-going ν showers, react differently to variations of the neutrino cross section and tau energy loss. By comparing these rates one can therefore constrain significant deviations of neutrino interactions from SM predictions, see for example [3] for more details.

The neutrino-nucleon cross section is related to parton densities in the yet unmeasured low Bjorken-x region $x \sim 10^{-5}$. Some models even propose substantial modifications of neutrino interactions at high energies, including theories of TeV-gravity and production of microscopic black holes (BH), a domain that is to be tackled in the near future by the LHC. Measuring the flux of ultra high energy neutrinos would not only allow to put limits on cosmic ray production and propagation models. It would also probe fundamental interactions at energies that lie well above the TeV scale, and open a new window on possible physics beyond the Standard Model (SM) [4].

In this paper the scenario of microscopic BH production in neutrino nucleon collisions at the TeV scale is exemplified for the case of the surface detector (SD) of the Pierre Auger Observatory [5], which consists 1600 water Cherenkov detectors with $1.5\,\mathrm{km}$ spacing. In addition to hadrons and photons the Auger Observatory is also sensitive to UHE neutrinos with energies above $\sim 10^{17}\,\mathrm{eV}$ [6], [7].

The outline of the paper is as follows. In section II a short description of microscopic BH physics is given. In section III a full MC simulation chain starting with the injection of a neutrino into the Earth's atmosphere, its propagation, interactions and eventually the air shower production up to the actual response of the Auger SD array is described. Finally, in section IV results of the calculations event rates are presented.

II. Black hole production

In conventional 4-dimensional theories the Planck scale $\sim 10^{19}\,\mathrm{GeV}$ (at which quantum effects of gravity become strong) is fundamental and the study of black holes lies beyond the realm of experimental particle physics. In theories where the existence of larger warped

extra dimensions is suggested, the 4-dimensional Planck scale is derived from the D-dimensional fundamental Planck scale, which can be of $\mathcal{O}(\mathrm{TeV})$, bringing the possible observation of BH production and evaporation into reach of available experiments [8], [9].

Microscopic BHs might be produced in high energy particle collisions with the center of mass (CM) energies above the fundamental scale of gravity. When the impact parameter of two incident particles drops below the Schwarzschild radius r_s of a BH with mass equal to their CM energy, BH formation should occur with a mass $M_\mathrm{BH} = \sqrt{\hat{s}}$. In case of a neutrino-nucleon collision the squared CM energy $\hat{s}$ is given by $\hat{s} = x \cdot 2 m_\mathrm{N} E_\nu$, where m_N is the nucleon mass and E_ν the energy of the interacting neutrino. Within a semi-classical approach this suggests a geometric cross section of $\hat{\sigma} \approx \pi r_\mathrm{s}^2$ with

$$r_\mathrm{s}\left(M_\mathrm{BH}\right) = \frac{1}{M_D}\left[\frac{M_\mathrm{BH}}{M_\mathrm{D}}\right]^{\frac{1}{1+n}}\left[\frac{2^n \pi^{\frac{n-3}{2}} \Gamma\left(\frac{n+3}{2}\right)}{n+2}\right]^{\frac{1}{1+n}} \tag{1}$$

so that $\hat{\sigma} \propto \hat{s}^{\frac{1}{n+1}}$, where n is the number of extra dimensions.

The quantity M_D denotes the lightest possible BH with a trans-Planckian Schwarzschild-radius.

The total cross section for the formation of a BH in neutrino-nucleon collisions can then be written as

$$\sigma\left(\nu N \to BH\right) = \sum_i \int_{(M_\mathrm{BH}^\mathrm{min})^2/s}^{1} dx\, \hat{\sigma}_i\left(\sqrt{xs}\right) f_i\left(x, Q\right), \tag{2}$$

where $f_i(x, Q)$ denotes the parton distributions functions (PDF) and $M_\mathrm{BH}^\mathrm{min}$ is the minimal BH mass for which a semi-classical treatment of BH formation is expected to be valid and not understood effects of quantum gravity can be neglected. Due to the rapidly rising nucleon PDF at low x, the effective BH mass M_BH does not exceed several tens of $\mathrm{TeV/c^2}$, even for neutrinos with an energy up to $10^{21}\,\mathrm{eV}$.

Once produced, microscopic BHs are expected to decay within time scales of $\sim 10^{-25}\,\mathrm{s}$ through three major phases:

- The balding phase, in which the 'hair' (asymmetry and moments due to the violent production process) is shed.
- The Hawking evaporation phase [10], which consists of a short spin-down phase (the Kerr (rotating) BH loses its angular momentum) and then a longer Schwarzschild phase, which accounts for the greatest proportion of mass loss [11].
- A Planck phase at the end, when the BH mass or the Hawking temperature reach the Planck scale.

Given the validity of the semiclassical description, a BH will mainly evaporate due to Hawking radiation and behave like a thermodynamical system with the temperature $T_\mathrm{H} = \frac{n+1}{4\pi r_\mathrm{s}}$. During the decay the Hawking temperature will rise as the BH mass drops. The lifetime can be described as $\tau \sim \frac{1}{M_\mathrm{D}}\left(\frac{M_\mathrm{BH}}{M_\mathrm{D}}\right)^{\frac{3+n}{1+n}}$. Approximately the decay may be treated as instantaneous on detector time scales, since for $M_\mathrm{D} \sim 1\,\mathrm{TeV}$ and $M_\mathrm{BH} \sim 10\,\mathrm{TeV}$, the BH lifetime τ is smaller than 10^{-25} s. During the decay process particles of all SM channels will be produced in a 'flavor-democratic' fashion with energies of order T_H or above, typically at relatively high multiplicities $\langle n \rangle \approx \frac{1}{2}\frac{M_\mathrm{BH}}{T_\mathrm{H}}$.

III. METHOD

In order to calculate the expected event rate from microscopic BH-induced showers at SD array of the Auger Observatory, a full MC simulation chain was set. Simulation consists of three phases: propagation and interaction of neutrinos inside the Earth and atmosphere to produce primaries able to initiate potentially detectable showers in the atmosphere; simulation of lateral profiles of shower developments in the atmosphere and, finally, simulation of detector response.

The decay and the resulting particle spectrum of BH was simulated using a modified version of the CHARYBDIS code [12]. The original version has been developed as an event generator for the production of microscopic BHs at the LHC. One characteristic feature to be pointed out is the inclusion of the recently calculated *grey-body* factors for BH production in extra dimensions [13]. Grey body factors account for the fact that particles have to be transmitted through a curved space-time outside the horizon, and result in a modified emission spectrum from that one of a perfect thermal black body, even in 4 dimensions. For sake of simplicity and due to the fact that the decay balding and Planck phase are not well understood, only the Hawking evaporation phase for a non-rotating BH is implemented. In CHARYBDIS the fragmentation and hadronization process of the radiated particles is realized by an interface to the generator PYTHIA [14].

There is no BH generator for collisions of neutrinos and nucleons available so far. Among other generators also CHARYBDIS was originally designed for pp and $\bar{p}p$ collisions and motivated by collider experiments like the upcoming LHC. Modifications had to be introduced allowing for the study of neutrino-nucleon collisions. The neutrino has to be treated as a beam particle without substructure. This affects the calculation of the BH mass as well as the cross section, the handling of PDF and the initialization routine of PYHTIA. A Lorentz boost from the LAB system to the CM system before the collision and back after the decay was added to ensure the numerical stability even at highest energies. The implemented changes were verified by cross-checking the cross sections and distribution of the generated BH mass $M_\mathrm{BH} = \sqrt{xs}$ (which depends on the involved PDF) calculated in our cross section generator, CSGEN, according to the cited literature against the results obtained with the modified version of CHARYBDIS. The cross-section generator, CSGEN, is a self-written tool to

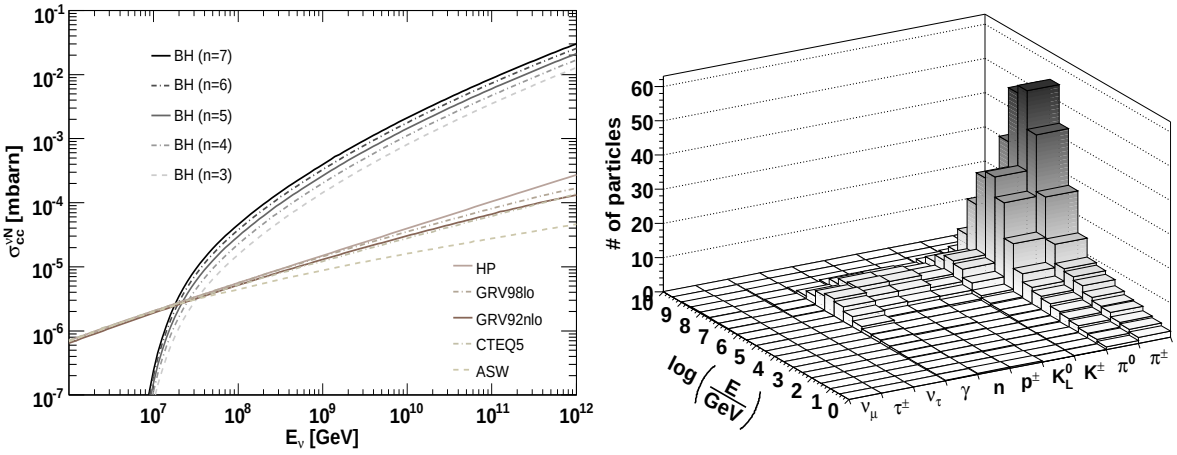

Fig. 1. (Left panel) The BH formation cross section calculated for $x_{\rm min} = 3$. For comparison the SM CC $\nu_\tau N$ cross section [15] is shown; (right panel) particle spectrum of a BH decay with $E_{\nu_\tau} = 10^{19}\,{\rm eV}$, averaged over 100 events. The mean BH mass is $\langle M_{\rm BH}\rangle = 6730.8\,{\rm TeV}$, the multiplicity $\langle M\rangle = 614.4$.

calculate cross sections. In CSGEN typical SM structure functions [15] were implemented as the parametrisation and other PDF included as the LHAPDF [16] FORTRAN libraries.

All calculations were performed with the minimal black hole mass given by $x_{\rm min} \equiv M_{\rm BH}^{\rm min}/M_{\rm D} = 3$ which corresponds to a lower cutoff where the semi-classical description of microscopic BHs is still valid, and the number of extra spacial dimensions set to $3 \leq n \leq 7$.

We determine the flux of neutrinos reaching the detector volume and initiating an extensive air shower (EAS). CSGEN is used to calculate cross sections, the distributions of involved kinematic variables and the tau energy loss for various interaction models and predictions [17]. The data are input to a modified version of ANIS [18], [19] to simulate the propagation of incident neutrinos towards the detector and calculate the vertices of initiated air showers.

The probability to detect neutrinos and microscopic BH by the SD array of the Auger Observatory is done by means of the packages PYTHIA and CHARYBDIS, which are used to simulate the production of secondary particles in neutrino-nucleon interactions that eventually initiate an EAS. These particles are input to the air shower simulation software AIRES [20] to create shower profiles and footprints, which are then analyzed with the Auger Offline software framework [21] in order to determine the detector response and identification efficiency.

IV. Results

The actual BH formation cross section for neutrino nucleon collisions calculated with CSGEN is shown in Fig. 1 (left panel) for different assumptions on the number of additional spacial dimensions n. When the CM energy reaches values high enough to form a BH with the minimum mass $M_{\rm BH}^{\rm min}$ (which occurs between $E_\nu = 10^{15}\,{\rm eV}$ and $E_\nu = 10^{16}\,{\rm eV}$), the BH cross section rises rapidly, exceeding the SM cross sections by about two orders of magnitude at the highest energies. As an example the averaged spectrum of a BH decay at $E_{\nu_\tau} = 10^{19}\,{\rm eV}$ is shown in Fig. 1 (right panel). It is evident that the secondaries consist mainly of charged and neutral pions, and kaons.

For the scenario of microscopic BH production, the neutrino interaction length in air is still larger than the atmospheric depth, so that BH showers can be initiated deep in the atmosphere and hence can be distinguished from hadronic cosmic rays in the same way like neutrino induced showers, i.e. looking for inclined young showers [6], [22].

Neutrinos are able to penetrate deep into the atmosphere before interacting and generating a *young shower* close to the detector as opposed to *old showers* of hadronic or photon origin shortly after entering the atmosphere. At large zenith angles the purely electromagnetic part of such old showers is usually absorbed within the first $2000\,{\rm g\,cm^2}$. Practically only the high energy muons reach the ground, especially in inclined showers. This results in a thin and flat shower front which generates a short detector signal, lasting only a few ten nanoseconds. Young showers however reach the ground with a significant electromagnetic component still existent, showing a curved and thick shower front at ground that leads to broad signals with durations of up to a few microseconds. Together with the time information of the particles detected at ground and the elongated shape of the footprint, young inclined showers can be identified and their origin eventually attributed to neutrinos. The larger the considered zenith angle, the more pronounced are these features.

To calculate the expected event rate from microscopic BHs we have defined a set of cuts where the number of events passing is maximal while the background contamination (due to hadron-induced showers) is kept minimal. A method similar to the one presented in [6] was used. Applying the cuts to simulated neutrino and microscopic BH showers yield to the neutrino/BH identification efficiency, which is defined as the ratio of showers triggering the detector and passing the cuts over

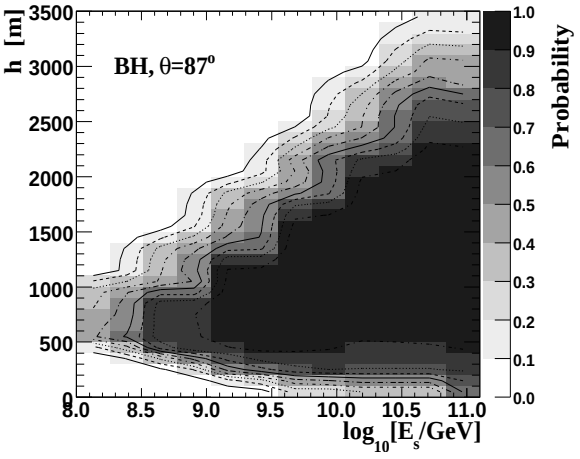

Fig. 2. The SD identification efficiency maps calculated for down-going $\nu_{\rm e}$ neutrinos producing microscopic BH. The efficiency is ploted as the function of shower energy $E_{\rm s}$ and the injection height h.

the total number of simulated AIRES showers. In Fig. 2 an example of identification efficiencies is shown.

Once the identification is known the event rate can be calculated. The total observable rates (number of expected events) were calculated according to $N = \Delta T \times \int_{E_{\rm th}}^{E_{\rm max}} A(E_\nu) \times \Phi(E_\nu) \times dE$, where $\Phi(E_\nu)$ is the isotropic ν-flux, ΔT the observation time and $A(E_\nu)$ the acceptance for a given initial neutrino energy, E_ν.

In Tab. I the rates (number of events per year), for different injected ν-fluxes are listed. The rates labeled with "WB" are obtained for the Waxman-Bahcall bound [23]. Other rates are calculated for the GZK flux [24] and a flux due to Topological Defects (TD) [25]. In addition in Tab. I the ratio R between expected up- and down-going neutrino events is presented for different interaction models. One finds that this ratio is indeed sensitive to the underlying neutrino-nucleon cross section. A higher cross section results in a decrease of up-going and increase of down-going event rates, and vice versa. But given the fact that for a non-exotic interaction model more than ten years of data-taking (depending on the incoming neutrino flux) might be necessary to detect a single down-going neutrino, the statistical relevance of the measured data will at best allow to put a limit on the cross section or energy loss model. In the case of BH production the picture looks different: the non-observation of up-going neutrinos in conjunction with a high rate of down-going inclined air showers, initiated deep in the atmosphere, would be a strong indicator of physics beyond the SM.

TABLE I
THE EXPECTED EVENT RATES AND THE RATIO BETWEEN UP- AND DOWN-GOING EVENT RATES FOR DIFFERENT NEUTRINO FLUX AND CROSS SECTIONS.

Scenario	flux Φ	rate 1/yr up-g.	rate 1/yr down-g.	ratio R
GRV92nlo	WB	0.44	0.22	2.0
	GZK	0.12	0.05	2.5
	TD	0.49	0.32	1.6
HP	WB	0.23	0.26	0.9
	GZK	0.07	0.05	1.2
	TD	0.25	0.39	0.7
ASW	WB	0.54	0.13	4.2
	GZK	0.15	0.03	4.8
	TD	0.61	0.17	3.6
BH, n=5	WB	0.02	11.30	$\approx \frac{1}{500}$
	GZK	0.01	2.01	$\approx \frac{1}{300}$
	TD	0.02	19.31	$\approx \frac{1}{1000}$

V. CONCLUSIONS

A complete MC simulation chain to study the microscopic BH-induced showers has been presented. Our calculations show a significant deviation of the expected event rate in comparison to the rate calculated by SM predictions. The non observation of up-going neutrinos by the Pierre Auger Observatory in conjunction with a high rate of down-going neutrino-induced showers, would be a strong indication of physics beyond the SM.

VI. ACKNOWLEDGMENT

The authors gratefully acknowledge the fruitful discussions with our Pierre Auger collaborators, in particular we thank J. Alvarez-Muñiz for his strong interest. We are very much in dept to the authors of the Auger Offline software used for the analysis. We gratefully acknowledge the financial support by the HHNG-128 grant of the Helmholtz association and the Ministry of Science and Higher Education under Grant 2008 No. NN202 127235.

REFERENCES

[1] D. Fargion, B. Mele, and A. Salis, Astrophys. J. 517 (1999) 725.
[2] E. Zas, New J. Phys. 7 (2005) 130.
[3] L.A. Anchordoqui *et al.* , Phys. Rev. D74 (2006) 043008.
[4] Anchordoqui *et al.* , Astropart. Phys. 25 (2006) 14.
[5] J. Abraham *et al.* , Nucl. Instrum. Meth. A523 (2004) 50.
[6] J. Abraham *et al.* , Phys. Rev. Lett. 100 (2008) 211101; J. Abraham *et al.* , Phys. Rev. D 79 (2009) 102001.
[7] J. Tiffenberg [The Pierre Auger Collaboration], these proceedings; D. Góra [The Pierre Auger Collaboration], these proceedings.
[8] L. Randall and R. Sundrum, Phys. Rev. Lett. 83 (1999) 3370.
[9] S.B. Giddings and E. Katz, J. Math. Phys. 42 (2001) 3082.
[10] S.W. Hawking, Commun. Math. Phys. 43 (1975) 199.
[11] D. N. Page, Phys. Rev. D13 (1976) 198.
[12] C.M. Harris *et al.* , JHEP 08 (2003) 033.
[13] P. Kanti and J. March-Russell, Phys. Rev. D67 (2003) 104019.
[14] T. Sjostrand, S. Mrenna, and P. Skands, JHEP 05 (2006) 026.
[15] The following models were chosen in this work: **GRV98lo, GRV92nlo** M. Glück S. Kretzer and E. Reya, Astropart. Phys. 11 (1999) 327; **CTEQ5** CTEQ Collaboration, H.L. Lai *et al.* , Eur. Phys. J. C12 (2000) 375; **HP** A. Donnachie and P.V. Landshoff, Phys. Lett. B437 (1998) 408; **ASW** J.L. Albacete *et al.* , Eur. Phys. J. C43 (2005) 353.
[16] LHAPDF home page: http://projects.hepforge.org/lhapdf.
[17] M. Haag, Diploma Thesis, Universtät Karlsruhe, Germany (2008).
[18] A. Gazizov and M.P. Kowalski, Comput. Phys. Commun. 172 (2005) 203.
[19] D. Góra *et al.* , Astropart. Phys. 26 (2007) 402.
[20] S. Sciutto, "AIRES a system for air shower simulation, version 2.6.0,". http://www.fisica.unlp.edu.ar/auger/aires/.
[21] S. Argiro *et al.* , Nucl. Instrum. Meth. A580 (2007) 1485.
[22] J. Alvarez-Muñiz [The Pierre Auger Collaboration], Proc. 30th ICRC 2007; I. Valiño (PhD thesis) Univ. de Santiago de Compostela, ISBN 9788497509664, 2008.
[23] E. Waxman and J.N. Bahcall, Phys. Rev. D59 (1999) 023002.
[24] R. Engel *et al.* , Phys. Rev. D64 (2001) 093010.
[25] P. Bhattacharjee and G. Sigl,Phys. Rept. 327 (2000) 109.

3D Air Shower Simulations Using CONEX in CORSIKA

Tanguy Pierog, Ralph Engel, and Dieter Heck

Forschungszentrum Karlsruhe, Institut für Kernphysik, Postfach 3640, Karlsruhe, Germany

***Abstract*. Interpretation of EAS measurements strongly depends on detailed air shower simulations. The reliability of these simulations is limited by our current knowledge and modeling of hadronic multiparticle production. Another severe limitation, though of technical nature, is the calculation time of Monte Carlo programs at very high energy. In this contribution we will present improvements implemented in the latest versions of the shower simulation codes CORSIKA and CONEX, addressing these limitations.**

***Keywords*: CORSIKA, CONEX, air-shower**

I. Introduction

The experimental method of studying ultra-high energy cosmic rays is an indirect one. Typically, one investigates various characteristics of extensive air showers (EAS), a huge nuclear-electromagnetic cascade induced by a primary particle in the atmosphere, and uses the obtained information to infer the properties of the original particle, its energy, type, direction, etc. Hence, the reliability of ultra-high energy cosmic ray analyses depends on the use of proper theoretical and phenomenological descriptions of the cascade processes.

The most natural way to predict atmospheric particle cascading in detail seems to be a direct Monte Carlo (MC) simulation of EAS development, like it is done, for example, in the CORSIKA program [1]. As very large computation times are required at high energy, an alternative procedure was developed to describe EAS development numerically, based on the solution of the corresponding cascade equations (CE). Combining this with an explicit MC simulation of the most energetic part of an EAS allows us to obtain accurate results both for average EAS characteristics and for their fluctuations in the CONEX program [2].

After briefly describing recent changes introduced in CORSIKA and CONEX in their latest release, we will present the latest results on important EAS observables obtained with these programs. In the second part of this article we will discuss how the two programs can be combined to achieve fast and accurate 3-dimensional EAS simulations. First results of this ongoing work are shown.

II. Improvements of CORSIKA and CONEX

One of the aims of releasing new versions of CORSIKA and CONEX is to provide the users with up-to-date versions of hadronic interaction models.

Two years ago, the new hadronic model EPOS 1.61 [3] brought a quite different philosophy in the hadronic models used for EAS simulations: Designed for high energy physics, unless others, EPOS is detailed enough to be compared to any type of accelerator data experiment. While the results on muon production were very promising [4], the model was shown to be incompatible with hadron data of the KASCADE experiment [5]. As a result of accounting for constraints given by cosmic ray experiments and further model developments to describe accelerator data, EPOS has been improved to version 1.99, which has been introduced this year in both CORSIKA and CONEX as new hadronic interaction model. Some results are presented in the following. Details on EPOS 1.99 are given in [6].

Concerning the particle tracking algorithms, the most important improvement in the last release of CORSIKA (6.900) is the possibility to follow [7] charmed particles produced by QGSJET01 [8] and DPMJET 2.55 [9]. Only with increasing collision energy above 10^{16} eV the production cross section becomes large enough [10], [11] for a noticeable number of charmed hadrons. In the new CHARM option these particles are tracked to the point of decay. As their life times are generally short ($\approx 10^{-12}$ sec) and their interaction cross sections unknown, currently only the decay is considered, neglecting all possible interactions. The new extension of CORSIKA introduces the masses and life times of all ground states of charmed hadrons, as well as of their first excited resonance states, and of the strange charmed

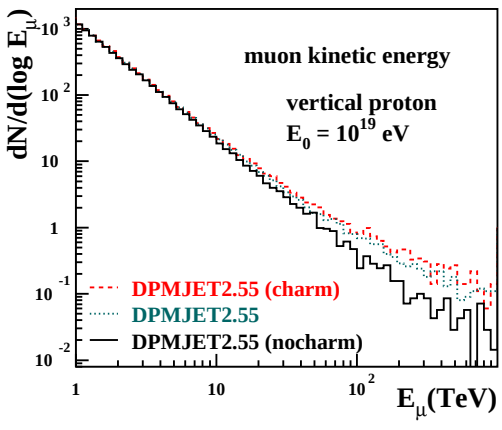

Fig. 1. Sensitivity of muon energy spectra influenced to charm particle production using standard DPMJET (charmed particles decay at production, dotted line), with charm production and tracking (dashed line), and with charm production suppressed (full line).

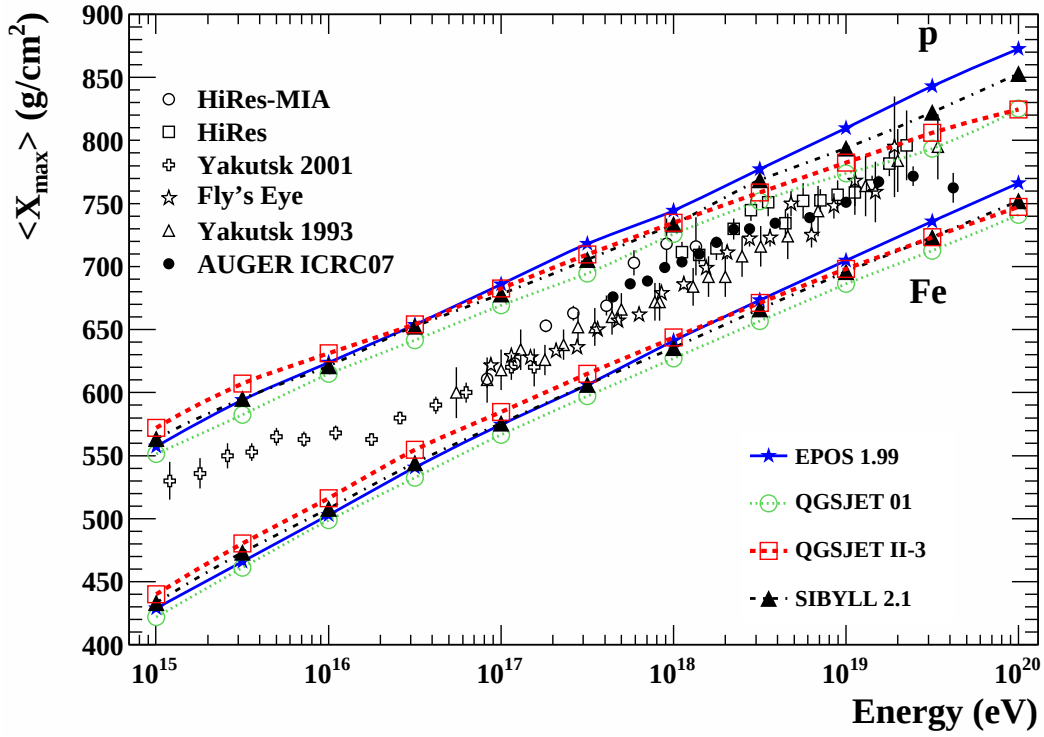

Fig. 2. Mean X_{max} for proton and iron induced showers as a function of the primary energy. Predictions of different high-energy hadronic interaction models, QGSJET01 (dotted), QGSJET II-3 (dashed), SIBYLL 2.1 (dashed-dotted), and EPOS 1.99 (solid), are compared to data. Refs. to the data can be found in [13].

hadrons. The decays are treated by the PYTHIA package [12] which is coupled [7] with CORSIKA.

The number of high energy muons in EAS, which emerge at a low percentage from the decay of charmed mesons, is sensitive to charm production. Fig. 1 shows the muon energy spectra of vertical proton induced EAS of 10^{19} eV primary energy (averaged over 100 EAS), one set simulated with the standard DPMJET/GHEISHA [14] interaction models. In the standard version DPMJET produces charmed particles, which decay immediately at the production vertex and are implicitly treated in the interaction. In a second set of showers (denoted by 'charm') the produced charmed hadrons are transported to the point of their decay. In a third set the charm production is suppressed artificially (denoted by 'nocharm'). The influence on the muon energy spectra is visible only above 10 TeV, in average only very few additional muons are produced by the charmed mesons.

A technical improvement was achieved in CORSIKA by replacing the shell script `corsika-install` by the perl program `coconut` to manage in a portable way the `autoconf/automake` tools for the installation and selection of options in CORSIKA. Options are selected by a shell script using `autoconf` and standard C preprocessor commands in the CORSIKA source code.

Finally, the interface to FLUKA2008.3b [15] has been updated.

III. LATEST RESULTS

In the following EAS simulation results using EPOS 1.99 [6] and QGSJET II-3 [16] are presented and compared to former results using QGSJET01 [8] or SIBYLL 2.1 [17], [18].

As shown in Fig. 2, the mean depth of shower maximum, X_{max}, for proton and iron induced showers simulated with CONEX is quite different for EPOS 1.99. EPOS proton induced showers show a significantly higher elongation than QGSJET II. Above 10^{19} eV, both QGSJET01 and QGSJET II elongation rates decrease due to the very large multiplicity of these models at ultra-high energy. Below 10^{18} eV, an analysis of X_{max} data would lead to a composition of primary cosmic rays that is heavier using QGSJET II compared to EPOS. Above 10^{18} eV the situation is reversed.

In Fig. 3 CONEX-based estimates for the value of the Cherenkov signal in Auger tanks [19] due to muon component, $S_\mu(1000\,\mathrm{m})$, are plotted as a function of the zenith angle. The tank signal has been simulated in a simplified way, that is why only the relative differences between the model results are shown here (reference is proton induced showers with QGSJET II). Due to a much larger muon number at ground in EPOS [4], the density at 1 km is higher by about 25% for proton induced showers and up to 90% in case of iron induced showers if compared to the proton prediction of QGSJET II. Such a difference is of crucial importance for the reconstruction

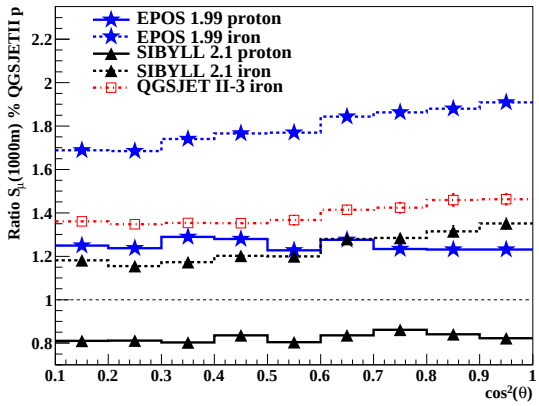

Fig. 3. Muon contribution to S(1000m) as measured by the Pierre Auger Observatory for 10^{19} eV air showers simulated with different high-energy hadronic interaction models and primary mass: EPOS 1.99 (stars) proton (full) and iron (dashed), SIBYLL 2.1 (triangles) proton (full) and iron (dashed), and QGSJET II-3 iron (squares dashed-dotted), relative to proton with QGSJET II-3.

of the primary energy and composition with ground array experiments. Compared to other models, using EPOS would decrease the energy reconstructed from lateral densities and could lead to a more consistent cosmic ray composition obtained from muon number and mean X_{max} data [20]. On the other hand, SIBYLL 2.1 shows about a 20% lower muon signal than QGSJET II.

The higher muon number from EPOS is due mainly to a larger baryon-antibaryon pair production rate in the individual hadronic interactions in showers. By predicting more baryons, more energy is kept in the hadronic shower component even at low energy. As a consequence, the calorimetric energy – as measured by fluorescence light detectors – is reduced since more energy is transferred to neutrinos and muons. In Fig. 4 the conversion factor from the visible calorimetric energy to the real energy is plotted as a function of the primary energy of the showers. As expected, EPOS 1.99 shows a conversion factor which is up to 2% higher than QGSJET II. SIBYLL results (not shown) are very similar to QGSJET II.

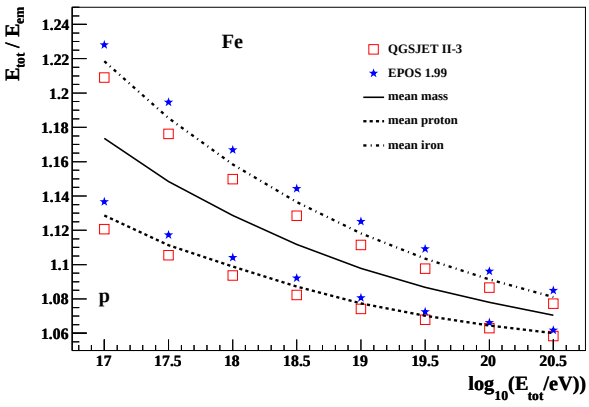

Fig. 4. Mean factor for the conversion of observed (calorimetric) energy to total energy for iron (dashed-dotted) or proton (dashed) induced showers. The conversion factor is shown for QGSJET II-3 (squares) and EPOS 1.99 (stars). The mean conversion factor (solid line) is calculated by averaging all proton and iron predictions.

IV. Outlook

For the next release of CORSIKA, two important improvements are in preparation. First of all work is in progress to run CONEX in the framework of CORSIKA both for 1-dimensional fast simulations and detailed 3-dimensional simulations. Secondly, CORSIKA is being modified to take advantage of modern computing clusters by simulating showers in a controlled parallel way.

A. CONEX *in* CORSIKA

In order to have the best of CONEX and CORSIKA in one single program, we are using the method already implemented in SENECA [21] and outlined in Fig. 5. The CORSIKA installation scheme and steering files are used to set the simulation parameters. Then, internally, these parameters are transferred to CONEX to start the MC simulation with the given primary energy. Depending on their energy, the secondary particles stay either in CONEX MC if $E > E_{\rm thr}$, or go into the CORSIKA stack if $E < E_{\rm low}$, or are used as source for 1-dimensional CE in between. When no more particles with $E > E_{\rm thr}$ are stored on the CONEX stack, the CE are solved down to $E_{\rm low}$. The solution of the CE can be sampled into individual particles saved on the CORSIKA stack. At this point, a weight can be attributed to these particles to reduce the simulation time. Finally all these particles with $E < E_{\rm low}$ stored in the stack are tracked in CORSIKA as usual in a 3-dimensional space until they reach the observation level where they are stored in the chosen output file.

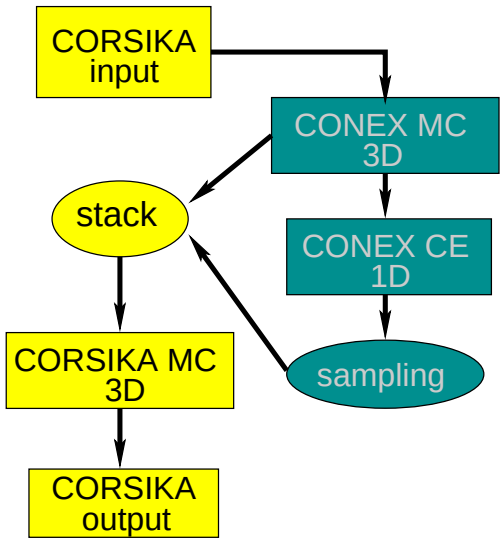

Fig. 5. Implementation of CONEX in CORSIKA.

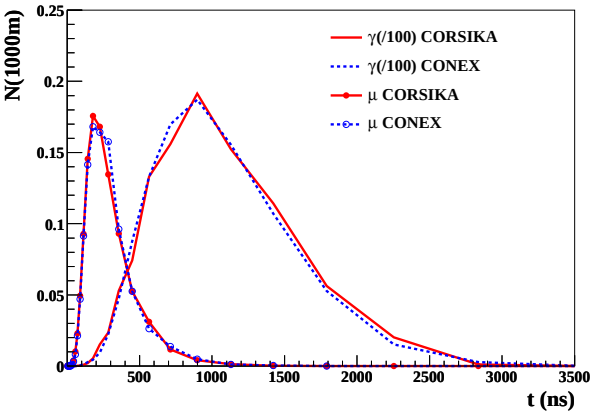

Fig. 6. Arrival time distribution function at 1000 m for photons and muons from vertical proton induced shower at 10^{19} eV simulated with CORSIKA (full line only MC) or with CONEX in CORSIKA (dashed line using CE at intermediate energies).

As a result, simulations can be done either in 1D (only the longitudinal profile) or in 3D (lateral distribution function (LDF)) depending on the parameters $E_{\rm thr}$ and $E_{\rm low}$ used. The simulation time depends mostly on the weight given to the particles sampled from the CE since the thresholds can not have arbitrary values in order to preserve the precision of the simulations. For instance, if $E_{\rm low}$ is too low, the LDF will not be correctly reproduced. For an equivalent precision level, a gain factor of 10 in time can be expected using this method instead of standard thinning. As a first result, the arrival time distribution of muons and photons (divided by 100) at 1000 m from the shower core is shown Fig. 6 for vertical proton induced showers at 10^{19} eV (average over many showers) generated with the usual CORSIKA thinning option (full lines) and with the CONEX option ($E_{\rm low} = 10$ TeV for hadrons and 10 GeV for electromagnetic particles). The results are in a very good agreement.

B. Parallelization

To perform parallel simulations of a single shower in which the results are controlled in a unique way by seeds for the random number generator given by the user, a new option is under development. It will be possible to save all particles above a user-defined threshold in an external file, which can be used to run all the subshowers induced by these particles on different CPU's. If the seeds are well defined for each subshower, it is possible to reproduce the same shower under different technical conditions.

V. CONCLUSIONS

New versions of CORSIKA and CONEX have been released recently with an update of the new hadronic interaction model EPOS 1.99. The available hadronic interaction models differ in several important aspects in the approach of reproducing data. SIBYLL 2.1 and QGSJET 01 are fast and simple models focusing on the description of the main observables a priori needed for EAS simulations. In QGSJET II-3, high parton density effects are treated by re-summing enhanced Pomeron graphs to all orders, but energy conservation at amplitude level is not implemented. On the other hand, in EPOS, energy conservation at amplitude level is fully implemented, but high-density effects are treated by a phenomenological approach. EPOS is particularly well-tuned to describe available accelerator data including heavy ion collisions measured at RHIC. The differences of the model predictions are large: At high energy, proton induced air showers simulated with EPOS have even more muons at ground than iron induced showers simulated with QGSJET II and air showers developed deeper in the atmosphere.

In the near future, the fusion of CONEX in CORSIKA will allow fast detailed 3D simulations of ultra-high energy EAS. Combined with the parallelization of CORSIKA, simulation of unthinned showers corresponding to real observed events will even become feasible.

Acknowledgments: The CORSIKA and CONEX authors would like to thank all users who contributed to the development of the programs by their help in detecting and solving problems. We are particularly grateful to R. Cady (Utah) who started the work on the parallelization of CORSIKA.

REFERENCES

[1] D. Heck *et al.*, Report FZKA 6019, Forschungszentrum Karlsruhe, 1998.
[2] T. Bergmann *et al.*, Astropart. Phys. 26 (2007) 420–432.
[3] K. Werner *et al.*, Phys. Rev. C74 (2006) 044902.
[4] T. Pierog and K. Werner. *Phys. Rev. Lett.* 101:171101 2008.
[5] W. D. Apel et al., *J. Phys. G: Nucl. Part. Phys.* 36:035201, 2009
[6] T. Pierog and K. Werner, These proceedings (2009) .
[7] D. Heck, Report FZKA 7366, Forschungszentrum Karlsruhe, 2008.
[8] N. N. Kalmykov, S. S. Ostapchenko, and A. I. Pavlov, Nucl. Phys. Proc. Suppl. 52B (1997) 17–28.
[9] J. Ranft, hep-ph/9911213 and 9911232, 1999.
[10] P. Berghaus *et al.*, Journ. Cosm. Astropart. Phys. 06 (2008) 003.
[11] U. Dev Goswami, Astropart. Phys. 28 (2007) 251.
[12] T. Sjöstrand, S. Mrenna, P. Skands, Report LU TP 06-13 (2006); hp-ph/0603175 (2006).
[13] R. Engel and H. Klages, Comptes Rendus Physique 5 (2004) 505–518.
[14] H. Fesefeldt, Report PITHA-85/02, RWTH Aachen, 1985.
[15] A. Fassò *et al.*, CERN-2005-010 (2005).
[16] S. Ostapchenko, Phys. Rev. D74 (2006) 014026.
[17] R. S. Fletcher, T. K. Gaisser, P. Lipari, and T. Stanev, Phys. Rev. D50 (1994) 5710–5731.
[18] R. Engel, T. K. Gaisser, P. Lipari, and T. Stanev, in Proceedings of 26^{th} ICRC (Salt Lake City) vol. 1, p. 415, 1999.
[19] J. Abraham *et al.* (Pierre Auger Collab.), Nucl. Instrum. Meth. A523 (2004) 50–95.
[20] A. Castellina *et al.* (Pierre Auger Collab.), These proceedings (2009) .
[21] H. J. Drescher and G. R. Farrar, Phys. Rev. D **67** (2003) 116001.

How to Relate Particle Physics and Air Shower Development : the EPOS Model

Tanguy Pierog*, Klaus Werner†

*Forschungszentrum Karlsruhe, Institut für Kernphysik, Postfach 3640, Karlsruhe, Germany
†SUBATECH, Université de Nantes - IN2P3/CNRS - EMN, Nantes, France

***Abstract*. In detailed air shower simulations, the uncertainty in the prediction of shower observables for different primary particles and energies is currently dominated by differences between hadronic interaction models. Recently a new hadronic interaction model EPOS 1.61 has been introduced in air shower simulation programs. This model has originally been used to analyze hadron-hadron as well as heavy ion physics at RHIC and SPS energies. Used for air showers, it gives a much larger number of muons at ground. The cross section of this model being too high, the correlation between the number of muons and the number of electrons at ground was not consistent with the KASCADE measurements. New developments in EPOS lead to a strong reduction of the proton-nucleus cross section whose consequences are important both for LHC predictions and air shower measurement. In this contribution, we will show the results of the new version of EPOS 1.99 and how cosmic ray physic can be used to constrain particle physic.**

***Keywords*: EPOS, air-shower, simulation**

I. INTRODUCTION

Air shower simulations are a very powerful tool to interpret ground based cosmic ray experiments. However, most simulations are still based on hadronic interaction models being more than 10 years old. Much has been learned since, in particular due to new data available from the SPS and RHIC accelerators.

In this paper, we discuss air shower simulations based on EPOS, the latter one being a hadronic interaction model, which does very well compared to RHIC data [1], and also other particle physic experiments (especially SPS experiments at CERN). But used in air shower simulation program like CORSIKA [2] or CONEX [3], some results where in contradiction with KASCADE data [4], while it was better for other experiments [5].

Due to the constrains of particle physics, air shower simulations using EPOS present a larger number of muons at ground [6]. On the other hand, we will explain in this paper, how the constrains given by cosmic ray experiments can compensate the lack of accelerator data in some given kinematic regions (very forward) to improve hadronic interaction models and in particular the new EPOS 1.99.

II. EPOS MODEL

One may consider the simple parton model to be the basis of high energy hadron-hadron interaction models, which can be seen as an exchange of a "parton ladder" between the two hadrons.

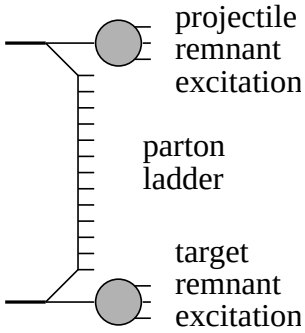

Fig. 1. Elementary parton-parton scattering: the hard scattering in the middle is preceded by parton emissions attached to remnants. The remnants are an important source of particle production even at RHIC energies.

In EPOS, the term "parton ladder" is actually meant to contain two parts [7]: the hard one, as discussed above, and a soft one, which is a purely phenomenological object, parameterized in Regge pole fashion.

In additions to the parton ladder, there is another source of particle production: the two off-shell remnants, see fig. 1. We showed in ref. [8] that this "three object picture" can solve the "multi-strange baryon problem" of conventional high energy models, see ref. [9].

Hence EPOS is a consistent quantum mechanical multiple scattering approach based on partons and strings [7], where cross sections and the particle production are calculated consistently, taking into account energy conservation in both cases (unlike other models where energy conservation is not considered for cross section calculations [10]). Nuclear effects related to Cronin transverse momentum broadening, parton saturation, and screening have been introduced into EPOS [11]. Furthermore, high density effects leading to collective behavior in heavy ion collisions are also taken into account [12].

Energy momentum sharing and remnant treatment are the key points of the model concerning air shower simulations because they directly influence the multiplicity and the inelasticity of the model. At very high energies or high densities, the so-called non-linear ef-

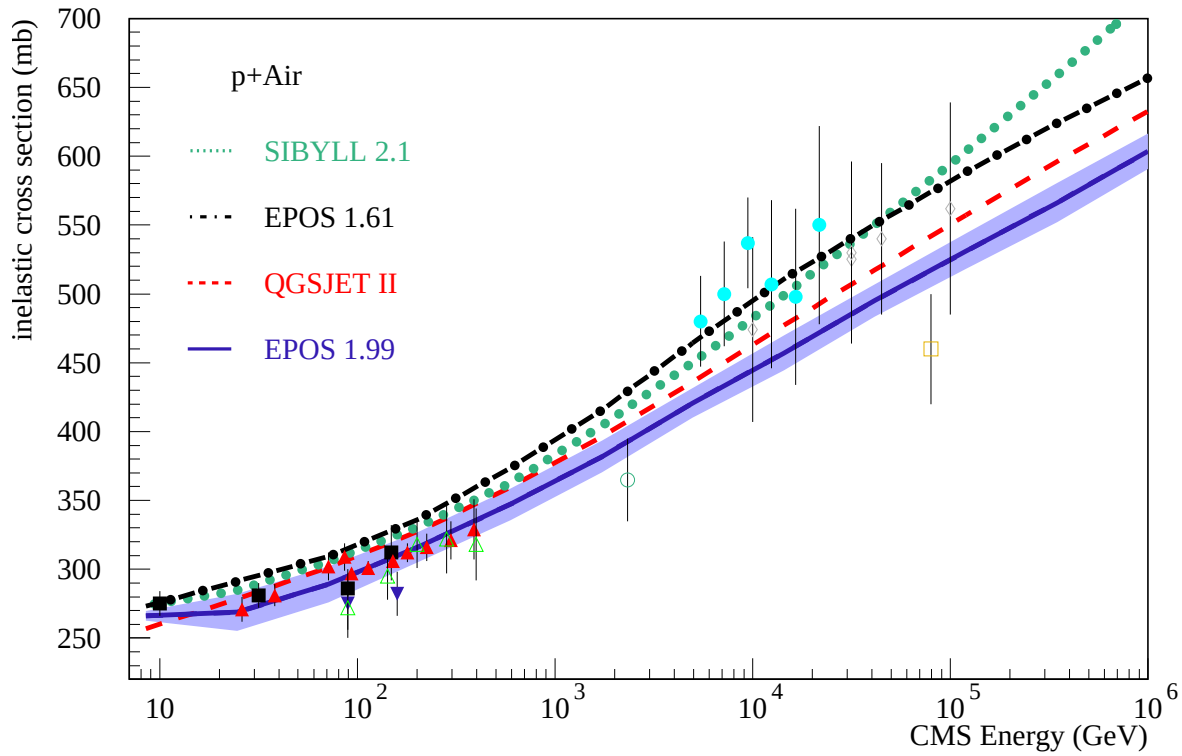

Fig. 2. Inelastic cross section of proton-air interactions. EPOS 1.99, QGSJETII, EPOS 1.61 and SIBYLL 2.1 hadronic interaction models (lines) are compared to data of air shower experiment (points).

fects described in [11] are particularly important for the extrapolation for EAS and it's one of the parts which has been changed in EPOS 1.99.

A. Cross section

We learned from KASCADE data [4], that the energy carried by hadrons in EPOS 1.61 simulations is too low. It means than the showers are too old when they reach ground and it was due to a problem in the calculation of the nuclear cross section and to a too large remnant break-up at high energy (leading to a high inelasticity).

To improve the predictive power of the model, the effective treatment of non-linear effects describe in [11] has been made consistent to describe both proton-proton, hadron-nucleus and nucleus-nucleus data with a unique saturation scale which can be fixed thanks to proton-proton cross section and Cronin effect in dAu collisions at RHIC. Details will be published in a dedicated article.

The EPOS 1.99 (full line) proton-carbon total cross section is shown Fig 3. It is now in very good agreement with the data [13] and with the other hadronic interaction models used for air shower physics QGSJET01 [14] (dashed-dotted line), QGSJETII [15] (dashed line) and SIBYLL [16] (dotted line). In fig 2, the extrapolation to proton-air data up to the highest energies is shown in comparison with measurement from cosmic ray experiments. The surface around the line for EPOS 1.99 represents the uncertainty due to the definition of the

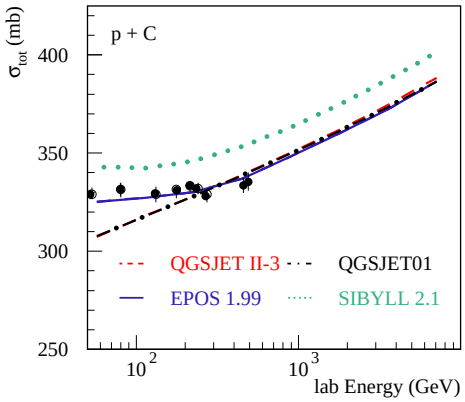

Fig. 3. Total cross section of proton-carbon interactions. EPOS 1.99, QGSJETII, QGSJET01 and SIBYLL 2.1 hadronic interaction models (lines) are compared to data [13] (points)

inelastic cross section as measured by cosmic ray experiments. The difference between the top and the bottom of the area is the part of the cross-section where secondary particles are produced without changing the projectile (target diffraction). So any cross section chosen in this band would give the same result in term of air shower development. Cross section of other models includes this target diffraction (top of the band). In comparison with

EPOS 1.61 (dashed-dotted line), the EPOS 1.99 cross section has been notably reduced.

B. Particle production and inelasticity

Thanks to a Monte Carlo, first the collision configuration is determined: i.e. the number of each type of Pomerons exchanged between the projectile and target is fixed and the initial energy is shared between the Pomerons and the two remnants. Then particle production is accounted from two kinds of sources, remnant decay and cut Pomeron. A Pomeron may be regarded as a two-layer (soft) parton ladder attached to projectile and target remnants through its two legs. Each leg is a color singlet, of type $q\bar{q}$, qqq or $\bar{q}\bar{q}\bar{q}$ from the sea, and then each cut Pomeron is regarded as two strings, cf. Fig. 4a.

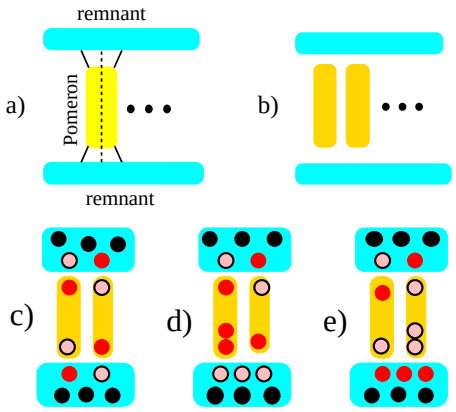

Fig. 4. a) Each cut Pomeron is regarded as two strings b). c) The most simple and frequent collision configuration has two remnants and only one cut Pomeron represented by two $q-\bar{q}$ strings. d) One of the $\bar{q}$ string ends can be replaced by a qq string end. e) With the same probability, one of the q string ends can be replaced by a $\bar{q}\bar{q}$ string end.

It is a natural idea to take quarks and anti-quarks from the sea as string ends for soft Pomeron in EPOS, because an arbitrary number of Pomerons may be involved. In addition to this soft Pomerons, hard and semi-hard Pomerons are treated differently.

Thus, besides the three valence quarks, each remnant has additionally quarks and anti-quarks to compensate the flavors of the string ends, as shown in fig. 4c. According to its number of quarks and anti-quarks, to the phase space, and to an excitation probability, a remnant decays into mesons and/or (anti)baryons [8]. Furthermore, this process leads to a baryon stopping phenomenon in which the baryon number can be transfered from the remnant to the string ends (for instance in 4d, depending on the process, the $3\bar{q}+3q$ can be seen as 3 mesons or a baryon-antibaryon pair).

In case of meson projectile, this kind of diquark pair production at the string ends leads to an increase of the (anti)baryon production in the forward production

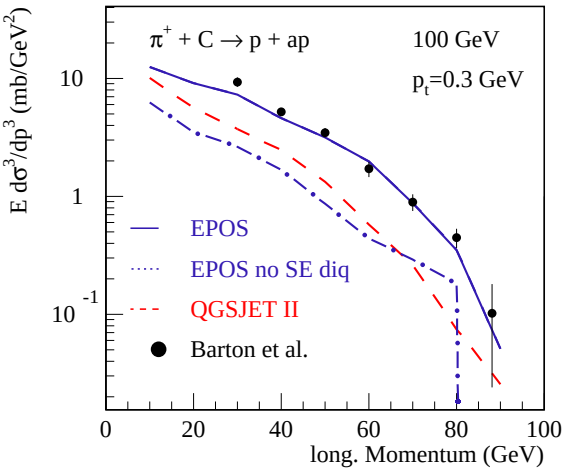

Fig. 5. Model comparison: longitudinal momentum distributions of pion carbon collisions at 100 GeV from EPOS with (full) or without (dashed-dotted) sting-end diquarks and QGSJETII (dashed) compared to data [17].

in agreement with low energy pion-nucleus data [17] as shown fig. 5. As a consequence it is part of the larger number of muons in EAS simulations with EPOS.

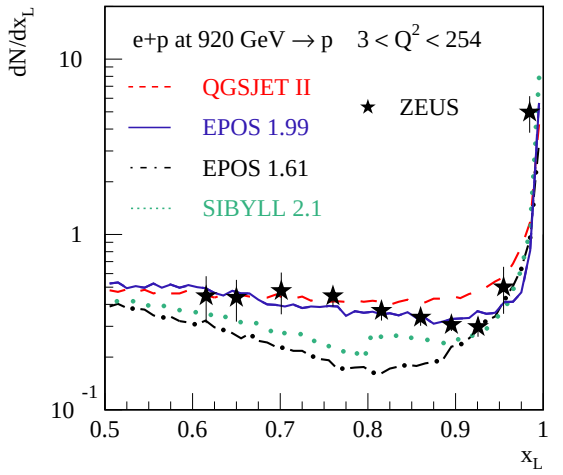

Fig. 6. Proton longitudinal momentum fraction $x_{\rm L}$ distribution in electron-proton interactions. EPOS 1.99 (full), QGSJETII (dashed), EPOS 1.61 (dashed-dotted) and SIBYLL 2.1 (dotted) hadronic interaction models (lines) are compared to HERA data from ZEUS experiment [18] (stars).

As shown on fig. 6, the deficit of leading proton in EPOS 1.61 was very strong around $x_{\rm L} = 0.75$. It has been corrected in EPOS 1.99. As a consequence, EPOS 1.99 has a reduced excitation probability at high energy compared to EPOS 1.61, increasing the number of protons in the forward direction and reducing the inelasticity.

III. AIR SHOWERS

In the following, we discuss air shower simulations, based on the shower programs CONEX, using the old EPOS 1.61 (dashed-dotted line), the new EPOS 1.99 (full line) and QGSJETII (dashed line) (as a reference) as high energy hadronic interaction models.

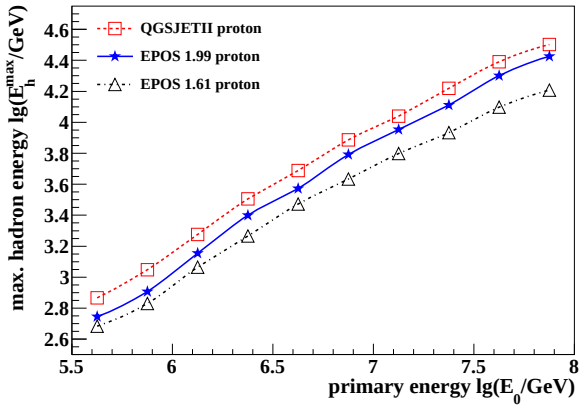

Fig. 7. Maximum hadron energy as a function of the primary energy for proton induced showers using EPOS 1.99 (full line), EPOS 1.61 (dashed-dotted line) and QGSJETII (dashed line) as high energy hadronic interaction models.

The effect of the reduced cross section and inelasticity is clearly visible on the maximum energy of hadrons at ground as shown fig. 7. The shower being younger at ground with EPOS 1.99, the maximum energy is up to 60% higher than in the previous release 1.61. The results are now close to QGSJETII results but with a different slope due to a different elongation rate.

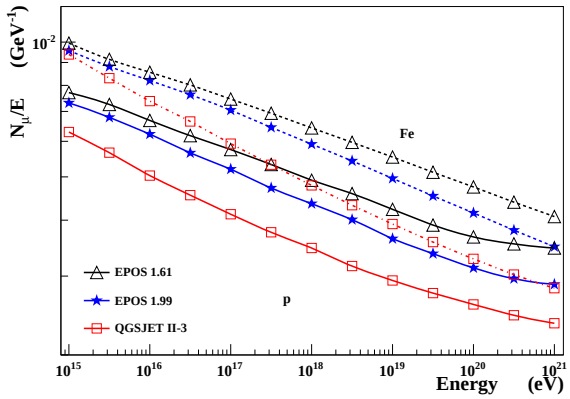

Fig. 8. Total number of muons at ground divided by the primary energy as a function of the primary energy for proton (full lines) and iron (dashed lines) induced showers using EPOS 1.99 (stars), EPOS 1.61 (triangles) and QGSJET II-3 (squares) as high energy hadronic interaction model.

Furthermore, the reduced excitation probability of the remnants leads to a reduction of the muon production compared to EPOS 1.61. Indeed, remnant break-up is an important factor of the muon production in air showers [19] in particular for the mesons. Since less excitation means less break-up, we can see on fig. 8 that EPOS 1.99 produces about 15% less muons than EPOS 1.61 (depending on the primary energy since the slope is different too). It is important to notice that air showers simulated with EPOS will still have about 25% more muons than QGSJETII at Auger energies.

As a consequence, EPOS 1.99 with less muons and more electrons and hadrons at ground does not have the problems pointed out in [4] anymore and should be compatible with KASCADE data.

IV. SUMMARY

EPOS is an interaction model constructed on a solid theoretical basis. It has been tested very carefully against all existing hadronic data, also those usually not considered important for cosmic rays. In EAS simulations, EPOS provides more muons than other models, which was found to be linked to an increased diquark production in both string ends and string fragmentation. To solve the problems pointed out by the comparison with KASCADE data, the treatment of screening effects in nuclear collisions has been improved in EPOS. The new EPOS 1.99 has now a reduced cross section and inelasticity compared to the previous EPOS 1.61 which leads to deeper shower development. But since the number of muons and the elongation rate are different than in the other models, the resulting analysis will be significantly different.

REFERENCES

[1] R. Bellwied. *Acta Phys. Hung.*, A27:201–204, 2006.
[2] D. Heck et al. FZKA-6019, 1998.
[3] T. Bergmann et al. *Astropart. Phys.*, 26:420–432, 2007.
[4] W. D. Apel et al., *J. Phys. G: Nucl. Part. Phys.* 36:035201, 2009
[5] A. V. Glushkov et al., *JETP Lett.*, 87:190 2008.
[6] T. Pierog and K. Werner. *Phys. Rev. Lett.* 101:171101 2008.
[7] H. J. Drescher et al. *Phys. Rept.*, 350:93–289, 2001.
[8] F. M. Liu et al. *Phys. Rev.*, D67:034011, 2003.
[9] M. Bleicher et al. *Phys. Rev. Lett.*, 88:202501, 2002.
[10] M. Hladik et al. *Phys. Rev. Lett.*, 86:3506–3509, 2001.
[11] K. Werner et al. *Phys. Rev.*, C74:044902, 2006.
[12] K. Werner. *Phys. Rev. Lett.*, 98:152301, 2007.
[13] U. Dersch et al. *Nucl. Phys.* B579:277, 2000.
[14] N. N. Kalmykov, S. S. Ostapchenko, and A. I. Pavlov, *Nucl. Phys. Proc. Suppl.* 52B:17–28, 1997.
[15] S. Ostapchenko. *Phys. Rev.*, D74:014026, 2006.
[16] R. Engel, T. K. Gaisser, P. Lipari, and T. Stanev, *Proceedings of 26th ICRC* (Salt Lake City) vol. 1, p. 415, 1999.
[17] D. S. Barton et al. *Phys. Rev.*, D27:2580, 1983.
[18] ZEUS Coll., S. Chekanov et al.,*Nucl. Phys.* B658:3 2003.
[19] H. J. Drescher, *Phys. Rev. D* 77:056003, 2008.

Abstracts of all contributions by the Pierre Auger Observatory:

Measurement of the cosmic ray energy spectrum above 10^{18} eV with the Pierre Auger Observatory

F. Schüssler
Karlsruhe Institute of Technology, Postfach 3640, D-76021 Karlsruhe, Germany

The flux of high energy cosmic rays above $10^{18.5}$ eV has been measured with the Pierre Auger Observatory using an unprecedented number of events. Here we present the energy spectrum derived using two data analysis methods. Above 3 x 10^{18} eV air showers measured with the array of water-Cherenkov detectors and an energy-independent aperture, calibrated by energy measurements made using fluorescence telescopes, are used to obtain a measurement of the energy spectrum. Using air showers detected with the fluorescence telescopes and at least one water-Cherenkov detector (so called hybrid events) a spectrum is derived for energies above 10^{18} eV. The two spectra are found to be consistent and a combined spectrum is derived. The impact of systematic uncertainties and in particular the influence of the energy resolution, on the spectral shape is addressed.

The cosmic ray flux observed at zenith angles larger than 60 degrees with the Pierre Auger Observatory

R. Vazquez
University of Santiago de Compostela, Campus Sur s/n, 15782 Santiago de Compostela, Spain

The cosmic ray energy spectrum is obtained using inclined events detected with the surface detectors of the Pierre Auger Observatory. Air showers with zenith angles between 60 and 80 degrees add about ~30% to the exposure. Events are identified from background based on compatibility between the arrival time and the detector location enabling the elimination of random signals. The arrival direction is computed using the time information. The core position and a shower size parameter are obtained for each event by fitting measured signals to those obtained from predictions of two-dimensional distributions of the patterns of the muon densities at ground level. The shower size parameter, a zenith angle independent energy estimator, is calibrated using the shower energy measured by the fluorescence technique in a sub-sample of high-quality hybrid events. The measured flux is in agreement with that measured using showers of zenith less than 60 degrees.

Energy calibration of data recorded with the surface detectors of the Pierre Auger Observatory

C. Di Giulio
Universitá di Roma II and INFN Roma II, Via della Ricerca Scientifica 1, 00133 Roma, Italy

The energy of the primary particles of the air showers recorded using the water-Cherenkov detectors of the Pierre Auger Observatory is inferred from simultaneous measurement of the showers with the fluorescence telescopes. The signal on the ground at 1000 m from the shower axis obtained using the water-Cherenkov detectors is related directly to the calorimetric energy measured with the telescopes. The energy assignment is therefore independent of air-shower simulations except for the assumptions that must be made about the energy carried into the ground by neutrinos and muons. The correlation between the signal at ground and the calorimetric energy is used to derive a calibration curve. A detailed description of the method used to determine the energy scale is presented. The systematic uncertainties on the calibration procedure are discussed.

Correlation of the Highest Energy Cosmic Rays with Nearby Extragalactic Objects in Pierre Auger Observatory Data

J. D. Hague
University of New Mexico, Albuquerque NM, USA.

We update the analysis of correlation between the arrival directions of the highest energy cosmic rays and the positions of nearby active galaxies. We report and discuss the results of a scan of the full data set in terms of energy threshold, maximum distance and angular separation.

Discriminating potential astrophysical sources of the highest energy cosmic rays with the Pierre Auger Observatory

J. Aublin
Université Paris 6, LPHNE, 4 place Jussieu, 75252 PARIS Cedex 05, France..

We compare the distribution of arrival directions of the highest energy cosmic rays detected by the Pierre Auger Observatory from January 2004 to March 2009 with that of populations of potential astrophysical sources. For this purpose, we present several complementary statistical tests allowing to describe and quantify the degree of compatibility between data and a given sources catalogue. We applied these tests to AGNs detected in X-rays by SWIFT-BAT and to galaxies found in the HI Parkes and in the 2 Micron All-Sky Surveys.

Search for sidereal modulation of the arrival directions of events recorded at the Pierre Auger Observatory

R.Bonino
Istituto di Fisica dello Spazio Interplanetario (INAF), Università di Torino and Sezione INFN Torino.

The Auger Observatory has accumulated important statistics of cosmic rays at energies above 1 EeV. Using data collected from 1 January 2004 to March 2009, we search for large-scale anisotropies in different energy windows. We implement and adapt 3 different methods. The first accounts for various systematic effects affecting the calculation of the exposure that could generate spurious modulations in sidereal time and corrects for these effects. The second method is used to disentangle the sidereal modulation from the solar and anti-sidereal modulations. The third method is based on a differential counting rate analysis and is therefore largely independent of spurious time variations. We present the results of these 3 complementary analyses. No significant anisotropies have been observed and accordingly upper limits to possible sidereal modulations have been set.

Ultra-high energy photon studies with the Pierre Auger Observatory

P. Homola
Institute of Nuclear Physics PAN, ul. Radzikowskiego 152, 31-342 Krakow, Poland

While the most likely candidates for cosmic rays above 10^{18} eV are protons and nuclei, many of the scenarios of cosmic ray origin predict in addition a photon component. Detection of this component is not only of importance for cosmic-ray physics but would also open a new research window with impact on astrophysics, cosmology, particle and possibly fundamental physics. The Pierre Auger Observatory can be used for photon searches of unprecedented sensitivity. At this conference, the status of this search will be reported. In particular the first experimental limits at EeV energies will be presented.

Limits on the flux of diffuse ultra high energy neutrinos set using the Pierre Auger Observatory

J. Tiffenberg
Universidad de Buenos Aires, Argentina

The array of water–Cherenkov detectors of the Pierre Auger Observatory is sensitive to neutrinos of > 1 EeV of all flavors. These interact through charged and neutral currents in the atmosphere (down-going) and, for ν_τ, through the "Earth skimming" mechanism (upgoing). Both types of neutrinos can be identified by the presence of a broad time structure of signals in the water-Cherenkov detectors in the inclined showers that they induce when interacting close to ground. Using data collected from 1 January 2004 to 28 February 2009, we present for the first time an analysis based on down-going neutrinos and place a competitive limit on the all-flavor diffuse neutrino flux. We also update the previous limit for up-going tau neutrinos. Sources of possible backgrounds and systematic uncertainties are discussed.

Comparison of data from the Pierre Auger Observatory with predictions from air shower simulations: testing models of hadronic interactions

Antonella Castellina,
Istituto di Fisica dello Spazio Interplanetario (INAF) and INFN Torino, Via P.Giuria 1, 10125 Torino, Italy

The Pierre Auger Observatory is a hybrid instrument that records the longitudinal, lateral and temporal particle distributions of very high-energy air showers and is thus sensitive to their electromagnetic and muonic components. Such observables depend on energy and on the type of primary particle that initiates the shower and are sensitive to the hadronic interaction properties. Independent analyses of the combined distributions, direct tests of the predictions of hadronic interaction models are performed at ~ 10^{19} eV, which corresponds to $\sqrt{s}$ ~ 140 TeV for proton primaries: discrepancies are discussed

Measurement of the average depth of shower maximum and its fluctuations with the Pierre Auger Observatory

Jose Bellido
The University of Adelaide

The depth of maximum (X_{max}) of air-showers above 10^{18} eV can be measured with an average resolution of 20 g cm^{-2} using the fluorescence telescopes of the Pierre Auger Observatory. The dependence of the average value of X_{max} and the magnitude of the fluctuations in X_{max} are reported as a function of energy and compared with predictions made from shower simulations. Some inferences about the mass composition of primary cosmic rays will be drawn.

Study of the nuclear mass composition of UHECR with the surface detectors of the Pierre Auger Observatory

Hernan Wahlberg
IFLP-Departamento de Fisica, Universidad Nacional de La Plata cc 67 - 1900 La Plata – Argentina

We investigate observables that can be measured with the water-Cherenkov detectors of the Pierre Auger Observatory. In particular we explore the use of the rise time of the signals at the detectors and the azimuthal features of the time distributions. A correlation of these observables with the position of shower maximum (X_{max}), as measured with the fluorescence telescopes is obtained. The dependence of the parameters with energy is also presented.

Cosmic Ray Solar Modulation Studies in the Pierre Auger Observatory

H. Asorey
Centro Atomico Bariloche (CNEA and CONICET), Av. E. Bustillo 9500 (8400) San Carlos de Bariloche, Rio Negro, Argentina

Since data-taking began in January 2004, the Pierre Auger Observatory has been recording low threshold background rates for the self-calibration of its surface detectors. After atmospheric corrections are applied, solar modulation and transient events are observed. A strong correlation with neutron monitor rates is found. In this study, we present an analysis of the available background data, with special emphasis on the observation of Forbush Decreases. The high total count rates allow us to determine temporal variations of solar origin with high accuracy.

Atmospheric Monitoring and its Use in Air Shower Analysis at the Pierre Auger Observatory

S. Y. BenZvi
University of Wisconsin – Madison, 222 W. Washington Ave., Suite 500, Madison, WI 53703, USA

In the analysis of air showers measured using the air fluorescence technique, it is essential to understand the behavior of the atmosphere. At the Pierre Auger Observatory, the atmospheric properties which affect the production of UV light in air showers and the transmission of the light to the fluorescence telescopes are monitored regularly. These properties include the altitude profiles of temperature, pressure, and humidity; the optical depth and scattering behavior of aerosols; and the presence of clouds in the field of view of the telescopes. The atmospheric measurements at the Observatory characterise a detector volume in excess of 30,000 km^3. Since 2004, the data have been compiled in a multigigabyte record of nightly conditions, a record that is vital to the analysis of events observed by the fluorescence telescopes. We will review the atmospheric monitoring techniques used at the Observatory and discuss the influence of atmospheric measurements on estimates of shower observables using true and simulated data.

The Northern Pierre Auger Observatory

John L. Harton
Colorado State University, Fort Collins, Colorado, USA.

It is planned to build the northern part of the Pierre Auger Observatory in southeast Colorado, USA. Results from the southern section of the Auger Observatory, which has recently been completed, imply a scientific imperative to create a much larger acceptance for the extremely rare cosmic rays of energy above a few times 10^{19} eV. The plan for Auger North is to cover an area greater than 20,000 km2, seven times the area of Auger South in Argentina. The motivation for Auger North and the status of preparations will be presented including: R&D work at the Colorado site on a small surface detector array; atmospheric monitoring measurements; R&D on new electronics and communications equipment; and outreach and relations with the local community.

Extension of the Pierre Auger Observatory using high-elevation fluorescence telescopes (HEAT)

Matthias Kleifges
Forschungszentrum Karlsruhe, IPE , H.-v.-Helmholtz-Platz 1, 76344 Eggenstein-Leopoldshafen, Germany

The original fluorescence telescopes of the southern Pierre Auger Observatory have a field of view from about 1° to 29° in elevation. The construction of three additional telescopes (High Elevation Telescopes - HEAT) is nearing completions and observations with one telescope have started. A second telescope will be running by the time of the conference. These new instruments have been designed to improve the quality of reconstruction of showers down to energies of 10^{17} eV. The extra telescopes are pivot-mounted for operation with a field of view from 30° to 60°. The design is optimised to record near-by showers in combination with the existing telescopes at one of the telescope sites, as well as to take data in the hybrid mode using the measurements from an infilled area of surface detectors and additional muon detectors (AMIGA). The design, expected performance, status of construction, and first measurements will be presented.

AMIGA - Auger Muons and Infill for the Ground Array of the Pierre Auger Observatory

M. Platino
Comisión Nacional de Energía Atómica, Av. Gral. Paz 1499 (1650) San Martín – Buenos Aires, Argentina

AMIGA consists of detector pairs composed of a water-Cherenkov detector on the ground and a muon detector buried at a certain depth. The detector pairs are arranged in arrays with 433 and 750 m spacing thus allowing a detailed study of the spectrum region known as the ankle. Design parameters and performance requisites will be outlined. Construction of the first muon detectors, associated software and hardware, and the results of laboratory tests will be described. Preliminary results on the performance of the 750 m array of surface detectors will be presented.

Exposure of the Hybrid Detector of The Pierre Auger Observatory

Francesco Salamida
Dept. of Physics, University of L'Aquila, Italy

The exposure of the Pierre Auger Observatory for events observed by the fluorescence telescopes in coincidence with at least one water-Cherenkov detector of the surface array is calculated. Relevant monitoring data collected during the operation, such as the status of the fluorescence detector, background light and atmospheric conditions are considered in both simulation and reconstruction. This allows better understanding of the time-dependent conditions under which data were taken.

A Monte Carlo exploration of methods to determine the UHECR composition with the Pierre Auger Observatory

D. D'Urso
Universitá di Napoli "Federico II" and INFN Napoli, Via Cintia, 80126

The understanding of the mass composition of the cosmic ray radiation is a key to the solution of the puzzle of the origin of ultra high energy cosmic rays. We present statistical methods which might be used to determine the elemental composition comparing observables measured with the Pierre Auger Observatory with corresponding Monte Carlo predictions for different mass groups obtained using different hadronic interaction models. The techniques make use of the mean and fluctuations of X_{max}, the log-likelihood fit of the X_{max} distributions and the multi-topological analysis of a selection of parameters describing the shower profile. We show their sensitivity to the input composition of simulated samples of known mixing and the comparison with the standard analysis.

Intrinsic anisotropy of the UHECR from the Pierre Auger Observatory

João de Mello Neto
Instituto de Física, Universidade Federal do Rio de Janeiro, Rio de Janeiro, Brazil

We discuss techniques which have been developed for determining the intrinsic anisotropy of UHECR datasets containing small numbers of events, including autocorrelation, an improved two point method and a three point method. The sensitivity to uncertainties in energy and angle reconstruction is examined. The application of these techniques to data obtained with the Pierre Auger Observatory is reported.

Atmospheric effects on extensive air showers observed with the Array of Surface Detectors of the Pierre Auger Observatory

Benjamin Rouillé d'Orfeuil
Laboratoire AstroParticule et Cosmologie (APC), Université Paris 7, CNRS-IN2P3

Atmospheric parameters, such as pressure, temperature and density, affect the development of extensive air showers (EAS) initiated by energetic cosmic rays. We have studied the impact of atmospheric variations on EAS using the surface detectors of the Pierre Auger Observatory, analyzing the dependence of the rate of events on pressure and density. We show that the observed behavior is explained by a model including variations of pressure and density and validated with full EAS simulations. As changes in the atmosphere influence the EAS development, these are expected also to have an effect on the measured signal, with a consequent impact on the determination of the energy of the primary particle. We show that the energy estimation can be corrected for such effects.

Energy scale derived from Fluorescence Telescopes using Cherenkov Light and Shower Universality

S. Müller
Karlsruher Institut für Technologie, Postfach 3640, 76021 Karlsruhe, Germany

We use the universal shape of longitudinal shower profiles to determine the energy scale deduced using the fluorescence detection of air-showers. For this purpose, the fraction of scattered Cherenkov and fluorescence light are adopted as free parameters while fitting the individual profiles of the longitudinal deposit of the energy to the universal shape. We demonstrate the validity of the method using a Monte Carlo study based on the Offline framework of the Pierre Auger Observatory and estimate systematic uncertainties due to the choice of high energy interaction model and atmospheric conditions.

An alternative method for determining the energy of hybrid events at the Pierre Auger Observatory

Patrick Younk
1875 Campus Delivery, Fort Collins, Colorado 80523-1875

An important feature of the Pierre Auger Observatory is the detection of hybrid events; i.e. extensive air showers simultaneously detected with at least one of the water-Cherenkov detectors and one fluorescence telescope. Here we describe an alternative method of estimating the energy of these events. The shower axis is determined using data from both detector systems. The shower energy is determined from the integrated water-Cherenkov signals and the distance of each detector from the shower axis. This is done by characterizing an average lateral distribution function as a function of the shower energy and the zenith angle. The statistical uncertainty in the energy estimate is approximately 40%. The method requires only the signal from one surface detector. Thus, it is useful for estimating the energy of hybrid events for which the geometry cannot be estimated with the surface detectors alone and the longitudinal profile measured by the fluorescence instrument is not well determined. The majority of events in this category have an energy below 10^{18} eV.

The electromagnetic component of inclined air showers at the Pierre Auger Observatory

I. Valiño
Karlsruhe Institute of Technology, 76021 Karlsruhe, Germany

Muons, accompanied by secondary electrons, dominate the characteristics of inclined air showers above 60º. The characteristics of the signal induced by the electromagnetic component in the water-Cherenkov detectors of the Pierre Auger Observatory are studied using Monte Carlo simulations. The relative contributions of the electromagnetic component to the total signal in a tank are characterized as a function of the primary energy, for different assumptions about mass composition of the primary cosmic rays and for different hadronic models.

The delay of the start-time measured with the Pierre Auger Observatory for inclined showers and a comparison of its variance with models

L. Cazon
Department of Astronomy & Astrophysics, The University of Chicago, Kavli Institute for Cosmological Physics, Chicago, IL 60637-1433

Using a sub-sample of high quality events at zenith angles above 60 degrees the delays in the start-time of the signals detected with water-Cherenkov detectors of the Pierre Auger Observatory with respect to a plane front are compared to those from a model for the arrival time distribution of muons at different angles, different distances to the shower axis and different primary energies. Good agreement is found. The variance of the start-time obtained from this model is compared to the variance model currently used in the Auger reconstruction chain, which is based on the assumption of a uniform distribution of the particle arrival times in the shower front. The distribution of the chi2 probability of the angular reconstruction is discussed.

UHE neutrino signatures in the surface detector of the Pierre Auger Observatory

D. Góra
Karlsruhe Institute of Technology (KIT), 76021 Karlsruhe, Germany

The Pierre Auger Observatory has the capability of detecting ultra-high energy neutrinos. The method adopted is to search for very inclined showers with a broad time structure. The properties of such showers that start deep in the atmosphere are very different at ground level from those of showers initiated in the upper atmosphere by protons or nuclei. The neutrino events would have a significant electromagnetic component leading to a broad time structure of detected signals in contrast to nucleonic-induced showers. In this paper we present several observables that are being used to identify neutrino candidates and show that the configuration of the surface detectors of the Auger Observatory has a satisfactory discrimination power against the larger background of nucleonic showers over a broad angular range.

Investigation of the Displacement Angle of the Highest Energy Cosmic Rays Caused by the Galactic Magnetic Field

B. M. Baughman
The Ohio State University and the Center for Cosmology and Astro-Particle Physics

Ultra-high energy cosmic rays (UHECR) are deflected by magnetic fields during their propagation. Different theoretical parametrisations of the Galactic magnetic field are examined using a numerical tool which simulates their propagation through models of these fields. We constrain the possible parameter space of the models by comparing data on UHECR obtained with the Pierre Auger Observatory with the results of the simulations.

Search for coincidences with astrophysical transients in Pierre Auger Observatory data

Dave Thomas
Colorado State University, Fort Collins

We analyze data collected by the Pierre Auger Observatory to search for coincidences between the arrival directions of ultra-high energy cosmic rays and the positions of astrophysical sources that are transients. We also search for coincident increases above the average background particle rate over the whole array correlated with gamma ray bursts.

The monitoring system of the Pierre Auger Observatory and its additional functionalities

Julian Rautenberg
University of Wuppertal, Department of Physics, D-42119 Wuppertal

To ensure smooth operation of the Pierre Auger Observatory a monitoring tool has been developed. Data from different sources, e.g. the detector components, are collected and stored in a single database. The shift crew and experts can access these data using a web interface that displays generated graphs and specially developed visualizations. This tool offers an opportunity to monitor the long term stability of some key quantities and of the data quality. Quantities derived such as the on-time of the fluorescence telescopes can be estimated in nearly real-time and added to the database for further analysis. In addition to access via the database server the database content is distributed in packages allowing a wide range of analysis off-site. A new functionality has been implemented to manage maintenance and intervention in the field using the web interface. It covers the full work-flow from an alarm being raised to the issue being resolved.

Nightly Relative Calibration of the Fluorescence Detector of the Pierre Auger Observatory

Rossella Caruso
Dipartimento di Fisica e Astronomia dell'Università di Catania and Sezione INFN, Catania

A relative calibration of the photomultipliers in the fluorescence telescopes is made every night. The calibration allows the long term performance of the photomultipliers to be monitored and permits an absolute calibration database to be created each night. A stable procedure has been developed to produce absolute calibration constants, typically 2 x 10^6 calibration constants/year. Three years (2006-2008) of data were analysed to produce the latest version of the database, including for the first time calibration constants for the final six telescopes that were commissioned in February 2007.

Rapid monitoring of the atmosphere after the detection of high-energy showers at the Pierre Auger Observatory

B. Keilhauer
Karlsruhe Institute of Technology (KIT) Forschungszentrum Karlsruhe, Institut für Kernphysik, Postfach 3640, 76021 Karlsruhe, Germany

The atmospheric monitoring program of the Pierre Auger Observatory has been upgraded to make measurements of atmospheric conditions possible directly following the detection of very high-energy showers. Measurements of the optical transmittance due to aerosols and clouds are time-critical. Therefore, observations of atmospheric regions close to a shower track of interest are performed within ten minutes of a shower detection using lidar and telescope monitors. Measurements of the altitude dependence of atmospheric state variables such as air temperature, pressure, and humidity are performed within about two hours following the detection of a very high-energy event using meteorological radio soundings. Both programs are triggered using a full online reconstruction with analysis-level quality cuts. We describe the implementation of the online trigger, and discuss the impact of the monitoring data with high resolution on the analysis of air shower events.

Atmospheric Aerosol Measurements at the Pierre Auger Observatory

L. Valore
Universit`a degli Studi di Napoli "Federico II" and INFN Napoli, Complesso Universitario di Monte Sant'Angelo -Via Cintia, 80126 Napoli, Italy

The Pierre Auger Observatory uses the atmosphere as a huge calorimeter. This calorimeter requires continuous monitoring, especially for the measurements made with the fluorescence telescopes. A complex monitoring program has been developed. LIDARs at the sites of each of the fluorescence detectors are used to record the presence of local haze and cloud. Beams from calibrated laser sources located near the centre of the Observatory are used to measure the light attenuation due to aerosols. The attenuation is highly variable even on small time scales. The Central Laser Facility has been used to provide hourly aerosol characterisations over five years based on two independent but fully compatible procedures. The Extreme Laser Facility (XLF) has just started operation. The level of cloud cover is measured using cameras sensitive to the infra red and can also be detected with the sky background data.

Radio detection of Cosmic Rays at the southern Auger Observatory

A.M. van den Berg,
Kernfysisch Versneller Insitittut, University of Groningen, Zernikelaan 25, 9747AA Groningen, The Netherlands

An integrated approach has been developed to study radio signals induced by cosmic rays entering the Earth's atmosphere. An engineering array will be co-located with the infill array of the Pierre Auger Observatory. Our R&D effort includes the physics processes leading to the development of radio signals, end-to-end simulations of realistic hardware configurations, and tests of various systems on site, where coincidences with the surface detectors of the Observatory are used to benchmark the systems under development.

Hardware Developments for the AMIGA enhancement at the Pierre Auger Observatory

Peter Buchholz
Universität Siegen, Fachbereich Physik, Walter-Flex-Str.3, D 57068 Siegen, Germany

To extend the energy threshold of the Auger Observatory to lower energies and to measure the number of muons in extensive air showers, the AMIGA (Auger Muons and Infill for the Ground Array) enhancement is being developed. The complete muon detector system, including the scintillation detectors, the analogue front-end, trigger and the digital readout electronics, as well as the power supplies and slow-control electronics, have been designed. Prototypes of all components have been produced and tested separately in system tests. The performances of all components and the complete system will be discussed..

A simulation of the fluorescence detectors of the Pierre Auger Observatory using GEANT 4

Pedro Assis
LIP - Laboratório de Instrumentação e Física Experimental de Partículas Av. Elias Garcia, 14 -1 1000-149 Lisboa, Portugal

A simulation of the fluorescence telescopes of the Pierre Auger Observatory was developed, taking advantage of the capabilities of GEANT 4 to describe complex 3D geometries realistically and to allow the required optical processes such as refraction, reflection, Rayleigh scattering and bulk absorption to be included in the simulation. Each telescope features Schmidt optics consisting of a ring shaped corrector lens placed at the entrance pupil and a 11 m^2 spherical mirror. The incoming light is focused on to a spherical camera, made of an array of 440 hexagonal photo-multipliers and the light guides. In this simulation all components of the optical system were implemented. Account was taken of the description of the corrector lens profile, the details of the mirror geometry, including the parameters of each individual mirror, and the different components of the camera, including light guides and photomultipliers. The Geant4 FD simulation is included in the Auger simulation and reconstruction framework and is being used in several studies of the FD performance. The main features of the simulation will be reviewed.

Education and Public Outreach of the Pierre Auger Observatory

Gregory Snow
Department of Physics and Astronomy, 116 Brace Hall, University of Nebraska, Lincoln, Nebraska, USA

The scale and scope of the physics studied at the Auger Observatory offer significant opportunities for original outreach work. Education, outreach and public relations of the Auger collaboration are coordinated in a separate task whose goals are to encourage and support a wide range of education and outreach efforts that link schools and the public with the Auger scientists and the science of cosmic rays, particle physics, and associated technologies. The presentation will focus on the impact of the collaboration in Mendoza Province, Argentina, as: the Auger Visitor Center in Malargüe that has hosted over 40,000 visitors since 2001, a collaboration-sponsored science fair held on the Observatory campus in November 2007, the Observatory Inauguration in November 2008, public lectures, school visits, and courses for science teachers. A Google-Earth model of the Observatory and animations of extensive air showers have been created for wide public release. As the collaboration prepares its northern hemisphere site proposal, plans for an enhanced outreach program are being developed in parallel and will be described.

Performance and operation of the Surface Detectors of the Pierre Auger Observatory

Tiina Suomijärvi
Institut de Physique Nucleaire, Universit´e Paris-Sud, IN2P3-CNRS, Orsay, France

The Surface Array of the Pierre Auger Observatory consists of 1660 water Cherenkov detectors that sample the charged particles and photons of air showers initiated by energetic cosmic rays at the ground. The construction of the array in Malargue, Argentina is now complete. A large fraction of the detectors have been operational for more than five years. Each detector records data locally with timing obtained from GPS units and power from solar panels and batteries. In this paper, the performance and the operation of the array are discussed. We emphasise the accuracy of the signal measurement, the stability of the triggering, the performance of the solar power system and other hardware, and the long-term purity of the water.

BATATA: A device to characterize the punch-through observed in underground muon detectors and to operate as a prototype for AMIGA

G. Medina-Tanco,
Instituto de Ciencias Nucleares, Univ. Nacional Autónoma de México Circ. Exterior S/N, Ciudad Universitaria, México

BATATA is a hodoscope comprising three X-Y planes of plastic scintillation detectors. This system of buried counters is complemented by an array of 3 water-Cherenkov detectors, located at the vertices of an equilateral triangle with 200 m sides. This small surface array is triggered by extensive air showers. The BATATA detector will be installed at the centre of the AMIGA array, where it will be used to quantify the electromagnetic contamination of the muon signal as a function of depth, and so to validate, in situ, the numerical estimates made of the optimal depth for the AMIGA muon detectors. BATATA will also serve as a prototype to aid the design of these detectors.

Hadron Production Measurements with the NA61/SHINE Experiment and their Relevance for Air Shower Simulations

Ioana C. Mariş* for the NA61/SHINE Collaboration
**Karlsruhe Institute of Technology (KIT), D-76021 Karlsruhe, Germany*

***Abstract*. NA61/SHINE is a fixed-target experiment to study hadron production in hadron-nucleus and nucleus-nucleus collisions at the CERN SPS. Due to a large acceptance and good particle identification capabilities in forward direction, NA61/SHINE is well suited for measuring particle production to improve the reliability of air shower simulations. During its pilot run in 2007 proton-carbon collisions at 31 GeV/c were recorded. Dedicated runs for pion-carbon collisions at 158 and 350 GeV/c are planned for 2009. We will study the phase space regions of secondary particles that are of importance for understanding the muon production in air showers as measured by KASCADE and the Pierre Auger Observatory. The performance of the NA61/SHINE detector is discussed and preliminary results from the pilot run are presented.**

***Keywords*: NA61/SHINE, cosmic rays**

I. Introduction

Cosmic rays at very high energy ($E > 10^{14}\,\mathrm{eV}$) can be measured only indirectly by observing the secondary particles produced in cascade processes in the atmosphere. Therefore it is not surprising that many open questions in cosmic ray physics are related to the difficulty of determining the energy and mass/type of primary shower particle at these energies. For example, the mass composition of the primary particles can be obtained only from comparing air shower data with simulations of the air shower development in the atmosphere [1], [2].

The simulations involve detailed descriptions of the hadronic, muonic and electromagnetic components of the air showers. The present implementations rely on phenomenological models for the hadronic interactions and cannot describe the observed air shower properties with a good precision [3], [4]. For example, at the Pierre Auger Observatory, the observed number of muons is underestimated in simulations with commonly used hadronic interaction models [4].

Hadronic interaction models are based on extrapolations of the particles interaction properties in phase space regions which are presently not covered by particle physics experiments. The energies of the first interactions in high energy showers are not accessible by current accelerators. Furthermore, at low energies, there is a lack of precise data in the forward region and for projectiles and targets relevant for air showers [5]. The impact of the uncertainty of hadronic interaction characteristics on air shower observables does currently prevent an unambiguous analysis of air shower data in terms of e.g. the primary mass composition [1], [6].

While high energy interactions are of direct relevance to the longitudinal shower profile [7], particle production at low energy is important for the lateral distribution of shower particles at ground. The use of different hadronic interaction models for low-energy interactions ($E < 200\,\mathrm{GeV}$) leads to significant differences of the expected particles at ground [8], [9]. For example, in the case of the Auger Observatory [10], the predicted muon densities differ by more than 20% [8] with a difference of $\approx 40\%$ expected between proton and iron.

The NA61/SHINE (SHINE $\equiv$ SPS Heavy Ion and Neutrino Experiment) experiment [11] combines a rich physics program in an efficient and cost effective way offering the possibility to reach physics goals in three different fields: neutrino experiment calibration, cosmic ray simulations, and the behavior strongly interacting matter at high density.

The NA61/SHINE apparatus is an upgrade of the NA49 experiment [12]. A new time of flight detector has been tested and installed in the forward beam direction, increasing the accuracy of the particle identification. Moreover the update of the DAQ and of the readout of tracking detectors provides an increase of the maximum detection rate by a factor of 10 with respect to NA49. During its 10 years of operation the NA49 experiment delivered high precision data with beams ranging from proton to lead [13]. Among other results, the minimum bias analysis of p+p [14] and p+C [15] collisions at a beam momentum of 158 GeV/c provided information about the inclusive production of charged pions which already have been used to improve the precision of air shower simulations [16].

In the following we will investigate the phase space region important for cosmic ray experiments and compare it with the measurement capabilities of the NA61/SHINE experiment. Data taken in the 2007 pilot run are presented.

II. Muon production in air showers

The electromagnetic component of extensive air showers originates from π^0 decays, bremsstrahlung and $e^{\pm}$ pair production with a small component from $\mu^{\pm}$ decays. The electromagnetic particles are well described by QED. The muonic component, produced mainly in decays of charged pions and kaons, depends upon the phenomenological models used to overcome the problems of perturbative QCD calculations for processes with low momentum transfer.

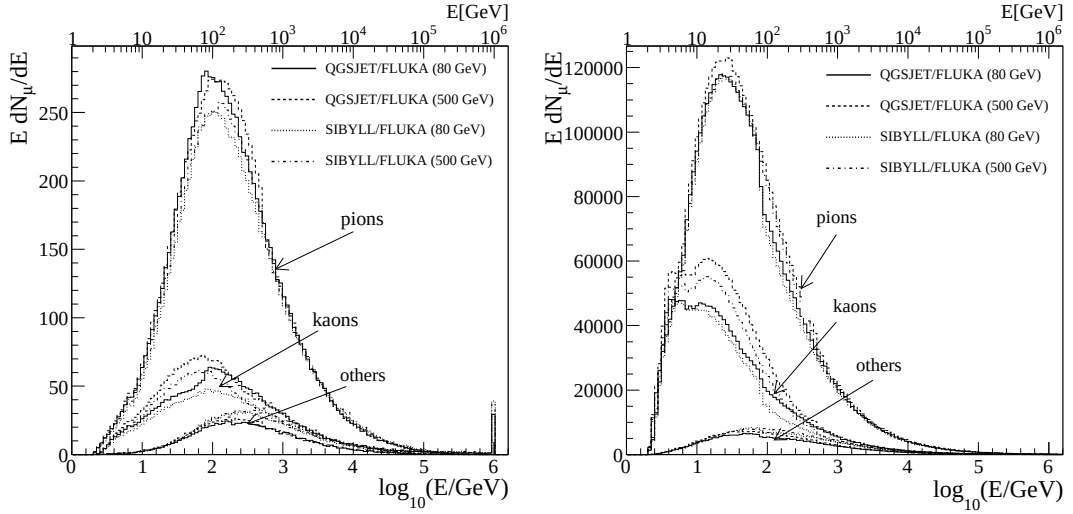

Fig. 1. Energy spectra of the grandmothers for a primary cosmic ray at 10^{15} eV (left) and 10^{19} eV (right). The transition energy between different interaction models is indicated in brackets. Only the grandmother particles of muons with a total energy larger than 250 MeV (left) and 150 MeV (right) were taken into account. The distance of the muons to the shower axis was required to be between 40 and 200 m (left) and 900 and 1100 m (right). The spectra are averaged over the total number of simulated air-showers.

In order to investigate the muon production, air shower simulations were performed assuming vertical incident protons as primary particles. To cover the knee energy range 1000 air-showers at 10^{15} eV were simulated and the particles were stored at an altitude of 100 m asl. The KASCADE experiment is sensitive to muons above 250 MeV and the distribution of particles on ground is mostly important at distances between 40 and 200 m from the air shower axis, therefore only muons in these ranges are considered. For ultra high energy cosmic rays, 5 events at 10^{19} eV were generated and the particles reaching an altitude of 1400 m were stored. At this energy the most important region is between 900 m and 1100 m from the shower axis, distance where the energy estimator and the mass composition parameters for the cosmic rays recorded by the surface detector of the Pierre Auger Observatory are evaluated. The water Cherenkov detectors are observing light from muons above 150 MeV.

The air showers were generated with a modified version of the CORSIKA [17] code for which the history of the muon production is available in the output [18]. In the following we refer by the term *grandmother* to the hadron inducing the last hadronic interaction that leads to a meson that decays into the corresponding muon. Each air shower was generated four times using different hadronic interaction models. FLUKA [19] was utilized for the description of the hadronic interaction in the low energy range and QGSJet II [20] or Sibyll 2.1 [21] to handle the high energy region. The assumption of the transition energy where the switch between the interaction models occurs influences the particle distributions at ground [22]. Therefore simulations with two transition energies were generated: at 80 GeV and 500 GeV. At the highest energies the available CPU time and storage do not allow to track all the particles in the cascade processed, therefore the electromagnetic component of these showers was neither tracked nor stored.

The energy spectra of the grandmother particles are depicted in Fig. 1. The difference in the distributions of the particles predicted by different high energy interaction models is compatible with the difference induced only by switching the transition energy. Small discontinuities at 80 and 500 GeV are observed indicating a miss-match between the predictions of low energy and high energy hadronic interaction models. The majority of muons are produced by charged pions ($\approx 95\%$) in the energy range 10-500 GeV. A $\approx 4\%$ contribution comes from kaons at 10-200 GeV.

Grandmother particles are equivalent to the beam particles for fixed target experiments. The majority of pions cover mostly the forward direction (polar angle, $\theta < 0.2\,\mathrm{rad}$). Giving the momentum range and the direction, the current and future data of the NA61/SHINE experiment are perfectly suited for improving the hadronic interaction models.

III. NA61/SHINE EXPERIMENT

The NA61/SHINE detector is located in the H2 beam line of the North experimental hall of the SPS. It employs a large hadron spectrometer for the study of the hadronic states produced in interaction of π, p, C, S or In beam particles with a variety of fixed targets at the SPS energies.

The layout of the NA61/SHINE experiment is presented in Fig. 2. The detector inherits the main components of the NA49 experiment [12]. A set of upstream scintillation or Cherenkov counters and beam position detectors (BPD) provides precise timing reference, charge and position measurement of the incoming beam particles. The components for tracking are four

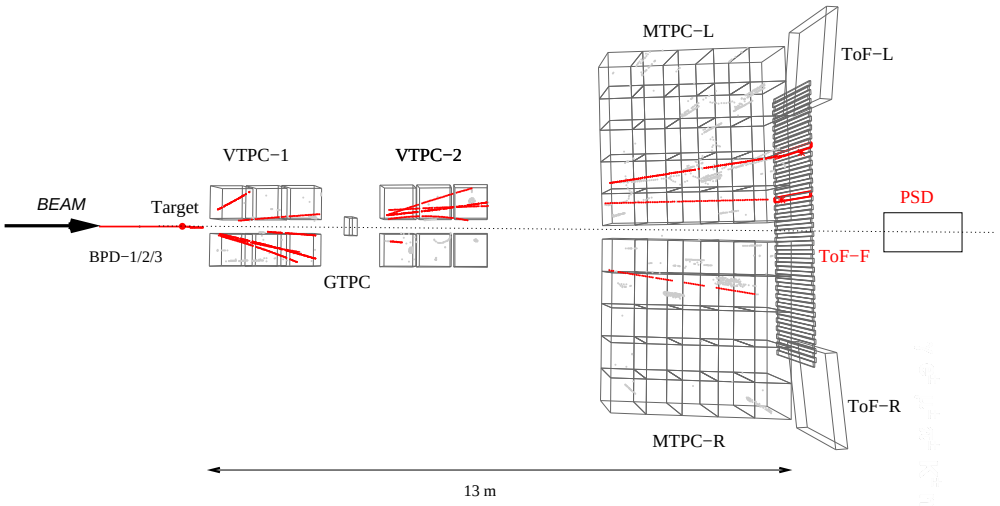

Fig. 2. A typical event recorded during the pilot run for a proton beam (31 GeV/c) on a thin carbon target. The NA61/SHINE detector layout is sketched with the exception of the vertex magnets surrounding the vertex TPCs. Two of the particles have left a signal in the forward ToF detector.

large volume Time Projection Chambers (TPCs). The vertex TPCs (VTPC-1 and VTPC-2) are located in the magnetic field of two super-conducting dipole magnets with a maximum combined bending power of 9 Tm at currents of 5000 A. The other two (MTPC-L and MTPC-R) are positioned symmetrically with respect to the beam line, downstream of the magnets. An additional gap TPC (GTPC) is located on the beam axis between the vertex TPCs.

At minimum ionization particle identification by energy loss measurement alone is not possible and even with a very good dE/dx resolution kaon selection on a track-by-track basis is not feasible. Therefore the NA49 detector was equipped with time-of-flight detectors (ToF-L and ToF-R) placed behind the MTPCs. The time resolution achieved is of 60 ps. In 2007 the experiment has been updated with a new forward time of flight detector (ToF-F), installed downstream of the MTPCs and closing the gap between ToF-L and ToF-R. The ToF-F provides a very good particle identification in the low momentum domain ($p < 6\,\mathrm{GeV/c}$). In the pilot run data for cosmic rays and T2K neutrino experiment [23] on p+C interactions at 31 GeV/c were recorded [24]. One super-module of the Particle Spectator Detector (PSD) was installed downstream of the TOF-F and tested [25]. A major enhancement for the detector performance, i.e. the TPC readout and DAQ upgrade, was achieved in the 2008 run. It results in an increase of the data rate by a factor of about 10 compared to the old setup.

An example of the combined ToF and dE/dx particle identification capabilities is illustrated in Fig. 3 for positive particles using the pilot run data. Four clusters, corresponding to positrons, pions, kaons and protons can

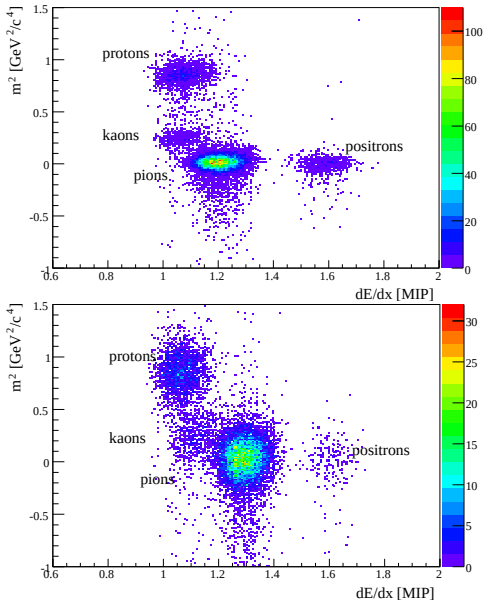

Fig. 3. Particle identification for positively charged particles using the combined ToF and dE/dx measurements in the momentum range 2-3 GeV/c (upper panel) and 4-5 GeV/c (lower panel).

be seen. At momenta above 4 GeV/c the separation of the lighter particles (e, π) from the group of heavier ones is performed essentially by dE/dx, whereas the ToF measurement is needed to distinguish between kaons and protons. Below 4 GeV/c particle identification can be performed almost exclusively by the ToF.

The detector acceptance, determined by its geometry and magnetic field, is shown in Fig. 4 for beam momenta

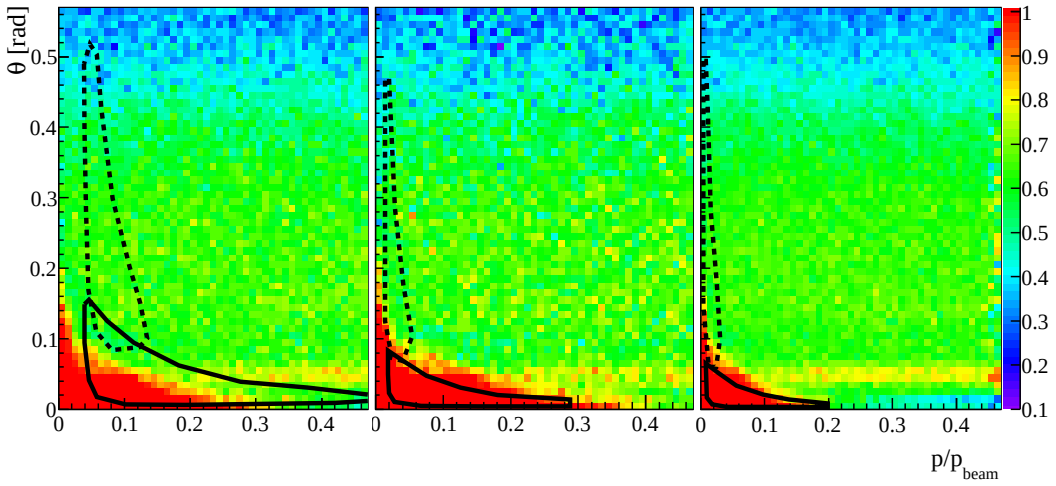

Fig. 4. The detector acceptance at beam momenta of 50 GeV/c (left), 158 GeV/c (middle) and 350 GeV/c (right). Lines correspond to the 68% contour of the cosmic ray phase space relevant for KASCADE (continuous) and Pierre Auger Observatory (dashed).

of 50 GeV/c, 158 GeV/c and 350 GeV/c. It is plotted in the plane of the polar angle, θ, versus the fraction of beam momentum carried by the secondary particles. Only tracks that were well reconstructed were selected, requiring at least 10 hits in the TPCs. The phase space of relevance for the KASCADE experiment, shown in the same figures with continuous contours is covered at full acceptance, close to 100%. At higher energies, relevant for the Pierre Auger Observatory (dashed contour), the acceptance of the detector is between 60 and 80%. The particles are at larger angles with respect to the beam due to the larger distance to the air shower axis that was required.

IV. Outlook

In 2009 the data taking program will start with p and π beams on C targets for cosmic ray and for the T2K experiments at energies of 30, 158 and 350 GeV with an expected statistics of about 18M minimum bias events. The data will cover a large region of the forward phase space of low energy hadronic interactions as needed for improving air shower modeling.

Acknowledgements

This work was supported by the Virtual Institute VI-146 of Helmholtz Gemeinschaft, Germany, Korea Research Foundation (KRF-2008-313-C00200), the Hungarian Scientific Research Fund (OTKA 68506), the Polish Ministry of Science and Higher Education (N N202 3956 33), the Federal Agency of Education of the Ministry of Education and Science of the Russian Federation (grant RNP 2.2.2.2.1547) and the Russian Foundation for Basic Research (grant 08-02-00018), the Ministry of Education, Culture, Sports, Science and Technology, Japan, Grant-in-Aid for Scientific Research (18071005, 19034011, 19740162), Swiss Nationalfonds Foundation 200020-117913/1 and ETH Reseach Grant TH-01 07-3.

References

[1] T.Antoni *et al.* [KASCADE Collaboration], Astroparticle Phys. 24 (2005) 1–25 [arXiv:astro-ph/0505413].
[2] J. Knapp, D. Heck, S.J. Sciutto, M.T. Dova, and M. Risse, Astropart. Phys. 19 (2003) 77-99 [arXiv:astro-ph/0206414].
[3] J. R. Hörandel [KASCADE Collaboration], these proceedings.
[4] R. Engel [Pierre Auger Collaboration], arXiv:0706.1921 [astro-ph]. A. Castellina [Pierre Auger Collaboration], these proceedings.
[5] R. Engel, Nucl. Phys. Proc. Suppl. **122**, 437 (2003) [arXiv:hep-ph/0212340].
[6] R. Ulrich, R. Engel, S. Müller, T. Pierog, F. Schüssler and M. Unger, these proceedings.
[7] R. Ulrich, R. Engel, S. Müller, F. Schüssler and M. Unger, to appear in Proceedings of the 15^{th} ISVHECRI, Paris 2008.
[8] H. J. Drescher and G. Farrar., Astropart. Phys. 19(2003) 325. H. J. Drescher, M. Bleicher, S. Soff, H. Stöcker, Astropart. Phys. 21(2004) 87.
[9] C. Meurer, J. Blümer, R. Engel, A. Haungs, M. Roth, Czech. J. Phys. 56 (2006) A211 [arXiv:astro-ph/0512536].
[10] J. Abraham *et al.* [Pierre Auger Collaboration], Nucl. Instrum. Meth. A523 (2004) 50.
[11] N. Antoniou *et al.* [NA61/SHINE Collaboration], CERN-SPSC-2006-034.
[12] S. Afanasiev *et al.* [NA61/SHINE Collaboration], Nucl. Instrum. Meth. A430 (1999) 210.
[13] C. Alt *et al.* [NA49 Collaboration], Phys. Rev. C 94 052301 (2005). P. Dinkelaker *et al.* [NA49 Collaboration], J. Phys. G 31 S1131 (2005).
[14] C. Alt *et al.* [NA49 Collaboration], Eur. Phys. J. C45 (2006) 343.
[15] C. Alt *et al.* [NA49 Collaboration], Eur. Phys. J. C49 (2007) 897.
[16] T. Pierog and K. Werner, Phys. Rev. Lett. 11 (2008) 171101.
[17] D. Heck, J. Knapp, J. Capdevielle, G. Schatz and T. Thouw, 1998, FZKA-6019.
[18] C. Meurer *et al.* , Nuclear Physics B (Proc. Suppl.) 175-176 (2008) 113
[19] G. Battistoni *et al.* , AIP Conf. Proc., 896 (2007) 31.
[20] N. N. Kalmykov, S. S. Ostapchenko, A.I. Pavlov Nucl. Phys. (Proc. Suppl.) B52 (1997) 17.
[21] R. S. Fletcher, T. K. Gaisser P. Lipari and T. Stanev, Phys. Rev. D50 (1994) 5710 R. Engel, T. K. Gaisser, T. Stanev and P. Lipari, Proc. 26^{th} Int. Cosmic Ray Conf., Salt Lake City, Utah 1 (1999) 415.
[22] I. C. Mariş, R. Engel, X. Garrido, A. Haungs, M. Roth, R. Ulrich and M. Unger, to appear in Proceedings of the 15^{th} ISVHECRI, Paris 2008.
[23] N. C. Hastings, arXiv:0905.1211 [hep-ex].
[24] N. Abgrall *et al.* [NA61/SHINE Collaboration], CERN-SPSC-2008-018, CERN-SPSC-SR-033, Jul. 2008.
[25] M. Golubeva *et al.* ,Nucl. Instrum. Meth. A589 (2009) 268.

Correlations between solar events and the cosmic muon flux measured with WILLI detector

I.M. Brancus*, A. Saftoiu*, B. Mitrica*, M. Petcu*, O. Sima†, A. Haungs‡, G. Toma*, M. Duma*, A. Bercuci§

*Horia Hulubei National Institute for Physics and Nuclear Engineering, 077125, Bucharest, Romania
†Department of Physics, University of Bucharest, Romania
‡Institut für Kernphysik, Forschungszentrum Karlsruhe, 76021 Karlsruhe, Germany
§on leave of absence from NIPNE

***Abstract*. The WILLI detector, built in IFIN-HH Bucharest in collaboration with FZ Karlsruhe, is a compact rotatable system, with an incident surface of 1 m^2, consisting of 16 modules, each module having a scintillator layer (3 cm thickness) and Al support (1 cm thickness). The modular system is surrounded by 4 anticoincidence modules. With WILLI detector we can measure simultanenously muon events with energy $\geq$ 0.4 GeV and the muon events with energy lower than 0.6 GeV (coresponding only to events stopped in the detector layers).**

The measurements performed with WILLI detector have shown a variation of the muon intensity which can be correlated with the solar effects. Taking into account muon events with energy $\geq$ 0.4 GeV, a modulation of the muon intensity as a diurnal variation is observed.

The analysis of the muon events for a smaller energy range, lower than 0.6 GeV, has shown an aperiodic variation of the muon intensity, which could be correlated with magnetic activity indicated by the planetary K-index.

***Keywords*: low energy atmospheric muons, solar modulation**

I. Introduction

When galactic cosmic rays enter the heliosphere they enter a region dominated by our Sun. Magnetic fields and processes such as diffusion, convection and drifts affect cosmic particles on different timescales and with various intensities corresponding to the solar activity. For solar modulation surveys the low energy part of the cosmic rays spectrum is relevant as it is the part most influenced by the solar activity. As the particle's energy increases it tends to travel less influenced.

The Earth's atmosphere and magnetic field also play an important role. A cosmic particle hitting the Earth's atmosphere will suffer nuclear interactions, loose energy and generate a shower or secondary particles that will continue interacting as they propagate towards ground. The muons component of such a shower is the most abundant at ground level.

The fact that cosmic rays and the secondary particles that are observed at ground level are linked to the solar activity gives us the opportunity to investigate the solar activity.

The two different types of solar effects that can be observed using particle detectors at ground level are periodic or sporadic effects, [1], [2], [3], [4], [5], on the flux of neutrons and muons. Periodic events are well connected to the solar cycle and geometry of the Sun-Earth connection and present important subjects for solar studies but do not pose a threat on ourselves. Phenomena that can also affect life on Earth and are of solar origin may be expected if spaceweather is taken into account because particle detectors at ground level can record annomalies in the cosmic rays propagation before dangerous magnetic storms reach and affect us.

II. The detector

The detector, WILLI (Weakly Ionizing Lead-Lepton Interaction), is a sampling calorimeter for atmospheric muons, designed initially for muon charge ratio measurements [6]. It is located in IFIN-HH, at 44^0 21' N, 26^0 E, 75 m above sea level and 5.6 GV rigidity cutoff. It consists of 20 modules 16 plates placed in a stack and 4 as anticounters, fig. 1. All the modules are identical, scintillator plates, 3 cm thick, encased in 1 cm thick aluminium box, read by 2 photomultipliers placed at opposite corners of the plate. The detector has the possibility to rotate both in zenith (up to 45^0) and azimuth (no restriction).

The acquisition trigger can be chosen from 1 or 2 different plates in the stack. This means that there exists the possibility to record muons with different energy threshold, $\geq$ 0.4 GeV or $\geq$ 0.6 GeV, if the trigger is set for the first 2 plates or for the first and the last plates in the stack.

Also the detector can register muons stopped inside the detector which gives us the possibility to investigate muons in a small energy range, 0.4-0.6 GeV. The selection for a small range of energies is performed after the acquisition on the usual run when all the incoming muons are recorded. Thus we have access to both types of data, all passing the trigger condition and energy range selection, simultaneously.

The detector dead time is 50 μs. For muons that are stopped in the detector an additional 80 ns time window

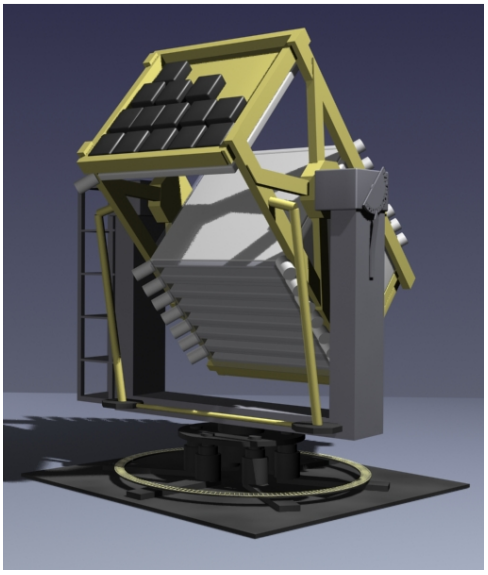

Fig. 1. The WILLI detector.

is reserved for the observation of the delayed electron resulted from the muon decay inside the detector, thus increasing the overall dead time.

III. Solar modulation

Solar modulation means time variation of cosmic radiation intensity due to solar activity.

Solar modulation of cosmic rays takes place in the heliosphere (i.e. the region where solar influence is dominant). Galactic cosmic rays are influenced by the solar wind and heliospheric magnetic field (HMF) when entering the heliosphere. The solar activity, through all kinds of magnetic disturbances, affects the shape of the cosmic rays energy spectrum and the direction of particle propagation. The modulation effects decrease with increasing energy and become less significant for particles with rigidities in excess of ≈10 GeV/nucleon, i.e. a rigidity of 10 GV for protons and 20 GV for He [7].

The amplitude of this activity is time dependent and manifests periodic as well as aperiodic features on different time scales (see table I). In this study we intend to investigate the possibility to observe the types of effects listed in table I.

IV. Muon intensity variations

We have performed measurements of integral vertical muon intensity, computed as below, for various periods of time.

$$I_v(E > E_{th}) = \frac{dN}{dAdtd\Omega}[cm^{-2}s^{-1}sr^{-1}] \qquad (1)$$

where E_{th} is given by the type of acquisition/trigger chosen.

After recording the raw muon count rate we have corrected it for atmospheric pressure, [7]. The fractional change of muon intensity, $\delta j_\mu/j_\mu$, is related to the pressure change, δp, by:

$$\delta j_\mu/j_\mu = -\alpha_\mu \delta p \qquad (2)$$

where α_μ is the *pressure coefficient* of the muonic component, $\alpha_\mu \simeq 0.12\%$ [mm^{-1} Hg] for atmospheric pressure measured in [mm Hg].

So far no additional data, e.g. height of the production layer, are available and therefore no other correction for the atmospheric influence is made.

A. Periodic variations

Periodic variations in sea level muon intensity have been documented [3], [5]. They include data recording on extensive periods of time as well as daily monitoring.

Given the short amount of time our detector has been taking data for solar modulation monitoring we will reffer only to short period periodic variations, namely the daily variation.

Data sets contain time stamp and PMT signal amplitude information for each individual event. They are divided into user defined time intervals after the acquisition process. Figure 2 shows raw count rate for a period of 3 days for E $\geq$ 0.4 GeV.

For time periods of 24 hours 10-minute rates were normalized to a daily average obtained from data taken 7 days before and fitted with a 24 and 12 hour periodicity function, see figure 3,

$$Averaged\ rate = 1 - 0.008 \cdot sin(\frac{2\pi}{12}x - 1.21) - \\ -0.03 \cdot sin(\frac{2\pi}{24}x - 1.47). \qquad (3)$$

The amplitude of the sinusoidal variation relative to the average is ∼3% for the diurnal variation and ∼1% for the semi-diurnal variation. The maximum is around 11 a.m.

B. Aperiodic variations

Aperiodic variations are mainly characterized by their relative unpredictability. They are linked to the solar activity, therefore a solar maximum period is expected to present more aperiodic events, but this is not a rule. This type of variations can vary both in intensity (see table I) and time scale. Sporadic events have been detected with muon telescopes [9].

Small intensity variations may be caused by geomagnetic field perturbations which are usually linked with the solar activity.

Our detector, being able to 'see' small variations as the daily variation and due to its good counting possibility, can be also used to investigate these aperiodic events.

Low energy muons are mostly produced by low energy primaries which are strongest affected by solar modulation. Because of the stack configuration of the detector we can measure the muon intensity at low energies and for small energy ranges. This enables us to exclude all the high energy muons and measure only the muons most influenced by solar and local

type	amplitude	nature
Periodic variations		
11- and 22-year	up to 30%	Solar modulation of GCR in the heliosphere
27-day	<2%	Long-lived longitudinal asymmetry in HMF of solar wind structure
diurnal	few%	Anisotropy of CR fluxes due to convection by solar wind and diffusion along HMF lines
Aperiodic variations		
GLE	1-300%	Increase of CR intensity due to arrival of solar cosmic rays
Forbush decreases	up to 30%	GCR decrease due to the shielding by an interplanetary shock passing the Earth
increase before Forbush decrease	<2%	CR increase due to "collection" of CR particles in front of the interplanetary shock causing a Forbush decrease
magnetic cloud effect	few%	GCR decrease due to the shielding by a magnetic cloud passing the Earth

TABLE I
CR INTENSITY VARIATIONS: EXTRA-TERRESTRIAL EFFECTS [8]

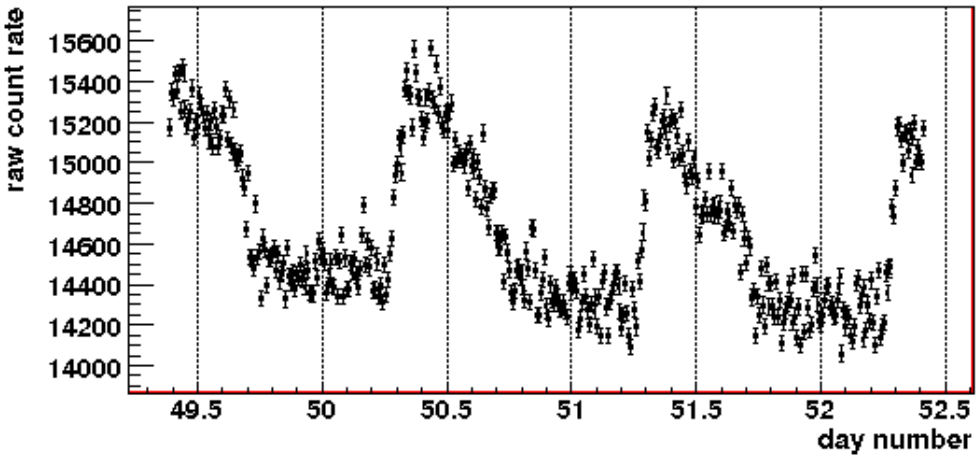

Fig. 2. Raw muon count rate, measured with WILLI, as a function of day number of the year divided into 10 minutes intervals for E $\geq$ 0.4 GeV. Error bars represent statistical errors.

magnetic activities. Such an example is depicted in fig. 4. The figure shows 60-minutes count rates for muons in the energy range 0.4-0.6 GeV. In this energy range a significant decrease is observed that was not significant in the E $\geq$ 0.4 GeV measurements. After investigation, an increase in the K_p index was found to coincide, as time period during that day, with the observed decrease [10].

V. CONCLUSIONS

In this study we investigated the possibility to detect solar modulation of cosmic rays, both periodic and aperiodic effects, with our detector, WILLI, a sampling calorimeter for atmospheric muons.

Due to the configuration of our detector we can perform various types of measurements, selecting only a small energy range, 0.4-0.6 GeV, or all the muons passing through the detector which sets an energy lower limit.

Our detector is capable of recording variations in the muon count rate that are of the same order as those expected for solar modulation effects. A few examples stand to prove it.

VI. ACKNOWLEDGEMENTS

The authors would like to thank the Romanian Ministry of Education, Research and Innovation for funding of this study and Prof. Rebel for his continuous support and advice.

REFERENCES

[1] H.L. Hall, M.L. Duldig, J.E. Humble, Space Science Review **78**, (1996), p.401
[2] M.S. Potgieter, Space Science Reviews **83**, (1998), 147-158
[3] M.L. Duldig, Publication of Astronomical Society of Australia **18**, (2001), 12-40
[4] B. Heber, H. Fichtner, K. Scherer, Space Science Reviews **125**, (2006), 81-93
[5] N.S. Barbashina et al., astro-ph/0701288 (2007)

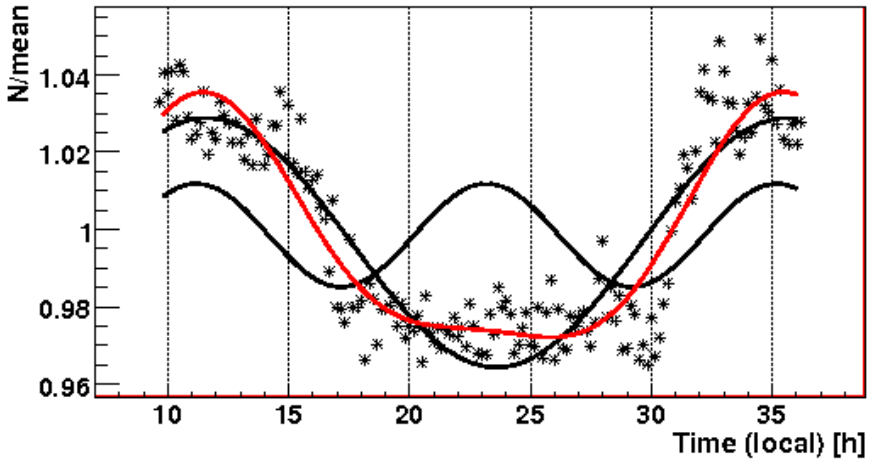

Fig. 3. Daily variation of muon count rate for E $\geq$ 0.4 GeV as a function of local time averaged with a daily mean and fitted with 12 and 24 hour periodicity functions. The third curve represents the fit with the sum of the 2 sine functions.

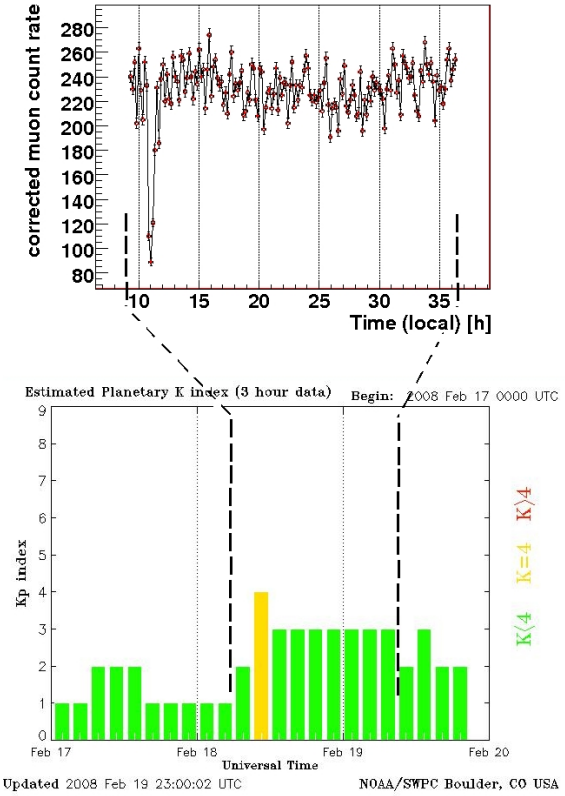

Fig. 4. Upper panel: variation of 60 minutes count rate, measured with WILLI, for an aperiodic decrease registered around 10 a.m. local time on February 2008; the line connecting the points is only meant to help the eye. Lower panel: planetary K_p index indicating an unsettled magnetic field around the same period of time that the decrease was observed, [10].

[6] B. Vulpescu et al., Nucl. Instum, Meth. A **414**, (1998), p. 205-217

[7] P. Grieder, *Cosmic Rays at Earth. Researcher's Reference Manual and Data Book*, Elsevier, 2001

[8] R. Rasinkangas, K. Mursula, T. Ulich, and J. Kangas, *The Online Space Physics Textbook of the University of Oulu*, http://www.oulu.fi/~spaceweb/textbook/

[9] I. Braun et al., Advances in Space Research **43** (2009), 480488

[10] NOAA, *Space Weather Prediction Center* http://www.swpc.noaa.gov/

Studies of hadronic interaction models by measuring the flux and the charge ratio of atmospheric muons with the WILLI detector

B.Mitrica*, I.M.Brancus*, A.Saftoiu*, H.Rebel†, O.Sima‡, A.Haungs†, G.Toma*, M.Petcu* and M.Duma*

**Horia Hulubei Institute of Physics and Nuclear Engineering (IFIN-HH), Bucharest, Romania, P.O.B.MG-6*
†Institut fr Kernphysik, Forschungszentrum Karlsruhe, P.O.B. 3640, Germany
‡Department of Physics, University of Bucharest, P.O.B. MG-11, Romania

***Abstract*. Measurements of the of the low energy (<1 GeV) muon charge ratio and muon flux have been perfomed using WILLI detector. We investigate the azimuthal and the zenithal dependence of the muon flux. The results are compared with complex Monte-Carlo simulation using CORSIKA code taking into account 2 hadronic interaction models (DPMJET and QGSJET2). The results of the energetic, azimuthal and zenithal dependence of the atmospheric muon charge ratio was compared with CORSIKA simulations (DPMJET model). The simulations of the EAS muon charge ratio was performed using CORSIKA code and 2 hadronic interaction models (QGSJET2 and EPOS), in order to to investigate a new experiment WILLI-EAS that will be focused on measurements of the muon charge ratio from individual EAS at primary energy between $10^{14} - 10^{15}$ eV. The results of the simulations shows that the EAS muon charge ratio is influenced by hadronic interaction models.**

***Keywords*: muon, simulation, WILLI**

I. INTRODUCTION

Measurements of the low energy ($<$ 1 GeV) muon flux and muon charge ratio were performed using the WILLI detector [1], [2] which is a compact, modular rotatable system. Each module is formed by a plastic scintillator layer of 3 cm thickness, in 1 cm Al frame box. The detector was used to measure the muon charge ratio and the muon flux, for different azimuthal direction (N,S,E,W) for a mean zenithal angle of 35°. The results were compared with Monte-Carlo simulations performed with CORSIKA code [3] using 2 hadronic interaction models DPMJET [4] and QGSJET [5]. Beside the studies of the atmospheric muons, we will focuse in the future on the investigation of the charge ratio of the muon density in EAS, so the WILLI detector is extended by a mini array of 12 scintillator plates of $1m^2$. Simulations performed with CORSIKA using 2 hadronic interaction models (QGSJET2[5] and EPOS[6]) shows that EAS muon charge ratio is quite sensitive to the hadronic model.

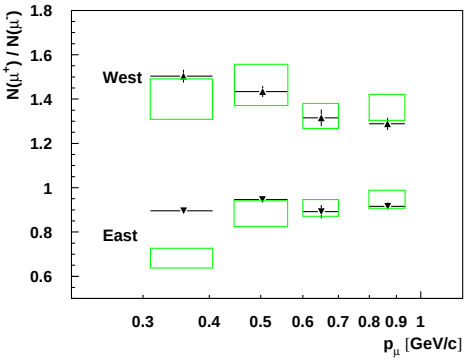

Fig. 1. The energy variation of the muon charge ratio (points) compared with CORSIKA simulations (rectangles)

II. THE MUON CHARGE RATIO

The charge ratio of atmospheric muons has been analysed under various theoretical aspects [7], [8]. The merit of the WILLI detector is that it approaches the very low muon energy range with excellent accuracy. The detector determines the charge ratio of atmospheric muons by measuring the life time of stopped muons in the detector layers: the stopped positive muons decay with a lifetime of 2.2 μs, while negative muons are captured in the atomic orbits, leading to an effectively smaller lifetime depending on the stopping material. The muon charge ratio is determined from the measured decay curve of all muons stopped in the detector, by fitting the measured decay spectrum with the theoretical curve.

For the investigation of the azimuth dependence of the charge ratio of atmospheric muons, a series of measurements [9] has been performed on four azimuth directions of incidence of the atmospheric muons: North, East, South, West, (N, E, S, W) for muons with inclined incidence, mean value at 35^{o} and mean incident energy 0.5 GeV/c.

The results (see Fig.1,2) show that CORSIKA simulations, based on DPMJET model reproduce relativ well the azimuthal and the variation i.e. the East-West effect as observed by WILLI. The Okayoma Group [10] reported a less pronounced azimuth dependence

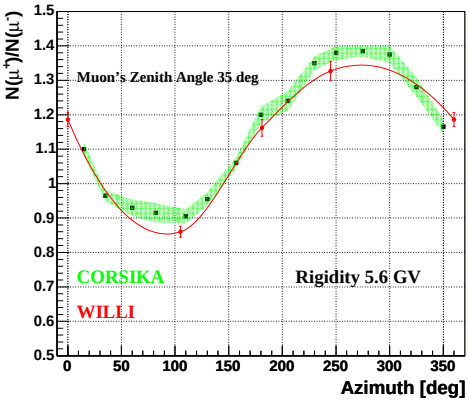

Fig. 2. The azimuthal variation of the muon charge ratio (preliminary)

but considering muons with higher energies (> 1 GeV). The observed asymmetry is attributed to the anisotropy of primary proton flux caused by the geomagnetic cut-off, as well as to the geomagnetic influence on the atmospheric muon propagation.

III. Muon flux measuremnts

Measurements of the flux of low energy muons have been performed by use of the WILLI detector. The results have been compared to Monte Carlo simulations based on DPMJET model and semiempirical approaches of Judge and Nash [11] and of Gaisser [12]. The results agree with the predictions of of the simulations, while the semiemprical formulae have a restricted range of validity (Fig.3). Obviously the approach of Gaisser is only applicable at muon energies above 10 GeV [9].

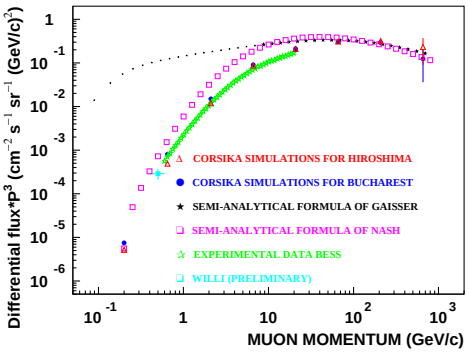

Fig. 3. The muon flux data compared with Monte Carlo simulations and semi-analytical formulae

We have aplied another hadronic interaction model (QGSJET) for simulationg the muon flux in the energy range 0.2 GeV - 1 TeV. Figure 4 shows the muon flux simulated with QGSJET and DPMJET models for a mean zenith angle of 35 ^{o}. Comparing with previoulsly simulation results (DPMJET) we note only very small differences between their predictions.

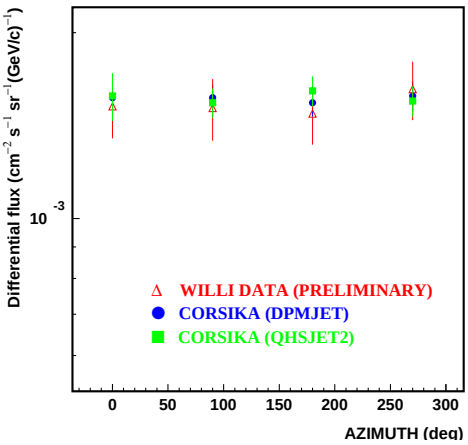

Fig. 4. The azimuthal variation of the muon flux measure by WILLI compared with CORSIKA simulatiuons

IV. WILLI-EAS, a detection system for measuring muon charge ratio in EAS

The difficulty in studying the high cosmic rays is their low intensity, what requires systems of detection covering large surfaces.

KASCADE-Grande [13] is a complex array, area 700 m^2, for investigating the energy spectrum and the mass composition of primary cosmic particle with energies in the knee range, 10^{14} -10^{18} eV. At ISVHECRI 2004 [14] Okayoma group reported results from LAAS experiments for measuring integral cosmic ray spectrum by requiring coincidences at multiple EAS arrays, formed by mini-arrays.

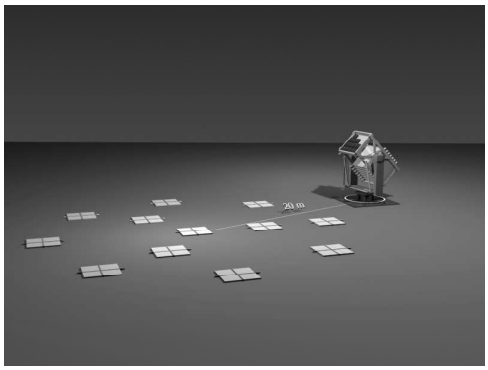

Fig. 5. A possible layout for the mini-array for triggering the WILLI detector.

There are currently some experimental approaches under discussion to measure the charge ratio of the muon density in EAS [15], [16]. Our approach [17] for an appropriate detector installation follows the considerations of [18], which have theoretically (on basis of simulations) revealed very detailed features of the geomagnetic influence on the radial and azimutal variation of muon charge ratio. The forseen installation will link the WILLI device to a nearby located miniarray of detectors for EAS registration which data will help to

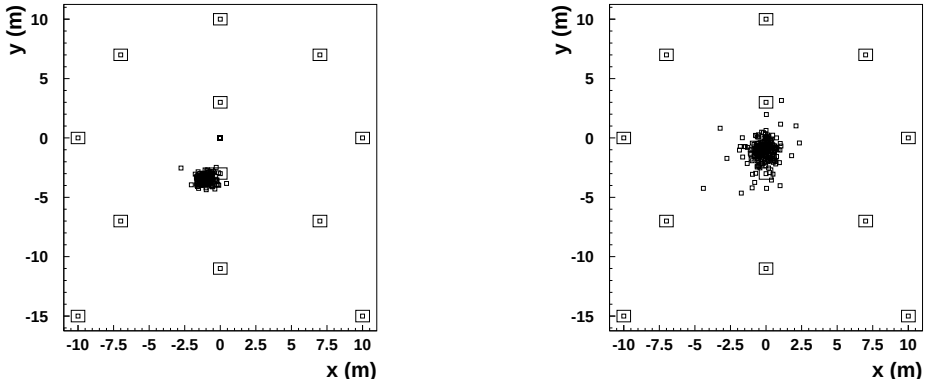

(a) (b)

Fig. 6. The reconstructed shower cores for 250 H incident showers placed in the same position for 20^0 (a) and 30^0 (b)

reconstruct the characteristics (core location , direction of incidence etc.).

We have presented [17] the experimental concept for investigating muon charge ratio in EAS by correlating WILLI detector with a mini-array. was develop based on the simulations prediction [18], [19] that shows an integral excess of positive muons in showers, prediction that has been never experimentally tested. The simulations shows that this small effect can slightly vary with the mass of the primary. The mean charge ratio is affected by the geomagnetic field, especially for low energy muons and the simulations show different azimuth variation of the muon densities of opposite charges and an azimuth variation of the muon charge ratio dependent on the direction of EAS incidence and the position of the observer in respect with the Earth's magnetic field.

We have started to scrutinize by simulations the performance of various possible configurations (see Fig.6) and the dependence of the results of acceptance of the WILLI spectrometer [19]. In particular, the layout studies must also include an adequate electronic system for triggering and data acquisition since only one stopped muon per shower can be handled in the present system. We investigate, how the finite angular acceptance of the WILLI spectrometer, positioned at a particular accurately defined distance from the shower core and observing muons from a particular direction will affect the pronounced predicted variation of the charge ratio of the observed muon density.

Using CORSIKA and GEANT codes, simulation studies have been performed for H and Fe generated showers ($10^{14} - 10^{15}$ eV) to study the configuration of EAS array to optimise reconstruction of the shower and the configuration WILLI-EAS for obtaining a significant feature for muon charge ratio in EAS. In order to investigate the best configuration of the array a modified version of SHOWREC[20] program was used. The program perform the reconstruction of the detector response using a parametrisation of the energy deposit in the scintillator plates from the mini-array.

Figure 6 a,b shows the quality of the reconstruction, given by the difference between the reconstructed and the true core position.

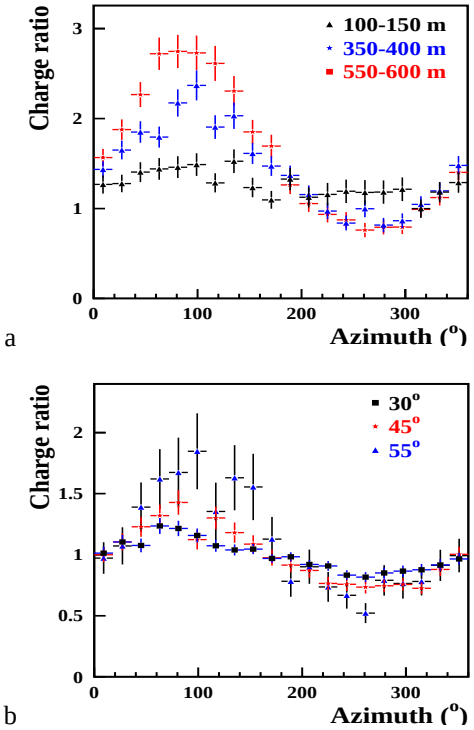

Fig. 7. The dependence of the charge ratio on the azimuth position of WILLI for different positions from the showere core (a) and for different zenith angles (b).

Considering that the H showers are coming from North, angle 45^0, and WILLI is oriented parallel to the shower axis, Fig. 7 a,b shows the dependence of the charge ratio on the azimuth position of WILLI around shower core for various radial ranges and for different

zenith angles.

The WILLI-EAS system for measuring muon charge ratio in EAS is under construction, see Fig.5, consisting by a core finder system composed by 12 independent stations, arranged as a mini-array close to WILLI. Each unit is a scintillator plate of 1 m^2, 3 cm thickness, consisting of 4 parts (0.25 x 0.25m^2), measuring the arrival times of the shower front and the energy deposits in the detectors.

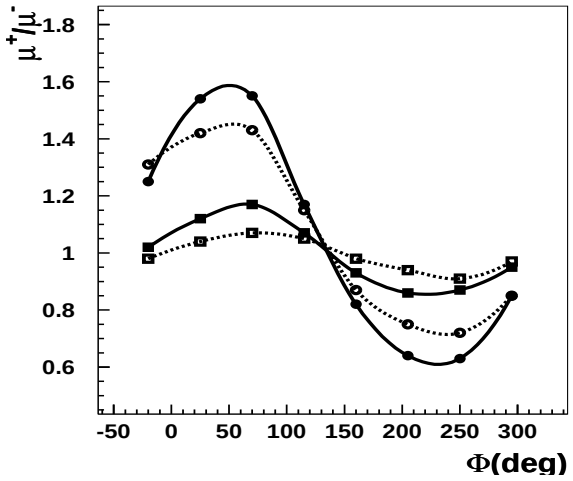

Fig. 8. The dependence of the charge ratio on the azimuth position of WILLI for proton (rectangles) and iron (circles) induced showers using QGSJET (solid line) and EPOS (dotted line) models

Fig. 8 show the dependence of the charge ratio on azimuth position of WILLI around shower core for H and Fe showers using 2 different hadronic interaction models implemented in CORSIKA code QGSJET2 and EPOS. The results of the simulations shows a quite sensitive difference between the two models also for the H an for the Fe showers.

V. Conclusions

The results (charge ratio and flux of atmospheric muons), obtained with the WILLI detector are in good agreement with the predictions of Monte Carlo simulations and a strong difference between the hadronic interaction models was not observe. Simulation studies for the EAS muon charge ratio present a high sensitivity at the hadronic interaction model, and the measurements (we estimate the start of the measurements till the end of 2009), if sufficiently accurate,could be used as a test for different models. The effectcs of the geomagnetic field could be also explore by measuring the EAS muon charge ratio, in order to improve the implementation of the geomagnetic field in simulation codes.

VI. Acknowledgements

One of the authors (B.Mitrica) would like to thanks to the Local Organising Committee of ICRC 2009 for the financial support.

References

[1] B.Vulpescu et al. Nucl. Instr.Meth. A414(1998)205
[2] I. M. Brancus et al, Nucl. Phys. A721 (2003) 1044c.
[3] D.Heck et al., Report FZKA 6019 (1998)
[4] J. Ranft, Phys. Rev. D 51 (1996) 64
[5] S. S. Ostapchenko, Phys. Rev. D 74 (2006 014026)
[6] K. Werner, F. M. Liu and T. Pierog, Phys. Rev. C 74 (2006) 044902
[7] P.Lipari, Astropart.Phys 16 (2002) 295
[8] J.Wentz et al., Phys. Rev D67(2003) 073020
[9] B. Mitrica, AIP Conf. Proc., 972 (2008) 500-504
[10] S.Tsuji et al., Proc.29th ICRC Pune (India) 2005,vol.6, p.211
[11] R.J.R.Judge and W.F.Nash, Il Nuovo Cimento XXXV-4 (1965) 999
[12] T.K. Gaisser, Astropart. Phys.16(2002)285
[13] G. Navarra et al, Nucl. Instr. Meth. Phys. Res. A518, (2004) 207.
[14] A. Iyono et al., Proc.ISVHECRI Pylos, 2004, Nucl. Phys.B. Proc. Suppl. 151 (2006)69.
[15] A.Iyono et al., Proc.ISVHECRI 2006, Nucl.Phys B (Proc. suppl.) 175-176(2008)366
[16] I,M Brancus et al., Proc. ISVHECRI 2008, in print
[17] I,M Brancus et al., Proc. ISVHECRI 2006, Nucl.Phys B (Proc. suppl.) 175-176(2008)370
[18] H. Rebel et al., J. Phys. G: Nucl. Part. Phys. 35(2008)085203
[19] B. Mitrica et al., Proc 30th ICRC Merida (Mexico) 2007 vol.5 p.1569
[20] O. Sima et al, FZKA 6985(2004)

Observation of Forbush Degreases and Solar Events in the 10-20 GeV Energy Range with the Karlsruhe Muon Telescope

Isabel Braun*, Joachim Engler§, Jörg R. Hörandel¶ and Jens Milke‖

* *Institute for Particle Physics, ETH Zurich, 8092 Zurich, Switzerland*
§*Institut für Experimentelle Kernphysik, Universiät Karlsruhe, D-76021 Karlsruhe, Germany*
¶*Radboud University Nijmegen, Department of Astrophysics, P.O. Box 9010, 6500 GL Nijmegen, The Netherlands*
‖*Institut für Wissenschaftliches Rechnen, Forschungszentrum Karlsruhe, D-76021 Karlsruhe, Germany*

***Abstract*. Since 1993, a muon telescope located at Forschungszentrum Karlsruhe (Karlsruhe Muon Telescope) has been recording the flux of single muons mostly originating from primary cosmic-ray protons with dominant energies in the 10 - 20 GeV range. The data are used to investigate the influence of solar effects on the flux of cosmic-rays measured at Earth. Non-periodic events like Forbush decreases and ground level enhancements are detected in the registered muon flux. Events of the 23rd solar cycle will be presented and compared to data from the Jungfraujoch neutron monitor. The data of the Karlsruhe Muon Telescope help to extend the knowledge about Forbush decreases and ground level enhancements to energies beyond the neutron monitor regime.**

***Keywords*: Forbush decreases, Ground Level Enhancements, Muon Telescope**

I. Introduction

The association of solar activity with the cosmic-ray intensity has been studied for various observed effects including Forbush decreases [1], i.e. a rapid decrease in the observed galactic cosmic-ray intensity, and Ground Level Enhancements connected to large solar flares. They can be related to magnetic disturbances in the heliosphere that create transient cosmic-ray intensity variations [2], [3]. From the observation of such events with different experiments, an energy dependent description can be obtained. The heliospheric influence is mostly pronounced for primary particles with low rigidity and has been studied mainly using data of the worldwide neutron monitor network [4]. With its unique median primary energy of 40 GeV for protons, the Karlsruhe Muon Telescope fills the energy gap between neutron monitors (from $\approx 11-15$ GeV, depending on solar activity state, to ≈ 33 GeV) and other muon telescopes ($\approx 53-119$ GV rigidity). In the following, we report on the detection of Forbush decreases and the investigation of Ground Level Enhancements with the Karlsruhe Muon Telescope.

II. Experimental Set-Up

The flux of single muons from the zenith region has been recorded continuously since 1993 with the Karlsruhe Muon Telescope located at Forschungszentrum Karlsruhe, Germany (49.094°N, 8.431°E, 120 m a.s.l). Details on the set-up are given in [5] and [6].

The response of the muon detector has been evaluated with simulations based on the CORSIKA [7] and GEANT 3.21 [8] packages. The median energy of the Karlsruhe Muon Telescope is 40 GeV, the maximum occurs at primary energies of about 15 GeV.

Corrections were applied to the recorded muon rate using the atmospheric pressure measured at the Forschungszentrum Karlsruhe. In addition, balloon ascends at noon and midnight conducted by the German weather service (DWD) in Stuttgart provide the heights of specific pressure layers including the 150 g/cm^2 layer (≈ 13.6 km) which is close to the typical production layer of muons triggering the telescope at 130 g/cm^2, as determined from simulations.

For each year, the muon rate was iteratively corrected for a pressure of 1013 hPa and a nominal height of the 150 g/cm^2 layer of 13.6 km, yielding correction parameters of $d(Rate)/dp = (-0.12 \pm 0.04)$ %/hPa and $d(Rate)/dh = (-3.8 \pm 1.2)$ %/km. This correction eliminates rate variations caused by changing atmospheric conditions from the data-set.

III. Forbush Decreases

The muon data were searched for days where the average rate was significantly lower than that of a background region. The background level was determined from hourly count rates within two times two weeks (14 d before the test region and 14 d afterwards), separated by three days from the tested day. The significances for each day were computed according to [9]. Trial factors were not taken into account.

The Karlsruhe Muon Telescope has detected several significant structures.

The strongest Forbush decreases in the years from 1998 to 2006 are compiled in Table I. Shown are: a sequential number, the date, the significance and the amplitude A of the minimum rate (r_{FD}) relative to the

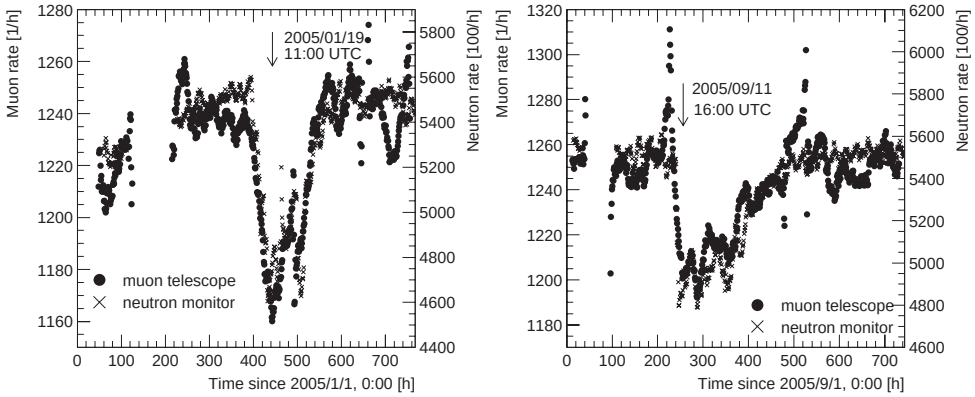

Fig. 1: Count rates of the Karlsruhe Muon Telescope and the Jungfraujoch neutron monitor for the two most recent Forbush decreases. The corresponding dates and times are indicated in the figure. Jungfraujoch data scaled by a factor 100, muon counting rate smoothed over a period of 24 hours.

TABLE I: Very significant Forbush decreases detected since 1998. A sequential number and the dates are listed. Significances are pre-trials, the amplitudes of the Karlsruhe Muon Telescope refer to the hourly data (not smoothed). The fifth column gives the amplitudes detected by the Jungfraujoch neutron monitor. The last column gives an estimate for the energy dependence of the detected amplitudes, expressed in amplitude change per decade in energy.

#	date	significance(μ)	amplitude(μ) [%]	amplitude(n) [%]	amplitude change [% / energy decade]
1	1998/08/26	6.1σ	10.1	7.1	5.7
2	1998/09/25	6.2σ	11.7	5.7	11.5
3	1999/01/23	4.7σ	8.1	7.0	2.1
4	2000/07/15	8.3σ	12.3	10.5	3.5
5	2000/11/10	6.1σ	6.8	1.5	10.2
6	2001/08/03	8.7σ	9.4	1.7	14.8
7	2003/10/30	8.4σ	11.3	17.0	-10.9
8	2004/11/10	5.0σ	10.5	6.6	7.6
9	2005/01/19	10.6σ	13.2	13.2	0.02
10	2005/09/11	5.5σ	8.4	10.4	-3.9

average rate before the decrease (r_b) computed as

$$A = (r_b - r_{FD})/r_b. \quad (1)$$

The amplitudes A_μ and A_n have been calculated according to (1) for the muon telescope (based on hourly rates) and the Jungfraujoch 18-IGY neutron monitor (46.55°N / 7.98°E, 3570 m asl), respectively. The latter has an effective vertical cutoff rigidity of 4.49 GV [10]. It was chosen for this comparison because of its geographic proximity to Karlsruhe. The two most recent detected events compared to the neutron monitor counting rate are depicted in Fig. 1. To display their development, the muon telescope rates are smoothed by a running mean over 24 hours. Attention should be paid to the different scales for the muon rate (left-hand scale) and for the neutron monitor rate (right-hand scale). The apparently significant excesses on 2005/09/09-10 and 2005/09/22 are artefacts of the smoothing and caused by individual high data-points at the boundaries of detector downtime. It is worth to point out that the rate development observed at 4.5 GV (Jungfraujoch) and for the muon telescope (15 GeV) are quite similar, despite of their different energy thresholds. This illustrates that Forbush decreases are clearly detectable with a muon detector with 15 GeV peak energy. Forbush decreases were already detected with the GRAND muon detector [11] at 10 GeV peak energy. With the Karlsruhe Muon Telescope, we push the detection towards higher energies.

Many structures in these Forbush decreases are visible at both energies. A closer look [6] reveals that for events 7, 8, 9, and 10 (close to the solar minimum), the rates of both detectors follow each other extremely closely. On the other hand, for events 1, 2, 4, and 6 there are systematic differences between the two energies in the behavior before or after the Forbush decrease. For the Forbush decrease in the year of the solar maximum (# 5), the strongest differences between the two rates are observed. It appears as during solar maximum there are significant differences between the fluxes observed at 4.5 GV and 15 GeV, while the fluxes are correlated well during periods of low solar activity.

To study the energy dependence of the amplitudes of a Forbush decrease, the spectral index γ, i.e. the change of amplitude per decade in energy has been calculated according to

$$\gamma = (A_\mu - A_n) \ / \ (log(E_M^\mu) - log(E_M^n)), \quad (2)$$

$E_M^\mu \sim 15$ GeV and $E_M^n \sim 4.5$ GeV being the most

propable primary energies for the muon telescope and the neutron monitor, respectively. γ is listed in the last column of Table I. No clear correlation between the amplitude change per energy decade and the international sunspot number (taken from [12]) is found [6]. Thus, earlier claims by [13] cannot be confirmed. A study of the energy-dependence of the recovery time of Forbush decreases including data from Karlsruhe Muon Telescope is published elsewhere [14].

IV. Ground Level Enhancements

Due to their relatively short duration, Ground Level Enhancements (GLEs) are difficult to detect with the Karlsruhe Muon Telescope. Therefore, the data were scanned for correlations with all events marked in the GLE database, as provided by the Bartol group [15]. For a detailed list of muon telescope activity at the time of these events see [6].

For GLE 57, no significant excess was observed in the muon counting rate. However, about seven hours before the Ground Level Enhancement a small peak is visible in the registered muon flux. For GLE 58, no significant muon excess has been observed.

GLE 59, the "Bastille day event" on July 14, 2000 has been registered by many detectors, including neutron monitors and space crafts [16], [17]. In particular, the event could be measured for primary cosmic rays with GeV energies [18]. It has been detected by the GRAND muon detector (10 GeV most probable energy) [19], by the L3+C detector at CERN (≈ 40 GeV primary energy) [20] and also by the Karlsruhe Muon Telescope. An excess in the muon counting rate can be recognized a few hours before the event. The significance of this structure is under investigation. If real, it is a possible hint for energy dependent propagation effects or the strongly anisotropic nature of this event.

On Easter day 2001 (April 15), an event occured (GLE 60) which has been observed and discussed by several groups [21], [22], [23], [24], [17]. A muon count excess can be recognized at the time of GLE 60, while no signal is observed from GLE 61. It should also be noted that the Jungfraujoch neutron monitor detects GLE 60 with a large signal. On the other hand, the muon flux is only slightly increased at the time of the event.

Some of the greatest bursts in the 23rd solar cycle occurred on 28/29 October and 2 November 2003 (GLE $65 - 67$). They are extensively discussed in the literature, e.g. [25], [26], [27], [28]. Unfortunately, the muon telescope was not active during GLEs 65 and 67. At the time of GLE 66, no significant signal is seen in the muon count rate. However, about one day before GLEs 65 and 66 a peak can be recognized in the registered muon flux. It is not clear whether these increases are statistically significant, since there are gaps in the observing time. Thus, it is not obvious whether the detected rate variations are correlated with the Ground Level Enhancements.

V. Conclusions

The Karlsruhe Muon Telescope provides information about effects of solar activity on the cosmic-ray flux observed at Earth since 1993. The recorded muon flux corresponds to 15 GeV peak energy (40 GeV median energy) for primary protons.

Several strong Forbush decreases, i.e. a rapid decrease in the observed galactic cosmic-ray intensity, could be measured with the muon telescope, indicating that these effects can be seen at energies exceeding the typical energies of neutron monitors. Comparing the observed amplitudes to the Jungfraujoch neutron monitor data, the spectral index of the events has been estimated. No dependence of the spectral index on the sunspot number has been found. However, there are significant differences in the timely development of the rates observed at 4.5 GV and 15 GeV for different states of solar activity. For Forbush decreases during solar maximum, the rates of the muon telescope and the neutron monitor behave quite differently, while they are well correlated for periods of low solar activity.

It has been investigated whether Ground Level Enhancements connected to large solar flares, observed between 1997 and 2005 can be detected in the registered muon flux. For the strong Ground Level Enhancements 59 and 60, a clear signal can be seen in the muon count rate at the times of the events. This provides direct evidence for particles being accelerated to energies as high as 15 GeV during solar flares. Indirect evidence has been previously obtained by observations of lines in the gamma ray spectrum measured during solar flares [29], [30]. On the other hand, no signal has been detected for the GLEs 58, 61, 66, 68, and 69. If the underlying physics processes of all Ground Level Enhancements are the same, this means that the energy spectra of GLEs 59 and 60 differ from the spectra of the other GLEs. Another possibility is that the angular distribution of the emitted particles is different for different GLEs, i.e. in cases with highly anisotropic emission no signal was detected in the muon counting rate.

Acknowledgments

We are grateful to Mrs. Heike Bolz for her enthusiastic efforts in continuously operating the Karlsruhe Muon Telescope and to Jürgen Wochele for his help during the construction of the detector. We thank the team operating the Jungfraujoch neutron monitor for making their data publicly available. We acknowledge the help of the Deutscher Wetter-Dienst (DWD) and the Institut für Meteorologie und Klimaforschung of Forschungszentrum Karlsruhe providing atmospheric data.

References

[1] S. E. Forbush, *Worldwide cosmic ray variations*, J. Geophys. Res., 59, 525 - 542, 1954.

[2] E.N. Parker, *The passage of energetic charged particles through interplanetary space*, Planetary and Space Science 13, 9-49, 1965.

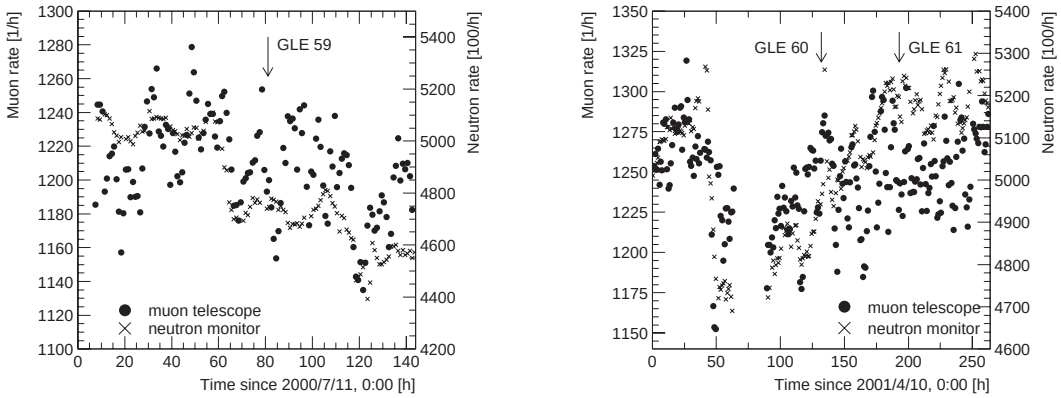

Fig. 2: Hourly count rates registered by the Karlsruhe Muon Telescope and the Jungfraujoch neutron monitor for several Ground Level Enhancements, as marked in the figures, see also [6]. Jungfraujoch data are scaled by factor 100, muon counting rates smoothed over a period of three hours.

[3] M-B. Kallenrode, *Current views on impulsive and gradual solar energetic particle events*, J. Phys. G: Nucl. Part. Phys., 29, 956-981, 2003.

[4] J.A. Simpson, *The cosmic ray nucleonic component: the invention and uses of the neutron monitor*, Space Sci. Rev. 93, 11-32, 2000.

[5] J. Engler, F. Fessler, J.R. Hörandel *et al.* , *A warm-liquid calorimeter for cosmic-ray hadrons*, Nuclear Instruments and Methods A 427, 528-542, 1999.

[6] I. Braun, J. Engler, J.R. Hrandel *et al.* , *Forbush decreases and solar events seen in the* $10 - 20$ *GeV energy range by the Karlsruhe Muon Telescope*, Advances in Space Research 43, 480-488, 2008.

[7] Heck, D., Knapp, J., Capdevielle, J. *et al.* , *CORSIKA: a Monte Carlo code to simulate extensive air showers*, Report FZKA 6019, Forschungszentrum Karlsruhe, 1998.

[8] GEANT 3.15, *Detector Description and Simulation Tool*, CERN Program Library Long Writeup W5013, CERN, 1993.

[9] T.-P. Li and Y.-Q. Ma, *Analysis methods for results in gamma-ray astronomy*, Astrophysical Journal, 272, 317-324, 1983.

[10] Bern Cosmic Ray Group, Physikalisches Institut, University of Bern http://cosray.unibe.ch.

[11] J. Poirier, M. Herrera, P. Hemphill, *et al.* , *A study of the Forbush decrease event of September 11, 2005 with GRAND*, Proceedings 30th International Cosmic Ray Conference, Merida, 2007.

[12] SIDC: Sunspot Index Data Center, Royal Observatory of Belgium, http://sidc.oma.be

[13] S.O. Ifedili, *Spacecraft measurement of forbush decreases in the cosmic radiation*, Solar Physics 168, 195-203, 1996.

[14] I.G.Usoskin, I. Braun, O.G. Gladysheva *et al.* , *Forbush decreases of cosmic rays: Energy dependence of the recovery phase*, Journal of Geophysical Research, 2008.

[15] Bartol Research Institute neutron monitor program, http://neutronm.bartol.udel.edu.

[16] J.W. Bieber, W. Dröge, P.A. Evenson *et al.* , *Energetic Particle Observations during the 2000 July 14 solar event*, Astrophysical Journal 567, 622-634, 2002.

[17] E.V. Vashenyuk, Y.V. Balabin, P.H. Stoker, *Response to solar cosmic rays of neutron monitors of a various design*, Advances in Space Research 40, 331-337, 2007.

[18] R. Wang and J. Wang, *Spectra and solar energetic protons over 20 GeV in Bastille Day event*, Astroparticle Physics 25, 41-46, 2006.

[19] J. Poirier, C. D'Andrea, M. Dunford, *A project GRAND study of the GLE of July 14, 2000*, Proceedings 27th International Cosmic Ray Conference, Hamburg, 3557-3559, 2001.

[20] L3 Collaboration, *et al.* , *The solar flare of the 14th of July 2000 (L3+C detector results)*, Astronomy and Astrophysics 456, 351-357, 2006.

[21] M.A. Shea and D.F. Smart, *Solar proton and GLE event frequency: 1955 - 2000*, Proc. 27th Int. Cosmic Ray Conf., Hamburg 3401-3404, 2001.

[22] C. D'Andrea and J. Poirier, *A study of the ground level event of April 15, 2001 with GRAND*, Proc. 28th Int. Cosmic Ray Conference, Tsukuba, 3423-3426, 2003.

[23] J.W. Bieber, P. Evenson, W. Dröge *et al.* , *Spaceship Earth observations of the Easter 2001 solar particle event*, Astrophysical Journal 601, L103-106, 2004.

[24] A.J. Tylka, C.M.S. Cohen, W.F. Dietrich, *et al.* , *Shock geometry, seed populations, and the origin of variable elemental composition at high energies in large gradual solar particle events*, Astrophysical Journal 625, 474-495, 2005.

[25] K. Watanabe, M. Gros, P.H. Stoker *et al.* , *Solar Neutron Events of 2003 OctoberNovember*, Astrophysical Journal 636, 1135-1144, 2006.

[26] Y. Liu and K. Hayashi, *The 2003 October-November fast halo coronal mass ejections and the large-scale magnetic field structures*, Astrophysical Journal 640, 1135-1141, 2006.

[27] G.J. Hurford, S. Krucker, R.P. Lin *et al.* , *Gamma-ray imaging of the 2003 October/November solar flares*, Astrophysical Journal 644, L93-96, 2006.

[28] E. Eroshenko, A. Belov, H. Mavromichalaki *et al.* , *Cosmic-ray variations during the two greatest bursts of solar activity in the 23rd solar circle*, Solar Physics 224, 345-358, 2004.

[29] E. Rieger, *Solar flares: high-energy radiation and particles*, Solar Physics 121, 323-345 1989.

[30] L. Fletcher, *Energetic particles in the solar atmosphere*, Proc. 10th European Solar Physics Meeting, Prague, Czech Republic, ESA SP-506, 223-232, 2002.

KASCADE-Grande COLLABORATION

W.D. Apel[1], J.C. Arteaga[2,10], F. Badea[1], K. Bekk[1], M. Bertaina[3], J. Blümer[1,2], H. Bozdog[1], I.M. Brancus[4], M. Brüggemann[5], P. Buchholz[5], E. Cantoni[3,6], A. Chiavassa[3], F. Cossavella[2], K. Daumiller[1], V. de Souza[2,11], F. Di Pierro[3], P. Doll[1], R. Engel[1], J. Engler[1], M. Finger[1], D. Fuhrmann[7], P.L. Ghia[6], H.J. Gils[1], R. Glasstetter[7], C. Grupen[5], A. Haungs[1], D. Heck[1], J.R. Hörandel[2,12], T. Huege[1], P.G. Isar[1], K.-H. Kampert[7], D. Kang[2], D. Kickelbick[5], H.O. Klages[1], P. Łuczak[8], C. Manailescu[9], H.J. Mathes[1], H.J. Mayer[1], J. Milke[1], B. Mitrica[4], C. Morariu[9], C. Morello[6], G. Navarra[3], S. Nehls[1], J. Oehlschläger[1], S. Ostapchenko[1,13], S. Over[5], M. Petcu[4], T. Pierog[1], H. Rebel[1], M. Roth[1], H. Schieler[1], F. Schröder[1], O. Sima[9], M. Stümpert[2], G. Toma[4], G.C. Trinchero[6], H. Ulrich[1], A. Weindl[1], J. Wochele[1], M. Wommer[1], J. Zabierowski[8]

[1]Institut für Kernphysik, Forschungszentrum Karlsruhe, 76021 Karlsruhe, Germany
[2]Institut für Experimentelle Kernphysik, Universität Karlsruhe, 76021 Karlsruhe, Germany
[3]Dipartimento di Fisica Generale dell'Università di Torino, 10125 Torino, Italy
[4]National Institute of Physics and Nuclear Engineering, 077125 Bucharest-Magurele, Romania
[5]Fachbereich Physik, Universität Siegen, 57068 Siegen, Germany
[6]Istituto di Fisica dello Spazio Interplanetario, INAF, 10133 Torino, Italy
[7]Fachbereich Physik, Universität Wuppertal, 42097 Wuppertal, Germany
[8]Soltan Institute for Nuclear Studies, 90950 Lodz, Poland
[9]Department of Physics, University of Bucharest, 7690 Bucharest, Romania
[10]now at: Universidad Michoacana, Morelia, Mexico
[11]now at: Universidade de São Paulo, Instituto de Física de São Carlos, Brasil
[12]now at: Dept. of Astrophysics, Radboud University Nijmegen, The Netherlands
[13]now at: University of Trondheim, Norway

LOPES COLLABORATION

W.D. Apel[1], J.C. Arteaga[2,14], T. Asch[3], F. Badea[1], L. Bähren[4], K. Bekk[1], M. Bertaina[5], P.L. Biermann[6], J. Blümer[1,2], H. Bozdog[1] I.M. Brancus[7], M. Brüggemann[8], P. Buchholz[8], S. Buitink[4], E. Cantoni[5,9], A. Chiavassa[5], F. Cossavella[2], K. Daumiller[1], V. de Souza[2,15], F. Di Pierro[5], P. Doll[1], M. Ender[1], R. Engel[1], H. Falcke[4,10], M. Finger[1], D. Fuhrmann[11], H. Gemmeke[3], P.L. Ghia[9], R. Glasstetter[11], C. Grupen[8], A. Haungs[1], D. Heck[1], J.R. Hörandel[4], A. Horneffer[4], T. Huege[1], P.G. Isar[1], K.-H. Kampert[11], D. Kang[2], D. Kickelbick[8], O. Krömer[3], J. Kuijpers[4], S. Lafebre[4], K. Link[1], P. Łuczak[12], M. Ludwig[2], H.J. Mathes[1], H.J. Mayer[1], M. Melissas[2], B. Mitrica[7], C. Morello[9], G. Navarra[5], S. Nehls[1], A. Nigl[4], J. Oehlschläger[1], S. Over[8], N. Palmieri[2], M. Petcu[7], T. Pierog[1], J. Rautenberg[11], H. Rebel[1], M. Roth[1], A. Saftoiu[7], H. Schieler[1], A. Schmidt[3], F. Schröder[1], O. Sima[13], K. Singh[4,16], G. Toma[7], G.C. Trinchero[9], H. Ulrich[1], A. Weindl[1], J. Wochele[1], M. Wommer[1], J. Zabierowski[12], J.A. Zensus[6]

[1]Institut für Kernphysik, Forschungszentrum Karlsruhe, Germany
[2]Institut für Experimentelle Kernphysik, Universität Karlsruhe, Germany
[3]IPE, Forschungszentrum Karlsruhe, Germany
[4]Department of Astrophysics, Radboud University Nijmegen, The Netherlands
[5]Dipartimento di Fisica Generale dell'Università di Torino, Italy
[6]Max-Planck-Institut für Radioastronomie Bonn, Germany
[7]National Institute of Physics and Nuclear Engineering, Bucharest, Romania
[8]Fachbereich Physik, Universität Siegen, Germany
[9]Istituto di Fisica dello Spazio Interplanetario, INAF Torino, Italy
[10]ASTRON, Dwingeloo, The Netherlands
[11]Fachbereich Physik, Universität Wuppertal, Germany
[12]Soltan Institute for Nuclear Studies, Lodz, Poland
[13]Department of Physics, University of Bucharest, Bucharest, Romania
[14]now at: Universidad Michoacana, Morelia, Mexico
[15]now at: Universidade de São Paulo, Instituto de Física de São Carlos, Brasil
[16]now at: KVI, University of Groningen, The Netherlands

PIERRE AUGER COLLABORATION

J. Abraham[8], P. Abreu[71], M. Aglietta[54], C. Aguirre[12], E.J. Ahn[87], D. Allard[31], I. Allekotte[1], J. Allen[90], J. Alvarez-Muñiz[78], M. Ambrosio[48], L. Anchordoqui[104], S. Andringa[71], A. Anzalone[53], C. Aramo[48], E. Arganda[75], S. Argirò[51], K. Arisaka[95], F. Arneodo[55], F. Arqueros[75], T. Asch[38], H. Asorey[1], P. Assis[71], J. Aublin[33], M. Ave[96], G. Avila[10], T. Bäcker[42], D. Badagnani[6], K.B. Barber[11], A.F. Barbosa[14], S.L.C. Barroso[20], B. Baughman[92], P. Bauleo[85], J.J. Beatty[92], T. Beau[31], B.R. Becker[101], K.H. Becker[36], A. Bellétoile[34], J.A. Bellido[11, 93], S. BenZvi[103], C. Berat[34], P. Bernardini[47], X. Bertou[1], P.L. Biermann[39], P. Billoir[33], O. Blanch-Bigas[33], F. Blanco[75], C. Bleve[47], H. Blümer[41, 37], M. Boháčová[96, 27], D. Boncioli[49], C. Bonifazi[33], R. Bonino[54], N. Borodai[69], J. Brack[85], P. Brogueira[71], W.C. Brown[86], R. Bruijn[81], P. Buchholz[42], A. Bueno[77], R.E. Burton[83], N.G. Busca[31], K.S. Caballero-Mora[41], L. Caramete[39], R. Caruso[50], A. Castellina[54], O. Catalano[53], L. Cazon[96], R. Cester[51], J. Chauvin[34], A. Chiavassa[54], J.A. Chinellato[18], A. Chou[87, 90], J. Chudoba[27], J. Chye[89d], R.W. Clay[11], E. Colombo[2], R. Conceição[71], B. Connolly[102], F. Contreras[9], J. Coppens[65, 67], A. Cordier[32], U. Cotti[63], S. Coutu[93], C.E. Covault[83], A. Creusot[73], A. Criss[93], J. Cronin[96], A. Curutiu[39], S. Dagoret-Campagne[32], R. Dallier[35], K. Daumiller[37], B.R. Dawson[11], R.M. de Almeida[18], M. De Domenico[50], C. De Donato[46], S.J. de Jong[65], G. De La Vega[8], W.J.M. de Mello Junior[18], J.R.T. de Mello Neto[23], I. De Mitri[47], V. de Souza[16], K.D. de Vries[66], G. Decerprit[31], L. del Peral[76], O. Deligny[30], A. Della Selva[48], C. Delle Fratte[49], H. Dembinski[40], C. Di Giulio[49], J.C. Diaz[89], P.N. Diep[105], C. Dobrigkeit [18], J.C. D'Olivo[64], P.N. Dong[105], A. Dorofeev[85, 88], J.C. dos Anjos[14], M.T. Dova[6], D. D'Urso[48], I. Dutan[39], M.A. DuVernois[98], R. Engel[37], M. Erdmann[40], C.O. Escobar[18], A. Etchegoyen[2], P. Facal San Luis[96, 78], H. Falcke[65, 68], G. Farrar[90], A.C. Fauth[18], N. Fazzini[87], F. Ferrer[83], A. Ferrero[2], B. Fick[89], A. Filevich[2], A. Filipčič[72, 73], I. Fleck[42], S. Fliescher[40], C.E. Fracchiolla[85], E.D. Fraenkel[66], W. Fulgione[54], R.F. Gamarra[2], S. Gambetta[44], B. García[8], D. García Gámez[77], D. Garcia-Pinto[75], X. Garrido[37, 32], G. Gelmini[95], H. Gemmeke[38], P.L. Ghia[30, 54], U. Giaccari[47], M. Giller[70], H. Glass[87], L.M. Goggin[104], M.S. Gold[101], G. Golup[1], F. Gomez Albarracin[6], M. Gómez Berisso[1], P. Gonçalves[71], D. Gonzalez[41], J.G. Gonzalez[77, 88], D. Góra[41, 69], A. Gorgi[54], P. Gouffon[17], S.R. Gozzini[81], E. Grashorn[92], S. Grebe[65], M. Grigat[40], A.F. Grillo[55], Y. Guardincerri[4], F. Guarino[48], G.P. Guedes[19], J. Gutiérrez[76], J.D. Hague[101], V. Halenka[28], P. Hansen[6], D. Harari[1], S. Harmsma[66, 67], J.L. Harton[85], A. Haungs[37], M.D. Healy[95], T. Hebbeker[40], G. Hebrero[76], D. Heck[37], C. Hojvat[87], V.C. Holmes[11], P. Homola[69], J.R. Hörandel[65], A. Horneffer[65], M. Hrabovský[28, 27], T. Huege[37], M. Hussain[73], M. Iarlori[45], A. Insolia[50], F. Ionita[96], A. Italiano[50], S. Jiraskova[65], M. Kaducak[87], K.H. Kampert[36], T. Karova[27], P. Kasper[87], B. Kégl[32], B. Keilhauer[37], E. Kemp[18], R.M. Kieckhafer[89], H.O. Klages[37], M. Kleifges[38], J. Kleinfeller[37], R. Knapik[85], J. Knapp[81], D.-H. Koang[34], A. Krieger[2], O. Krömer[38], D. Kruppke-Hansen[36], F. Kuehn[87], D. Kuempel[36], K. Kulbartz[43], N. Kunka[38], A. Kusenko[95], G. La Rosa[53], C. Lachaud[31], B.L. Lago[23], P. Lautridou[35], M.S.A.B. Leão[22], D. Lebrun[34], P. Lebrun[87], J. Lee[95], M.A. Leigui de Oliveira[22], A. Lemiere[30], A. Letessier-Selvon[33], M. Leuthold[40], I. Lhenry-Yvon[30], R. López[59], A. Lopez Agüera[78], K. Louedec[32], J. Lozano Bahilo[77], A. Lucero[54], H. Lyberis[30], M.C. Maccarone[53], C. Macolino[45], S. Maldera[54], D. Mandat[27], P. Mantsch[87], A.G. Mariazzi[6], I.C. Maris[41], H.R. Marquez Falcon[63], D. Martello[47], O. Martínez Bravo[59], H.J. Mathes[37], J. Matthews[88, 94], J.A.J. Matthews[101], G. Matthiae[49], D. Maurizio[51], P.O. Mazur[87], M. McEwen[76], R.R. McNeil[88], G. Medina-Tanco[64], M. Melissas[41], D. Melo[51], E. Menichetti[51], A. Menshikov[38], R. Meyhandan[14], M.I. Micheletti[2], G. Miele[48], W. Miller[101], L. Miramonti[46], S. Mollerach[1], M. Monasor[75], D. Monnier Ragaigne[32], F. Montanet[34], B. Morales[64], C. Morello[54], J.C. Moreno[6], C. Morris[92], M. Mostafá[85], C.A. Moura[48], S. Mueller[37], M.A. Muller[18], R. Mussa[51], G. Navarra[54], J.L. Navarro[77], S. Navas[77], P. Necesal[27], L. Nellen[64], C. Newman-Holmes[87], D. Newton[81], P.T. Nhung[105], N. Nierstenhoefer[36], D. Nitz[89], D. Nosek[26], L. Nožka[27], M. Nyklicek[27], J. Oehlschläger[37], A. Olinto[96], P. Oliva[36], V.M. Olmos-Gilbaja[78], M. Ortiz[75], N. Pacheco[76], D. Pakk Selmi-Dei[18], M. Palatka[27], J. Pallotta[3], G. Parente[78], E. Parizot[31], S. Parlati[55], S. Pastor[74], M. Patel[81], T. Paul[91], V. Pavlidou[96c], K. Payet[34], M. Pech[27], J. Pękala[69], I.M. Pepe[21], L. Perrone[52], R. Pesce[44], E. Petermann[100], S. Petrera[45], P. Petrinca[49], A. Petrolini[44], Y. Petrov[85], J. Petrovic[67], C. Pfendner[103], R. Piegaia[4], T. Pierog[37], M. Pimenta[71], T. Pinto[74], V. Pirronello[50], O. Pisanti[48], M. Platino[2], J. Pochon[1], V.H. Ponce[1], M. Pontz[42], P. Privitera[96], M. Prouza[27], E.J. Quel[3], J. Rautenberg[36], O. Ravel[35], D. Ravignani[2],

A. Redondo[76], B. Revenu[35], F.A.S. Rezende[14], J. Ridky[27], S. Riggi[50], M. Risse[36], C. Rivière[34], V. Rizi[45], C. Robledo[59], G. Rodriguez[49], J. Rodriguez Martino[50], J. Rodriguez Rojo[9], I. Rodriguez-Cabo[78], M.D. Rodríguez-Frías[76], G. Ros[75], [76], J. Rosado[75], T. Rossler[28], M. Roth[37], B. Rouillé-d'Orfeuil[31], E. Roulet[1], A.C. Rovero[7], F. Salamida[45], H. Salazar[59b], G. Salina[49], F. Sánchez[64], M. Santander[9], C.E. Santo[71], E.M. Santos[23], F. Sarazin[84], S. Sarkar[79], R. Sato[9], N. Scharf[40], V. Scherini[36], H. Schieler[37], P. Schiffer[40], A. Schmidt[38], F. Schmidt[96], T. Schmidt[41], O. Scholten[66], H. Schoorlemmer[65], J. Schovancova[27], P. Schovánek[27], F. Schroeder[37], S. Schulte[40], F. Schüssler[37], D. Schuster[84], S.J. Sciutto[6], M. Scuderi[50], A. Segreto[53], D. Semikoz[31], M. Settimo[47], R.C. Shellard[14], [15], I. Sidelnik[2], B.B. Siffert[23], G. Sigl[43], A. Śmiałkowski[70], R. Šmída[27], B.E. Smith[81], G.R. Snow[100], P. Sommers[93], J. Sorokin[11], H. Spinka[82], [87], R. Squartini[9], E. Strazzeri[32], A. Stutz[34], F. Suarez[2], T. Suomijärvi[30], A.D. Supanitsky[64], M.S. Sutherland[92], J. Swain[91], Z. Szadkowski[70], A. Tamashiro[7], A. Tamburro[41], T. Tarutina[6], O. Taşcău[36], R. Tcaciuc[42], D. Tcherniakhovski[38], D. Tegolo[58], N.T. Thao[105], D. Thomas[85], R. Ticona[13], J. Tiffenberg[4], C. Timmermans[67], [65], W. Tkaczyk[70], C.J. Todero Peixoto[22], B. Tomé[71], A. Tonachini[51], I. Torres[59], P. Travnicek[27], D.B. Tridapalli[17], G. Tristram[31], E. Trovato[50], M. Tueros[6], R. Ulrich[37], M. Unger[37], M. Urban[32], J.F. Valdés Galicia[64], I. Valiño[37], L. Valore[48], A.M. van den Berg[66], J.R. Vázquez[75], R.A. Vázquez[78], D. Veberič[73], [72], A. Velarde[13], T. Venters[96], V. Verzi[49], M. Videla[8], L. Villaseñor[63], S. Vorobiov[73], L. Voyvodic[87‡], H. Wahlberg[6], P. Wahrlich[11], O. Wainberg[2], D. Warner[85], A.A. Watson[81], S. Westerhoff[103], B.J. Whelan[11], G. Wieczorek[70], L. Wiencke[84], B. Wilczyńska[69], H. Wilczyński[69], C. Wileman[81], M.G. Winnick[11], H. Wu[32], B. Wundheiler[2], T. Yamamoto[96a], P. Younk[85], G. Yuan[88], A. Yushkov[48], E. Zas[78], D. Zavrtanik[73], [72], M. Zavrtanik[72], [73], I. Zaw[90], A. Zepeda[60b], M. Ziolkowski[42]

[1] Centro Atómico Bariloche and Instituto Balseiro (CNEA-UNCuyo-CONICET), San Carlos de Bariloche, Argentina

[2] Centro Atómico Constituyentes (Comisión Nacional de Energía Atómica/CONICET/UTN-FRBA), Buenos Aires, Argentina

[3] Centro de Investigaciones en Láseres y Aplicaciones, CITEFA and CONICET, Argentina

[4] Departamento de Física, FCEyN, Universidad de Buenos Aires y CONICET, Argentina

[6] IFLP, Universidad Nacional de La Plata and CONICET, La Plata, Argentina

[7] Instituto de Astronomía y Física del Espacio (CONICET), Buenos Aires, Argentina

[8] National Technological University, Faculty Mendoza (CONICET/CNEA), Mendoza, Argentina

[9] Pierre Auger Southern Observatory, Malargüe, Argentina

[10] Pierre Auger Southern Observatory and Comisión Nacional de Energía Atómica, Malargüe, Argentina

[11] University of Adelaide, Adelaide, S.A., Australia

[12] Universidad Catolica de Bolivia, La Paz, Bolivia

[13] Universidad Mayor de San Andrés, Bolivia

[14] Centro Brasileiro de Pesquisas Fisicas, Rio de Janeiro, RJ, Brazil

[15] Pontifícia Universidade Católica, Rio de Janeiro, RJ, Brazil

[16] Universidade de São Paulo, Instituto de Física, São Carlos, SP, Brazil

[17] Universidade de São Paulo, Instituto de Física, São Paulo, SP, Brazil

[18] Universidade Estadual de Campinas, IFGW, Campinas, SP, Brazil

[19] Universidade Estadual de Feira de Santana, Brazil

[20] Universidade Estadual do Sudoeste da Bahia, Vitoria da Conquista, BA, Brazil

[21] Universidade Federal da Bahia, Salvador, BA, Brazil

[22] Universidade Federal do ABC, Santo André, SP, Brazil

[23] Universidade Federal do Rio de Janeiro, Instituto de Física, Rio de Janeiro, RJ, Brazil

[26] Charles University, Faculty of Mathematics and Physics, Institute of Particle and Nuclear Physics, Prague, Czech Republic

[27] Institute of Physics of the Academy of Sciences of the Czech Republic, Prague, Czech Republic

[28] Palacký University, Olomouc, Czech Republic

[30] Institut de Physique Nucléaire d'Orsay (IPNO), Université Paris 11, CNRS-IN2P3, Orsay, France

[31] Laboratoire AstroParticule et Cosmologie (APC), Université Paris 7, CNRS- IN2P3, Paris, France

[32] Laboratoire de l'Accélérateur Linéaire (LAL), Université Paris 11, CNRS-IN2P3, Orsay, France

[33] Laboratoire de Physique Nucléaire et de Hautes Energies (LPNHE), Universités Paris 6 et Paris 7, CNRS-IN2P3, Paris, France

[34] Laboratoire de Physique Subatomique et de Cosmologie (LPSC), Université Joseph Fourier, INPG, CNRS-IN2P3, Grenoble, France

[35] *SUBATECH, Nantes, France*
[36] *Bergische Universität Wuppertal, Wuppertal, Germany*
[37] *Forschungszentrum Karlsruhe, Institut für Kernphysik, Karlsruhe, Germany*
[38] *Forschungszentrum Karlsruhe, Institut für Prozessdatenverarbeitung und Elektronik, Karlsruhe, Germany*
[39] *Max-Planck-Institut für Radioastronomie, Bonn, Germany*
[40] *RWTH Aachen University, III. Physikalisches Institut A, Aachen, Germany*
[41] *Universität Karlsruhe (TH), Institut für Experimentelle Kernphysik (IEKP), Karlsruhe, Germany*
[42] *Universität Siegen, Siegen, Germany*
[43] *Universität Hamburg, Hamburg, Germany*
[44] *Dipartimento di Fisica dell'Università and INFN, Genova, Italy*
[45] *Università dell'Aquila and INFN, L'Aquila, Italy*
[46] *Università di Milano and Sezione INFN, Milan, Italy*
[47] *Dipartimento di Fisica dell'Università del Salento and Sezione INFN, Lecce, Italy*
[48] *Università di Napoli "Federico II" and Sezione INFN, Napoli, Italy*
[49] *Università di Roma II "Tor Vergata" and Sezione INFN, Roma, Italy*
[50] *Università di Catania and Sezione INFN, Catania, Italy*
[51] *Università di Torino and Sezione INFN, Torino, Italy*
[52] *Dipartimento di Ingegneria dell'Innovazione dell'Università del Salento and Sezione INFN, Lecce, Italy*
[53] *Istituto di Astrofisica Spaziale e Fisica Cosmica di Palermo (INAF), Palermo, Italy*
[54] *Istituto di Fisica dello Spazio Interplanetario (INAF), Università di Torino and Sezione INFN, Torino, Italy*
[55] *INFN, Laboratori Nazionali del Gran Sasso, Assergi (L'Aquila), Italy*
[58] *Università di Palermo and Sezione INFN, Catania, Italy*
[59] *Benemérita Universidad Autónoma de Puebla, Puebla, Mexico*
[60] *Centro de Investigación y de Estudios Avanzados del IPN (CINVESTAV), México, D.F., Mexico*
[61] *Instituto Nacional de Astrofisica, Optica y Electronica, Tonantzintla, Puebla, Mexico*
[63] *Universidad Michoacana de San Nicolas de Hidalgo, Morelia, Michoacan, Mexico*
[64] *Universidad Nacional Autonoma de Mexico, Mexico, D.F., Mexico*
[65] *IMAPP, Radboud University, Nijmegen, Netherlands*
[66] *Kernfysisch Versneller Instituut, University of Groningen, Groningen, Netherlands*
[67] *NIKHEF, Amsterdam, Netherlands*
[68] *ASTRON, Dwingeloo, Netherlands*
[69] *Institute of Nuclear Physics PAN, Krakow, Poland*
[70] *University of Łódź, Łódź, Poland*
[71] *LIP and Instituto Superior Técnico, Lisboa, Portugal*
[72] *J. Stefan Institute, Ljubljana, Slovenia*
[73] *Laboratory for Astroparticle Physics, University of Nova Gorica, Slovenia*
[74] *Instituto de Física Corpuscular, CSIC-Universitat de València, Valencia, Spain*
[75] *Universidad Complutense de Madrid, Madrid, Spain*
[76] *Universidad de Alcalá, Alcalá de Henares (Madrid), Spain*
[77] *Universidad de Granada & C.A.F.P.E., Granada, Spain*
[78] *Universidad de Santiago de Compostela, Spain*
[79] *Rudolf Peierls Centre for Theoretical Physics, University of Oxford, Oxford, United Kingdom*
[81] *School of Physics and Astronomy, University of Leeds, United Kingdom*
[82] *Argonne National Laboratory, Argonne, IL, USA*
[83] *Case Western Reserve University, Cleveland, OH, USA*
[84] *Colorado School of Mines, Golden, CO, USA*
[85] *Colorado State University, Fort Collins, CO, USA*
[86] *Colorado State University, Pueblo, CO, USA*
[87] *Fermilab, Batavia, IL, USA*
[88] *Louisiana State University, Baton Rouge, LA, USA*
[89] *Michigan Technological University, Houghton, MI, USA*
[90] *New York University, New York, NY, USA*
[91] *Northeastern University, Boston, MA, USA*
[92] *Ohio State University, Columbus, OH, USA*
[93] *Pennsylvania State University, University Park, PA, USA*
[94] *Southern University, Baton Rouge, LA, USA*
[95] *University of California, Los Angeles, CA, USA*
[96] *University of Chicago, Enrico Fermi Institute, Chicago, IL, USA*

[98] *University of Hawaii, Honolulu, HI, USA*
[100] *University of Nebraska, Lincoln, NE, USA*
[101] *University of New Mexico, Albuquerque, NM, USA*
[102] *University of Pennsylvania, Philadelphia, PA, USA*
[103] *University of Wisconsin, Madison, WI, USA*
[104] *University of Wisconsin, Milwaukee, WI, USA*
[105] *Institute for Nuclear Science and Technology (INST), Hanoi, Vietnam*
‡ *Deceased*
[a] *at Konan University, Kobe, Japan*
[b] *On leave of absence at the Instituto Nacional de Astrofisica, Optica y Electronica*
[c] *at Caltech, Pasadena, USA*
[d] *at Hawaii Pacific University*